

https://dspace.org/

A geochemical and petrological study of the crystalline basement and associated megablocks of the Eyreville-B drillcore, Chesapeake Bay impact structure, USA

Townsend, Gabrielle Nicole

2015-05-07
http://hdl.handle.net/10539/17653

Downloaded from a DSpace repository. https://dspace.org/

A GEOCHEMICAL AND PETROLOGICAL STUDY OF THE CRYSTALLINE BASEMENT AND ASSOCIATED MEGABLOCKS OF THE EYREVILLE-B DRILLCORE, CHESAPEAKE BAY IMPACT STRUCTURE, USA

Gabrielle Nicole Townsend

A dissertation submitted to the Faculty of Science, University of the Witwatersrand, in fulfilment of the requirements for the degree of Master of Science

Johannesburg, 2015

STATEMENT OF ORIGINAL CONTRIBUTION

I declare that this dissertation is my own, unaided work. It is being submitted for the Degree of Master of Science in the University of the Witwatersrand, Johannesburg, South Africa. It has not been submitted before for any degree or examination in any other university.

Signed this 21st day of January, 2015.

_____

Gabrielle Nicole Townsend

ABSTRACT

The ca. 36 Ma Chesapeake Bay impact event on the east coast of Virginia, USA, formed an 85 km complex crater in Cretaceous to Eocene sediments and underlying crystalline basement rocks belonging to the Appalachian orogen. Appalachian rocks are well exposed along the Appalachian Mountains to the west, however, little is known of the basement along the Atlantic Coastal Plain owing to the covering sedimentary sequence. This study investigates the crystalline rocks intersected by the 2006 ICDP (International Continental Scientific Drilling Program) – USGS (United States Geological Survey) drilling of the Chesapeake Bay impact structure (CBIS) on the Eyreville Farm near Cape Charles, Virginia.

The crystalline rocks of the Eyreville-B borehole core are found in the lower basement-derived section (between 1551.19 m and 1766.32 m depth), in the amphibolite megablock (between 1376.38 m and 1389.35 m depth) and in the upper granite megablock (between 1095.74 m and 1371.11 m depth). The lower basement-derived section consists of foliated metasediments, which include mica schist, amphibolite and calc-silicate rock, and coarse-grained to pegmatitic granite. The amphibolite megablock is a black to dark grey to dark green, fine- to medium-grained, locally foliated, relatively homogenous, lithic block. The upper granite megablock is divided into gneissic and massive varieties, with a minor component of biotite schist xenoliths. The crystalline rocks contain foliations and related structures, fractures and breccias, microstructures and porphyroblast microstructures; however, none of the three lithic blocks is in situ and, consequently, structural measurements cannot be fully interpreted tectonically. Mineral assemblages and microstructural evidence in the mica schists suggest the rocks in the lower basement-derived section experienced a syn-D1 amphibolite facies peak metamorphic event (M1a) followed by retrograde metamorphic conditions (M1b) limited to D1b mylonitic and D2 brittle deformation. Similar metamorphic conditions in the upper megablocks suggest that the three sections likely formed part of a single metamorphic terrane.

Geochemistry in the lower basement-derived mica schists revealed a strong intermediate igneous provenance, whereas the upper megablock biotite schist xenoliths showed a quartzose sedimentary provenance; the precursors to both appear to have been deposited in active continental margin settings. The lower basement-derived amphibolite appears to be derived from a sedimentary source. The precursor to the upper amphibolite megablock, on the other hand, was probably a tholeittic gabbro generated in an island arc setting. The peraluminous, S-type nature of the lower basement-derived granite suggests it was most likely generated in a within-plate tectonic setting. In contrast, the massive and gneissic granites from the upper megablock are metaluminous, I-type granites that were most likely generated in a syn-collisional environment.

Metamorphic conditions of the M1 event were constrained using mineral assemblages mainly from the lower basement-derived section, which limited the $X(H_2O)$ value to 0.8, *P* to >0.4 GPa and the *T* range to 600-670°C. Using the 0.4 GPa pressure constraint, Zr-in-rutile thermometry revealed a peak metamorphic temperature for the M1 event of 606 ± 18°C, which is consistent with mid-amphibolite facies metamorphism. These estimates suggest a very steep geothermal gradient approaching ~44°C/km.

Rutile U/Pb geochronology revealed that the M1 event recorded in the lower basement-derived metasediments occurred at 259 ± 13 Ma, with Ar/Ar geochronology indicating the cooling path through to greenschist metamorphic conditions. Zircon U/Pb SHRIMP geochronology performed by Horton *et al.* (2009b) on the massive and gneissic megablock granites dated their crystallisation ages at 254 ± 3 Ma and 615 ± 7 Ma, respectively, with the former age in agreement with the rutile U/Pb peak metamorphism results from the lower basement-derived section. These ages, together with petrography, structural observations, geochemistry and geothermobarometry suggests that the amphibolite and granite megablocks form part of the same metamorphic terrane as the lower basement-derived section and that the D1 and M1 events recorded in the lower basement-derived section and upper megablocks of the Eyreville-B borehole core likely occurred during the late stages of the Alleghanian orogeny.

Based on mineralogy, geochemistry, metamorphic grade and structural evidence, comparisons with the neighbouring terranes within the Appalachian basement beneath the Atlantic Coastal Plain sediments suggest that the lower basement-derived and upper amphibolite and granite megablocks of the Eyreville-B borehole core most likely formed part of the Hatteras terrane prior to the Chesapeake Bay impact event. This terrane, together with 5 other terranes, forms part of the Carolina Zone, a peri-Gondwanan micro-continent formed by the amalgamation of magmatic arcs during the Penobscottian and Taconian orogenies, which was then accreted onto the Laurentian margin during the Salinic and Acadian orogenies.

DEDICATION

I would like to dedicate this dissertation first and foremost to my supervisor, Professor Roger Gibson. His mentorship has grown my skills far beyond the scientific and I am enormously grateful for his patience and continued faith in me.

Secondly, I dedicate this dissertation to my family: Henry and Olga Townsend, Priscilla and Zane Roux, Richard and Robyn Beneke, and to my husband, Graham Beneke. I will never be able to fully express my gratitude for your support all these years.

Finally, I dedicate this dissertation to the One who created everything in all its beauty and glorious splendour.

ACKNOWLEDGEMENTS

Funding for the Chesapeake Bay Deep Drilling Project was provided by the International Continental Scientific Drilling Program (ICDP), the US Geological Survey (USGS) and the National Aeronautics and Space Administration (NASA). Drilling operations were managed by DOSECC (Drilling, Observation and Sampling of the Earth's Continental Crust), and core drilling was performed by Major Drilling America.

Funding for this MSc dissertation, including analytical and travel expenses, was provided by the National Research Foundation of South Africa (GUN 2074407).

A number of analytical techniques were performed in the study. The following people are thanked for their assistance:

- P. Czaja and L. Hecht (Museum für Naturkunde, Berlin, Germany), and P. Graser (University of Pretoria) for their technical assistance with electron microprobe geochemical analysis.
- R.T. Schmitt (Museum für Naturkunde, Berlin, Germany) and S. Farrell-Turner (University of the Witwatersrand) for performing the XRF analyses.
- S. Farrell-Turner (University of the Witwatersrand) for performing ICP-MS analysis.
- R. McAleer (USGS, Reston, Virginia, USA) for technical assistance during mineral separate preparation.
- M.J. Kunk and R. McAleer (USGS, Reston, Virginia, USA) for performing the Ar/Ar geochronology.
- T. Zack (Institut für Geowissenschaften, Universität Mainz, Germany) for performing the Zr-in-rutile geothermobarometry and the U/Pb rutile geochronology.
- P. Ogilvie (University of the Witwatersrand) for assistance with conventional geothermobarometry.

K. Bartosova, K. Born, G.S. Gohn, L. Hecht, J.W. Horton, Jr., M.J. Kunk, M.L. Malinconico, R. McAleer, D. Powars, U.W. Reimold and R.T. Schmitt are thanked for their cooperation on scientific papers as well as their guidance and participation in discussions at the Museum für Naturkunde in Berlin, Germany, and at the USGS in Reston, Virginia, USA. J.W. Horton, Jr., is additionally thanked for discussions and reviews on the geology of the Appalachian Mountains and the east coast of North America.

D. Blithental, S. Cannell, M. Kitching and M. van Wyngaard are thanked for their logistical support during the course of this dissertation. L. Whitfield is thanked for assisting with drafting Figure 4.9 in Chapter 4. G. Drennan is thanked for her guidance, encouragement and support throughout the study. L. Jolly is thanked for introducing me to this project and for sharing an office and supervisor in a companion study to this dissertation.

Finally, I thank my family and friends for their continued support and encouragement over the years. My husband, Graham Beneke, is thanked for his unceasing love, motivation and support, which empowered me to complete this dissertation.

TABLE OF CONTENTS

STATEMENT OF ORIGINAL CONTRIBUTION ii

ABSTRACT iii

DEDICATION vi

ACKNOWLEDGEMENTS vii

TABLE OF CONTENTS ix

LIST OF FIGURES xiv

LIST OF TABLES xxxiv

LIST OF APPENDICES xxxviii

1 INTRODUCTION 1

1.1 Geological setting 2

1.1.1 Evolution of the Appalachian orogen 4

1.1.2 Tectonostratigraphic terranes of the Appalachian orogen 12

1.1.3 Sedimentation following the cessation of the Appalachian orogenies 28

1.2 The Chesapeake Bay impact structure 30

1.2.1 Previous studies of the Chesapeake Bay impact structure 32

1.2.2 Evolution of the Chesapeake Bay impact event 34

1.3 The ICDP-USGS Eyreville borehole core 37

1.3.1 ICDP-USGS drilling of the Chesapeake Bay impact structure 37

1.4 This study 39

2 PETROGRAPHIC AND STRUCTURAL ANALYSIS 42

2.1 Introduction 42

2.2 Methodology 42

2.3 Petrographic Analysis 43
2.3.1 Lower basement-derived section 43
2.3.2 Upper amphibolite megablock 58
2.3.3 Upper granite megablock 60
2.4 Structural analysis 67
2.4.1 Foliations and related structures 67
2.4.2 Fractures and breccias 73
2.4.3 Microstructures 79
2.4.4 Porphyroblast microstructures 82
2.5 Discussion 86
2.5.1 Lower basement-derived section 86
2.5.2 Upper amphibolite megablock 89
2.5.3 Upper granite megablock 90
2.6 Summary 91
3 GEOCHEMICAL ANALYSIS 93
3.1 Introduction 93
3.2 Methodology 93
3.3 Major element analysis 98
3.3.1 Mica schists 102
3.3.2 Amphibolites and calc-silicate rock 108
3.3.3 Granites 109
3.3.4 Alteration within the Eyreville-B borehole core 114
3.4 Trace element analysis 118
3.4.1 Mica schists 122

3.4.2 Amphibolites and calc-silicate rock 125

3.4.3 Granites 127

3.5 Rare earth element analysis 129

3.5.1 Mica schists 132

3.5.2 Amphibolites and calc-silicate rock 133

3.5.3 Granites 133

3.6 Discussion 135

3.6.1 Provenance of the metasedimentary rocks 135

3.6.2 Provenance of the amphibolites 141

3.6.3 Granite petrogenesis 146

3.7 Summary 150

4 MINERAL CHEMISTRY AND GEOTHERMOBAROMETRY 152

4.1 Introduction 152

4.2 Mineral Chemistry 152

4.2.1 Methodology 152

4.2.2 Mica schists 160

4.2.3 Amphibolites and calc-silicate rock 166

4.2.4 Granites 170

4.3 Geothermobarometry 174

4.3.1 Introduction 174

4.3.2 Constraints on peak *P*-*T*-X(H_2O) estimates 179

4.3.3 Methodology 182

4.3.4 Results 186

4.4 Discussion 198

4.4.1 Metamorphic grade 198

4.4.2 Geothermal gradient and possible metamorphic evolution 201

4.4.3 Terrane relationships 202

4.5 Summary 205

5 GEOCHRONOLOGY 208

5.1 Introduction 208

5.2 Rutile U/Pb geochronology 211

5.2.1 Methodology 212

5.2.2 Results 214

5.3 $^{40}Ar/^{39}Ar$ geochronology 217

5.3.1 Methodology 218

5.3.2 Results 221

5.4 Discussion 233

5.5 Summary 235

6 DISCUSSION AND CONCLUSIONS 238

6.1 Geological setting 239

6.2 Lithologies 247

6.2.1 Lower basement-derived section 247

6.2.2 Upper megablocks section 253

6.3 Structure 258

6.3.1 D1 event 259

6.3.2 D2 event 262

6.3.3 Chesapeake Bay impact event 263

6.4 Metamorphic grade 264

6.5 Timing and nature of metamorphism 266

6.6 Age and nature of intrusions 269

6.7 Tectonic implications 271

6.8 Conclusions 276

6.9 Recommendations 277

REFERENCES 279

LIST OF FIGURES

Figure 1.1: Locality map of the CBIS and the ICDP-USGS Eyreville drill site (after Gohn *et al.*, 2006). 1

Figure 1.2: Simplified tectonic map of the Appalachian orogen showing the exposed Northern and Central/Southern Appalachians divisions as well as pre-Silurian lithotectonic divisions with respect to the current North American eastern coastline (diagram modified after Hibbard *et al.*, 2007a and Pollock, 2008). The location of the CBIS has been included for reference purposes. 3

Figure 1.3: Reconstructions of Pangaea during the Palaeozoic, illustrating the closing of the Iapetus and Rheic oceans between Gondwana and Laurentia (diagram modified Stampfli and Borel, 2002, and Murphy *et al.*, 2010). Abbr. A-C = Avalonia-Carolina. 5

Figure 1.4: Illustration of the proposed tectonic models for the Taconian (left) and Penobscottian (right) orogenies along the Laurentian and Gondwanan margins in the Dunnage domain of the Northern Appalachians (modified after Hibbard *et al.*, 2007a and Murphy *et al.*, 2010). The details and timing depicted may not be necessarily true for the Central and Southern Appalachians but is used here to illustrate subduction processes of the Iapetus Ocean. 6

Figure 1.5: Palaeozoic reconstructions of the formation of Pangaea through the preferential subduction of the Iapetus and Rheic oceanic lithosphere (diagram modified after Murphy and Nance, 2013 and references therein). Abbr. A-C- Avalonia-Carolina. 8

Figure 1.6: Illustrations of the oblique rotational collision between Laurentia and Gondwana as suggested by Hatcher (2002). The red lines and symbols represent active features in the interval shown in each figure (after Hatcher, 2002; Nance and Linnemann, 2008). 10

Figure 1.7: Schematic cross-section of the Alleghanian orogeny (modified after Fichter and Baedke, 1999) showing Gondwana over-riding Laurentia to the west through décollement tectonics. 11

Figure 1.8: Plate reconstruction of the Palaeozoic Iapetus, Rheic (also known as Theic; Nance and Linnemann, 2013) and Mauritanian sutures (dashed lines) between Laurentia and Gondwana with the location of Chesapeake Bay included (modified after Lefort, 1988; Lefort and Max, 1991). 13

Figure 1.9: Tectonostratigraphic terrane map of the Central Appalachians showing the location of the Chesapeake Bay suture (after Horton *et al.*, 1991), Chesapeake block, CBIS, ICDP-USGS Eyreville-B drill site and the proposed extrapolated boundary between the Roanoke Rapids and Hatteras terranes (modified slightly, after Horton *et al.*, 1991; 2005b). Terranes have been grouped according to the three orogenic realms (Laurentia, Iapetan and Gondwanan) proposed by Hibbard *et al.* (2007a). 15

Figure 1.10: (a) Location of the suprastructural and infrastructural terranes of the Carolina Zone separated from the Piedmont Zone by the Central Piedmont shear zone within the Appalachian orogen. The approximate location of the CBIS has been included for reference purposes. (b) Depiction of the progressive accretion model for the docking of the Carolina Zone onto the Laurentian passive margin during the Salinic orogeny. Both diagrams modified after Hibbard (2000) and references therein, and Horton *et al.* (2005b) and references therein. 17

Figure 1.11: Generalised stratigraphic column for the pre-impact and post-impact sediments in southeastern Virginia in the vicinity of the CBIS (modified after Poag *et al.*, 2004). Undulating horizontal lines represent unconformities. Legend: 1 = Era; 2 = Epoch; 3 = Time of deformation relative to the impact; 4 = Rock units. 29

Figure 1.12: Geological cross-section of the CBIS from NW to SE showing the relative locations of the central zone (inner basin, central peak, peak ring), the annular trough and the ICDP-USGS Eyreville drill site (modified after Poag *et al.*, 1999, 2004; Gohn *et al.*, 2008, 2009). 31

Figure 1.13: Regional map of the CBIS with the locations of borehole cores in southeastern Virginia, including the ICDP-USGS Eyreville borehole core (after Horton *et al.,* 2005a, 2005b; Gohn *et al.*, 2008, 2009). Symbols: B = Bayside; D = Dismal Swamp; E = Exmore; EF = ICDP-USGS Eyreville; F = Fentress; H = Haynesville; J = Jamestown; JB = Jenkins Bridge; K = Kiptopeke; L = USGS-NASA Langley; M = MW4-1; N = North; NN = Newport News Park 2; W = Windmill Point; WS = Watkins School. 33

Figure 1.14: Schematic cross-sections illustrating the proposed sequence of events for the formation of the CBIS (Horton *et al.,* 2005a): (a) Pre-impact target. (b) Contact and compression stage of the impact followed by excavation of the target material. (c) Crater modification by collapse, slumping blocks and resurging water (A and B represent crater units; see text for explanation). (d) Burial of the impact crater by post-impact marine sediments. Locations of the USGS-NASA Langley and ICDP-USGS Eyreville borehole cores in (d) are included for reference purposes. Diagram modified after Horton *et al.* (2005a). 35

Figure 1.15: Composite geological column of the Eyreville borehole core with cored intervals A, B and C (after Gohn *et al.*, 2006). 39

Figure 2.1: (a) Composite stratigraphic column for Eyreville-B borehole core (after Gohn *et al.*, 2006) with (b) a detailed column for the lower basement-derived section between 1551 m and 1766 m depth (after Horton *et al.*, 2009a). 44

Figure 2.2: Corebox and thin section photographs of the lower basement-derived mica schists. (a) Corebox 322 showing the highly foliated nature of the mica schists. (b) Sample RG60 showing folds that locally deform the mica schist foliation (PPL). (c) Sample RG34 showing an

elongated Qz grain within the Ms-Bt foliae and adjacent irregular masses of Gr (PPL). (d) Zoned Pl porphyroblasts with Gr-rich cores in sample RG68 (PPL). Abbr.: Bt = biotite; Cal = calcite; Gr = Graphite; Ms = muscovite; Pl = plagioclase; PPL = plane polarised light; Py = pyrite; Qz = quartz; Sil = sillimanite (mineral abbreviations after Whitney and Evans, 2010). 45

Figure 2.3: Photomicrographs of samples from the lower basement-derived mica schist. (a) Sample RG44 showing a Fi knot (PPL). (b) Skeletal and elongated garnet in sample RG53 (PPL). (c) Sample RG38 illustrating the intercalation of Tur and Py with Ms and Pl (PPL). (d) Brecciated fracture in Qz with Py, Cal and Chl fracture-fill in sample RG43 (PPL). Abbr.: Bt = biotite; Cal = calcite; Chl = chlorite; Fi = Fibrolite; Gr = Graphite; Grt = garnet; Ms = muscovite; Pl = plagioclase; PPL = plane polarised light; Py = pyrite; Qz = quartz; Tur = tourmaline. 47

Figure 2.4: (a) Photomicrograph (PPL) and (b) hand specimen photograph of the lower basement-derived biotite schist sample RG70 showing the large amount of Bt that defines the lithology. (c) Hand specimen and (b) photomicrograph (PPL) of the lower basement-derived amphibolite sample RG51 where alternating bands of Bt-rich and Bt-poor assemblages are shown. Abbr.: Amp = amphibole; Bt = biotite; Ep = epidote; Pl = plagioclase; PPL = plane polarised light; Py = pyrite; Qz = quartz; Ttn = titanite. 48

Figure 2.5: Hand specimen and thin section (PPL) photographs of the lower basement-derived calc-silicate sample RG50 showing (a) its highly brecciated nature, (b) the peak metamorphic assemblage, (c) the retrograde metamorphic assemblage and (d) the Amp component. Abbr.: Amp = amphibole; Cal = calcite; Chl = chlorite; Ep = epidote; Pl = plagioclase; PPL = plane polarised light; Qz = quartz; Ves = vesuvianite. 50

Figure 2.6: (a) Hand specimen and (b) thin section (PPL) photographs of sample RG54 showing the abundance and fine-grained nature of the lower basement-derived tourmalinite. (c) Thin section (PPL) and (d) hand specimen photographs of sample RG57 showing the coarse grain

size of Tur-rich layers within the lower basement-derived mica schist. Abbr.: Ms = muscovite; Pl = plagioclase; PPL = plane polarised light; Py = pyrite; Qz = quartz; Tur = tourmaline. 51

Figure 2.7: Corebox and thin section photographs of the lower basement-derived granite. Coreboxes (a) 313 and (b) 324 showing the pink/orange and white granite varieties, respectively. (c) Poikilitic Kfs grain with Bt and Pl inclusions and local replacement by Cal in sample RG40a (XPL). (d) Large Ms and Pl grains within dynamically recrystallised Qz grains in sample RG32 (XPL). (e) Fractured and locally poikilitic Grt in sample RG40a (PPL). (f) Fractured Amp grains in a Qz-Pl matrix in sample RG61 (PPL). Abbr.: Amp = amphibole; Bt = biotite; Cal = calcite; Kfs = K-feldspar; Ms = muscovite; Pl = plagioclase; PPL = plane polarised light; Qz = quartz; XPL = cross polarised light; Zrn = zircon. 53

Figure 2.8: Photograph of corebox 310 illustrating the fine-grained alternating mica schist and granite layers in the lower basement-derived mylonite zone. Abbr.: CV = chlorite vein; GR = granite; MS = mica schist; QV = quartz vein. 55

Figure 2.9: Photographs of the suevite and polymict impact breccia dykes in the lower basement-derived section. (a) Corebox 297 showing the deepest suevite dyke intercalated with MS and GR. (b) Corebox 285 showing interplay between the SV dykes and MS. (c) Corebox 282 showing the beginning of the polymict impact breccia dyke. (d) Hand specimen of sample RG71 showing the local brecciation with plucked PQz clasts. Abbr.: BR = breccia; GN = granite gneiss; GR = granite; Gr = graphite; M = melt; MS = mica schist; PQz = polycrystalline quartz; Py = pyrite; SH = shale; SV = suevite. 56

Figure 2.10: Photographs of the suevite and polymict impact breccia dykes in the lower basement-derived section. (a) Hand specimen of sample RG62 showing the variation in clast size and type within a matrix-support suevite. (b) Hand specimen of sample RG73 showing a clast-supported suevite with a melt vein and quartzite clasts. (c) Hand specimen of sample RG77 showing the large variation in grain size and clast type in polymict impact breccia. (d)

Photomicrograph of sample RG77 showing fractured and toasted quartz with PDFs within an altered matrix (PPL). Abbr.: Cal = calcite; GN = granite gneiss; GR = granite; M = melt; PDF = plane deformation features; PPL = plane polarised light; Py = pyrite; QZ = quartzite; Qz = quartz; SH = shale. 57

Figure 2.11: Composite stratigraphic column for the Eyreville-B borehole core (after Gohn *et al.*, 2006) with the detailed column for the upper megablocks section from 1095.74 m to 1389.71 m depth (after Horton *et al.*, 2009a). 59

Figure 2.12: Photographs of the upper amphibolite megablock. (a) Corebox 226 showing the zone of coarse-grained amphibolite that contains a relict igneous texture within the generally homogenous megablock. (b) Photomicrograph (PPL) of sample W51 showing aggregates of Amp in certain parts of the megablock. (c) Hand specimen and (d) photomicrograph (PPL) of the brecciated GR vein within a Cal matrix (sample RG04) showing the brecciation at macro and microscopic scale. (e) Photomicrograph (PPL) of sample RG04 showing the contact zone between the granite-bearing calcite vein and the amphibolite where Bt has been intensely altered to Chl. Abbr.: Amp = amphibole; Bt = biotite; Cal = calcite; Chl = chlorite; GR = granite; Kfs = K-feldspar; Pl = plagioclase; Qz = quartz. 61

Figure 2.13: Photographs of the gneissic granite in the upper megablock. (a) Corebox 158 illustrating the gneissic banding. Photomicrographs (XPL) of (b) sample RG151 and (c) sample RG152 illustrating altered, poikilitic Kfs and altered Pl grains as well as Bt retrogressing to Chl in the gneissic megablock granite. Abbr.: Bt = biotite; Chl = chlorite; Kfs = K-feldspar; Mag = magnetite; Pl = plagioclase; Qz = quartz; XPL = cross polarised light. 63

Figure 2.14: Photographs of the massive granite of the upper megablock. (a) Corebox 142 showing the medium-grained nature of the massive megablock granite with an intruding GP and QV. (b) Photomicrograph of sample W46 showing the poikilitic Kfs phenocrysts exhibiting microcline twinning and myrmekitic texture (XPL). (c) Photomicrograph of sample W37 showing

alteration in Kfs and Pl (PPL). Abbr.: Bt = biotite; GP = granite pegmatite; GR = massive granite; Kfs = K-feldspar; Pl = plagioclase; PPL = plane polarised light; Qz = quartz; QV = quartz vein; XPL = cross polarised light. 64

Figure 2.15: Photographs of the schist xenoliths in the upper granite megablock. (a) Corebox 147 illustrating the location of the xenoliths within the massive and gneissic granite. Photomicrographs (PPL) of sample W39 showing (b) the irregular contact between the schist and granite. (c) Photomicrograph of sample W36b showing the relative size and abundance of Bt compared to the massive and gneissic megablock granites. Abbr.: Bt = biotite; GN = gneissic granite; GP = granite pegmatite; GR = massive granite; Pl = plagioclase; PPL = plane polarised light; Qz = quartz; SX = schist xenoliths. 66

Figure 2.16: (a) Portion of corebox 321 from the lower basement-derived section showing the prograde foliation (S1a) as well as intrafolial folds and QV within the MS that is locally intruded by GR. Photomicrographs of sample RG41 showing (a) the locally chaotic foliation adjacent to intrafolial folds (XPL) and (c) the lack of enhanced retrogression despite Gr, Cal and Py occurring in interclast regions (PPL). Abbr.: Cal = calcite; GR = granite vein; Gr = graphite; MS = mica schist; Ms = muscovite; Pl = plagioclase; PPL – plane polarised light; Py = pyrite; Qz = quartz; Tur = tourmaline; XPL = cross-polarised light. 69

Figure 2.17: Photographs of the S1b foliation in the lower basement-derived mylonite. (a) Corebox 310 showing the mylonite zone with interlayered GR, MS and QV. (b) Hand specimen of sample RG56 showing the S1a and S1b foliations in the retrogressed MS. (c) Hand specimen of sample RG40 showing the S1b foliation in the fine-grained mylonitised Gr. (d) Photomicrograph (PPL) of sample RG57 showing the S1a foliation defined by elongated Pl and Py inclusions in Tur. Abbr.: GR = granite; MS = mica schist; Pl = plagioclase; PPL = plane polarised light; Py = pyrite; QV = quartz vein; Tur = tourmaline; Zrn = zircon. 70

Figure 2.18: Photograph of corebox 160 showing the gneissic foliation in GN and the massive nature of GR in the upper granite megablock. Abbr.: GN = gneissic megablock granite; GR = massive megablock granite. 72

Figure 2.19: Hand specimen photographs of (a) sample RG172 showing the biotite-defined foliation in the biotite schist xenoliths in the upper granite megablock, (b) sample RG02 showing the foliation in the upper amphibolite megablock that is locally cut by Cal and Qz veins, (c) sample RG176 showing the mineral lineation relative to the orientation of the core in the upper amphibolite megablock, and (d) sample RG06 showing the coarse-grained, phaneritic texture preserved in parts of the upper amphibolite megablock. Abbr.: Cal = calcite; Qz = quartz. 73

Figure 2.20: Corebox photographs showing fracturing containing varying amounts of Cal, Chl, Py and Qz within the (a) the lower basement-derived mica schist (Corebox 307) and granite (Corebox 314), and within the (c) gneissic megablock granite (Corebox 159). Abbr.: Cal = calcite; CCV = calcite and chlorite vein; Chl = chlorite; PV = pyrite vein; Py = pyrite; QV = quartz vein; Qz = quartz. 74

Figure 2.21: Corebox photographs showing fracturing within containing varying amounts of Cal, Py and Qz within the (a) massive megablock granite (Corebox 165), (b) the biotite schist xenoliths in the upper granite megablock (Corebox 147) and (c) the upper amphibolite megablock (Corebox 224). Abbr.: Cal = calcite; CV = calcite vein; PV = pyrite vein; Py = pyrite; QCV = quartz and calcite vein; Qz = quartz. 76

Figure 2.22: Photographs of fracturing and brecciation in the lower basement-derived section. (a) Hand specimen of MS sample RG178 showing a Chl+Cal fracture that is locally brecciated. (b) Portion of corebox 328 showing splaying Chl+Cal fractures in the GR. (c) Portion of corebox 317 showing a Cal+Chl fracture between the MS and GR. (d) Hand specimen and (e) photomicrograph (PPL) of sample RG46 showing D2 chloritic fracturing in the GR. Abbr.: Cal = calcite; Chl = chlorite; GR = granite; MS = mica schist; PPL = plane polarised light. 77

Figure 2.23: (a) Photomicrograph of mica schist sample RG44 showing a fibrolitic knot (PPL). (b) Photomicrograph of mica schist sample RG68 showing the prograde S1a foliation and extensional shear bands (PPL). (c) Photomicrograph of mica schist sample RG60 showing the cleavage orientations of Ms grains (XPL). (d) Photomicrograph of granitic sample RG40a showing mylonitic S1b S-C and S-C' (white dashed lines) structures (PPL) consistent with dextral shear sense. (e) PPL and (f) XPL photomicrograph of granitic sample RG40 showing Ms and Bt fish, Kfs bookshelf sliding and Qz ribbons illustrating dextral shear sense. Abbr.: Bt = biotite; Fi = fibrolite; Gr = graphite; Grt = garnet; Kfs = K-feldspar; Ms = muscovite; Pl = plagioclase; PPL = plane polarised light; Py = pyrite; Qz = quartz; Tur = tourmaline; XPL = cross-polarised light. 80

Figure 2.24: Photomicrographs of (a) sample RG154 showing the extensive seritisation of plagioclase grains in the gneissic megablock granite (PPL), (b) sample RG158 showing bent twins in K-feldspar phenocrysts in the gneissic megablock granite (PPL), and sample W49 showing (c) the less altered nature of the massive megablock granite (XPL) with (d) K-feldspar bent twins and myrmekitic textures (XPL). Abbr,: Bt = biotite; Cal = calcite; Kfs = K-feldspar; Pl = plagioclase; PPL = plane polarised light; Qz = quartz; XPL = cross polarised light. 82

Figure 2.25: Photomicrographs of (a) sample W39 showing rotated plagioclase porphyroblasts (XPL) and (b) boudinaged quartz ribbons (PPL) in the biotite schist xenoliths of the upper granite megablock, and (c) samples RG177 (PPL) and (d) RG176 (XPL) showing monomineralic aggregates of amphibole and biotite, respectively. Abbr.: Amp = amphibole; Bt = biotite; Ep = epidote; Pl = plagioclase; PPL = plane polarised light; Qz = quartz; XPL = cross polarised light. 83

Figure 2.26: Photomicrographs of (a) sample RG53 showing a poikilitic garnet porphyroblast in the lower basement-derived mica schist with a weak internal foliation defined by biotite, rutile needles and elongated quartz inclusions (XPL), sample RG68 showing an internally zoned plagioclase porphyroblast in (b) PPL and (c) XPL views in the lower basement-derived mica

schist, and (d) sample RG34 showing an internally zoned plagioclase porphyroblast with deformed muscovite inclusions in the lower basement-derived mica schist (XPL). Abbr.: Bt = biotite; Grt = garnet; Ms = muscovite; Pl = plagioclase; PPL = plane polarised light, Py = pyrite; Qz = quartz; XPL = cross polarised light. 85

Figure 3.1: Variations in major element concentrations (wt%) with depth (m) for the four target rock units in the lower basement-derived section of the Eyreville-B borehole core. Samples from the CB6 and W series (after Schmitt *et al.*, 2009) have been included to increase the data set size. The geologic column, as described in Chapters 1 and 2 (after Horton *et al.*, 2009a), has been placed on the right side for reference purposes. Dashed lines represent observed groupings. 101

Figure 3.2: Variations in major element concentrations (wt%) with depth (m) for the four target rock units in the upper granite and amphibolite megablocks of the Eyreville-B borehole core. Samples from the CB6 series (after Schmitt *et al.*, 2009) have been included to increase the data set size. The geologic column, as described in Chapters 1 and 2 (after Horton *et al.*, 2009a), has been placed on the right side for reference purposes. Dashed lines represent observed groupings. 103

Figure 3.3: Harker diagrams showing major element oxides (TiO_2, Al_2O_3, Fe_2O_3, MnO, MgO, CaO, Na_2O, K_2O and P_2O_5) plotted against SiO_2 for the eight target rocks units of the Eyreville-B borehole core. Abbr.: NASC = North American Shale Composite (after Gromet *et al.*, 1984); PAAS = Post Achaean Australian Shale (after Taylor and McLennan, 1985). Dashed lines represent observed groupings. 104

Figure 3.4: Ternary diagrams indicating normative An-Or-Ab content calculated for (a) the mica schist, amphibolite and calc-silicate, and (b) the granite rock units of the Eyreville-B borehole core. Abbr.: An = anorthite; Or = orthoclase; Ab = albite; NASC = North American Shale

Composite (after Gromet *et al.*, 1984); PAAS = Post-Achaean Australian Shale (after Taylor and McLennan, 1985). Dashed lines represent observed groupings. 106

Figure 3.5: Bivariate diagrams for the granite rock units of the Eyreville-B borehole core: (a) TAS diagram for the classification of plutonic rocks (after Middlemost, 1994), and (b) ASI (after Shand, 1927; Chappell and White, 1974). All data in wt%. 111

Figure 3.6: Ternary diagrams indicating the AFM abundances (wt%) for (a) the lower basement-derived granite, (b) the upper megablock granite and (c) the upper megablock granite gneiss rock units of the Eyreville-B borehole core. Red dashed line shows the chemical boundary between tholeiitic and calc-alkaline magma series (after Irving and Baragar, 1971). Abbr.: A (alkalis) = $Na_2O + K_2O$; F = $Fe_2O_{3(total)}$; M = MgO. 113

Figure 3.7: Variations in LOI (wt%) with depth (m) for the metasedimentary target rock units of the (a) lower basement-derived section and (b) upper granite and amphibolite megablocks of the Eyreville-B borehole core. The geologic column, as described in Chapters 1 and 2 (after Horton *et al.*, 2009a), has been placed on the right side for reference purposes. Dashed lines represent observed groupings. 115

Figure 3.8: Variations in LOI with CaO concentrations for (a) the mica schists and (b) the amphibolites and calc-silicate rock units of the Eyreville-B borehole core. All data in wt%. 116

Figure 3.9: Variations in CIA with depth (m) for the metadeismentary target rock units of the (a) lower basement-derived section and (b) upper granite and amphibolite megablocks of the Eyreville-B borehole core. The geologic column, as described in Chapters 1 and 2 (after Horton *et al.*, 2009a), has been placed on the right side for reference purposes. Abbr.: CIA = chemical index of alteration. Dashed lines represent observed groupings. 117

Figure 3.10: Variations in trace element concentrations (ppm) with depth (m) for the four target rock units in the lower basement-derived section of the Eyreville-B borehole core. Not all samples could be plotted for Zr, Ba, V and Zn graphs as their concentrations were below the lower limit of detection. Samples from the CB6 and W series (after Schmitt *et al.*, 2009) have been included to increase the data set size. The geologic column, as described in Chapters 1 and 2 (after Horton *et al.*, 2009a), has been placed on the right side for reference purposes. Dashed lines represent observed groupings. 120

Figure 3.11: Variations in trace element concentrations (ppm) with depth (m) for the four target rock units in the upper granite and amphibolite megablocks of the Eyreville-B borehole core. The geologic column, after Horton *et al.* (2009), has been placed on the right side for reference purposes. Not all samples could be plotted for Rb, Cr, Ba, V and Zn graphs as their concentrations were below the lower limit of detection. Samples from the CB6 series (after Schmitt *et al.*, 2009) have been included to increase the data set size. The geologic column, as described in Chapters 1 and 2 (after Horton *et al.*, 2009a), has been placed on the right side for reference purposes. Dashed lines represent observed groupings. 121

Figure 3.12: Harker diagrams showing trace element (Rb, Sr, Zr, Ba, Cr, V, Ni and Zn) concentrations (in ppm) plotted against SiO_2 for the eight target rocks units of the Eyreville-B borehole core. Abbr.: NASC = North American Shale Composite (after Gromet *et al.*, 1984); PAAS = Post Archean Australian Shale (after Taylor and McLennan, 1985). Dashed lines represent observed groupings. 123

Figure 3.13: Harker diagrams showing trace element concentrations (in ppm) plotted against Al_2O_3 (Rb, Ba, Cr and V) and against Fe_2O_3 (Cr and V) for the eight target rocks units of the Eyreville-B borehole core. Abbr.: NASC = North American Shale Composite (after Gromet *et al.*, 1984); PAAS = Post Archean Australian Shale (after Taylor and McLennan, 1985). Dashed lines represent observed groupings. 126

Figure 3.14: Harker diagrams showing trace element concentrations (in ppm) plotted against Na_2O (Rb, Zr and Cr) and against K_2O (Rb and Ba) for the eight target rocks units of the Eyreville-B borehole core. Abbr.: NASC = North American Shale Composite (after Gromet *et al.*, 1984); PAAS = Post Archean Australian Shale (after Taylor and McLennan, 1985). Dashed lines represent observed groupings. 128

Figure 3.15: C1 chondrite-normalised REE distribution patterns for the eight target rock units of the Eyreville-B borehole core (after after McDonough and Sun, 1995). Average REE data from Schmitt *et al.* (2009) have been included for reference purposes. Pr, Dy, Ho and Er were estimated due to insufficient data for trending purposes; these points are omitted in the figure. 134

Figure 3.16: Bivariate diagrams for the basement and megablock mica schists and basement amphibolite and calc-silicate rock units of the Eyreville-B borehole core. (a) Classification scheme for terrigenous clastic sediments (after Herron, 1988); and (b) K_2O/Na_2O versus SiO_2 diagram indicating tectonic environment for sandstone-mudstone suites (after Roser and Korsch, 1986). All data in wt%. 137

Figure 3.17: Discriminant diagrams showing provenance signatures for sandstone-mudstone suites using major elements based on (a) raw oxides and (b) oxide ratios for the megablock and basement mica schists and basement amphibolite and calc-silicate rock units of the Eyreville-B borehole core (after Roser and Korsch, 1988). All data in wt%. 138

Figure 3.18. Ternary diagram indicating CaO-MgO-FeO abundances for the discrimination between ortho- and para-amphibolites for the megablock and basement amphibolites and calc-silicate (after Walker *et al.*, 1960) of the Eyreville-B borehole core. FeO was calculated using the CIPW norm. 142

Figure 3.19: Bi-variate TAS diagram illustrating possible protoliths for the megablock amphibolite rock unit (after Middlemost, 1994) of the Eyreville-B borehole core. All data in wt%. 144

Figure 3.20. Ternary diagrams indicating AFM abundances (wt%) for the megablock amphibolite rock units rock unit of the Eyreville-B borehole core. Black dashed line shows the chemical boundary between tholeiitic and calc-alkaline magma series (after Irving and Baragar, 1971). Abbr.: A (alkalis) = $Na_2O + K_2O$; F = $Fe_2O_{3(total)}$; M = MgO. 145

Figure 3.21: Discriminant diagrams showing the tectonic setting for the amphibolite rock units of the Eyreville-B borehole core. (a) TiO_2 versus Zr diagram (after Pearce *et al.*, 1981), and (b) Zr/Y versus Zr diagram (after Pearce and Norry, 1979). Abbr.: IAB = island arc basalt; OFB = ocean floor basalt; WPB = within-plate basalt; MORB = mid-oceanic ridge basalt. 146

Figure 3.22: (a) Rb versus Y + Nb and (b) Nb versus Y discriminant diagrams for the granites of the Eyreville-B borehole core, indicating different tectonic setting (after Pearce *et al.*, 1984). All data in ppm. Abbr.: VAG = volcanic-arc granite; syn-COLG = syncollisional granite; WPG = within-plate granite; ORG = ocean-ridge granite. 147

Figure 3.23: Ternary discrimination diagrams for the granites of the Eyreville-B borehole core. (a) Hf-Rb/10-Tax3 diagram showing different tectonic settings (data in ppm; after Harris *et al.*, 1986). (b) Ab-Qtz-Or diagram showing cotectic curves in an H_2O-undersaturated system. Dashed line represents the water-undersaturated curve for a_{H2O} = 0.8 crustal fluids in equilibrium with graphite (after Johannes and Holtz, 1991). Abbr.: VAG = volcanic-arc granite; syn-COLG = syncollisional granite; WPG = within-plate granite; ORG = ocean-ridge granite; Ab = albite; Q = quartz = Or = orthoclase. 149

Figure 4.1: (a) Ca-K-Na ternary diagram showing the albite to labradorite range of Pl (n = 159) in the lower basement-derived mica schist and (b) a compositional profile of a Pl grain in the

basement mica schist sample RG48 (n = 9). (c) Ca-K-Na ternary diagram showing the tightly constrained andesinitic natures of Pl in both the lower basement-derived biotite schist (n = 13) and the upper megablock biotite schist (n = 104). (d) Compositional profile of a Pl grain in sample RG157b from the upper megablock biotite schist (n = 18). Dashed lines represent observed groupings. Abbr.: n = number of analyses; Pl = plagioclase. 160

Figure 4.2: (a) X_{Mg} vs. Al^{vi} and (b) K vs. Ti abundances in Bt (apfu for 11 oxygens) and (c) X_{Mg} vs Al^{vi} abundances in Ms (apfu for 11 oxygens) for the lower basement-derived mica schist (Bt n = 41; Ms n = 130) and biotite schist (Bt n = 19) and upper megablock biotite schist xenoliths (Bt n = 25; Ms n = 4). Dashed lines represent observed groupings. Abbr.: Bln = EMP analyses obtained in Berlin; Bt = biotite; Ms = muscovite (white mica); n = number of analyses; Pta = EMP analyses obtained in Pretoria. 162

Figure 4.3: Bivariate diagrams showing (a) X_{Mn}, (b) X_{Mg} and (c) X_{Ca} elemental ratios of Grt plotted against Si (apfu for 12 oxygens) for both mica schist (n = 109) and granite (n = 296) in the lower basement-derived section. Abbr.: Bln = EMP analyses obtained in Berlin; Grt = garnet; n = number of analyses; Pta = EMP analyses obtained in Pretoria. 165

Figure 4.4: Elemental compositional profiles for garnet in the lower basement-derived (a) mica schist (sample RG53 n = 15) with (b) accompanying reference photomicrograph (XPL), and in the lower basement-derived (c) granite (sample RG40; n = 15) with (d) accompanying reference photomicrograph (XPL). White dashed lines in the photomicrographs indicate the approximate locations of each compositional profile. Abbr.: Bt = biotite; Grt = garnet; n = number of analyses; Pl = plagioclase; Qz = quartz; XPL = cross polarised light. 166

Figure 4.5: Ca-K-Na ternary diagrams for Pl in (a) the lower basement-derived amphibolite (n = 25) and (b) the upper megablock amphibolite (n = 55). Abbr.: Bln = EMP analyses obtained in Berlin; n = number of analyses; Pl = plagioclase; Pta = EMP analyses obtained in Pretoria. 167

Figure 4.6: (a) X_{Mg} vs. Al^{vi} and (b) K vs. Ti abundances (apfu for 11 oxygens) in Bt for the lower basement-derived amphibolite (n = 5) and megablock amphibolite (n = 4). (c) Amphibole classification diagram (after Leake, 1978; Deer *et al.*, 1992) using Na + K abundances plotted against Si (apfu for 23 oxygens) for the lower basement-derived amphibolite (n = 31) and the upper megablock amphibolite (n = 44). Dashed lines represent observed groupings. Abbr.: Bln = EMP analyses obtained in Berlin; Bt = biotite; n = number of analyses; Pta = EMP analyses obtained in Pretoria. 168

Figure 4.7: Ca-K-Na ternary diagrams for Pl in (a) the lower basement-derived granite (n = 144) and (b) the upper gneissic (n = 10) and massive (n = 97) megablock granites. Abbr.: Bln = EMP analyses obtained in Berlin; n = number of analyses; Pl = plagioclase; Pta = EMP analyses obtained in Pretoria. 171

Figure 4.8: (a) X_{Mg} vs. Al^{vi} and (b) K vs. Ti abundances (apfu for 11 oxygens) in Bt and (c) X_{Mg} vs. Al^{vi} abundances (apfu for 11 oxygens) in Ms for the lower basement-derived granite (Bt n = 25; Ms n = 115) and upper gneissic (Bt n = 22; Ms n = 4) and massive (Bt n = 105; Ms n = 9) megablock granites. Dashed lines represent observed groupings. Abbr.: Bln = EMP analyses obtained in Berlin; Bt = biotite; Ms = muscovite (white mica); n = number of analyses; Pta = EMP analyses obtained in Pretoria. 172

Figure 4.9: *P-T* diagram indicating the relative positions of reactions occurring within the lower basement-derived mica schists within the CKNASH system (modified after Pattison and Tracy, 1991) with the Als phase boundaries (after Holland and Powell, 1998) superimposed. Dashed lines represent the fluid-present Ms melting curves within the CKNASH system (Thompson and Tracy, 1990). Solid lines represent the displaced Ms melting curves where the fluid is in equilibrium with Gr at $X(H_2O)$ = 0.8 (Ashworth and Tyler, 1983). Grey area represents the probable *P-T* conditions, based on mineral stability, under which the basement mica schists formed. P (after Pattison, 1992) and H (after Holdaway, 1971) are triple points that delimit the possible range in *P-T* space for the And-Sil transition as discussed in Pattison and Tracy

(1991). Abbr.: Als = aluminosilicate; And = andalusite; Bt = biotite; Chl = chlorite; Crd = cordierite; Gr = graphite; Grt = garnet; Kfs = K-feldspar; Ky = kyanite; L = liquid; Ms = muscovite; Pl = plagioclase; Qtz = quartz; Sil = sillimanite; St = staurolite. 181

Figure 4.10: Distribution of temperatures calculated from Zr-in-rutile thermometry (assuming 0.4 GPa) for the lower basement-derived samples RG54 and RG57. 188

Figure 4.11: *P-T* phase equilibria diagrams using THERIAK-DOMINO for the basement mica schist sample RG53. Assemblages: 1 = Grt (2)Pl Bt Ms *β*Qz H_2O; 2 = Grt Pl Bt Ms Crd *α*Qz H_2O; 3 = Grt Pl Bt Ms Chl *α*Qz H_2O; 4 = Grt (2)Pl Bt Ms Chl *α*Qz H_2O; 5 = Pl Bt Ms Crd *α*Qz H_2O; 6 = (2)Pl Bt Crd *α*Qz H_2O; 7 = (2)Pl Bt Crd *β*Qz H_2O. Symbols: Blue shaded area/dashed line = range of estimated peak *P-T* conditions. Abbr.: Bt = biotite; Chl = chlorite; Crd = cordierite; Grt = garnet; Ms = muscovite (white mica); Pl = plagioclase; (2)Pl = albite and anorthite; Qz = quartz. 196

Figure 4.12: *P-T* phase equilibria diagrams using THERIAK-DOMINO for the basement granite sample RG40. Assemblages: 1 = Grt Pl Bt Ms Crd *α*Qz H_2O; 2 = Grt Kfs Pl Ms Crd *α*Qz H_2O; 3 = Kfs Pl Crd *α*Qz Sil H_2O; 4 = Pl Bt Ms Chl *α*Qz H_2O; 5 = Grt Pl Bt Ms Chl *α*Qz H_2O; 6 = Grt Kfs Pl Bt Ms *α*Qz H_2O. Symbols: Blue shaded area/dashed line = range of estimated peak *P-T* conditions; thick blue line = possible minimum *P-T* constraint. Abbr.: And = andalusite; Bt = biotite; Chl = chlorite; Crd = cordierite; Grt = garnet; Kfs = K-feldspar; Ms = muscovite (white mica); Pl = plagioclase; Qz = quartz; Sil = sillimanite. 197

Figure 4.13: *P-T* phase equilibria diagrams using THERIAK-DOMINO for the megablock amphibolite sample W51. Assemblages: 1 = Ol Spl Grt Pl Bt Amp H_2O; 2 = Ol Grt Pl Bt Omp Amp H_2O. Symbols: Blue shaded area/dashed line = range of estimated peak *T* for *P* range of 0.3-0.5 GPa. Abbr.: Amp = amphibole; Bt = biotite; Grt = garnet; Ol = olivine; Omp = omphacite; Pl = plagioclase; Spl = spinel; Qz = quartz. 198

Figure 5.1: Photomicrograph of (a) RG54 (tourmalinite) and (b) RG57 (tourmaline-rich schist) showing the rutile-bearing mineral assemblages. Abbr. (after Siivola and Schmid, 2007; Whitney and Evans, 2010): Fsp – feldspar; Gr – graphite; Py – pyrite; Qz – quartz; Rt – rutile; Tur – tourmaline. 210

Figure 5.2: Schematic of the prograde formation of rutile from ilmenite under low- to medium-grade metamorphic conditions (after Luvizotto *et al.*, 2009b, and Meinhold, 2010). Abbr. Chl = chlorite; Ilm = ilmenite; Rt = rutile. 212

Figure 5.3: (a) Concordia plot and (b) $^{206}Pb/^{238}U$ ages for LA-ICP-MS data of rutiles from samples RG54 and RG57. Errors, MSWD (mean square of weighted deviates) and degree of concordance were calculated using Isoplot (after Ludwig, 2003; Zack *et al.*, 2011). 215

Figure 5.4: Tera-Wasserburg diagram illustrating uncorrected data for rutiles from samples RG54 and RG57. The regression line (black dashed line) intersects the y-axis $^{207}Pb/^{206}Pb$ ratio within error of the current estimate for the continental crust (grey star; Stacey and Kramers, 1975) Abbr.: MSWD = mean square of weighted deviates. 216

Figure 5.5: Hand specimen photographs for samples (a) RG177, (b) RG176, (c) RG40, (d) RG167, (e) RG169, (f) RG56, (g) MJK18 and (h) MJK21. 219

Figure 5.6: Amphibole (a) age spectrum, K/Ca and (b) inverted isochron diagrams for the amphibolite megablock sample RG177. For (a) plateau ages (±1σ), age maxima and age minima are as indicated. For (b), the inverted isochron age is meaningful as MSWD < 2.5 and $(^{40}Ar/^{36}Ar)_i \geq 295.5$ (Kunk *et al.*, 2005). Points A, B, C and D were dropped to improve the fit of the data. Abbr.: MSWD = mean square of weighted deviates. 223

Figure 5.7: K-feldspar age spectra, K/Cl and K/Ca diagrams for samples (a) RG40 and (b) RG167. Age maxima and age minima are as indicated. 226

Figure 5.8: White mica age spectra, K/Cl and K/Ca diagrams for mica schist samples (a) RG169, (b) RG56, (c) MJK18 and (d) MJK21. Plateau ages (±1σ), age maxima and age minima are as indicated. Symbols: * = forced plateau age; *P* = probability. 228

Figure 5.9: White mica age spectra, K/Cl and K/Ca diagrams for granitic samples (a) RG167 and (b) RG40. Plateau ages (±1σ), age maxima and age minima are as indicated. 231

Figure 5.10: Thermal decay curve showing the cooling path for the target rocks of Eyreville-B borehole core based on this study's results. Refer to the explanation of numbered labels in text. Closure temperatures used: rutile = 606 ± 18°C (Chapter 4, Section 4.3.4.1); amphibole = 500 ± 50°C (Harrison, 1981); muscovite/white mica = 350 ± 50°C (Hames and Bowring, 1994). Symbols: black squares and lines = data points with errors from this study; grey dashed line = projected cooling history. 234

Figure 5.11: (a) Thermal-decay curve showing complete crystallisation and cooling history as recorded in the target rocks of the Eyreville-B borehole core. (b) Magnified view of the cooling history from 280 to 200 Ma. Refer to the explanation of numbered labels in text. Granite crystallisation temperature is 675 ± 50°C (after Kerrick, 1972). Closure temperatures: rutile = 606 ± 18°C (Chapter 4, Section 4.3.4.1); amphibole = 500 ± 50°C (Harrison, 1981); muscovite/white mica = 350 ± 50°C (Hames and Bowring, 1994). Symbols: red squares and lines = data points with errors derived from Horton *et al.* (2009b); black squares and lines = data points with errors from this study; grey dashed lines = projected cooling history; red dashed line = alternative cooling history. 236

Figure 6.1: (a) Plate reconstruction of the Palaeozoic sutures between Laurentia and Gondwana showing the location of the CBIS (after Lefort, 1988; Lefort and Max, 1991). (b) Tectonostratigraphic terrane map of the Central Appalachians showing the location of the CBIS (after Horton *et al.*, 2005b). 241

Figure 6.2: Comparisons between the granites from the Eyreville-B borehole core, the Langley Granite from the Langley borehole core and the Alleghanian-age granitic plutons from the eastern portion of the Appalachian orogen (data from Russell *et al.*, 1985; Coler *et al.*, 1995; Horton *et al.*, 2005b). (a) ASI diagram (after Shand, 1927; Chappell and White, 1974) and (b) ternary Ab-Qz-Or diagram including cotectic curves in an H_2O-undersaturated system (after Johannes and Holtz, 1991). Dashed line represents the water-undersaturated curve for a_{H2O} = 0.8 crustal fluids in equilibrium with graphite (after Johannes and Holtz, 1991). Abbr. ASI = alumina saturation index (after Shand, 1927); Ab = albite; Or = orthoclase; Qz = quartz (mineral abbreviations after Whitney and Evans, 2010). 251

Figure 6.3: Harker diagrams showing selected major element oxides (TiO_2, Al_2O_3, Fe_2O_3, MgO, CaO and Na_2O) plotted against SiO_2 for the megablock amphibolite of the Eyreville-B borehole core and the mafic-ultramafic rocks of the Halifax County Complex (data from Kite and Stoddard, 1984). Abbr.: HCC = Halifax County Complex. 255

Figure 6.4: Schematic cross sections showing the latter stages of the Carolina Zone accretion onto the Laurentian margin from (a) the Silurian to Lower Devonian, (b) the Middle-Late Devonian and (c) the Middle Devonian, followed by (d) the Late Permian collision between Laurentia and Gondwana (diagrams modified after Fichter and Baedke, 1999). See text for explanation. Abbr. ROB = remnant ocean basin. 273

LIST OF TABLES

Table 2.1: Average orientation angle of foliations measured from the core axis for the metapelites from the lower basement-derived section (LB), the amphibolite from the upper megablock amphibolite (MBA) and biotite schist xenoliths (MBS) and the gneissic granite (MBGn) from the upper megablock granite. 68

Table 3.1: Analytical precision for major and trace element analysis by XRF at the Museum für Naturkunde, Humboldt University (after Schmitt *et al.*, 2004 and Coney, 2009). 95

Table 3.2: Analytical precision for major and trace element analysis by XRF in the School of Geosciences at the University of the Witwatersrand (after Coney, 2009). 96

Table 3.3: Trace element compositions of the standards used for ICP-MS analysis in the School of Geosciences at the University of the Witwatersrand (A. Wilson, pers. comm., 2008). 98

Table 3.4: Mean and standard deviation (data in wt%) of major element oxides obtained by XRF analysis for the eight target rock units of the Eyreville-B borehole core. Abbr.: n = number of samples; SD = standard deviation; LOI = loss on ignition. 99

Table 3.5: Mean and standard deviation (data in ppm) of trace element abundances obtained by XRF analysis for the eight target rock units of the Eyreville-B borehole core. Abbr.: n = number of samples; SD = standard deviation; bdl = below detection limit. 119

Table 3.6: Mean and standard deviation (data in ppm) of trace elements obtained by ICP-MS analysis for the eight target rock units of the Eyreville-B borehole core. Abbr.: n = number of samples; SD=standard deviation. 130

Table 4.1: List of samples analysed using EMPA at the Museum für Naturkunde, Humboldt University (Berlin) and at the University of Pretoria (Pretoria). 153

Table 4.2: Representative electron microprobe analyses for the Eyreville-B lower basement-derived and upper megablocks sections obtained in Pretoria[1] and Berlin[2]. Abbr.: Amp = amphibole; Bt = biotite; Chl = chlorite; Ep = epidote; Grt = garnet; Kfs = K-feldspar; Ms = muscovite; Pl = plagioclase; Ttn = titanite; Tur = tourmaline; Ves = vesuvianite. B-A = basement amphibolite; B-BS = basement biotite schist; B-G = basement; B-MS = basement mica schist; MB-A = megablock amphibolite; MB-G = megablock massive granite; MB-Gn = megablock gneissic granite; MB-MS = megablock mica schist. 154

Table 4.3: Definitions of symbols used in Equation 4.1 (after Spear, 1989, 1993; Powell *et al.*, 1998). 176

Table 4.4: Geobarometers and geothermometers used on selected samples from the Eyreville-B borehole core. Abbr.: Bt = biotite; Grt = garnet; Hbl = hornblende; Pl = plagioclase; N/A = not applicable. 183

Table 4.5: Trace element compositions of the NIST SRM 610 (after Jochum *et al.*, 2011) and R10 (after Luvizotto *et al.*, 2009a) standards used for LA-ICP-MS analysis at the Institut für Geowissenschaften at the Universität Mainz, Germany. 184

Table 4.6: Equilibrium reactions for geothermometers and geobarometers used. 186

Table 4.7: Oxide wt.% and normalised mole values used for THERIAK-DOMINO modelling input data from samples RG53 (from the lower basement-derived mica schist), RG40 (from the lower basement-derived granite) and W52 (from the upper megablock amphibolite). 187

Table 4.8: Average temperature estimates (2σ) from Zr-in-rutile thermometry for samples RG54 and RG57 from the lower basement-derived section. Temperatures calculated at a fixed pressure of 0.4 GPa. 187

Table 4.9: Temperature estimates from the Grt-Bt mineral pair geothermometer for samples RG48 and RG53 (from the lower basement-derived mica schist) and samples RG40a and RG46 (from the lower basement-derived granite) using seven calibrations (see footnote). Temperatures are calculated at a fixed pressure of 0.4 GPa. Abbr.: c = core; r = rim. 190

Table 4.10: Temperature estimates from the Hbl-Pl mineral pair thermometer (after Blundy and Holland, 1990; Holland and Blundy, 1994) for sample RG51 (from the lower basement-derived para-amphibolite) and samples W51 and W52 (from the upper amphibolite megablock). Temperatures are calculated at a fixed pressure of 0.4 GPa. Abbr.: c = core; r = rim. 193

Table 4.11: Pressure estimates from the GASP and GPMB geobarometers (Holland and Powell, 1998) for samples RG48 and RG53 (from the lower basement-derived mica schist) and sample RG40a (from the lower basement-derived granite). Abbr.: c = core; r = rim. 194

Table 5.1: Dwell times for isotopes. 214

Table 5.2: LA-ICP-MS data for rutile in samples RG54 and RG57 215

Table 5.3: Mineral separates obtained for Ar/Ar geochronological analysis by rock type, sample and depth. Abbr. (after Siivola and Schmid, 2007; Whitney and Evans, 2010): Amp = amphibole; Bt = biotite; Kfs = K-feldspar; WM = white mica. 218

Table 5.4: Compilation of interpreted $^{40}Ar/^{39}Ar$ ages. Abbr.: A = amphibolite; G = granite; LB = lower basement-derived section; MB = megablock section; MS = mica schist; MSWD = mean square of weighted deviates; *P* = probability. 222

Table 6.1: Characteristics of terranes in the vicinity of the CBIS (as seen in Figure 6.1b). 242

Table 6.2: Tectonic setting and proposed source of origin for terranes in the vicinity of the CBIS (as seen in Figure 6.1b). 247

Table 6.3: Summary of estimated conditions and timing of metamorphism and deformation experienced by the Eyreville-B rock units analysed in this study. 267

LIST OF APPENDICES

Appendix 1a: Sample numbers and lithology with corresponding depth (MJK-series collected by M.J. Kunk, RG-series collected by R.L. Gibson, W-series collected by W.U. Reimold). Abbr.: Basement = lower basement-derived section.

Appendix 1b: Sample descriptions based on hand specimen and thin section petrographic analysis (MJK-series collected by M.J. Kunk, RG-series collected by R.L. Gibson, W-series collected by W.U. Reimold). Refer to Appendix 1c for hand specimen photographs. Abbr.: Amp = amphibole; Bt = biotite; Cal = calcite; Ccd = chalcedony; Ccp = chalcopyrite; Chl = chlorite; Ep = epidote; Fi = fibrolite; Gr = graphite; Grt = garnet; Ilm = ilmenite; Kfs = K-feldspar; Mag = magnetite; Ms = muscovite; Pl = plagioclase; Po = pyrrhotite; Py = pyrite; Qz = quartz; Rt = rutile; Ser = Ser; Sil = sillimanite; Ttn = titanite; Tur = tourmaline; Ur = uralite; Ves = vesuvianite; Zrn = zircon (after Whitney and Evans, 2010).

Appendix 1c: Hand specimen photographs of samples corresponding to descriptions in Appendix 1b. Photographs are catalogued from the top to the base of the Eyreville-B borehole core (MJK-series collected by M.J. Kunk, RG-series collected by R.L. Gibson, W-series collected by W.U. Reimold).

Appendix 1d: Foliation structural measurements with increasing depth for the gneissic granite and schist xenoliths from the upper granite megablock, the amphibolite from the upper amphibolite megablock and for the metapelites from the lower basement-derived section of the Eyreville-B borehole core. All measurements are taken from the core axis.

Appendix 2a.1: Major and trace element bulk rock geochemical data for the Eyreville-B borehole core lower basement-derived and upper megablocks sections obtained at the Museum für Naturkunde, Humboldt University, Berlin, Germany (total Fe calculated as Fe_2O_3).

Appendix 2b: ICP-MS trace element analyses for the Eyreville-B borehole core lower basement-derived and upper megablocks sections obtained at the School of Geosciences, University of the Witwatersrand, South Africa.

Appendix 3a.1: Amphibole electron microprobe analyses for the Eyreville-B borehole core lower basement-derived and upper megablocks sections obtained at the Museum für Naturkunde, Humboldt University, Berlin, Germany.

Appendix 3a.2: Biotite electron microprobe analyses for the Eyreville-B borehole core lower basement-derived and upper megablocks sections obtained at the Museum für Naturkunde, Humboldt University, Berlin, Germany.

Appendix 3a.3: Chlorite electron microprobe analyses for the Eyreville-B borehole core lower basement-derived and upper megablocks sections obtained at the Museum für Naturkunde, Humboldt University, Berlin, Germany.

Appendix 3a.4: Garnet electron microprobe analyses for the Eyreville-B borehole core lower basement-derived and upper megablocks sections obtained at the Museum für Naturkunde, Humboldt University, Berlin, Germany.

Appendix 3a.5: K-feldspar electron microprobe analyses for the Eyreville-B borehole core lower basement-derived and upper megablocks sections obtained at the Museum für Naturkunde, Humboldt University, Berlin, Germany.

Appendix 3a.6: Plagioclase electron microprobe analyses for the Eyreville-B borehole core lower basement-derived and upper megablocks sections obtained at the Museum für Naturkunde, Humboldt University, Berlin, Germany.

Appendix 3a.7: White mica electron microprobe analyses for the Eyreville-B borehole core lower basement-derived and upper megablocks sections obtained at the Museum für Naturkunde, Humboldt University, Berlin, Germany.

Appendix 3b.1: Amphibole electron microprobe analyses for the Eyreville-B borehole core lower basement-derived and upper megablocks sections obtained at the University of Pretoria, South Africa.

Appendix 3b.2: Biotite electron microprobe analyses for the Eyreville-B borehole core lower basement-derived and upper megablocks sections obtained at the University of Pretoria, South Africa.

Appendix 3b.3: Chlorite electron microprobe analyses for the Eyreville-B borehole core lower basement-derived and upper megablocks sections obtained at the University of Pretoria, South Africa.

Appendix 3b.4: Epidote electron microprobe analyses for the Eyreville-B borehole core lower basement-derived and upper megablocks sections obtained at the University of Pretoria, South Africa.

Appendix 3b.5: Garnet electron microprobe analyses for the Eyreville-B borehole core lower basement-derived and upper megablocks sections obtained at the University of Pretoria, South Africa.

Appendix 3b.6: K-feldspar electron microprobe analyses for the Eyreville-B borehole core lower basement-derived and upper megablocks sections obtained at the University of Pretoria, South Africa.

Appendix 3b.7: Plagioclase electron microprobe analyses for the Eyreville-B borehole core lower basement-derived and upper megablocks sections obtained at the University of Pretoria, South Africa.

Appendix 3b.8: Titanite electron microprobe analyses for the Eyreville-B borehole core lower basement-derived and upper megablocks sections obtained at the University of Pretoria, South Africa.

Appendix 3b.9: Tourmaline electron microprobe analyses for the Eyreville-B borehole core lower basement-derived and upper megablocks sections obtained at the University of Pretoria, South Africa.

Appendix 3b.10: Vesuvianite electron microprobe analyses for the Eyreville-B borehole core lower basement-derived and upper megablocks sections obtained at the University of Pretoria, South Africa.

Appendix 3b.11: White mica electron microprobe analyses for the Eyreville-B borehole core lower basement-derived and upper megablocks sections obtained at the University of Pretoria, South Africa.

Appendix 4a: Mineral compositional data and temperature estimates from Zr-in-rutile thermometry using the NIST SRM 610 (Jochum *et al.*, 2011) and R10 (Luvizotto *et al.*, 2009a) standards.

Appendix 4b: Mineral compositional data used for conventional geothermobarometry. Abbr.: Amp = amphibolite; Bt = biotite; Grt = garnet; Ms = muscovite; Pl = plagioclase (after Whitney and Evans, 2010). Abbr.: c = core; r = rim.

Appendix 5a.1: Uncorrected LA-ICP-MS data for rutile U/Pb geochronology in samples RG54 and RG57.

Appendix 5a.2: Corrected LA-ICP-MS data for rutile U/Pb geochronology in samples RG54 and RG57.

Appendix 5a.3: Rutile U/Pb geochronological data diagrams.

Appendix 5b.1: Argon isotopic step-heating results for amphibole, biotite, K-feldspar and muscovite mineral separates.

Appendix 5b.2: Age spectra diagrams for results listed in Table 1.

Appendix 5b.3: Inverted isochron diagrams for results listed in Table 1.

Appendix 6a: Journal article (Townsend *et al.*, 2009)

Appendix 6b: Journal article (Gibson *et al.*, 2009)

1 INTRODUCTION

The ca. 36 Ma (Horton and Izett, 2005) Chesapeake Bay impact event on the east coast of Virginia, USA, formed an 85 km complex crater in Cretaceous to Eocene sediments and underlying crystalline basement rocks belonging to the Appalachian orogen (Horton *et al.*, 1989; Poag *et al.*, 2004; Horton *et al.*, 2005a). Appalachian rocks are well exposed along the Appalachian Mountains to the west, however, little is known of the basement along the Atlantic Coastal Plain owing to the covering sediment (Horton *et al.*, 2005b; Hibbard *et al.*, 2007a). This study investigates the crystalline rocks intersected by the 2006 ICDP (International Continental Scientific Drilling Program) – USGS (United States Geological Survey) drilling of the Chesapeake Bay impact structure (CBIS) on the Eyreville Farm near Cape Charles, Virginia (Figure 1.1).

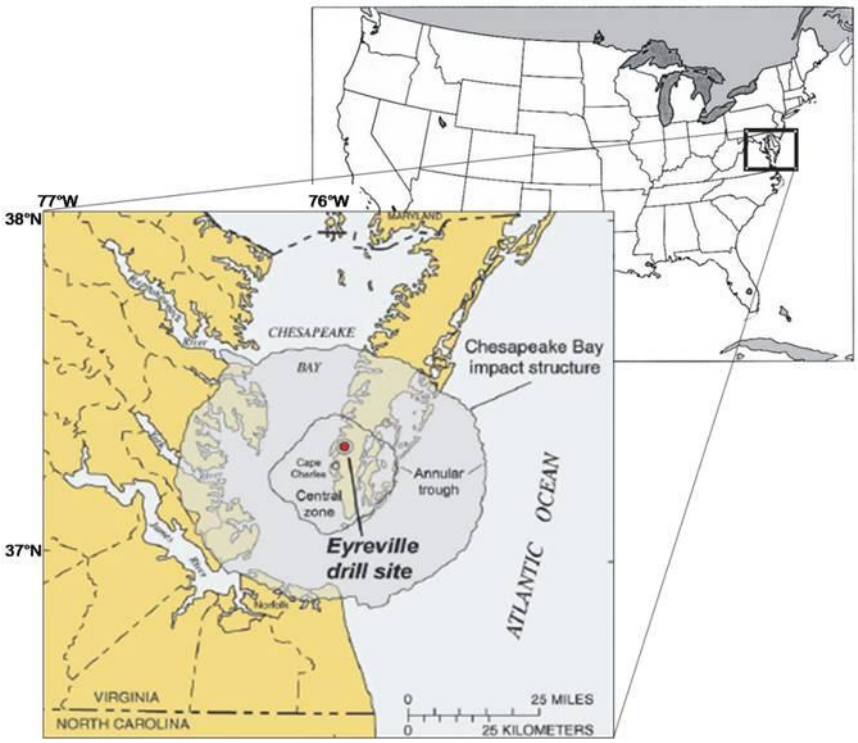

Figure 1.1: Locality map of the CBIS and the ICDP-USGS Eyreville drill site (after Gohn *et al.*, 2006).

1.1 Geological setting

The Appalachian orogenic belt is an elongate tectonic region that is exposed along the eastern margin of the North American continent, extending 3200 km from Alabama to Newfoundland with an exposed width varying from 150 to 600 km (Figure 1.2; Everett *et al.*, 1986; Faill, 1997). The eroded elements of the orogenic belt are separated into the Northern and Central/Southern Appalachians by the New York promontory (Rodgers, 1970; Horton *et al.*, 1989; Taylor, 1989; Faill, 1997; Hibbard *et al.*, 2007a); the CBIS is located in the latter division (Figure 1.2). The tectonic history for this orogenic belt spans more than one billion years, beginning with the Mesoproterozoic assembly of the supercontinent, Rodinia, and ending during the Mesozoic break-up of the supercontinent, Pangaea (Faill, 1997). The orogenic belt is characterised by a series of tectonostratigraphic terranes, each having its own stratigraphy, which were juxtaposed and accreted during the belt's complex history of various plate-plate interactions (Everett *et al.*, 1986; Horton *et al.*, 1989). Overlying the eastern and southern parts of the Appalachian orogenic belt, the Atlantic Coastal Plain sediments comprise a ~18 km updip, seaward-thickening sequence of Early Cretaceous to Holocene (145 Ma to present time) deposits; these sediments comprise dominantly unconsolidated to poorly consolidated siliciclastic sands, silts and both marine and non-marine clays (Poag *et al.*, 2004).

Determining the evolution of this highly complex region has led to much controversy owing to the inherent complexity associated with multiple major continent-continent collisions, which is combined with the region's poor rock exposures due to post-Mesozoic geological processes (glacial drift in the north, deep weathering in the south, eastern parts covered by the Atlantic Ocean, and deposition of Mesozoic and Cenozoic sediments on the Atlantic Coastal Plain's southern extent; Horton *et al.*, 1989). For the most part, the tectonostratigraphic terranes appear to have evolved independently of Proterozoic North America (Laurentia) and can be used to constrain certain aspects of the orogen based on their accretionary history during the Palaeozoic (Horton *et al.*, 1991).

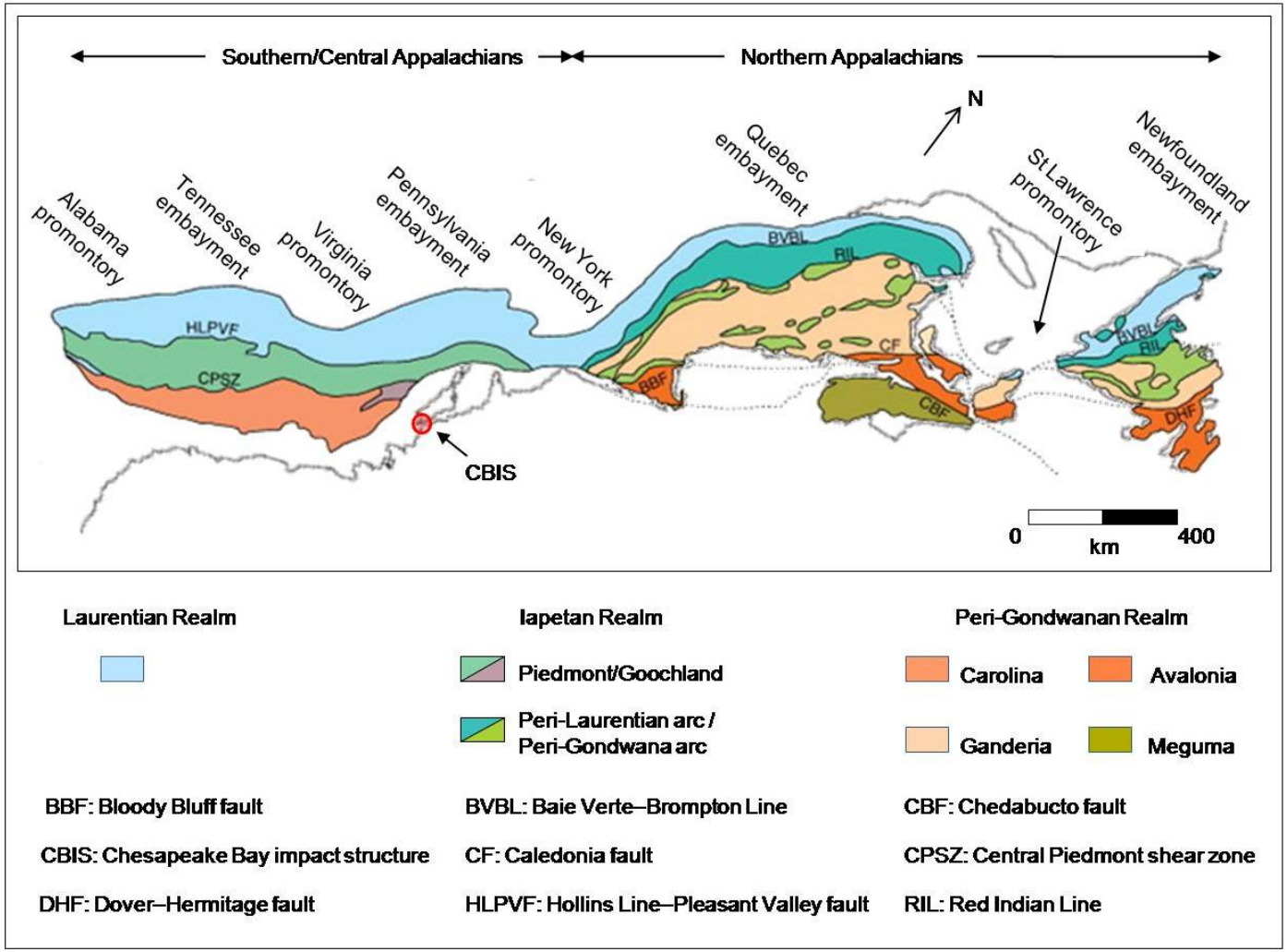

Figure 1.2: Simplified tectonic map of the Appalachian orogen showing the exposed Northern and Central/Southern Appalachians divisions as well as pre-Silurian lithotectonic divisions with respect to the current North American eastern coastline (diagram modified after Hibbard *et al.*, 2007a and Pollock, 2008). The location of the CBIS has been included for reference purposes.

1.1.1 Evolution of the Appalachian orogen

The evolution of the Appalachian orogen began with the late Mesoproterozoic assembly of the supercontinent Rodinia (McMenamin and McMenamin, 1990; also known as Panchaos after Thompson *et al.*, 1993, and Kanatia after Young, 1995 and Dalziel and McMenamin, 1995) at the end of the Grenville orogeny, which brought the Wilson cycle to a close (Faill, 1997). The Grenville Province, located on the Laurentian margin, underwent a widespread granulite facies metamorphism between 1.0 and 1.1 Ga, and was later uplifted and exposed by erosion from approximately 700 Ma with the initiation of the continental rifting of Rodinia (Horton *et al.*, 1989). The final rifting of Rodinia during the late Neoproterozoic led to the opening of the Iapetus Ocean between Laurentia, West Gondwana and Baltica, which was at its widest around 540 Ma (Figure 1.3; Murphy and Nance, 2008; Nance and Linnemann, 2008).

During the Late Cambrian/Early Ordovician, the closure of the Iapetus Ocean and resultant opening of the Rheic Ocean (also known as the Theic Ocean; Nance and Linnemann, 2008) was initiated by coeval subduction on both the Laurentian and Gondwanan passive margins, causing both margins to founder (Figure 1.3; Stevens, 1970; Williams and Stevens, 1974; Williams, 1979; van Staal *et al.*, 1998; Murphy *et al.*, 2010). As illustrated in Figure 1.4, Pacific-type arc/back arc systems developed on both margins, producing ophiolitic complexes in supra-subduction zones relatively early on in the Iapetus oceanic tract's subduction history, which were then obducted and involved in arc-continent collisions during the Early to Middle Ordovician (550-440 Ma; Williams, 1979; Dewey *et al.*, 1983; Searle and Stevens, 1984; Horton *et al.*, 1989; Rankin, 1994; van Staal *et al.*, 1998, 2009; Hibbard *et al.*, 2007a; Murphy *et al.*, 2010). The above process has been termed the Penobscottian orogeny along the peri-Gondwanan margin, and the Taconian orogeny along the peri-Laurentian margin (Figure 1.4; Hibbard *et al.*, 2007a).

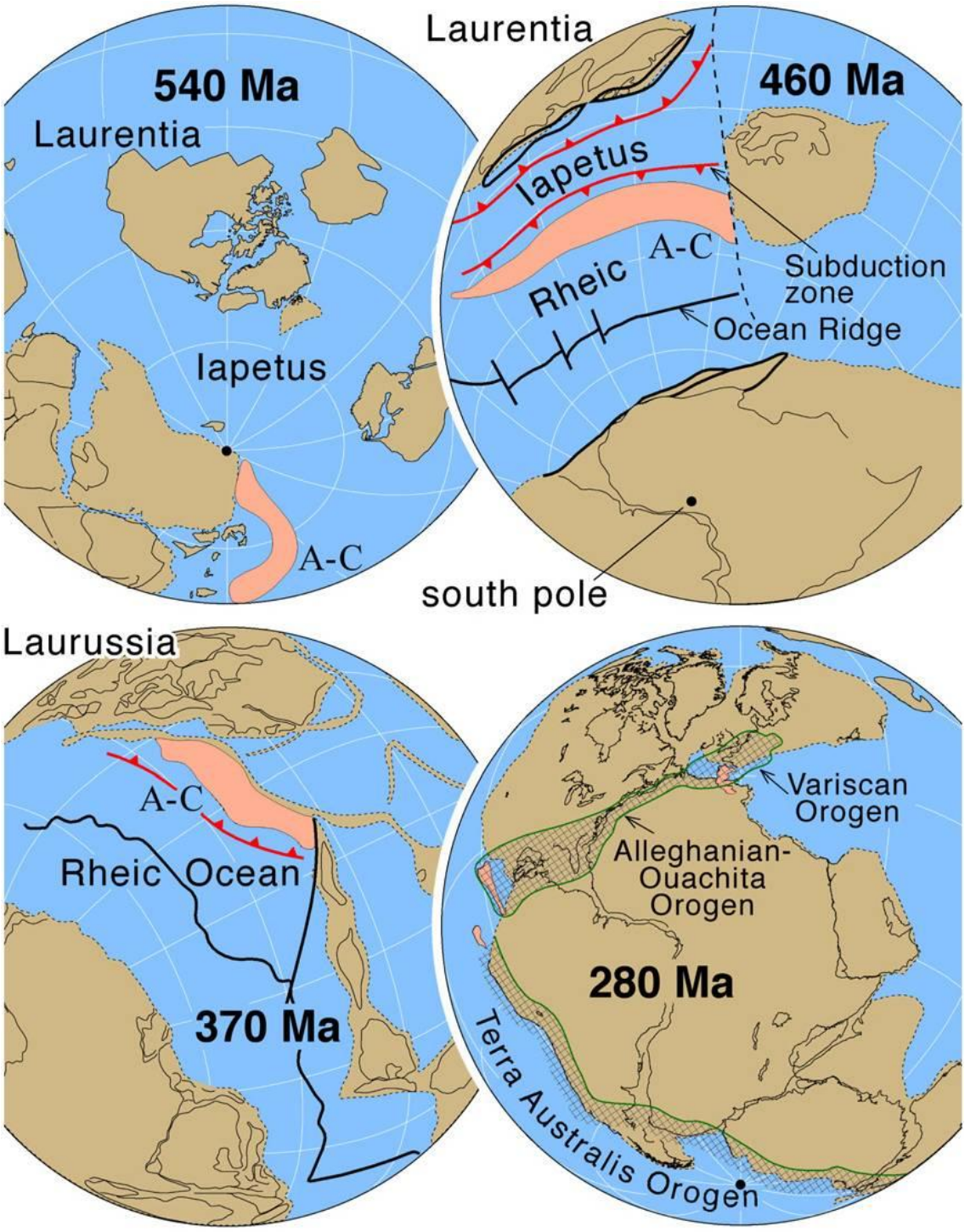

Figure 1.3: Reconstructions of Pangaea during the Palaeozoic, illustrating the closing of the Iapetus and Rheic oceans between Gondwana and Laurentia (diagram modified Stampfli and Borel, 2002, and Murphy *et al.*, 2010). Abbr. A-C = Avalonia-Carolina.

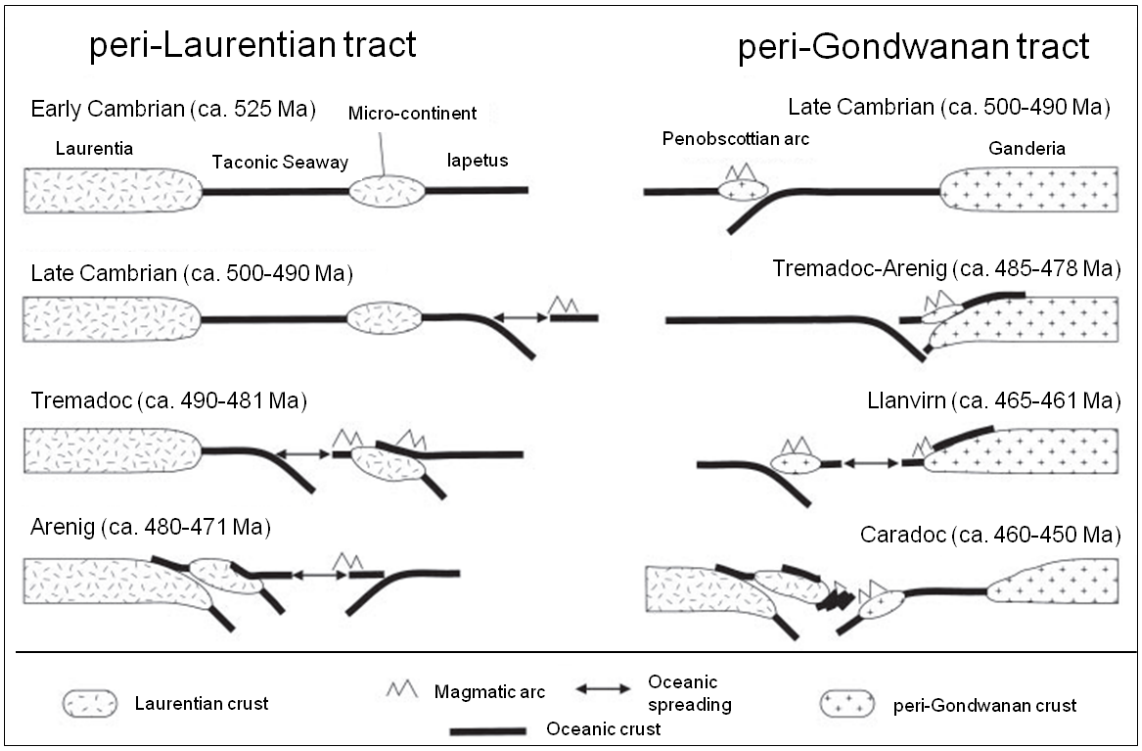

Figure 1.4: Illustration of the proposed tectonic models for the Taconian (left) and Penobscottian (right) orogenies along the Laurentian and Gondwanan margins in the Dunnage domain of the Northern Appalachians (modified after Hibbard *et al.*, 2007a and Murphy *et al.*, 2010). The details and timing depicted may not be necessarily true for the Central and Southern Appalachians but is used here to illustrate subduction processes of the Iapetus Ocean.

The Penobscottian orogeny, first identified by Neuman (1967), is thought to have commenced around 550 Ma (Drake *et al.*, 1989; Rankin, 1994) with the formation of a magmatic arc in the peri-Gondwanan margin (Hibbard *et al.*, 2007a). The westward subduction beneath the magmatic arc resulted in its obduction onto the passive margin of a peri-Gondwanan micro-continent (Ganderia in Figure 1.4; Hibbard *et al.*, 2007a). Such micro-continents, also known as ribbon continents and/or arc terranes, formed as a result of the amalgamation of several Neoproterozoic arc terranes that had separated from Gondwana with the opening of the Rheic Ocean (Faill, 1997; Hibbard *et al.*, 2007a; Murphy *et al.*, 2010; Nance and Linnemann, 2008). The obduction of the magmatic arc onto the micro-continent signalled the end of the Penobscottian orogeny (ca. 480 Ma; Zagorevski *et al.* 2007; van Staal *et al.*, 2009) and initiated a reverse in polarity of the subduction direction (Colman-Sadd *et al.*, 1992; Hibbard *et al.*,

2007a; van Staal *et al.*, 2009). A back-arc basin ensued, opening along the peri-Gondwanan micro-continent margin (Figure 1.4; van Staal, 1994; Valverde-Vaquero *et al.*, 2005; Hibbard *et al.*, 2007a).

The Taconian orogeny, which took place along the Laurentian margin of the Iapetus Ocean, commenced towards the end of the Penobscottian orogeny around 495 Ma (Fig 1.5; van Staal *et al.*, 2009; Murphy and Nance, 2013). Subducting eastwards beneath the Iapetus Ocean, a magmatic arc was formed outboard of a micro-continental block (e.g. Dashwoods in the Northern Appalachians; van Staal *et al.*, 2009) that had rifted from the Laurentian margin in the Late Neoproterozoic/Early Cambrian (Figure 1.4; Hibbard *et al.*, 2007a). The magmatic arc was then obducted onto the micro-continent, resulting in the stepping back of subduction into the Taconic Seaway and the subsequent generation of a magmatic arc and its associated forearc ophiolitic crust (Figure 1.4; Hibbard *et al.*, 2007a; van Staal *et al.*, 2009). The final elements of the Taconian orogeny relate to the closure of the Taconic Seaway by subduction processes, which led to the re-accretion of the micro-continent and the obduction of Taconic Seaway oceanic crust onto the Laurentian margin and the development of reverse polarity subduction beneath the accreted system (Figure 1.4; Hibbard *et al.*, 2007a). The peri-Gondwanan arc system produced by the Penobscottian orogeny subsequently collided with this peri-Laurentian configuration, after which the Taconian orogeny concluded (ca. 440 Ma; Figure 1.4; Horton *et al.*, 1989; Rankin, 1994; Hibbard *et al.*, 2007a).

The final closure of the Iapetus Ocean occurred owing to successive collisional events, which took place from the Late Ordovician into the Silurian (~460-420 Ma; Figure 1.5; Murphy *et al.*, 2010; Murphy and Nance, 2013). These collisional events relate to the docking of several peri-Gondwanan arc terranes to form Laurussia (e.g. Avalonia-Carolina; Figure 1.5), the sequence of which is the cause for much controversy, although there is consensus that the northern margin of Laurentia collided with Baltica and that peri-Gondwanan terranes accreted to Laurentia along the remaining portion of the margin (Nance and Linnemann, 2008; Murphy *et al.*, 2010; Nance *et al.*, 2012).

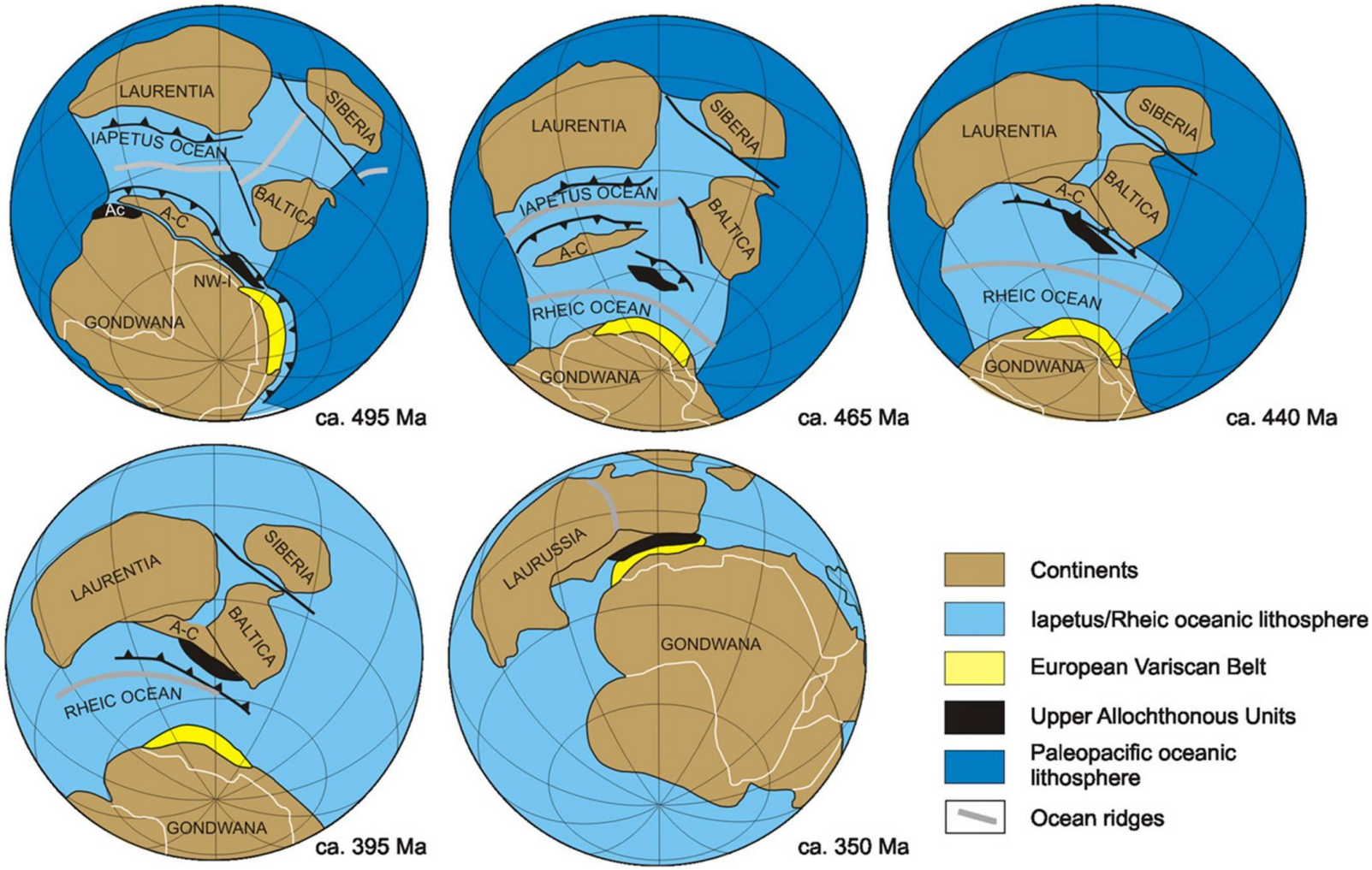

Figure 1.5: Palaeozoic reconstructions of the formation of Pangaea through the preferential subduction of the Iapetus and Rheic oceanic lithosphere (diagram modified after Murphy and Nance, 2013 and references therein). Abbr. A-C- Avalonia-Carolina.

According to Murphy *et al.* (2010), there are two main models regarding the amalgamation of Laurussia: (1) The Ganderia, Avalonia and Meguma peri-Gondwanan micro-continents accreted to Laurentia as separate crustal blocks during the Palaeozoic; each accretion involved a distinct orogeny, namely the Late Ordovician–Early Silurian Salinic (450-423 Ma), Late Silurian–Devonian Acadian (421-400 Ma) and the Neoacadian (395-350 Ma), respectively (van Staal *et al.*, 1998, 2009; Waldron *et al.*, 2009). Hibbard *et al.* (2002) proposed that the Carolina micro-continent accreted to Laurentia during the Late Ordovician-Silurian Salinic orogeny, the concept of which is further hypothesised by Hibbard *et al.* (2007b) where they correlate Carolina with Ganderia. (2) Ganderia, Carolina and Meguma form part of a single composite Avalonian micro-continent that separated from Gondwana during the Late Cambrian, forming the Rheic Ocean, and which then accreted to Baltica by the Early Silurian and to Laurussia by the Middle Silurian (Figure 1.3; Keppie *et al.*, 1996; Murphy and Keppie, 2005). In this model, the Salinic orogeny is thought to represent a protracted orogenic episode relating to the accretion of Avalonia to Laurussia, with northward flat slab subduction of the Rheic Ocean beneath Laurussia demonstrated by the Late Silurian to Late Devonian tectonothermal events assigned to the Acadian orogeny (Murphy *et al.*, 1999; Murphy and Keppie, 2005).

The final closing of the Rheic Ocean by the collision of the African side of Gondwana and Laurussia during the late Palaeozoic formed the supercontinent, Pangaea (Figure 1.3; Faill, 1998; Hatcher, 2002). This final stage of accretionary history recorded in the Appalachian orogen is known as the Alleghanian orogeny (Horton *et al.*, 1989, 1991; Rankin, 1994; Faill, 1998; Hatcher 2002). Hatcher (2002) proposed a possible zippered collisional sequence for formation of the Alleghanian orogeny (Figure 1.6):

(a) The beginning of the closure of the Rheic Ocean initiated the first contact of Gondwana with Laurentia during the Early Carboniferous (ca. 325 Ma), indicated by the early strike-slip deformation and formation of step-over basins. After the initial contact, Gondwana began to rotate clockwise relative to Laurentia, which allowed more of the continental margins farther south to come into contact with Laurentia (Figure 1.6a).

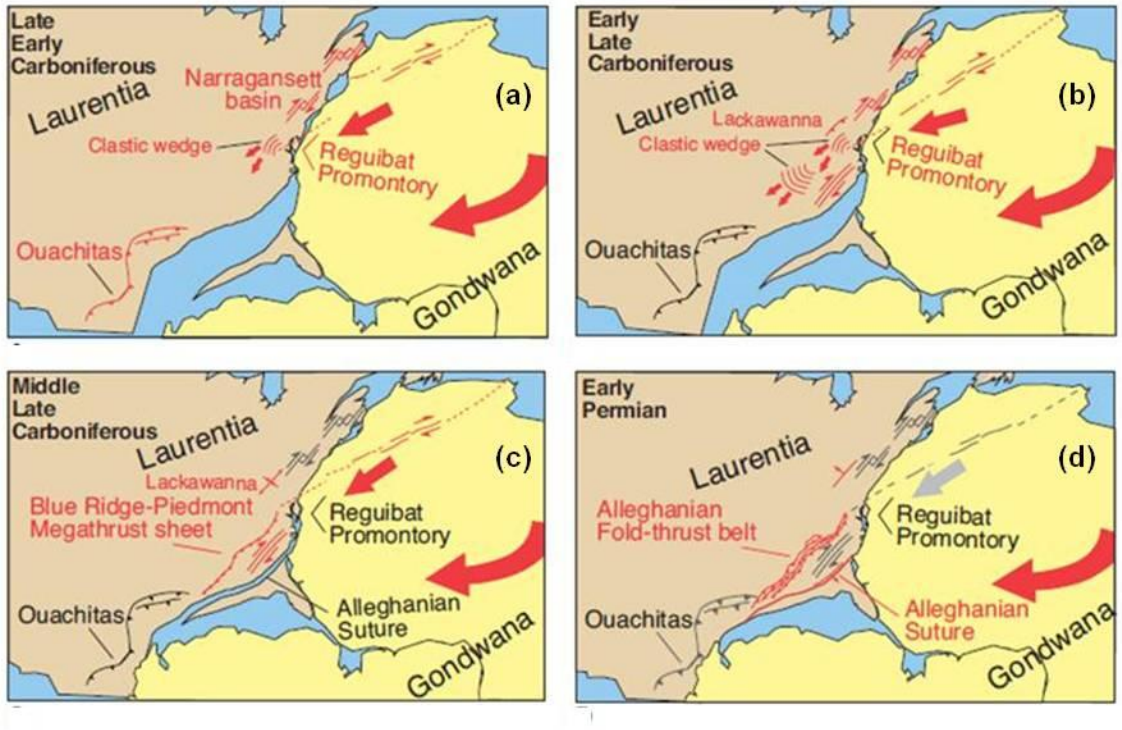

Figure 1.6: Illustrations of the oblique rotational collision between Laurentia and Gondwana as suggested by Hatcher (2002). The red lines and symbols represent active features in the interval shown in each figure (after Hatcher, 2002; Nance and Linnemann, 2008).

(b) The Reguibat promontory came into contact with the Central Appalachian margin during the early Late Carboniferous (ca. 310 Ma; Figure 1.6b). The first deformation occurred parallel to the promontory on the nearby foreland. The deformation consists of the Lackawanna Phase in the Central Appalachians, dextral strike-slip deformation in the Central and Southern Appalachian internides (see Lackawanna region in Figure 1.6b), and the formation of dextral pull-apart basins in New England.

(c) The continuing encroachment of the promontory onto the Laurentian margin and the rotation of Gondwana southward created dextral motion on many faults, plus fault reactivation, from the Late Carboniferous to Early Permian (ca. 300-280 Ma; Figure 1.6c).

(d) Gondwana collided head-on with southeastern Laurentia during the Early Permian (ca. 270 Ma), propagating and driving the Blue Ridge-Piedmont megathrust sheet onto the continental margin (Figure 1.6d). This deformed the foreland and clastic wedge that

formed ahead of the advancing sheet. This represents the termination of the Alleghanian orogeny.

This collision occurred northeast-southwest, as seen in the predominantly dextral motion both in New England and the Southern Appalachians (Hatcher, 1989). It produced a Himalayan-size mountain range and structurally overprinted the structures related to the older events. All present landforms, physiographic provinces, structures, rock fabrics and micro-textures in this region reflect this event (Fitcher, 2000).

A fundamental element of the Alleghanian orogeny, specifically in the Central and Southern Appalachians, is the basal décollement that originated within the crust east of the presently exposed Appalachian Mountains (Figure 1.7; Faill, 1998; Fichter and Baedke, 1999). The décollement formed a sub-horizontal sole thrust fault that gradually rose westward from mid-crustal levels, tipping out at some horizons within the Palaeozoic section of the Appalachian basin (Figure 1.7; Faill, 1998). The décollement ramped over older detached terranes accreted during the Taconic and Acadian orogenies (Figure 1.7; Fichter and Baedke, 1999). The Valley and Ridge foreland basin was caused by the successive collisional events experienced by the subducting Laurentian margin (Figure 1.7; Ettensohn, 2008).

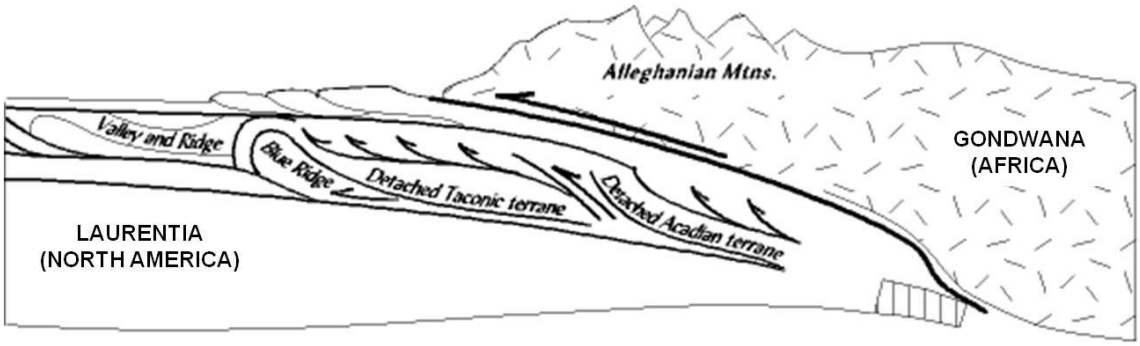

Figure 1.7: Schematic cross-section of the Alleghanian orogeny (modified after Fichter and Baedke, 1999) showing Gondwana over-riding Laurentia to the west through décollement tectonics.

The décollement deformation of the Alleghanian orogeny was concurrent with abundant magmatic activity, where at least 60 plutons, mostly granitoid in composition, were emplaced between 330 and 260 Ma (Horton *et al.*, 1987; Coler *et al.*, 1997; Speer *et al.*, 1994). Of the granitoid plutons, most are leucocratic, metaluminous granites and granodiorites, although a minor amount of peraluminous granitoids also occur (Speer *et al.*, 1994). Notable plutons in relatively close proximity to the CBIS include the Langley Granite (Horton *et al.*, 2005b), Portsmouth Granite (Horton *et al.*, 1989) and Petersburg Granite (Gates and Glover, 1989).

Geochemical and Nd isotopic studies by Coler *et al.* (1997) revealed that textural and mineralogical differences between and within many of the Alleghanian granitoids reflect isotopically variable sources, suggesting that the Alleghanian magmatism was probably a result of partial melting of multiple geochemically similar tectonostratigraphic terranes. The relative synchronicity of granite emplacement with the Alleghanian décollement led Coler *et al.* (1997) to propose that the majority of the plutons were emplaced during and/or after the thrusting-related deformation occurred.

1.1.2 Tectonostratigraphic terranes of the Appalachian orogen

As previously mentioned, a number of distinct tectonostratigraphic terranes characterise the Appalachian orogen (Everett *et al.*, 1986; Horton *et al.*, 1989). These terranes were accreted to Laurentia through the sequence of orogenic events described above during the closure of the Iapetus and Rheic oceans and the formation of Pangaea. Lying mostly beneath the Atlantic Coastal Plain sediments, the precise locations of the associated Iapetus and Rheic (also known as Theic; Nance and Linnemann, 2013) suture zones have been much debated with interpretations based largely on geophysical data (e.g. Lefort, 1988; Lefort *et al.*, 1988; Lefort and Max, 1991; West, 1998; Hibbard, 2000; Murphy *et al.*, 2006). According to Lefort (1988) and Lefort and Max (1991), both sutures lie west of the Chesapeake Bay (Figure 1.8).

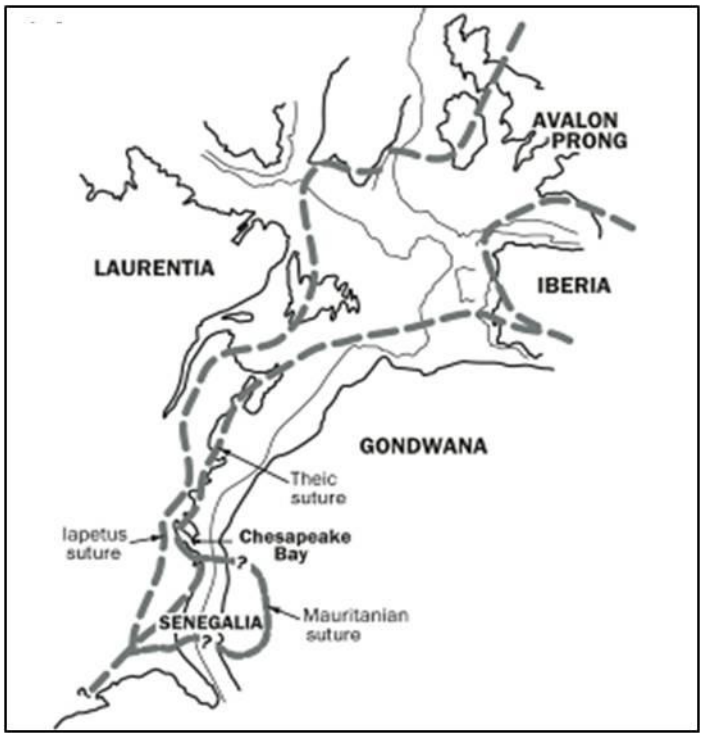

Figure 1.8: Plate reconstruction of the Palaeozoic Iapetus, Rheic (also known as Theic; Nance and Linnemann, 2013) and Mauritanian sutures (dashed lines) between Laurentia and Gondwana with the location of Chesapeake Bay included (modified after Lefort, 1988; Lefort and Max, 1991).

Based on their origins, Horton *et al.* (1989, 1991, 1994) proposed that the Appalachian terranes can be subdivided into seven groups using the terrane terminology adopted from Coney *et al.* (1980), Jones (1983), Jones *et al.* (1983) and Howell and Jones (1984):

(i) Laurentian native terranes – Outliers of the Grenville Province, these terranes comprise Middle Proterozoic basement, rift-related Late Proterozoic clastic and volcanic sequences, and Palaeozoic shelf and platform sediments deposited on Laurentia's eastern margin;

(ii) Internal continental terranes of the Appalachian orogen – These terranes are composed of Middle Proterozoic continental basement and sedimentary cover sequences and are located within the Appalachian metamorphic core;

(iii) Disrupted terranes – Terranes that are characterised by mélange complexes intermingled with coherent volcanic, ophiolitic and/or continental terrane fragments;

(iv) Possible oceanic crustal remnants – Terranes that may possibly be remnants of oceanic crust that occur as mafic and ultramafic complexes;

(v) Volcanic terranes – Terranes generated by volcanic arc systems of both oceanic and continental origin;

(vi) Continental terrane of Gondwanan affinity – A terrane comprising an unmetamorphosed, little-deformed sequence of fossiliferous Ordovician to Devonian sandstones and shales (known as the Suwannee Basin) derived from Gondwanan crust; and

(vii) Metamorphic complexes of undetermined affinity – Terranes that are composed of metamorphic complexes whose origins could not be determined.

Subsequently, Hibbard *et al.* (2007a) proposed that the Appalachian orogen can also be separated into three realms based on pre-Silurian orogenic crustal building blocks, namely the Laurentian, Iapetan and peri-Gondwanan realms (see Figure 1.2). Although on a much smaller scale, the seven terrane types identified by Horton *et al.* (1989, 1991, 1994) can be placed in context within the three orogen-scale realms (Figure 1.9; Hibbard *et al.*, 2007a).

Prior to the discovery of the CBIS, the basement rocks beneath the Atlantic Coastal Plain sediments were assigned to the Chesapeake block (Figure 1.9; Horton *et al.*, 1991), a roughly circular terrane that was inferred to comprise rocks of mostly greenschist facies, including argillite, chloritic schist, phyllitic metavolcanic rock, and serpentinised gabbro (Horton *et al.*, 1989, 1991). Owing to the lack of surface outcrop, the provenance of the Chesapeake block was cause for much debate. The strongly curved southern and western edge of the Chesapeake Bock (Figure 1.9) was inferred by Lefort (1988) and Lefort and Max (1991) through gravimetric and magnetic geophysical surveys. This led the authors to suggest the suture reflected an indentation by western Gondwana onto the Carboniferous margin of Laurentia, consequently they named it the Chesapeake Bay suture (Lefort, 1989; Lefort and Max, 1989; Horton *et al.*, 1991), and Lefort (1988) and Lefort and Max (1991) concluded that the Chesapeake Bay was underlain by crust of Gondwanan affinity.

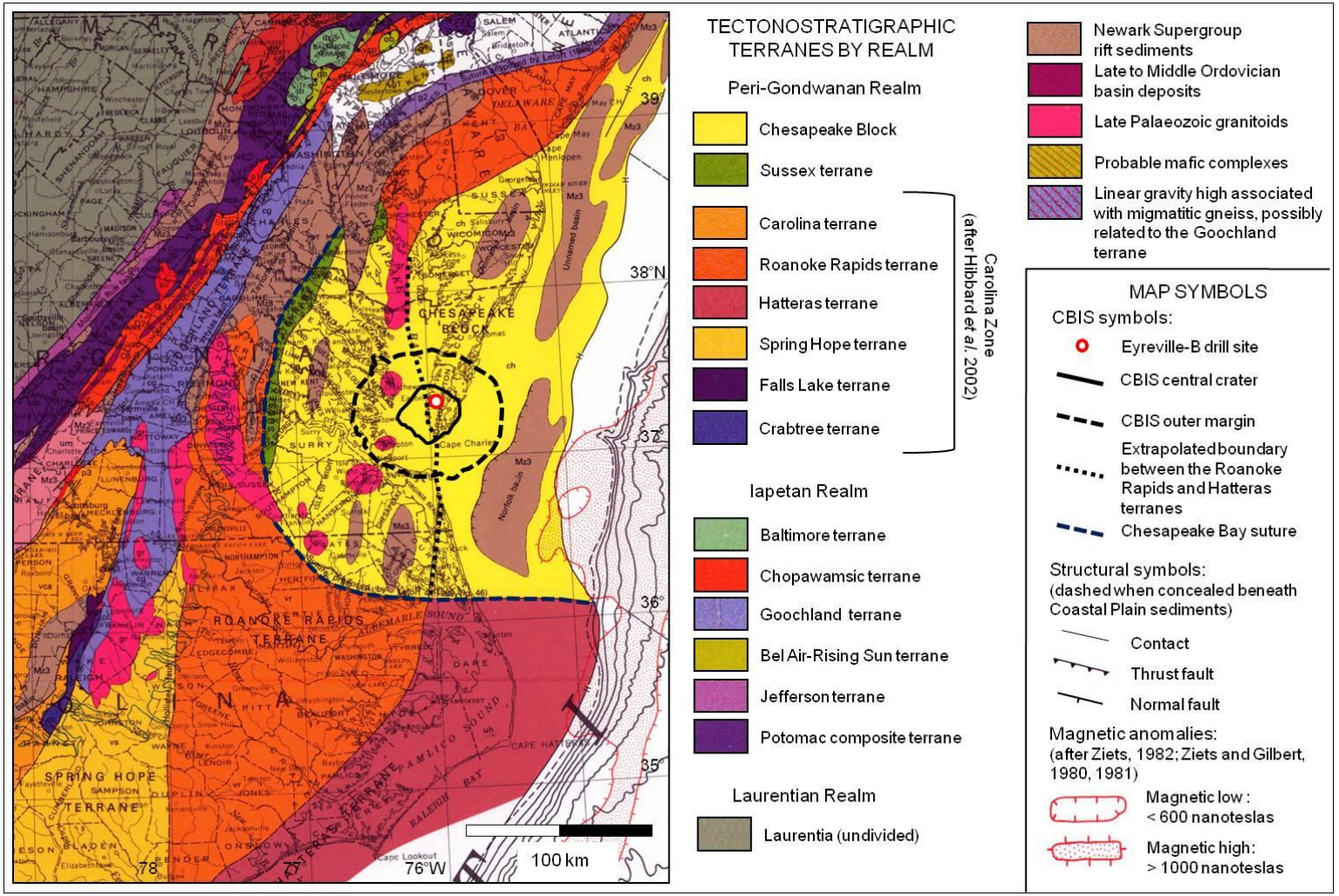

Figure 1.9: Tectonostratigraphic terrane map of the Central Appalachians showing the location of the Chesapeake Bay suture (after Horton *et al.*, 1991), Chesapeake block, CBIS, ICDP-USGS Eyreville-B drill site and the proposed extrapolated boundary between the Roanoke Rapids and Hatteras terranes (modified slightly, after Horton *et al.*, 1991; 2005b). Terranes have been grouped according to the three orogenic realms (Laurentia, Iapetan and Gondwanan) proposed by Hibbard *et al.* (2007a).

Lefort's (1988) and Lefort and Max's (1991) interpretation has been questioned by Horton *et al.* (2005a, 2005b) who found that the characteristics of rocks recovered from drill cores in the Chesapeake Bay are more consistent with peri-Gondwanan origins. Furthermore, Horton *et al.* (2005b) proposed that the geophysical features previously associated with the Chesapeake block can be attributed to the CBIS and do not reflect traditional terrane boundaries. As a result, Horton *et al.* (2005b) suggested that the CBIS overlapped the boundary between the Roanoke Rapids and Hatteras terranes (Figure 1.9), both of which comprise rocks of analogous composition, metamorphic grade and age to that previously assigned to the Chesapeake block. A discussion of these terranes and others in close proximity to the CBIS (as seen in Figure 1.9) follows.

1.1.2.1 Carolina Zone

The Carolina Zone is a cluster of volcanic arc supracrustal (suprastructure) and infracrustal (infrastructure; Figure 1.10a) terranes lying along the eastern flank of the Southern Appalachians (Figure 1.10; Hibbard *et al.*, 2002). The synthesis of the Carolina Zone involved at least three stages of magmatism and sediment deposition, namely, Stage I: pre-600 Ma, Stage II: ca. 590-560 Ma and Stage III: ca. 550-440 Ma (Hibbard *et al.*, 2002), and docking onto the Laurentian passive margin is thought to have occurred at the end of Stage III during the Late Ordovician to Early Silurian Salinic orogeny (460-440 Ma; Hibbard *et al.*, 2002, 2007b). Hibbard *et al.* (1998, 2002) proposed that the original suture between the Carolina Zone and the Piedmont Zone of the Laurentian passive margin is marked by the Central Piedmont shear zone, an Alleghanian ductile thrust that tectonically truncated and buried the suture beneath the Carolina Zone (Figure 1.10b).

The mainly meta-igneous terranes that comprise the Carolina Zone include the supercrustal Roanoke Rapids, Spring Hope, Carolina, Augusta and Milledgeville terranes, and the infracrustal Charlotte, Crabtree, Raleigh, Triplet, Falls Lake, Dreher Shoals, Savannah River and Uchee terranes (Hibbard *et al.*, 2002). Based on observations made by Horton *et al.* (1989, 1991, 1994), the Hatteras terrane may be a possible higher grade extension of the Roanoke Rapids terrane (see discussion below). Consequently, the Hatteras terrane has been tentatively assigned to the Carolina Zone. Adjacent to the CBIS, Carolina Zone terranes of significance include the Roanoke Rapids and Hatteras terranes,

as mentioned above, as well as the Carolina, Spring Hope, Falls Lake and Crabtree terranes (Figure 1.9).

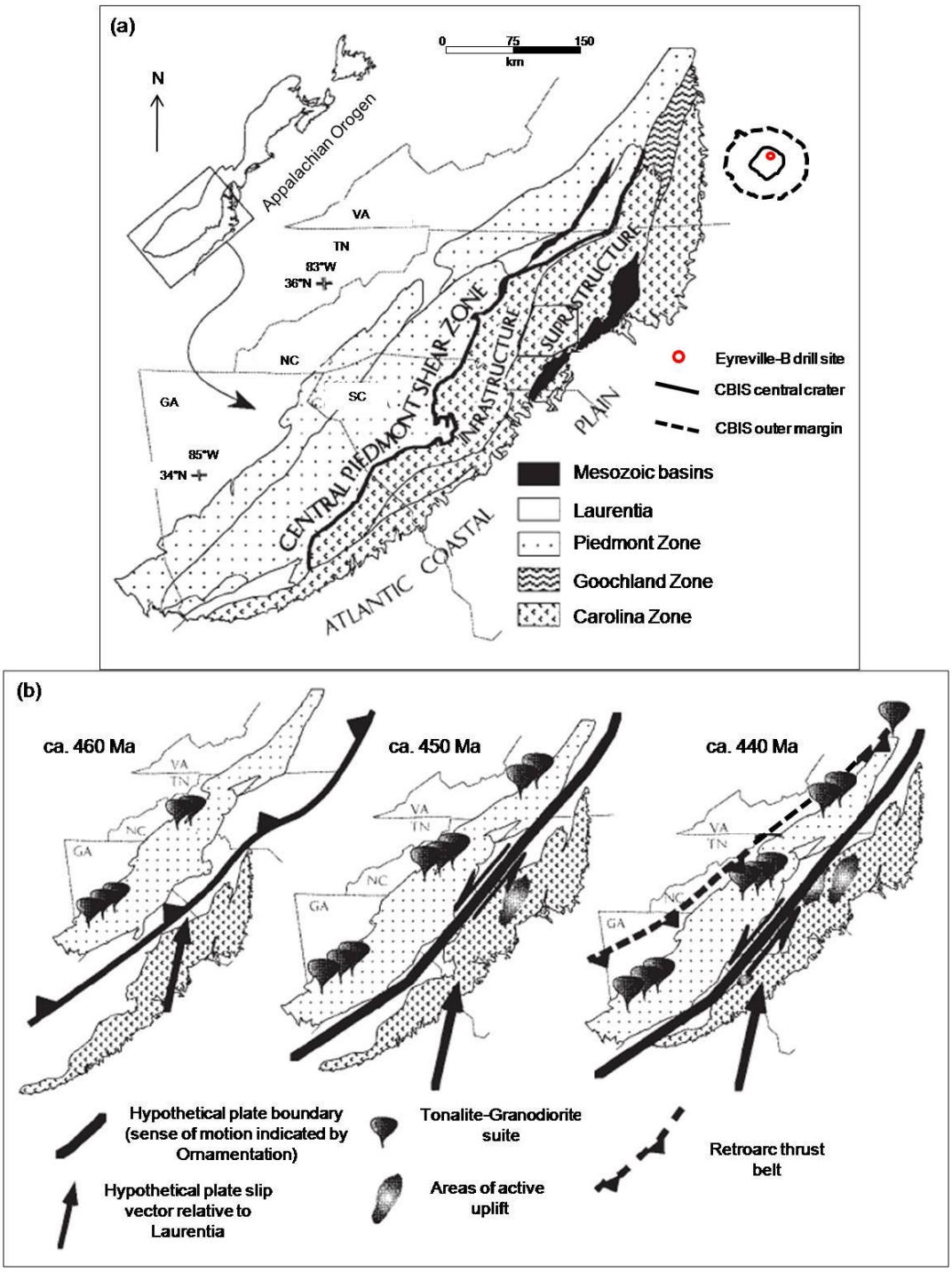

Figure 1.10: (a) Location of the suprastructural and infrastructural terranes of the Carolina Zone separated from the Piedmont Zone by the Central Piedmont shear zone within the Appalachian orogen. The approximate location of the CBIS has been included for reference purposes. (b) Depiction of the progressive accretion model for the docking of the Carolina Zone onto the Laurentian passive margin during the Salinic orogeny. Both diagrams modified after Hibbard (2000) and references therein, and Horton *et al.* (2005b) and references therein.

Roanoke Rapids terrane

The Roanoke Rapids terrane is a greenschist to epidote-amphibolite facies metavolcanic and metasedimentary sequence (Horton *et al.*, 1989; 1991; 2005b; Rankin, 1994). The volcanic arc terrane is divided into three major units: the Halifax County complex, the Roanoke Rapids complex and the Easonburg formation (Hibbard *et al.,* 2002).

Kite and Stoddard (1984) described the Halifax County complex as a low-grade mafic-ultramafic rock suite that ranges in composition from ultramafics to gabbroids to felsic plutonics to basaltic rocks. The Roanoke Rapids complex is a volcanic-plutonic complex, which comprises a trondhjemitic to quartz-diorite core surrounded by mainly metavolcanic and metavolcaniclastic rocks (Farrar, 1985; Hibbard *et al.*, 2002). The Easonburg Formation, a felsic volcanic and phyllitic volcaniclastic rock suite, appears to surround both the Halifax County and Roanoke Rapids complexes, even though the exact relationship between the formation and the two complexes has yet to be established (Farrar, 1985; Hibbard *et al.*, 2002).

Limited geochronological studies of the Roanoke Rapids terrane have resulted in a poorly constrained age for the terrane (Horton *et al.*, 1989; Hibbard *et al.*, 2002). However, the oldest dated rocks in the Carolina Zone occur within this terrane (Hibbard *et al.*, 2002). Horton and Stern (1994) obtained preliminary $^{207}Pb/^{206}Pb$ zircon ages of ca. 668 Ma for a metatonalite in the Roanoke Rapids complex and ca. 607 Ma for a metatonalite in the Easonburg formation (Hibbard *et al.*, 2002). Samson and Coler (2000) reported a U/Pb zircon age of 672 ± 2 Ma for a metagranodiorite that intrudes into the Roanoke Rapids complex, corresponding with Horton and Stern's (1994) study (Hibbard *et al.*, 2002). Kite and Stoddard (1984) proposed that the mafic-ultramafic Halifax County complex could be an island-arc ophiolite, which suggests that the terrane originated at least in part in an oceanic tectonic setting (Horton *et al.*, 1989; Rankin, 1994; Hibbard *et al.*, 2002). The ages reported above correspond to the first stage of magmatism and deposition recorded in the Carolina Zone (Stage I: pre-600 Ma; Hibbard *et al.*, 2002).

Hatteras terrane

Other than what is discussed in Horton *et al.* (1989, 1991, 1994), very little information is available for the Hatteras terrane. The amphibolite facies metamorphic complex comprises biotite gneiss and garnetiferous schist intruded by a suite of plutonic rocks, which range from granite to diorite in composition (Denison *et al.*, 1967; Daniel and Zietz, 1978; Horton *et al.*, 1989). Rb/Sr dating of these plutonic rocks has revealed ages of 583 to 685 Ma (Denison *et al.*, 1967; Russell *et al.*, 1981; Horton *et al.*, 1989, 1991, 1994). Despite the higher sensitivity of Rb/Sr whole rock systems to isotopic disturbance and resetting compared with U/Pb zircon systems (Pidgeon and Johnson, 1974), subsequent higher precision geochronological studies of the Hatteras terrane plutonic rocks have not been undertaken. Using the Rb/Sr results, however, it is possible that the wide age range may reflect Stage I and Stage II magmatism, as observed in other parts of the Carolina Zone (Stage I: pre-600Ma; Stage II: ca. 590-560 Ma; Hibbard *et al.*, 2002). The tectonic setting in which the Hatteras terrane was derived is currently unknown, although Horton *et al.* (1989) surmised that it may be a higher grade equivalent of the Roanoke Rapids terrane. Consequently, the Hatteras terrane may also be associated with island-arc volcanism.

Carolina terrane

Although exposed mainly in the Southern Appalachians, the Carolina terrane extends almost to the southwestern edge of the CBIS (Figures 1.9 and 1.10a; Horton *et al.*, 1989; Hibbard, 2000; Hibbard *et al.*, 2002). The terrane is subdivided into four metavolcanic-dominated sequences that comprise generally low-grade meta-igneous and metasedimentary rocks, namely the Virgilina, Albemarle, South Carolina and Cary sequences (Hibbard *et al.*, 2002). The Virgilina sequence, located in the northern portion of the Carolina terrane and closest to the CBIS, can be further subdivided into the Hyco Formation (a thick felsic-intermediate metavolcanic base), the Aaron Formation (overlying metaclastic turbidites) and the Virgilina Formation (a metabasalt that caps the previous two formations), which collectively form a roughly 8 km thick sequence (Hibbard *et al.*, 2002).

There is a general consensus that the Carolina terrane is a peri-Gondwanan terrane exotic to Laurentia and that it represents a long-lived supra-subduction zone magmatic arc system (Hibbard *et al.*, 2002; Hackley *et al.*, 2007). Based on isotopic data, Ingle *et al.* (2003) postulated that the Carolina

terrane was initially an oceanic arc (Virgilina sequence) that migrated towards Laurentia prior to the formation of the upper sequences, progressing from a juvenile arc to a more mature arc tectonic setting.

Stage I magmatism (pre-600 Ma) associated with the Carolina Zone is best documented in the Virgilina sequence in the Carolina terrane (Hibbard *et al.*, 2002). Glover and Sinha (1973) and Horton *et al.* (1999) dated the Hyco Formation of the Virgilina sequence using U/Pb zircon geochronology as Late Neoproterozoic (~620 ± 20 Ma and 620-616 Ma, respectively; Hackley *et al.*, 2007). These ages for the Virgilina sequence were confirmed by Wortman *et al.* (2000), who constrained the arc magmatism to have occurred during a limited time-frame of ~20 Myr, from 633 to 612 Ma (U/Pb zircon geochronology; Hibbard *et al.,* 2002). Additionally, Wortman *et al.* (2000) determined a tightly constrained U/Pb zircon age of 546 ± 3 Ma for the intruding Roxboro Metagranite (Hibbard *et al.*, 2002); the metagranite had previously been dated at 575 ± 20 Ma by Briggs *et al.* (1978) using Rb/Sr whole rock geochronology (Horton *et al.*, 1989). The new minimum age from the Roxboro Metagranite for the Virgilina sequence, thus, reflects Stage III (550-440 Ma) magmatism in the Carolina Zone (Hibbard *et al.*, 2002; Hackley *et al.*, 2007).

Spring Hope terrane

The Spring Hope terrane, located southwest of the Roanoke Rapids terrane (Figure 1.9), is dominated by greenschist facies mafic to felsic metavolcanic rocks with associated metaplutonic and metasedimentary rocks (Horton *et al.*, 1989; Hibbard *et al.*, 2002). The stratigraphy of the Spring Hope terrane is divided into a lower, predominantly felsic, metavolcanic sequence and an upper, predominantly metasedimentary sequence (after Carpenter *et al.*, 1995; Hibbard *et al.*, 2002). The terrane had previously been divided by Farrar (1985) into the lower Spring Hope, middle Stanhope and upper Smithfield formations but was later reclassified based on subsequent geochronological data (Hibbard *et al.*, 2002).

A metatuff from the lowest portion of the lower metavolcanic sequence was preliminarily dated at ca. 544 Ma by Horton and Stern (1994) using $^{207}Pb/^{206}Pb$ zircon geochronology, whilst Goldberg (1994) obtained a U/Pb zircon age of 590 ± 3 Ma for a felsic crystal tuff in the middle portion of the lower

metavolcanic sequence (Hibbard *et al.*, 2002). High-K tholeiitic metabasalts were identified by Boltin and Stoddard (1987), leading them to suggest that these rocks were generated in a supra-subduction zone environment built on either oceanic crust or very thin continental crust (Horton *et al.*, 1989; Hibbard *et al.*, 2002). This most likely occurred during Stage II magmatism in the Carolina Zone (Hibbard *et al.*, 2002).

Falls Lake terrane

The Falls Lake terrane, located to the southwest of the CBIS (Figure 1.9), is a mélange complex that consists of metamorphosed mafic and ultramafic blocks as well as bodies of micaceous quartzofeldspathic material located within pelitic schists (Horton *et al.*, 1989, 1991; Hibbard *et al.*, 2002). Horton *et al.* (1986) and Stoddard *et al.* (1989) noted that the blocks and bodies ranged from pebbles to up to entities ca. 2 km in length (Hibbard *et al.*, 2002). Horton *et al.* (1989) suggested that the terrane formed as a result of both sedimentary and tectonic processes, such as observed in an accretionary wedge. According to Horton *et al.* (1986, 1989, 1991), the Falls Lake terrane and underlying Carolina terrane were thrust together onto the Crabtree terrane, after which all three terranes underwent Late Palaeozoic folding and metamorphism.

Although previously thought to be a coarser facies of the pelitic schist matrix, geochronological evidence suggests that the quartzofeldspathic bodies are of different origin to the matrix and mafic and ultramafic blocks and that they could be either meta-igneous blocks or intrusive bodies (Horton *et al.*, 1994; Hibbard *et al.*, 2002). Goldberg (1994) determined that the quartzofeldspathic bodies crystallised at approximately 590 Ma based on $^{207}Pb/^{206}Pb$ zircon dating methods; an inherited component of Proterozoic age (~2.2 Ga) was also revealed (Hibbard *et al.*, 2002). These age data have proved ambiguous since the ~590 Ma age could represent crystallisation if the quartzofeldspathic body were a structural block, or the ~590 Ma age could represent the minimum age of the melange complex if the body intruded into the pelitic schist matrix (Horton *et al.*, 1994; Hibbard *et al.*, 2002).

Crabtree terrane

The Crabtree terrane is located to the southwest of the CBIS (Figure 1.9) and comprises a mainly metasedimentary sequence that is intruded by the Crabtree Creek pluton (Blake, 1994; Hibbard *et al.*, 2002). The amphibolite facies metasedimentary sequence consists of felsic gneiss, garnet-staurolite schist, garnet-kyanite schist and graphitic schist (Blake, 1994; Robitaille, 2004). Stoddard *et al.* (1978) proposed felsic igneous or arkosic protoliths for the felsic gneiss, and Horton *et al.* (1986) suggested that the highly aluminous and graphitic schists were derived from muds deposited in a restricted basin environment. Lumpkin *et al.* (1994) suggested that the Crabtree terrane is linked to the Spring Hope terrane based on the presence of graphitic schist and phyllite in the latter terrane immediately east of the Nutbush Creek fault, and is, thus, a deeper crustal equivalent of the Spring Hope terrane (Hibbard *et al.*, 2002).

The leucogranitic to granitic Crabtree Creek pluton (Blake and Stoddard, 1993) was dated by $^{207}Pb/^{206}Pb$ zircon geochronology, producing preliminary ages of 542 Ma by Horton and Stern (1994) and 554, 564 and 566 Ma by Goldberg (1994). These ages have been interpreted to represent the crystallisation age (Hibbard *et al.*, 2002). Consequently, the metasedimentary sequence it intruded into is Neoproterozoic in age or older (Hibbard *et al.*, 2002).

1.1.2.2 Sussex terrane

The Sussex terrane lies entirely beneath the Atlantic Coastal Plain sediments, directly to west of the CBIS (Figure 1.9; Horton *et al.*, 1989, 1991). The terrane consists of low grade, foliated, mafic volcanic rocks, ultramafic rocks, gabbro, metadiorite and phyllite and has been suggested to represent a mélange complex; the predominant fraction of mafic rocks may be reflective of an oceanic crust source (Horton *et al.*, 1989, 1991; Rankin, 1994). The age of the terrane has yet to be constrained.

Although it is not considered to form part of the Carolina Zone, the Sussex terrane lies east of the Goochland terrane (a Grenville-age terrane of disputed Laurentian or peri-Gondwanan origins; Bartholomew and Tollo, 2004; Bailey and Owens, 2012) and appears to be interleaved with the Roanoke Rapids terrane in Figure 1.9. The western border of the Sussex terrane was interpreted by

Glover (1989) to represent the suture between the Carolina and Goochland terranes. Located northeast of the Central Piedmont shear zone, which marks the location of the Rheic suture (Hibbard *et al.*, 2000, 2002), the Sussex terrane appears to lie outboard of this feature, and, consequently to be part of the peri-Gondwanan realm.

1.1.2.3 Goochland terrane

The Goochland terrane lies to the northwest of the CBIS and is separated from the Roanoke Rapids terrane by the late Palaeozoic Hylas fault zone (Figure 1.9); it comprises multiply deformed and metamorphosed gneiss, amphibolite, granite and anorthosite (Farrar, 1984; Spears *et al.*, 2004). For the purposes of this study, the Goochland terrane includes the Raleigh terrane, which was previously thought to be a southern extension of the Goochland terrane (Farrar, 1984).

The structurally lowest unit is the State Farm Gneiss, a felsic to intermediate gneiss derived from both igneous and sedimentary sources that outcrops in a series of domes (Farrar, 1984; Rankin, 1994; Spears *et al.*, 2004). The State Farm Gneiss is intruded by a small suite of Neoproterozoic A-type granitoids (~630 Ma; Owens and Tucker, 2003) and is structurally overlain by the Sabot Amphibolite and the Maidens Gneiss (Horton *et al.*, 1989; Rankin, 1994; Aleinikoff *et al.*, 1996; Spears *et al.*, 2004). The Sabot Amphibolite is a 700-1000 m thick amphibolite inter-layered with biotite gneiss (Farrar, 1984; Aleinikoff *et al.*, 1996). The protoliths for the Sabot Amphibolite are mafic lava flows or volcaniclastic rocks intercalated with sediments (Goodwin, 1970; Poland, 1976; Marr, 1985; Aleinikoff *et al.*, 1996). The Maidens Gneiss is a heterogeneous metamorphic suite of layered metavolcanic and metasedimentary units (Poland, 1976; Farrar, 1984; Rankin, 1994; Aleinikoff *et al.*, 1996). The State Farm Gneiss and the Sabot Amphibolite are exposed in three en echelon doubly plunging antiforms, surrounded by the Maidens Gneiss (Rankin, 1994). Aleinikoff *et al.* (1996) suggested that the Sabot Amphibolite and Maidens Gneiss belong to the same lithostratigraphic unit based on the similarities of the intercalated gneisses and amphibolites, with only their relative proportions differing.

Mapping by Farrar (1984) and Marr (1985) revealed that a small anorthosite body, the Montpelier Anorthosite, intrudes all major units of the Goochland terrane, including that of the Sabot Amphibolite and Maidens Gneiss (Rankin, 1994; Horton *et al.*, 1989; Aleinikoff *et al.*, 1996; Spears *et al.*, 2004).

Farrar (1984) also observed relict granulite facies metamorphism throughout the Goochland terrane overprinted by a later amphibolite facies metamorphic event (Rankin, 1994; Horton *et al.*, 1989; Aleinikoff *et al.*, 1996). Farrar (1984) interpreted the granulite facies metamorphism as Mesoproterozoic (Grenvillian) and the amphibolite facies metamorphic event as Palaeozoic (Alleghanian; Spears *et al.*, 2004).

Using U/Pb zircon geochronology, Mesoproterozoic ages were determined for the State Farm Gneiss (~1046-1023 Ma; Owens and Tucker, 2003), the Montpelier Anorthosite (1045 ± 10 Ma; Aleinikoff *et al.,* 1996) and a granitic gneiss within the Maidens Gneiss (1035 ± 5 Ma; Horton *et al.*, 1995). Based on mapping by Farrar (1985) and Marr (1985) and the inferred cross-cutting relationships, Aleinikoff *et al.* (1996) postulated that the Sabot Amphibolite and Maidens Gneiss are older than the emplacement and crystallisation of the Montpelier Anorthosite and are thus at least Mesoproterozoic in age. Recent U/Pb zircon geochronology of the Sabot Amphibolite and Maidens Gneiss, however, has brought this hypothesis into question. Martin and Owens (2012) obtained a Late Neoproterozoic age (552 ± 11 Ma) for protolith crystallization from fine-grained felsic layers within the Sabot Amphibolite whilst Owens *et al.* (2010a) obtained three Devonian crystallisation ages (407 ± 2 Ma; 390 ± 3 Ma; 371 ± 3 Ma) from meta-igneous layers in the Maidens Gneiss. Shirvell *et al.* (2004) attempted to date the granulite facies metamorphic event based on electron microprobe Th-U-total Pb chemical dating of monazite in the more typical lithologies of the Maidens Gneiss. Her results yielded ages no older than ~420 Ma, which led her to conclude that the Goochland terrane reflects high-grade Acadian, not Grenvillian, metamorphism. This conclusion is supported by Martin and Owens' (2012) determination of an Upper Ordovician to Early Devonian zircon age (450-410 Ma) for the metamorphic event preserved in felsic interlayers within the Sabot Amphibolite.

Interestingly, the Mesoproterozoic State Farm Gneiss and Montpelier Anorthosite are located in the eastern-most extent of the Goochland terrane, whereas the Palaeozoic ages for the Maidens Gneiss were obtained in the western portion of the terrane (Spears *et al.*, 2004). Furthermore, no Neoproterozoic granites have been identified within the Maidens Gneiss; they appear to only occur within the State Farm Gneiss (Owens and Tucker, 2003; Spears *et al.*, 2004). Spears *et al.* (2004)

suggested that this is evidence that an unconformity or structural discontinuity exists between the western and eastern parts of the Goochland terrane.

Various authors have suggested that the Goochland terrane is of Laurentian origin based on similarities of the Mesoproterozoic rocks and Neoproterozoic A-type granites with exposed rocks of Laurentian heritage in the northern Virginia Blue Ridge (Glover *et al.*, 1978; Farrar, 1984; Glover, 1989; Aleinikoff *et al.*, 1996; Owens and Tucker, 2003; Owens and Samson, 2004). It was suggested by Bartholomew and Tollo (2004) that the Goochland terrane is a translated block of Laurentian crust that was originally rifted from the northern part of the Central Appalachians during the break-up of the supercontinent Rodinia (Bailey and Owens, 2012). Previously, other authors suggested a peri-Gondwanan origin for the Goochland terrane (Rankin *et al.*, 1989; Horton *et al.*, 1989. 1991; Hibbard and Samson, 1995; Bailey *et al.*, 1995).

1.1.2.4 Chopawamsic terrane

The Chopawamsic terrane, to the northwest of the CBIS (Figure 1.9), is separated from the Goochland terrane by the Spotsylvania high-strain zone (Rankin, 1994; Spears *et al.*, 2004). The Chopawamsic terrane is composed of mixed mafic and felsic volcanic arc rocks interlayered with non-volcanic metagreywacke and metapelite that are intruded by plagiogranite and trondhjemite (Horton *et al.*, 1989, 1991; Rankin, 1994). Three units make up the Chopawamsic terrane: the Ta River Metamorphic Suite, the Chopawamsic Formation and the James Run Formation (Rankin, 1994). The Ta River Metamorphic Suite has been interpreted to be an eastern, more mafic (possibly oceanic) facies of the Chopawamsic terrane consisting of amphibolite interlayered with biotite gneiss and schist (Pavlides, 1980; Horton *et al.*, 1989, 1991; Rankin, 1994). The Chopawamsic Formation (the most extensive subunit of the Chopawamsic terrane; Spears *et al.*, 2004) exhibits rare earth and trace element geochemical signatures typical of a tholeiitic island arc suite with some calc-alkalic components (Horton *et al.*, 1989, 1991). The James Run Formation is a correlative of the Chopawamsic Formation in Maryland (Rankin, 1994).

Horton *et al.* (1998) and Coler *et al.* (2000) determined the age of the Chopawamsic Formation to be ~470 Ma (Spears *et al.*, 2004). Intruding the terrane in central Virginia, the Columbia Granite was

dated at 457 ± 7 Ma using U/Pb SIMS (secondary ion mass spectrometry) zircon geochronology (Wilson, 2001; Spears *et al.*, 2004). The Occoquan Granite, which intrudes both the Chopawamsic and Potomac terranes where the former is thrusted onto the latter (Horton *et al.*, 1989), was determined by Aleinikoff *et al.* (2002) using SHRIMP (sensitive high resolution ion microprobe) U/Pb zircon geochronology to be Middle Ordovician in age (472 ± 4 Ma). Mose and Nagel (1982) previously determined a Late Cambrian age of 494 ± 14 Ma (Rb/Sr whole rock) for the Occoquan Granite, which led them to suggest that the Chopawamsic and Potomac terranes were amalgamated during the Penobscottian orogeny (Horton *et al.*, 1989, 1991; Rankin, 1994). Based on the newer, more reliable age evidence, Drake (1998) and Aleinikoff *et al.* (2002) proposed that the Chopawamsic terrane accreted to Laurentia during the Taconian orogeny (ca. 495-440 Ma; Hibbard *et al.*, 2007a). This corresponds with Coler *et al.*'s (2000) hypothesis that the Chopawamsic terrane is a volcanic arc of Ordovician age that developed on continental crust, outboard of Laurentia, and that it was accreted in the Late Ordovician during the Taconian orogeny (Glover *et al.*, 1989; Spears *et al.*, 2004).

1.1.2.5 Potomac composite terrane

The Potomac composite terrane is located approximately 200 km to the northwest of the CBIS (Figure 1.9) and consists of a stack of thrust sheets containing mélange complexes (both tectonic and olistostromal) and fragments of probable ophiolites, volcanic arcs and submarine-fan turbidites (Drake and Morgan, 1981; Horton *et al.*, 1989, 1991; Rankin, 1994). Horton *et al.* (1989, 1991) interpreted a number of terrane fragments to be part of the Potomac composite terrane; these include the Piney Branch Complex (ophiolite fragment), the Peters Creek Schist (a high-energy submarine-fan ophiolitic mélange), the Piney Run Formation (ophiolitic mélange; Crowley, 1976), the Annandale Group (a suprafan deposit) and the Wissahickon Formation (turbidite-ophiolitic mélange ; Drake, 1986). In the vicinity of the CBIS, the Potomac composite terrane can be divided into three mappable units in Virginia, namely, the Mather Gorge (turbidites), Sykesville (diamictite and amphibolite) and Laurel formations (quartz and meta-arenite; Drake and Froelich, 1997; Drake, 1998; Kunk *et al.*, 2004).

In the northern part of the Central Appalachians (northern Virginia to the Pennsylvania-Maryland state border), thrust sheets of the Potomac composite terrane are underlain by precursor sedimentary mélanges characterised by olistoliths of the overlying thrust sheets; such sedimentary mélange

complexes have not been identified south of Virginia (Drake, 1985; Horton *et al.*, 1989, 1991). The thrust stack was amalgamated and deformed and then unconformably overlain by the Popes Head Formation, a turbiditic and tuffaceous rock unit that includes upright isoclinal folds with strong axial-surface schistosity known as the Clifton folds (Drake and Lyttle, 1981; Drake, 1987; Milici, 1987; Horton *et al.*, 1989, 1991; Rankin, 1994; Aleinikoff *et al.*, 2002). The previously mentioned Occoquan Granite (see Section 1.1.2.5) intruded into this package along with the Chopawamsic terrane at 472 ± 4 Ma (Aleinikoff *et al.*, 2002). The contact between the Occoquan Granite and Popes Head Formation is characterised by veins of granite concordant to the schistosity of the Popes Head Formation, with foliation observed in the granite approximately parallel to the schistosity (Drake, 1987; Aleinikoff *et al.*, 2002). Drake (1987) noted that quartz-rod lineations in the Occoquan Granite appear to be related to the Clifton phase folding, indicating a synkinematic emplacement of the granite (Rankin, 1994; Aleinikoff *et al.*, 2002). Based on these observations, Drake (1998) and Aleinikoff *et al.* (2002) proposed that the Clifton phase folding, associated schistosity and regional metamorphism are early manifestations of the Taconian orogeny.

1.1.2.6 Jefferson terrane

The Jefferson terrane (also known as the Eastern Blue Ridge Province; Tull *et al.*, 2007) is an elongated terrane located west of the Potomac composite terrane (Figure 1.9), which extends the length of the Central and Southern Appalachians (Horton *et al.*, 1989, 1991). It is a metamorphosed accretionary wedge, comprising gneiss (metasandstone), schist (metapelite), amphibolite (metabasalt) and ultramafics (fragmented ophiolite), that was thrust onto the Laurentian margin during the Taconian orogeny (Horton *et al.*, 1989, 1991; Rankin, 1994).

According to Rankin *et al.* (1986, 1988, 1989), Stanley and Ratcliff (1985) and Horton *et al.* (1989, 1991), the Jefferson terrane's accretionary wedge developed over an east-dipping subduction zone on eastern, non-Laurentian basement during closing of the Iapetus Ocean's eastern margin. This resulted in an arc complex and is analogous with the western portion of the Brompton-Cameron terrane in New England (Rankin, 1994). Horton *et al.* (1989) noted that the easiest way to generate a westward-verging, subduction-related accretionary wedge that contains ophiolitic fragments would be if the formation of the accretionary wedge also occurred on the eastern side of the Iapetus Ocean.

This interpretation implies that the western leading edge of the accretionary wedge forms the Iapetus or Taconic suture; and makes the Jefferson terrane exotic in nature (Rankin, 1988; Horton *et al.*, 1989). On the other hand, however, lithologic similarities between the accretionary wedge and the Laurentian slope-rise deposits (Taconic allochthons and Hamburg klippe) led Zen *et al.* (1986) to argue that these rocks were a deep-sea facies of pre-Silurian Laurentian cover rocks that were later obducted onto the North American craton; the westward vergence of the accretionary wedge may have formed through underplating of an obducting ocean slab, incorporating ophiolitic fragments into the underplating material (Horton *et al.*, 1989).

1.1.3 Sedimentation following the cessation of the Appalachian orogenies

Continental rifting and the resultant break-up of the supercontinent Pangaea began during the Carboniferous and Permian with transtensional graben formation (Rankin, 1994; Thomas, 2006; Withjack *et al.*, 2012). Final continental break-up of Pangaea occurred during the Middle Jurassic, with the formation of oceanic crust and subsidence of the new continental margin being followed by deposition of onlapping sediments, concluding the rifting cycle (Veevers, 1994). The North American continental margin evolved from an active extensional margin during the rifting stage into a passive margin during the drifting stage (opening of the Atlantic Ocean; Rankin, 1994).

The subsequent sedimentation onto the North American passive margin is preserved in the Atlantic Coastal Plain, a ~18-km-thick, seaward-thickening sequence of Early Cretaceous to Holocene (ca. 145 Ma to present time) deposits that fill the southern end of the elongate offshore Baltimore Canyon trough (Poag *et al.*, 2004). Covering the underlying Appalachian orogen, 27 formal sedimentary formations have been identified in the Atlantic Coastal Plain proximal to the CBIS in southeastern Virginia (Poag *et al.*, 2004 and references therein). These dominantly unconsolidated to poorly consolidated sediments can be separated into seven pre-impact and 20 post-impact sedimentary formations (Figure 11; Poag *et al.*, 2004).

The seven pre-impact sedimentary units of the Atlantic Coastal Plain in the vicinity of the CBIS are Lower Cretaceous to lowermost Upper Eocene in age (ca. 145-35.5 Ma) and are recognised based on the combination of lithology and biozonation (Figure 1.11; Poag *et al.*, 2004). In ascending order

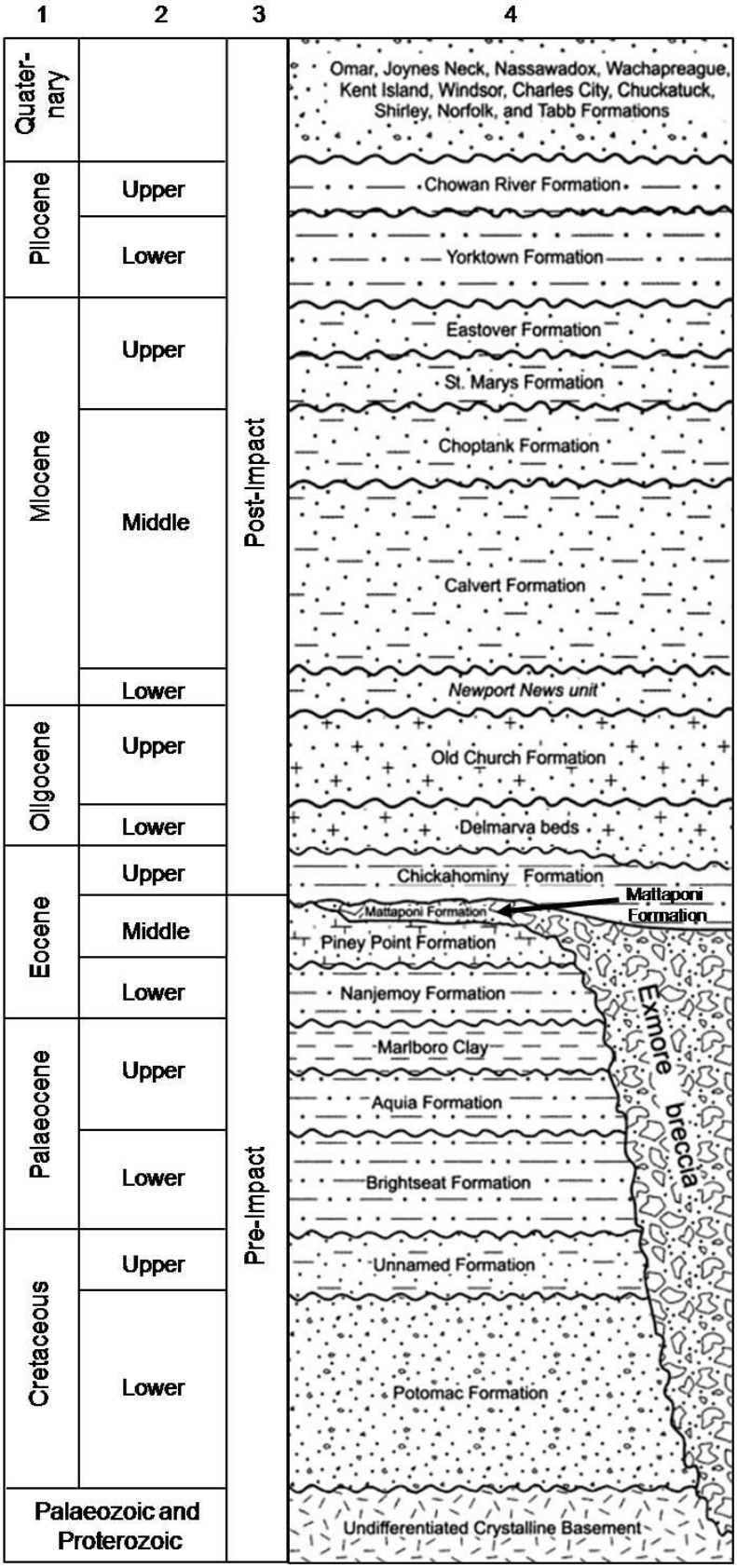

Figure 1.11: Generalised stratigraphic column for the pre-impact and post-impact sediments in southeastern Virginia in the vicinity of the CBIS (modified after Poag *et al.*, 2004). Undulating horizontal lines represent unconformities. Legend: 1 = Era; 2 = Epoch; 3 = Time of deformation relative to the impact; 4 = Rock units.

these sedimentary units comprise the Potomac, Unnamed Upper Cretaceous Beds, Brightseat, Aquia, Marlboro Clay, Nanjemoy and Piney Point formations (Figure 1.11; Poag *et al.*, 2004).

Immediately following the Chesapeake Bay impact event (see Section 1.2), deposition of marine sediments resumed owing to the location of the CBIS in a relatively deep continental shelf (Poag *et al.*, 2004). This prevented the erosion of original features of the crater other than those of distal margins (Poag *et al.*, 2004). However, just prior to this resumption of deposition, the wash-back of impact-generated tsunami waves produced an unusually thick impact breccia body inside the crater, known as the Exmore breccia, named after the town of Exmore in Virginia, where it was first cored (Powars *et al.*, 1992; Poag *et al.*, 1997a; Poag *et al.*, 2004). Poag *et al.* (2004) inferred that the bulk of this syn-impact crater-fill deposit formed from fragments of sedimentary rocks and crystalline basement rocks, sand-sized particles up to km-sized blocks, that were violently disrupted initially by the impact and then further deformed and turbulently mixed together by the resulting water-column collapse and surge-back. The Exmore breccia completely covers and fills the inner basin and annular trough of the impact crater (see Section 1.2), with the proposed thickness of the breccia in the inner crater of ~ 1.2 km, while in the annular trough it is ~ 200 m in the western half, but thickens up to ~ 400 m eastwards (Poag *et al.*, 2004).

After the generation of the Exmore breccia, the resumption of sedimentation onto the crater was immediate (Poag *et al.*, 2004), burying it beneath 20 post-impact sediment formations (Figure 1.11). These formations include the Chickahominy, Delmarva beds, Old Church, Calvert, Choptank, St. Mary's, Eastover, Yorktown, Chowan River formations and the Quaternary Tabb, Norfolk, Shirley, Chuckatuck, Charles City, Windsor, Kent Island, Wachapreague, Nassawadox, Joynes Neck and Omar formations (Figure 1.11; Poag *et al.*, 2004).

1.2 The Chesapeake Bay impact structure

The CBIS is a late Eocene (35.4 ± 1 Ma; Horton and Izett, 2005) complex marine crater (Horton *et al.*, 2005a). Despite being buried beneath several hundreds of metres of post-impact sediments (see Section 1.1.3; Figure 1.11), geophysical studies and drilling programmes have revealed that the

structure is approximately 1.3-2 km deep and 85 km across and is characterised by an ~38 km wide central crater (inner basin in Figure 1.12) and an ~24 km wide annular trough, creating a distinctive "inverted sombrero" shape (Figure 1.1; Poag *et al.*, 2004; Horton *et al.*, 2005b; Gohn *et al.*, 2004a, 2009). The central crater has three elements: the central uplift (central peak in Figure 1.12), an irregular peak ring and the intervening crater floor or moat, the deepest part of the CBIS (Poag *et al.*, 1999, 2004; Horton *et al.*, 2005a, 2009a; Gohn *et al.*, 2004, 2008, 2009).

The central uplift consists of crystalline rock with a diameter of 15-20 km, rising to a peak 900 m above the central crater floor (Figure 1.12; Poag *et al.*, 2002; Horton *et al.*, 2005a). The irregular peak ring on the margin of the central crater is composed of uplifted basement material and rises to a maximum height of 1000 m above the central crater floor (Figure 1.12; Poag *et al.*, 1999, 2004; Horton *et al.*, 2005a; Gohn *et al.*, 2009). The moat of the central crater is 2 km at its deepest point, and contains fallback and slump deposits (Figure 1.12; Poag *et al.*, 2004; Horton *et al.*, 2005a). Surrounding the central crater, the annular trough is a roughly circular, flat-floored, highly faulted and inwardly slumped structure (Figure 1.12; Poag *et al.*, 1999, 2004; Horton *et al.*, 2005a; Gohn *et al.*, 2009).

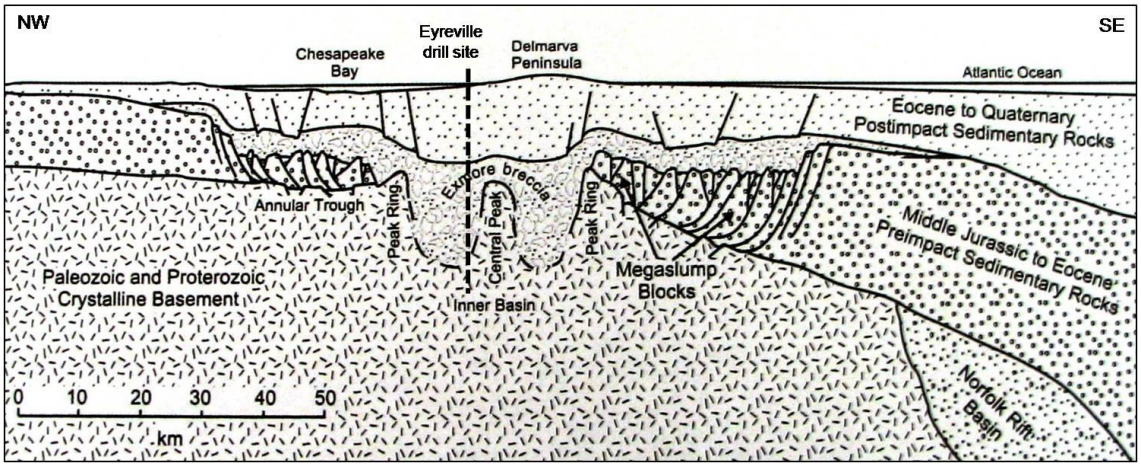

Figure 1.12: Geological cross-section of the CBIS from NW to SE showing the relative locations of the central zone (inner basin, central peak, peak ring), the annular trough and the ICDP-USGS Eyreville drill site (modified after Poag *et al.*, 1999, 2004; Gohn *et al.*, 2008, 2009).

The character of the target into which the Chesapeake Bay bolide excavated into can be divided into three components with increasing depth: sea water, clastic sediments and crystalline rocks (Horton *et al.*, 2005a). The uppermost target component, sea water, is estimated to have been 0-340 m deep at

the impact site, with water depth increasing eastwards across the crater (Horton *et al.*, 2005a). The second component, clastic sediments, forms part of the Atlantic Coastal Plain sediments and has already been discussed in Section 1.1.3. Crystalline rocks comprise the deepest target component and include Proterozoic and Palaeozoic basement rocks of the Appalachian orogen discussed in Section 1.1.2.

1.2.1 Previous studies of the Chesapeake Bay impact structure

Sedimentary and structural evidence for a large crater in the Chesapeake Bay have been recorded since the 1940's through geo-hydrological studies, although the extraterrestrial significance of the evidence was not fully realized until 50 years later when it was linked to a late Eocene impact (Poag *et al.*, 1992, 1994b; Poag, 1996; 1997a, 1999c; Koeberl *et al.*, 1996; Powars and Bruce, 1999). During the intervening years, a large database of subsurface stratigraphic analyses, derived from more than 200 uncored boreholes, was produced and published by several authors, including (amongst others) Cederstrom (1945a, 1945b, 1946), Brown *et al.* (1972), Teifke (1973), Gibson (1983), Ward and Krafft (1984), Ward and Strickland (1985), Mixon *et al.* (1989) and Poag and Ward (1993; Poag *et al.*, 2004). This database was combined with extensive outcrop studies to establish a regional and structural framework for the south-eastern Virginia sedimentary rocks located outside the crater rim (Poag *et al.*, 2004). A complementary geological framework for the crystalline basement beneath the Virginia Coastal Plain was generated from regional geophysical surveys and rare deep well data published by many authors, including (amongst others) Ewing *et al.* (1937), Woollard *et al.* (1957), LeVan and Pharr (1963), Taylor *et al.* (1968), Sabet (1973), Johnson (1977), Hawarth *et al.* (1980) and Thomas *et al.* (1989; Poag *et al.*, 2004).

The existence of the Chesapeake Bay impact crater was revealed through a combination of sample analysis from borehole cores drilled by the USGS and Virginia Department of Environmental Quality (VDEQ) between 1986 and 1992, the recognition of an offshore layer of late Eocene impact ejecta at the Deep Sea Drilling Site 612 and subsequent analysis of marine seismic-reflection data (Powars *et al.*, 1987, 1990, 1992, 1993; Bohor *et al.*, 1988; Glass, 1989; Obradovich *et al.*, 1989; Poag *et al.*, 1991, 1992, 1994; Horton *et al.*, 2005a). Extensive structural and stratigraphic documentation of the

CBIS based on the seismic-reflection data followed (Poag and Aubrey, 1995; Koeberl *et al.*, 1996, 2001; Poag, 1996, 1997, 2000; Poag *et al.*, 1999a, 1999b; Powars and Bruce, 1999; Powars, 2000).

Poag and Aubry (1995), Koeberl *et al.* (1996), Poag (1996, 1997, 2000), Poag *et al.* (1999a, 1999b), Powars and Bruce (1999) and Powars (2000) provided the initial structural and stratigraphic documentation of the CBIS. However, many fundamental concepts regarding the CBIS were based on untested hypotheses (Horton *et al.*, 2005a). As a result, the Chesapeake Bay Impact Crater Drilling Project was established in 2000 to elucidate the various aspects of the CBIS, including the physical characteristics, geologic history, formative processes, hydrologic effects, and water-resource implications (Horton *et al.*, 2005a). Figure 1.13 shows the locations of a number of other borehole cores drilled into the CBIS, including the ICDP-USGS Eyreville borehole core. The five borehole cores (Bayside, USGS-NASA Langley, North and Watkins School and ICDP-USGS Eyreville borehole cores) have been drilled since 2000 (Horton *et al.*, 2005a; Gohn *et al.*, 2008, 2009).

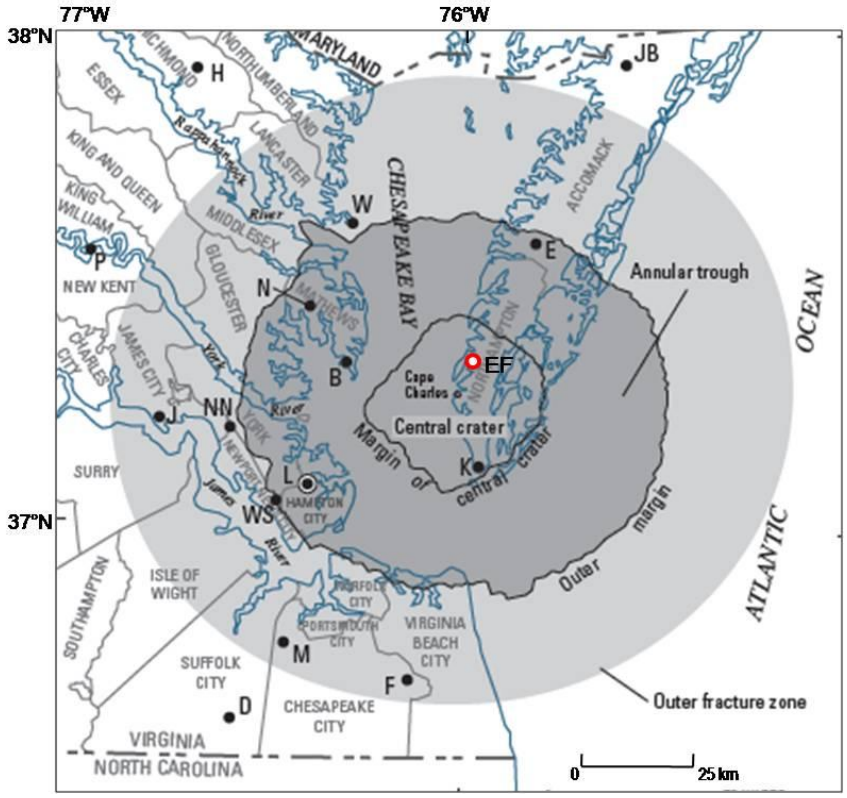

Figure 1.13: Regional map of the CBIS with the locations of borehole cores in southeastern Virginia, including the ICDP-USGS Eyreville borehole core (after Horton *et al.,* 2005a, 2005b; Gohn *et al.*, 2008, 2009). Symbols: B = Bayside; D = Dismal Swamp; E = Exmore; EF = ICDP-USGS Eyreville; F = Fentress; H = Haynesville; J = Jamestown; JB = Jenkins Bridge; K = Kiptopeke; L = USGS-NASA Langley; M = MW4-1; N = North; NN = Newport News Park 2; W = Windmill Point; WS = Watkins School.

1.2.2 Evolution of the Chesapeake Bay impact event

Prior to the Chesapeake Bay impact, passive margin sediments of the Atlantic Coastal Plain covered the Appalachian orogen (Figure 1.14a; Section 1.1.3). At 35.4 ± 1 Ma, the Chesapeake Bay bolide impacted into these sediments and the underlying crystalline basement rocks (Figure 1.14b; Horton and Izett, 2005). Excavation and subsequent inward slumping of unconsolidated, wet sediments of the shallow ocean created the wide, shallow, annular trough; the central crater excavated into the underlying consolidated sediments and crystalline basement rocks (Figure 1.14b; Horton *et al.*, 2005a). This excavation of a multi-layered target created the inverted sombrero" shape characteristic of the CBIS (Figure 1.12; Horton *et al.*, 2005a).

The shockwave produced by the impact of the bolide into the target material initially forced the transport of material outward and upward, causing vaporisation, melting and shock metamorphism in the target material (Figure 1.14b; Horton *et al.*, 2005a). The formation of the bowl-shaped transient crater (transient cavity in Figure 1.14b) was due to the downward expansion of the shockwave, which produced shock deformation (and the associated faulting and fracturing), the formation of melts lining the transient cavity, the generation of an ejecta curtain, and the upliftment of the crater rim (Figure 1.14b; Horton *et al.*, 2005a). The sudden lack of overburden caused fractures to open, allowing the emplacement of lithic and suevitic dike breccias (Gohn *et al.*, 2008).

Once expansion of the transient crater ceased, the central crater and central uplift experienced rebound and collapse concurrently with massive rock failure and inward slumping of water-saturated sediments (crater units A and B in Figure 1.14c) within the annular trough, continuing into the central crater beyond, and surge-back effects from subsequent water-column collapse (Figure 1.14c; Poag *et al.*, 2004; Horton *et al.*, 2005a). Included in the fallback and slump deposits within the central crater are displaced rock slabs (megablocks), which were transported into the central crater by the ocean resurge processes from either the transient crater rim or adjacent areas outside of the transient crater (Gohn *et al.*, 2008). Distances travelled by these megablocks may be in excess of 5 km (Gohn *et al.*, 2008; Horton *et al.*, 2009a).

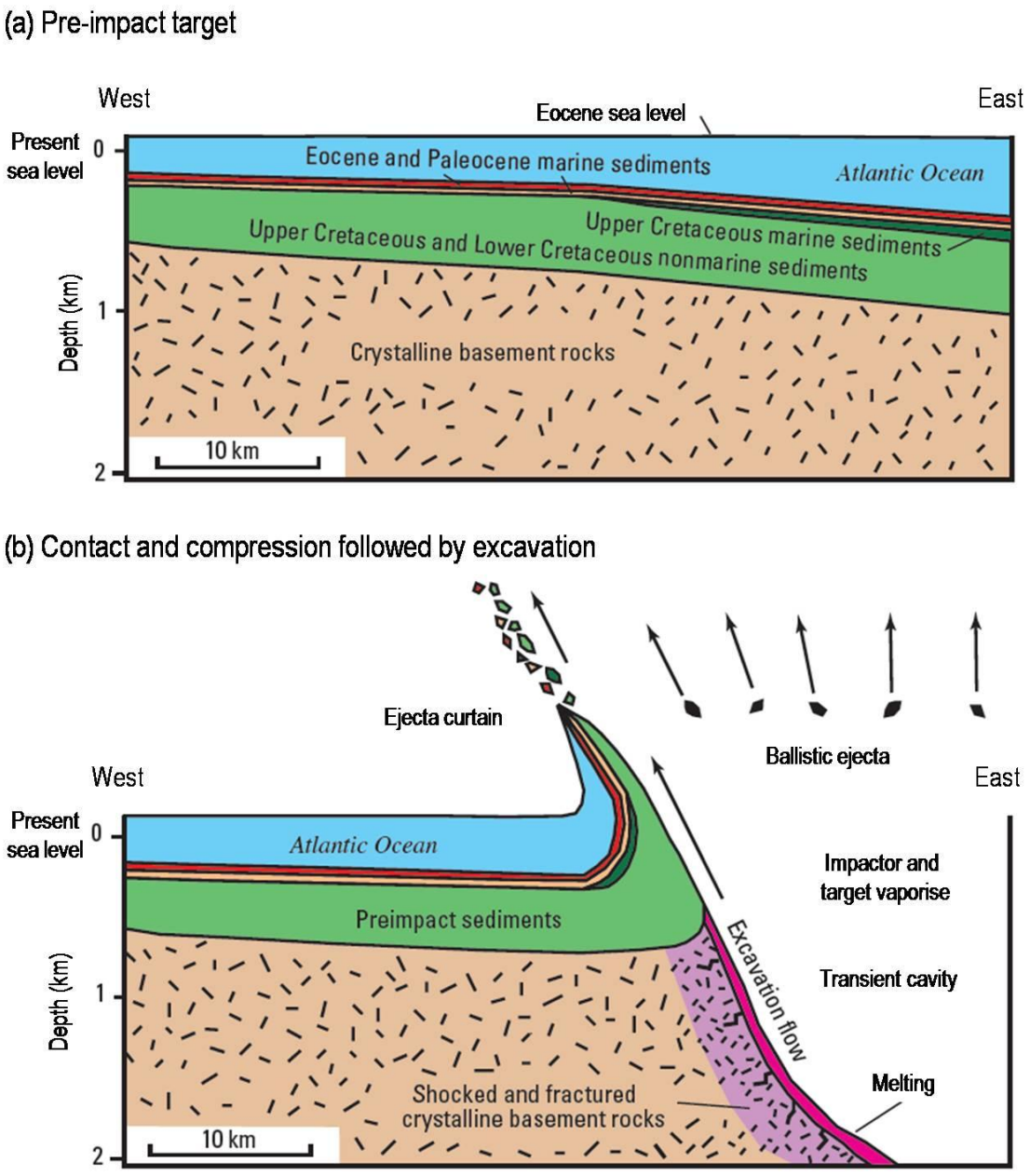

Figure 1.14: Schematic cross-sections illustrating the proposed sequence of events for the formation of the CBIS (Horton *et al.*, 2005a): (a) Pre-impact target. (b) Contact and compression stage of the impact followed by excavation of the target material. (c) Crater modification by collapse, slumping blocks and resurging water (A and B represent crater units; see text for explanation). (d) Burial of the impact crater by post-impact marine sediments. Locations of the USGS-NASA Langley and ICDP-USGS Eyreville borehole cores in (d) are included for reference purposes. Diagram modified after Horton *et al.* (2005a).

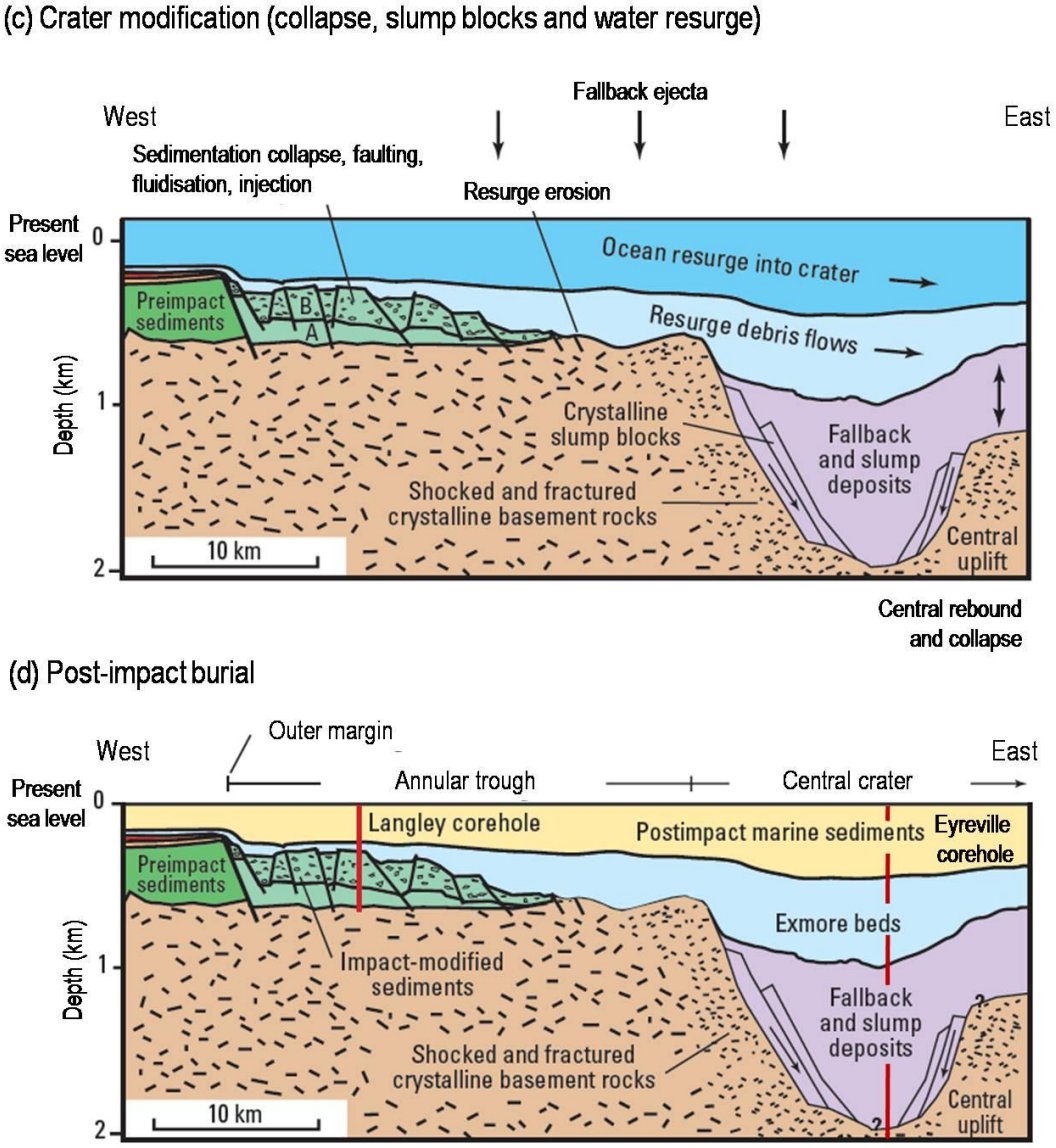

Figure 1.14 (continued): **Schematic cross-sections illustrating the proposed sequence of events for the formation of the CBIS (Horton *et al.*, 2005a): (a) Pre-impact target. (b) Contact and compression stage of the impact followed by excavation of the target material. (c) Crater modification by collapse, slumping blocks and resurging water (A and B represent crater units; see text for explanation). (d) Burial of the impact crater by post-impact marine sediments. Locations of the USGS-NASA Langley and ICDP-USGS Eyreville borehole cores in (d) are included for reference purposes. Diagram modified after Horton *et al.* (2005a).**

Unlike the USGS-NASA Langley borehole core, which intersected crater units from the CBIS annular trough and underlying crystalline basement (as shown in Figure 1.14d), the location of the ICDP-USGS Eyreville borehole core in the central crater suggests that it may have intersected such

slumped megablocks. Coeval with the collapse of the transient crater was the fallback of particles and other material ejected during the formation of the transient crater (Horton *et al.*, 2005a; Gohn *et al.*, 2008). Burial of the final crater by post-impact sediments commenced following the deposition of the Exmore beds by late ocean resurge currents (Figure 1.14d; Horton *et al.*, 2005a).

1.3 The ICDP-USGS Eyreville borehole core

1.3.1 ICDP-USGS drilling of the Chesapeake Bay impact structure

As part of the Chesapeake Bay Impact Crater Drilling Project, the ICDP and USGS completed a drilling project within the Chesapeake Bay impact structure near Cape Charles, Virginia, in May 2006 (Figure 1.1; Gohn *et al.*, 2006). The drilling resulted in three holes with a combined depth of 1766 m within the central zone or inner rim of the structure, approximately 9 km from the presumed centre of the impact structure (Gohn *et al.*, 2006; 2009). The project drilling objectives were to (i) recover continuous cores from a complete section of upper Eocene and younger sediments covering the impact structure, from the complete section of crater-filling impactites and from a short section of breccias from the crater floor, and (ii) investigate the post-impact continental-margin geology, impact effects on the regional groundwater system and groundwater quality, and impact effects and other aspects of the deep biosphere, in addition to studies of impact processes and products (Gohn *et al.*, 2006).

Field operations began in July 2005 when three borehole cores were drilled at the Eyreville Farm site located in Northampton County, Virginia (Figure 1.1; Gohn *et al.*, 2006). The Eyreville-A borehole core was cored at a depth of 125 to 941 m from September through to early October of 2005; the cessation in the drilling of the Eyreville-A borehole core was caused by swelling clays and a loss of mud circulation (Gohn *et al.*, 2006; 2009). Drilling of the Eyreville-B borehole core at a depth of 738 to 1766 m took place from October to early December of 2005 (Gohn *et al.*, 2006; 2009). The Eyreville-C borehole core was cored through post-impact sediments to a depth of 140 m during April and May of 2006 (Gohn *et al.*, 2006; 2009).

The three Eyreville borehole cores uncovered rocks from the lower crystalline basement, the impactite succession, granite and amphibolite megablocks, impact-modified pre-impact sediments, and post-impact marine sediments (Figure 1.15; Gohn *et al.*, 2006; Horton *et al.*, 2009a). A brief description of these five crater fill units (after Gohn *et al.*, 2008, and Horton *et al.*, 2009a) follows.

- The crystalline basement (1766.3-1551.2 m depth) comprises amphibolite-facies metasediments that are intruded by coarse-grained to pegmatitic granite. Minor polymict impact breccia dykes and veins occur towards the top of basement sequence. Rocks of the basement section are pre-Mesozoic in age and record the pre-impact regional metamorphic history.
- Suevitic and lithic impact breccias constitute the impactite succession (1551.3-1397.2 m depth). The succession has a lower melt-poor section containing boulders of cataclased gneiss, while the upper section of the impactite succession is considered to be melt-rich.
- The amphibolite (1397.2-1371.1 m depth) and granite (1371.1-1095.7 m depth) megablocks lie above the impactite sequence. These rocks were transported to their present locations during the collapse of the transient crater.
- The thickest crater-filling unit of the CBIS is the impact-modified pre-impact sediment sequence (1095.7-443.9 m depth). Brecciated target sediments and polymict, sediment-dominated breccias make up this section, with the Exmore breccia the dominant unit.
- The post-impact marine sediments constitute the upper 443.9 m of the geological column, burying the CBIS.

Seismic profiling of the Eyreville borehole cores by Catchings *et al.* (2008) revealed that the ICDP-USGS drilling of the CBIS did not intersect in situ crystalline basement but rather a portion of basement rocks that had been dislodged by the impact event. Despite this, the lower basement-derived section still provides a unique sample set of previously inaccessible material that, in combination with previous studies, contributes to the understanding of the regional pre-impact geological setting.

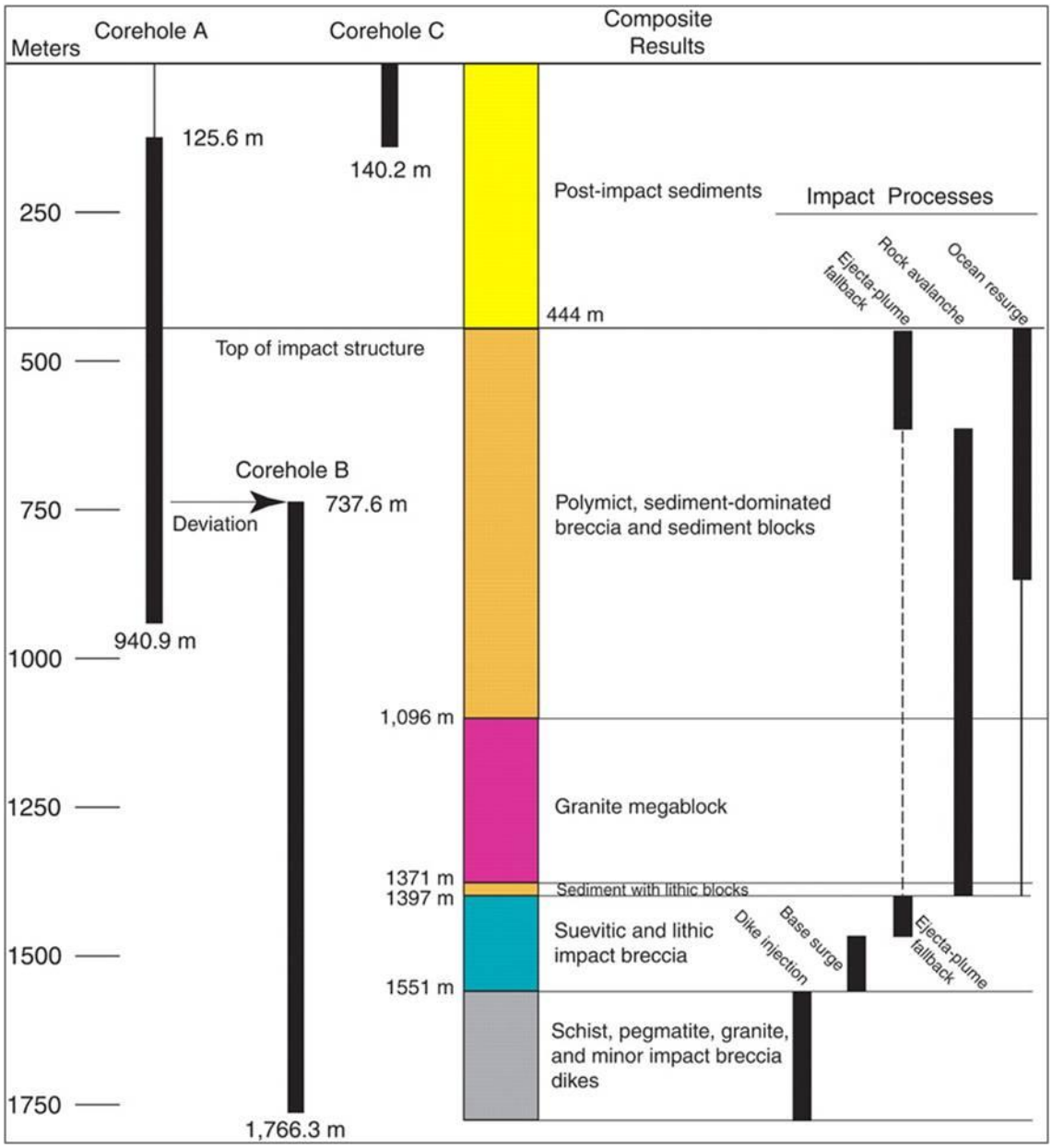

Figure 1.15: Composite geological column of the Eyreville borehole core with cored intervals A, B and C (after Gohn *et al.*, 2006).

1.4 This study

The main objective of this study is to describe and analyse samples from the lower crystalline basement-derived section (1551.2-1766.3 m depth) and upper granite and amphibolite megablocks (1095.7-1397.2 m depth) of the Eyreville-B borehole core in order to characterise the crystalline part of the target into which the Chesapeake Bay bolide impacted. The sample set analysed in this study comprises 106 discrete samples collected from the Eyreville-B borehole core. Of the 106 samples, 85

samples are from the RG-series (54 collected by Roger Gibson in June, 2006; 31 collected by G.N. Townsend in November, 2007), 19 samples from the W-series (collected by Uwe Reimold in June, 2006) and 2 samples from the MJK-series (collected by Mick Kunk in June, 2006, and included into this study in November, 2007). The additional W-series and MJK-series samples were incorporated to improve the reliability of the data set owing to sample size restrictions (each sample was limited to quarter cores up to a maximum length of 150 mm). A parallel MSc of the impactite sequence from the Eyreville-B borehole core was completed by Jolly (2011).

The methods of investigation undertaken in this study include hand specimen and thin section petrography (Chapter 2), structural analysis (Chapter 2), bulk rock major, trace and rare earth element geochemistry (Chapter 3), electron microprobe analysis (Chapter 4), geothermobarometry (Chapter 4) and geochronology (Chapter 5). The results and observations of this study are then combined with previous studies in Chapter 6 to generate a potential regional model for the target rocks of the CBIS in terms of lithology, structure, metamorphic grade, age and nature of intrusions and the age and nature of metamorphism. The above methods were employed to produce results that gave both detailed information regarding how specific minerals and rock samples were formed as well as providing information that could be used for large-scale regional comparisons.

Objectives of this study on the lower basement-derived section and the upper amphibolite and granite megablocks of the Eyreville-B borehole core include:

- Petrographic description and structural analysis through micro- and macroscopic observations;
- Geochemical analysis in terms of mineralogy (electron microprobe analysis) and bulk rock composition (X-ray fluorescence for major and trace elements; inductively coupled plasma mass spectrometry for rare earth elements);
- Establishing the metamorphic conditions experienced by the target rocks prior to the impact event by geothermobarometric analyses;
- Geochronological determination of the age of intrusive and metamorphic events recorded in the Eyreville-B target rocks; and
- Comparisons of this project's results with regional studies to contribute to understanding of the Appalachian evolution of the region.

Two peer-reviewed papers (Appendix 6) have been published from this MSc project by the Geological Society of America in a Special Paper dedicated to the ICDP-USGS drilling of the Chesapeake Bay impact crater:

- **Townsend, G.N.**, R.L. Gibson, J.W. Horton, Jr., W.U. Reimold, R.T. Schmitt & K. Bartosova, 2009, Chapter 13: Petrographic and geochemical comparisons between the lower crystalline basement-derived section and the granite megablock and amphibolite megablock of the Eyreville B core, Chesapeake Bay impact structure, USA: Geological Society of America Special Paper 458, p. 255-275.
- Gibson, R.L., **G.N. Townsend**, J.W. Horton, Jr. & W.U. Reimold, 2009, Chapter 12: Pre-impact tectonothermal evolution of the crystalline basement-derived rocks in the ICDP-USGS Eyreville B core, Chesapeake Bay impact structure: Geological Society of America Special Paper 458, p. 235-254.

Co-author Roger Gibson (University of the Witwatersrand, South Africa) was the supervisor for this MSc project and collected the initial sample set. Owing to time constraints, Roger Gibson took the lead on the second peer-reviewed paper, focusing on metamorphic and structural aspects of the study. Wright Horton is a collaborator at the USGS in Reston, USA, and supervised the geochronology and regional comparison sections. Uwe Reimold is a collaborator at the Museum für Naturkunde–Leibniz Institute at the Humboldt University in Berlin, Germany, and both facilitated geochemical analyses in Berlin and provided the W-series sample set. Ralf Schmitt (Museum für Naturkunde–Leibniz Institute at the Humboldt University in Berlin, Germany) and Katerina Bartosova (University of Vienna, Austria), who undertook parallel studies of the Eyreville drill cores from the Chesapeake Bay impact structure that were also published in the Special Paper by the Geological Society of America, contributed to the peer-reviewed paper by sharing geochemical data sets to improve data reliability. The project included time at the Museum für Naturkunde–Leibniz Institute at the Humboldt University in Berlin, Germany, performing scanning electron microscopy and electron microprobe analysis. At the USGS in Reston, USA, an additional 30 samples were collected additional core descriptions and measurements were completed, and mineral separations were performed for the geochronological analyses in the laboratory of Michael Kunk, who provided the MJK-series sample set.

2 PETROGRAPHIC AND STRUCTURAL ANALYSIS

2.1 Introduction

This chapter presents a detailed petrographic and structural analysis of the lower basement-derived section (between 1551.19 m and 1766.32 m depth) and upper amphibolite (between 1376.38 m and 1389.35 m depth) and the granite (between 1095.74 m and 1371.11 m depth) megablocks of the Eyreville-B borehole core. Identifying and describing the macro- and microscopic characteristics and textures of the various rock types within the Eyreville-B borehole core allows for initial interpretations regarding the petrogenesis of the rocks and provides the foundation on which interpretations from scientific analyses in the following chapters are based.

2.2 Methodology

A total suite of 106 samples were selected from the Eyreville-B core hole for petrographic and structural analysis based on macroscopic and transmitted (and reflected) light optical microscopy. This suite comprises 85 samples from the RG-series (54 collected by R.L. Gibson in June 2006; 31 collected by G.N. Townsend in November 2007), 19 samples from the W-series (collected by W.U. Reimold in June 2006) and 2 samples from the MJK-series (collected by M.J. Kunk in June 2006 and included into this study in November 2007). Of these, 56 samples are from the lower, crystalline basement-derived section (28 mica schist, 13 granite, 8 breccia, 2 amphibolite, 1 biotite schist, 1 calc-silicate, 1 tourmalinite, 1 quartz vein and 1 chlorite fracture), 10 are from the amphibolite megablock (9 amphibolite and 1 granite-bearing calcite vein) and 40 are from the granite megablock (20 gneissic granite, 13 massive granite, 6 biotite schist xenoliths and 1 chlorite fracture). 107 thin sections were prepared for transmitted (and reflected) microscopy: 56 from RG-series of samples at the SGS Lakefield Laboratories in Johannesburg, South Africa, 19 from the W-series of samples at the Humboldt University in Berlin, Germany, and 29 from the RG-series and 1 from the W-series at the University of the Witwatersrand, South Africa. Two thin sections were prepared from the following samples: RG01, RG40, RG50, RG51 and RG156. Macroscopic structural measurements were undertaken at the USGS in Reston, Virginia, in November 2007. Each measurement was taken from

the core axis for each relevant sample. All samples collected are presented in Appendix 1a, with petrographic summary descriptions and hand specimen photographs presented in Appendix 1b and 1c, respectively. Structural measurements are presented in Appendix 1d. Mineral abbreviations in the figure captions are from Whitney and Evans (2010).

2.3 Petrographic Analysis

2.3.1 Lower basement-derived section

The lower basement-derived section of the Eyreville-B borehole core is located between 1551.19 m and 1766.32 m depth (Figure 2.1) and consists of foliated metasediments, which include mica schist, amphibolite and calc-silicate rock, and coarse-grained to pegmatitic granite. The section is characterised by a dominant mica schist component in the upper part of the section, whereas the granite becomes increasingly abundant towards the base, solely comprising the lowermost ~75 m of the borehole core (Figure 2.1). Between 1640 m and 1655 m depth, alternating layers of granite and metasediments define a distinct mylonitic zone, although thin mylonites occur locally above and below this zone. Additionally, several thin dikes of suevite and polymict impact breccia occur above 1611 m depth (Figure 2.1).

2.3.1.1 Mica schists

The mica schists (between 1560 m and 1718 m depth) are black to silver-grey in colour, fine-grained (average grain size less than 1 mm) and foliated (Figure 2.2a). Locally porphyroblastic, the mica schists are observed to contain highly deformed relict sedimentary layering, are intruded by granite dykes and cut by secondary fractures containing quartz, chlorite and/or calcite (see Section 2.4.2). In terms of mineralogy, the mica schists comprise mainly muscovite (20-40 vol%), plagioclase (20 vol%), quartz (15-30 vol%), biotite (10-15 vol%) and graphite (5-10 vol%). Accessory phases include garnet, fibrolite (sillimanite), tourmaline, rutile, pyrite, chalcopyrite, pyrrhotite and zircon.

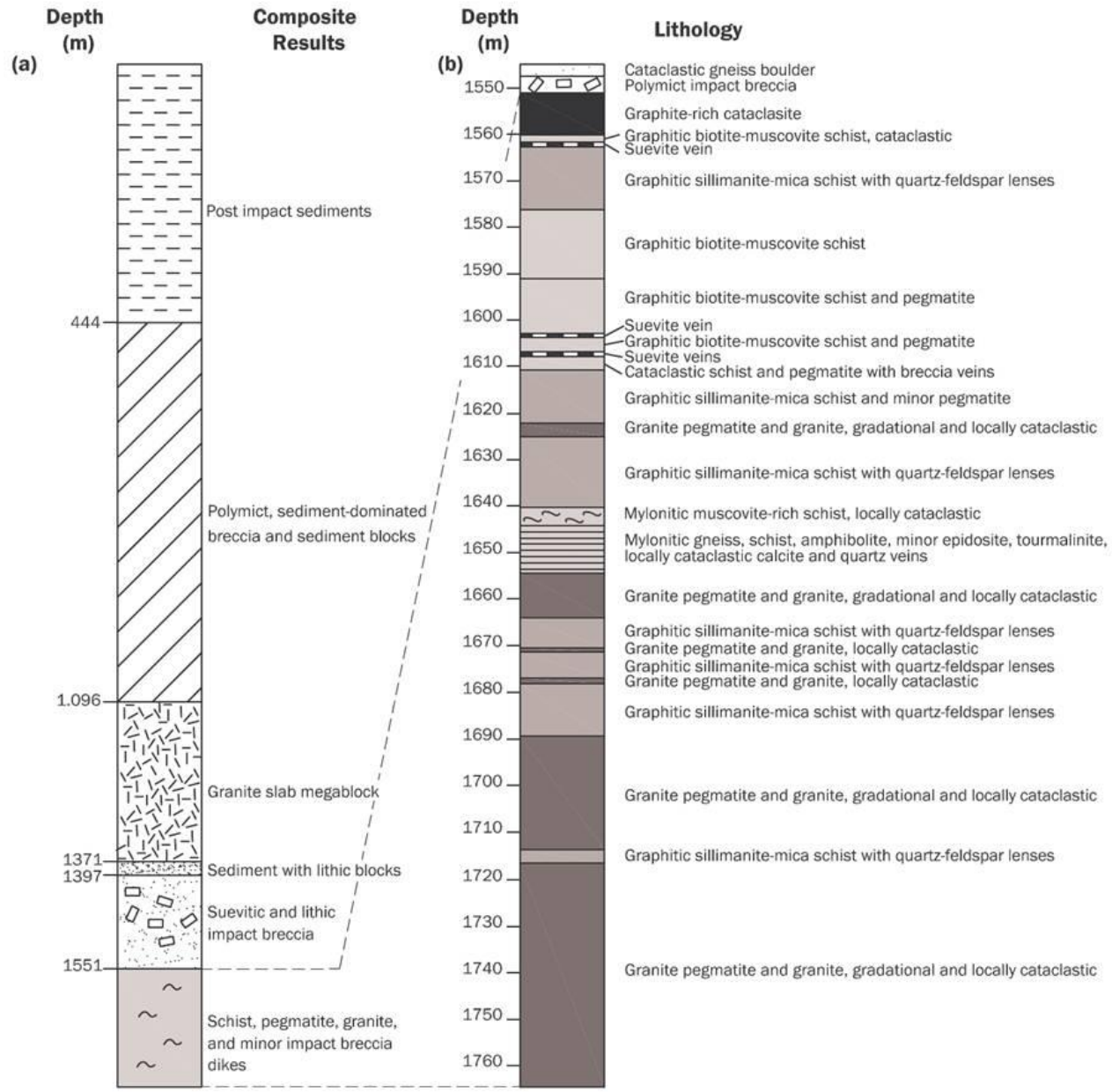

Figure 2.1: (a) Composite stratigraphic column for Eyreville-B borehole core (after Gohn *et al.*, 2006) with (b) a detailed column for the lower basement-derived section between 1551 m and 1766 m depth (after Horton *et al.*, 2009a).

The mica schist foliation is defined by alternating millimetre-scale mica (Ms > Bt) and Qz-Pl foliae (Figure 2.2b), which is locally folded (see Section 2.4.1). Muscovite is fine-grained (~0.5-1 mm), subidioblastic and platy, and exhibits variable degrees of internal strain (e.g. kink banding, undulose extinction; Figure 2.2b) caused by localised mylonitic deformation (see Section 2.3.1.7). Muscovite is also common as lath-shaped inclusions in the graphite-rich cores of plagioclase porphyroblasts (see

Section 2.4.4). Fine-grained (~0.6 mm), subidioblastic and commonly intergrown with muscovite (Figure 2.2c), biotite is commonly kinked and altered to chlorite in the vicinity of mylonitic deformation bands as well as fracture and breccia zones (see Section 2.4). In addition to occurring in the matrix, porphyroblasts of plagioclase are poikilitic, texturally zoned and up to 2 mm in diameter (Figure 2.2d). Plagioclase porphyroblasts tend to have a graphite-rich core, an inclusion-rich intermediate zone (including quartz, tourmaline, muscovite, graphite and/or rutile), an inclusion-poor rim, and exhibit variable amounts of dissolution along the mylonitic foliation (Figure 2.2d; see Section 2.4.4). Plagioclase is commonly altered to sericite, epidote and/or calcite.

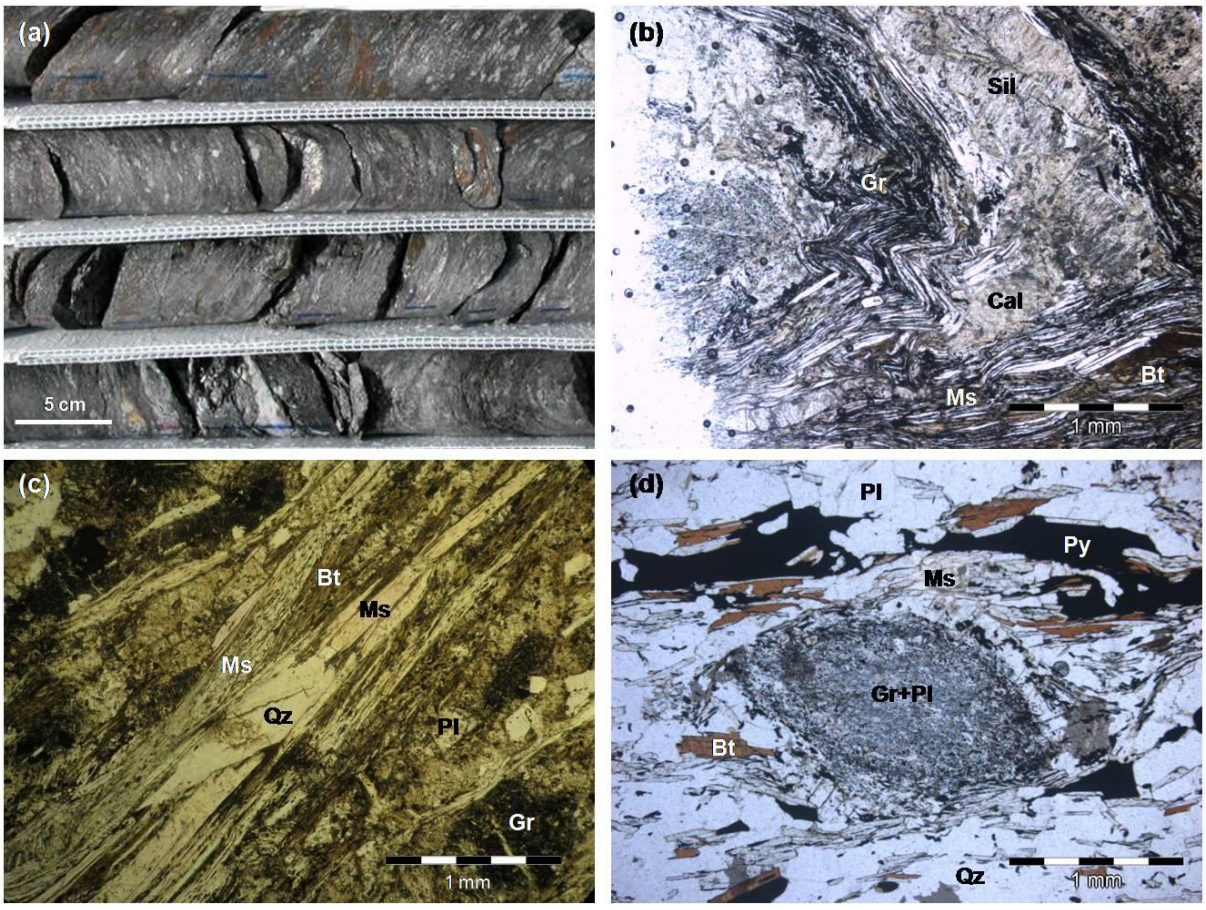

Figure 2.2: Corebox and thin section photographs of the lower basement-derived mica schists. (a) Corebox 322 showing the highly foliated nature of the mica schists. (b) Sample RG60 showing folds that locally deform the mica schist foliation (PPL). (c) Sample RG34 showing an elongated Qz grain within the Ms-Bt foliae and adjacent irregular masses of Gr (PPL). (d) Zoned Pl porphyroblasts with Gr-rich cores in sample RG68 (PPL). Abbr.: Bt = biotite; Cal = calcite; Gr = Graphite; Ms = muscovite; Pl = plagioclase; PPL = plane polarised light; Py = pyrite; Qz = quartz; Sil = sillimanite (mineral abbreviations after Whitney and Evans, 2010).

Quartz is granoblastic to lensoid (0.2-1 mm; Figure 2.2c) and exhibit varying degrees of internal strain demonstrated by undulose extinction and grain boundary migration recrystallisation. Graphite is observed to occur in disseminated form, large irregular masses (Figure 2.2c) and as inclusions in plagioclase porphyroblasts (Figure 2.2d). The abundance of graphite increases in concentration with depth (Figure 2.1) and is found within breccia matrices and fractures towards the base of the lower basement-derived section.

Sillimanite is observed as knots of fibrolite, up to 3 mm long in places (Figure 2.3a), as well as rarer, highly altered grains (Figure 2.2b). More commonly skeletal and highly fractured with varying levels of alteration (Figure 2.3b), porphyroblasts of garnet can also be poikilitic containing biotite, quartz and rutile inclusions (see Figure 2.26a). Tourmaline is brown in colour (i.e. dravitic) and idioblastic to subidioblastic in nature (Figure 2.3c). Pyrite forms idioblastic to subidioblastic grains as well as blebs and/or stringers as inclusions in plagioclase porphyroblasts (Figure 2.2c and d) and is locally associated with other fracture fill minerals (e.g. chlorite and calcite) in veins and fractures (Figure 2.3d). Rutile and zircon occur as very fine-grained (≤0.1 mm), idioblastic to rounded grains. Pyrrhotite grains are xenoblastic and form either individual blebs (0.2 mm) or aggregates up to 3.5 mm in diameter. Epidote and chlorite are alteration products of plagioclase and biotite, respectively, and form part of the retrograde metamorphic assemblage adjacent to calcite-filled veins, fractures and/or breccias (Figure 2.3d).

2.3.1.2 Biotite schist

A thin layer (22 cm) of Qz-Pl-Bt schist is located in the upper portion of the lower basement-derived section between 1578.74 m to 1578.96 m depth. Unlike the other mica schists, this schistose layer comprises quartz (35 vol%), plagioclase (35 vol%), biotite (25 vol%) and graphite (5 vol%), with only trace amounts of rutile and muscovite (Figure 2.4a). The biotite schist is characterised by a distinctive lensoid microstructure where biotite is observed to wrap around fine-grained, lensoid Qz-Pl aggregates (≤1 mm), which locally exhibit internal strain and dynamic recrystallisation. Plagioclase forms subidioblastic grains with oscillatory zoning, whereas biotite grains, locally up to 2.5 mm in diameter, show strong kinking and bent cleavage and contain fine-grained graphite inclusions. More commonly, graphite occurs as coarse-grained aggregates and seams, which lie parallel to the biotite

foliation, as well as in cross-cutting fractures (Figure 2.4b). Rare, very fine-grained white mica aggregates appear to possibly be pseudomorphs after highly poikilitic cordierite porphyroblasts. Unfortunately, mineral chemistry for the biotite schist could not confirm this possibility (see Chapter 4, Section 4.2.2).

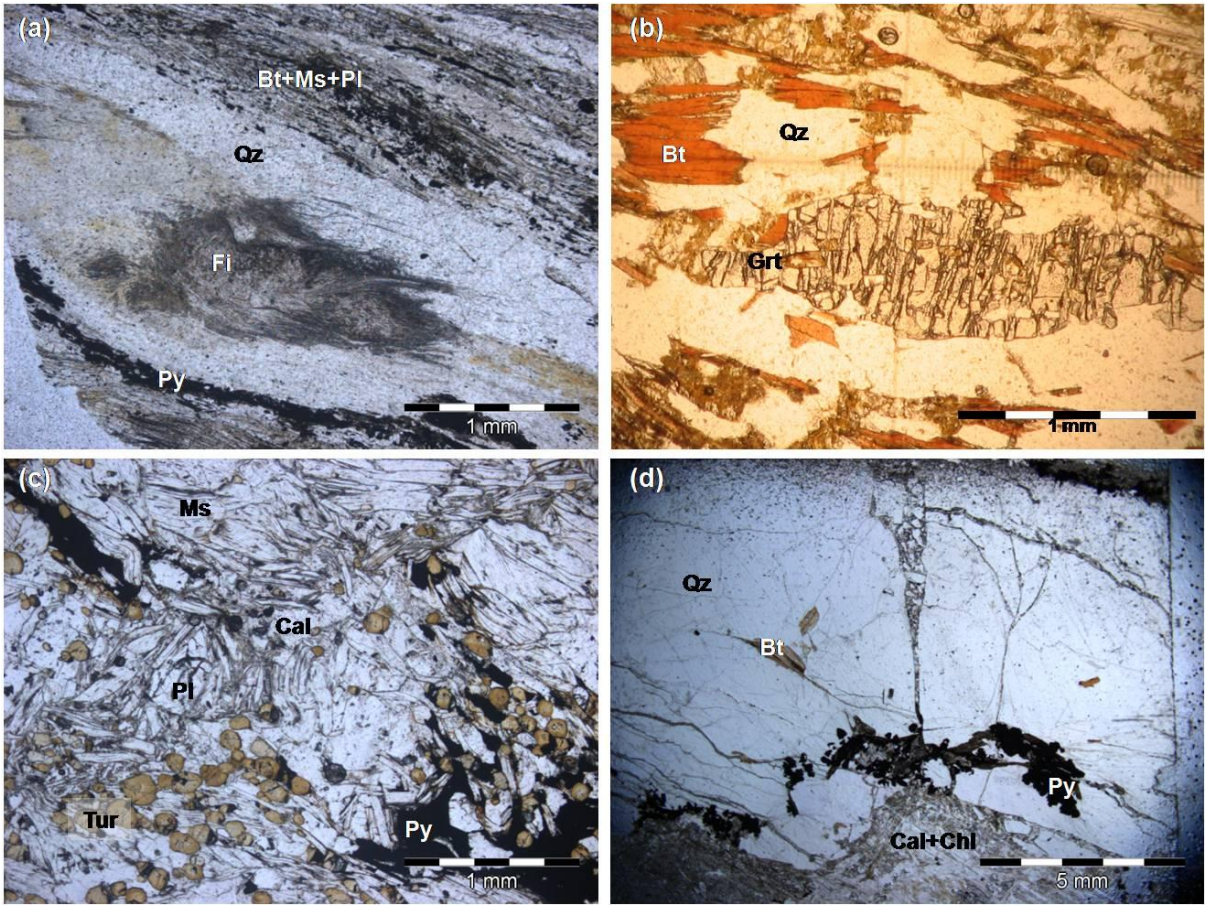

Figure 2.3: Photomicrographs of samples from the lower basement-derived mica schist. (a) Sample RG44 showing a Fi knot (PPL). (b) Skeletal and elongated garnet in sample RG53 (PPL). (c) Sample RG38 illustrating the intercalation of Tur and Py with Ms and Pl (PPL). (d) Brecciated fracture in Qz with Py, Cal and Chl fracture-fill in sample RG43 (PPL). Abbr.: Bt = biotite; Cal = calcite; Chl = chlorite; Fi = Fibrolite; Gr = Graphite; Grt = garnet; Ms = muscovite; Pl = plagioclase; PPL = plane polarised light; Py = pyrite; Qz = quartz; Tur = tourmaline.

2.3.1.3 Amphibolite

A very thin layer (~58 cm) of fine-grained banded amphibolite is located within the mylonite zone of the lower basement-derived section between 1644.58 m and 1645.16 m (Figure 2.1). This 58-cm-thick layer exhibits a subidioblastic mineral texture with seriate-polygonal aggregates and contains

mm- to cm-scale bands of alternating dark to light grey material of highly variable mineralogy, with some individual bands comprising up to 50 vol% epidote (Figure 2.4c). More commonly, amphibole and plagioclase together comprise >50 vol% of the lithology, with variable amounts of quartz, biotite, K-feldspar, calcite, epidote and titanite in different layers (Figure 2.4d). The alternating bands of strongly varying mineralogy and its close association with the calc-silicate (see Section 2.3.1.4) may suggest a sedimentary origin (i.e. para-amphibolite), rather than forming through igneous processes.

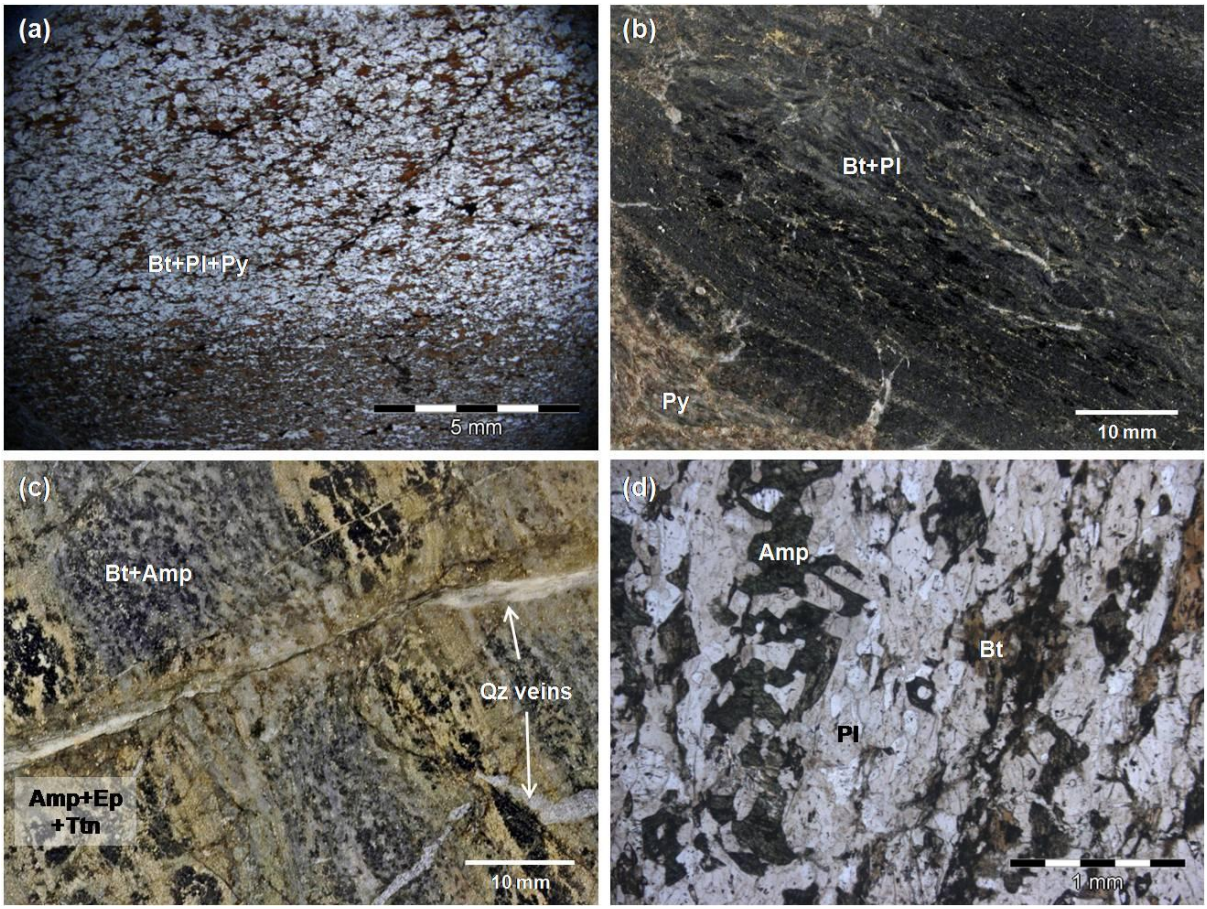

Figure 2.4: (a) Photomicrograph (PPL) and (b) hand specimen photograph of the lower basement-derived biotite schist sample RG70 showing the large amount of Bt that defines the lithology. (c) Hand specimen and (b) photomicrograph (PPL) of the lower basement-derived amphibolite sample RG51 where alternating bands of Bt-rich and Bt-poor assemblages are shown. Abbr.: Amp = amphibole; Bt = biotite; Ep = epidote; Pl = plagioclase; PPL = plane polarised light; Py = pyrite; Qz = quartz; Ttn = titanite.

The alternating bands are oriented parallel to the foliation defined by aligned amphibole grains (Figure 2.4d). Reaching up to 2.5 mm in diameter, amphibole grains are idioblastic to highly irregular poikiloblasts, containing quartz, plagioclase, epidote and titanite inclusions (Figure 2.4d). In some cases, the amphibole grains have been pseudomorphed by uralite and chlorite adjacent to fractures

and calcite veins. Biotite is locally replaced by chlorite and forms both as interstitial grains between quartz and feldspar and as somewhat irregular seams oriented parallel to the foliation (Figure 2.4d). Epidote (≤ 0.8 mm) and titanite (≤ 0.5 mm) are idioblastic and form part of the prograde peak assemblage. Quartz is observed to form large, irregular grains that locally exhibit dynamic recrystallisation. This observation combined with relatively coarse Pl-Qz myrmekitic texture suggests the rock experienced a hydrothermal component during mylonitisation. This is in agreement with disrupted calcite veins (Figure 2.4c) that may be related to a subsequent deformation event (see Section 2.4.2).

2.3.1.4 Calc-silicate rock

In close spatial association with the lower basement-derived amphibolite is the calc-silicate rock located between 1645.77 m and 1646.44 m depth (~67 cm; Figure 2.1). It is strongly cataclased, dark to light green in colour (Figure 2.5a) and contains a peak metamorphic assemblage, consisting of vesuvianite (70 vol%), plagioclase (15 vol%) and quartz (15 vol%), and a retrograde metamorphic assemblage, which comprises epidote (40 vol%), calcite (25 vol%), quartz (20 vol%), chlorite (10 vol%) and amphibole (5 vol%). In the peak assemblage, vesuvianite forms coarse-grained, interlocking aggregates (Figure 2.5b), which locally enclose plagioclase and quartz. Rare, irregularly-shaped relics of an isotropic mineral (possibly garnet) are also observed within the peak metamorphic assemblage.

The retrograde metamorphic assemblage, which comprises approximately 35% of the calc-silicate, is closely related to the brecciation observed in the calc-silicate rock (Figure 2.5a), which extends from hand specimen to micro-scale where intense fracturing of the vesuvianite occurs (Figure 2.5b). Commonly filled by Ep-Chl-Cal-Qz fracture-fill (Figure 2.5c), the fractures can be large and irregularly shaped or as sets of intersecting, closely-spaced, parallel fractures. Epidote forms subidioblastic grains up to 1.5 mm diameter in the larger fractures, with xenoblastic, medium-grained calcite (2 mm), very fine-grained (0.1 mm) quartz and fine-grained (0.5 mm) chloritic masses (Figure 2.5c). Aggregates of fine-grained (1 mm) amphibole (possibly actinolite owing to lighter green colour, compared to hornblende in the basement amphibolite, and acicular nature) are observed along a single fracture (Figure 2.5d).

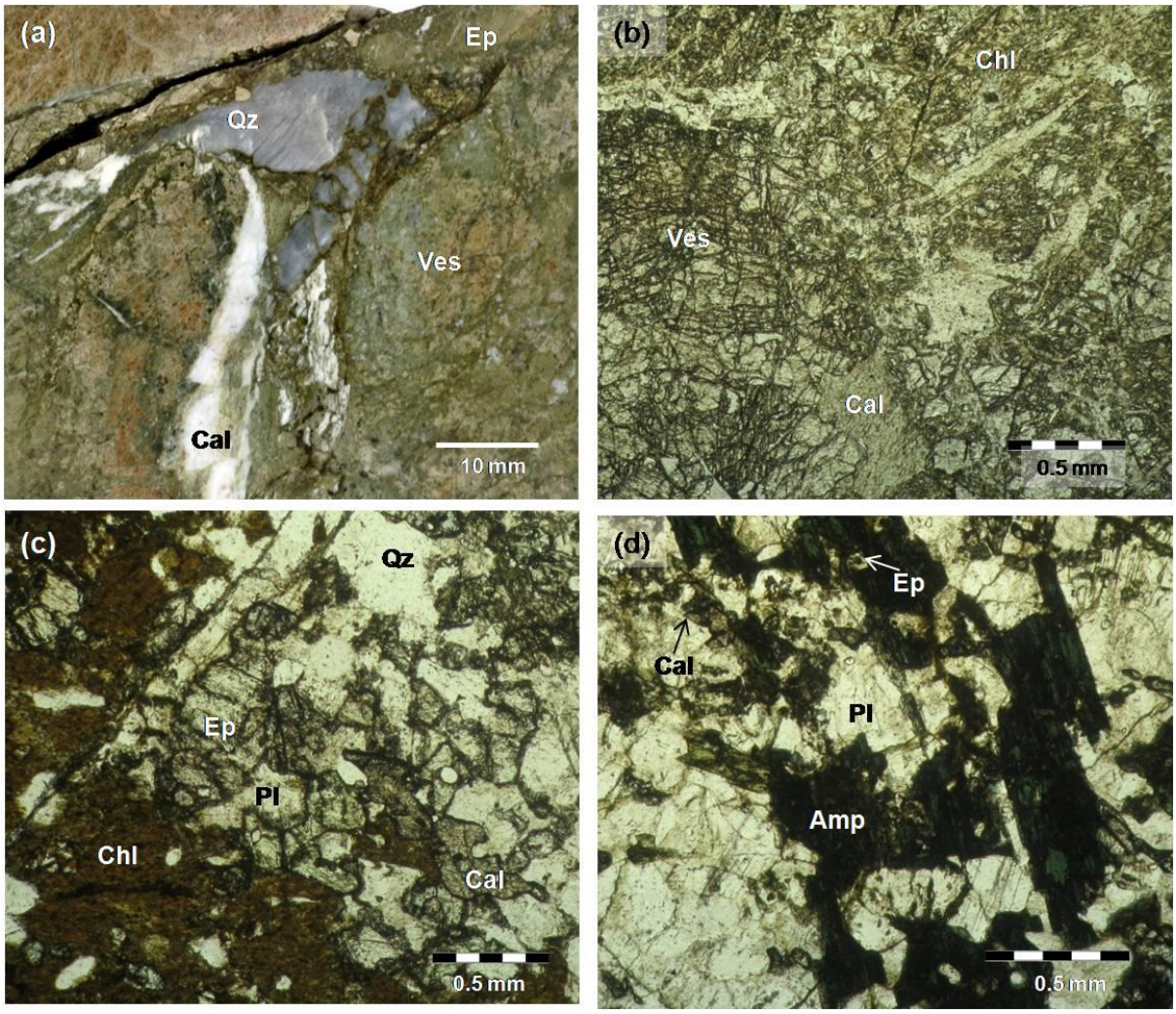

Figure 2.5: Hand specimen and thin section (PPL) photographs of the lower basement-derived calc-silicate sample RG50 showing (a) its highly brecciated nature, (b) the peak metamorphic assemblage, (c) the retrograde metamorphic assemblage and (d) the Amp component. Abbr.: Amp = amphibole; Cal = calcite; Chl = chlorite; Ep = epidote; Pl = plagioclase; PPL = plane polarised light; Qz = quartz; Ves = vesuvianite.

2.3.1.5 Tourmalinite

The tourmalinite, a banded rock that constitutes up to 80 vol% tourmaline in a single band, is located at approximately 1639 m depth (Figures 2.1 and 2.6a). The remainder of the assemblage comprises plagioclase, quartz, pyrite, graphite, rutile and zircon (Figure 2.6b). Similar to the tourmaline observed in the lower basement-derived mica schist, tourmaline forms brown (dravite), fine-grained (0.5 mm) and idioblastic to subidioblastic grains (Figure 2.6b). However, unlike the mica schist tourmaline, these grains are highly poikilitic (Figure 2.6b). The intensive nature of the tourmalinite coupled with its position adjacent to granite dykes within the mylonite zone (1640 m and 1655 m depth; see Section

2.3.1.6) is consistent with tourmaline from pegmatitic injections into metamorphic terranes (Krynine, 1946), which suggests that the lithology may have formed as a result of fluid escape from the granite veins. It is also possible that the mylonite zone included a tourmaline metasomatic component (see Section 2.5).

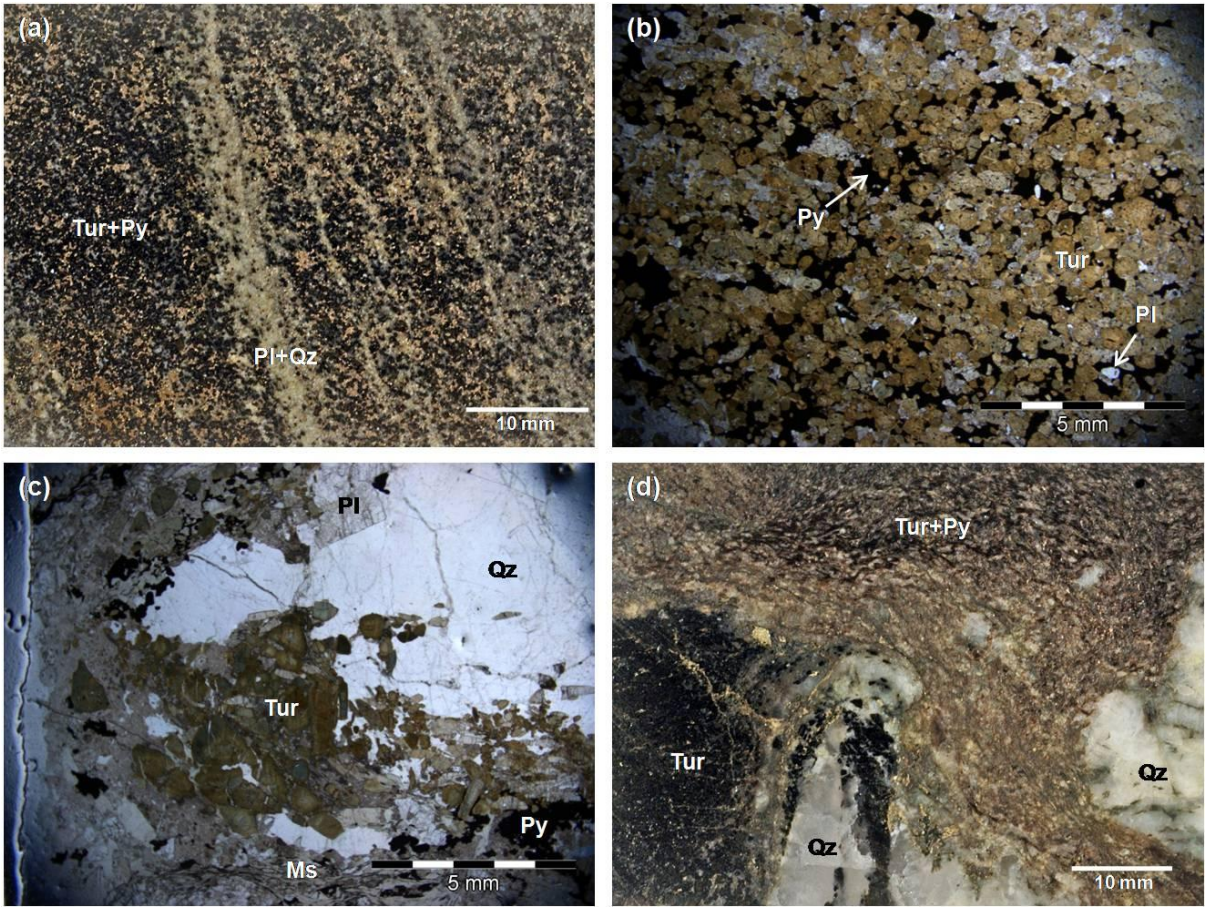

Figure 2.6: (a) Hand specimen and (b) thin section (PPL) photographs of sample RG54 showing the abundance and fine-grained nature of the lower basement-derived tourmalinite. (c) Thin section (PPL) and (d) hand specimen photographs of sample RG57 showing the coarse grain size of Tur-rich layers within the lower basement-derived mica schist. Abbr.: Ms = muscovite; Pl = plagioclase; PPL = plane polarised light; Py = pyrite; Qz = quartz; Tur = tourmaline.

A second, more common tourmaline-rich assemblage occurs within the lower basement-derived mica schist. Tourmaline in these assemblages form dense, poikilitic to locally monomineralic, aggregates (Figure 2.6c) that can reach up to several centimetres in width in close proximity to Qz and/or Qz-Fsp lenses (Figure 2.6d). The large size of the monomineralic tourmaline grains, which commonly occur within these lenses, is consistent with a pegmatitic provenance (Krynine, 1946). As a result, these lenses are interpreted to be boudinaged quartz veins and granite dykes (Figure 2.6d). Textural zoning

occurs in the larger tourmaline grains (1 mm), with blue-green irregular cores and yellow-brown rims (Figure 2.6c). Although somewhat erratic, the zoning is consistent with a blue-green, schorlitic core and a brown, dravitic rim (Krynine, 1946; Klein, 2002). Henry and Guidotti (1985) observed that this type of textural observation commonly occurs in pyrrhotite-rich rocks. Tourmaline grains are observed to be locally bent or broken, with micro-fractures locally filled by quartz (Figure 2.6c).

2.3.1.6 Granite

The lower basement-derived granite occurs as coarse-grained to pegmatitic dykes which intrude the metasediments, becoming the dominant lithology in the lower portion of the borehole core (from 1690 m depth; Figure 2.1). Exhibiting an idiomorphic to hypidiomorphic, inequigranular-polygonal texture, the granite varies from a pink/orange variety (Figure 2.7a), which is dominated by K-feldspar (20-40 vol%) megacrysts (pink) that are locally altered to sericite (orange), and a white variety (Figure 2.7b), which comprises mainly plagioclase (30-35 vol%) and quartz (20-25 vol%). Other mineral phases include muscovite (0-13 vol%), biotite (0-5 vol%), garnet (0-2 vol%) and amphibole (0-1 vol%).

K-feldspar forms coarse- (~8 mm) to very coarse-grained (up to 40 mm in pegmatites), idiomorphic to subidiomorphic, perthitic, poikilitic grains which display patchy microcline twinning (Figure 2.7c). Similar to K-feldspar, fine- to coarse-grained (0.4-6 mm) plagioclase grains are idiomorphic to subidiomorphic and locally poikilitic (Figure 2.7d). Muscovite, plagioclase and quartz form inclusions in both K-feldspar and plagioclase poikiloblasts (Figure 2.7c and d). Quartz grains are fine-grained (0.1-0.6 mm) and, together with the feldspars, show internal deformation and dynamic recrystallisation features (Figure 2.7d) associated with the mylonitic S1b deformation and cataclasis (see Section 2.4.1). Seritisation and saussuritisation is observed in both K-feldspar and plagioclase feldspars (Figure 2.7c and d). Calcite is commonly observed to replace twin lamellae in feldspar grains (Figure 2.7c and d).

Muscovite is the most common mica in the lower basement-derived granite (Figure 2.7d) and varies in grain size from fine- (0.4-0.8 mm) to very coarse-grained (~3 cm), whereas biotite only occurs a fine (0.2-0.4 mm) grains that are locally replaced by very fine-grained (≤ 1 mm) chlorite adjacent to fractures and cataclastic zones. Garnet occurs as fine- to medium-grained (0.5-2 mm), idiomorphic to

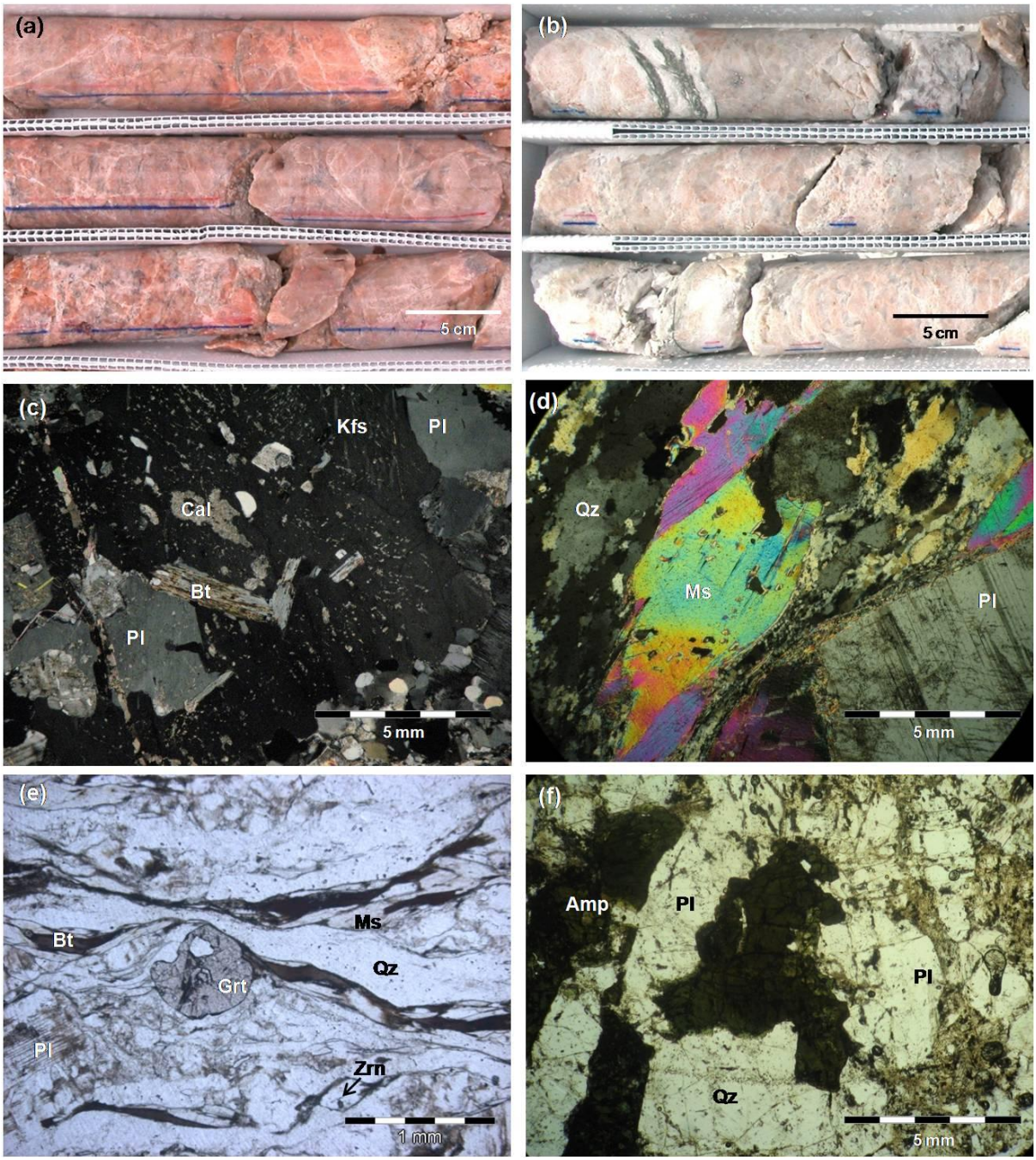

Figure 2.7: Corebox and thin section photographs of the lower basement-derived granite. Coreboxes (a) 313 and (b) 324 showing the pink/orange and white granite varieties, respectively. (c) Poikilitic Kfs grain with Bt and Pl inclusions and local replacement by Cal in sample RG40a (XPL). (d) Large Ms and Pl grains within dynamically recrystallised Qz grains in sample RG32 (XPL). (e) Fractured and locally poikilitic Grt in sample RG40a (PPL). (f) Fractured Amp grains in a Qz-Pl matrix in sample RG61 (PPL). Abbr.: Amp = amphibole; Bt = biotite; Cal = calcite; Kfs = K-feldspar; Ms = muscovite; Pl = plagioclase; PPL = plane polarised light; Qz = quartz; XPL = cross polarised light; Zrn = zircon.

subidiomorphic, locally poikilitic (quartz and plagioclase inclusions), fractured porphyroclasts (Figure 2.7e). Amphibole is fine- to medium-grained (0.5-1 mm), subidiomorphic, fractured, locally poikilitic and surrounded by locally altered plagioclase (Figure 2.7f).

2.3.1.7 Mylonite zone

The mylonite zone is located between 1640 m and 1655 m depth (Figure 2.1), although thin mylonites are observed to occur locally above and below this portion of the lower basement-derived section. The amphibolite, calc-silicate and tourmalinite (Sections 2.3.1.3, 2.3.1.4 and 2.3.1.5, respectively) are all located within this zone. Figure 2.8 shows the very fine-grained (< 1 mm) nature of the alternating bands of mica schist (dark grey to light brown) and granite (light pink) within the mylonite zone. Mica schist samples typically comprise plagioclase (20-30 vol%), quartz (10-20 vol%), muscovite (20-30 vol%), biotite/chlorite (0-20 vol%), graphite (0-10 vol%), fibrolite (0-5 vol%), garnet (0-2 vol%), and pyrite (0-2 vol%), whereas granite samples typically comprise K-feldspar (20-30 vol%), plagioclase (20-30 vol%), quartz (30-40 vol%), muscovite (10 vol%), biotite (0-8 vol%), and garnet (2 vol%). Qualitatively, the light brown mica schists appear to have experienced greater intensities of retrogression compared with the dark grey schists, owing to replacement of biotite by chlorite and muscovite.

2.3.1.8 Breccias

Rare injections of suevites and polymict impact breccia are observed in the lower basement-derived section above 1611 m depth (Figure 2.1), with the deepest dyke intruding cataclastic granite pegmatites and mica schists (Figure 2.9a). Suevite dykes vary from 5 cm to 2 m in thickness, generally increasing with decreasing depth (Figure 2.9b), and are more common than polymict impact breccias in the lower basement-derived section, the latter only observed above 1551 m depth (Figures 2.1 and 2.9c). A graphite-rich biotite and muscovite schist, observed between 1576.64 m and 1591.36 m depth, exhibits local brecciation and includes polycrystalline quartz mineral clasts (Figure 2.9d), possibly plucked from the lower basement-derived granite.

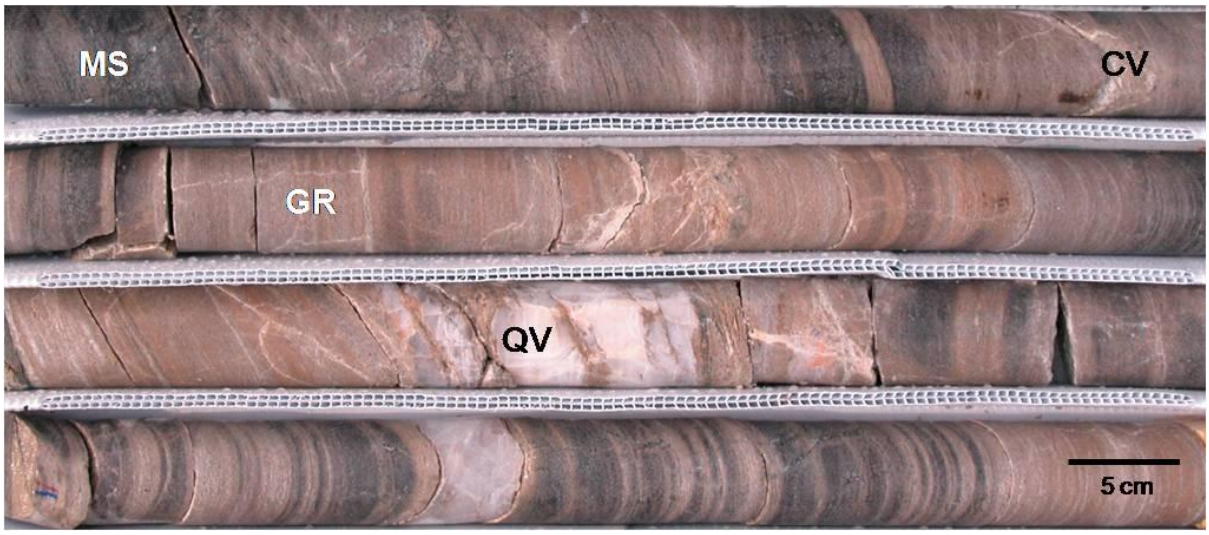

Figure 2.8: Photograph of corebox 310 illustrating the fine-grained alternating mica schist and granite layers in the lower basement-derived mylonite zone. Abbr.: CV = chlorite vein; GR = granite; MS = mica schist; QV = quartz vein.

Suevite matrices vary from black to dark grey in colour (evidence of its graphite-rich component) and exhibit weak to strong clast alignment (Figure 2.9b). Suevites become increasingly clast-supported with decreasing depth, directly correlating with increasing clast size (Figure 2.9a and b). Clasts vary from very fine-grained, acicular to subhedral, locally altered, individual minerals (Figure 2.10a), to larger than 6 cm, subrounded, lithic clasts (Figure 2.10b). Mineral clasts include muscovite, quartz, plagioclase, graphite and pyrite (Figure 2.10a), and lithic clasts include granite (Figure 2.9b) and quartzite (Figure 2.10b). The mineral clasts and granite lithic clasts are interpreted to have been included into the suevitic dykes from the lower basement-derived section; however, quartzite is not a lithology observed in this section and may have been included as a result of impact mixing processes (see Chapter 1, Figure 1.14). Melt in the suevite dykes occurs as dark grey to brown black, locally altered clasts (Figure 2.10a) and as light brown veins containing subrounded quartzitic material (Figure 2.10b).

Polymict impact breccias contain much more altered and diverse material compared with the suevites (Figure 2.9c). The breccias vary from matrix- to clast-supported with no apparent correlation with depth. Owing to their highly graphitic nature, breccia matrices are dark brown to dark grey in colour (Figure 2.9c). In a single sample, clast size ranges from 0.1 mm to 5 cm and clast type ranges from quartz and calcite mineral grains to granite gneiss and shale lithic clasts (Figure 2.10c).

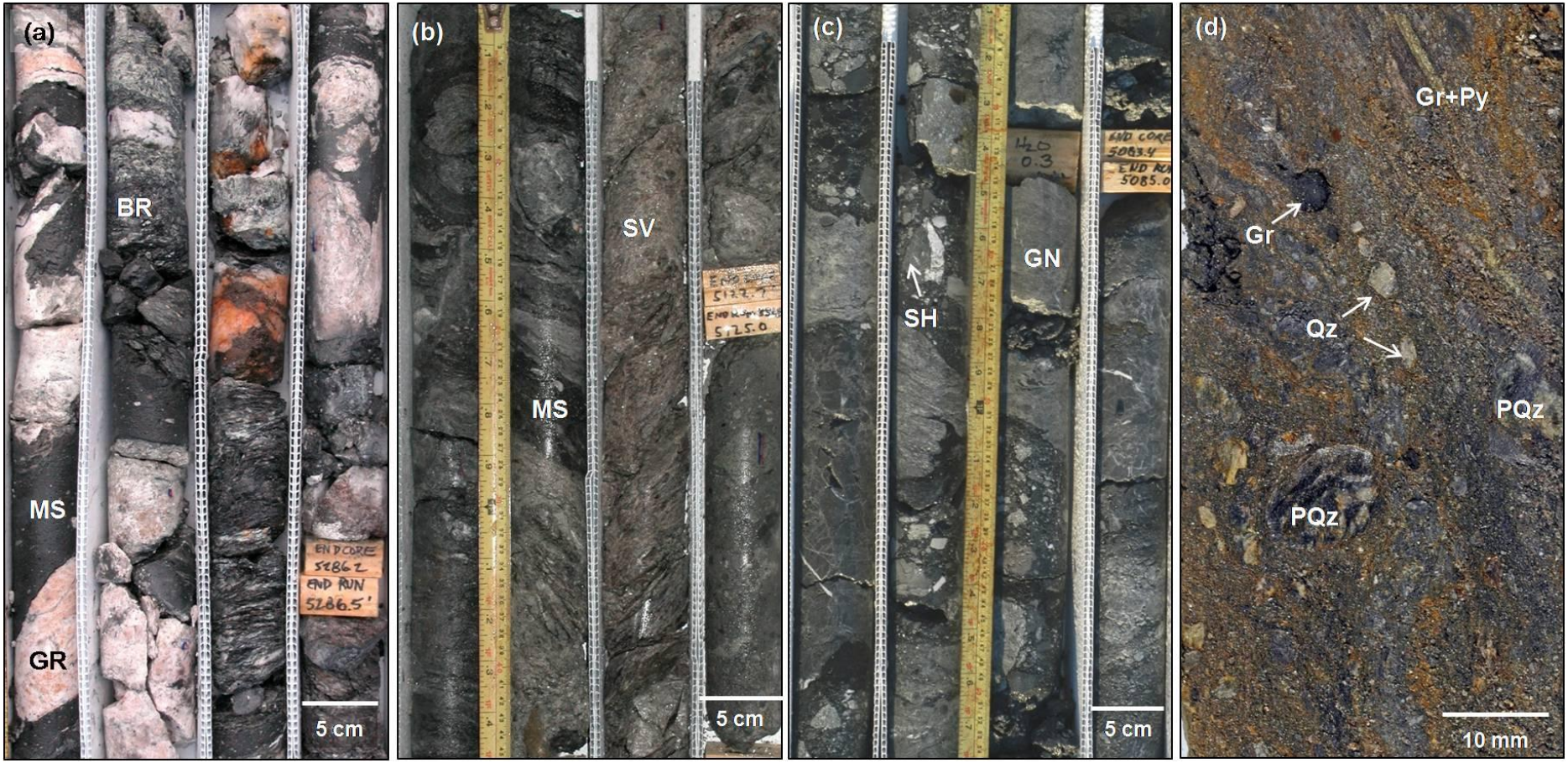

Figure 2.9: Photographs of the suevite and polymict impact breccia dykes in the lower basement-derived section. (a) Corebox 297 showing the deepest suevite dyke intercalated with MS and GR. (b) Corebox 285 showing interplay between the SV dykes and MS. (c) Corebox 282 showing the beginning of the polymict impact breccia dyke. (d) Hand specimen of sample RG71 showing the local brecciation with plucked PQz clasts. Abbr.: BR = breccia; GN = granite gneiss; GR = granite; Gr = graphite; M = melt; MS = mica schist; PQz = polycrystalline quartz; Py = pyrite; SH = shale; SV = suevite.

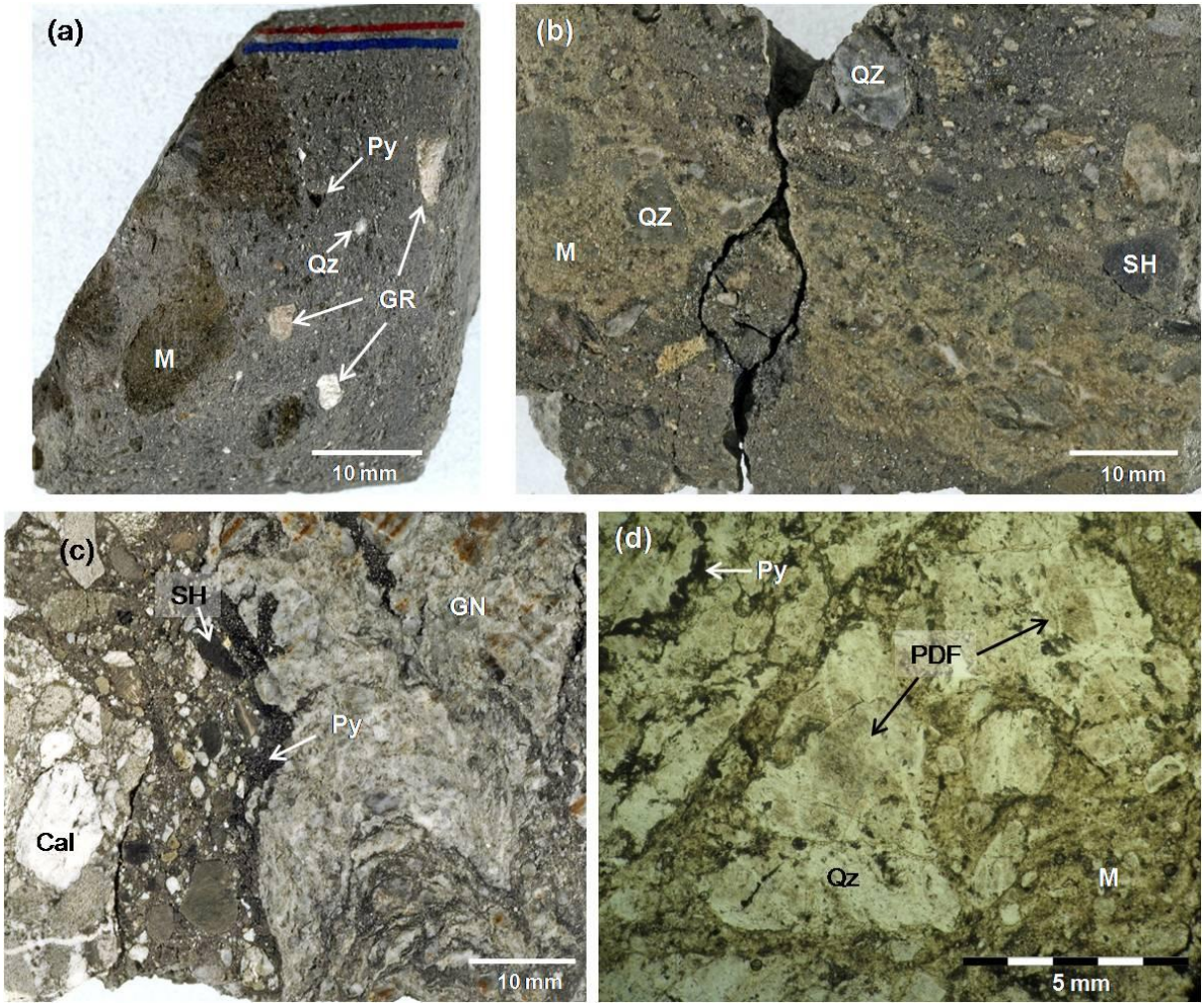

Figure 2.10: Photographs of the suevite and polymict impact breccia dykes in the lower basement-derived section. (a) Hand specimen of sample RG62 showing the variation in clast size and type within a matrix-support suevite. (b) Hand specimen of sample RG73 showing a clast-supported suevite with a melt vein and quartzite clasts. (c) Hand specimen of sample RG77 showing the large variation in grain size and clast type in polymict impact breccia. (d) Photomicrograph of sample RG77 showing fractured and toasted quartz with PDFs within an altered matrix (PPL). Abbr.: Cal = calcite; GN = granite gneiss; GR = granite; M = melt; PDF = plane deformation features; PPL = plane polarised light; Py = pyrite; QZ = quartzite; Qz = quartz; SH = shale.

Calcite, along with pyrite, is also observed along fractures and adjacent to large lithic clasts (Figure 2.10c). Evidence for shock metamorphism includes fractured minerals and toasted quartz grains with planar deformation features (PDFs; Figure 2.10d). Toasted quartz grains in Figure 2.10d are orange-brown in colour and become 'toasted' when quartz grains experience vesiculation after pressure release at high post-shock temperatures (Ferrière *et al.*, 2009). This evidence suggests that these dykes experienced pressures approximating 10 GPa (French, 1998; see Section 2.4.2).

2.3.2 Upper amphibolite megablock

Lying in sand between the overlying granite megablock and underlying impactite succession (Figure 2.11), the amphibolite megablock is a black to dark grey to dark green, fine- to medium-grained (1-44 mm), locally foliated, relatively homogenous, lithic block located between 1376.38 m to 1389.71 m depth (Figure 2.12a). The amphibolite megablock comprises amphibole (40-50 vol%), plagioclase (20-25 vol%), biotite (10-20 vol%) and quartz (10 vol%), with variable amount of epidote (0-5 vol%), chalcopyrite (0-2 vol%), pyrrhotite (0-2 vol%), pyrite (< 1 vol%), magnetite (< 1 vol%) and titanite (< 1 vol%).

The amphibolite megablock generally displays an idioblastic to subidioblastic inequigranular-interlobate metamorphic texture; however, between 1386.93 m and 1387.54 m depth (corresponding with samples RG03 and RG06), lies a zone of coarse-grained, phaneritic material that is dominated by plagioclase (up to 60 vol%; Figure 2.12a). Horton *et al.* (2009a) interpreted the phaneritic texture to be of igneous origin and suggested that this zone within the amphibolite was either a metagabbro or metadiorite. The relative enrichment in plagioclase combined with presence of hornblende and biotite as the chief mafic minerals within this zone, while pyroxene and olivine are notably absent, supports a more dioritic than gabbroic component (Streckeisen, 1974).

Amphibole is commonly idioblastic and relatively unaltered (minor alteration to uralite and chlorite) (Figure 2.12b) and occurs as up to 40 mm in diameter glomerocrysts located between 1381 m and 1382 m depth (Figure 2.12a). These glomerocrysts locally enclose very fine-grained (0.1 mm) quartz and plagioclase grains. Plagioclase forms fine-grained (0.6 mm), subidioblastic grains that are locally altered to calcite and epidote. Although biotite generally forms very fine-grained (0.4 mm), subhedral grains that are locally altered to chlorite, large monomineralic aggregates up to 30 mm in diameter do occur. The abundance of biotite tends to increase with depth. Quartz and epidote are both very fine-grained (0.1 mm), with the former exhibiting undulose extinction in subhedral grains and the latter forming xenoblastic grains. Accessory chalcopyrite, pyrrhotite, pyrite, magnetite and titanite form very fine-grained (0.3 mm) subidioblastic grains.

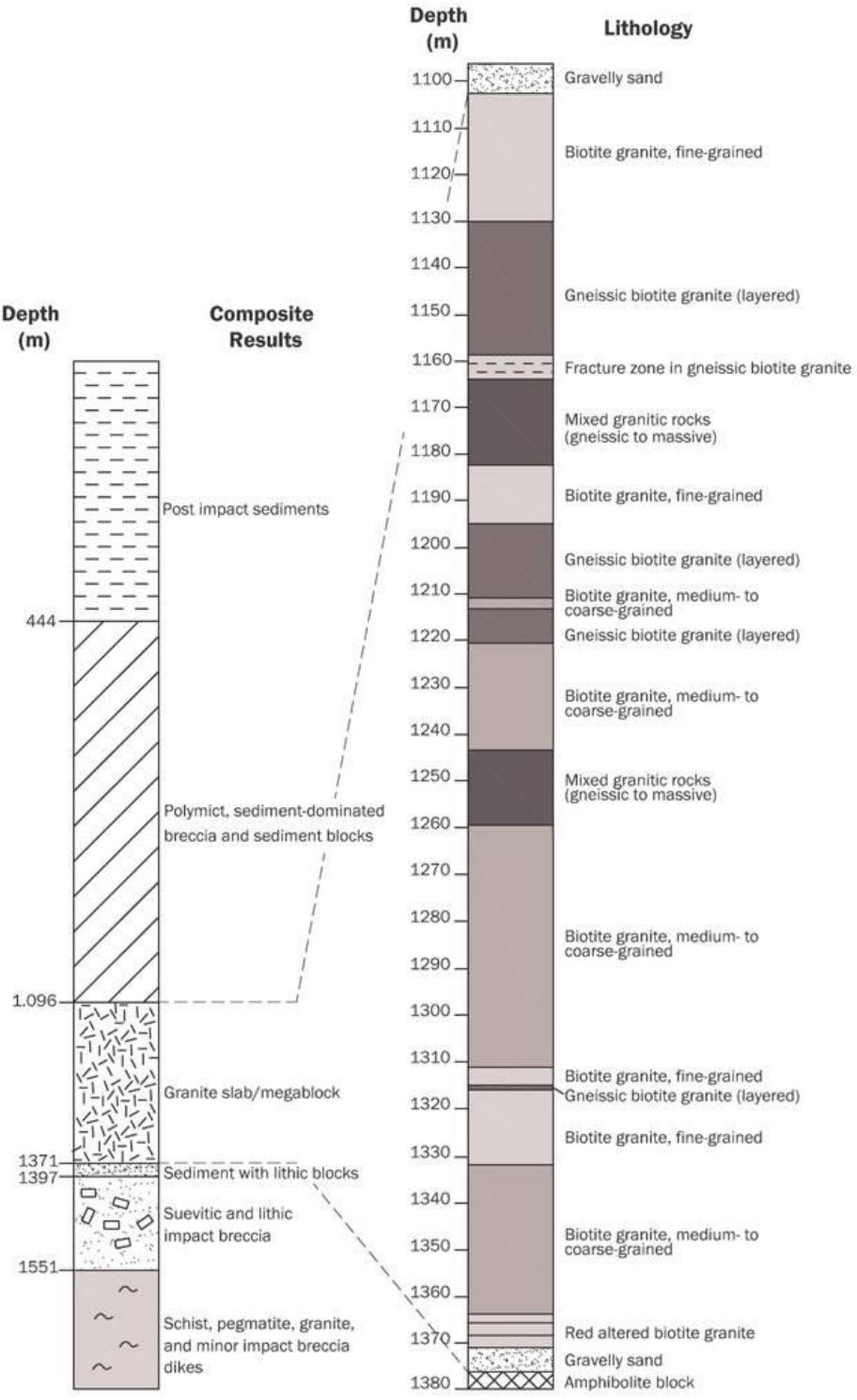

Figure 2.11: Composite stratigraphic column for the Eyreville-B borehole core (after Gohn *et al.*, 2006) with the detailed column for the upper megablocks section from 1095.74 m to 1389.71 m depth (after Horton *et al.*, 2009a).

Although the block is locally cut by multiple calcite-, quartz- and chalcedony-filled veins, varying in width from 0.5-20 mm (Figure 2.12a), a 40 mm wide brecciated granite vein within a calcite matrix (sample RG04; 1389.32 m depth; Figure 2.12c) intrudes roughly 40 cm above the base of the amphibolite megablock (1389.72 m depth), which comprises K-feldspar (45%), plagioclase (25%), quartz (25%) and biotite (5%; Figure 2.12c and d). K-feldspar in the brecciated granite is fine- to medium-grained (1-3 mm), subidiomorphic and variably altered to sericite. Plagioclase and quartz are both very fine- to fine-grained (0.2-1 mm) and subidiomorphic, with the latter locally poikilitic (very fine-grained, subidiomorphic quartz and biotite inclusions), twinned and variably altered to sericite and calcite. Biotite is very fine-grained (0.1-0.4 mm) and hypidiomorphic to subidiomorphic. The very fine-grained (<0.1 mm) calcite matrix also includes very fine-grained (<0.5 mm), angular mineral clasts of K-feldspar, plagioclase, quartz and biotite (Figure 2.12d). Along the contact zone between the brecciate granite vein and the amphibolite, an even finer-grained breccia comprising 80% of very fine-grained (0.3-0.5 mm) biotite that has experienced intense chloritisation, with the remaining 20% consisting of very fine-grained (<0.1 mm), recrystallised plagioclase and quartz grains (Figure 2.12d). The much finer-grained and recrystallised nature of the Bt-Chl breccia suggests a more ductile process (compared to the granite breccia) formed it.

2.3.3 Upper granite megablock

The upper granite megablock is the least shallow crystalline block in the Eyreville-B borehole core, located between 1095.71 m and 1371311 m depth, and can be divided into gneissic and massive varieties with a minor component of biotite-plagioclase±amphibole schist xenoliths (Figure 2.11). Unlike the lower basement-derived granite (Section 2.3.1.6), the dominant mica in the granite megablock is biotite. The gneissic granite, which tends to mainly occur above 1260 m depth, is intruded by the massive granite, the dominant lithology in the lower portion of the megablock (Figure 2.11). Contacts between the gneissic and massive granites tend to be sharp to lit-par-lit and, in some rare cases, appear gradational. The biotite schist xenoliths are almost exclusively found within the massive granite; however, rare exceptions within the gneissic granite do occur.

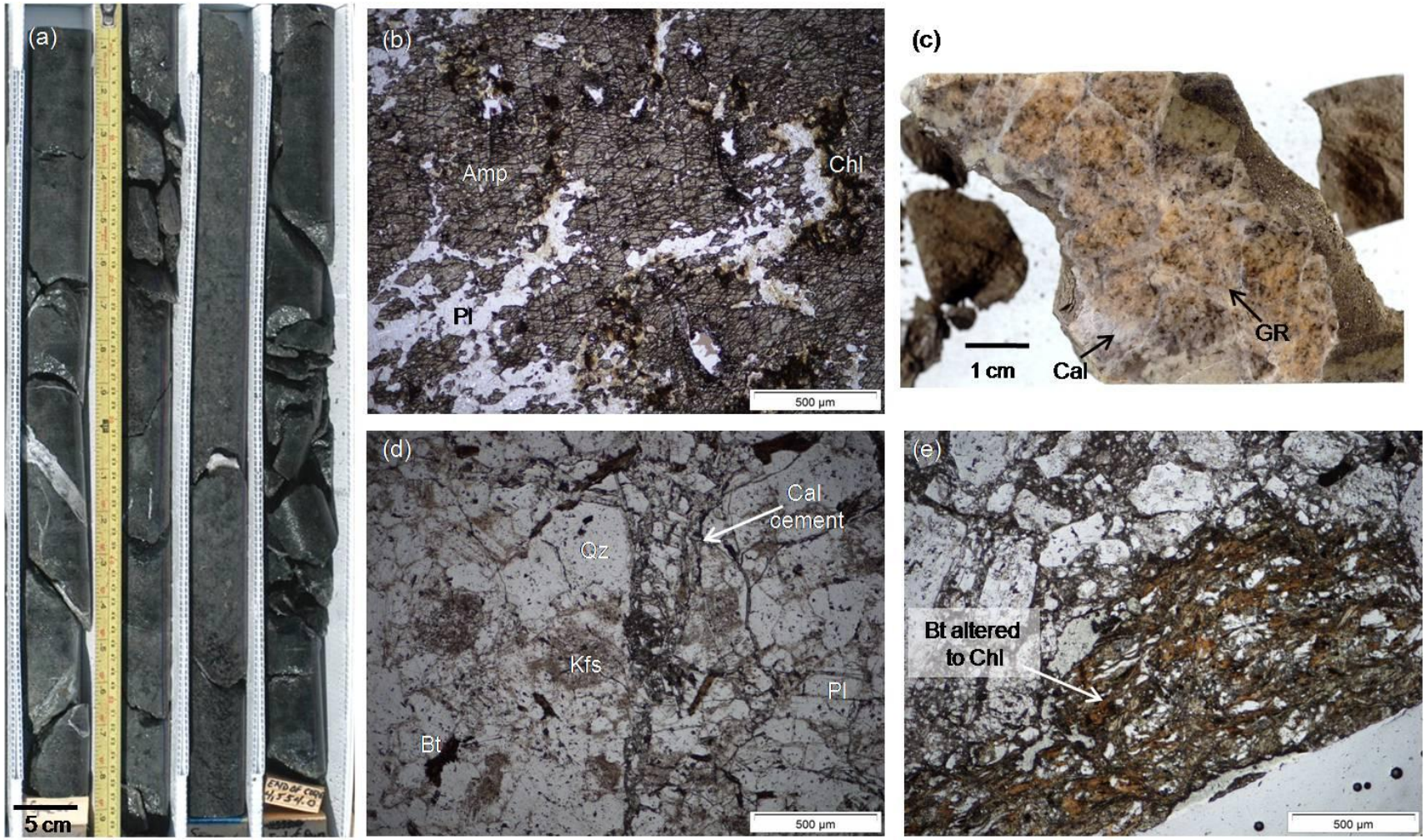

Figure 2.12: Photographs of the upper amphibolite megablock. (a) Corebox 226 showing the zone of coarse-grained amphibolite that contains a relict igneous texture within the generally homogenous megablock. (b) Photomicrograph (PPL) of sample W51 showing aggregates of Amp in certain parts of the megablock. (c) Hand specimen and (d) photomicrograph (PPL) of the brecciated GR vein within a Cal matrix (sample RG04) showing the brecciation at macro and microscopic scale. (e) Photomicrograph (PPL) of sample RG04 showing the contact zone between the granite-bearing calcite vein and the amphibolite where Bt has been intensely altered to Chl. Abbr.: Amp = amphibole; Bt = biotite; Cal = calcite; Chl = chlorite; GR = granite; Kfs = K-feldspar; Pl = plagioclase; Qz = quartz.

2.3.3.1 Gneissic biotite granite

The gneissic biotite granite comprises approximately 29 vol% of the granite megablock core intersection (Figure 2.11), displaying a hypidiomorphic, inequigranular-interlobate texture. Other characteristics of the gneissic granite include its light grey to pink colour, its fine- to coarse-grained (1-2.5 mm) nature and that it contains alternating mm- to cm-scale bands (Figure 2.13a). The banding occurs as a result of varying K-feldspar and biotite content within the gneiss. The composition of the granite gneiss consists of K-feldspar (25-35 vol%), quartz (25 vol%), plagioclase (25 vol%) and biotite (10-15 vol%), with lesser amounts of pyrite (0-5 vol%) and magnetite (0-5 vol%).

K-feldspar tends to form hypidiomorphic and poikilitic phenocrysts that can reach up to 2.5 mm in diameter (Figure 2.13b). Phenocrysts display flame perthite and microcline twinning and contain inclusions of quartz, plagioclase and biotite/chlorite (Figure 2.13b). Medium-grained (2 mm) plagioclase and quartz grains form the matrix (Figure 2.13c). Feldspars exhibit varying degrees of alteration to sericite and saussurite (Figure 2.13b and c). Biotite forms very fine- to medium-grained (0.1-2 mm), hypidiomorphic grains, which are locally altered to chlorite, and defines the foliation (Figure 2.13c). Pyrite and magnetite both form fine-grained (1-2 mm; Figure 2.13c), idiomorphic crystals with the latter observed to locally be surrounded by diffusion haloes.

2.3.3.2 Massive biotite granite

The massive biotite granite comprises approximately 70 vol% of the megablock granite core (Figure 2.11), has a hypidiomorphic, inequigranular-interlobate texture and exhibits considerably less alteration than observed in the gneissic granite. Generally massive, the medium- to coarse-grained (5-10 mm) biotite granite varies from pink to grey-white in colour, owing to variations in K-feldspar and biotite content, and is locally pegmatitic (Figure 2.14a). A weak foliation, defined by K-feldspar and/or biotite, is best observed adjacent to the gneissic granite (Figure 2.14a) and is interpreted to be magmatic based on the lack of evidence for significant crystal plastic flow in the matrix. The mineralogy of the massive granite includes K-feldspar (20-50 vol%), quartz (20-

35 vol%), plagioclase (15-30 vol%), biotite (2-10 vol%), muscovite (2 vol%), magnetite (0-3 vol%), pyrite (0-2 vol%) and zircon (0-1%).

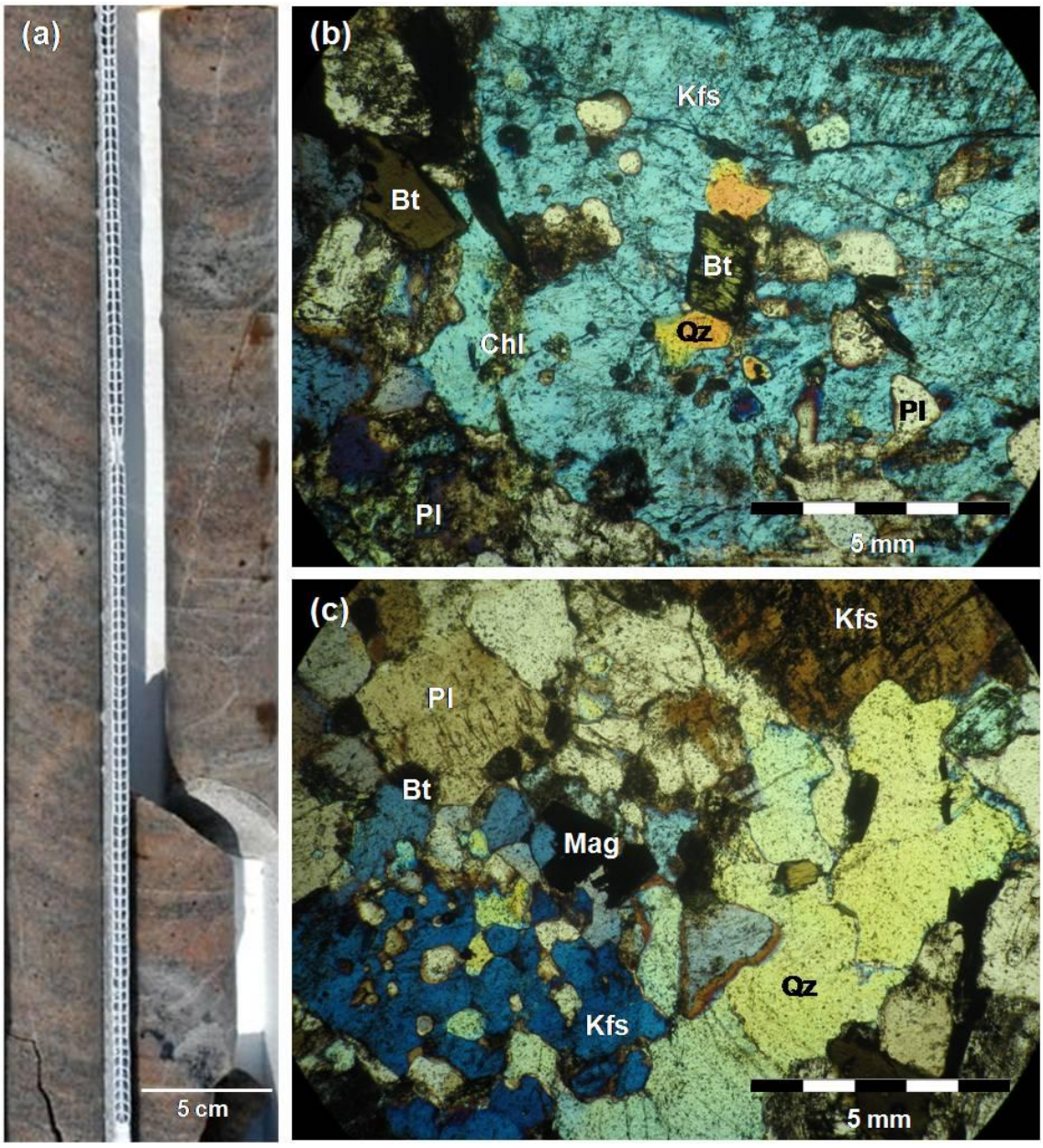

Figure 2.13: Photographs of the gneissic granite in the upper megablock. (a) Corebox 158 illustrating the gneissic banding. Photomicrographs (XPL) of (b) sample RG151 and (c) sample RG152 illustrating altered, poikilitic Kfs and altered Pl grains as well as Bt retrogressing to Chl in the gneissic megablock granite. Abbr.: Bt = biotite; Chl = chlorite; Kfs = K-feldspar; Mag = magnetite; Pl = plagioclase; Qz = quartz; XPL = cross polarised light.

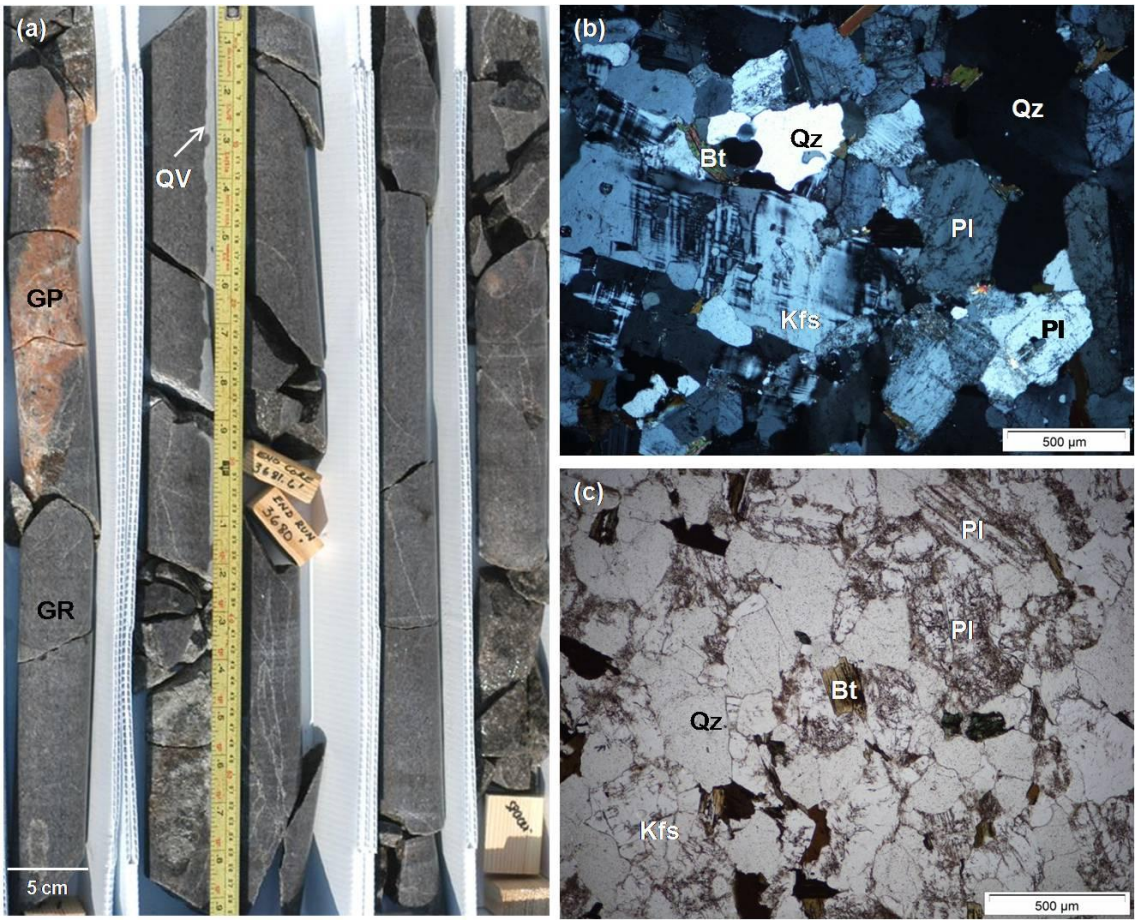

Figure 2.14: Photographs of the massive granite of the upper megablock. (a) Corebox 142 showing the medium-grained nature of the massive megablock granite with an intruding GP and QV. (b) Photomicrograph of sample W46 showing the poikilitic Kfs phenocrysts exhibiting microcline twinning and myrmekitic texture (XPL). (c) Photomicrograph of sample W37 showing alteration in Kfs and Pl (PPL). Abbr.: Bt = biotite; GP = granite pegmatite; GR = massive granite; Kfs = K-feldspar; Pl = plagioclase; PPL = plane polarised light; Qz = quartz; QV = quartz vein; XPL = cross polarised light.

Similar to the gneissic granite, K-feldspar in the massive granite forms idiomorphic to hypidiomorphic, poikilitic phenocrysts up to 15 mm in diameter, which exhibit flame perthite, microcline twinning and myrmekitic textures (Figure 2.14b). Quartz, plagioclase and biotite form inclusions in the K-feldspar phenocrysts (Figure 2.14b). Plagioclase forms medium-grained (2 mm), hypidiomorphic grains (Figure 2.14b). Although not to the same extent as in the gneissic granite, feldspar alteration to sericite and saussurite is observed (Figure 2.14b and c). Quartz forms fine- to medium-grained (1-3 mm), subhedral grains that exhibit undulose extinction and

locally sutured grain boundaries (Figure 2.14c). Together with chlorite, very fine-grained (0.3 mm) muscovite is observed to pseudomorph fine- to medium-grained (up to 2 mm) biotite (Figure 2.14b). Pyrite and magnetite are both fine-grained (1 mm) and hypidiomorphic, with the latter surrounded by diffusion haloes in close proximity to the gneissic granite. Zircon is very fine-grained (0.1-0.5 mm) and idiomorphic to subidiomorphic.

A zone of highly altered red granite lies between 1371.11 m and 1363.83 m depth at the base of the granite megablock (Figure 2.11). A similar lithology is identified in a 1-2 cm zone approximately 15 cm from the top of the megablock. The red colour is may have possibly been caused by comprehensive hydrothermal alteration of plagioclase to K-feldspar grains along pre-impact fractures (Mauldin *et al.*, 1997).

2.3.3.3 Biotite schist xenoliths

Usually less than 10 cm wide, but can reach up to 24 cm wide, several very fine- to medium-grained (0.2-2 mm), black to dark green, schistose xenoliths are observed mainly within the massive granite of the upper megablock (Figure 2.15a). Highly irregular contacts between the schist xenoliths and the massive granite are observed and are commonly accompanied by coarse plagioclase aggregates adjacent to the contacts (Figure 2.15b). The schist xenoliths comprise biotite (35 vol%), plagioclase (35-40 vol%), quartz (10-18 vol%), pyrite (2-10 vol%), epidote (2-10 vol%) and amphibole (0-10 vol%).

Biotite forms very fine- to medium-grained (0.2-2 mm), idioblastic to subidioblastic grains and defines the foliation (Figure 2.15c). Plagioclase occurs as very fine-grained (0.2 mm), subidioblastic to xenoblastic grains in the matrix and as rarer elongated to subrounded, poikilitic porphyroblasts (1 mm), which appear to locally overgrow the foliation (Figure 2.15c). Fine-grained (1 mm) pyrite more commonly occurs as subidioblastic aggregates. Epidote forms fine-grained (0.8 mm), subidioblastic poikiloblasts (Figure 2.15b). Very rare amphibole forms radiating or sheaf-like aggregates up to 1.5 mm wide.

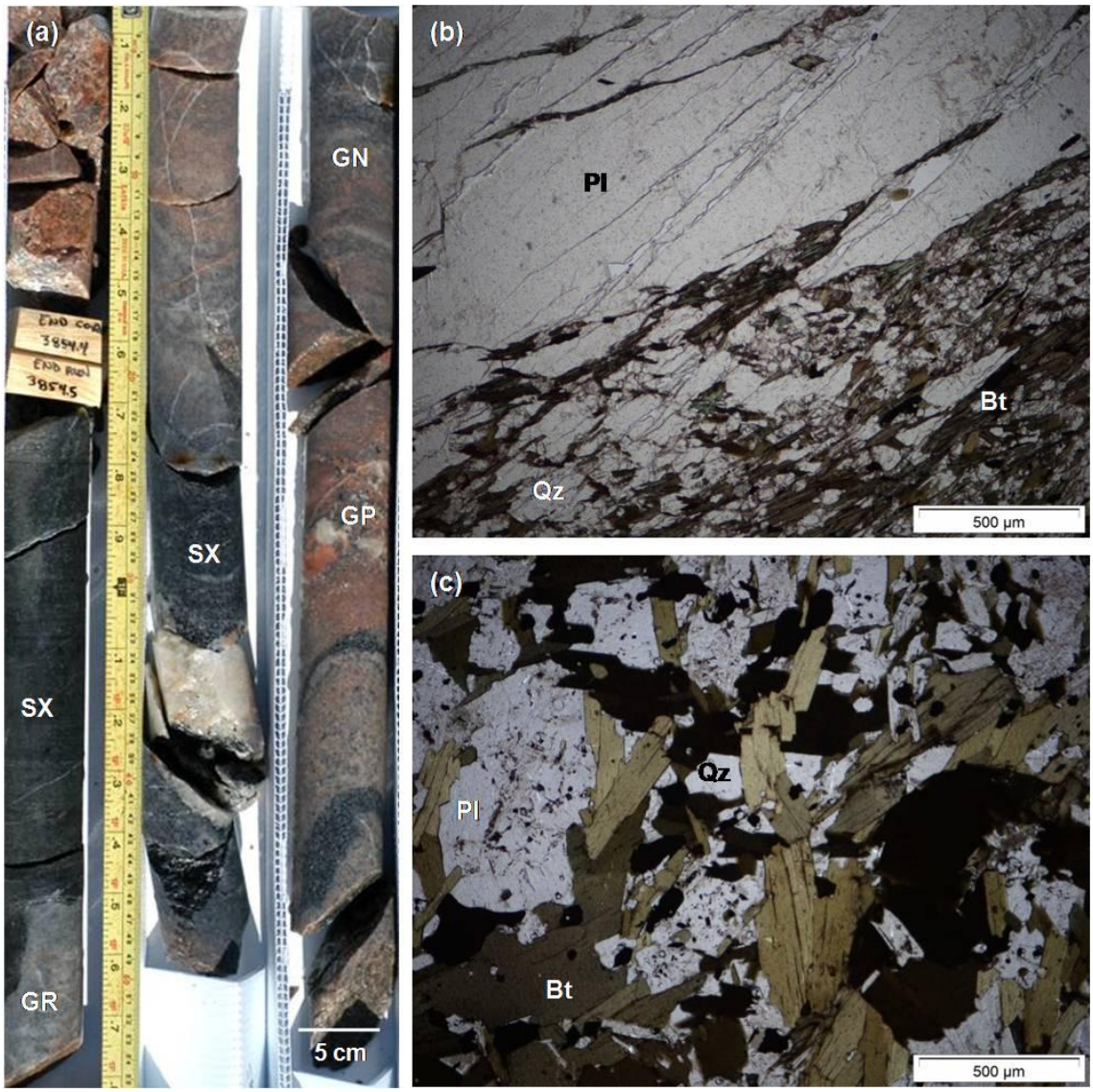

Figure 2.15: Photographs of the schist xenoliths in the upper granite megablock. (a) Corebox 147 illustrating the location of the xenoliths within the massive and gneissic granite. Photomicrographs (PPL) of sample W39 showing (b) the irregular contact between the schist and granite. (c) Photomicrograph of sample W36b showing the relative size and abundance of Bt compared to the massive and gneissic megablock granites. Abbr.: Bt = biotite; GN = gneissic granite; GP = granite pegmatite; GR = massive granite; Pl = plagioclase; PPL = plane polarised light; Qz = quartz; SX = schist xenoliths.

2.4 Structural analysis

In general, there are four main types of structures observed within the lower basement-derived and upper megablocks sections of the Eyreville-B borehole core; these include foliations and related structures, fractures and breccias, microstructures and porphyroblast microstructures. However, it must be noted that measurements taken from the upper amphibolite and granite megablocks are not considered to reflect true orientation based on their position above the impactite sequence in the stratigraphic column (see Chapter 1, Figure 1.15). As for the lower basement-derived section, seismic profiling of the lower basement-derived section by Catchings *et al.* (2008) indicates that this section is also a slumped block and, consequently, structural measurements taken from this section of the core are not interpreted to reflect the original orientation of the observed structures.

2.4.1 Foliations and related structures

In Table 2.1, the average dip angles for foliations measured in the lower basement-derived and upper megablocks sections of the Eyreville-B borehole core are presented (see Appendix 1d for the full list of measurements). Owing to the fact that the true orientation of the borehole core could not be determined, measurements of the dip angle were the only data that could be obtained as there was no strike data available. Other than the massive granite in the upper granite megablock and the pegmatitic granite in the lower basement-derived section, the target rocks of the Eyreville-B borehole core contain at least one foliation. In the lower basement-derived metapelites, structural measurements for the prograde-to-peak mica foliation (S1a; mean 54 ± 9°; Table 2.1; Figure 2.16a) shows that it dips at a moderate angle from the core axis.

Intrafolial fold hinges defined by either layering or quartz veins are observed in the lower basement-derived metapelites and can reach up to tens of centimetres in some cases (Figure 2.16a). The intrafolial folds tend to be shallowly inclined and have isoclinal to open interlimb angles, with some intrafolial folds in the graphite-rich mica schist containing secondary open M-

folds with wavelengths up to 10 cm in some cases (Figure 2.16a). In the vicinity of these intrafolial fold hinges zones of chaotic foliations are observed (Figure 2.16b). Although superficially resembling breccias, these graphite-rich zones typically contain crenulated minerals (e.g. muscovite) and plagioclase porphyroblasts as well as a highly micaceous matrix (Figure 2.16b and c). The localised nature of these zones (only within fold hinges) combined with the presence of graphite and the absence of significant retrogression of the mica and plagioclase grains suggests that the zones may be related to localised strain partitioning and slip facilitated by graphite and phyllosilicates during the prograde metamorphic path close to peak conditions.

Table 2.1: Average orientation angle of foliations measured from the core axis for the metapelites from the lower basement-derived section (LB), the amphibolite from the upper megablock amphibolite (MBA) and biotite schist xenoliths (MBS) and the gneissic granite (MBGn) from the upper megablock granite.

Section	Number of measurements	Angle (°)	Error (°)
LB (S1a)	20	54	9
LB (S1b)	19	71	7
MBA	10	49	10
MBS	2	48	9
MBGn	19	60	6

A mylonitic foliation (S1b) in the lower basement-derived section, defined by a heterogeneous zone of alternating bands of granite and mica schist, is observed mainly between 1640 m and 1655 m (Figure 2.17a), although mylonitisation is also seen locally above and below this zone. Dipping at a shallow angle from the core axis (S1b; mean 71 ± 7°; Table 2.1), this foliation is generally observed to be oriented subparallel to the schistose (S1a) foliation (Figure 2.17b) and is associated with an oblique dip-slip mineral lineation. Mylonitised mica schist samples are light brown (Figure 2.17b), owing to the extensive retrogressive replacement of biotite by chlorite and muscovite, whereas mylonitised granite is much more fine-grained compared with pegmatitic veins in other parts of the lower basement-derived section (Figure 2.17c). Lister and Snoke (1984) defined mylonites that form under retrograde conditions and exhibit non-coaxial laminar

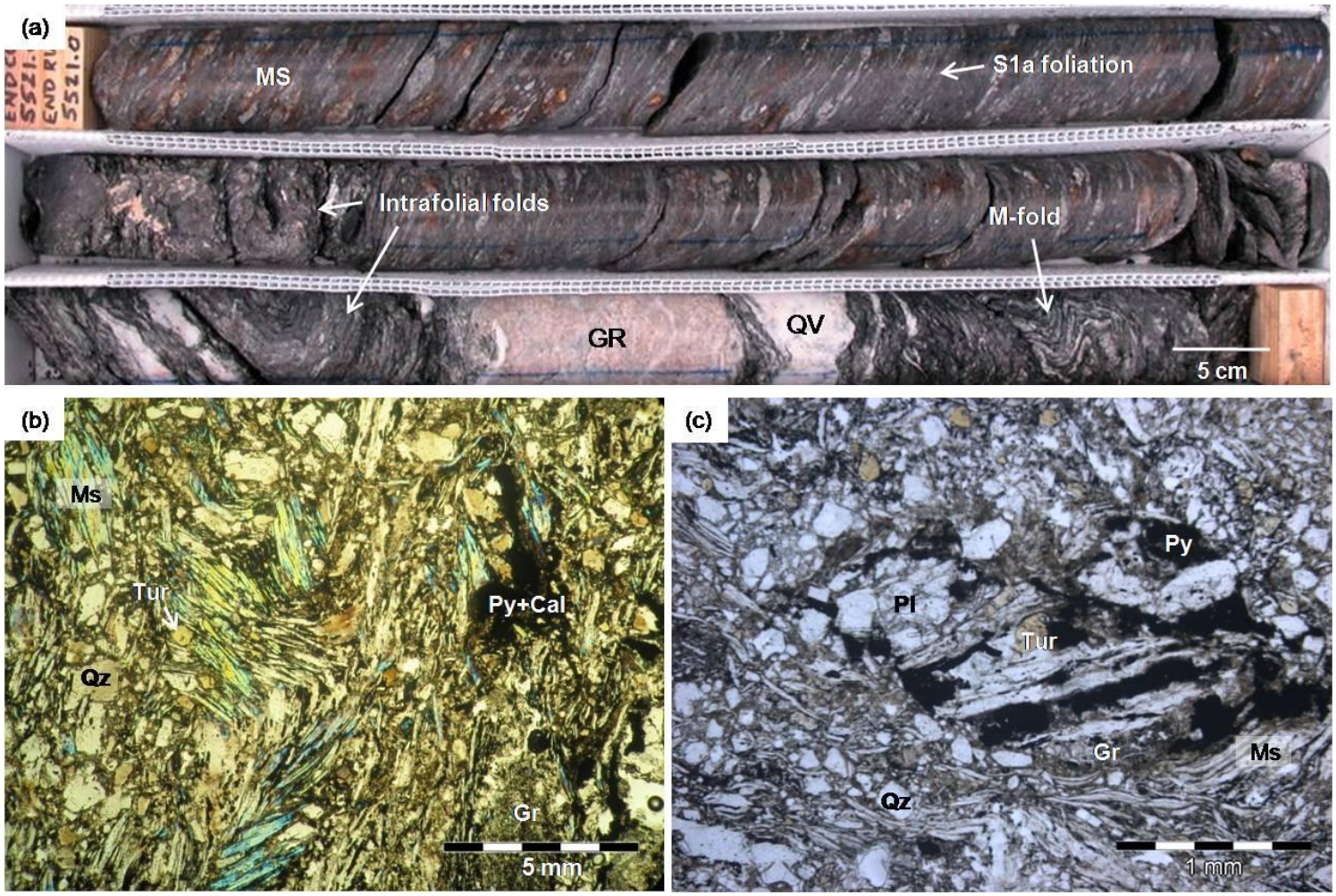

Figure 2.16: **(a) Portion of corebox 321 from the lower basement-derived section showing the prograde foliation (S1a) as well as intrafolial folds and QV within the MS that is locally intruded by GR. Photomicrographs of sample RG41 showing (a) the locally chaotic foliation adjacent to intrafolial folds (XPL) and (c) the lack of enhanced retrogression despite Gr, Cal and Py occurring in interclast regions (PPL). Abbr.: Cal = calcite; GR = granite vein; Gr = graphite; MS = mica schist; Ms = muscovite; Pl = plagioclase; PPL – plane polarised light; Py = pyrite; Qz = quartz; Tur = tourmaline; XPL = cross-polarised light.**

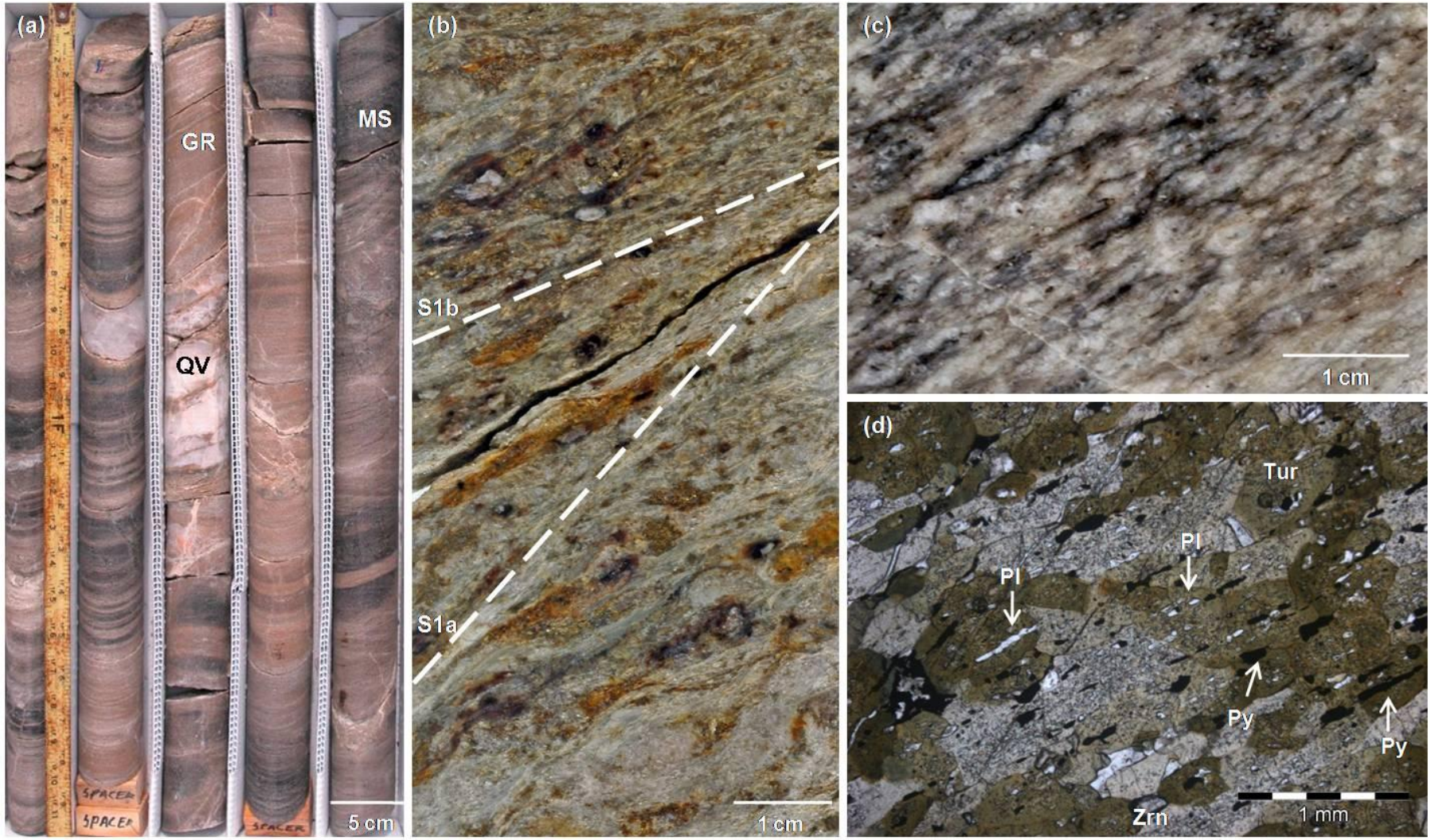

Figure 2.17: Photographs of the S1b foliation in the lower basement-derived mylonite. (a) Corebox 310 showing the mylonite zone with interlayered GR, MS and QV. (b) Hand specimen of sample RG56 showing the S1a and S1b foliations in the retrogressed MS. (c) Hand specimen of sample RG40 showing the S1b foliation in the fine-grained mylonitised Gr. (d) Photomicrograph (PPL) of sample RG57 showing the S1a foliation defined by elongated Pl and Py inclusions in Tur. Abbr.: GR = granite; MS = mica schist; Pl = plagioclase; PPL = plane polarised light; Py = pyrite; QV = quartz vein; Tur = tourmaline; Zrn = zircon.

flow microstructures (e.g. mica fish, S-C fabric; see Section 2.4.3) as Type II S-C mylonites. The fact that the basement granite does not contain the S1a foliation but is affected by the retrogressive mylonitic S1b foliation indicates that the granite intruded the mica schists after peak conditions had mostly passed but before the onset of the retrograde metamorphism in the latter part of D1. This is confirmed by the presence of metasomatic tourmaline aggregates overgrowing the prograde foliation in the wall rocks to granite veins, where elongated inclusions within the tourmaline preserve the S1a foliation (Figure 2.17d).

The dip magnitude of the gneissic foliation in the upper megablock section (mean 60 ± 6° from the core axis; Table 2.1) is similar to that of the lower basement-derived mica foliation (Figure 2.18). A weak mineral lineation (L1b) subparallel to the dip is also observed along fractures (see Section 2.4.2). Rare, thin (<10 cm), mylonitic zones occur locally (e.g. at 1096.59 m in core-box 119 and at 1359.80 m in core-box 216). Unfortunately, the absence of clear evidence that the gneissic foliation developed only during shearing, or that the mylonite formed during a separate event, prevents correlating these foliations with either S1a or S1b in the lower basement-derived section.

The foliation in the granite gneiss is interpreted to be tectonic rather than magmatic based on the presence of aligned biotite and amphibole monomineralic and polymineralic aggregates (more typical of metamorphic foliations; see Section 2.4.3), strain-related recrystallisation and elongation of K-feldspar and quartz grains (see Section 2.4.3) as well as the presence of local mylonite zones also relating to heterogeneous strain conditions (Paterson *et al.*, 1989). The generally massive granite (Figure 2.18), on the other hand, shows a weak foliation defined by K-feldspar and/or biotite adjacent to the gneiss. However, the lack of significant crystal plastic flow in this granite suggests that it is more likely that the weak foliation was not caused by the same process as the gneissic granite but rather by magmatic flow (Paterson *et al.*, 1989).

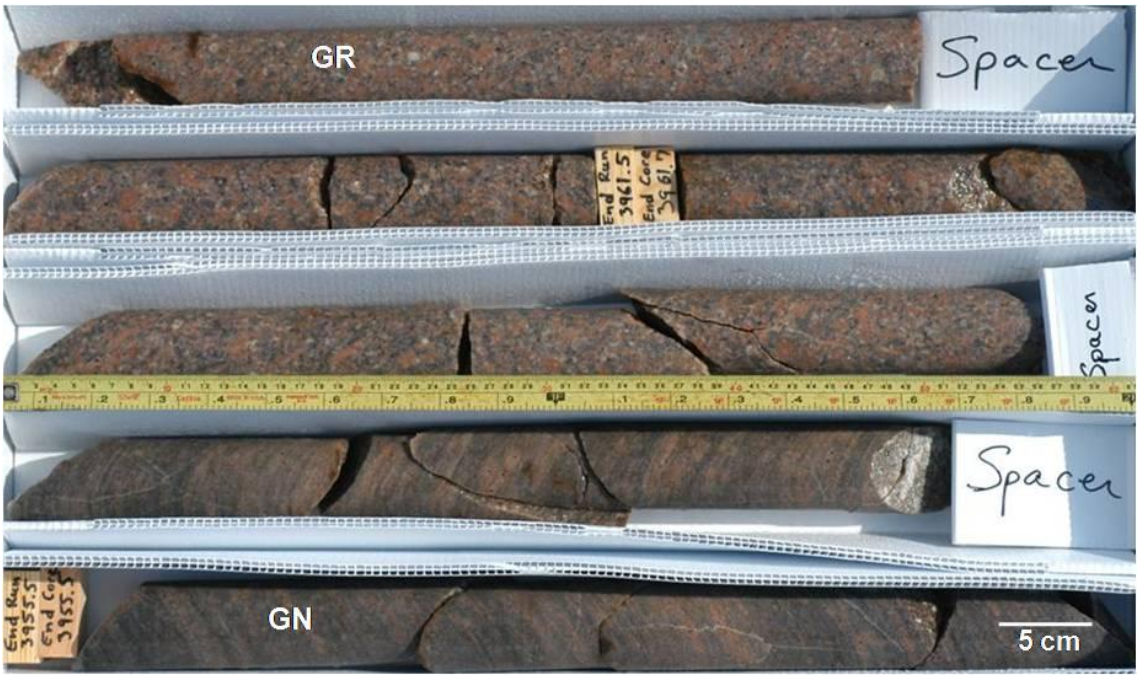

Figure 2.18: Photograph of corebox 160 showing the gneissic foliation in GN and the massive nature of GR in the upper granite megablock. Abbr.: GN = gneissic megablock granite; GR = massive megablock granite.

The foliation in the biotite schist xenoliths in the upper granite megablock is defined by fine- to medium-grained biotite (Figure 2.19a) and is oriented 48 ± 9° (measured from the core axis; Table 2.1). This is more steeply dipping than that seen in the gneissic granite variety of the megablock section. The upper amphibolite megablock includes a foliation, oriented at 49 ± 10 (measured from the core axis; Table 2.1; Figure 2.19b) as well as a lineation oriented obliquely to the amphibolite foliation (Figure 2.19c) on dip-slip slickenside fractures (see Section 2.4.2) based on the present orientation of the core. Although the amphibolite is strongly foliated in most of the amphibolite megablock, samples RG03 (1387.51 m depth) and RG06 (1387.24 m depth) are enriched in plagioclase and contain a coarse-grained, phaneritic texture that may have been inherited from the igneous protolith (Figure 2.19d; see Section 2.3.2). These observations correspond with those made for the amphibolite megablock between 1386.93 m and 1387.54 m depth by Horton *et al.* (2009a), who interpreted the relict igneous texture to be either metagabbroic or metadioritic in nature.

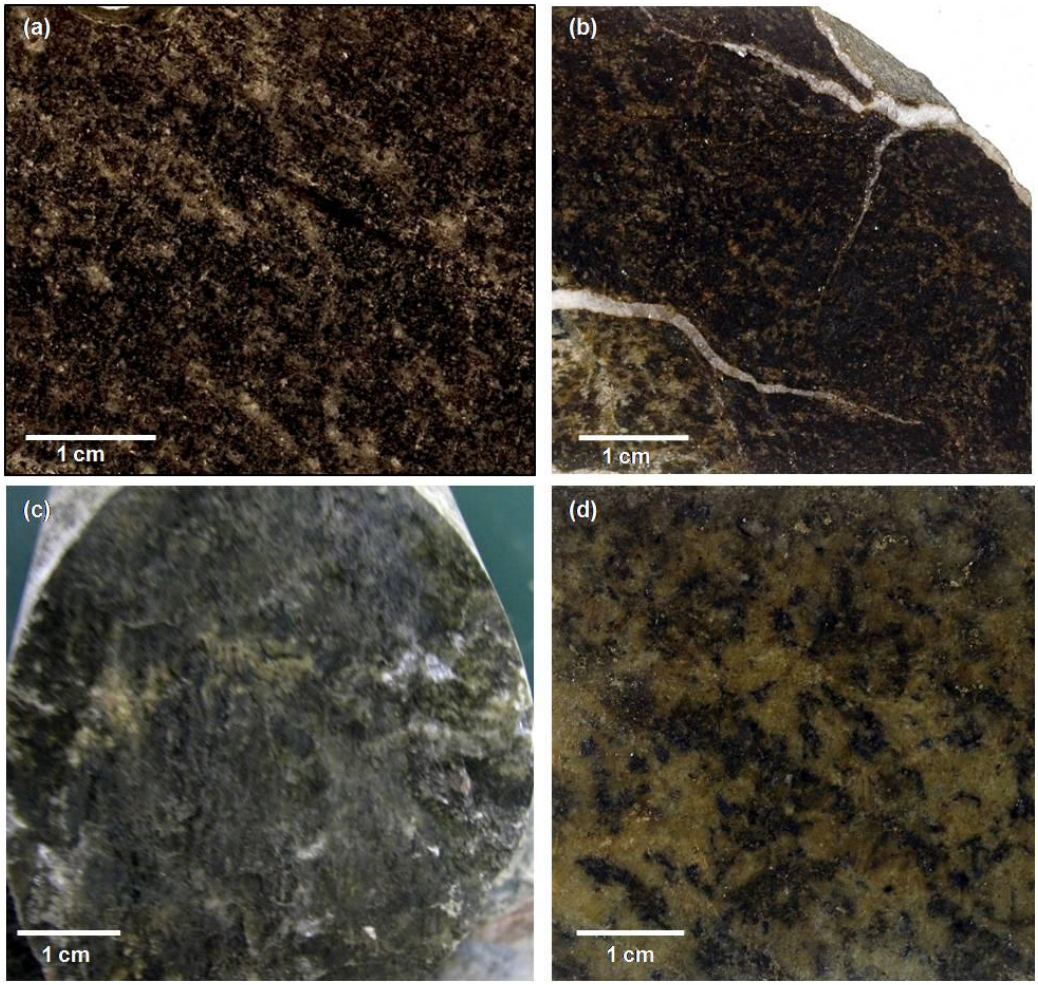

Figure 2.19: Hand specimen photographs of (a) sample RG172 showing the biotite-defined foliation in the biotite schist xenoliths in the upper granite megablock, (b) sample RG02 showing the foliation in the upper amphibolite megablock that is locally cut by Cal and Qz veins, (c) sample RG176 showing the mineral lineation relative to the orientation of the core in the upper amphibolite megablock, and (d) sample RG06 showing the coarse-grained, phaneritic texture preserved in parts of the upper amphibolite megablock. Abbr.: Cal = calcite; Qz = quartz.

2.4.2 Fractures and breccias

A major characteristic of both the lower basement-derived and upper megablock sections is the evidence of at least one fracturing event oriented subparallel to the core axis. Fractures are generally observed to overprint the foliations and related structures and are, thus, designated D2; these fractures are commonly filled by chlorite, calcite, pyrite, quartz and/or graphite, and range from fine- to coarse-grained and millimetre to decimetre scale (Figures 2.20 and 2.21). Within the fracture network observed throughout the lower basement-derived and upper

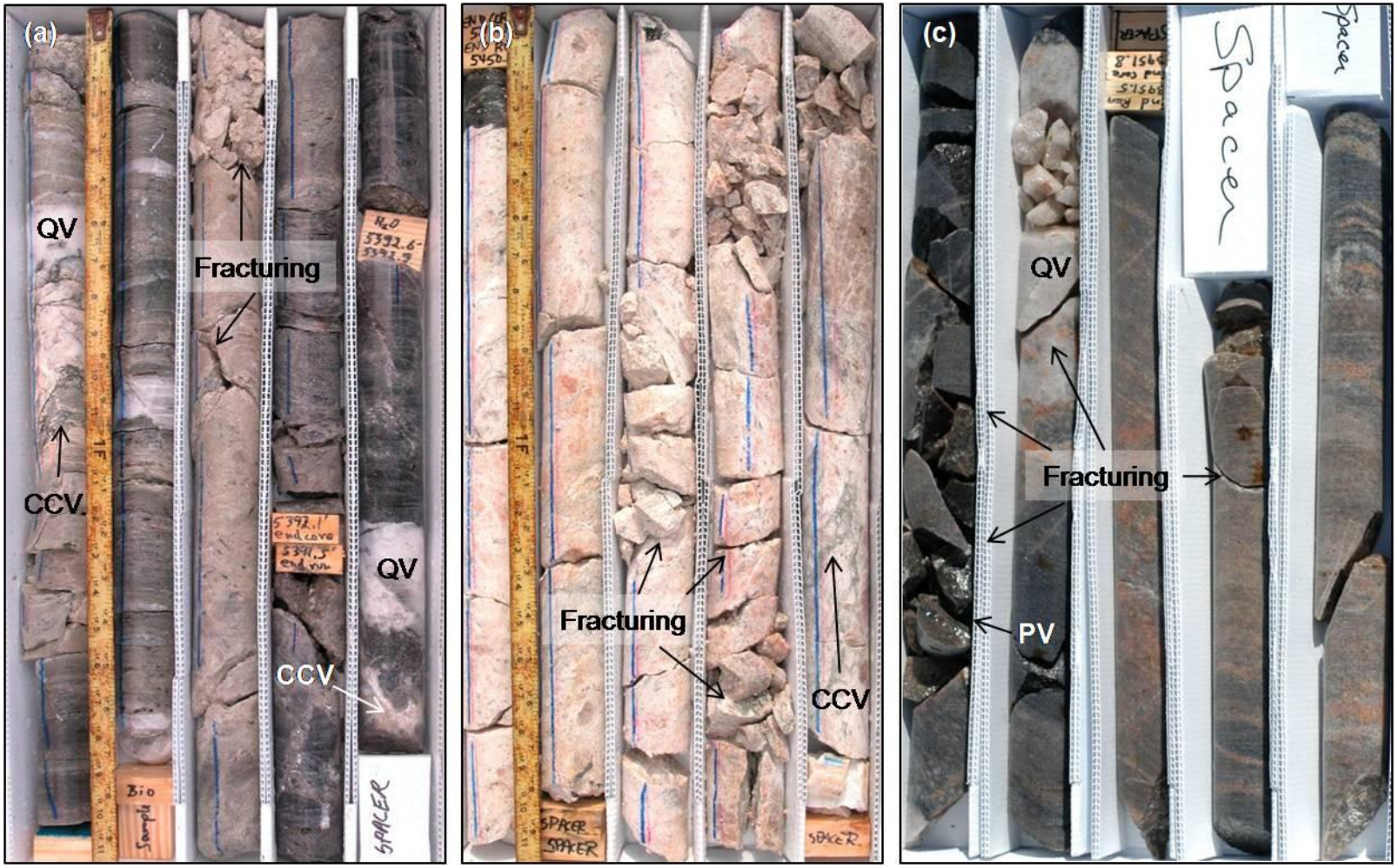

Figure 2.20: Corebox photographs showing fracturing containing varying amounts of Cal, Chl, Py and Qz within the (a) the lower basement-derived mica schist (Corebox 307) and granite (Corebox 314), and within the (c) gneissic megablock granite (Corebox 159). Abbr.: Cal = calcite; CCV = calcite and chlorite vein; Chl = chlorite; PV = pyrite vein; Py = pyrite; QV = quartz vein; Qz = quartz.

megablock section, calcite is typically granoblastic, with rare fibrous growths, and chlorite occurs both as spherulitic aggregates and as alteration products of biotite adjacent to calcite veins. Pyrite mineralisation along fractures typically occurs as stringers. Quartz veins tend to be coarse-grained. Graphite tends to occur as coarse, irregular aggregates.

In the lower basement-derived section, the most common type of D2 fracture is anastomosing/branching in nature, with chlorite and/or calcite as the typical fracture fill, and is associated with mesoscopic brecciation (Figure 2.22a). As mentioned in Section 2.4.2, an obliquely plunging lineation is apparent along chloritic slickensides where the core has split along the fractures. Although individual fractures are not typically very wide (<5 mm), splaying of the fractures to form up to 1 cm wide breccia lenses is observed (Figure 2.22b). Additionally, although displacements across fractures are generally <5 mm, displacements can be up to decimetres in extent (Figure 2.22c). Cataclastic brecciation within this fracture set in sample RG46 superficially resembles pseudotachylyte (Figure 2.22d), such as that observed in the impactite sequence of the Eyreville-B borehole core (Jolly, 2011). Matrix alteration, however, prevents the ability to assess whether or not its formation involved melting. The absence of truncation or displacement at a microscopic level in sample RG46 (Figure 2.22e) where macroscopic evidence of what appears to be fractures cross-cutting the brecciation suggests that the formation of the fracture set and brecciation in this sample were penecontemporaneous.

Brecciation observed in the calc-silicate rock in the lower basement-derived mylonite zone is closely associated with the extensive calcite + epidote + quartz ± chlorite fracture fill (Figure 2.5a). Unlike the microscopic to mesoscopic brecciation associated with the D2 fracture network described previously, the calc-silicate brecciation is more extensive in nature, is matrix-supported and is cut locally by D2 calcite veins (Figure 2.5a). This might suggest that the calc-silicate brecciation is related to the earlier D1b event, with the extensive brecciation a reflection of its greater competence relative to the mylonitised mica schists. Alternatively, this brecciation does form part of the D2 fracture network, which is a complicated process commonly involving



Figure 2.21: Corebox photographs showing fracturing within containing varying amounts of Cal, Py and Qz within the (a) massive megablock granite (Corebox 165), (b) the biotite schist xenoliths in the upper granite megablock (Corebox 147) and (c) the upper amphibolite megablock (Corebox 224). Abbr.: Cal = calcite; CV = calcite vein; PV = pyrite vein; Py = pyrite; QCV = quartz and calcite vein; Qz = quartz.

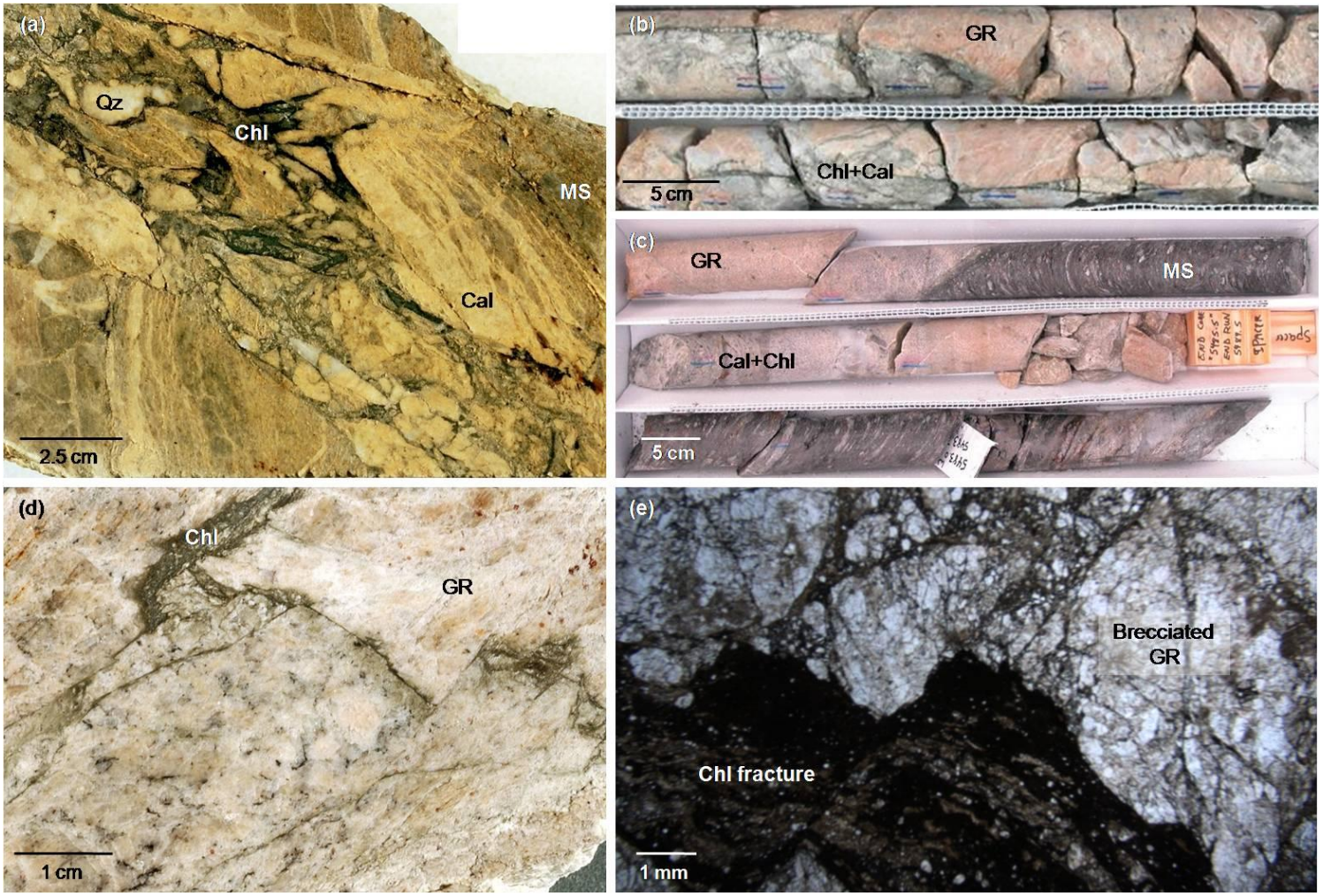

Figure 2.22: Photographs of fracturing and brecciation in the lower basement-derived section. (a) Hand specimen of MS sample RG178 showing a Chl+Cal fracture that is locally brecciated. (b) Portion of corebox 328 showing splaying Chl+Cal fractures in the GR. (c) Portion of corebox 317 showing a Cal+Chl fracture between the MS and GR. (d) Hand specimen and (e) photomicrograph (PPL) of sample RG46 showing D2 chloritic fracturing in the GR. Abbr.: Cal = calcite; Chl = chlorite; GR = granite; MS = mica schist; PPL = plane polarised light.

the overprinting of fracture sets. The retrogressive nature of the mineral assemblage, however, suggests that it is related to D2.

As mentioned in Section 2.3.2, the upper megablock amphibolite is intruded by a brecciated granite vein within a calcite matrix (sample RG04; Figure 2.12 c and d), and it is the only such vein observed within the lower basement-derived and upper megablocks sections of the Eyreville-B borehole core. The brecciated granite more closely resembles the coarser-grained massive granite of the upper megablock compared with the lower basement-derived granite owing to the absence of muscovite. If the brecciated granite was derived from the massive megablock granite, it implies that both amphibolite and granite megablocks form part of a single terrane. Furthermore, the association between the brecciation and calcite matrix-fill within this granite vein suggests that brecciation occurred either prior to or during calcite veining (D2) within the amphibolite megablock and, thus, the D2 fracturing event predates the Chesapeake Bay impact event.

In the upper 60 m of the lower basement-derived section of the Eyreville-B borehole core a number of polymict impact breccia dykes and suevite veins are observed (Figures 2.1, 2.9 and 2.10). Granite clasts within the deeper suevite veins (1600-1610 m depth) are observed to locally contain D2 chlorite-filled fractures. In this study, the breccia samples RG62, RG63, RG65, RG71, RG73, RG74, RG75 and RG77 contain the only evidence of shock metamorphism in the lower basement-derived section (see Section 2.3.1.8; Figure 2.10). Horton *et al.* (2009b) observed that clasts in these breccias record shock pressures from unshocked to whole-rock melt at pressures greater than 60 GPa (Stöffler, 1971). The fact that the breccias are located in typically unshocked basement indicates that they were probably injected into dilatant fractures in the lower basement-derived section adjacent to the transient crater wall at the onset of inward slumping when overburden pressure was absent (Gohn *et al.*, 2008; Horton *et al.*, 2009b).

2.4.3 Microstructures

In the lower basement-derived mica schists, the prograde metamorphic path is defined by the alignment of micas (muscovite > biotite) alternating with quartz + plagioclase layering (Figure 4.3a; see Section 2.3.1.1). Other characteristics of the prograde foliation include the preservation of rare isoclinal fold hinges by polygonal mica arcs (see Figure 2.2b) as well as within fibrolitic knots (Figure 2.23a). Where the prograde foliation evolves from planar to sinuous in nature, listric extensional shear bands are locally observed oriented at ≤30° to the mica foliation (Figure 2.23b). Muscovite grains with basal cleavages oriented obliquely to the prograde foliation exhibit rhomb shapes indicating slip along the (0001) cleavage plane whereas those with aligned basal cleavages give axial ratios up to 20:1 (Figure 2.23c). In some cases, the long axes of plagioclase porphyroblasts also slow consistent oblique alignment to the prograde foliation (Figure 2.23b). Based on the absence of significant retrogression, intracrystalline strain and/or grain size reduction along the extensional shear bands, it is interpreted that the bands formed under relatively high temperature conditions and, thus, form part of a composite shear fabric with the prograde foliation that may have evolved during prograde to peak metamorphic conditions.

As discussed in Section 2.4.1, a Type II S-C mylonitic foliation is preserved in certain parts of the lower basement-derived section, defined by alternating mica schist and granite bands (Figure 2.17a). Although the granite does not contain the prograde foliation seen in the mica schists, boudinaged granite veins as well as quartz veins within the prograde foliation are observed. Unfortunately, the subparallel nature of the mylonitic foliation to the prograde foliation combined with the fact that all rocks exhibit some degree of retrograde grain-scale effects precludes the ability to distinguish pre- to syn-peak metamorphic shearing from post-peak shearing in the mica schists. However, the retrograde mylonitic event in the lower basement-derived section is clearly defined by distinctive fine-grained microstructures produced by the associated grain-size reduction. This is especially so in the mylonitised granite where strong S-C and S-C' structures are observed (Figure 2.23d). Other microstructures include muscovite and biotite (rarer) fish with fine-grained and neoblastic tails, respectively, which tend to be bent

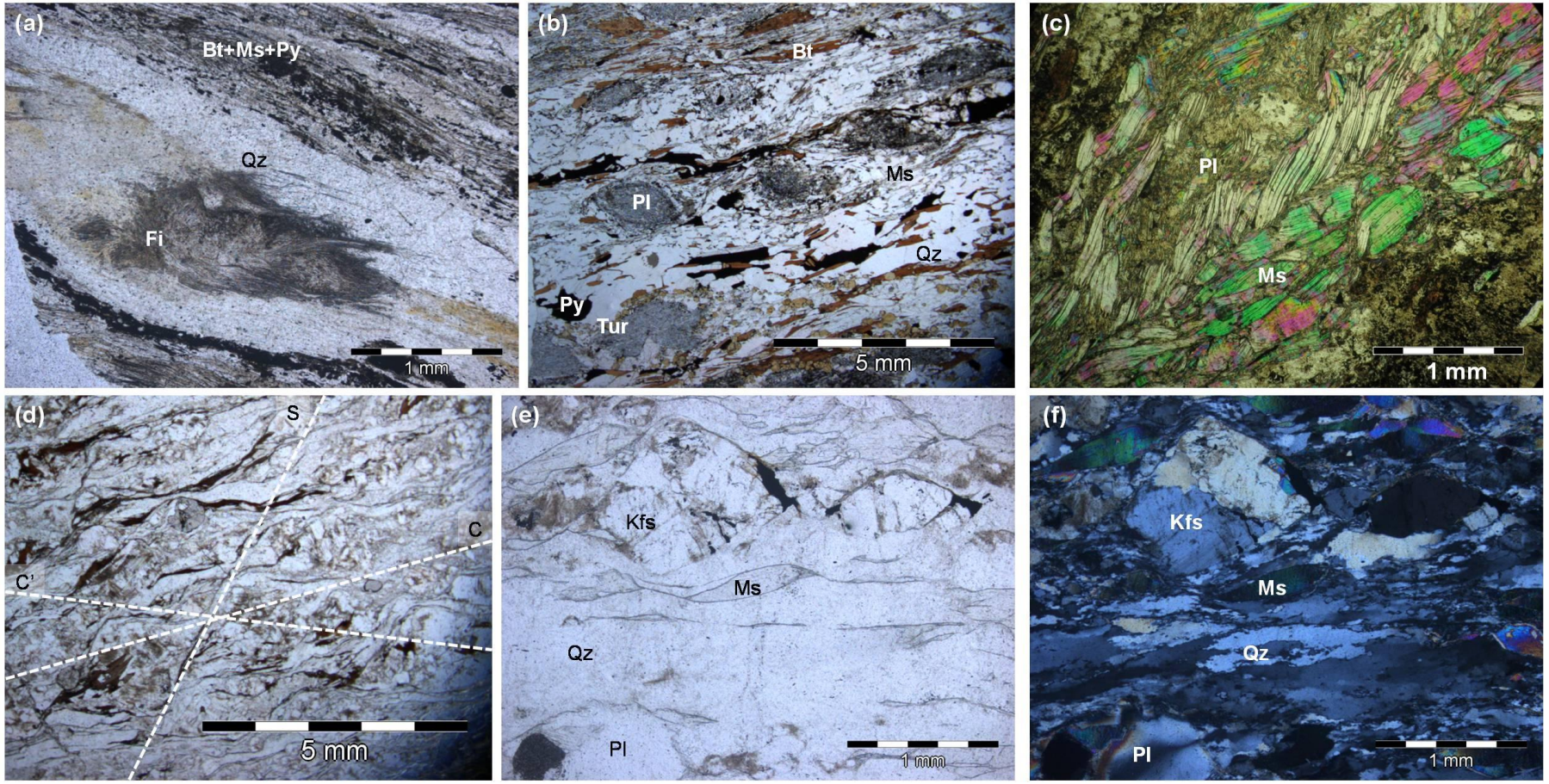

Figure 2.23: (a) Photomicrograph of mica schist sample RG44 showing a fibrolitic knot (PPL). (b) Photomicrograph of mica schist sample RG68 showing the prograde S1a foliation and extensional shear bands (PPL). (c) Photomicrograph of mica schist sample RG60 showing the cleavage orientations of Ms grains (XPL). (d) Photomicrograph of granitic sample RG40a showing mylonitic S1b S-C and S-C' (white dashed lines) structures (PPL) consistent with dextral shear sense. (e) PPL and (f) XPL photomicrograph of granitic sample RG40 showing Ms and Bt fish, Kfs bookshelf sliding and Qz ribbons illustrating dextral shear sense. Abbr.: Bt = biotite; Fi = fibrolite; Gr = graphite; Grt = garnet; Kfs = K-feldspar; Ms = muscovite; Pl = plagioclase; PPL = plane polarised light; Py = pyrite; Qz = quartz; Tur = tourmaline; XPL = cross-polarised light.

and exhibit undulose extinction (Figure 2.23e), rare, σ-shaped, feldspar porphyroclast mantles (Figure 2.23d; Passchier and Trouw, 2005), and bookshelf sliding in porphyroclastic feldspars with resultant interstices filled with relatively coarse-grained, unstrained quartz (Figure 2.23d and e). Quartz grains in the mylonitic foliation are characterised by extensive subgrain and ribbon development, with grains typically elongated parallel to C-surfaces and displaying highly sutured quartz-quartz grain boundaries (Figure 2.23f). Undulose extinction and subgrain formation in quartz are most common where quartz ribbons are pinched against C'-surfaces (Figure 2.23f). These microstructures can be used to infer kinematic information about sense of shear (Lister and Snoke, 1984), which, in this case, indicate a dextral sense of shear (Figure 2.23d, e and f).

The gneissic granite in the upper megablock section shows strong alteration of feldspar grains, and, in some cases, plagioclase grains are completely altered to sericite (Figure 2.24a). K-feldspar phenocrysts are commonly poikilitic in nature (see Section 2.4.4) and may contain bent twins (Figure 2.24b) and/or rare myrmekitic rims. In contrast, the massive megablock granite is significantly less altered, although some seritisation of plagioclase cores is observed (Figure 2.24c). Similar to the gneissic granite, bent twins and myrmekitic textures occur in the K-feldspar phenocrysts of the massive granite (Figure 2.24d).

Elongated to subrounded plagioclase porphyroblasts in the biotite schist xenoliths of the upper granite megablock (Figure 2.25a) suggest late syntectonic growth rather than as a result of ductile deformation. However, the presence of retrogressive chloritic seams, oriented at an oblique angle to the biotite-dominated foliation (consistent with extensional shear bands), boudinaged quartz ribbons and quartz subgrain development may suggest an association with the mylonitic foliation in the lower basement-derived section (Figure 2.25b). Unfortunately, there is insufficient evidence to fully support this argument owing to the limited sample material available.

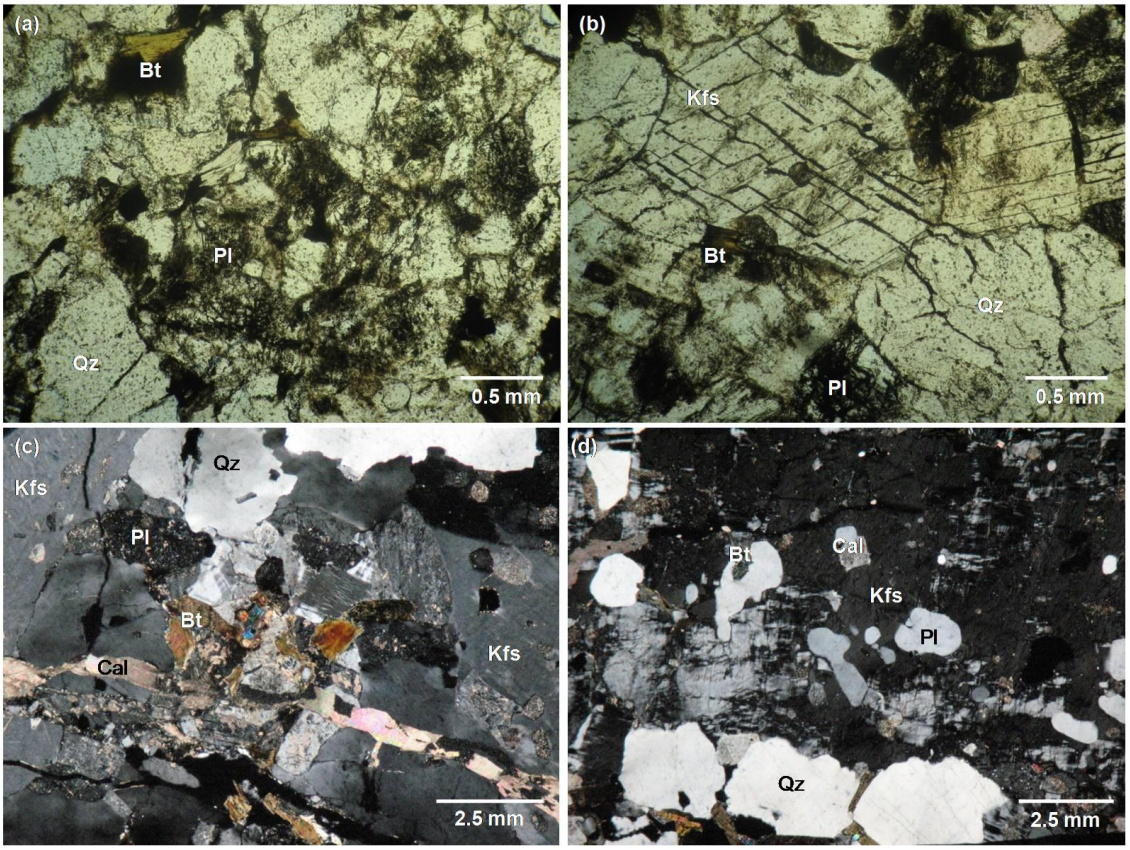

Figure 2.24: Photomicrographs of (a) sample RG154 showing the extensive seritisation of plagioclase grains in the gneissic megablock granite (PPL), (b) sample RG158 showing bent twins in K-feldspar phenocrysts in the gneissic megablock granite (PPL), and sample W49 showing (c) the less altered nature of the massive megablock granite (XPL) with (d) K-feldspar bent twins and myrmekitic textures (XPL). Abbr,: Bt = biotite; Cal = calcite; Kfs = K-feldspar; Pl = plagioclase; PPL = plane polarised light; Qz = quartz; XPL = cross polarised light.

The upper amphibolite megablock is characterised by large monomineralic aggregates (~30 mm) of amphibole (Figure 2.25c) and biotite (Figure 2.25d). Cleavage planes for both amphibole and biotite are observed to be strongly aligned, with individual amphibole and biotite grains slightly bent, indicating a minor intracrystalline strain component (Figure 2.25c and d).

2.4.4 Porphyroblast microstructures

Comparisons between internal porphyroblastic microstructures and those in the adjacent matrix assist in the deduction of the relative timing of porphyroblast growth and, by extrapolation, metamorphism, with respect to deformation (Passchier and Trouw, 2005). As noted in Sections

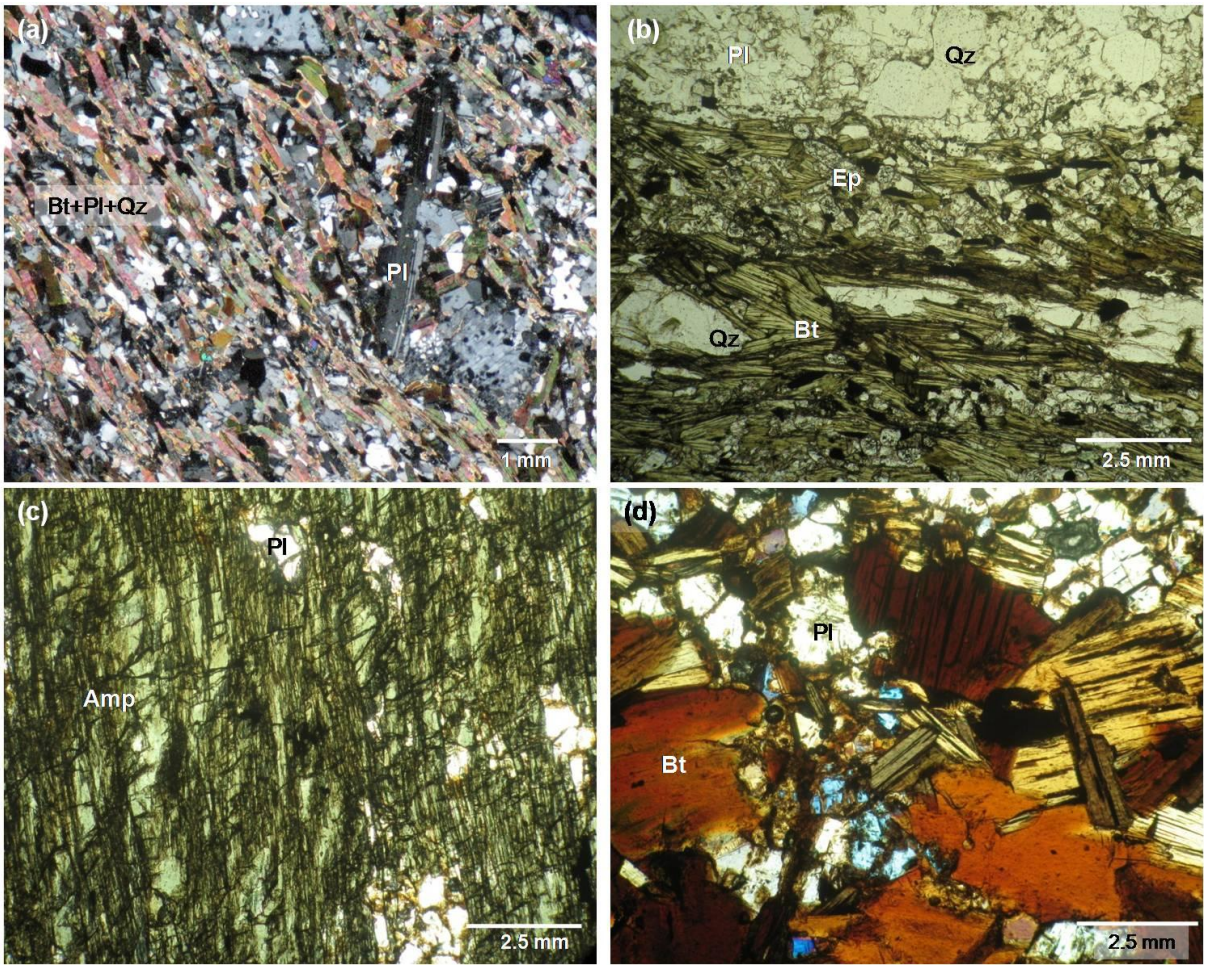

Figure 2.25: Photomicrographs of (a) sample W39 showing rotated plagioclase porphyroblasts (XPL) and (b) boudinaged quartz ribbons (PPL) in the biotite schist xenoliths of the upper granite megablock, and (c) samples RG177 (PPL) and (d) RG176 (XPL) showing monomineralic aggregates of amphibole and biotite, respectively. Abbr.: Amp = amphibole; Bt = biotite; Ep = epidote; Pl = plagioclase; PPL = plane polarised light; Qz = quartz; XPL = cross polarised light.

2.4.1 and 2.4.3, evidence within the lower basement-derived section suggests that it experienced at least one non-coaxial deformation event with dextral shear sense. Plagioclase, and less commonly garnet, porphyroblasts preserve internal microstructures, which can be used to identify the relative timing of porphyroblastesis under progressive simple shear (Johnson, 1999, 2009). Specifically, inclusion trails can provide critical information relating to the tectonometamorphic evolution experienced by metamorphic rocks as they commonly preserve records of multiple fabric-forming deformational events (Barker, 1994), whereas chemical and

textural zoning caused by strain-induced dissolution can provide information regarding the pathway along which the final bulk mineral assemblage was formed (Bell and Cuff, 1989).

Garnet-bearing mica schists are only found within the mylonite zone (1640-1655 m depth) in the lower basement-derived section. As a result, porphyroblasts of garnet in the mylonitised mica schist are located within the composite prograde-retrograde matrix fabric, complicating microstructural interpretations (Figure 2.26a). A weak foliation (S_i) oriented obliquely to the matrix foliation (S_e) in a highly poikilitic garnet porphyroblast in sample RG53 (Figure 2.26a) is defined by biotite, rutile needles and slightly elongated quartz inclusions. Barker (1994) observed that straight to slightly curved inclusion trails are usually formed under normal crustal strain rates caused by progressive simple, non-coaxial shear. It is possible that the weak foliation within the porphyroblast formed during the prograde growth of garnet, with differential rotation of the porphyroblast occurring during the subsequent retrograde mylonitic event.

Plagioclase porphyroblasts in the lower basement-derived section tend to exhibit concentric textural zonation, comprising a dusty, inclusion-rich core, an intermediate zone of coarser inclusions and an outer rim with few to no inclusions (Figure 2.26b). The porphyroblasts locally show sector twinning across all zones (Figure 2.26c). In mica schists that are more strongly foliated, plagioclase porphyroblasts are more elongated with their long edges oriented parallel to the matrix foliation (Figure 2.26b and c). Within the plagioclase cores, inclusions of elongate muscovite laths and very fine-grained graphite occur, with the former observed to locally overgrow the latter in random to orthogonal orientations (Figure 2.26b and c). Very rarely do these inclusions preserve a deformation-related orientation (Figure 2.26d). In the intermediate zone, inclusions consist of pyrite, graphite (large size than in the core), tourmaline and rutile (Figure 2.26b and c). The outer, inclusion-poor rims of the plagioclase porphyroblasts exhibit asymmetrical development in the form of so-called “quarter structures” (Figure 2.26b and c).

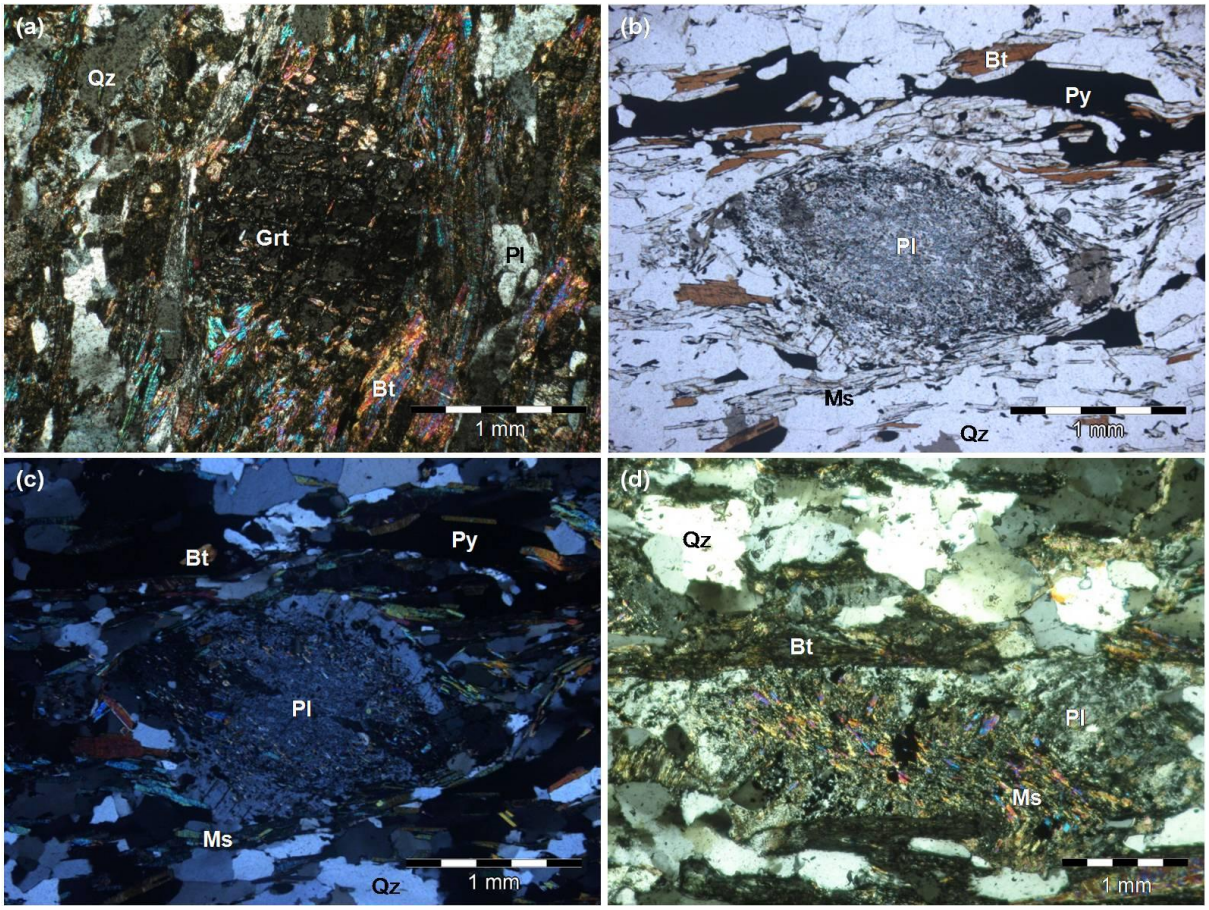

Figure 2.26: Photomicrographs of (a) sample RG53 showing a poikilitic garnet porphyroblast in the lower basement-derived mica schist with a weak internal foliation defined by biotite, rutile needles and elongated quartz inclusions (XPL), sample RG68 showing an internally zoned plagioclase porphyroblast in (b) PPL and (c) XPL views in the lower basement-derived mica schist, and (d) sample RG34 showing an internally zoned plagioclase porphyroblast with deformed muscovite inclusions in the lower basement-derived mica schist (XPL). Abbr.: Bt = biotite; Grt = garnet; Ms = muscovite; Pl = plagioclase; PPL = plane polarised light, Py = pyrite; Qz = quartz; XPL = cross polarised light.

The lensoid-shaped, graphite-rich core of the elongated plagioclase porphyroblasts coupled with an inclusion-poor rim may suggest that initial porphyroblastic growth was followed by strain-induced dissolution which was then followed by renewed growth. This is supported by the similar grain-size of the inclusions within the intermediate zone to the adjacent matrix (Figure 2.26b and c). This suggests growth of the intermediate zone and outer rim of plagioclase porphyroblasts took place during or shortly after peak metamorphic conditions. Furthermore, the increased concentration as well as grain size of graphite in the intermediate zone compared to

the core, the increased size of silicate mineral inclusions within this zone as well as a stepped increase in An content in plagioclase composition between cores and rims (see Section 2.4.2) all agree with dissolution prior to rim growth (Figure 2.26b and c). Porphyroblasts with multiple stages of growth, dissolution and regrowth are regularly preserved in metamorphic terranes owing to the inherent variations in strain conditions at the porphyroblast-matrix interface (Bell and Cuff, 1989). The asymmetry of the plagioclase porphyroblast rims might suggest that rims grew before the prograde C' shear bands were developed and were later dissolved against these surfaces. Alternatively, the plagioclase rims may have grown concurrently with the C' shear bands in the strain shadows while simultaneous dissolution against the C' surfaces occurred. The inclusion-poor nature of the plagioclase rims compared to their cores implies an increase in temperature occurred since the absence of matrix phases at the growing porphyroblast margins is consistent with increased diffusion rates (Passchier and Trouw, 2005). The increase in temperature combined with the absence of retrogression along the C' surfaces suggest that they grew close to peak metamorphic conditions and that the S1a foliation developed on the prograde path had a shear origin. It is consequently inferred that these C' surfaces in the mica schist are older than the S-C' structures in the mylonitised granite, which are defined by retrograde mineral assemblages (Figure 2.23d, e and f).

2.5 Discussion

2.5.1 Lower basement-derived section

In Section 2.3.1, the lower basement-derived section was observed to exhibit both prograde-to-peak and retrograde metamorphic paths. Along the prograde-to-peak path, mineral parageneses within the metasediments include muscovite + plagioclase + biotite + quartz + graphite ± sillimanite(fibrolite) ± garnet ± tourmaline ± rutile ± pyrite ± chalcopyrite ± pyrrhotite ± zircon (mica schist; Section 2.3.1.1), quartz + plagioclase + biotite + graphite ± rutile ± muscovite (biotite schist; Section 2.3.1.2), amphibole + plagioclase + quartz + epidote + titanite (amphibolite; Section 2.3.1.3) and vesuvianite + plagioclase + quartz (calc-silicate; Section 2.3.1.4). Deformation (D1a) accompanying prograde-to-peak metamorphism (M1a) produced a

composite shear fabric (S1a) comprising the pervasive, planar to sinuous, mica (muscovite and biotite) foliation (Section 2.4.1) and listric extensional shear bands (Section 2.4.3), with the asymmetrically zoned plagioclase porphyroblasts suggesting that the development of the S1a fabric experienced varying rates of shear strain (Section 2.4.4). Using the prograde-to-peak metamorphic mineral parageneses in the basement metasediments, it is possible to estimate the pressure and temperature conditions they experienced at peak metamorphism. For example, the presence of garnet and sillimanite in the mica schists (Section 2.3.1.1), amphibole in the amphibolite (Section 2.3.1.3) and vesuvianite in the calc-silicate (Section 2.3.1.4) suggests that peak metamorphism in the lower basement-derived section reached medium pressures and temperatures, most likely under mid-amphibolite facies conditions (e.g. Mason, 1990; Barker, 1998; Winter, 2001; Smulikowski *et al.*, 2007).

Evidence for retrograde cooling (M1b) and accompanying deformation (D1b) in the lower basement-derived section includes the development of a mylonitic fabric (S1b) as well as the retrogressive alteration of mineral assemblages associated (Section 2.4.1). The S1b fabric is observed to locally overprint S1a and incorporates the coarse-grained to pegmatitic granite (K-feldspar + plagioclase + quartz ± muscovite ± biotite ± garnet; Section 2.3.1.6). The granite, which does not contain the S1a fabric, is interpreted to have intruded the basement metasediments after D1a but prior to the onset of D1b (Sections 2.3.1.7 and 2.4.1). Strong retrogressive alteration of minerals occurs in the vicinity of the S1b fabric. In the mylonitised mica schist, biotite is locally replaced by chlorite and muscovite, garnet by chlorite, plagioclase by sericite, calcite and epidote and K-feldspar by sericite, which is similar to the alteration observed in the mylonitised granite where biotite and garnet is also locally replaced by chlorite, K-feldspar by sericite and plagioclase by sericite and calcite (Section 2.3.1.7). Retrogressive mineral alteration in the para-amphibolite includes local replacement of amphibole to uralite and chlorite and plagioclase locally replaced by sericite and calcite (Section 2.3.1.3). In the calc-silicate, the prograde-to-peak mineral assemblage is locally replaced by epidote + calcite + quartz + chlorite + amphibole (Sections 2.3.1.4 and 2.4.2).

Inferences regarding the relative metamorphic conditions under which the retrograde M1b event terminated in the lower basement-derived section can be obtained using the combination of retrograde mineral assemblages with certain observable microstructures. Typically, neoblastic biotite tails and feldspar subgrain aggregates, such as those seen in the mylonitised granite (Section 2.4.3), form under upper greenschist to lower amphibolite facies conditions, whereas the presence of bookshelf sliding of feldspar porphyroclasts (Section 2.4.3) suggests mylonitisation ceased under lower-grade conditions (e.g. Gaipas, 1989). When viewed in context with the presence of subhorizontal chlorite shears and intense chlorite-sericite alteration observed within the mylonitised mica schist (see Sections 2.3.1.1 and 2.3.1.7; Figure 2.8), these findings support a mid- to lower greenschist facies termination for the mylonitic D1b event in the lower basement-derived section. The D2 fracturing event in the lower basement-derived section, which overprints both the S1a and S1b fabrics, is accompanied by cataclasis and brecciation (Section 2.4.2), denoting lower greenschist to upper blueschist facies conditions (Etheridge, 1983; Scholz, 1988).

Deformation sequences can be described as major movement zones that have evolved through various rheological regimes with space and time, and the intense shear strain necessary to develop S-C mylonites suggests that the lower basement-derived section forms part of a shear zone (Lister and Snoke, 1984). The following deformation sequence, observed by Lister and Snoke (1984) to not be uncommon in shear zones, exhibits many similarities to that seen in the lower basement-derived section:

(a) A period of penetrative plastic deformation associated with large-scale non-coaxial laminar flow;

(b) Plastic deformation concentrating in increasingly narrow and high shear strain zones, resulting in S-C relationship formation;

(c) Brecciation and cataclasis where, depending on rock composition as well as the presence/absence of pore fluid, fault melts may have transient existence; and

(d) Formation of discrete, commonly anastomosing brittle faults that overprint structures relating to previous deformation.

In the conceptual model of a shear zone (e.g. Sibson, 1977; Scholz, 1988; Shimamoto, 1989), ductile deformation (such as S-C mylonites) typically occurs at deeper levels under amphibolite facies conditions, with cataclasis and brecciation occurring at shallower levels from greenschist to blueschist facies conditions. As a result, when viewed in context with the shear zone conceptual model, the above deformation sequence suggests progressive decreasing metamorphic grade and decompression. This is also true for the lower basement-derived section, where the penetrating foliation-forming event (D1a) coincided with prograde-to-peak mid-amphibolite facies metamorphism (M1a), with retrograde mylonitisation (D1b) occurring at lower amphibolite to upper greenschist facies metamorphism (M1b), and cataclasis and brecciation (D2) occurring at lower greenschist to upper blueschist facies metamorphism. It must be noted, however, that the D2 fracturing event in the lower basement-derived section is highly complicated and may have formed part of a separate event to that of D1.

2.5.2 Upper amphibolite megablock

The upper amphibolite megablock mineral assemblage comprises a prograde mineral assemblage of amphibole + plagioclase + biotite + quartz ± epidote ± chalcopyrite ± pyrrhotite ± pyrite ± magnetite ± titanite (Section 2.3.2). Although most of the megablock is strongly foliated (Section 2.4.1), a relict igneous texture is preserved between 1386.93 m and 1387.54 m depth, and is interpreted to reflect a metadioritic component (Sections 2.3.2 and 2.4.1). According to Eskola (1920, 1939), the amphibolite facies in mafic rocks comprises hornblendic amphibole and andesitic plagioclase. The mineral chemistry of amphibole and plagioclase in the amphibolite megablock corresponds with these parameters (see Chapter 4, Section 4.2.3), indicating peak metamorphism in the amphibolite megablock reached amphibolite facies conditions. In terms of retrograde metamorphism in the amphibolite megablock, although chloritisation of biotite and seritisation of feldspar is observed (Section 2.3.2), a discrete retrograde metamorphic assemblage, such as that seen in the lower basement-derived amphibolite and calc-silicate (Sections 2.3.1.3 and 2.3.1.4), is absent. Furthermore, the amphibolite megablock does not contain unequivocal retrograde microstructures. However, the

similar peak metamorphic conditions to that observed in the lower basement-derived section suggests that a common history may still have been shared by both blocks.

The megablock is locally cut by D2 calcite ± chlorite fractures as well as a single brecciated granite vein at the base of the megablock (Section 2.3.2). This granite superficially resembles the biotite-rich granites from the upper megablock owing to its lack of muscovite (Sections 2.3.2 and 2.3.3). The timing of the brecciation of the granite may be either pre- or syn-tectonic with the D2 veining event. If the brecciated granite did originate from the same source as the massive megablock granite, it is likely that the two megablocks formed part of a single terrane.

2.5.3 Upper granite megablock

The upper granite megablock consists of three distinct lithologies: a gneissic biotite granite (K-feldspar + quartz + plagioclase + biotite ± pyrite ± magnetite; Section 2.3.3.1), a massive biotite granite (K-feldspar + quartz + plagioclase + biotite + muscovite ± pyrite ± magnetite; Section 2.3.3.2) and biotite schist xenoliths predominantly incorporated into the massive biotite granite (biotite + plagioclase + quartz + epidote ± amphibole; Section 2.3.3.3). The foliation in the gneissic biotite granite is defined by millimetre- to centimetre-scale banding and is interpreted to be tectonic (Section 2.4.1; Paterson *et al.*, 1989). Unfortunately, a lack of clear evidence as to whether the development of gneissic foliation was a result of shearing alone or if it formed during a separate event to the D1b mylonite foliation seen in the lower basement-derived section precludes any correlations with foliations in other parts of the Eyreville-B borehole core (Section 2.4.1). The gneissic granite is intruded by the massive biotite granite along sharp contacts, and locally contains a magmatic foliation adjacent to these intrusive contacts (Section 2.4.1). Although structural evidence in the biotite schist xenoliths suggests an association with the D1b mylonitic event, there is insufficient evidence to clearly link it to the foliation-forming event in the lower basement-derived mica schists (Section 2.4.3).

Myers (1978) observed that gneissic foliations tend to require metamorphic conditions to be at least amphibolite facies to form. This agrees with evidence from the biotite schist xenoliths

where the presence of amphibole within the mineral assemblage also denotes amphibolite facies metamorphism (Eskola, 1920, 1939). Thus, it is likely that the upper granite megablock experienced amphibolite facies conditions at peak metamorphism, such as observed in the lower basement-derived section and upper amphibolite megablock. Much like the amphibolite megablock, varying degrees of biotite chloritisation and feldspar seritisation within all three granite megablock lithologies represent the retrograde metamorphic event in this section. The common metamorphic history suggests that the three sections formed part of a single metamorphic terrane. This is discussed in more detail in Chapter 4 (Section 4.4.1).

The incorporation of the biotite schist xenoliths into the massive granite might suggest that these are rare restite enclaves. Williamson *et al.* (1997) observed that restites varied in mineralogy and structure depending on the type of melt from which they formed. Restites in S-type granites, which form from sedimentary sources (Chappell and White, 1974, 1984), are typically foliated metasedimentary enclaves (Williamson *et al.*, 1997), whereas I-type granites, which form from igneous sources (Chappell and White, 1974, 1984), typically include randomly oriented pyroxene and amphibole phases (Wall *et al.*, 1987; Stephens, 2001). Thus, if the biotite schist xenoliths are in fact restitic, it would be expected that the massive granite in the megablock would be an S-type granite. However, geochemical analyses in Chapter 3 (Section 3.3.3) indicate that the upper megablock granites are both I-type. Consequently, it is interpreted that the biotite schist xenoliths were incorporated into the magma that gave rise to the massive granite through mechanical methods, such as stoping,

2.6 Summary

The target rocks of the Eyreville-B borehole core consists of a lower basement-derived section, comprising metasediments intruded by a pegmatitic granite, an amphibolite megablock, and an upper granite megablock, comprising a gneissic granite that is intruded by a massive granite that locally incorporates small biotite schist xenoliths. Mineral assemblages and microstructural evidence in all three blocks suggests these rocks experienced an amphibolite facies peak

metamorphic event (M1a) followed by retrograde metamorphic conditions (M1b). The latter event is most clearly observed in the lower basement-derived section, which is characterised by mylonitisation. This shared metamorphic history suggests that the three sections may have formed part of a single terrane, which is discussed in greater detail in Chapter 4.

3 GEOCHEMICAL ANALYSIS

3.1 Introduction

Geochemical analysis was performed on samples from the lower crystalline basement-derived section and the upper granite and amphibolite megablocks in order to constrain their chemical properties in terms of major, trace and rare earth elements (REE) and, in turn, determine their potential protoliths (in the case of the metasediments), tectonic setting of emplacement as well as the degree of similarity between characteristics of these samples and those of neighbouring terranes (the latter to be discussed in detail in Chapter 6). Two geochemical methods were used, namely X-ray fluorescence (XRF) spectrometry to determine major and trace elements, and inductively coupled plasma mass spectrometry (ICP-MS) to determine the REE signatures of the samples. Other geochemical studies of the lower crystalline basement-derived section and upper granite and amphibolite megablocks have been reported by Bartosova *et al.* (2009), Gibson *et al.* (2009), Horton *et al.* (2009b) and Schmitt *et al.* (2009).

3.2 Methodology

Fifty-two samples were selected for bulk-rock chemical analysis using XRF: 26 from the upper granite megablock (11 gneiss, 10 granite and 5 biotite schist xenoliths), 8 from the upper amphibolite megablock and 18 from the lower basement-derived section (12 mica schist, 3 granite, 2 amphibolite and 1 calc-silicate). All 52 samples were first crushed using a mechanical jaw crusher and then milled in tungsten carbide swing mills in the School of Geosciences at the University of the Witwatersrand. Precautionary methods, in the form of cleaning with acetone and the use of a pressurised air hose, were implemented to avoid contamination. Methods of sample preparation and instrumental analysis are detailed below.

Major and trace element analyses were obtained for the RG (1–3. 6, 38–40, 44, 53, 54, 61, 64, 68, 70, and 76) series and W (35-40) series using a SIEMENS SRS 3000 at the Museum für

Naturkunde, Humboldt University in Berlin. Fusion discs were prepared using 0.6 g of the milled sample that had been dried for 4 hours at 105°C, 3.6 g of Dilithiumtetraborate (BRA A10 Specflux), and approximately 0.5–2.0 g NH_4NO_3 for the oxidation of the sample material, depending on the degree of oxidation. The fusion discs were produced using Pt/Au-crucibles (950/50) on an OXIFLUX burner chain (CRB ANALYSE SERVICE; after Schmitt *et al.*, 2004). A modified Geoquant programme (SIEMENS) was used for measurement and data analysis based on the following international standards: CR-2CAS1, HG-BAH, MRG-1, NIM-D, NIM-G, NIM-L, NIM-N, NIM-P, NIM-S, SY-3, UN-SPS, VS-813, VS-2116, VS-2117, VS-2119, VS-2120, VS-2121, VS-2122, VS-2123, VS-2125, VS-2889, VS-5370, VS-7126, VS-7176, VS-MO7, VS-MO13, VS-MO15, X-39, X-41, X-44, X-45, X-48, X-50, Z-AN, Z-BM, Z-FK, Z-GM, Z-GNA, Z-KH, ZSW, Z-TB and Z-TS; the SIEM-01-SIEM-10 internal standard was also used. The analytical precisions for both major and trace elements are shown in Table 3.1.

Loss on ignition (LOI) was determined by drying approximately 1 g of pulverised sample material for 4 hours at 105ºC, then heating the sample material in Heldenwanger porcelain crucibles for a further 4 hours at 1000ºC. LOI was calculated by measuring the difference in weight of the sample from before and after the heating process. The LOI detection limit and standard error equal ~0.1 wt%.

Further geochemical analysis was undertaken for the RG (50-51, 151-152, 154-164, 166-167, 169, 171-174, and 176-179) and MJK series with a PW 1400 XRF machine which ran the rhodium X-ray tube at 50kV and 50 mA in the School of Geosciences at the University of the Witwatersrand. For major element analysis, fusion discs were prepared using 1.26 g of the milled sample with 1.5 g of flux, a mixture comprising lithium tetraborate, lithium carbonate and lanthanum oxide, and sodium nitrate as the oxidising agent. Pressed powder pellets were prepared for trace element analysis by mixing the milled sample with Mowiol 40-88™ glue in aluminium cups. The standards used for both major and trace element analyses were NIM-S (syenite), AN-G (anorthosite), NIM-D (dunite), MICA-FE (biotite), NIM-N (norite) and NIM-G (granite). Table 3.2 includes the analytical precisions for these analyses.

Table 3.1: Analytical precision for major and trace element analysis by XRF at the Museum für Naturkunde, Humboldt University (after Schmitt *et al.*, 2004 and Coney, 2009).

Major Element	Detection Limit (wt%)	Standard Error (wt%)	Standard Range (wt%)
SiO_2	1.0	0.50	1.00-100
TiO_2	0.01	0.01	0.01-4.00
Al_2O_3	0.5	0.10	0.50-50.00
Fe_2O_3*	0.05	0.05	0.05-25.00
MnO	0.01	0.01	0.01-0.50
MgO	0.01	0.05	0.01-50.00
CaO	0.01	0.05	0.01-50.00
Na_2O	0.01	0.05	0.01-10.00
K_2O	0.01	0.05	0.01-10.00
P_2O_5	0.01	0.01	0.01-2.50
SO_3	0.1	0.10	0.10-50.00

Trace Element	Detection Limit (ppm)	Standard Error (ppm)
V	15	5
Cr	15	5
Co	15	5
Ni	15	5
Cu	30	25
Zn	30	25
Rb	15	5
Sr	15	5
Y	10	5
Zr	15	5
Nb	10	5
Mo	10	10
Ba	30	30
Ce	30	20
Pb	15	20
Th	10	5
U	10	10

* Total Fe calculated as Fe_2O_3.

Table 3.2: Analytical precision for major and trace element analysis by XRF in the School of Geosciences at the University of the Witwatersrand (after Coney, 2009).

Major Element	Standard Deviation	Absolute Error (%)	Relative Error (%)	Standard Range (wt%)
SiO_2	0.36	0.06	-0.09	34.40-76.31
TiO_2	0.07	-0.04	13.7	0.00-2.69
Al_2O_3	0.07	0.07	1.3	0.30-30.04
Fe_2O_3*	0.09	-0.03	-3.7	0.09-26.65
MnO	0.01	-0.009	4.8	0.01-0.35
MgO	0.18	-0.05	-6.1	0.03-43.18
CaO	0.04	0.003	0.2	0.11-16.03
Na_2O	0.13	-0.05	-6.8	0.04-6.57
K_2O	0.07	0.005	-5.6	0.01-15.40
P_2O_5	0.02	-0.02	14.2	0.01-1.40
LOI	0.26	-0.21	7.1	
Total	0.58	-0.18	0.2	

Trace Element	Standard Deviation	Absolute Error (%)	Relative Error (%)	Lower Limit of Detection (ppm)
V	9	-3.8	-12.7	12
Cr	7	0.7	5.2	12
Co	2	0.7	-10.7	6
Ni	2	0.6	-9.3	6
Cu	5	1.9	-0.3	6
Zn	2	2.8	-6.2	6
As	2	4.7		15
Rb	2	1.0	-1.9	3
Sr	2	1.3	0.4	3
Y	2	-0.7	-3.7	3
Zr	3	4.3	1.2	8
Nb	1	-2.4	-8.5	3
Ba	7	12.0	3.1	20
Pb	2	3.1		10

* Total Fe calculated as Fe_2O_3.

Twenty-seven samples were selected for ICP-MS analysis of trace elements in the School of Geosciences at the University of the Witwatersrand: 20 from the upper granite megablock (12 gneiss, 4 granite and 2 biotite schist xenoliths), 2 from the upper amphibolite megablock, and 7 from the lower basement-derived section (3 mica schist, 2 amphibolite, 1 calc-silicate and 1

granite). ICP-MS analysis is achieved by ionising a sample with an argon inductively coupled plasma after which the ions are separated and quantified by a mass spectrometer (Jarvis, 1988). As with XRF, samples were crushed and milled to make a powder in the School of Geosciences at the University of the Witwatersrand.

ICP-MS analysis of the samples was obtained using a Perkin Elmer DRC-e machine. For each sample, 50 mg of powder was used and individually digested in a microwave with a 60:40 high purity HF:HNO_3 solution. A MARS microwave digester was used. Before the aliquot was run on the ICP-MS, a 50 ml sample mixture was generated using 5% HNO_3-solution which contains 50 ppb Rh, Re, Bi and In. Samples were analysed against the certified primary solution standards BCR1 and BVHO1 (see Table 3.3). Analytical precision (agreement with accepted values of standards) was better than 10%; in many cases, this improved to within 5%.

The above sample set has been supplemented with chemical analyses of an additional 70 samples from CB6 series (33 samples) and W series (37 samples) of the Eyreville-B borehole core previously reported by Schmitt *et al.* (2009). Of these 70 samples, 15 are from the upper granite megablock (13 granite and 2 biotite schist xenoliths), 1 is from the upper amphibolite megablock, and 54 are from the lower basement-derived section (28 mica schist, 23 granite and 3 calc-silicate). These samples have been included in the analyses in order to enhance data analysis and interpretation due to the limited number of samples for certain sections of the Eyreville-B borehole core as well as the sample size limitation of the borehole core. Major element data was obtained for all 70 samples by XRF analysis at the Museum für Naturkunde, Humboldt University in Berlin (see above for XRF methodology), while 32 samples from the CB6 series underwent trace element analysis obtained by instrumental neutron activation analysis (INAA) at the Department for Lithospheric Research, University of, Vienna, Austria (see Bartosova *et al.*, 2009, for INAA methodology). The INAA method entails the bombardment of a sample with an intense neutron flux, causing the elements in that sample to form radioactive isotopes (e.g. Winter, 2001). The radioactive emissions, which occur as the atoms return to their stable configurations, are then analysed based on their characteristic spectra.

Table 3.3: Trace element compositions of the standards used for ICP-MS analysis in the School of Geosciences at the University of the Witwatersrand (A. Wilson, pers. comm., 2008).

Trace Element	BCR-1 (ppm)	BHVO-1 (ppm)	Trace Element	BCR-1 (ppm)	BHVO-1 (ppm)
P	1571	1191	Ce	53.7	39
Sc	32.6	31.8	Pr	6.8	5.7
Ti	13428	16246	Nd	28.8	25.2
V	407	317	Sm	6.59	6.2
Cr	16	289	Eu	1.95	2.06
Co	37	45	Gd	6.68	6.4
Ni	13	121	Tb	1.05	0.96
Cu	19	136	Dy	6.34	5.2
Zn	130	105	Ho	1.26	0.99
Ga	22	21	Er	3.63	2.4
As	0.65	0.4	Tm	0.56	0.33
Rb	47.2	11	Yb	3.38	2.02
Sr	330	403	Lu	0.51	0.29
Y	38	27.6	Hf	4.95	4.38
Zr	190	179	Ta	0.81	1.23
Nb	14	19	W	0.44	0.27
Ba	681	139	Pb	13.6	2.6
Cs	0.96	0.13	Th	5.98	1.08
La	24.9	15.8	U	1.75	0.42

3.3 Major element analysis

The mean values and standard deviations of the major element oxides for the eight target rock units of the Eyreville-B borehole core are included in Table 3.4 (see Chapter 2, Section 2.3 and Figure 2.1). Major element data for all samples are presented in Appendix 2a. Where applicable, the anhydrous CIPW norm calculation program was used to determine mineral compositions from major element data.

Table 3.4: Mean and standard deviation (data in wt%) of major element oxides obtained by XRF analysis for the eight target rock units of the Eyreville-B borehole core. Abbr.: n = number of samples; SD = standard deviation; LOI = loss on ignition.

Major Element Oxide (wt%)	Basement Mica Schist		Basement Amphibolite		Basement Calc-silicate	Basement Granite	
	n = 12		n = 2		n = 1	n = 3	
	Mean	SD	Mean	SD	Mean	Mean	SD
SiO_2	57.45	9.78	56.47	2.90	52.37	73.38	0.90
TiO_2	0.81	0.41	0.71	0.01	0.53	0.10	0.06
Al_2O_3	18.34	3.35	13.37	0.34	11.06	14.89	0.53
Fe_2O_3*	7.96	5.08	5.95	0.33	4.60	1.09	0.44
MnO	0.08	0.04	0.15	0.05	0.22	0.11	0.02
MgO	1.72	1.28	1.51	0.42	1.03	0.19	0.17
CaO	2.14	1.55	11.07	0.35	20.39	1.58	0.77
Na_2O	2.16	1.44	1.24	0.60	0.17	3.66	2.22
K_2O	3.23	1.10	3.19	1.29	1.01	2.94	0.66
P_2O_5	0.08	0.04	0.13	0.04	0.02	0.03	0.00
LOI	5.24	2.14	5.15	3.44	9.35	2.01	1.50
Total	99.35	1.11	98.92	0.90	100.75	100.02	0.11

Major Element Oxide (wt%)	Megablock Massive Granite		Megablock Gneissic Granite		Megablock Biotite Schist Xenoliths		Megablock Amphibolite	
	n = 10		n = 11		n = 5		n = 8	
	Mean	SD	Mean	SD	Mean	SD	Mean	SD
SiO_2	74.04	1.51	73.31	2.48	55.99	12.32	47.88	5.48
TiO_2	0.27	0.18	0.29	0.14	2.37	1.57	1.34	0.45
Al_2O_3	13.47	0.74	13.34	1.08	14.76	1.91	18.53	0.83
Fe_2O_3*	2.04	0.73	2.57	0.80	12.62	6.06	10.66	2.66
MnO	0.04	0.01	0.04	0.01	0.20	0.08	0.20	0.09
MgO	0.31	0.21	0.23	0.16	2.81	1.84	5.32	1.71
CaO	1.61	0.73	1.31	0.46	3.25	1.29	7.86	1.74
Na_2O	3.46	0.71	3.35	0.50	2.94	1.15	2.83	1.08
K_2O	4.26	1.95	5.12	0.87	3.44	1.52	0.93	1.11
P_2O_5	0.06	0.05	0.08	0.07	0.58	0.43	0.22	0.13
LOI	0.47	0.13	0.37	0.13	0.67	0.50	3.95	1.54
Total	100.02	0.58	100.01	0.81	99.62	0.43	99.93	0.72

* Total Fe calculated as Fe_2O_3.

Major element concentrations of the eight target rock units of the Eyreville-B borehole core have been plotted against depth in Figures 3.1 (lower basement-derived section) and 3.2 (upper megablocks section) to illustrate the spatial variability of abundances within the borehole core. SiO_2 and MgO (Figure 3.1a and f) in the lower basement-derived section mica schists decrease with depth from 1540 m to aproximately 1610 m, while Al_2O_3 and Fe_2O_3 (Figure 3.1c and d) increase for the same depth interval. TiO_2, MnO and CaO (Figure 3.1b, e and g) in the lower basement-derived calc-silicate decreases slightly with depth; this is mirrored in the lower basement-derived amphibolite.

There is little to no variation in SiO_2, TiO_2, Fe_2O_3, MnO, MgO, CaO and P_2O_5 (Figure 3.1a. b, d, e, f,g and j) concentrations with depth for the lower basement-derived granite. While Na_2O (Figure 3.1h) does increase in the lower basement-derived granites with depth (specifically between 1720 and 1760 m), there is also a strong negative correlation in K_2O (Figure 3.1i) abundance at the same depths.

Most outliers in TiO_2, Fe_2O_3, MnO, MgO, CaO and P_2O_5 (Figure 3.1b, d, e, f, g and j) concentrations are located between 1620 m and 1660 m depth, which coincides with the strongly altered mylonite zone of the lower basement-derived section (see Chapter 2, Section 2.3.1.7 and Figure 2.1). Mica schist outliers, high in TiO_2, Fe_2O_3, and P_2O_5 (Figure 3.1b, d and j), are samples RG54 and W131b obtained from the tourmalinite in the mylonite zone.

The most common outliers in MnO, MgO and CaO (Figure 3.1e, f and g) are samples from the amphibolite and calc-silicate rock units (RG50-51, RG179, W132-134) of the lower basement-derived section. The two lower basement-derived granite outliers in Na_2O and K_2O (CB6-148, W128; Figure 3.1h and i) are pegmatitic to very coarse-grained samples and, thus, are not necessarily representative samples of bulk rock composition.

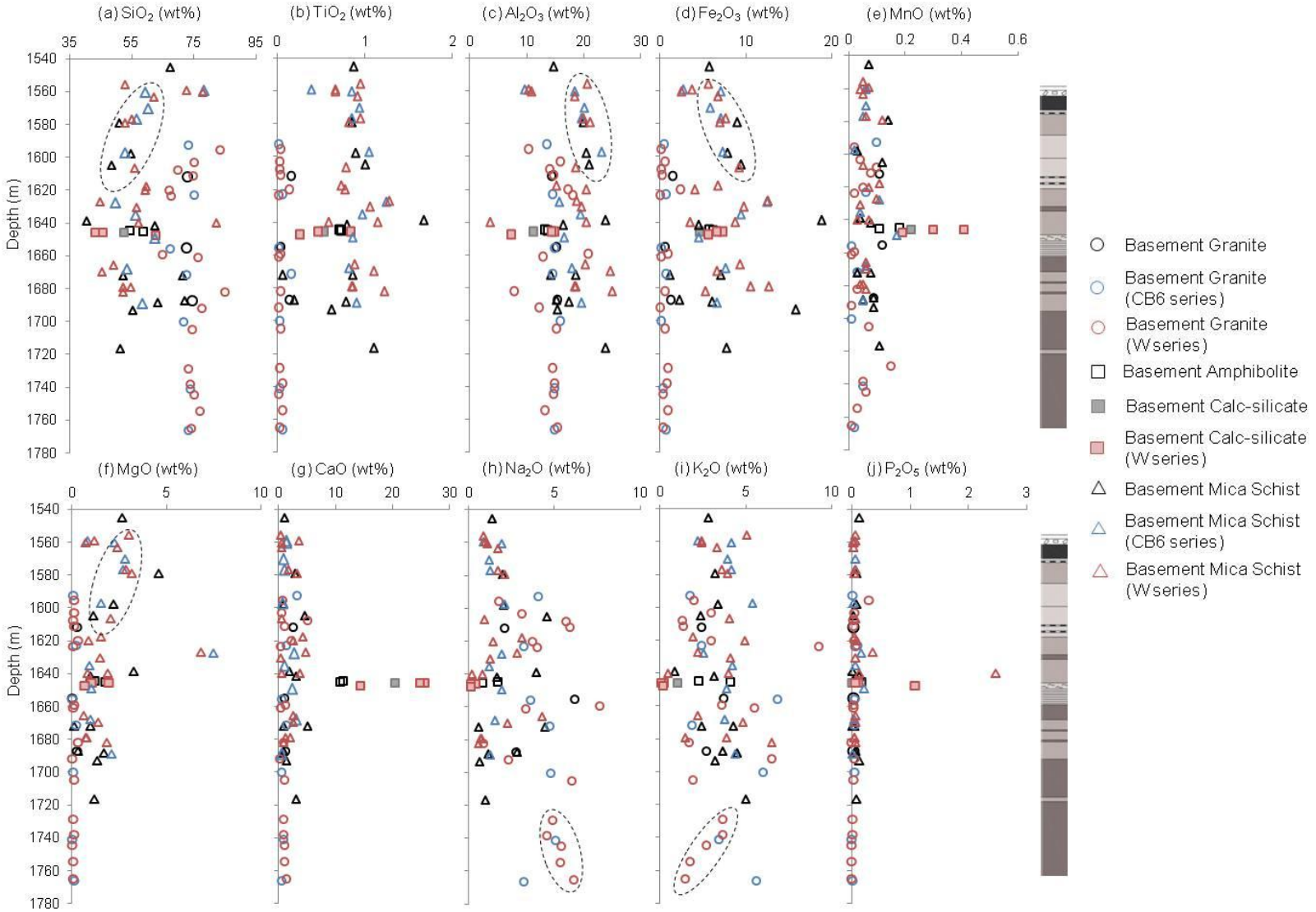

Figure 3.1: Variations in major element concentrations (wt%) with depth (m) for the four target rock units in the lower basement-derived section of the Eyreville-B borehole core. Samples from the CB6 and W series (after Schmitt *et al.*, 2009) have been included to increase the data set size. The geologic column, as described in Chapters 1 and 2 (after Horton *et al.*, 2009a), has been placed on the right side for reference purposes. Dashed lines represent observed groupings.

No significant variation of major element abundance with depth is observed between the massive and gneissic megablock granites (Figure 3.2); however, MnO content in the massive megablock granite does show a negative correlation with depth at the base of the megablock (Figure 3.2e). The biotite schist xenoliths within the massive megablock granite, on the other hand, do show signficant variability in concentrations with depth (Figure 3.2). SiO_2, TiO_2, Fe_2O_3, Na_2O and K_2O (Figure 3.2a, b, d, h and i) show a negative correlation of abundance in the biotite schist xenoliths with depth, while MnO, MgO, CaO and P_2O_5 (Figure 3.2e, f, g and j) indicate a positive correlation with depth; the biotite schist xenoliths show no significant trend in Al_2O_3 (Figure 3.2c) with depth. The amphibolite megablock increases slightly in TiO_2, Na_2O, K_2O and P_2O_5 (Figure 3.2b, h, i and j) with depth but decreases in Al_2O_3 and Fe_2O_3 (Figure 3.2c and d).

Figure 3.3 shows Harker diagrams for the eight target rock units of the Eyreville-B borehole core where major element oxides have been plotted against SiO_2. Average shale compositions are included in Figure 3.3 for comparison purposes. Generally, TiO_2, Al_2O_3, Fe_2O_3 and MgO (Figure 3.3a, b, c and e) all show negative correlations with SiO_2, while Na_2O and K_2O have a slightly positive correlation (Figure 3.3g and h). MnO, CaO and P_2O_5 show no significant correlation with SiO_2 (Figure 3.3d, f and i).

3.3.1 Mica schists

The lower basement-derived mica schists show a broad range in SiO_2 content from 40 to 82 wt% (Figure 3.3; Appendix 2a), consistent with the presence of fine-scale layering, highly disrupted quartz veins and the limited sample size. Steep negative trends of TiO_2, Al_2O_3 and Fe_2O_3 with increasing SiO_2 are evident in the mica schists of the lower section of the Eyreville-B borehole core (Figure 3.3b and c); a less defined negative trend can be seen with MgO (Figure 3.3e).

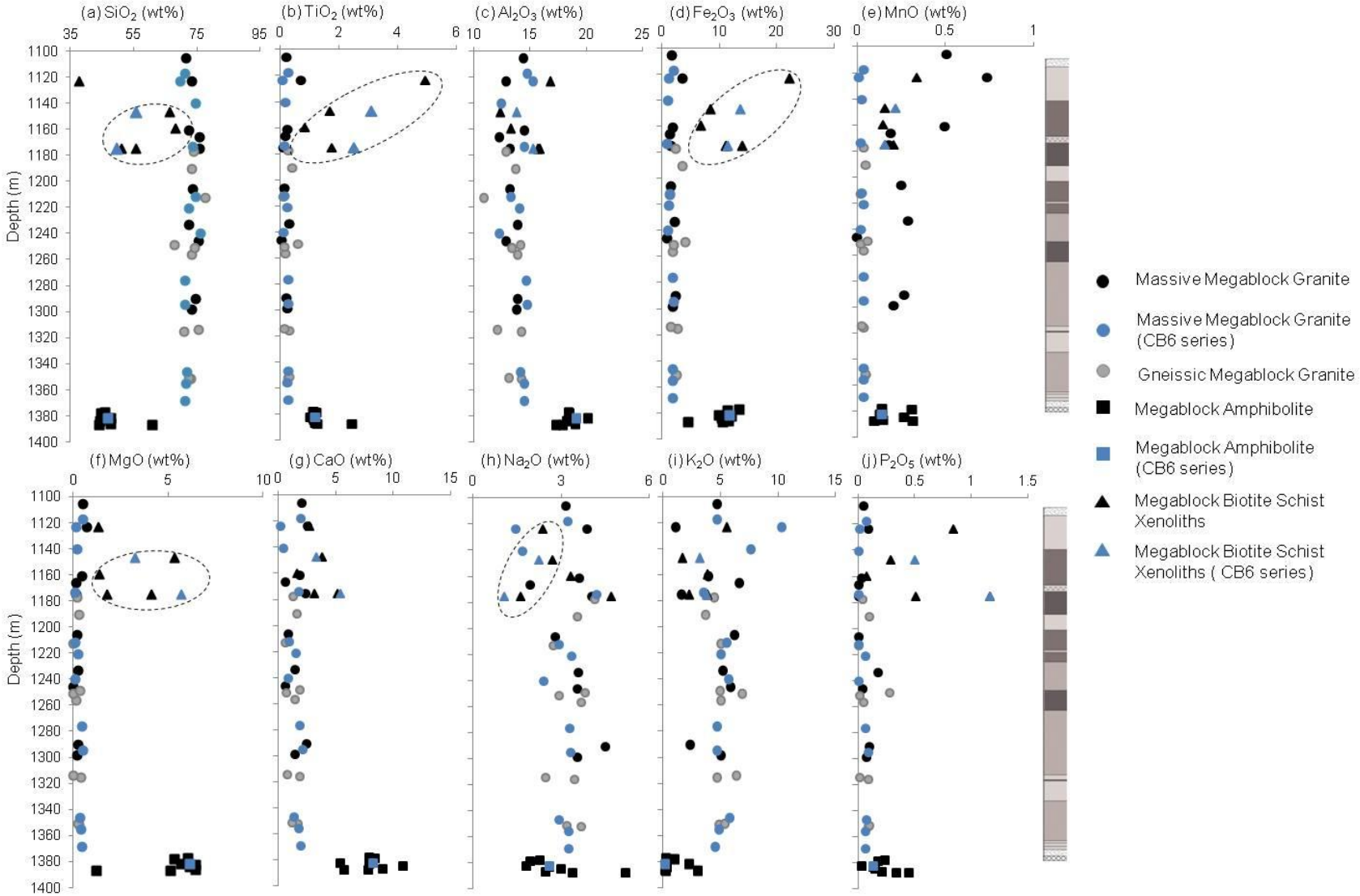

Figure 3.2: Variations in major element concentrations (wt%) with depth (m) for the four target rock units in the upper granite and amphibolite megablocks of the Eyreville-B borehole core. Samples from the CB6 series (after Schmitt *et al.*, 2009) have been included to increase the data set size. The geologic column, as described in Chapters 1 and 2 (after Horton *et al.*, 2009a), has been placed on the right side for reference purposes. Dashed lines represent observed groupings.

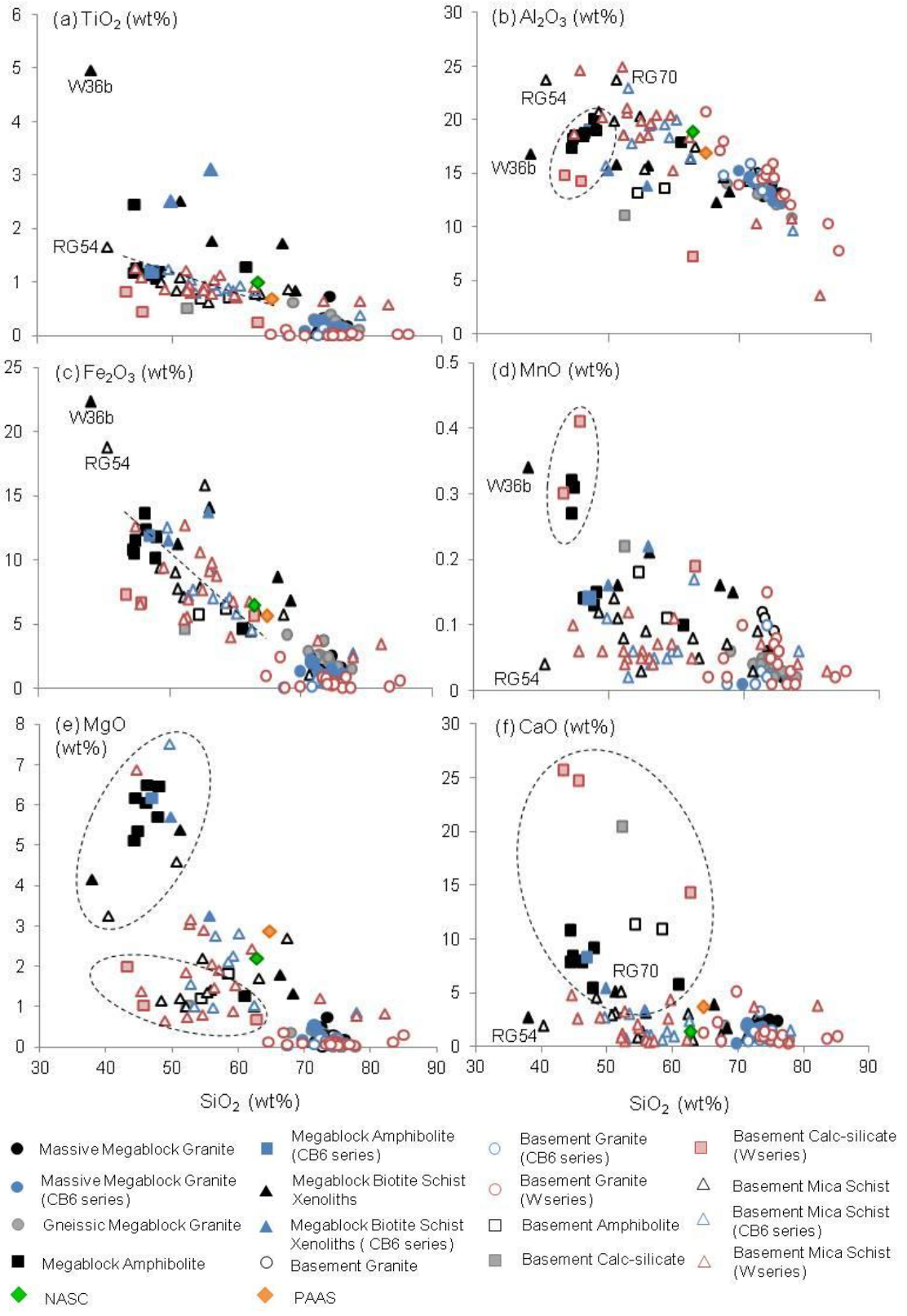

Figure 3.3: Harker diagrams showing major element oxides (TiO_2, Al_2O_3, Fe_2O_3, MnO, MgO, CaO, Na_2O, K_2O and P_2O_5) plotted against SiO_2 for the eight target rocks units of the Eyreville-B borehole core. Abbr.: NASC = North American Shale Composite (after Gromet *et al.*, 1984); PAAS = Post Achaean Australian Shale (after Taylor and McLennan, 1985). Dashed lines represent observed groupings.

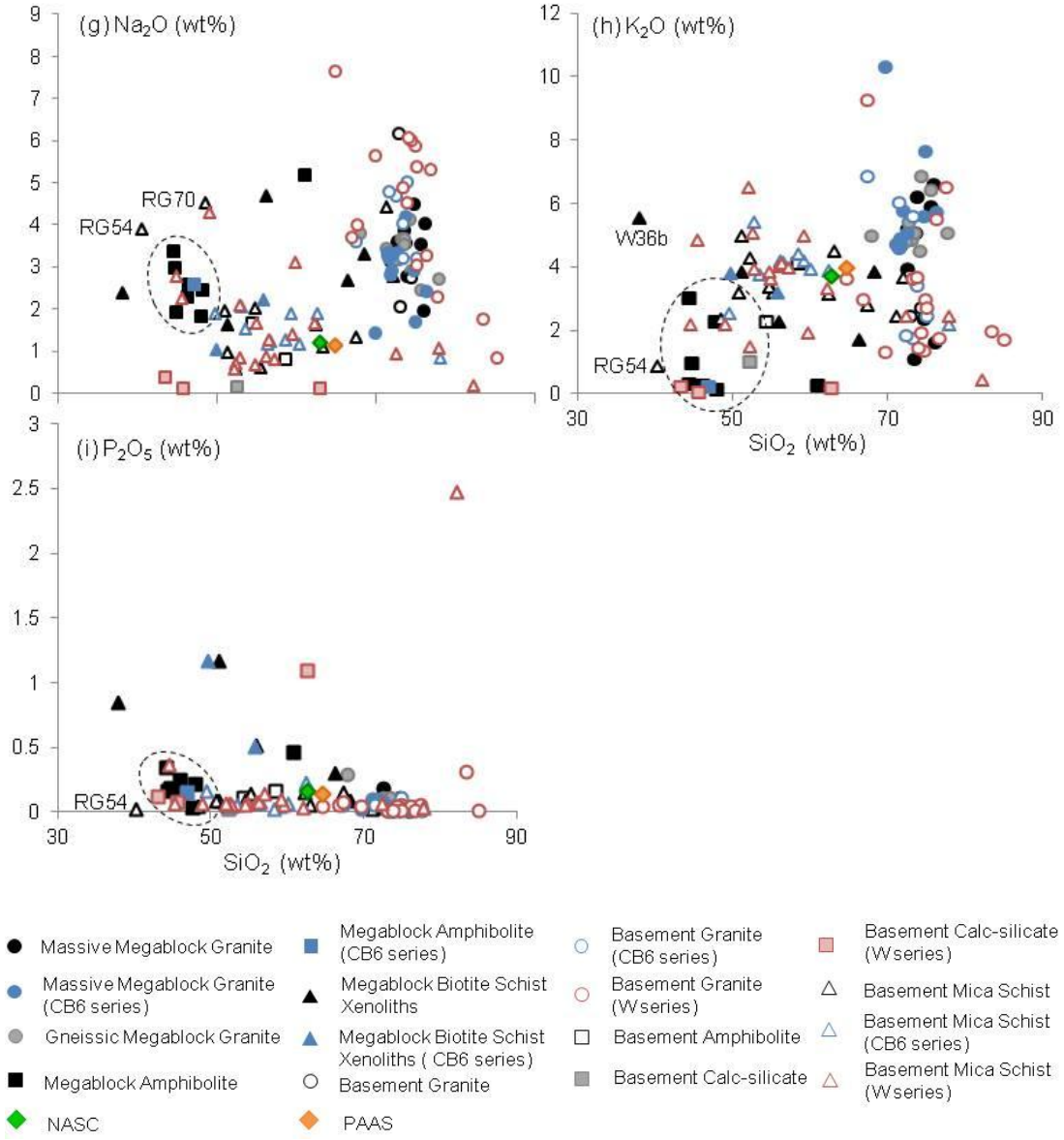

***Figure 3.3 (continued)*: Harker diagrams showing major element oxides (TiO_2, Al_2O_3, Fe_2O_3, MnO, MgO, CaO, Na_2O, K_2O and P_2O_5) plotted against SiO_2 for the eight target rocks units of the Eyreville-B borehole core. Abbr.: NASC = North American Shale Composite (after Gromet *et al.*, 1984); PAAS = Post Achaean Australian Shale (after Taylor and McLennan, 1985). Dashed lines represent observed groupings.**

The An-Or-Ab ternary diagrams in Figure 3.4 were constructed using are used to demonstrate differing feldspar compositions in the eight target rock units. The relative abundances for anorthite, orthoclase and albite were derived from the CIPW norm. Information regarding feldspar composition has been used to characterise lithic clasts in the impactite sequence (located between the lower basement-derived section and the upper granite and amphibolite megablocks; Figure 1.3) believed to be derived from the target rocks in which the impact

occurred (e.g. Jolly, 2011). The varied nature of feldspar in the lower basement-derived mica schists is illustrated in Figure 3.4a, being notably depleted in anorthite and slightly enriched in orthoclase compared to albite, consistent with petrographic observations (see Chapter 2, Section 2.3.1.1).

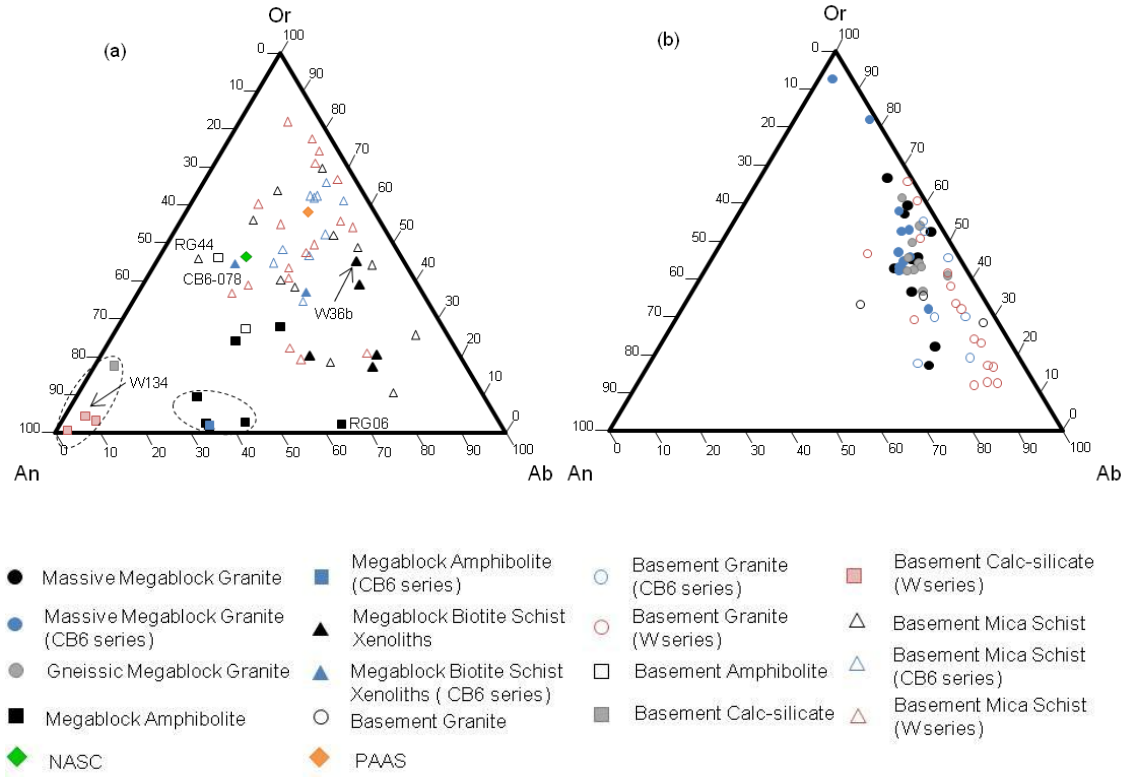

Figure 3.4: Ternary diagrams indicating normative An-Or-Ab content calculated for (a) the mica schist, amphibolite and calc-silicate, and (b) the granite rock units of the Eyreville-B borehole core. Abbr.: An = anorthite; Or = orthoclase; Ab = albite; NASC = North American Shale Composite (after Gromet *et al.*, 1984); PAAS = Post-Achaean Australian Shale (after Taylor and McLennan, 1985). Dashed lines represent observed groupings.

When compared to average shale compositions of the NASC (North American Shale Composite; Gromet *et al.*, 1984) and the PAAS (Post-Archean Australian Shale; Taylor and McLennan, 1985), the mica schists of the lower basement-derived section tend to be slightly higher in Fe_2O_3 and Na_2O concentrations, and slightly lower in SiO_2, MgO and CaO concentrations (Table 3.4; Figure 3.3; Appendix 2a). The basement mica schists also tend to be more albitic in composition (Figure 3.4a). Sample RG44 is seen to occur as an outlier indicating a higher CaO content compared to the other mica schists (Figure 3.4a).

The biotite schist xenoliths of the upper granite megablock are more scattered and are chemically distinct from the lower basement-derived mica schists, being significantly enriched in TiO_2, Fe_2O_3, MnO, MgO, CaO and P_2O_5, (Figure 3.3a, c, d, e, f and i) and depleted in Al_2O_3 and SiO_2 (38–68 wt%; Figure 3.3b). Feldspar in the biotite schist xenoliths tends to be albite-rich plagioclase (Figure 3.4a), corresponding to mineral chemical analyses in Chapter 4 (Section 4.1.2; Figure 4.1). As with the lower basement-derived mica schists, the biotite schist xenoliths typically have lower concentrations of SiO_2, higher concentration of Fe_2O_3, MgO and Na_2O, and are more albitic in nature than the NASC and PAAS composition averages (Table 3.4; Figures 3.3 and 3.4a; Appendix 2a). Sample CB6-078 contains the least amount of albitic plagioclase in the megablock biotite schist xenoliths (Figure 3.4a). Na_2O/K_2O ratios of the lower basement-derived mica schist and the megablock schist lie between 0.1 and 2.0, with an average of 0.7, which is slightly less than the average pelite ratio according to Taylor and McLennan (1985); a Na_2O/K_2O ratio outlier of 4.6 occurs for the tourmalinite sample RG54 (Appendix 2a). MnO enrichment in the biotite schist xenoliths

A single biotite schist xenolith sample (W36b) in the massive megablock granite contains the lowest SiO_2 content (Appendix 2a) observed within the Eyreville-B borehole core and is considerably higher in TiO_2, Fe_2O_3, MnO and K_2O (Figure 3.3b, c, d and h) compared to the other biotite schist xenoliths. This sample also contains the most orthoclase-rich feldspar observed in the biotite schist xenoliths (Figure 3.4a). The generally Fe_2O_3-rich, SiO_2-poor biotite schist xenoliths may reflect a restitic origin from partial melting that could have contributed to the granite found in the megablock.

The basement biotite schist sample RG70, which contains unusually magnesian biotite and lacks significant muscovite (see Chapter 2, Section 2.3.1.2), has a significantly higher MgO content (4.6 wt.%) than most other mica schist samples (Figure 3.3e; Appendix 2a), and is depleted in Al_2O_3 relative to the other mica schists (Figure 3.3b). It also shows slightly elevated Na_2O and, to a lesser extent, CaO values, which are consistent with the high plagioclase content (Figure 3.3f and g, respectively). The Na_2O/K_2O ratio for the biotite schist sample RG70

is 0.6 (Appendix 2a), which is only slightly less than the average pelite Na_2O/K_2O ratio (Taylor and McLennan, 1985).

The tourmalinite (sample RG54) contains both the highest Fe_2O_3 content (18.8 wt%; Figure 3.3c) and the lowest SiO_2 content (40.4 wt%) of the basement-derived mica schists (Figure 3.3c; Appendix 2a). This is consistent with the Fe-rich tourmaline (dravite to schorlite) mineralogy observed in Chapter 2, Section 2.3.1.5. The tourmalinite also has elevated TiO_2, Al_2O_3, MgO and Na_2O (Figure 3.3b, c, e and g) values and is depleted in K_2O (Figure 3.3d, h and i) values relative to the mica schists, reflecting the absence of micas (Figure 3.3b, e and h).

3.3.2 Amphibolites and calc-silicate rock

With the exception of the tourmalinite (sample RG54), which is interpreted as a highly metasomatised rock, and the low SiO_2 biotite schist xenolith (sample W36b), the megablock amphibolite samples show the lowest SiO_2 content (Figures 3.3 and 3.4a; Table 3.4; Appendix 2a), although one sample (RG06) contains >60 wt% SiO_2, which could reflect thin quartz veining. The megablock amphibolite is generally significantly enriched in MnO, MgO and CaO relative to the mica schists (Figure 3.3d, e and f) but has lower TiO_2 and Fe_2O_3 totals (Figure 3.3a and c). It is depleted in Al_2O_3 and K_2O (Figure 3.3b and h) but shows a spread of similar Na_2O contents to the mica schists (Figure 3.3g). There is a comparatively closer correlation between the upper amphibolite megablock and the biotite schist xenoliths of the upper granite megablock where the two target rock units have similar compositions depleted in SiO_2 and enriched in Fe_2O_3, MnO and MgO (Figure 3.3c, d and e; Appendix 2a). This reinforces Schmitt *et al.*'s (2009) suggestion that the schist xenoliths form a distinct suite separate from the mica schists below the impactites.

The lower basement-derived amphibolite is more enriched in SiO_2, CaO and K_2O than the upper amphibolite megablock (Table 3.1; Figure 3.3f and h), which is consistent with the comparatively Mg-depleted mineralogy described in Chapter 2, Section 2.3.1.3. The amphibolite of the lower basement-derived section is spatially associated with the calc-silicate (see Chapter

2, Figure 2.1) and contains similar Fe_2O_3, MgO and P_2O_5 values to the calc-silicate (Figure 3.3c, e and i).

The calc-silicate contains the highest CaO content observed in the Eyreville-B borehole core (14.3–25.6 wt%; Figure 3.3f), although a single sample reflects quartz veining (SiO_2 > 60 wt%; sample W134; Appendix 2a). This is also mirrored in the anorthite-rich plagioclase of the calc-silicate (Figure 3.4a). The calc-silicate also shows the lowest Na_2O values (0.11–0.37 wt%; Figure 3.3g) and low K_2O values (0.04-1.01 wt%; Figure 3.3h). The high CaO content as well as the relatively high Al_2O_3 (7.2–14.8 wt%; Figure 3.3b) and Fe_2O_3 (4.6–7.26 wt%; Figure 3.3c) values of the calc-silicate compare well to marly sediments, as recorded by Pettijohn (1957), and, thus, it is interpreted to be a metamarl.

Some of the greatest MnO values within the Eyreville-B borehole core are within the calc-silicate (0.19-0.41 wt%; Figure 3.3d; Appendix 2a). This enrichment might confirm the presence of garnet within the calc-silicate that was speculated in Chapter 2 (Section 2.3.1.4) with regards to possible relics of an isotropic mineral. Ordóñez-Calderón *et al.* (2008) observed that Mn is significantly mobile during calc-silicate metasomatism; consequently, it could be surmised that the MnO content may have been incorporated into the retrograde mineral assemblage as garnet became increasingly unstable (see Chapter 2, Section 2.3.1.4).

3.3.3 Granites

The granite of the lower basement-derived section strongly overlaps both the massive and gneissic granite varieties from the megablock in terms of composition (Figure 3.3). The coarse nature of the basement granite coupled with the small core samples has caused difficulty in obtaining representative chemical analyses for this rock unit. Consequently, the lower basement-derived granite shows the largest compositional range, including two samples (W119 and W140) comprising over 80 wt% SiO_2 (Appendix 2a).

The basement granite contains very minor opaque or ferromagnesian minerals (other than rare biotite and garnet; see Chapter 2, Section 2.3.1.6) which is consistent with the TiO_2-, Fe_2O_3-, MnO- and MgO-poor nature of these samples and distinguishes them from the megablock granites (Figure 3.3a, c, d and e). Furthermore, the basement granite displays the highest Na_2O content of all rock units analysed (Figure 3.1h; Figure 3.3g), which is reflected in the albitic plagioclase in this rock unit (Figure 3.4b) and is consistent with mineral chemistry in Chapter 4 (Section 4.1.4; Figure 4.8).

The gneissic megablock granite has slightly higher TiO_2, Fe_2O_3, MgO, CaO and P_2O_5 values than the massive megablock granite (Figure 3.3a, c, e, f and i). It also displays the highest K_2O content of the three granite types. The average CaO content (1.2 wt%) of the lower basement-derived granite is lower, and the Na_2O content (4.3 wt%) is slightly higher, than that of the megablock massive (CaO = 1.5 wt%; Na_2O = 3.2 wt%) and gneissic (CaO = 1.3 wt%; Na_2O = 3.3 wt%) granite varieties. Both megablock massive and gneissic granites show $Na_2O<K_2O$, while the lower basement-derived granite shows $Na_2O>K_2O$ (illustrated in normative feldspar compositions in Figure 3.4b).

Middlemost (1994) proposed a classification and nomenclature scheme for plutonic rocks based on the total alkali versus silica (TAS) diagram. Of the 60 samples from the three granite rock units plotted in Figure 3.5a, over 80% fall with the granite field with outliers plotting mainly in the quartz monzonite and granodiorite fields and, to a lesser extent, in the syenite and quartzolite fields. Two finer-grained samples (RG40 and RG61), which show more representative compositions than the coarser-grained samples, are located along the granite/granodiorite field boundary (Figure 3.5a). Petrographic analysis of these two samples in Chapter 2 (Section 2.3.1.6) observed that these two samples are located within the mylonite zone and are significantly enriched in SiO_2 compared to the other basement granite samples. This is consistent with quartz- and calcite-rich veining associated with hydrothermal alteration that is characteristic of the mylonite zone (Chapter 2, Section 2.3.1.7), and it is uncertain as to the amount of SiO_2 that introduced to the basement granite.

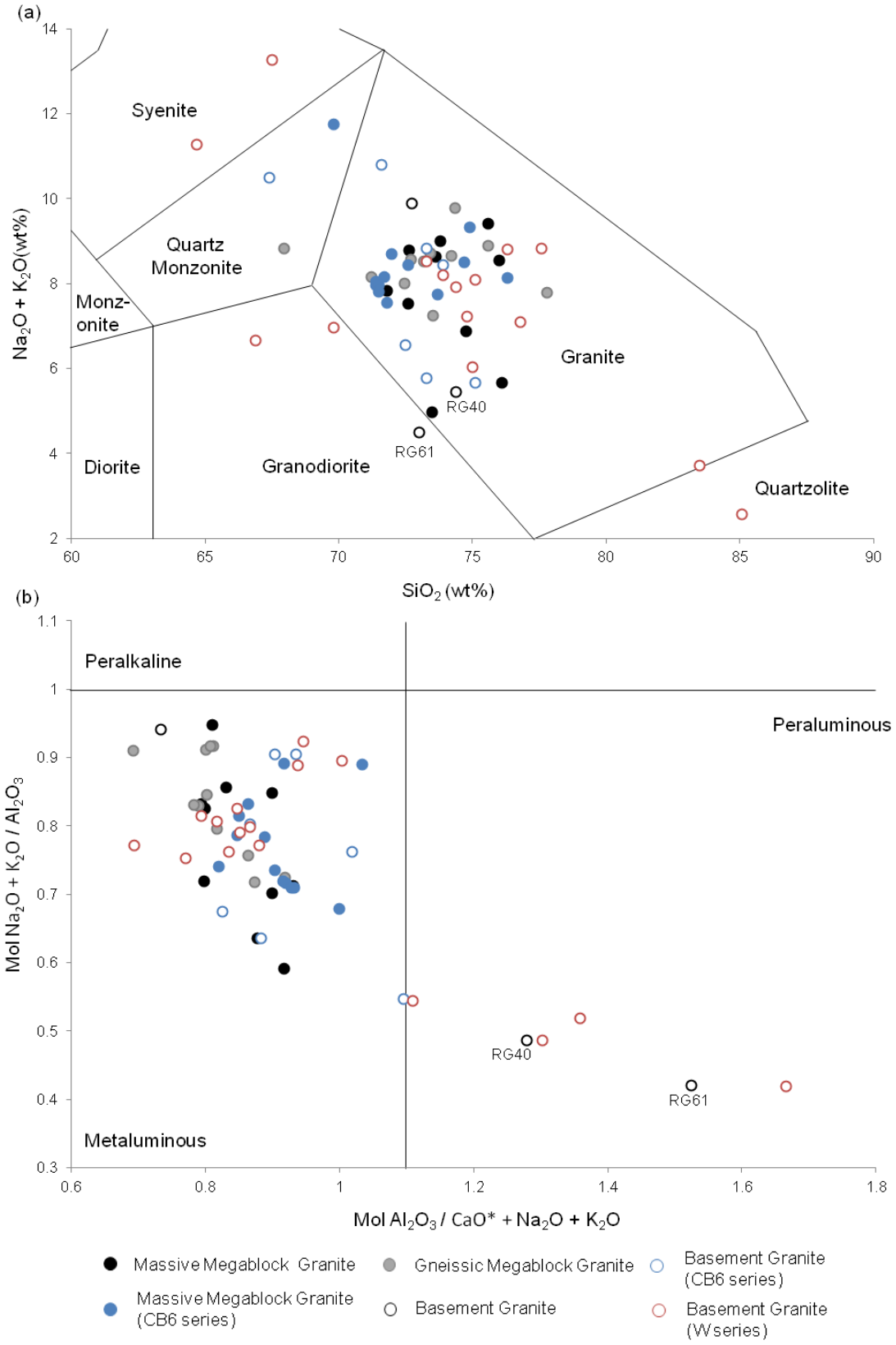

Figure 3.5: Bivariate diagrams for the granite rock units of the Eyreville-B borehole core: (a) TAS diagram for the classification of plutonic rocks (after Middlemost, 1994), and (b) ASI (after Shand, 1927; Chappell and White, 1974). All data in wt%.

Chappell and White (1974, 1984) observed two types of granites, namely I-type and S-type, based on petrological and geochemical features. I-type granites are those that are derived from an igneous source, wheras S-type granites are derived from sedimentary sources (Chappell *et al.*, 1998). One of the best ways to distinguish between the two types is the use of the alumina saturation index (ASI; after Shand, 1927). Chappell and White (1974) observed that I-type granites tend to be metaluminous in nature while S-type granites tend to be peraluminous.

Figure 3.5b illustrates the ASI for the three granites of the Eyreville-B borehole core. ASI is calculated by the following equation:

$$Al_2O_3 / (CaO^* + Na_2O + K_2O)$$

In order to obtain representative results, CaO* was first corrected for apatite and carbonate by the following equation (after Yan *et al.*, 2010):

$$CaO^* = (\text{mole } CaO - \text{mole } P_2O_5) \times (10 / 3)$$

If $CaO^* \leq Na_2O$, this value was adopted into the CIA equation; however, if $CaO^* \geq Na_2O$, CaO* was assumed to be equal to that of Na_2O (after McLennan, 1993). See Appendix 2a for calculated CIA values for all samples analysed.

The lower basement-derived granite is metaluminous to peraluminous in composition, with an ASI ratio range of 0.69–1.67 and an average of 0.99 (Appendix 2a). The wide ranges in both SiO_2 content and ASI in the lower basement-derived granite most likely reflect the strongly pegmatitic nature of this granite. ASI values for finer-grained granite samples (RG40 and RG61) indicate a narrower range that is peraluminous in character (ASI ratios are 1.28–1.53; Appendix 2a). Despite the fact that these samples may not be true representatives of the basement granite, the peraluminous nature of the granite corresponds with the observed mineral

assemblage suggesting it was derived from a crustal source i.e. an S-type granite (Chapter 2, Section 2.3.1.6; Chappell and White, 1974; Miller, 1985).

The massive and gneissic megablock granites are strongly metaluminous, with ASI ratio ranges of 0.80–1.04 and 0.69–0.92 and averages of 0.89 and 0.82, respectively. Chappell and White (1992) noted that I-type granites could be further distinguished by other parameters, such the Na_2O/K_2O ratio. The massive and gneissic megablock granites show Na_2O/K_2O ratio ranges of 0.1 to 3.6 (average of 0.9) and 0.4 to 1.0 (average of 0.7), respectively; the Na_2O/K_2O averages for the megablock granite rock units correspond well with the expected ratio for a typical I-type granitoid (0.9; after Chappell and White, 1992).

Using AFM diagrams (based on bulk rock geochemical data; Figure 3.6), it is observed that all three granite rock units of the Eyreville-B borehole core are part of a calc-alkaline magma series (Irving and Baragar, 1971). However, the differences in ASI (Figure 3.5) preclude the deduction that the three granites were derived from the same parent magma.

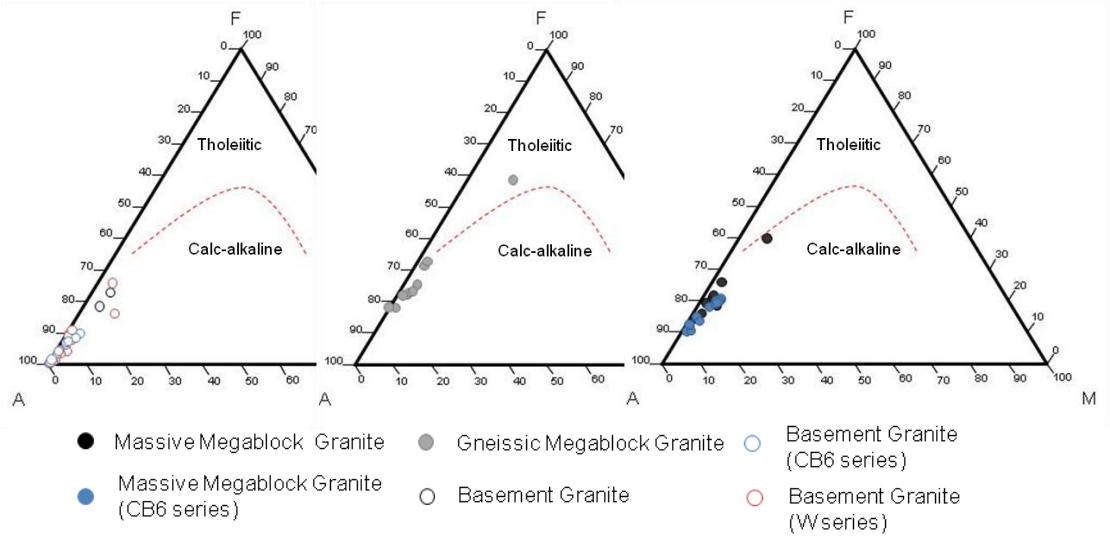

Figure 3.6: Ternary diagrams indicating the AFM abundances (wt%) for (a) the lower basement-derived granite, (b) the upper megablock granite and (c) the upper megablock granite gneiss rock units of the Eyreville-B borehole core. Red dashed line shows the chemical boundary between tholeiitic and calc-alkaline magma series (after Irving and Baragar, 1971). Abbr.: A (alkalis) = $Na_2O + K_2O$; F = $Fe_2O_{3(total)}$; M = MgO.

3.3.4 Alteration within the Eyreville-B borehole core

Breccias and veining were avoided as much as practicably possible when selecting samples for bulk-rock chemical analysis; however, the metasedimentary target rock units of the Eyreville-B borehole core show extensive hydrothermal alteration both in terms of their metamorphic mineral assemblages as well as in the abundant quartz and calcite veining (see Chapter 2, Section 2.3.1.1). This is further evidenced in the sericitisation of the feldspars, chloritisation of biotite, specifically in the mylonite zone, as well as the presence of metasomatised tourmalinite (see Chapter 2, Section 2.3.1.5). The upper amphibolite megablock and biotite schist xenoliths of the upper granite megablock also show alteration (see Chapter 2, Sections 2.3.2 and 2.3.3.3, respectively).

To determine the extent and nature of the hydrothermal alteration, loss on ignition (LOI), determined prior to XRF analysis, was plotted against depth (Figure 3.7) and against CaO (Figure 3.8). Price and Velbel (2003) noted that Ca, K, Na and Mg (alkali and alkaline earth elements) are the most mobile of the major elements and can be readily used in weathering indices and, thus, can be used to gauge the degree of alteration. Means and standard deviations of LOI for the eight target rock units of the Eyreville-B borehole core are listed in Table 3.4.

Average values of LOI range between 5.15 and 9.35 wt% in the metasediments of the lower basement-derived section and between 0.78 and 3.95 wt% for the upper amphibolite megablock and biotite schist xenoliths of the upper granite megablock (Table 3.4; Appendix 2a). Unsurprisingly, trends in LOI values are most clearly observed in the micas schists of the lower basement-derived section, and increase with depth toward the mylonite zone (~1640-1650 m depth), peaking at 10.7 wt% at 1680 m depth (sample W139b), below which LOI steadily decreases (Figure 3.7a). A positive trend of LOI with increasing depth is seen in the basement amphibolite and calc-silicate, indicating that alteration increases with depth in the mylonite zone (Figure 3.7a). This finding correlates with the increase in quartz and calcite veining with depth in this zone (see Chapter 2, Section 2.3.1.7).

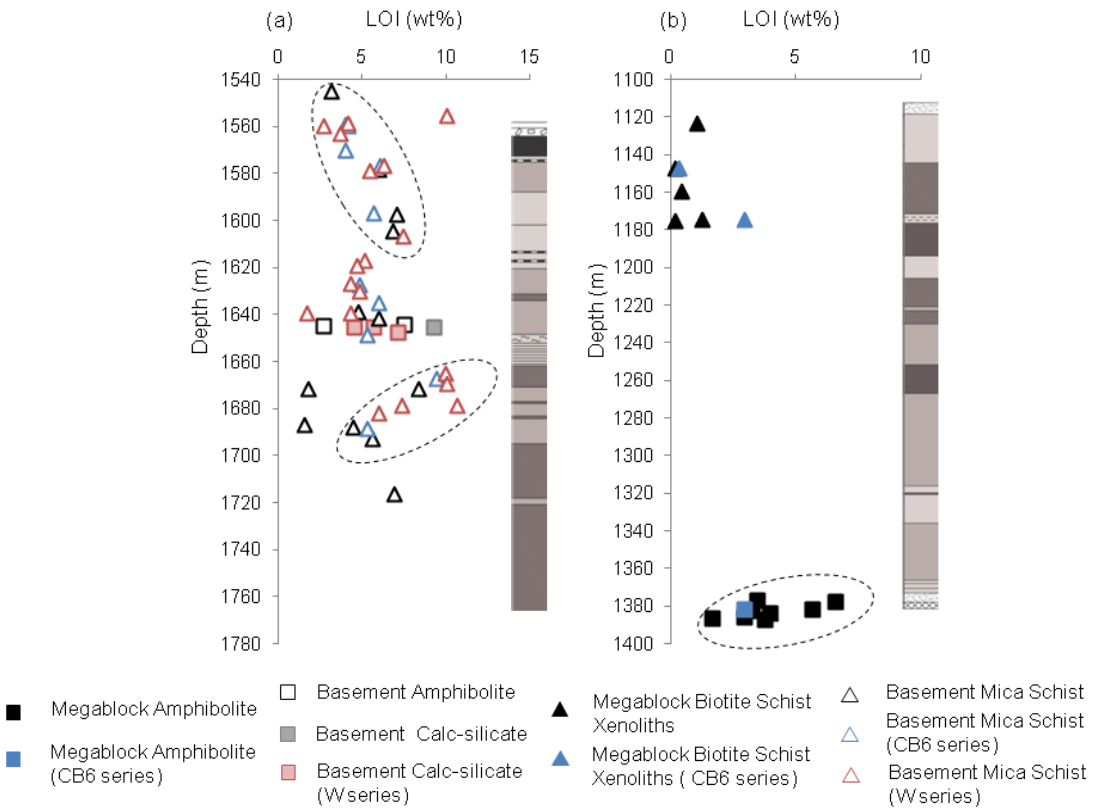

Figure 3.7: Variations in LOI (wt%) with depth (m) for the metasedimentary target rock units of the (a) lower basement-derived section and (b) upper granite and amphibolite megablocks of the Eyreville-B borehole core. The geologic column, as described in Chapters 1 and 2 (after Horton *et al.*, 2009a), has been placed on the right side for reference purposes. Dashed lines represent observed groupings.

CaO concentrations for the mica schists, amphibolites and calc-silicate are plotted against LOI in Figure 3.8. The noticeable lack of correlation between CaO and LOI in the lower basement-derived mica schists in Figure 3.8a is surprising when one considers the extensive quartz and calcite veining observed through petrographic analysis (Chapter 2, Section 2.3.1.1). This suggests that carbonate is not the predominant cause of LOI but rather that other effects, such as the presence of organic matter and/or H_2O in peak metamorphic phyllosilicate minerals (Bartosova *et al.*, 2009) or retrograde assemblages, have contributed to LOI. The biotite schist xenoliths of the upper granite megablock show a slightly positive trend between CaO and LOI (Figure 3.8a).

Figure 3.8b shows that, while the lower basement-derived amphibolite has a slightly positive correlation between CaO and LOI, the calc-silicate shows a distinctly negative trend. The finding

corresponds to what is observed in hand specimen where most fractures in the highly cataclased rock are filled with quartz, with a minor calcite component (Chapter 2, Section 2.3.1.4). The megablock amphibolite is the only lithology to show a clearly positive correlation between CaO and LOI (Figure 3.8b). Alteration in the megablock amphibolite occurs through locally intense quartz and calcite veining most evident in samples RG01, RG04 and RG05 (see Chapter 2, Section 2.3.2; Appendix 1b).

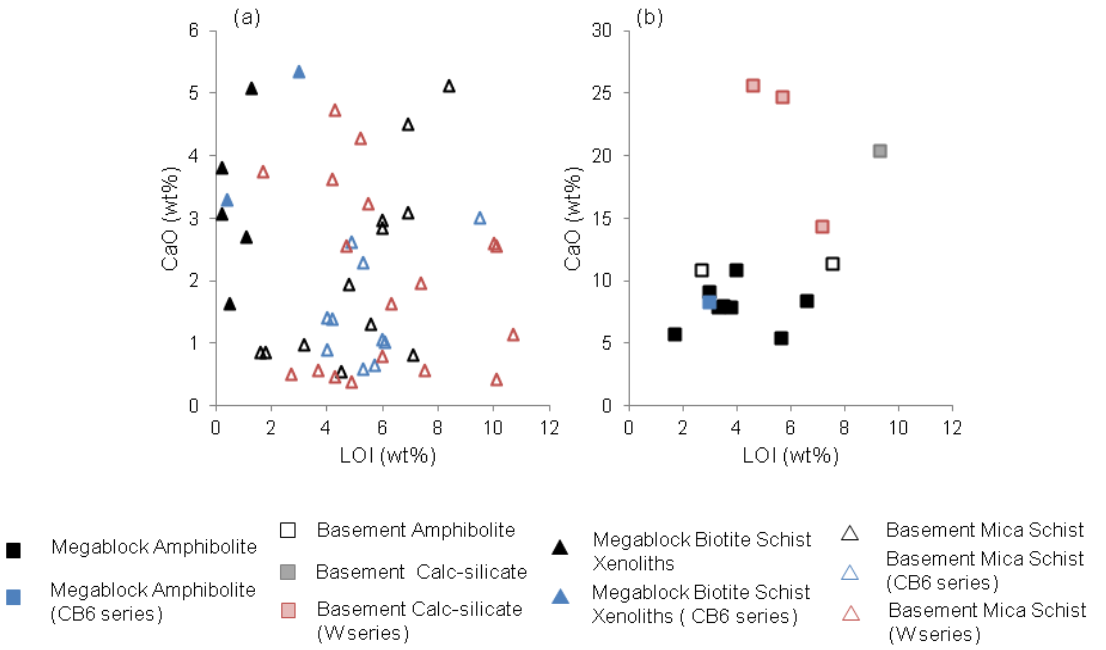

Figure 3.8: Variations in LOI with CaO concentrations for (a) the mica schists and (b) the amphibolites and calc-silicate rock units of the Eyreville-B borehole core. All data in wt%.

Nesbitt and Young (1982) observed that the proportion of alumina to alkalis typically increases with weathering and alteration. Thus, to best illustrate the extent of alteration, the chemical index of alteration (CIA; after Nesbitt and Young, 1982) has been plotted against depth for the lower basement-derived section (Figure 3.9a) and the upper megablocks section (Figure 3.9b). CIA is calculated using molecular proportions in the following formula:

$$CIA = [Al_2O_3 / (Al_2O_3 + CaO^* + Na_2O + K_2O)] \times 100$$

where CaO* is the amount of CaO included in the silicate fraction of the rock after it has been corrected for apatite and carbonate (see Section 3.3.3), and a calculated value of 100 represents the most altered material (after Nesbitt and Young, 1982).

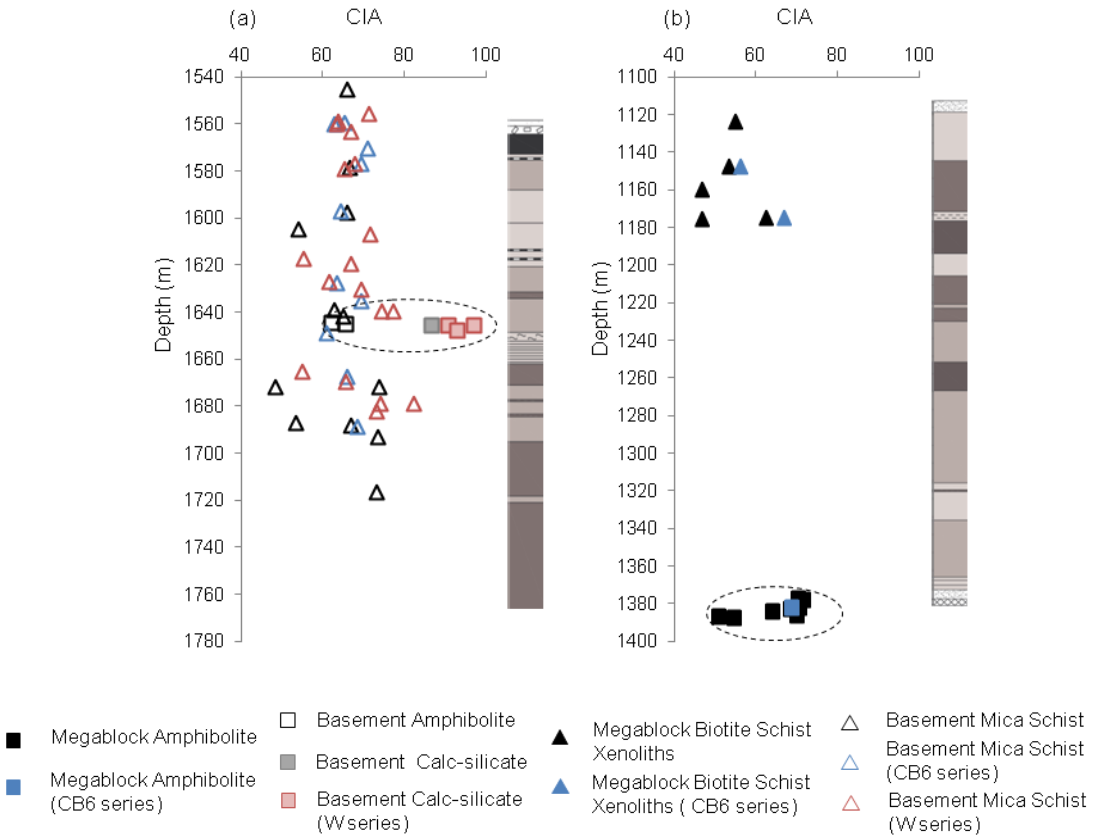

Figure 3.9: Variations in CIA with depth (m) for the metadeismentary target rock units of the (a) lower basement-derived section and (b) upper granite and amphibolite megablocks of the Eyreville-B borehole core. The geologic column, as described in Chapters 1 and 2 (after Horton *et al.*, 2009a), has been placed on the right side for reference purposes. Abbr.: CIA = chemical index of alteration. Dashed lines represent observed groupings.

The lower basement-derived mica schists show the largest range of CIA values (49-82), with the greatest variation observed at ~1680 m depth (Figure 3.9a). This corresponds with the base of the mylonite zone, which is characterised by hydrothermal alteration (see Chapter 2, Section 2.3.1.7). The average CIA value for the basement mica schists is 67, and the average CIA value for the mica schists in the mylonite zone is 68. These values are slightly less than and equal to the CIA values for the NASC (68) and PAAS (70) average shale compositions (Gromet *et al.*, 1984; Taylor and McLennan, 1985). Considering that optimum fresh values of CIA are less than

and equal to 50 (e.g. Price and Velbel, 2003), the slightly lower CIA values for the lower basement-derived mica schists compared with the NASC and PAAS suggests that the basement metasediments experienced average intensities of weathering.

The amphibolite of the lower basement-derived section ranges in CIA values between 62 and 66, with an average of 64 (Figure 3.9a). The calc-silicate has the highest CIA values of all rock types analysed, with an average of 92 (Figure 3.9a). This corresponds well with the petrographic characteristics of the calc-silicate, which is the most altered of all of the eight target rock units of the Eyreville-B borehole core (Chapter 2, Section 2.3.1.4, Figure 2.5).

CIA values for the megablock amphibolite range between 51 and 72, with an average of 65 (Figure 3.9b; Appendix 2a). These values are reflective of the hydrothermal alteration observed during petrographic analysis (Chapter 2, Section 2.3.2). The megablock amphibolite shows a slightly negative trend in CIA values with depth (Figure 3.9b). The biotite schist xenoliths of the megablock granite range between 47 and 67, with an average CIA value of 56 (Appendix 2a) very similar to that of the amphibolite. This suggests that the upper megablock amphibolite and biotite schist xenoliths experienced limited alteration.

3.4 Trace element analysis

Fifty-two samples from the Eyreville-B borehole core were analysed for trace elements by XRF (Table 3.5). Trace elements for the samples of the W series and CB6 series, also obtained by XRF analysis, have been included for comparison purposes (Bartosova *et al.*, 2009; Schmitt *et al.*, 2009). Trace element data for all samples obtained by XRF analysis are presented in Appendix 2a.

Figures 3.10 and 3.11 show selected trace elements plotted against depth for the eight target rock units of the Eyreville-B borehole core. These same trace elements have been plotted against SiO_2 in Figure 3.12.

Table 3.5: Mean and standard deviation (data in ppm) of trace element abundances obtained by XRF analysis for the eight target rock units of the Eyreville-B borehole core. Abbr.: n = number of samples; SD = standard deviation; bdl = below detection limit.

Trace Element (ppm)	Basement Mica Schist		Basement Amphibolite		Basement Calc-silicate	Basement Granite	
	n = 12		n = 2		n = 1	n = 3	
	Mean	SD	Mean	SD	Mean	Mean	SD
Rb	214.75	72.19	193.50	112.43	129.00	233.67	40.72
Sr	119.58	63.89	259.50	129.40	106.00	76.33	6.81
Y	50.08	11.70	30.50	6.36	17.00	43.00	24.76
Zr	163.08	72.01	235.00	14.14	38.00	65.67	37.21
Nb	23.42	21.99	29.50	19.09	8.00	49.67	6.43
Ba	364.25	212.28	1821.50	1939.59	73.00	128.33	58.23
Cr	135.90	38.86	68.00	8.49	14.00	107.00	76.74
V	162.36	69.97	81.50	23.33	54.00	21.00	4.24
Co	26.40	13.55	14.50	0.71	9.00	bdl	bdl
Ni	38.33	16.98	33.50	4.95	14.00	21.33	13.28
Cu	76.11	84.80	bdl	bdl	bdl	bdl	bdl
Zn	106.58	28.28	138.50	74.25	159.00	36.00	22.87

Trace Element (ppm)	Megablock Massive Granite		Megablock Gneissic Granite		Megablock Biotite Schist Xenoliths		Megablock Amphibolite	
	n = 10		n = 11		n = 5		n = 8	
	Mean	SD	Mean	SD	Mean		Mean	SD
Rb	218.70	82.68	219.09	19.69	323.40	104.41	87.43	99.58
Sr	185.50	103.79	191.73	76.08	252.80	329.03	305.88	68.55
Y	57.00	37.28	22.27	11.42	93.20	45.48	32.20	20.27
Zr	203.80	50.58	212.18	55.14	388.20	109.37	145.50	145.89
Nb	24.40	11.19	20.18	10.26	69.00	28.12	25.50	16.34
Ba	604.60	290.34	762.91	260.35	604.60	471.06	306.88	374.38
Cr	21.00	2.37	15.00	bdl	57.75	23.61	148.13	59.07
V	26.89	19.12	21.43	7.79	151.40	107.83	171.75	43.68
Co	6.00	bdl	6.50	0.58	31.50	27.60	42.63	16.49
Ni	21.50	10.77	8.45	1.51	54.20	76.27	67.75	32.83
Cu	7.00	bdl	9.80	3.42	11.50	4.95	46.75	18.00
Zn	50.11	19.59	43.27	14.40	214.40	77.15	81.25	28.19

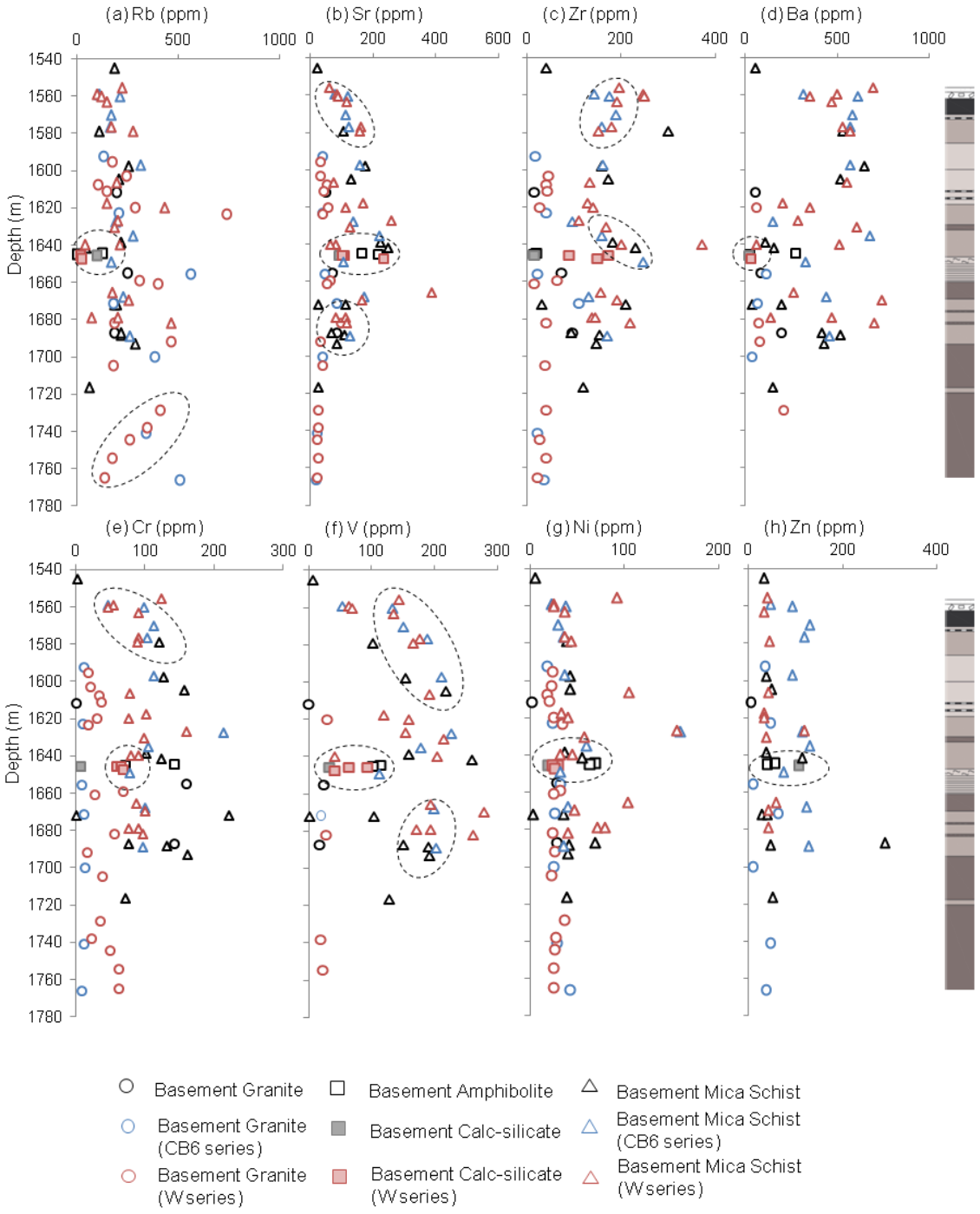

Figure 3.10: Variations in trace element concentrations (ppm) with depth (m) for the four target rock units in the lower basement-derived section of the Eyreville-B borehole core. Not all samples could be plotted for Zr, Ba, V and Zn graphs as their concentrations were below the lower limit of detection. Samples from the CB6 and W series (after Schmitt *et al.*, 2009) have been included to increase the data set size. The geologic column, as described in Chapters 1 and 2 (after Horton *et al.*, 2009a), has been placed on the right side for reference purposes. Dashed lines represent observed groupings.

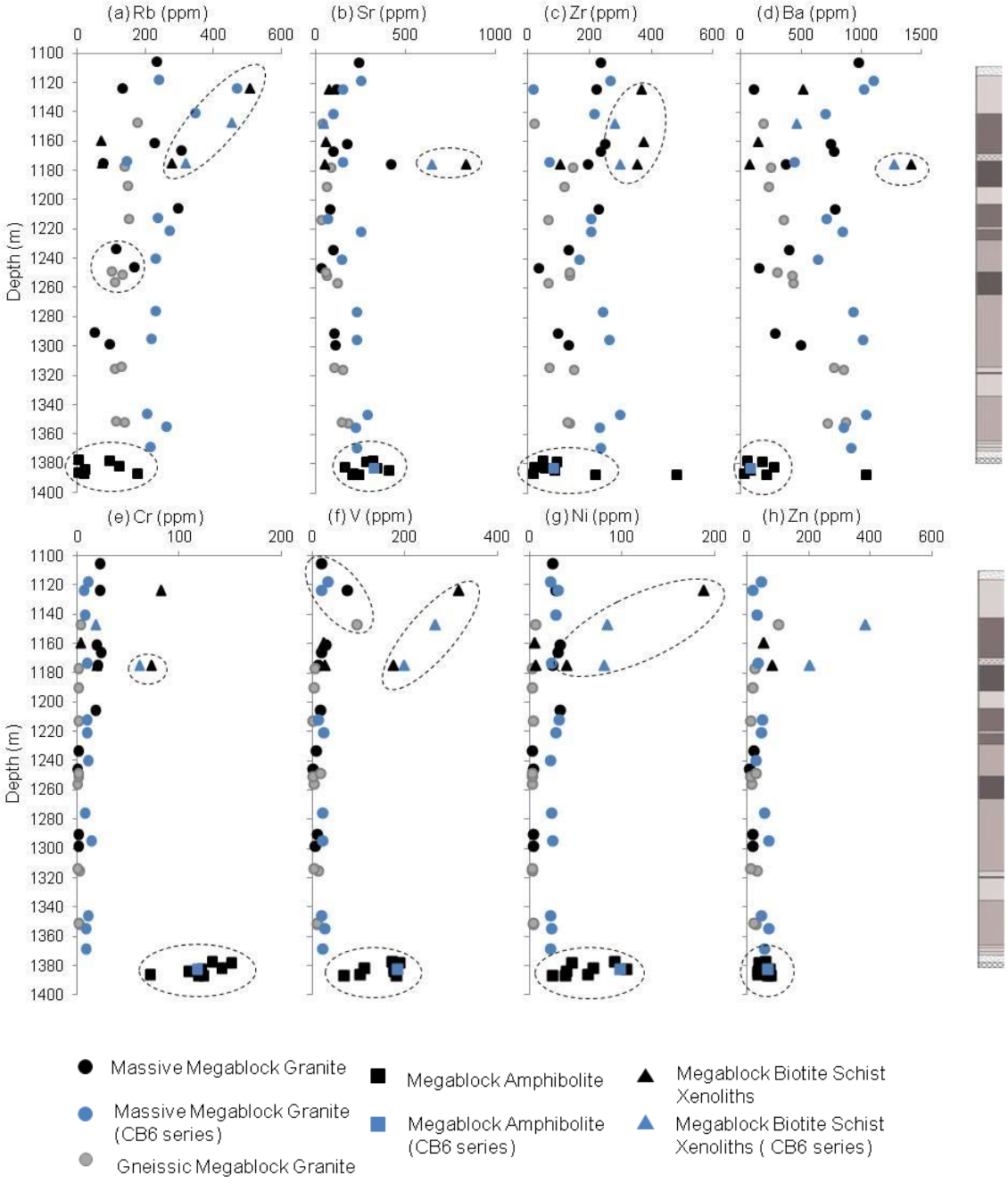

Figure 3.11: Variations in trace element concentrations (ppm) with depth (m) for the four target rock units in the upper granite and amphibolite megablocks of the Eyreville-B borehole core. The geologic column, after Horton *et al.* (2009), has been placed on the right side for reference purposes. Not all samples could be plotted for Rb, Cr, Ba, V and Zn graphs as their concentrations were below the lower limit of detection. Samples from the CB6 series (after Schmitt *et al.*, 2009) have been included to increase the data set size. The geologic column, as described in Chapters 1 and 2 (after Horton *et al.*, 2009a), has been placed on the right side for reference purposes. Dashed lines represent observed groupings.

3.4.1 Mica schists

Concentrations of Rb, Sr, Cr, V and Ni tend to increase with depth towards approximately 1610 m in the lower basement-derived mica schists, and then decrease with depth below 1660 m (Figure 3.10a, b, e, f and g). Zr concentrations in the basement mica schists differ in that there is a negative trend from around 1550 m to 1610 m, which changes to a positive trend from around 1610 m to 1640 m (the mylonite zone; Figure 3.10c). Zr concentrations return to a negative trend below 1670 m (Figure 3.10c). This signature is similar to that observed in the major element oxides SiO_2 and K_2O (Figure 3.1a and i) whereas Fe_2O_3 shows opposite trends at similar depths (Figure 3.1d).

The basement mica schists generally decrease in trace element abundance with increasing SiO_2, although no trend is observed in Zr and Zn abundances (Figure 3.12c and h). This negative correlation is mirrored in major element oxides TiO_2, Al_2O_3, Fe_2O_3, MgO, Na_2O and K_2O (Figure 3.3a, b, c, e, g and h). Rb, Ba, Cr and V abundances increase with increasing Al_2O_3 concentrations in the biotite schist xenoliths (Figure 3.10a, b, c and d). Cr and V also increase in abundance with increasing Fe_2O_3 (Figure 3.13e and f) and Rb and Ba increase with increasing K_2O (Figure 3.14c and d). Rb and Zr have negative trends with increasing Na_2O (Figure 3.14a and b).

Other than for V, average trace element concentrations for the lower basement-derived mica schists do not tend to agree with the NASC and PAAS trace element compositions (Table 3.5). Average Rb (215 ppm, NASC = 125 ppm; PAAS = 160 ppm) and Cr (136 ppm; NASC = 125 ppm; PAAS = 110 ppm) concentrations are higher while Sr (120 ppm; NASC = 142; PAAS = 200), Zr (163 ppm; NASC = 200; PAAS = 210), Ba (364 ppm; NASC = 636; PAAS = 650) and Ni concentrations (38 ppm; NASC = 58; PAAS = 55) are lower (Gromet *et al.*, 1984; Taylor and McLennan, 1985).

The biotite schist xenoliths of the upper granite megablock show the most scatter with depth in terms of trace element abundance (Figure 3.11). Rb, Zr, V and Ni abundances in the biotite

schist xenoliths tend to decrease with depth (Figure 3.11a, c, f and g), similar to that seen in the major element oxides TiO_2 and Fe_2O_3 (Figure 3.2b and d). Two outliers that occur in Sr, Ba and Cr abundances are samples CB6-078 and W39b (Figure 3.11b, d and e), and a single outlier in Zn is sample CB6-076 (Figure 3.11h).

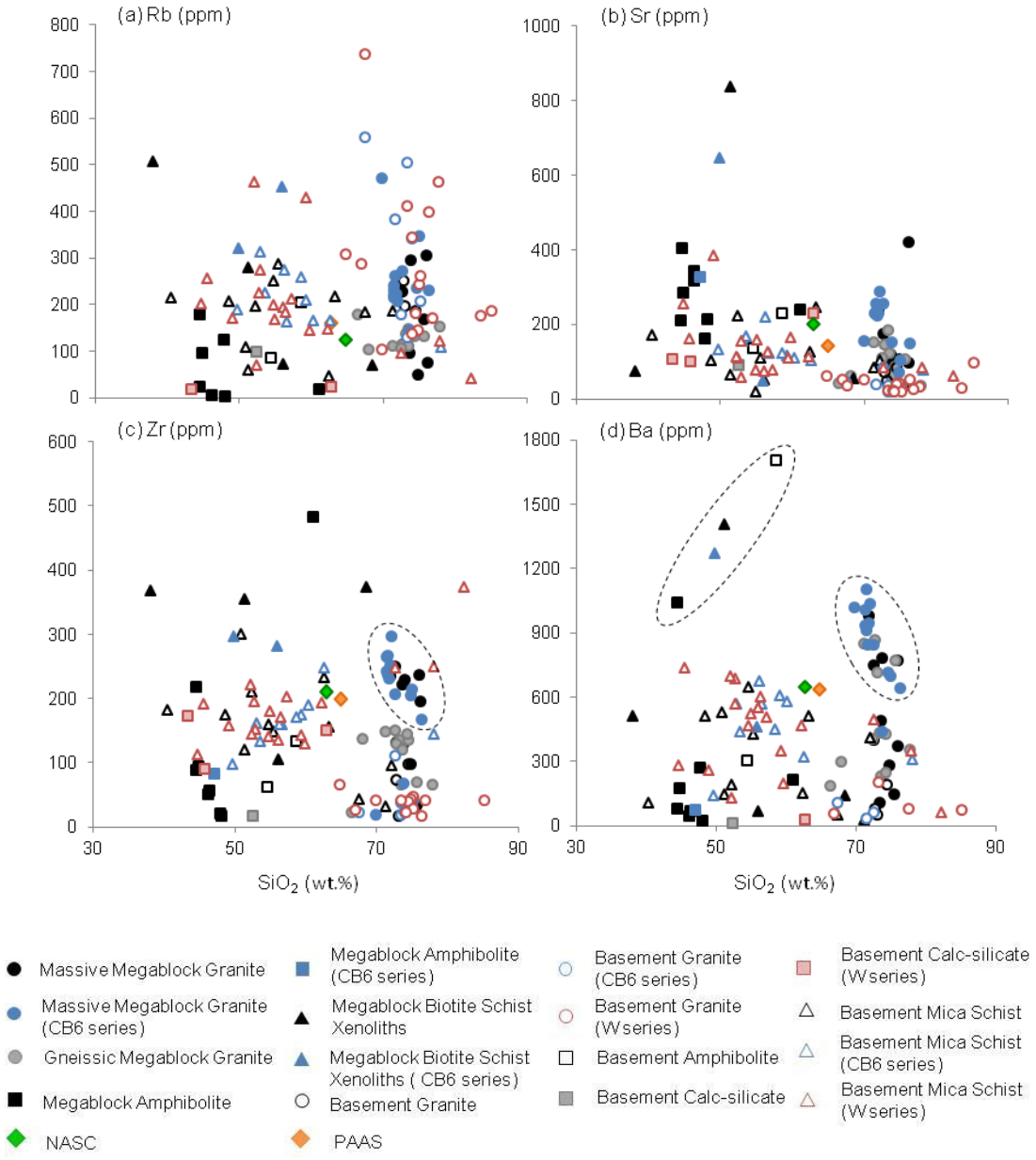

Figure 3.12: Harker diagrams showing trace element (Rb, Sr, Zr, Ba, Cr, V, Ni and Zn) concentrations (in ppm) plotted against SiO_2 for the eight target rocks units of the Eyreville-B borehole core. Abbr.: NASC = North American Shale Composite (after Gromet *et al.*, 1984); PAAS = Post Archean Australian Shale (after Taylor and McLennan, 1985). Dashed lines represent observed groupings.

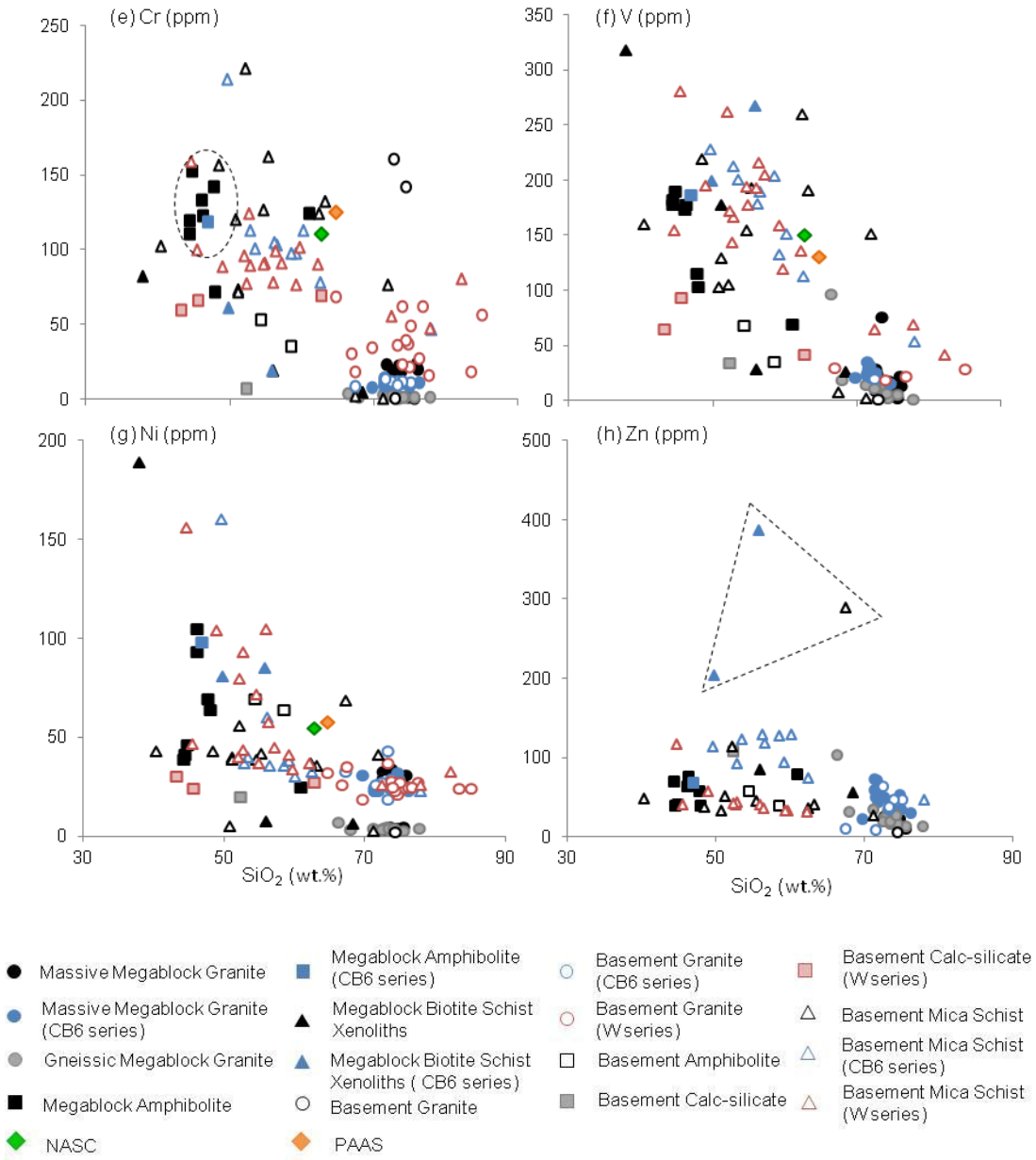

***Figure 3.12 (continued)*: Harker diagrams showing trace element (Rb, Sr, Zr, Ba, Cr, V, Ni and Zn) concentrations (in ppm) plotted against SiO_2 for the eight target rocks units of the Eyreville-B borehole core. Abbr.: NASC = North American Shale Composite (after Gromet *et al.*, 1984); PAAS = Post Archean Australian Shale (after Taylor and McLennan, 1985). Dashed lines represent observed groupings.**

Trace element abundances relative to SiO_2 also show the most scatter in the biotite schist xenoliths (Figure 3.12), mirroring what is observed in Figure 3.11. The xenoliths show positive correlations in Sr and Ba (Figure 3.12b and d) and correlate negatively in Rb and V abundance with increasing SiO_2 (Figure 3.12a and f). The biotite schist xenoliths tend to increase in V with

increasing Fe_2O_3 (Figure 3.13e and f), and Zr abundance with increasing Na_2O (Figure 3.14b). Negative correlations are between V and Al_2O_3 (Figure 3.10d), Cr and Fe_2O_3 (Figure 3.13e) and Rb and Na_2O (Figure 3.14a).

Unlike the basement-derived mica schists, the biotite schist xenoliths do generally agree with NASC and PAAS trace element concentrations for Sr, Ba, V and Ni (Table 3.5). However, the Rb and Zr concentrations (342 and 427 ppm, respectively) are more than double the NASC (Rb = 125 ppm; Zr = 200 ppm) and PAAS (Rb = 160; Zr = 210 ppm). Average Cr concentration (66 ppm) in the biotite schist xenoliths is half of that observed for the NASC (125 ppm) and PAAS (110 ppm) (Gromet *et al.*, 1984; Taylor and McLennan, 1985). A single biotite schist xenolith sample (W36b) is the most enriched in Rb (507 ppm), V (318 ppm) and Ni (198 ppm) of all the mica schist samples studied (Figure 3.11a, f and g; see Appendix 2a).

3.4.2 Amphibolites and calc-silicate rock

Trace element abundances in the lower basement-derived amphibolite and calc-silicate show similar major element concentrations with depth, with Sr, Zr, V, Ni and Zn showing the most variation in abundance (Figure 3.10b, c, f, g and h). The basement amphibolite shows an increase in Rb, Sr, Zr and Ba (Figure 3.12a, b, c and d) and a decrease in Cr, V, Ni and Zn with increasing SiO_2 (Figure 3.12e, f, g and h). Rb and Ba increase, and Cr and V decrease, in abundance with increasing Al_2O_3 (Figure 3.12a, b, c and d). Cr and V with increasing Fe_2O_3 (Figure 3.13e and f) and Rb and Zr with increasing Na_2O (Figure 3.14a and b) show negative trends in the basement amphibolite, while Rb and Ba show positive trends with increasing K_2O (Figure 3.14c and d).

The calc-silicate tends to have the opposite trend (or no trend at all) to that seen in the basement amphibolite, with the exception of Sr (Figure 3.12b). The calc-silicate tends to be more chemically associated, in terms of trace element abundance with increasing SiO_2, to the upper amphibolite megablock than that of the lower basement-derived section (Figure 3.12). This association can be seen in Figure 3.14c and d where Rb and Ba abundances are plotted

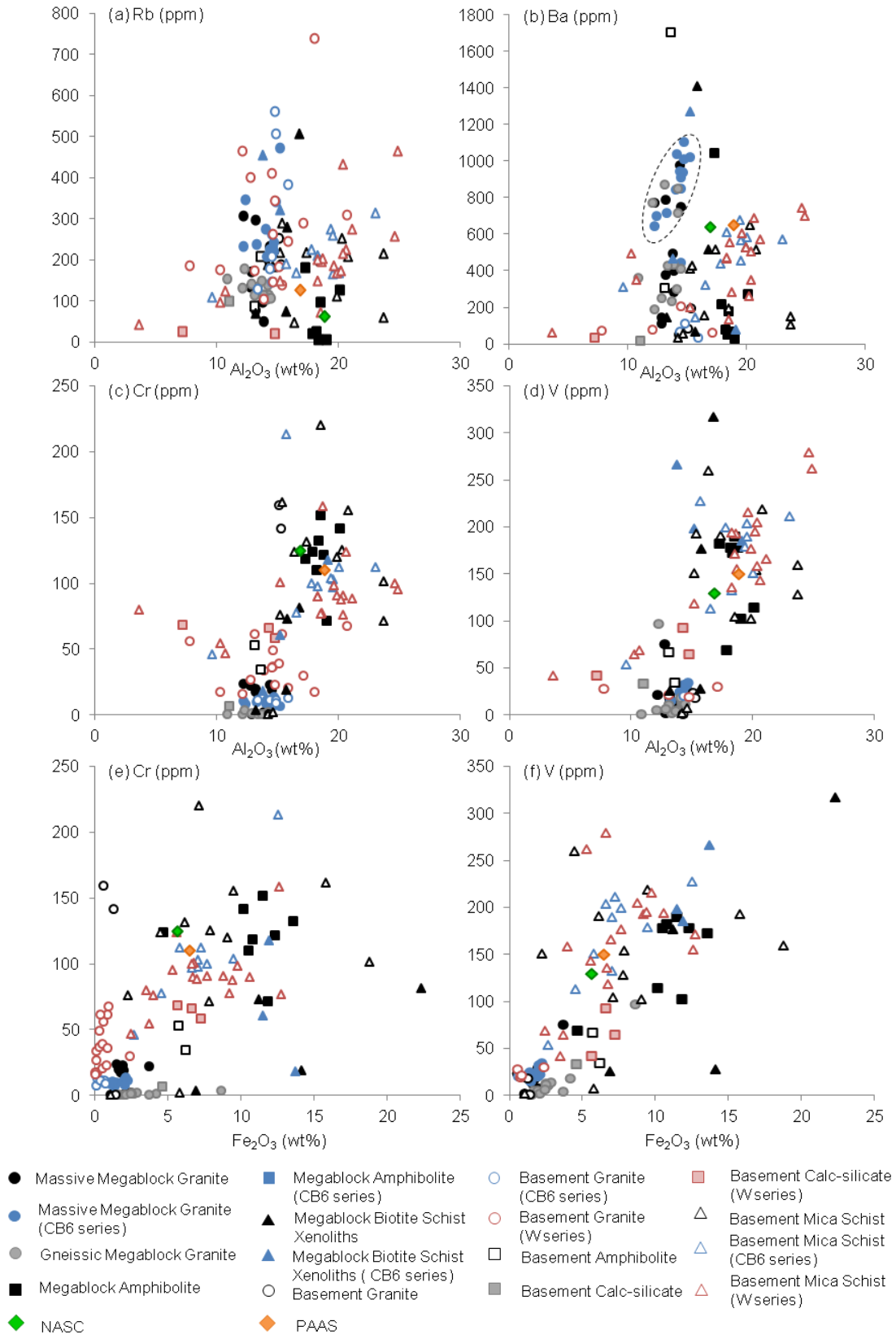

Figure 3.13: Harker diagrams showing trace element concentrations (in ppm) plotted against Al_2O_3 (Rb, Ba, Cr and V) and against Fe_2O_3 (Cr and V) for the eight target rocks units of the Eyreville-B borehole core. Abbr.: NASC = North American Shale Composite (after Gromet *et al.*, 1984); PAAS = Post Archean Australian Shale (after Taylor and McLennan, 1985). Dashed lines represent observed groupings.

against K_2O. Interestingly, the calc-silicate tends to be spatially associated with the basement amphibolite where trace elements have been plotted against other major element oxides (Figure 3.13 and 3.14).

Although samples from the upper amphibolite megablock show similar trace element concentrations to each other, there are no specific trends with depth (Figure 3.11) unlike those seen in the major element oxides (Figure 3.2). The upper megablock amphibolite shows more scatter in terms of trace element abundance (Figure 3.12) than that observed in the major element oxides with increasing SiO_2 (Figure 3.3) and tends to trend negatively with SiO_2 to varying degrees (Figure 3.12). Rb tends to decrease with increasing Na_2O in the upper megablock amphibolite (Figure 3.14a). Positive trends are observed in Ba, Cr and V with increasing Al_2O_3 (Figure 3.13b, c and d), Cr and V with increasing Fe_2O_3 (Figure 3.13e and f) and Rb with increasing K_2O (Figure 3.14c). A single upper megablock amphibolite sample (RG06) occurs as an outlier in Zr versus Na_2O (Figure 3.14b).

3.4.3 Granites

The lower basement-derived granite typically does not show any trends in trace element concentrations with depth (Figure 3.10); however, a notable negative trend in Rb is observed below 1730 m depth (Figure 3.10a). The basement granite shows much scatter in trace element abundance with increasing SiO_2 in comparison to the granite varieties of the upper granite megablock (Figure 3.12). Sr, Zr, Ni and Zn show the least scatter in the basement granite, with comparably low abundances (Figure 3.12b, c, g and h). The only significant trend of trace element abundance plotted against other major element oxides in the basement granite is that Rb tends to increase in abundance with increasing K_2O (Figure 3.14c).

The massive and gneissic megablock granites show the least scatter in trace element concentrations with depth, with the exceptions of Zr and Ba (Figure 3.11c and d). A strong positive correlation in Ba with depth is observed in the gneissic granite (Figure 3.11d). Both the

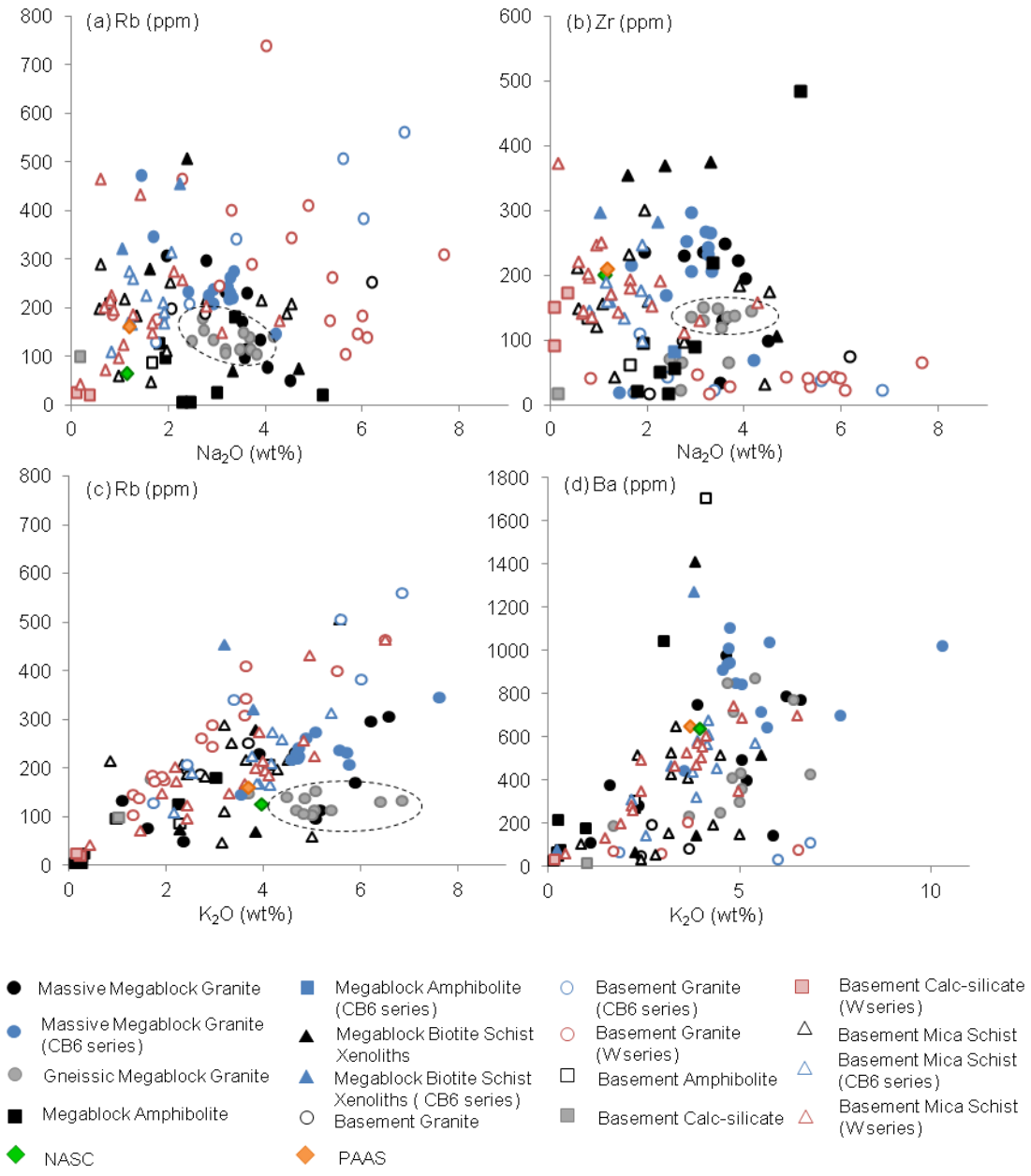

Figure 3.14: Harker diagrams showing trace element concentrations (in ppm) plotted against Na_2O (Rb, Zr and Cr) and against K_2O (Rb and Ba) for the eight target rocks units of the Eyreville-B borehole core. Abbr.: NASC = North American Shale Composite (after Gromet *et al.*, 1984); PAAS = Post Archean Australian Shale (after Taylor and McLennan, 1985). Dashed lines represent observed groupings.

massive and gneissic granites show similar trace element abundances, with increasing SiO_2 and are enriched in Sr Zr and Ba compared to the basement granite (Figure 3.11b, c and d). The gneissic megablock granite shows depletion in Zr and Ba abundance with SiO_2 compared to the massive megablock granite (Figure 3.12c and d) as well as where Rb and Zr are plotted

against Na_2O (Figure 3.14a and b) and Rb against K_2O (Figure 3.14c). Both megablock granite rock units show a negative trend in Zr and Ba abundance with increasing SiO_2 (Figure 3.12c and d) and a positive trend in Ba abundance with increasing Al_2O_3 (Figure 3.13b).

3.5 Rare earth element analysis

REE data were obtained for 27 samples by ICP-MS analysis (Table 3.6; see Section 3.2): 6 from the lower basement-derived section (3 mica schist, 2 amphibolite, 1 calc-silicate and 1 granite), 18 from the granite megablock (11 gneiss, 4 massive and 3 biotite schist xenoliths) and 2 from the upper megablock amphibolite. XRF analysis could not be used to measure REE data as results from this technique become unreliable when measuring abundances of light elements (atomic number less than 11), such as REEs, due to low X-ray yields of these elements as well as instrumental limitations (Winter, 2001). In contrast, the ICP-MS method can measure element abundances for the entire mass range; the REEs lie within the central part of this range (Jarvis, 1988). Appendix 2b shows all trace element data obtained by ICP-MS analysis.

Figure 3.15 shows the REE variation patterns for the eight target rock units of the Eyreville-B borehole core normalised to C1 chondrite composition (after McDonough and Sun, 1995). Average trace element data for the CB6 series were obtained by instrumental neutron activation analysis (INAA; after Bartosova *et al.*, 2009; see Section 3.2). Although a different technique, Little *et al.* (2004) found that data generated from the ICP-MS method was similar to that yielded by the INAA method. As such, the CB6 series trace element data has been included for comparison and interpretation purposes.

Mean Eu anomalies were determined for the eight target rock units of the Eyreville-B borehole core (see Appendix 2b). Eu anomalies reflect the Eu^{2+} substitution for Ca^{2+} in plagioclase feldspar since this substitution only takes place in a reducing magma where Eu^{2+} is preferentially incorporated into plagioclase; Eu^{3+} is incompatible in an oxidising magma (Weill

Table 3.6: Mean and standard deviation (data in ppm) of trace elements obtained by ICP-MS analysis for the eight target rock units of the Eyreville-B borehole core. Abbr.: n = number of samples; SD=standard deviation.

Trace Element (ppm)	Basement Mica Schist		Basement Amphibolite		Basement Epidosite	Basement Granite	Megablock Massive Granite		Megablock Gneissic Granite		Megablock Biotite Schist Xenoliths		Megablock Amphibolite	
	n = 3		n = 2		n = 1	n = 1	n = 4		n = 11		n = 3		n = 2	
	Mean	SD	Mean	SD	Mean	Mean	Mean	SD	Mean	SD	Mean	SD	Mean	SD
P	122.67	57.07	358.77	7.72	106.55	75.18	196.98	104.12	178.44	153.01	542.40	308.37	271.17	246.83
Sc	4.67	4.31	7.65	2.37	1.74	0.29	1.80	0.83	1.84	1.13	11.08	3.46	10.55	1.57
Ti	1534.48	1957.93	3376.00	373.61	2933.78	81.70	732.38	328.00	963.07	498.96	4504.64	1827.48	4017.09	544.03
V	45.94	71.83	51.04	23.22	33.46	0.73	7.63	4.23	8.56	5.23	50.44	40.19	108.82	8.13
Cr	24.85	40.55	44.08	12.84	6.62	0.40	1.26	0.59	1.39	0.58	8.91	8.77	106.87	49.64
Co	5.16	6.57	11.35	2.02	10.85	0.53	1.73	0.38	1.86	0.55	6.79	3.10	29.28	0.83
Ni	15.77	19.99	25.20	1.65	20.01	2.01	4.43	0.54	3.77	0.54	6.93	0.64	66.51	3.96
Cu	17.32	21.33	4.40	0.76	3.55	1.30	2.97	0.68	4.10	2.33	8.05	2.46	24.18	3.99
Zn	37.31	12.68	70.36	13.36	107.15	5.14	19.45	6.07	22.46	7.88	81.02	23.66	48.22	11.98
Ga	17.98	1.32	12.99	0.17	14.53	14.72	10.84	1.33	12.52	2.29	21.46	1.48	11.52	2.27
As	0.03	0.02	0.24	0.11	0.32	0.01	0.13	0.03	0.12	0.06	0.15	0.07	0.14	0.02
Rb	143.45	71.88	146.79	83.95	99.65	196.75	107.58	49.09	126.92	17.52	107.54	61.84	64.66	85.73
Sr	23.11	1.94	184.53	67.37	91.22	48.33	89.36	34.28	103.61	46.04	51.50	7.81	189.54	36.57
Y	10.42	3.37	18.75	4.87	14.32	8.15	9.93	4.35	9.66	2.81	40.26	10.67	8.26	0.44
Zr	64.87	48.20	97.50	50.64	17.35	16.34	98.01	45.60	117.96	34.06	167.23	184.25	18.66	3.23
Nb	35.94	20.87	20.75	10.75	4.96	39.37	14.47	5.21	14.31	8.03	38.82	19.21	7.14	3.65
Ba	79.47	61.20	1007.25	988.53	15.79	52.15	331.10	150.38	511.37	243.12	132.89	60.07	149.66	174.87
Cs	5.02	1.86	9.10	8.50	22.20	2.46	2.37	0.37	2.39	0.64	7.94	3.07	16.88	22.93

Trace Element (ppm)	Basement Mica Schist		Basement Amphibolite		Basement Epidosite	Basement Granite	Megablock Massive Granite		Megablock Gneissic Granite		Megablock Biotite Schist Xenoliths		Megablock Amphibolite	
	n = 3		n = 2		n = 1	n = 1	n = 4		n = 11		n = 3		n = 2	
	Mean	SD	Mean	SD	Mean	Mean	Mean	SD	Mean	SD	Mean	SD	Mean	SD
La	10.03	4.53	25.60	6.28	68.99	0.98	27.34	14.23	41.40	27.82	61.18	78.96	2.35	0.90
Ce	20.21	8.94	55.58	18.55	133.48	2.03	52.47	26.34	79.97	52.34	117.15	143.15	5.64	1.61
Pr	2.34	1.16	6.07	0.97	15.89	0.27	5.46	2.65	8.43	5.01	13.72	15.61	0.71	0.33
Nd	8.54	4.69	23.65	4.28	58.43	1.03	18.57	9.01	28.38	14.73	46.67	46.73	3.24	1.49
Sm	1.83	0.70	4.93	0.37	9.08	0.56	3.30	1.55	4.59	1.72	8.84	7.25	0.95	0.18
Eu	0.33	0.27	1.25	0.27	1.56	0.10	0.58	0.21	0.80	0.32	0.95	0.39	0.40	0.02
Gd	1.93	0.72	4.45	1.22	8.30	0.64	3.27	1.70	4.50	1.63	10.20	8.20	1.10	0.29
Tb	0.26	0.06	0.56	0.21	0.85	0.16	0.39	0.20	0.46	0.12	1.27	0.70	0.18	0.04
Dy	1.42	0.25	2.92	1.18	3.26	1.05	1.90	0.93	1.98	0.48	6.49	2.19	1.13	0.18
Ho	0.26	0.05	0.56	0.21	0.48	0.17	0.32	0.14	0.31	0.08	1.16	0.33	0.24	0.03
Er	0.68	0.16	1.53	0.58	1.26	0.41	0.85	0.32	0.82	0.21	2.82	0.94	0.60	0.06
Tm	0.12	0.04	0.24	0.10	0.14	0.09	0.13	0.06	0.11	0.03	0.41	0.21	0.10	0.00
Yb	0.89	0.29	1.61	0.57	0.89	0.72	0.84	0.47	0.75	0.28	2.70	1.52	0.66	0.01
Lu	0.13	0.04	0.24	0.08	0.13	0.10	0.13	0.07	0.11	0.03	0.39	0.23	0.10	0.00
Hf	2.07	0.71	2.38	0.78	0.60	1.33	2.90	1.12	3.36	0.77	4.08	4.58	0.44	0.05
Ta	3.12	2.12	0.93	0.14	0.55	9.29	0.70	0.12	0.81	0.53	2.13	0.93	0.81	0.79
W	2.43	1.12	1.44	1.11	10.75	0.83	0.35	0.22	0.26	0.07	0.69	0.12	0.69	0.41
Pb	17.22	4.45	8.28	2.46	1.03	21.47	18.99	4.11	18.98	2.35	8.12	3.80	2.38	0.86
Th	8.19	3.25	8.27	1.33	4.47	2.83	13.63	5.53	17.21	8.25	41.29	59.48	0.46	0.01
U	12.98	9.15	1.45	0.71	1.21	22.21	3.99	3.49	3.20	2.44	5.26	4.14	0.30	0.21

and Drake, 1973; Winter, 2001). As such, Eu anomalies may indicate whether plagioclase was removed (a negative Eu anomaly) or accumulated (a positive Eu anomaly) during the evolution of the magma (Winter, 2001). The mean Eu anomalies were calculated using the following formula:

$$Eu^{\#} = (Eu^* / [Sm^* + Gd^*] \times O.5) - 1$$

where Eu*, Sm* and Gd* represent chondrite-normalised values (after Pedersen *et al.*, 1996). Positive and negative values indicate positive and negative Eu anomalies, respectively. All eight target rock units have negative Eu anomalies (see Appendix 2b).

3.5.1 Mica schists

The biotite schist xenoliths of the upper granite megablock are enriched in REE compared to the lower basement-derived mica schists by a factor of 10 (Figure 3.15a). Both the basement mica schists and the biotite schist xenoliths are enriched in light rare earth elements (LREE) compared to their heavy rare earth element (HREE) counterparts (Figure 3.15a). Both the basement and megablock schists are observed to have the most significant negative Eu anomalies of all rock units (Figure 3.15a). The calculated mean Eu anomaly value for the basement mica schist is -0.88, and -0.92 for the megablock schists (see Appendix 2b). These findings are consistent with their plagioclase content (see Chapter 2, Section 2.3.1.1).

When compared to the RG series, the mean CB6 series REE values for the mica schists from both the lower basement-derived section (n = 9) and the upper granite megablock (n = 2) have relatively smooth slopes (Figure 3.15a). However, the mean values represent a large range for the REEs, much greater than that observed for the RG series samples (see Appendix 2b). The mean CB6 series REE values for the lower basement-derived mica schists are also more enriched in REEs compared to the RG series samples (Figure 3.15a). However, the mean CB6 series REE values show similar trends to the RG series values, being enriched in LREEs compared to HREEs; Eu anomalies for the lower basement-derived section (-0.80) and the

biotite schist xenoliths of the upper granite megablock (-0.75) are not as pronounced (Figure 3.15a; Appendix 2b).

3.5.2 Amphibolites and calc-silicate rock

The upper amphibolite megablock shows a relatively flat REE signature with a single sample (RG176) showing a slightly positive Eu anomaly (Figure 3.15b). The lower basement-derived calc-silicate is observed to be enriched in LREE but depleted in HREE compared to the basement amphibolite (Figure 3.15b). The Eu anomaly observed in the calc-silicate is a function of its high plagioclase content, similar to that seen in the mica schists (Figure 3.15a and b).

REE values in the basement amphibolite trend similar to that seen in the basement mica schists, although a single sample in this rock unit also has a slightly positive Eu anomaly (Figure 3.15a and b). Mean Eu anomalies for the upper and basement amphibolites are observed to be negative and equal to -0.79 and –0.70, respectively, while the calc-silicate negative Eu anomaly value is -0.87 (see Appendix 2b).

3.5.3 Granites

The massive and gneissic granites of the upper granite megablock correlate well together in terms of REE values (Figure 3.15c). LREE values tend to be higher than HREE values although a massive granite sample (RG161) shows enrichment in Yb and Lu compared to the other massive megablock granite samples (Figure 3.15c). The mean CB6 series REE values tend to be slightly higher than those observed in the RG series (Figure 3.15c). Unlike the granites of the upper megablock, the lower basement-derived granite has lower LREE values compared to HREEs (Figure 3.15c). However, it may be possible that this single sample (RG167) is not representative as the average CB6 series REE values for the basement granite tend to be greater by factors between 10 and 100 (Figure 3.15c). Calculated mean Eu anomalies for the massive and gneissic megablock granites equal -0.86 and -0.87, respectively; the Eu anomaly value for the basement granite equals -0.87 (see Appendix 2b). These values are similar to

what is observed for the CB6 series massive megablock granite REE values (-0.86) and basement granite (-0.85).

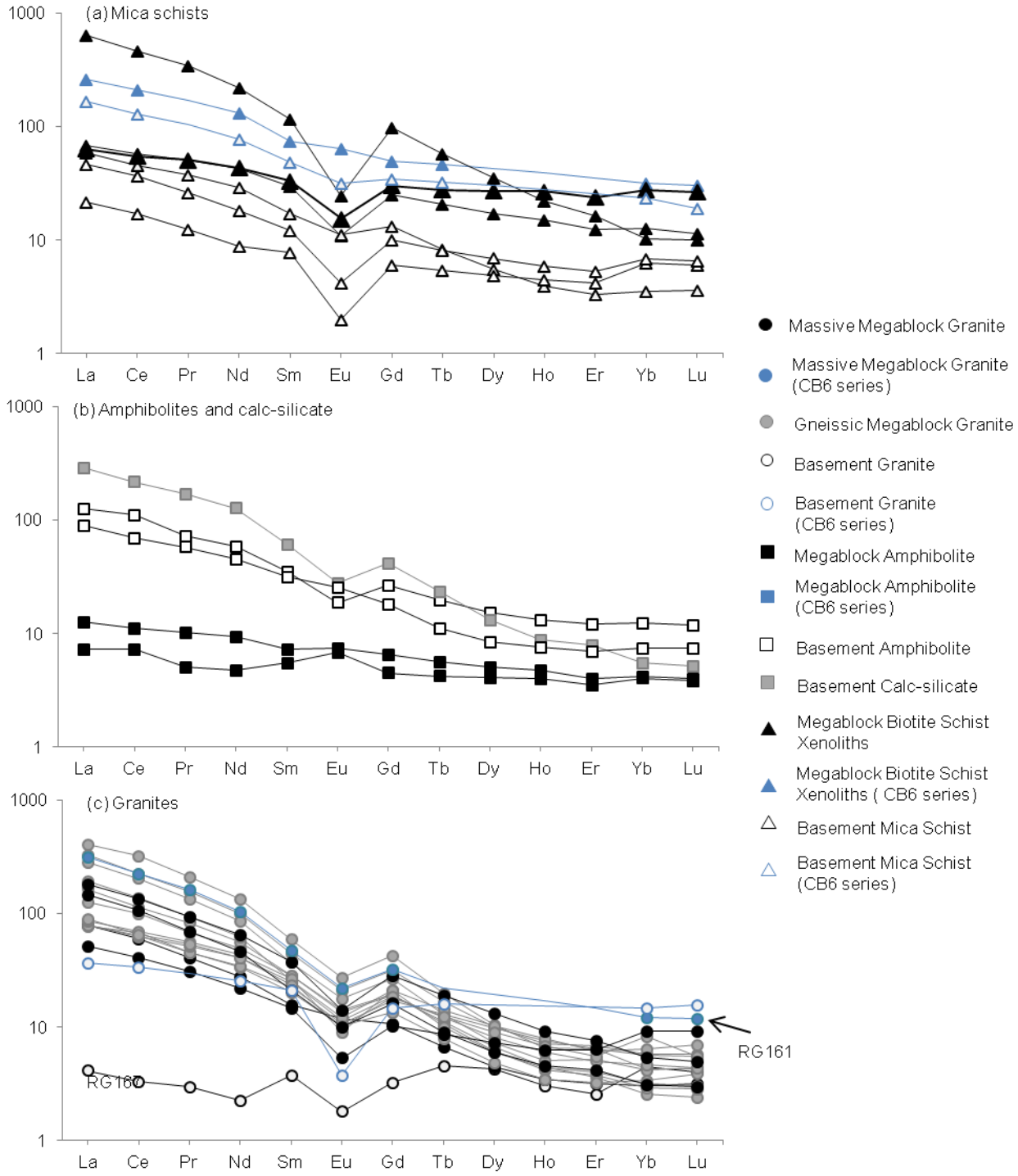

Figure 3.15: C1 chondrite-normalised REE distribution patterns for the eight target rock units of the Eyreville-B borehole core (after after McDonough and Sun, 1995). Average REE data from Schmitt *et al.* (2009) have been included for reference purposes. Pr, Dy, Ho and Er were estimated due to insufficient data for trending purposes; these points are omitted in the figure.

3.6 Discussion

3.6.1 Provenance of the metasedimentary rocks

The mica schists of the lower basement-derived section have chemical features that support their derivation from pelitic protoliths based on petrographic observations made in Chapter 2. This is confirmed using the classification scheme for terrigenous clastic sediments (after Herron, 1988), which shows that the basement mica schists have a dominantly shale protolith (Figure 3.16a). Although the majority of the samples plot within the shale and Fe-shale fields, samples RG39, RG53, RG76, CB6-143 and W126 plot in the wacke field, samples CB6-132 and W113 plot in the litharenite field and samples MJK21, RG169 and W114 plot in the arkose field, suggesting that the protolith for the basement-derived mica schists may have a quartzo-feldspathic element (Figure 3.16a). Protolith determination for the biotite schist xenoliths of the upper granite megablock is more ambiguous than that seen in the basement mica schists, with three samples plotting within the shale field, two samples (RG174 and CB6-076) in the wacke field, one sample (RG172) in the Fe-shale field and one sample (RG164) in the Fe-sandstone field (Figure 3.16a). Although it is possible that the two samples (RG164 and RG172) were enriched by Fe-rich metamorphic fluids, the CIA values for these two samples (53 and 47, respectively) suggest that these samples have experienced very low levels of alteration by secondary processes (see Section 3.3.4; Appendix 2a).

The possible tectonic setting for the basement mica schists and megablock biotite schist xenoliths is indicated in Figure 3.16b where K_2O/Na_2O is plotted against SiO_2 in the discrimination diagram for sandstone-mudstone suites (after Roser and Korsch, 1986). The basement mica schist plot primarily in the passive margin field, but 11 samples plot in the active margin field (CB6-137; CB6-141; CB6-145; MJK21; RG68; RG70; W117; W118; W126; W138; W139b) and 4 samples in the island arc field (RG54; RG64; W129; W137; Figure 3.16b). The megablock biotite schist xenoliths, on the other hand, plot mostly within the active margin field with two samples in the island arc field (RG172; W36b; Figure 3.16b).

Provenance analysis for the schist rock units (Figure 3.17) was performed using discriminant function diagrams proposed by Roser and Korsch (1988) for sandstone-mudstone suites which differentiate between mafic igneous, intermediate igneous, felsic igneous and quartzose sedimentary provenances. The diagram in Figure 3.17a uses discriminant functions based on raw oxides while the diagram in Figure 3.17b uses discriminant functions based on oxide ratios. For Figure 3.17a, discriminant function 1 is calculated as ($-1.773TiO_2 + 0.607Al_2O_3 + 0.76Fe_2O_{3(total)} - 1.5MgO + 0.616CaO + 0.509Na_2O - 1.224K_2O – 9.09$), and discriminant function 2 is calculated as ($0.445TiO_2 + 0.07Al_2O_3 - 0.25Fe_2O_{3(total)} - 1.142MgO + 0.438CaO + 1.475Na_2O + 1.426K_2O - 6.861$), after Roser and Korsch (1988). For Figure 3.17b, discriminant function 1 is calculated as ($30.638TiO_2/Al_2O_3 - 12.541Fe_2O_{3(total)}/Al_2O_3 + 7.329MgO/Al_2O_3 + 12.031Na_2O/Al_2O_3 + 35.402K_2O/Al_2O_3 – 6.382$), and discriminant function 2 is calculated as ($56.500TiO_2/Al_2O_3 – 10.879Fe_2O_{3(total)}/Al_2O_3 – 30.875MgO/Al_2O_3 + 5.404Na_2O/Al_2O_3 + 11.112K_2O/Al_2O_3 – 3.89$), after Roser and Korsch (1988). Although the discriminant diagram based on raw oxides most effectively differentiates between the different provenance fields, the diagram based on oxide ratios circumvents errors caused by biogenic CaO in $CaCO_3$ and biogenic SiO_2 (Roser and Korsch, 1988; Rollinson, 1993).

Roser and Korsch (1988) noted that each provenance corresponded to specific tectonic settings. Sediments with a mafic igneous provenance were most likely deposited in an immature ocean island arc setting, sediments with an intermediate igneous provenance were most likely deposited in either a mature island arc or an immature continental magmatic arc setting, sediments with a felsic igneous provenance were most likely deposited in either a mature continental margin arc setting or at continental transform boundaries and sediments with a quartzose sedimentary provenance were most likely derived from old upper continental crust and deposited at passive continental margins, in intracratonic sedimentary basins or in recycled orogenic provenances (Roser and Korsch, 1988; McLennan *et al.*, 1993).

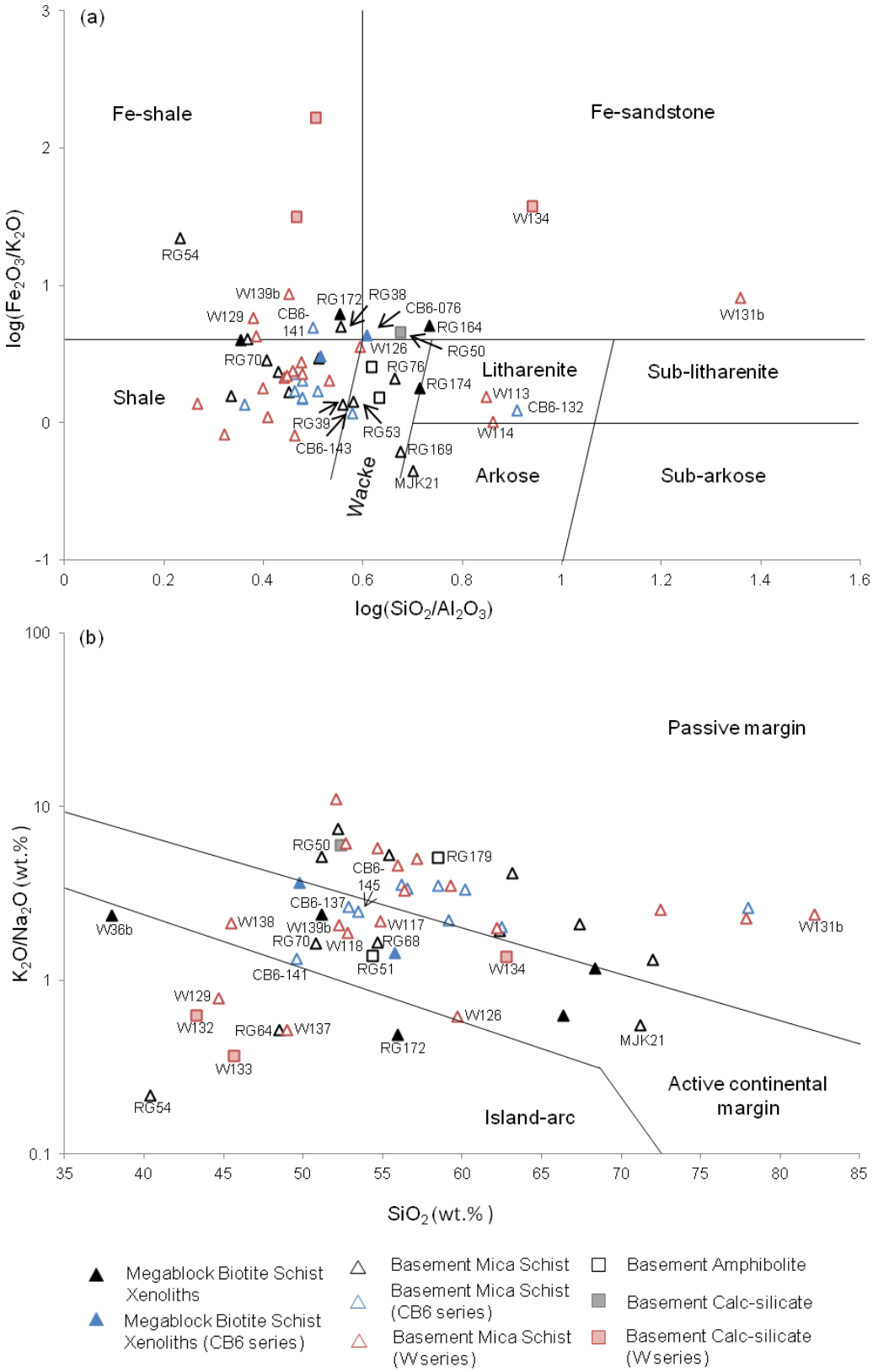

Figure 3.16: Bivariate diagrams for the basement and megablock mica schists and basement amphibolite and calc-silicate rock units of the Eyreville-B borehole core. (a) Classification scheme for terrigenous clastic sediments (after Herron, 1988); and (b) K_2O/Na_2O versus SiO_2 diagram indicating tectonic environment for sandstone-mudstone suites (after Roser and Korsch, 1986). All data in wt%.

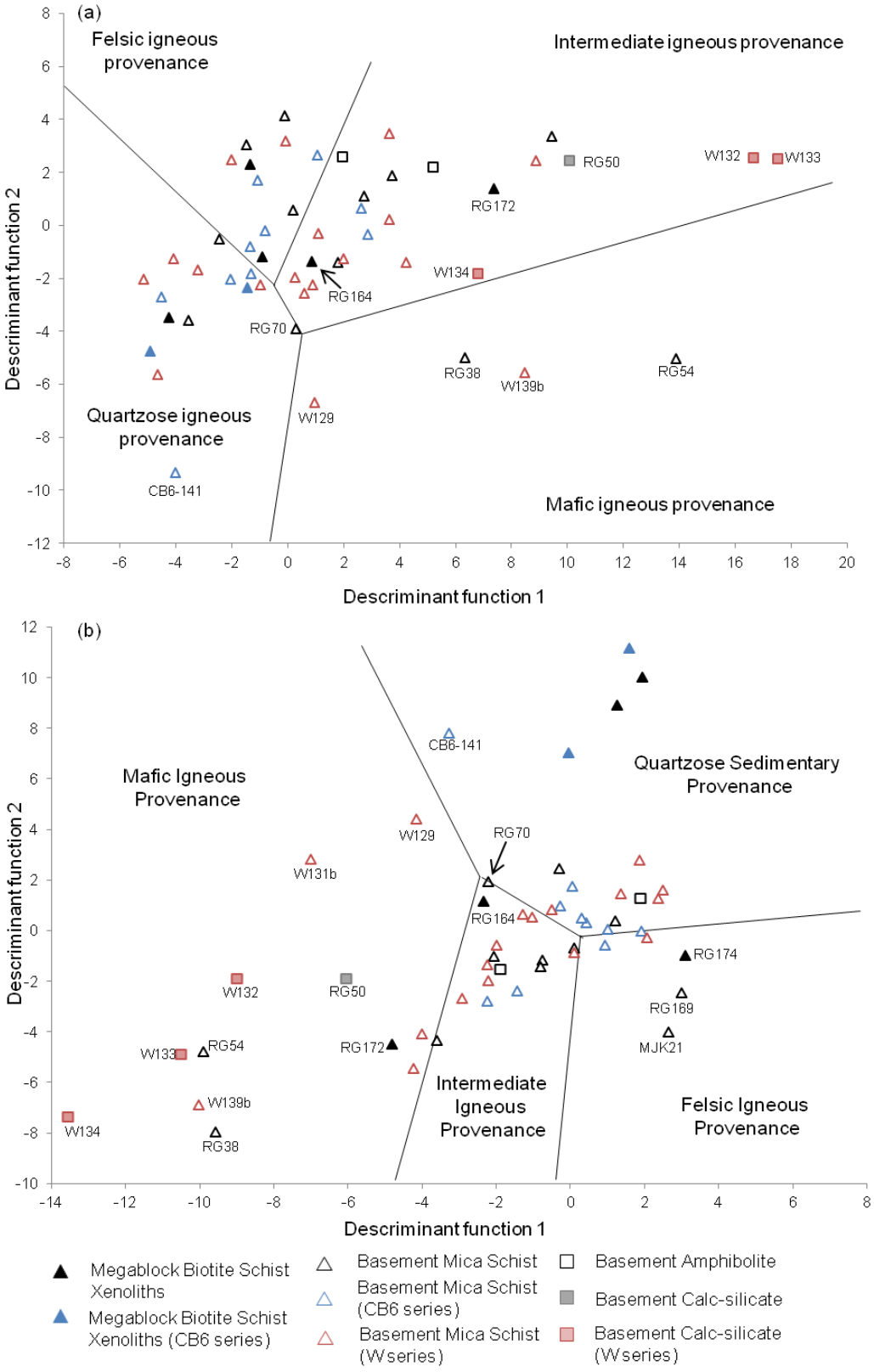

Figure 3.17: Discriminant diagrams showing provenance signatures for sandstone-mudstone suites using major elements based on (a) raw oxides and (b) oxide ratios for the megablock and basement mica schists and basement amphibolite and calc-silicate rock units of the Eyreville-B borehole core (after Roser and Korsch, 1988). All data in wt%.

The basement-derived mica schists show the most scatter within the different provenance fields of Figure 3.17a than in Figure 3.17b. In Figure 3.17a, the raw oxides of the basement mica schists cause most samples to plot within the intermediate igneous provenance field, with lesser numbers of samples within the quartzose sedimentary and felsic igneous provenance fields and only four samples plotting within the mafic igneous provenance field. However, where biogenic CaO and SiO_2 have been taken into account (Figure 3.17b), the basement mica schists samples have clearer groupings, most notably along the quartzose sedimentary, felsic igneous and intermediate igneous provenance field boundaries. In both diagrams, however, the basement mica schists show a strong intermediate igneous provenance with a minor quartzose sedimentary component (Figure 3.17).

Based on Figures 3.16 and 3.17, the basement-derived mica schists were deposited in a primarily passive margin setting and have an intermediate igneous provenance. However, as noted above, sediments with such a provenance generally are deposited either in mature island arc or immature continental magmatic arc settings (Roser and Korsch, 1988). This apparent contradiction can be a result of the secondary alteration effects, causing provenance analysis to be erroneous (Schmitt *et al.*, 2009). However, just over a third (38%) of the basement mica schist samples plotted in the active (10 samples) and island arc (4 samples) tectonic settings in Figure 3.16b. Furthermore, only 28% of the basement mica schist samples plotted in the quartzose sedimentary provenance fields (denoting a passive margin depositional setting; Roser and Korsch, 1988) in Figure 3.17. As such, the active margin component of the samples cannot be discounted.

As with the basement schists, the upper megablock biotite schist xenoliths show the most scatter in Figure 3.17a compared to Figure 3.17b, with three of the six samples plotting within the quartzose sedimentary provenance field, two in the felsic igneous provenance field and one in the intermediate igneous field. Provenance is much clearer in Figure 3.17b, where the xenoliths show a strong quartzose sedimentary provenance signature with single samples in the mafic igneous provenance field (RG172) and the felsic igneous provenance field (RG174). In

Chapter 2, Section 2.3.3.3, the biotite schist xenoliths were observed to be primarily incorporated into the biotite granite of the upper megablock, although rare xenoliths are included in the megablock granite gneiss. It is possible that this generally Fe_2O_3-rich, SiO_2-poor lithology could represent a restite component that was generated from partial melting during the metamorphic event associated with the formation of the megablock granite. However, as discussed in Chapter 2, Section 2.5, the mineralogy and texture of the biotite schist xenoliths differs from what is expected to be observed in a restite within an I-type metaluminous granite. It is more likely that the biotite schist xenoliths were scavenged from wall rock as the magma that gave rise to the megablock granite ascended through the crust (see Chapter 2, Section 2.5). The biotite schist xenoliths probably formed part of a package of old continental crust sediments (such as the hinterland of an over-riding plate during subduction; Simpson, 2010) that were eroded and deposited in an active margin tectonic setting.

The most likely source of the eroded continental crust would be from the hinterland of a convergent margin during continental collision (Simpson, 2010). Roser and Korsch (1988) noted that eroded old upper continental crust sediments are often deposited at passive continental margins, in intracratonic sedimentary basins or in recycled orogenic provenances. The active margin tectonic setting observed for the biotite schist xenoliths (see Chapter 3, Section 3.6.1, Figure 3.16b) favours a recycled orogenic provenance. Although Dickinson and Suczek (1979) noted that recycled orogen sedimentary suites tended to low in feldspar content, they also suggested caution when interpreting sedimentary suites in complex orogenic belts as they may include components from residual subduction complexes and foreland fold-thrust belts. This may explain the higher than expected Fe- and Mg-content and feldspar composition observed in the megablock biotite schists.

The biotite schist of the lower basement-derived section (RG70) plots within the shale protolith field in Figure 3.16a, within the active tectonic setting field in Figure 3.16b, in the quartzose sedimentary provenance field in Figure 3.17a, and in the intermediate igneous provenance field in Figure 3.17b. Although it would appear that the biotite schist is derived in a different tectonic

setting than what is observed for the lower basement-derived mica schists, the biotite schist exhibits extensive hydrothermal alteration, both in terms of petrography (Chapter 2, Section 2.3.3.3) and chemistry demonstrated by its relatively high LOI (6 wt%) and CIA (67) content (Appendix 2a). Thus, any inferred information relating to potential protoliths and/or provenance based on bulk rock chemistry requires caution (Schmitt *et al.,* 2009). It is possible, however, that the biotite schist experienced localised hydrothermal alteration after deposition had taken place and is derived from the same metasedimentary sequence as that of the basement mica schists.

A number of outliers are observed in Figures 3.16 and 3.17. Three samples (MJK21, RG54 and W131b) occur as outliers in both Figure 3.16a and b, while five samples (CB6-141, RG38, RG54, W129 and W139b) are outliers in both Figure 3.17a and b, with a further three samples (MJK21, RG169 and W131b) occurring as outliers in Figure 3.17b. With the exception of samples MJK21 and W131b which are enriched in SiO_2, the outlying samples notably depleted in SiO_2 and are enriched in Fe_2O_3 compared to the other basement mica schists (Figures 3.16 and 3.17). The only common outlier in all four of the diagrams is the tourmalinite (RG54) which is the most SiO_2-depleted and Fe_2O_3-enriched outlier and is interpreted to be a metasomatically-altered rock (see Chapter 2, Section 2.3.1.5). These findings correspond well with observed alteration by iron-rich fluids in the form of pyrite in the basement-derived section (see Chapter 2, Section 2.3.1), and the large volume of biotite in the schist xenoliths of the upper granite megablock (see Chapter 2, Section 2.3.3.3). Sample RG64 of the basement mica schists is also notably enriched in plagioclase, consistent with the observed enrichment in Na (Appendices 2a and 3b).

3.6.2 Provenance of the amphibolites

The amphibolites from the lower basement-derived section and the upper megablock show chemically distinct characteristics from each other. This trend is illustrated in Figure 3.18a where the amphibolites and calc-silicate of the Eyreville-B borehole core were plotted on the CaO-MgO-FeO ternary diagram proposed by Walker *et al.* (1960) to discriminate between those amphibolites with an igneous (ortho-) source and those with a sedimentary (para-) source

(Figure 3.18). In Chapter 4, Section 4.1.3, mineral chemistry reveals that the lower basement-derived amphibolite contains pargasitic amphibole, Na-enriched plagioclase and alkali feldspar compared to that of the megablock, and is closely associated with the calc-silicate, which is interpreted to be a metamarl (see Section 3.3.2), and it was suggested that the lower basement-derived amphibolite could be a para-amphibolite (Chapter 2, Section 2.5). Figure 3.18 confirms this suggestion, where samples from the lower basement-derived section plot within the para-amphibolite field.

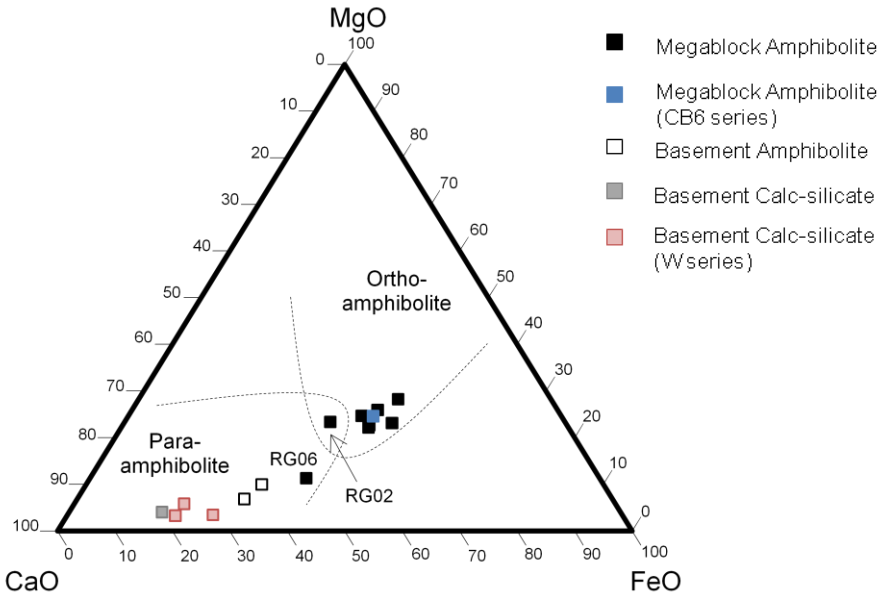

Figure 3.18. Ternary diagram indicating CaO-MgO-FeO abundances for the discrimination between ortho- and para-amphibolites for the megablock and basement amphibolites and calc-silicate (after Walker *et al.*, 1960) of the Eyreville-B borehole core. FeO was calculated using the CIPW norm.

Based on these findings, the basement para-amphibolite and calc-silicate rock units were plotted with the mica schists of the Eyreville-B borehole core in Figures 3.16 and 3.17. The basement amphibolite plots within the wacke protolith field in Figure 3.16a, consistent with observations that protoliths for para-amphibolites are often greywackes generated by turbiditic currents off continental shelves (Pettijohn, 1957; Bhatia and Crook, 1986; Winter, 2001). Figure 3.16b shows that sample RG51 plots in the active continental margin field while sample RG179 plots in the passive margin field. Unfortunately, this diagram does not clearly indicate the possible tectonic setting in which the para-amphibolites were generated (Figure 3.16b).

However, Figure 3.17 shows that the para-amphibolite does have an intermediate igneous source similar to that seen in the basement mica schists, suggesting either a mature island arc setting or immature continental magmatic arc setting (Roser and Korsch, 1988).

Possible protoliths for the calc-silicate vary from an Fe-rich shale to an Fe-rich sandstone (Figure 3.16a), corresponding with the interpretation that the calc-silicate is a metamarl based on the classification for sediments by Pettijohn (1957). In Figure 3.16b, the calc-silicate plots primarily in the island arc setting, although single samples also plot in the active (W134) and passive (RG50) margin fields. In Section 3.3.4 and Figure 3.9, the calc-silicate was shown to be the most highly altered rock unit within the Eyreville-B borehole core with an average CIA value of 92, where a value of 100 represents the most altered material (Nesbitt and Young, 1982). Furthermore, as discussed in Section 3.6.1, inference for protolith and provenance requires caution where samples are observed to be altered. In an attempt to overcome the errors associated with alteration effects, the calc-silicate was plotted in Figure 3.17b for which the discriminant functions are calculated to exclude biogenic $CaCO_3$ and SiO_2 (Roser and Korsch, 1988). The calc-silicate plots exclusively in the mafic igneous provenance field in Figure 3.17b in contrast to the intermediate igneous provenance in Figure 3.17a. Although the findings of Figure 3.17b are preferred, both provenances confirm an island arc depositional environment (Roser and Korsch, 1988).

Figure 3.18 indicates that the megablock amphibolite was derived from an igneous origin, in contrast to that of the lower basement-derived section. Although sample RG02 plots within the zone in which both fields overlap, and sample RG06 plots within the para-amphibolite field, these samples do not differ sufficiently to conclude that they do not form part of the same sequence as the other megablock amphibolite samples. These deviations could be attributed to alteration by quartz and calcite veining (see Chapter 2, Section 2.4.2).

Using the TAS classification scheme (after Middlemost, 1994), total alkalis ($Na_2O + K_2O$) for the megablock amphibolite were plotted against SiO_2 to determine the possible igneous protoliths

for this rock unit (Figure 3.19). Based on textural observations in Chapter 2, Section 2.4.1, the megablock amphibolite was plotted using intrusive igneous protoliths. Most samples plot within the gabbro protolith field and tend to be more alkalic in nature; the only significant outliers in Figure 3.19 are samples RG03 and RG06. Petrographic analysis for these two samples revealed a relict igneous texture resembling what would be expected in diorite (see Chapter 2, Section 2.3.2). Although this corresponds with geochemistry of sample RG06 (Figure 3.19), petrographic analysis also showed that sample RG03 to be particularly rich in pyrite and quartz veins (Appendix 1b), which would skew the accuracy of this sample's results. These two outliers are both located within the deepest two metres of the amphibolite megablock (Appendix 1b), suggesting this portion of the megablock was primarily dioritic, whereas the other ~11 m of the megablock is metamorphosed gabbro (Figure 3.19).

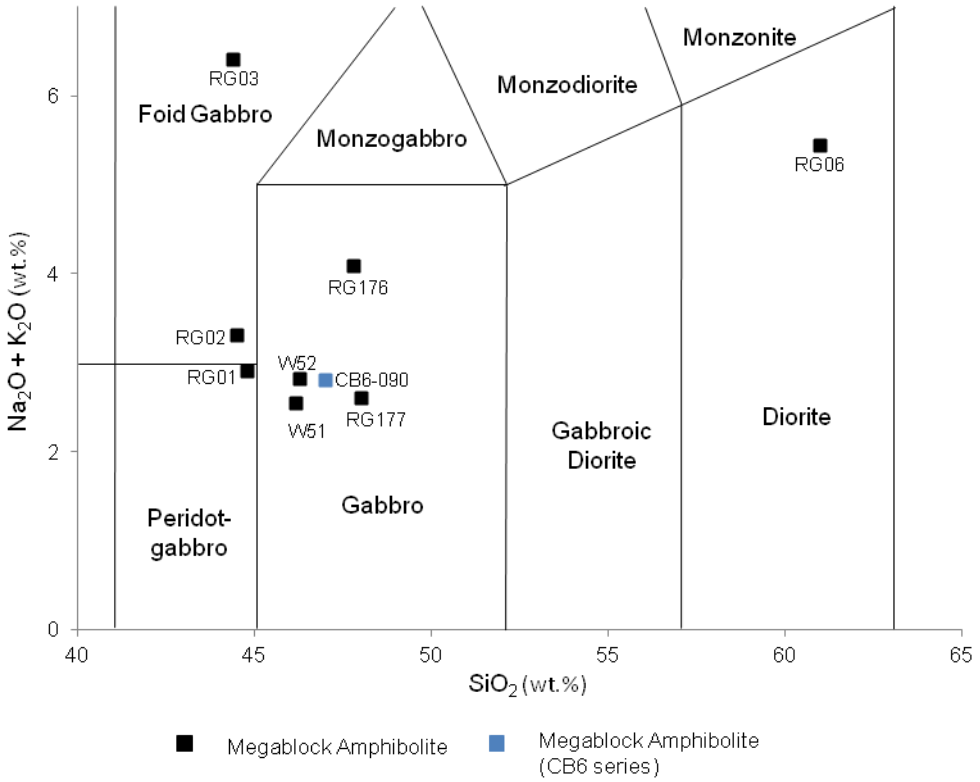

Figure 3.19: Bi-variate TAS diagram illustrating possible protoliths for the megablock amphibolite rock unit (after Middlemost, 1994) of the Eyreville-B borehole core. All data in wt%.

Determining the nature of the magma can assist with identifying the tectonic setting in which an igneous rock was derived. The megablock amphibolites have been plotted on an igneous AFM ternary diagram in Figure 3.20, in which A represents the alkalis, Na_2O+K_2O, F represents $Fe_2O_{3(total)}$ and M represents MgO (Winter, 2001). The AFM diagrams in Figure 3.20 are formulated for bulk rock compositions and are different from those based on mineral chemistry as devised by Thompson (1957). Irving and Baragar (1971) observed that fields denoting magma series type can be plotted on this AFM diagram. In Figure 3.20, it is observed that most samples plot within the tholeiitic magma series field.

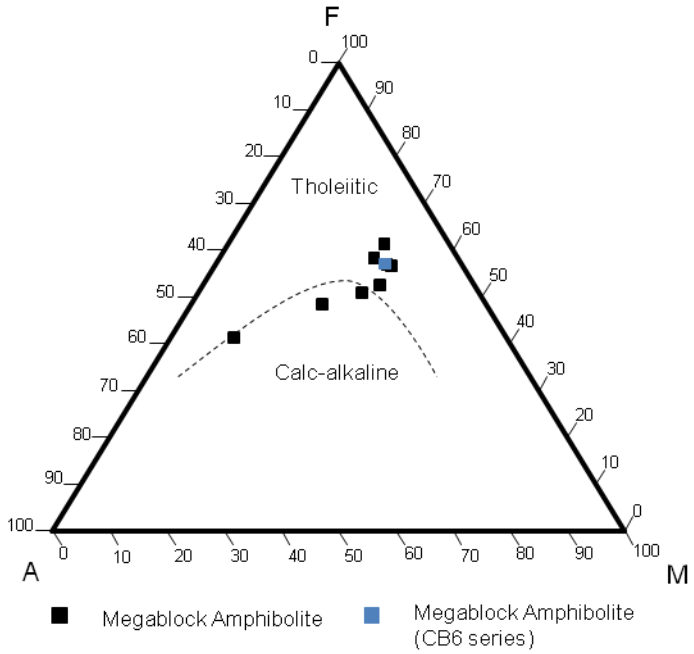

Figure 3.20. Ternary diagrams indicating AFM abundances (wt%) for the megablock amphibolite rock units rock unit of the Eyreville-B borehole core. Black dashed line shows the chemical boundary between tholeiitic and calc-alkaline magma series (after Irving and Baragar, 1971). Abbr.: A (alkalis) = $Na_2O + K_2O$; F = $Fe_2O_{3(total)}$; M = MgO.

The megablock amphibolite was plotted on Zr/Y versus Zr (Figure 3.21a; after Pearce *et al.*, 1981) and TiO_2 versus Zr (Figure 3.21b; after Pearce and Norry, 1979) diagrams to determine the possible tectonic setting in which the magma was formed. Although the samples do show much scatter, the trace element geochemistry suggests the upper megablock amphibolite formed within an island arc tectonic setting.

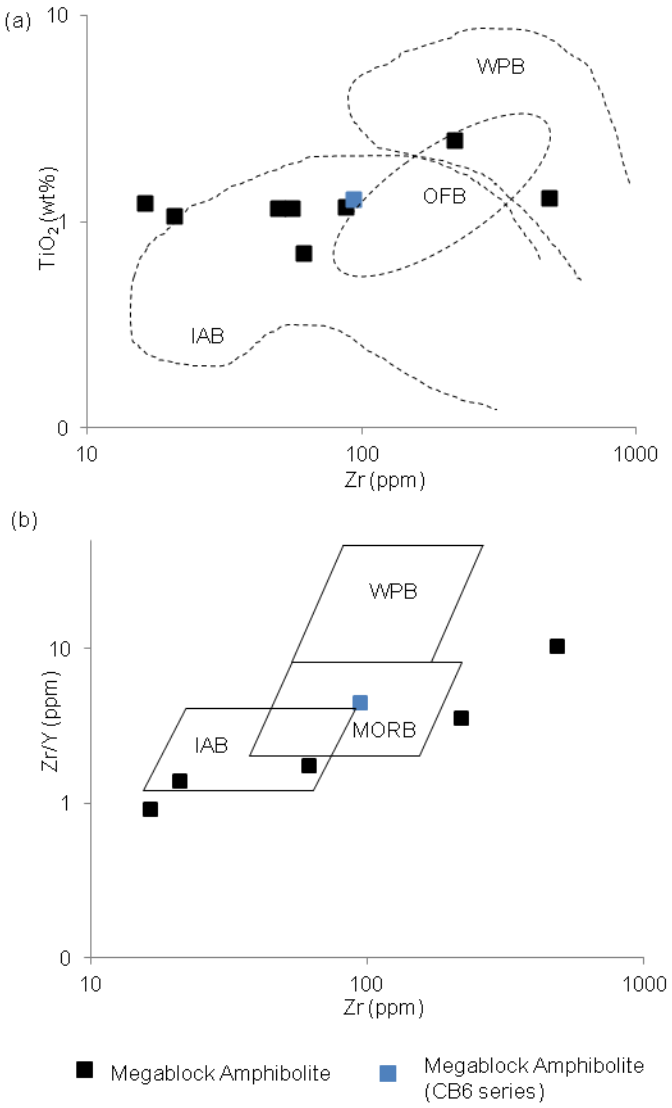

Figure 3.21: Discriminant diagrams showing the tectonic setting for the amphibolite rock units of the Eyreville-B borehole core. (a) TiO_2 versus Zr diagram (after Pearce *et al.*, 1981), and (b) Zr/Y versus Zr diagram (after Pearce and Norry, 1979). Abbr.: IAB = island arc basalt; OFB = ocean floor basalt; WPB = within-plate basalt; MORB = mid-oceanic ridge basalt.

3.6.3 Granite petrogenesis

ASI for the three granite rock units of the Eyreville-B borehole core revealed that the massive and gneissic granites of the upper megablock are strongly metaluminous whereas the basement granite is metaluminous to peraluminous (see Section 3.3.3, Figure 3.5b), indicating I-type and S-type sources for the three granites, respectively (Chappell and White, 1974; White and Chappell, 1983). In order to determine the tectonic settings in which the granite rock units

were emplaced, discriminant diagrams were used where Rb is plotted against the sum of Nb and Y, and where Nb is plotted against Y (after Pearce *et al.*, 1984; Figure 3.22). The granite samples show a significant overlap between both the megablock granites as well as the basement granite on the Rb versus Nb + Y (Figure 3.22a) and Nb versus Y (Figure 3.22b) discrimination diagrams (Pearce *et al.*, 1984).

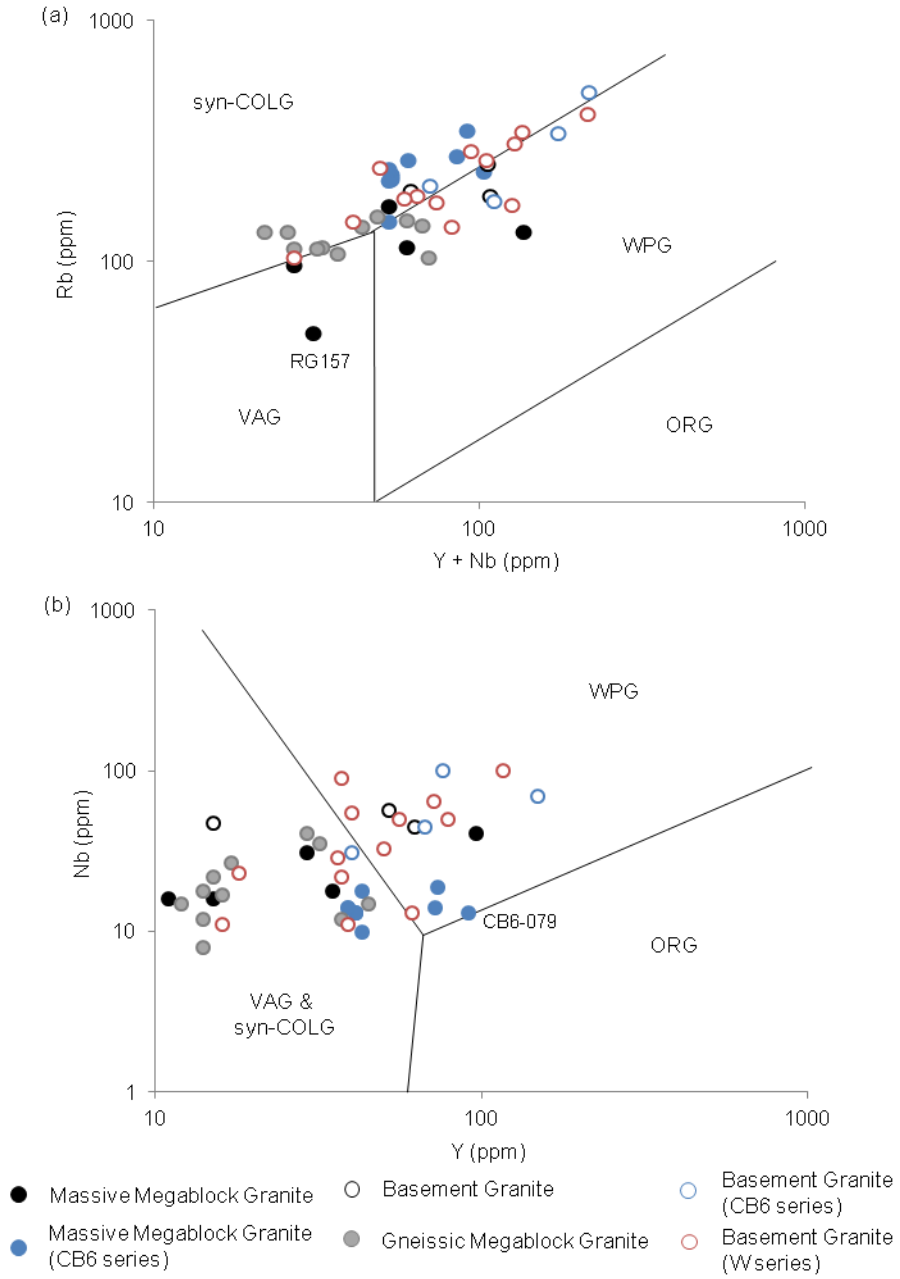

Figure 3.22: (a) Rb versus Y + Nb and (b) Nb versus Y discriminant diagrams for the granites of the Eyreville-B borehole core, indicating different tectonic setting (after Pearce *et al.*, 1984). All data in ppm. Abbr.: VAG = volcanic-arc granite; syn-COLG = syncollisional granite; WPG = within-plate granite; ORG = ocean-ridge granite.

In the Rb versus Y + Nb plot (Figure 3.22a), most samples plot in the within-plate granite (WPG) field, although close to the syncollisional granite (syn-COLG) field, and only a few samples fall into the volcanic-arc granite (VAG) field. The granite gneiss of the upper megablock tends to have lesser amounts of Rb compared to the other granite rock units, and thus favours the VAG field rather than the WPG field (Figure 3.22a). In the Nb versus Y diagram (Figure 3.22b), the granite rock units of the upper megablock plot primarily in the VAG & syn-COLG fields, with a few outliers in the WPG and ocean-ridge granite (ORG; sample CB6-079) fields.

The lower basement-derived granite samples are more dispersed, but have a distinctly WPG signature compared to the granite megablock, although a number of samples do plot within the VAG & syn-COLG field (Figure 3.22b). Schmitt *et al.* (2009) deduced a syn-COLG setting for the megablock granite rock units using a Rb versus Yb + Ta plot (after Pearce *et al.*, 1994). This is confirmed in the ternary Hf-Rb/10-Ta x 3 diagram (after Harris *et al.*, 1986) where the massive and gneissic megablock granites show a clear syn-COLG signature, whereas the basement granite plots more within the WPG field (Figure 3.23a).

In Figure 3.23b, samples from the basement granite and upper granite megablock are plotted relative to the cotectic curves for granitic melts in an H_2O-undersaturated system from Johannes and Holtz (1991). The difficulty of sampling pegmatite and the highly evolved nature of granite pegmatites may contribute to the large dispersion observed in samples from the lower basement-derived granite (Figure 3.23b). In an effort to evaluate more representative bulk compositions, two finer-grained mylonitised granite samples (RG40 and RG61) were analysed; however, both samples are characterised by significant enrichment in quartz relative to the other granite samples and they do not plot near the cotectic lines (Figure 3.23b). Petrographic and chemical evidence of the other basement granite samples suggests that silica enrichment most likely reflects hydrothermal fluids associated with mylonitisation. The strong dynamic recrystallisation in the mylonites, however, precludes the determination of how much silica might have been introduced during the retrograde event.

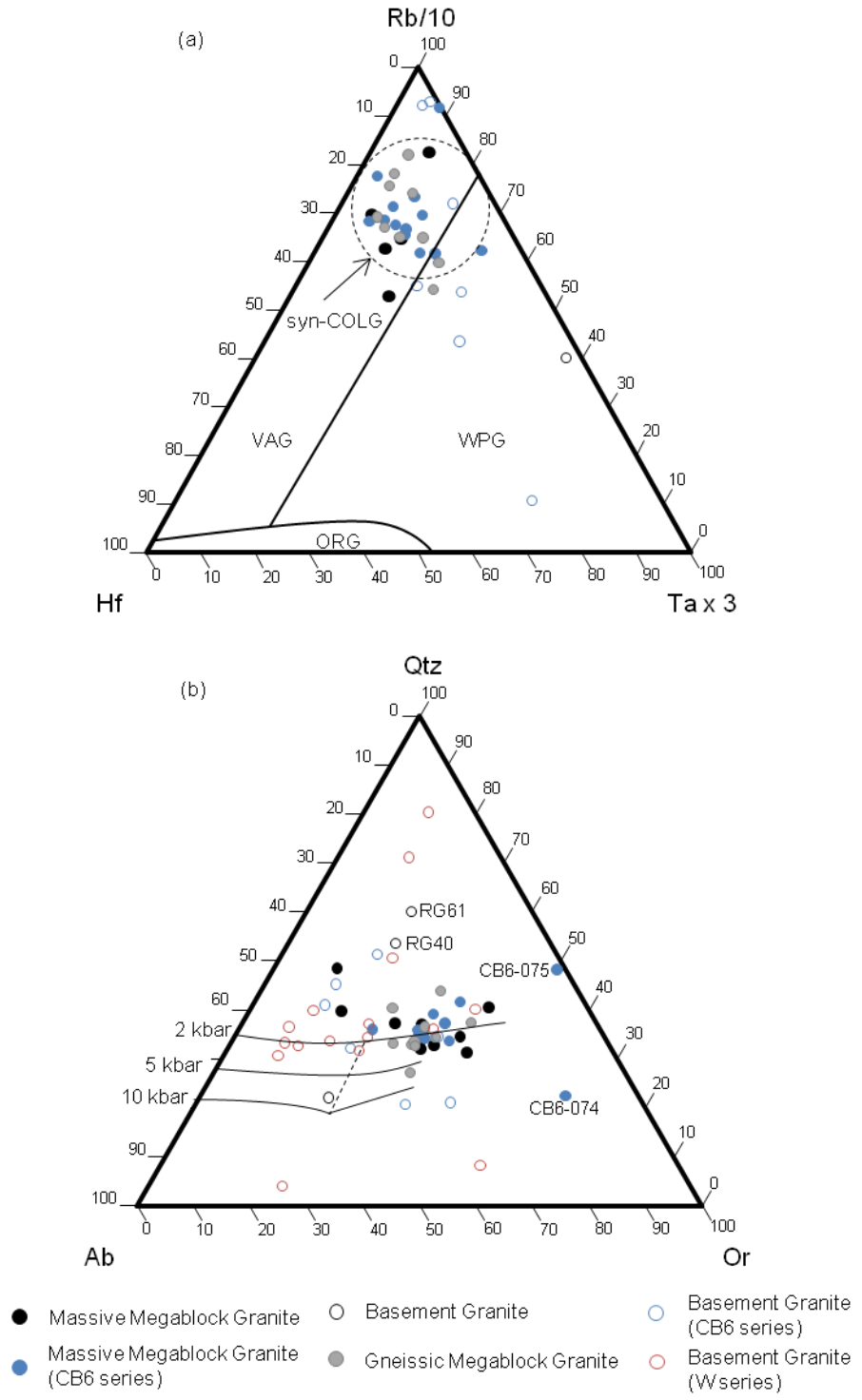

Figure 3.23: Ternary discrimination diagrams for the granites of the Eyreville-B borehole core. (a) Hf-Rb/10-Tax3 diagram showing different tectonic settings (data in ppm; after Harris *et al.*, 1986). (b) Ab-Qtz-Or diagram showing cotectic curves in an H_2O-undersaturated system. Dashed line represents the water-undersaturated curve for a_{H2O} = 0.8 crustal fluids in equilibrium with graphite (after Johannes and Holtz, 1991). Abbr.: VAG = volcanic-arc granite; syn-COLG = syncollisional granite; WPG = within-plate granite; ORG = ocean-ridge granite; Ab = albite; Q = quartz = Or = orthoclase.

In comparison, the slightly finer-grained, less altered massive and gneissic granites of the upper megablock show less scatter in Figure 3.23b. These samples tend to cluster around the 0.2-0.5 GPa cotectic curves (Figure 3.23b), indicating that emplacement occurred at intermediate crustal levels (after Johannes and Holtz, 1991). Furthermore, the granites of the upper megablock also show an enrichment in Or compared to Ab, especially in samples CB6-074 and CB6-075 (Figure 3.23b), which is common for H_2O-undersaturated partial melts (Johannes and Holtz, 1991). These findings coupled with the An- and mafic-poor composition of the megablock granite rock units suggest that they were formed at middle- to shallow-crustal levels in an H_2O-undersaturated system.

3.7 Summary

The lower basement-derived mica schists differ from the biotite schist xenoliths of the upper granite megablock both in terms of major and trace element chemistry, although some similarities do occur (Figures 3.3, 3.12, 3.13 and 3.14). Unsurprisingly, the biotite schist xenoliths are comparatively enriched in TiO_2, Fe_2O_3, and MgO (which corresponds to their muscovite-depleted mineralogy; see Chapter 2, Section 2.3.3.3) and are enriched in REEs to a factor of 10 compared to the basement-derived mica schists (Figure 3.15a). Although both schist rock units have shale protoliths (Figure 3.16a), they differ in terms of tectonic setting and provenance. The basement mica schists show passive margin signatures with a significant active margin component (Figure 3.16b) as well as a strongly intermediate igneous provenance, thus confirming the active margin signatures. The megablock biotite schist xenoliths were eroded from a quartzose sedimentary provenance, such as old upper continental crust, and later deposited in an active margin setting most likely associated with recycling of complex orogenic belts (Figures 3.16 and 3.17). Caution must be employed when interpreting these bulk rock chemical data, however, due to the significant alteration observed in the basement-derived mica schists.

Predictably, the amphibolites of the basement-derived section and upper megablock rarely share any chemical trends with each other, corresponding with their very different petrography (see Chapter 2, Sections 2.2.2.3 and 2.2.4). Figure 18 discriminates the two amphibolites from each other, indicating that the lower basement-derived variety is a para-amphibolite derived from sedimentary sources, while the upper amphibolite is an ortho-amphibolite derived from igneous sources. Based on these deductions, the lower basement-derived amphibolite was plotted with the mica schist rock units of the Eyreville-B borehole core to determine possible protolith, tectonic setting and provenance (Figures 3.16 and 3.17). Results from these figures indicate that the basement amphibolite was derived from greywackes that were probably generated in a passive margin setting although the intermediate igneous provenance suggests that a more tectonically active environment. The upper megablock amphibolite samples, on the other hand, have a tholeittic gabbro protolith (Figures 3.19 and 3.20) that was probably generated in an island arc tectonic setting (Figure 3.21). The calc-silicate is clearly shown to have been emplaced in an island arc tectonic setting (Figures 3.16 and 3.17).

The granite rock units of the Eyreville-B borehole core are chemically very similar as all three are classified as granites (Figure 3.5a; after Middlemost, 1994) and form part of calc-alkaline magmatic suites (Figure 3.6; after Irving and Baragar, 1971); however, the lower basement-derived granite is peraluminous whereas both megablock granites are metaluminous according to their ASI (Figure 3.5b; after Shand, 1927). These facts, coupled with the significant LREE-depletion in the basement-derived granite compared to the upper megablock granites (Figure 3.15c), suggest that basement and megablock granites were derived from different magmas. Determination of tectonic setting for the three granite rock units reveals a within-plate tectonic setting for the basement-derived granite whereas the massive and gneissic megablock granites were most likely generated in a syn-collisional environment (Figures 3.22 and 3.23a). Finally, eutectic curves in Figure 3.23b suggests that all three granites were emplaced at similar mid-crustal levels.

4 MINERAL CHEMISTRY AND GEOTHERMOBAROMETRY

4.1 Introduction

In Chapter 2, petrographic and structural analysis in the lower basement-derived and upper megablocks sections of the Eyreville-B borehole core revealed the presence of three main rock types (mica schists, amphibolites and granites) as well as a number of deformation-related textures and microstructures caused by at least one deformation event. In this chapter, the application of mineral chemistry and geothermobarometry to these rocks has been performed to determine the metamorphic conditions under which the relevant mineral assemblages formed, from which deductions regarding metamorphic grade, geothermal gradient and terrane relationships are examined. These findings are discussed in Chapter 6 in relation to the timing and inter-relationships of metamorphism and deformation, which is critical in understanding the broader tectono-metamorphic history of the target rocks beneath the Chesapeake Bay impact structure (Nesbitt and Essene, 1982; Bakker *et al.*, 1989; Williams, 1994).

4.2 Mineral Chemistry

4.2.1 Methodology

Mineral chemical analyses were obtained from 24 samples, of which 15 were from the lower basement-derived section (8 mica schist, 5 granite, 1 amphibolite and 1 calc-silicate), 2 from the megablock amphibolite and 7 from the megablock granite (4 massive granite, 2 gneissic granite and 1 biotite schist xenolith). 23 polished thin sections were prepared for EMPA: 12 from the RG-series of samples at the SGS Lakefield Laboratories in Johannesburg, South Africa, 5 from the W-series of samples at the Humboldt University in Berlin, Germany, and 5 from the RG-series and 1 from the W-series at the University of the Witwatersrand, South Africa. A number of the thin sections were embedded in epoxy owing to their disaggregated state.

Electron microprobe analysis (EMPA) was conducted at two locations: (1) at the Museum für Naturkunde, Humboldt University in Berlin and (2) at the University of Pretoria. Table 4.1 lists the samples analysed at each facility and Table 4.2 details the mineral chemistry of selected minerals within the analysed samples. Where low totals were unavoidable (owing to extensive alteration), analyses were selected according to the cation content (Table 4.1). The modified data set (with regards to the removal of poor analyses and quartz compositions) is presented in Appendix 3a for the Berlin analyses and Appendix 3b for the Pretoria analyses. Mineral abbreviations used in figure and table captions are from Whitney and Evans (2010).

Table 4.1: List of samples analysed using EMPA at the Museum für Naturkunde, Humboldt University (Berlin) and at the University of Pretoria (Pretoria).

Sample	Lithology	Berlin	Pretoria
Lower basement-derived section			
RG32	Granite	✓	
RG40	Granite		✓
RG40a	Granite	✓	✓
RG44	Mica schist	✓	
RG45	Mica schist	✓	
RG46	Granite	✓	✓
RG48	Mica schist	✓	✓
RG50	Calc-silicate		✓
RG51	Amphibolite	✓	✓
RG53	Mica schist		✓
RG55	Mica schist		✓
RG57	Mica schist		✓
RG68	Mica schist	✓	✓
RG70	Mica schist		✓
W130	Mica schist		✓
Upper amphibolite megablock			
W51	Amphibolite	✓	✓
W52	Amphibolite	✓	✓
Upper granite megablock			
RG156b	Massive granite		✓
RG157b	Schist xenolith		✓
RG163	Gneissic granite		✓
W35	Massive granite	✓	✓
W36a	Massive granite	✓	✓
W45	Massive granite		✓
W49	Gneissic granite	✓	

Table 4.2: Representative electron microprobe analyses for the Eyreville-B lower basement-derived and upper megablocks sections obtained in Pretoria[1] and Berlin[2]. Abbr.: Amp = amphibole; Bt = biotite; Chl = chlorite; Ep = epidote; Grt = garnet; Kfs = K-feldspar; Ms = muscovite; Pl = plagioclase; Ttn = titanite; Tur = tourmaline; Ves = vesuvianite. B-A = basement amphibolite; B-BS = basement biotite schist; B-G = basement; B-MS = basement mica schist; MB-A = megablock amphibolite; MB-G = megablock massive granite; MB-Gn = megablock gneissic granite; MB-MS = megablock mica schist.

Sample	RG51[1]	RG51[2]	W51[1]	W51[2]	W130[1]	RG45[2]	RG70[1]	RG157b[1]	RG51[1]	W52[2]	RG40a[1]	RG40a[2]	RG163[1]
Mineral	Amp	Amp	Amp	Amp	Bt	Bt	Bt	Bt	Bt	Bt	Bt	Bt	Bt
Lithology	B-A	B-A	MB-A	MB-A	B-MS	B-MS	B-BS	MB-MS	B-A	MB-A	B-G	B-G	MB-Gn
(wt%)													
SiO_2	41.17	42.55	43.70	42.75	36.79	35.90	39.34	34.93	36.86	37.30	34.83	34.24	34.54
TiO_2	0.68	0.52	0.77	0.78	2.05	2.21	1.53	2.68	2.51	1.44	2.23	1.97	3.49
Al_2O_3	12.77	10.91	13.66	14.83	20.37	16.40	16.17	16.64	15.77	16.91	18.80	18.50	17.92
Cr_2O_3	0.00	0.00	0.00	0.00	0.00	0.00	0.00	0.00	0.00	0.00	0.00	0.00	0.00
Fe_2O_3	4.62	3.66	2.47	2.75	0.06	0.00	2.06	0.08	0.00	2.28	0.00	0.00	0.02
FeO	14.87	14.13	11.99	11.93	12.98	21.95	10.49	21.61	18.12	11.62	25.78	24.27	25.26
MnO	0.49	0.56	0.23	0.19	0.34	0.34	0.35	0.40	0.30	0.11	0.58	0.26	0.60
MgO	9.06	10.00	11.01	10.53	13.14	8.76	17.64	8.36	11.89	15.02	4.25	4.34	5.08
CaO	12.24	11.90	11.53	11.19	0.00	0.00	0.00	0.01	0.00	0.02	0.02	0.00	0.00
Na_2O	1.32	1.40	1.64	1.88	0.21	0.10	0.20	0.14	0.10	0.26	0.10	0.08	0.07
K_2O	1.71	1.20	0.34	0.43	7.43	9.35	8.51	9.18	9.88	8.13	8.36	9.04	9.15
Total	98.93	96.83	97.09	97.27	93.37	95.01	96.29	94.03	95.44	93.09	94.96	92.70	96.13
Oxygens (apfu)	23.00	23.00	23.00	23.00	11.00	11.00	11.00	11.00	11.00	11.00	11.00	11.00	11.00
Si	6.19	6.47	6.43	6.31	2.73	2.78	2.83	2.74	2.80	2.79	2.74	2.75	2.69
Ti	0.08	0.06	0.09	0.09	0.11	0.13	0.08	0.16	0.14	0.08	0.13	0.12	0.21
Al	2.26	1.95	2.37	2.58	1.78	1.50	1.37	1.54	1.41	1.49	1.74	1.75	1.65
Cr	0.00	0.00	0.00	0.00	0.00	0.00	0.00	0.00	0.00	0.00	0.00	0.00	0.00
Fe^{3+}	0.52	0.42	0.27	0.31	0.00	0.00	0.11	0.01	0.00	0.13	0.00	0.00	0.00
Fe^{2+}	1.87	1.80	1.48	1.47	0.81	1.42	0.63	1.42	1.15	0.73	1.69	1.63	1.65
Mn	0.06	0.07	0.03	0.02	0.02	0.02	0.02	0.03	0.02	0.01	0.04	0.02	0.04
Mg	2.03	2.26	2.42	2.32	1.45	1.01	1.89	0.98	1.35	1.68	0.50	0.52	0.59
Ca	1.97	1.94	1.82	1.77	0.00	0.00	0.00	0.00	0.00	0.00	0.00	0.00	0.00
Na	0.39	0.41	0.47	0.54	0.03	0.02	0.03	0.02	0.02	0.04	0.02	0.01	0.01
K	0.33	0.23	0.06	0.08	0.70	0.93	0.78	0.92	0.96	0.78	0.84	0.93	0.91
Sum	15.88	15.76	15.52	15.58	7.63	7.81	7.75	7.80	7.84	7.72	7.69	7.73	7.74

Table 4.2: Representative electron microprobe analyses for the Eyreville-B lower basement-derived and upper megablocks sections obtained in Pretoria[1] and Berlin[2] (*continued).* Abbr.: Amp = amphibole; Bt = biotite; Chl = chlorite; Ep = epidote; Grt = garnet; Kfs = K-feldspar; Ms = muscovite; Pl = plagioclase; Ttn = titanite; Tur = tourmaline; Ves = vesuvianite. B-A = basement amphibolite; B-BS = basement biotite schist; B-G = basement; B-MS = basement mica schist; MB-A = megablock amphibolite; MB-G = megablock massive granite; MB-Gn = megablock gneissic granite; MB-MS = megablock mica schist.

Sample	W49[2]	W35[1]	W36[2]	W130[1]	RG45[2]	RG70[1]	RG51[1]	W51[1]	W51[2]	RG46[1]	RG163[1]	W35[1]	RG51[1]
Mineral	Bt	Bt	Bt	Chl	Chl	Chl	Chl	Chl	Chl	Chl	Chl	Chl	Ep
Lithology	MB-Gn	MB-G	MB-G	B-MS	B-MS	B-BS	B-A	MB-A	MB-A	B-G	MB-Gn	MB-G	B-A
(wt%)													
SiO_2	35.57	34.95	35.23	31.90	37.44	31.61	32.35	36.18	37.11	36.81	25.15	31.54	38.15
TiO_2	2.58	3.39	2.88	1.00	0.05	1.51	0.00	1.89	1.84	0.88	0.13	2.22	0.05
Al_2O_3	16.30	17.66	16.41	24.42	26.68	19.45	11.01	16.67	16.34	26.56	20.93	17.01	25.22
Cr_2O_3	0.00	0.00	0.00	0.00	0.00	0.00	0.00	0.00	0.00	0.00	0.00	0.00	0.00
Fe_2O_3	0.00	0.00	0.00	0.04	0.00	0.00	0.00	0.00	0.00	0.00	0.02	0.00	0.00
FeO	21.16	21.95	20.84	14.93	20.84	22.71	33.40	15.53	15.29	19.91	36.02	24.44	10.93
MnO	0.31	0.51	0.41	0.42	0.09	0.36	0.07	0.06	0.05	0.41	0.70	0.47	0.13
MgO	8.03	8.05	8.28	14.45	3.13	12.19	9.43	14.10	14.01	2.83	6.61	10.47	0.03
CaO	0.00	0.00	0.08	0.06	0.52	0.06	0.87	0.03	0.02	0.03	0.01	0.73	23.43
Na_2O	0.11	0.08	0.28	0.08	0.59	0.09	0.28	0.24	0.40	0.10	0.02	0.14	0.01
K_2O	9.96	9.90	9.43	2.55	0.78	3.86	0.23	6.72	6.47	2.83	0.05	4.72	0.01
Total	94.02	96.50	93.84	89.85	90.12	91.84	87.64	91.42	91.53	90.36	89.64	91.74	97.96
Oxygens (apfu)	11.00	11.00	11.00	14.00	14.00	14.00	14.00	14.00	14.00	14.00	14.00	14.00	12.50
Si	2.79	2.68	2.76	3.09	3.59	3.16	3.55	3.54	3.61	3.55	2.75	3.23	2.98
Ti	0.15	0.20	0.17	0.07	0.00	0.11	0.00	0.14	0.13	0.06	0.01	0.17	0.00
Al	1.51	1.60	1.52	2.79	3.02	2.29	1.43	1.92	1.87	3.02	2.70	2.05	2.32
Cr	0.00	0.00	0.00	0.00	0.00	0.00	0.00	0.00	0.00	0.00	0.00	0.00	0.00
Fe^{3+}	0.00	0.00	0.00	0.00	0.00	0.00	0.00	0.00	0.00	0.00	0.00	0.00	0.71
Fe^{2+}	1.39	1.41	1.37	1.21	1.67	1.90	3.07	1.27	1.24	1.61	3.29	2.09	0.01
Mn	0.02	0.03	0.03	0.03	0.01	0.03	0.01	0.01	0.00	0.03	0.07	0.04	0.01
Mg	0.94	0.92	0.97	2.08	0.45	1.82	1.54	2.05	2.03	0.41	1.08	1.60	0.00
Ca	0.00	0.00	0.01	0.01	0.05	0.01	0.10	0.00	0.00	0.00	0.00	0.08	1.96
Na	0.02	0.01	0.04	0.02	0.11	0.02	0.06	0.05	0.08	0.02	0.00	0.03	0.00
K	1.00	0.97	0.94	0.32	0.10	0.49	0.03	0.84	0.80	0.35	0.01	0.62	0.00
Sum	7.81	7.82	7.80	9.61	9.00	9.83	9.78	9.81	9.76	9.06	9.90	9.90	8.00

Table 4.2: Representative electron microprobe analyses for the Eyreville-B lower basement-derived and upper megablocks sections obtained in Pretoria[1] and Berlin[2] (*continued).* Abbr.: Amp = amphibole; Bt = biotite; Chl = chlorite; Ep = epidote; Grt = garnet; Kfs = K-feldspar; Ms = muscovite; Pl = plagioclase; Ttn = titanite; Tur = tourmaline; Ves = vesuvianite. B-A = basement amphibolite; B-BS = basement biotite schist; B-G = basement; B-MS = basement mica schist; MB-A = megablock amphibolite; MB-G = megablock massive granite; MB-Gn = megablock gneissic granite; MB-MS = megablock mica schist.

Sample	RG50[1]	RG48[1]	RG45[2]	RG40a[1]	RG32[2]	RG45[2]	RG51[1]	W51[2]	RG40a[2]	RG163[1]	W49[2]	W35[1]	W35[2]
Mineral	Ep	Grt	Grt	Grt	Grt	Kfs	Kfs	Kfs	Kfs	Kfs	Kfs	Kfs	Kfs
Lithology	B-CS	B-MS	B-MS	B-G	B-G	B-MS	B-A	MB-A	B-G	MB-Gn	MB-Gn	MB-G	MB-G
(wt%)													
SiO_2	37.58	36.65	38.30	36.18	36.17	64.94	63.73	61.02	63.25	64.57	64.27	63.18	64.88
TiO_2	0.07	0.06	0.03	0.08	0.00	0.00	0.02	0.06	0.00	0.02	0.03	0.03	0.02
Al_2O_3	25.55	20.56	21.54	21.14	20.37	18.32	18.87	18.78	17.88	19.01	17.91	18.99	17.92
Cr_2O_3	0.00	0.00	0.00	0.00	0.00	0.00	0.00	0.00	0.00	0.01	0.00	0.00	0.00
Fe_2O_3	0.00	1.35	0.00	0.65	0.52	0.02	0.09	0.37	0.04	0.02	0.00	0.00	0.00
FeO	9.71	20.94	29.48	29.51	27.06	0.00	0.00	0.00	0.00	0.00	0.00	0.00	0.00
MnO	0.18	16.03	3.22	10.44	14.41	0.04	0.00	0.02	0.00	0.01	0.00	0.01	0.00
MgO	0.04	1.92	4.43	0.81	0.20	0.00	0.00	0.05	0.01	0.01	0.01	0.01	0.00
CaO	24.12	2.50	3.26	1.19	0.71	0.00	0.00	0.20	0.00	0.00	0.00	0.04	0.03
Na_2O	0.01	0.01	0.05	0.06	0.07	0.97	0.83	1.58	0.54	1.51	1.29	0.83	1.09
K_2O	0.00	0.01	0.08	0.00	0.00	14.84	15.82	12.96	16.18	14.86	14.96	15.93	15.00
Total	97.27	100.02	100.39	100.00	99.51	99.13	99.36	95.04	97.90	100.02	98.47	99.04	98.94
Oxygens (apfu)	12.50	12.00	12.00	12.00	12.00	8.00	8.00	8.00	8.00	8.00	8.00	8.00	8.00
Si	2.97	2.97	3.02	2.96	3.00	3.01	2.97	2.94	2.99	2.97	3.01	2.96	3.02
Ti	0.00	0.00	0.00	0.01	0.00	0.00	0.00	0.00	0.00	0.00	0.00	0.00	0.00
Al	2.38	1.97	2.00	2.04	1.99	1.00	1.04	1.07	1.00	1.03	0.99	1.05	0.98
Cr	0.00	0.00	0.00	0.00	0.00	0.00	0.00	0.00	0.00	0.00	0.00	0.00	0.00
Fe^{3+}	0.53	0.08	0.00	0.04	0.03	0.00	0.00	0.01	0.00	0.00	0.00	0.00	0.00
Fe^{2+}	0.12	1.42	1.94	2.02	1.87	0.00	0.00	0.00	0.00	0.00	0.00	0.00	0.00
Mn	0.01	1.10	0.22	0.72	1.01	0.00	0.00	0.00	0.00	0.00	0.00	0.00	0.00
Mg	0.01	0.23	0.52	0.10	0.03	0.00	0.00	0.00	0.00	0.00	0.00	0.00	0.00
Ca	2.05	0.22	0.28	0.10	0.06	0.00	0.00	0.01	0.00	0.00	0.00	0.00	0.00
Na	0.00	0.00	0.01	0.01	0.01	0.09	0.08	0.15	0.05	0.14	0.12	0.08	0.10
K	0.00	0.00	0.01	0.00	0.00	0.88	0.94	0.80	0.98	0.87	0.89	0.95	0.89
Sum	8.07	8.00	7.99	8.00	8.00	4.98	5.02	4.99	5.02	5.02	5.01	5.03	4.99

Table 4.2: Representative electron microprobe analyses for the Eyreville-B lower basement-derived and upper megablocks sections obtained in Pretoria[1] and Berlin[2] (*continued).* Abbr.: Amp = amphibole; Bt = biotite; Chl = chlorite; Ep = epidote; Grt = garnet; Kfs = K-feldspar; Ms = muscovite; Pl = plagioclase; Ttn = titanite; Tur = tourmaline; Ves = vesuvianite. B-A = basement amphibolite; B-BS = basement biotite schist; B-G = basement; B-MS = basement mica schist; MB-A = megablock amphibolite; MB-G = megablock massive granite; MB-Gn = megablock gneissic granite; MB-MS = megablock mica schist.

Sample	RG68[1]	RG44[2]	RG157b[1]	RG40[1]	RG40a[2]	W49[2]	RG156b[1]	W36[2]	RG68[1]	RG45[2]	RG70[1]	RG157b[1]	RG51[1]
Mineral	Ms	Ms	Ms	Ms	Ms	Ms	Ms	Ms	Pl	Pl	Pl	Pl	Pl
Lithology	B-MS	B-MS	MB-MS	B-G	B-G	MB-Gn	MB-G	MB-G	B-MS	B-MS	B-BS	B-MS	B-A
(wt%)													
SiO_2	45.64	46.46	45.55	46.28	46.28	45.80	46.84	46.49	64.37	62.26	59.46	59.52	56.68
TiO_2	0.60	0.64	1.23	0.48	0.48	0.43	1.00	0.98	0.00	0.00	0.00	0.03	0.04
Al_2O_3	33.03	35.09	29.83	33.70	33.70	29.55	32.40	30.77	22.16	23.87	25.57	25.30	27.28
Cr_2O_3	0.00	0.00	0.00	0.00	0.00	0.00	0.01	0.00	0.00	0.00	0.00	0.02	0.00
Fe_2O_3	0.00	0.00	0.06	0.00	0.00	1.06	0.00	1.13	0.02	0.09	0.14	0.06	0.18
FeO	3.22	0.61	5.17	1.69	1.69	3.65	4.14	2.94	0.00	0.00	0.00	0.00	0.00
MnO	0.06	0.06	0.04	0.01	0.01	0.04	0.03	0.01	0.00	0.03	0.03	0.02	0.00
MgO	6.15	0.91	1.48	0.78	0.78	1.27	1.00	1.15	0.00	0.01	0.00	0.01	0.00
CaO	0.84	0.00	0.00	0.02	0.02	0.02	0.00	0.00	3.13	4.77	6.89	5.83	8.99
Na_2O	3.84	0.83	0.21	0.39	0.39	0.26	0.37	0.31	9.77	8.57	7.87	8.96	6.68
K_2O	0.03	9.23	10.28	10.69	10.69	10.58	7.62	9.94	0.10	0.15	0.11	0.29	0.16
Total	93.40	93.83	94.12	94.04	94.04	92.67	93.44	93.72	99.55	99.75	100.07	100.04	100.01
Oxygens (apfu)	11.00	11.00	11.00	11.00	11.00	11.00	11.00	11.00	8.00	8.00	8.00	8.00	8.00
Si	2.99	3.11	3.15	3.13	3.13	3.19	3.14	3.18	2.85	2.76	2.65	2.66	2.55
Ti	0.03	0.03	0.06	0.02	0.02	0.02	0.05	0.05	0.00	0.00	0.00	0.00	0.00
Al	2.55	2.77	2.43	2.69	2.69	2.43	2.56	2.48	1.16	1.25	1.34	1.33	1.45
Cr	0.00	0.00	0.00	0.00	0.00	0.00	0.00	0.00	0.00	0.00	0.00	0.00	0.00
Fe^{3+}	0.12	0.00	0.00	0.00	0.00	0.06	0.16	0.06	0.00	0.00	0.01	0.00	0.01
Fe^{2+}	0.05	0.03	0.30	0.10	0.10	0.21	0.07	0.17	0.00	0.00	0.00	0.00	0.00
Mn	0.00	0.00	0.00	0.00	0.00	0.00	0.00	0.00	0.00	0.00	0.00	0.00	0.00
Mg	0.60	0.09	0.15	0.08	0.08	0.13	0.10	0.12	0.00	0.00	0.00	0.00	0.00
Ca	0.06	0.00	0.00	0.00	0.00	0.00	0.00	0.00	0.15	0.23	0.33	0.28	0.43
Na	0.49	0.11	0.03	0.05	0.05	0.04	0.05	0.04	0.84	0.74	0.68	0.78	0.58
K	0.00	0.79	0.91	0.92	0.92	0.94	0.65	0.87	0.01	0.01	0.01	0.02	0.01
Sum	6.89	6.93	7.04	6.99	6.99	7.03	6.79	6.96	5.00	4.99	5.02	5.07	5.02

Table 4.2: Representative electron microprobe analyses for the Eyreville-B lower basement-derived and upper megablocks sections obtained in Pretoria[1] and Berlin[2] (*continued).* Abbr.: Amp = amphibole; Bt = biotite; Chl = chlorite; Ep = epidote; Grt = garnet; Kfs = K-feldspar; Ms = muscovite; Pl = plagioclase; Ttn = titanite; Tur = tourmaline; Ves = vesuvianite. B-A = basement amphibolite; B-BS = basement biotite schist; B-G = basement; B-MS = basement mica schist; MB-A = megablock amphibolite; MB-G = megablock massive granite; MB-Gn = megablock gneissic granite; MB-MS = megablock mica schist.

Sample	**RG51[2]**	**W51[1]**	**W51[2]**	**RG40[1]**	**RG46[2]**	**RG163[1]**	**W49[2]**	**W35[1]**	**W35[2]**	**RG51[1]**	**RG68[1]**	**RG50[1]**
Mineral	**Pl**	**Pl**	**Pl**	**Pl**	**Pl**	**Pl**	**Pl**	**Pl**	**Pl**	**Ttn**	**Tur**	**Ves**
Lithology	**B-A**	**MB-A**	**MB-A**	**B-G**	**B-G**	**MB-Gn**	**MB-Gn**	**MB-G**	**MB-G**	**B-A**	**B-MS**	**B-CS**
(wt%)												
SiO_2	57.54	57.19	58.50	64.40	64.77	66.76	67.51	61.38	61.89	31.14	39.48	36.96
TiO_2	0.02	0.01	0.03	0.00	0.01	0.00	0.00	0.00	0.00	36.90	0.69	1.08
Al_2O_3	26.06	26.69	25.50	22.31	20.88	20.52	19.35	24.34	23.28	1.98	35.27	17.67
Cr_2O_3	0.00	0.00	0.00	0.00	0.00	0.00	0.00	0.00	0.00	0.00	0.00	0.00
Fe_2O_3	0.10	0.04	0.18	0.00	0.02	0.00	0.21	0.03	0.00	0.00	0.00	0.00
FeO	0.00	0.00	0.00	0.00	0.00	0.00	0.00	0.00	0.00	0.75	4.49	3.52
MnO	0.00	0.01	0.00	0.01	0.00	0.00	0.02	0.01	0.02	0.10	0.09	0.07
MgO	0.01	0.01	0.02	0.00	0.00	0.01	0.02	0.00	0.02	0.00	8.23	1.71
CaO	8.68	8.86	7.82	2.96	2.02	0.50	0.40	5.44	5.01	28.61	0.91	36.05
Na_2O	6.91	6.52	7.25	10.09	10.66	11.65	11.16	8.65	8.58	0.01	1.89	0.14
K_2O	0.19	0.04	0.03	0.13	0.10	0.05	0.24	0.19	0.21	0.00	0.02	0.00
Total	99.51	99.37	99.33	99.90	98.46	99.49	98.91	100.04	99.01	99.49	91.07	97.23
Oxygens (apfu)	8.00	8.00	8.00	8.00	8.00	8.00	8.00	8.00	8.00	5.00	31.00	73.00
Si	2.59	2.58	2.63	2.84	2.89	2.94	2.99	2.73	2.77	1.02	7.59	17.93
Ti	0.00	0.00	0.00	0.00	0.00	0.00	0.00	0.00	0.00	0.91	0.10	0.39
Al	1.39	1.42	1.35	1.16	1.10	1.07	1.01	1.27	1.23	0.08	7.99	10.10
Cr	0.00	0.00	0.00	0.00	0.00	0.00	0.00	0.00	0.00	0.00	0.00	0.00
Fe^{3+}	0.00	0.00	0.01	0.00	0.00	0.0	0.01	0.00	0.00	0.00	0.00	0.00
Fe^{2+}	0.00	0.00	0.00	0.00	0.00	0.00	0.00	0.00	0.00	0.02	0.72	1.43
Mn	0.00	0.00	0.00	0.00	0.00	0.00	0.00	0.00	0.00	0.00	0.01	0.03
Mg	0.00	0.00	0.00	0.00	0.00	0.00	0.00	0.00	0.00	0.00	2.36	1.34
Ca	0.42	0.43	0.38	0.14	0.10	0.02	0.02	0.26	0.24	1.00	0.19	18.74
Na	0.60	0.57	0.63	0.86	0.92	1.00	0.96	0.75	0.74	0.00	0.70	0.13
K	0.01	0.00	0.00	0.01	0.01	0.00	0.01	0.01	0.01	0.00	0.00	0.00
Sum	5.02	5.00	5.01	5.01	5.02	5.03	4.99	5.02	5.00	3.03	19.67	49.99

At the Museum für Naturkunde, Humboldt University in Berlin, a JEOL JXA 8800 electron microprobe was used to obtain mineral chemical analyses. The microprobe used a 10 µm diameter beam with a 20 kV acceleration potential and a 20 nA current to obtain the average chemical composition for each mineral analysed. Counting times were 40 s and 20 s on peak and background positions, respectively. The microprobe was calibrated using the Smithsonian international mineral standards as defined in Jarosewich (2002). At the University of Pretoria, mineral chemical analyses were obtained using a Cameca SX 100 electron microprobe, with a 20 kV acceleration potential, a 20 nA beam current, and a defocused beam size of 10 µm. Counting times were 20 s on peak position and 10 s on each background position. The X-ray lines, spectrometer crystals, and standards (in brackets) used include: SiKα, TAP (KP garnet); CaKα, PET (KP garnet); AlKα, TAP (KP garnet); MgKα, TAP (diopside); FeKα, LLIF (KP garnet); MnKα, LLIF (rhodonite); TiKα, PET (rutile); BaLa, LLIF (barite); KKα, PET (KP hornblende); and NaKα, LTAP (KP hornblende).

Recalculation of the mineral chemistry data was performed using the AX activity-composition calculation program for rock-forming minerals (Holland and Powell, 2000) for amphibole, biotite, chlorite, garnet, K-feldspar, plagioclase and muscovite. Tourmaline, titanite and vesuvianite mineral chemical data and biotite, chlorite and muscovite Al^{vi} data were obtained using Excel spreadsheets available as part of the Andy Tindle Free Software package for mineral recalculation (http://www.open.ac.uk/earthresearch/tindle/AGTWebPages/ AGTSoft.html). Elemental ratios used in the sections below are defined by the following equations: $X_{Mg} = Mg/(Mg + Fe^{2+})$; $X_{Mn} = Mn/(Mn + Fe^{2+} + Mg + Ca)$; $X_{Ca} = Ca/(Ca + Fe^{2+} + Mg + Mn)$; $An = 100Ca/(Ca + Na)$; $Or = 100K/(K + Na)$; $Ps = 100Fe^{3+}/(Fe^{3+} + Al)$.

In Townsend *et al.* (2009), the plagioclase contents for all rock types obtained at the University of Pretoria were plotted on a single diagram (see Figure 6A; Townsend *et al.*, 2009). However, with the inclusion of the plagioclase analyses obtained at the Humboldt University, Berlin, mineral chemical trends for each rock type were obscured and, as a result, plagioclase analyses have been plotted per rock type in this study.

4.2.2 Mica schists

The composition of plagioclase in the lower basement-derived mica schist ranges from albite to andesine ($An_{0–38}$), with most analyses lying between An_{0-3}, An_{5-18} and An_{22-35} (Figure 4.1a; see Appendices 3a.6 and 3b.7). The An_{5-18} range is consistent with the peristerite miscibility gap (e.g. Goldsmith, 1982; Maruyama *et al.*, 1982; Klein, 2002), where peristerite intergrowths occur when oligoclase becomes stable along the transition from upper greenschist facies to amphibolite facies metamorphic conditions (Grapes and Otsuki, 1983).

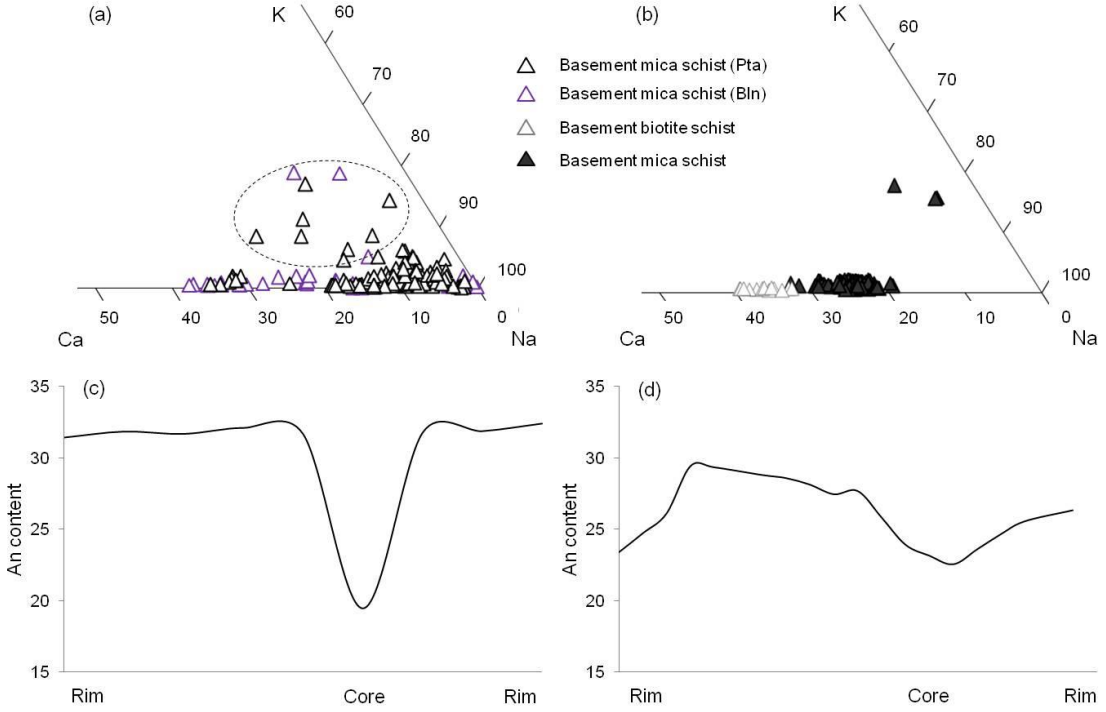

Figure 4.1: (a) Ca-K-Na ternary diagram showing the albite to labradorite range of Pl (n = 159) in the lower basement-derived mica schist and (b) a compositional profile of a Pl grain in the basement mica schist sample RG48 (n = 9). (c) Ca-K-Na ternary diagram showing the tightly constrained andesinitic natures of Pl in both the lower basement-derived biotite schist (n = 13) and the upper megablock biotite schist (n = 104). (d) Compositional profile of a Pl grain in sample RG157b from the upper megablock biotite schist (n = 18). Dashed lines represent observed groupings. Abbr.: n = number of analyses; Pl = plagioclase.

The 10 plagioclase analyses that show a slight enrichment in K compared with the other 149 analyses (Figure 4.1a) may have been contaminated through hydrothermal alteration, which is observed to be pervasive throughout the lower basement-derived and upper megablocks

sections of the Eyreville-B borehole core (see Chapter 2, Section 2.3). Although most plagioclase grains show flat compositional profiles, plagioclase grains that exhibit textural zoning correspond to reverse zonation patterns, with andesine rims with oligoclase cores (Figure 4.1b). Thin albitic rims (An_{0-9}) of plagioclase grains are also observed in the basement mica schists.

The plagioclase in the lower basement-derived biotite schist is tightly constrained as andesinitic in nature (An_{33-39}; Figure 4.1c). Despite a relatively wide range of An content in the megablock biotite schist xenoliths (An_{7-33}), the majority of analyses are andesinitic (An_{20-29}; Figure 4.1c; see Appendices 3a.6 and 3b.7). Similar to the basement mica schist, three plagioclase analyses within the megablock biotite schist xenoliths are comparatively enriched in K compared to the other 101 plagioclase analyses (Figure 4.1c), which was most likely caused by hydrothermal alteration. Reverse compositional zonation in plagioclase grains is more subdued in the megablock biotite schist xenoliths (Figure 4.1d) compared to the basement mica schist (Figure 4.1b). Rare K-feldspar grains analysed from the basement mica schist show a very narrow Or range (Or_{90-95}).

Biotite X_{Mg} values are highest for the lower basement-derived biotite schist (mean X_{Mg} = 0.73; range X_{Mg} = 0.62-0.76; Figure 4.2a; see Appendices 3a.2 and 3b.2) of all biotite-bearing rock types in the lower basement-derived and upper megablocks sections. Conversely, Ti (mean Ti = 0.09; range Ti = 0.07-0.18) and K (mean K = 0.70; range K = 0.49-0.81) abundances (atoms per formula unit [apfu] for 11 oxygens) for the basement biotite schist are amongst the lowest values of all analysed rocks types (Figure 4.2b). The broad ranges in both Ti and K are caused by a single biotite analysis in the basement biotite schist that is relatively enriched in Ti (0.18 apfu) and depleted in K (0.49 apfu) compared to the other biotite analyses (see Appendix 3b.2). Excluding this analysis, biotite K values range between 0.54 and 0.81 (mean K = 0.71) and Ti values range between 0.07 and 0.11 (mean Ti = 0.09) in the basement biotite schist (see Appendix 3b.2). Al^{vi} in the lower basement-derived biotite schist lies in the range 0.05-0.73

(mean Al^{vi} = 0.19; see Appendix 3b.2). The high magnesian values of biotite in the basement biotite schist are the most similar to the megablock amphibolite (see Section 4.2.3).

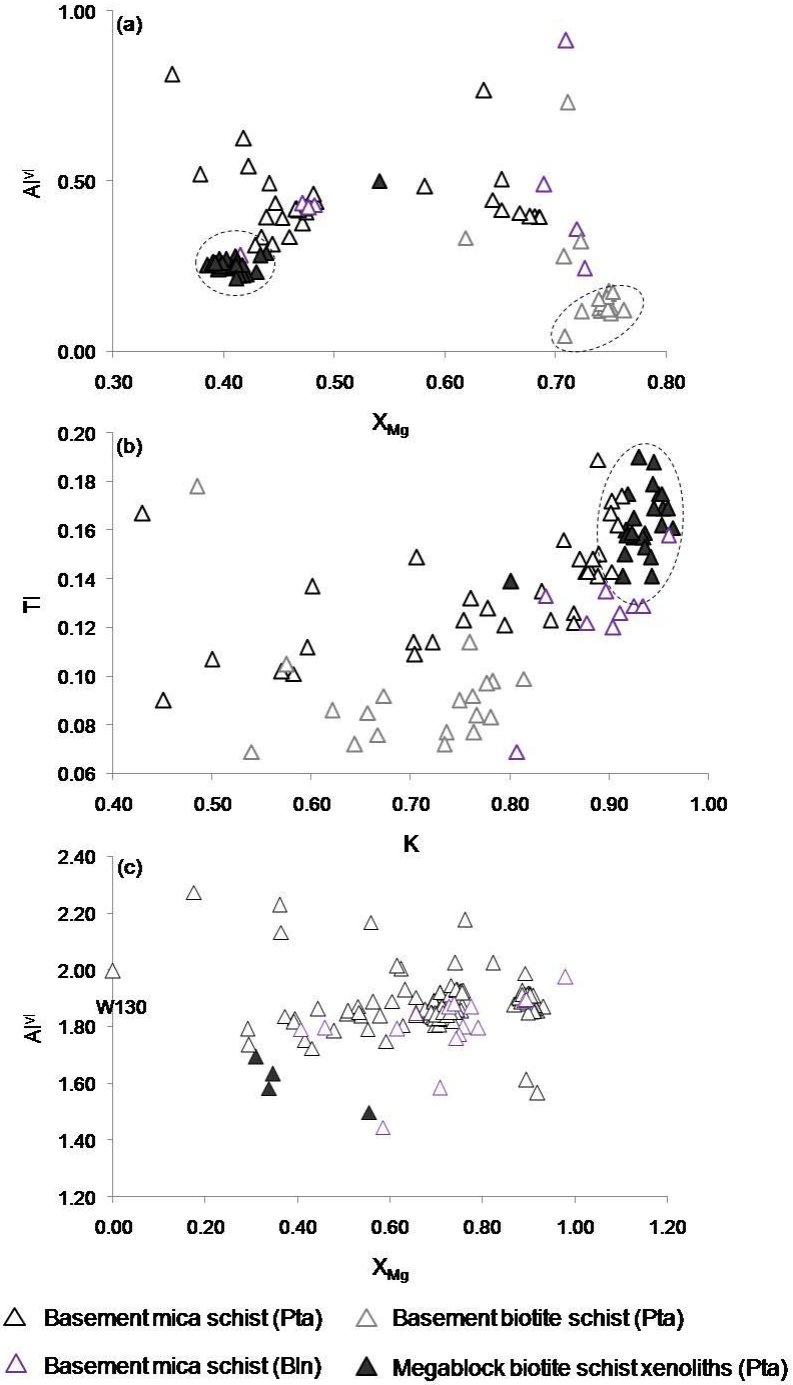

Figure 4.2: (a) X_{Mg} vs. Al^{vi} and (b) K vs. Ti abundances in Bt (apfu for 11 oxygens) and (c) X_{Mg} vs Al^{vi} abundances in Ms (apfu for 11 oxygens) for the lower basement-derived mica schist (Bt n = 41; Ms n = 130) and biotite schist (Bt n = 19) and upper megablock biotite schist xenoliths (Bt n = 25; Ms n = 4). Dashed lines represent observed groupings. Abbr.: Bln = EMP analyses obtained in Berlin; Bt = biotite; Ms = muscovite (white mica); n = number of analyses; Pta = EMP analyses obtained in Pretoria.

Average biotite Ti values (apfu for 11 oxygens) for the lower basement-derived mica schist (mean Ti = 0.13) and the upper megablock biotite schist xenoliths (mean Ti = 0.16) are generally quite similar but the former has slightly higher average X_{Mg} (0.52) and Al^{vi} (0.45) and lower average K (0.80) compared to the latter (X_{Mg} = 0.41, Al^{vi} = 0.26; K = 0.93; Figure 4.2a and b; see Appendices 3a.2 and 3b.2). The resemblance of the basement biotite schist to the cataclastic gneiss found in boulders and blocks in the impactite succession (Jolly, 2011) at a macro-scale and its bulk rock chemistry (see Chapter 3, Section 3.6.1) both suggest a volcanic precursor or volcaniclastic origin for the basement biotite schist, rather than a true pelite.

White mica in the Eyreville-B borehole core mica schists is predominantly muscovite, although a single analysis for sample RG68 contains a relatively elevated Na (0.49) abundance (apfu for 11 oxygens) compared with other analyses (see Appendix 3b.11), suggesting paragonite rather than muscovite. As observed in Chapter 2, Section 2.3.1.1, the dominant mica in the lower basement-derived mica schist is muscovite, whereas the upper megablock biotite schist xenoliths and lower basement-derived biotite schist contains little to no muscovite. The average muscovite K:Na and Si:Al ratios for the basement mica schist are K:Na = 9.00:1 and Si:Al = 1.10:1, and for the megablock biotite schist xenoliths are K:Na = 27.38:1 and Si:Al = 1.36:1 (see Appendices 3a.7 and 3b.11).

X_{Mg} for muscovite (Figure 4.2c) in the basement mica schist ranges from 0.29 to 0.98 (mean X_{Mg} = 0.72), and for the megablock biotite schist xenoliths ranges from 0.31 to 0.55 (mean X_{Mg} = 0.39; see Appendix 3). The relatively lower X_{Mg} values in muscovite for the biotite schist xenoliths (Figure 4.2c) compared to the basement mica schists is consistent with the X_{Mg} data for ferromagnesian minerals in the xenoliths (see Appendices 3a.7 and 3b.11). The large variation of muscovite X_{Mg} in the basement mica schists may be reflective of the presence of both prograde-to-peak muscovite and retrograde muscovite from the breakdown of biotite.

Chlorite in the lower basement-derived and upper megablocks sections of the Eyreville-B borehole core is observed to be an alteration product, forming through the retrogression of

biotite and/or garnet (see Chapter 2, Section 2.3). Chlorite X_{Mg} and Al^{vi} values (apfu for 14 oxygens) in the basement mica schist lie in the ranges 0.21-0.63 (mean X_{Mg} = 0.41) and 1.10-2.46 (mean Al^{vi} = 1.79), respectively, whereas chlorite X_{Mg} values for the basement biotite schist have a slightly narrower but elevated X_{Mg} range (X_{Mg} = 0.49-0.70; mean X_{Mg} = 0.59) but lower Al^{vi} values (Al^{vi} = 1.23-1.56; mean Al^{vi} = 1.40; see Appendices 3a.3 and 3b.3). The elevated X_{Mg} values of chlorite in the basement biotite schist are consistent with the X_{Mg} values for garnet and biotite that it commonly pseudomorphs/replaces.

For garnet in the lower basement-derived mica schist, X_{Mn} = 0.07-0.42 (mean X_{Mn} = 0.20; Figure 4.3a), X_{Mg} = 0.12-0.25 (mean X_{Mg} = 0.16; Figure 4.3b) and X_{Ca} = 0.04-0.10 (mean X_{Ca} = 0.06; Figure 4.3c; see Appendices 3a.4 and 3b.5). The mica schist garnets are enriched in spessartine compared to almandine (Fe), pyrope (Mg) and grossular (Ca). Continuous compositional profiling was inhibited owing to the highly fractured nature of the mica schist garnets (see Chapter 2, Figure 2.3b), but, where compositional profiling was possible, the garnets tend to show relatively flat profiles. However, a single garnet in sample RG53 contains a pyrope-rich, spessartine-poor core with a spessartine-richer marginal zone and rim (Figure 4.4a and b; see Appendices 3a.4 and 3b.5). This zonation is interpreted to reflect prograde growth zoning in the garnet core with retrograde diffusional zoning occurring in the marginal zone and rim owing to garnet break-down. This interpretation is supported by geothermometry in Section 4.3.4.2.

Tourmaline in the lower basement-derived mica schist is magnesian (mean Mg = 2.35; range Mg = 2.10-2.68 apfu for 31 oxygens; see Appendix 3b.9), consistent with the Mg-rich nature of dravite (Pichler and Schmitt-Riegraf, 1997), which corresponds to the petrographic observations made for tourmaline in the basement mica schist (see Chapter 2, Section 2.3.1.1). In comparison, large tourmalines in basement tourmaline-rich zones (see Chapter 2, Section 2.3.1.5) tend to have relatively higher and wider ranges of Mg (mean Mg = 0.91; range Mg = 2.05-2.80) and Fe (mean $Fe_{(tot)}$ = 0.91; range $Fe_{(tot)}$ = 0.70-1.27; see Appendix 3b.9). Despite the somewhat variable zoning patterns observed in thin section, a general zoning trend in the

large tourmalines corresponds with schorlite-rich cores and dravite-rich rims observed in Chapter 2, Section 2.3.1.5.

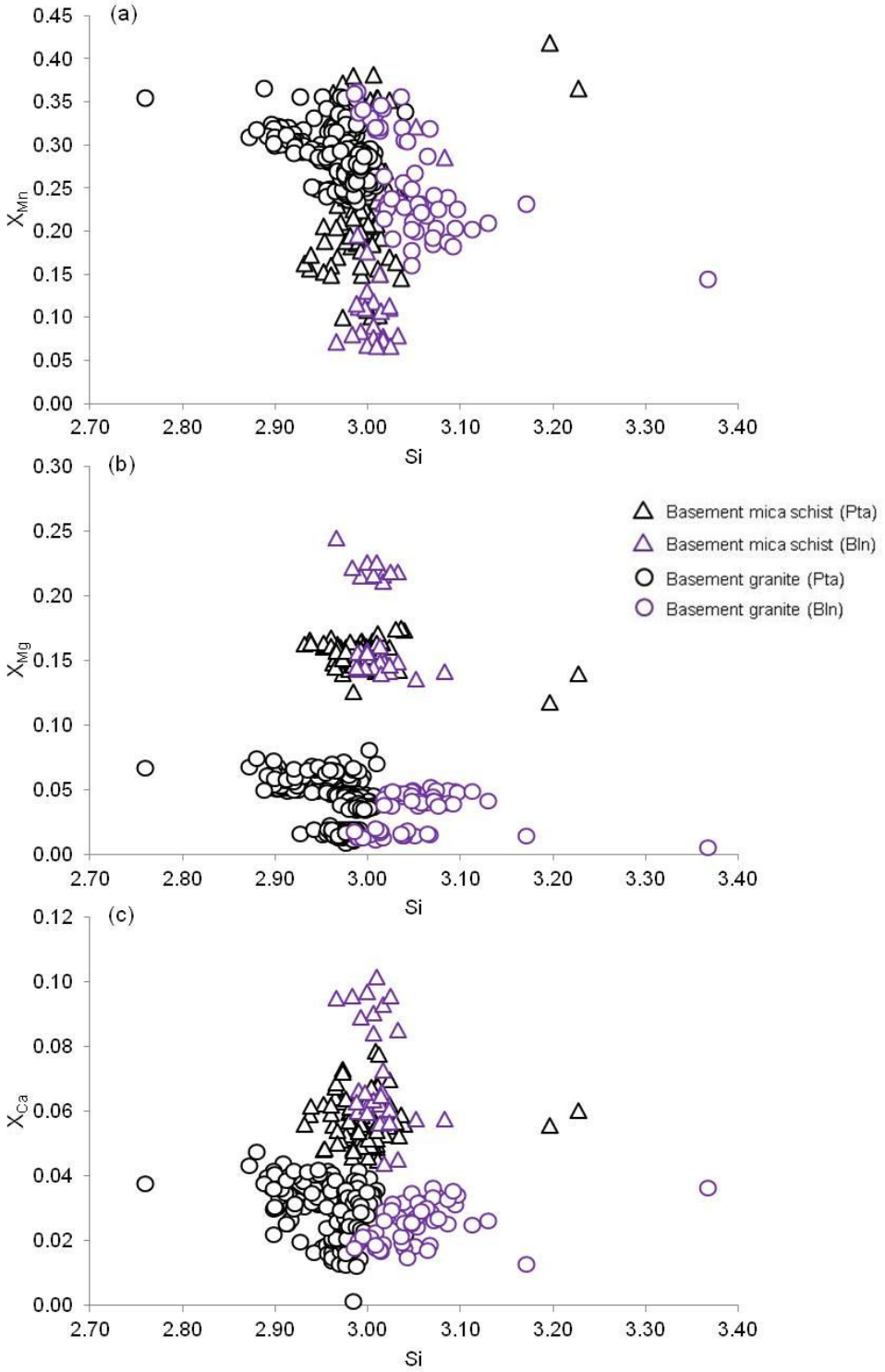

Figure 4.3: Bivariate diagrams showing (a) X_{Mn}, (b) X_{Mg} and (c) X_{Ca} elemental ratios of Grt plotted against Si (apfu for 12 oxygens) for both mica schist (n = 109) and granite (n = 296) in the lower basement-derived section. Abbr.: Bln = EMP analyses obtained in Berlin; Grt = garnet; n = number of analyses; Pta = EMP analyses obtained in Pretoria.

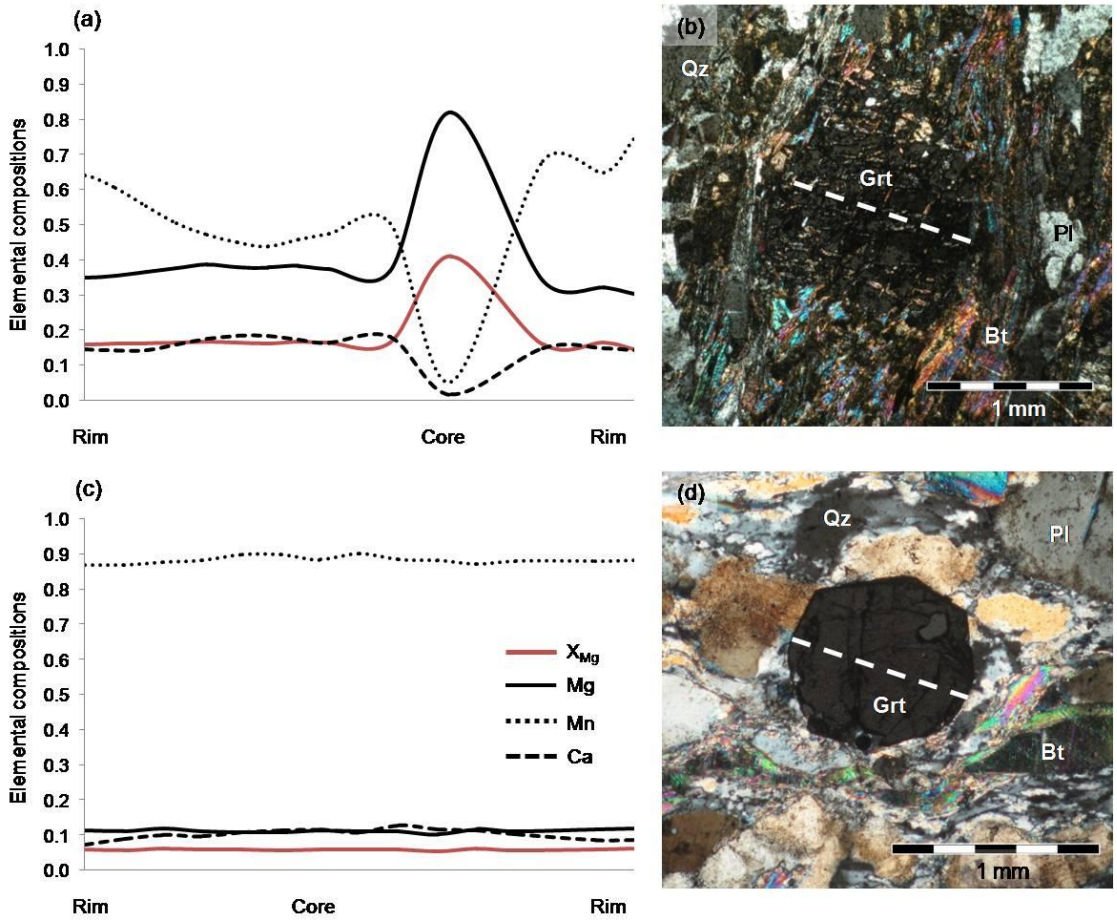

Figure 4.4: Elemental compositional profiles for garnet in the lower basement-derived (a) mica schist (sample RG53 n = 15) with (b) accompanying reference photomicrograph (XPL), and in the lower basement-derived (c) granite (sample RG40; n = 15) with (d) accompanying reference photomicrograph (XPL). White dashed lines in the photomicrographs indicate the approximate locations of each compositional profile. Abbr.: Bt = biotite; Grt = garnet; n = number of analyses; Pl = plagioclase; Qz = quartz; XPL = cross polarised light.

4.2.3 Amphibolites and calc-silicate rock

Plagioclase in the lower basement-derived amphibolite ranges in composition from albite to andesine (An_{0-43}), although most analyses are andesinitic in nature (An_{37-42}; Figure 4.5a; see Appendices 3a.6 and 3b.7). The megablock amphibolite, on the other hand, contains generally more calcic plagioclase than the basement amphibolite, ranging between oligoclase and labradorite (An_{22-56}; Figure 4.5b; see Appendices 3a.6 and 3b.7). Most plagioclase analyses from the megablock amphibolite also lie mainly within the andesine range (An_{42-49}; Figure 4.5b; see Appendices 3a.6 and 3b.7). The K-feldspar in the basement amphibolite has a relatively

wide Or range (Or_{77-98}), but no compositional zoning is apparent. Most of the analyses of K-feldspar in the basement amphibolite lie in the range Or_{92-95} (see Appendices 3a.5 and 3b.6). A single grain in the generally K-feldspar-deficient megablock amphibolite contains Or_{84} (see Appendices 3a.5 and 3b.6).

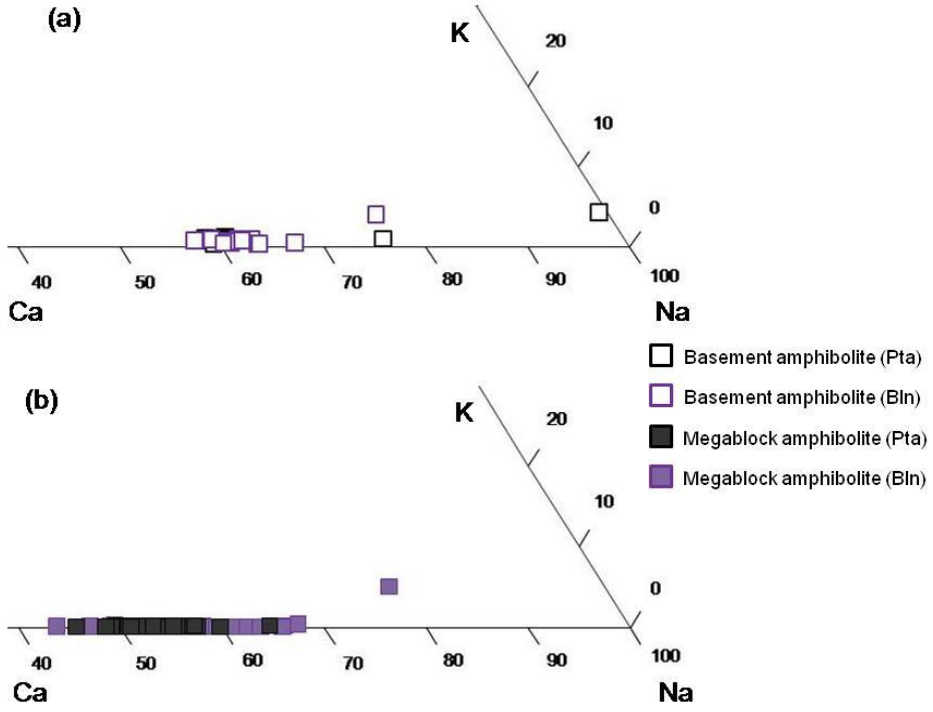

Figure 4.5: Ca-K-Na ternary diagrams for Pl in (a) the lower basement-derived amphibolite (n = 25) and (b) the upper megablock amphibolite (n = 55). Abbr.: Bln = EMP analyses obtained in Berlin; n = number of analyses; Pl = plagioclase; Pta = EMP analyses obtained in Pretoria.

As observed during petrographic analysis, biotite in the megablock amphibolite is much more abundant (see Chapter 2, Section 2.3.2) than in the lower basement-derived amphibolite (see Chapter 2, Section 2.3.1.3). This trend is also observed in the generally higher X_{Mg} values (mean X_{Mg} = 0.65; X_{Mg} = 0.55-0.70) in the megablock amphibolite compared with the basement amphibolite (mean X_{Mg} = 0.54; range X_{Mg} = 0.53-0.56; apfu for 11 oxygens; Figure 4.6a; see Appendices 3a.2 and 3b.2). However, the opposite trend in terms of Al^{vi}, K and Ti abundances is observed, with the basement amphibolite (mean Al^{vi} = 0.36; range Al^{vi} = 0.22-0.48; mean K = 0.97; range K = 0.96-0.98; mean Ti = 0.15; range Ti = 0.13-0.17) containing higher values than

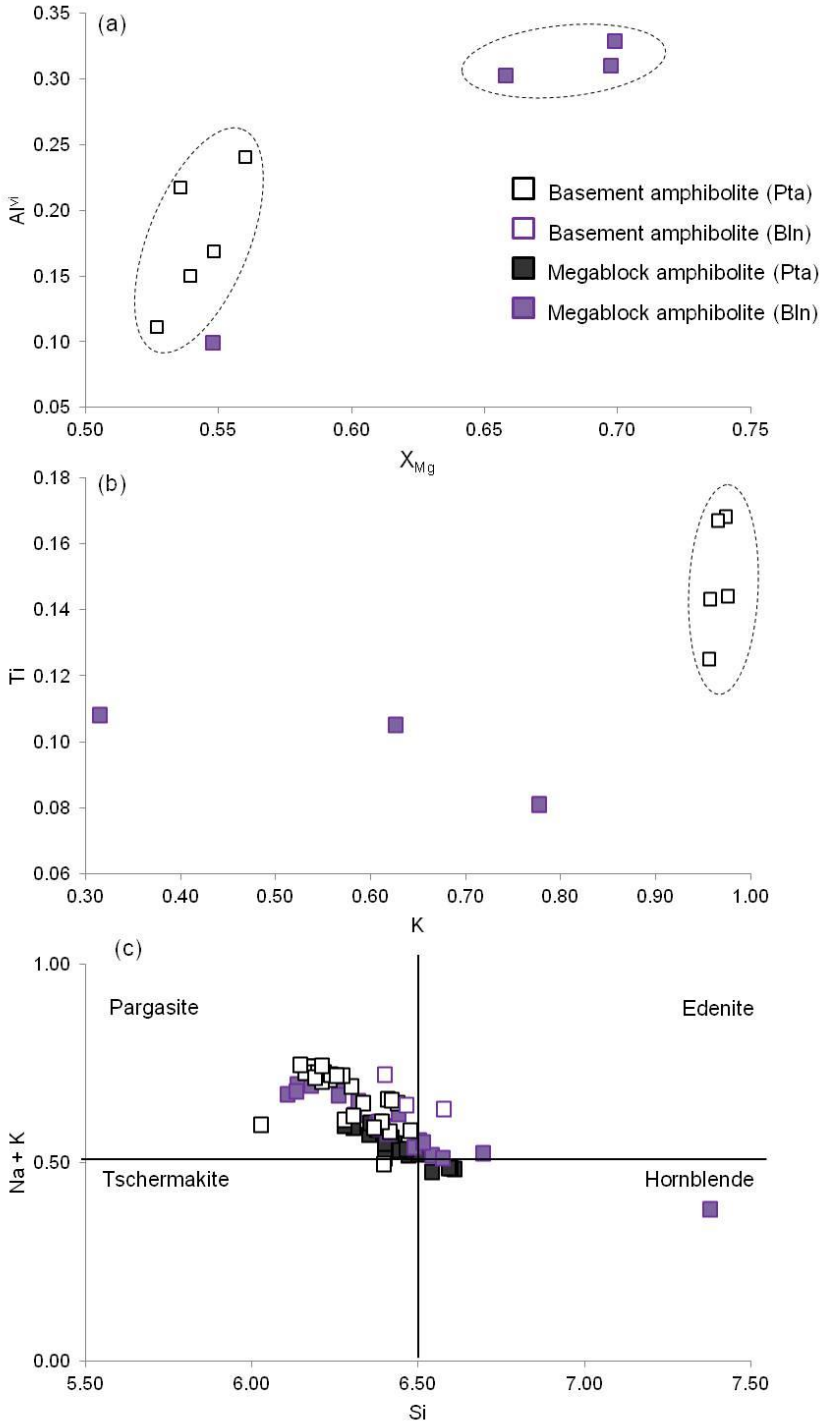

Figure 4.6: (a) X_{Mg} vs. Al^{vi} and (b) K vs. Ti abundances (apfu for 11 oxygens) in Bt for the lower basement-derived amphibolite (n = 5) and megablock amphibolite (n = 4). (c) Amphibole classification diagram (after Leake, 1978; Deer *et al.*, 1992) using Na + K abundances plotted against Si (apfu for 23 oxygens) for the lower basement-derived amphibolite (n = 31) and the upper megablock amphibolite (n = 44). Dashed lines represent observed groupings. Abbr.: Bln = EMP analyses obtained in Berlin; Bt = biotite; n = number of analyses; Pta = EMP analyses obtained in Pretoria.

the megablock amphibolite (mean Al^{vi} = 0.26; range Al^{vi} = 0.10-0.33; mean K = 0.62; K = 0.32-0.78; mean Ti = 0.09; Ti = 0.08-0.11; Figure 4.6; see Appendices 3a.2 and 3b.2). These observations are consistent with the presence and absence of K-feldspar in the basement and megablock amphibolites, respectively (see Chapter 2, Sections 2.2.2.3 and 2.2.3). Additionally, the low and wide range of K abundances in the megablock amphibolite is suggestive of chloritisation, which also corresponds to petrographic observations (see Chapter 2, Section 2.2.3). Similar to biotite, X_{Mg} values for retrograde chlorite in the megablock amphibolite are higher (mean X_{Mg} = 0.61; range X_{Mg} = 0.59-0.62; see Appendices 3a.2 and 3b.2) and Al^{vi} values (apfu for 14 oxygens) are lower (mean Al^{vi} = 1.30; range Al^{vi} = 1.27-1.34; see Appendix 3) than in the basement amphibolite (mean X_{Mg} = 0.34; range X_{Mg} = 0.32-0.40; mean Al^{vi} = 1.87; range Al^{vi} = 1.72-2.01; see Appendices 3a.2 and 3b.2).

Amphibole in the basement amphibolite contains slightly higher abundances of Na and K (range Na + K = 0.50-0.75; Figure 4.6c; see Appendices 3a.1 and 3b.1), indicating a pargasitic composition, compared to amphibole in the megablock amphibolite (Na + K = 0.38-0.70 apfu for 23 oxygens; Figure 4.6c), which is pargasitic to hornblendic in composition (Leake, 1978). Conversely, average X_{Mg} values in the megablock amphibolite (X_{Mg} = 0.62) are slightly greater than those in the basement amphibolite (X_{Mg} = 0.55).

As described in Chapter 2, Section 2.3.1.4, the lower basement-derived calc-silicate rock comprises a prograde-to-peak, vesuvianite-dominated mineral assemblage and a retrograde, epidote-dominated mineral assemblage. Vesuvianite compositions typically show very little variation despite its coarse-grain size, resulting in narrow elemental ranges (Ca = 18.60-18.95; Ti = 0.32-0.51; Na = 0.09-0.16; apfu for 73 oxygens based on 50 cation normalisation; see Appendix 3b.10). The average abundance of Ca + Na is 18.91 (standard deviation = 0.09), which is statistically identical to Groat *et al.*'s (1992) ideal value of 19 X sites for the 50 cation vesuvianite formula. Si varies very slightly (17.70 and 17.95 apfu) with a mean Si value of Si = 17.84 (standard deviation = 0.06). This is minimally less than the projected value of 18 Z sites (Groat *et*

al., 1992). Low values of kurtosis (-0.20) and skewness (-0.41) combined with the nearly identical Si value suggests that Al-for-Si substitution at the Z sites was minimal (Groat *et al.*, 1992). The mean value of the sum of the remaining cations (Al^{3+}, Mg^{2+}, Fe^{2+}, Fe^{3+}, Ti^{4+} and Mn^{2+}) is equal to 12.79, with a standard deviation of 0.08. As with the Z sites, the sum of the remaining cations is slightly less that the projected 13 Y sites (Groat *et al.*, 1992). The low Ti and Na values correspond to predictions by Groat *et al.* (1992) that Na values are typically less than 0.2 apfu where Ti values are less than 0.75 apfu.

Pistacite (Ps) values of epidote in the basement calc-silicate show a broad variation in composition (Ps_{5-26}), although most values lie in the range Ps_{15-24} (see Appendix 3b.4). Epidote in the basement amphibolite shows a narrower Ps range (Ps_{11-25}) but most analyses are in the range Ps_{19-24} (see Appendix 3b.4). Compositional zoning in epidote is strongest in the basement calc-silicate, although slight zoning is also observed in the basement amphibolite. Higher Ps values are more consistent with prograde-to-peak epidote growth, whereas the lower Ps values correspond to the retrograde mineral assemblages observed in the basement calc-silicate and amphibolite.

4.2.4 Granites

Anorthite (An) content of plagioclase in the lower basement-derived granite generally occurs in the range An_{10-15} (albite to oligoclase), although the full range is An_{6-32} (Figure 4.7a; see Appendices 3a.6 and 3b.7). Despite the broader An ranges in the gneissic (An_{1-8} and An_{20-25}) and massive (An_{2-34}) megablock granites, the majority of analyses from both megablock granites lie in the range An_{20-30}, which is slightly more calcic than the basement granite (Figure 4.7b and c; see Appendices 3a.6 and 3b.7). K-feldspar Or content in the basement granite, gneissic megablock granite and massive megablock granite lie in the ranges Or_{89-96}, Or_{64-98} and Or_{77-96}, respectively (see Appendices 3a.5 and 3b.6). The wider compositional ranges of K-feldspar in the megablock granites compared to the basement granite may suggest a greater sodium component to K-feldspar in the megablock granites.

X_{Mg} values for biotites in the gneissic megablock granite (mean X_{Mg} = 0.28; range X_{Mg} = 0.25-0.44) are slightly higher than those in the basement granite (mean X_{Mg} = 0.23; range X_{Mg} = 0.20-0.26) but less than the X_{Mg} values for biotites in the massive megablock granite (mean X_{Mg} = 0.42; range X_{Mg} = 0.35-0.52; Figure 4.8a; see Appendices 3a.2 and 3b.2). Al^{vi} values (apfu for 11 oxygens) are highest in biotites from the basement granite (mean Al^{vi} = 0.47; range Al^{vi} = 0.39-0.64; Figure 4.8a), with K = 0.53-0.98 (mean K = 0.87) and Ti = 0.08-0.17 (mean Ti = 0.13; Figure 4.8b; see Appendices 3a.2 and 3b.2). Biotite Al^{vi} values (apfu for 11 oxygens) in the gneissic megablock granite range between 0.26 and 0.41 (mean Al^{vi} = 0.26; Figure 4.8a) and in the massive megablock granite Al^{vi} values range between 0.19 and 0.44 (mean Al^{vi} = 0.24; Figure 4.8a; see Appendices 3a.2 and 3b.2). K and Ti values (apfu for 11 oxygens) for the gneissic and massive megablock granites have the following ranges: K = 0.71-1.00 (mean K = 0.88) and Ti = 0.12-0.21 (mean Ti = 0.18), and K = 0.67-0.98 (mean K = 0.92) and Ti = 0.05-0.23 (mean Ti = 0.17), respectively (Figure 4.8b; see Appendices 3a.2 and 3b.2).

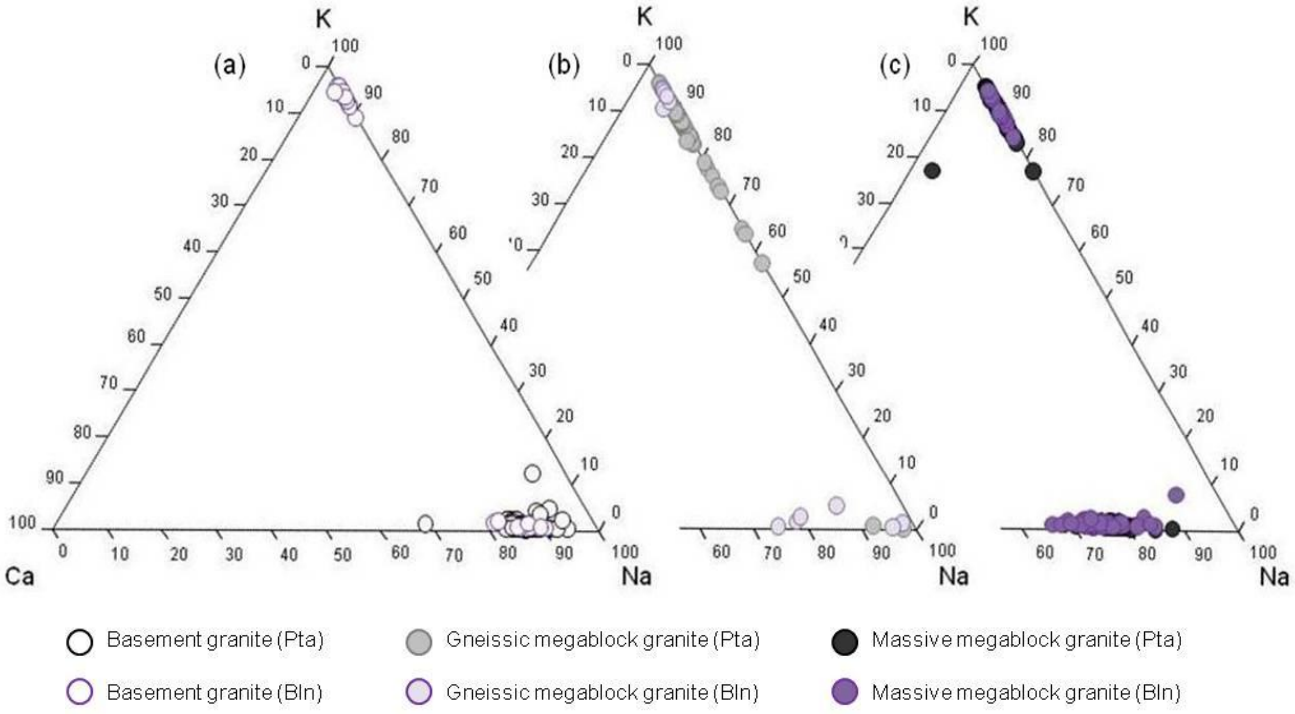

Figure 4.7: Ca-K-Na ternary diagrams for Pl in (a) the lower basement-derived granite (n = 144) and (b) the upper gneissic (n = 10) and massive (n = 97) megablock granites. Abbr.: Bln = EMP analyses obtained in Berlin; n = number of analyses; Pl = plagioclase; Pta = EMP analyses obtained in Pretoria.

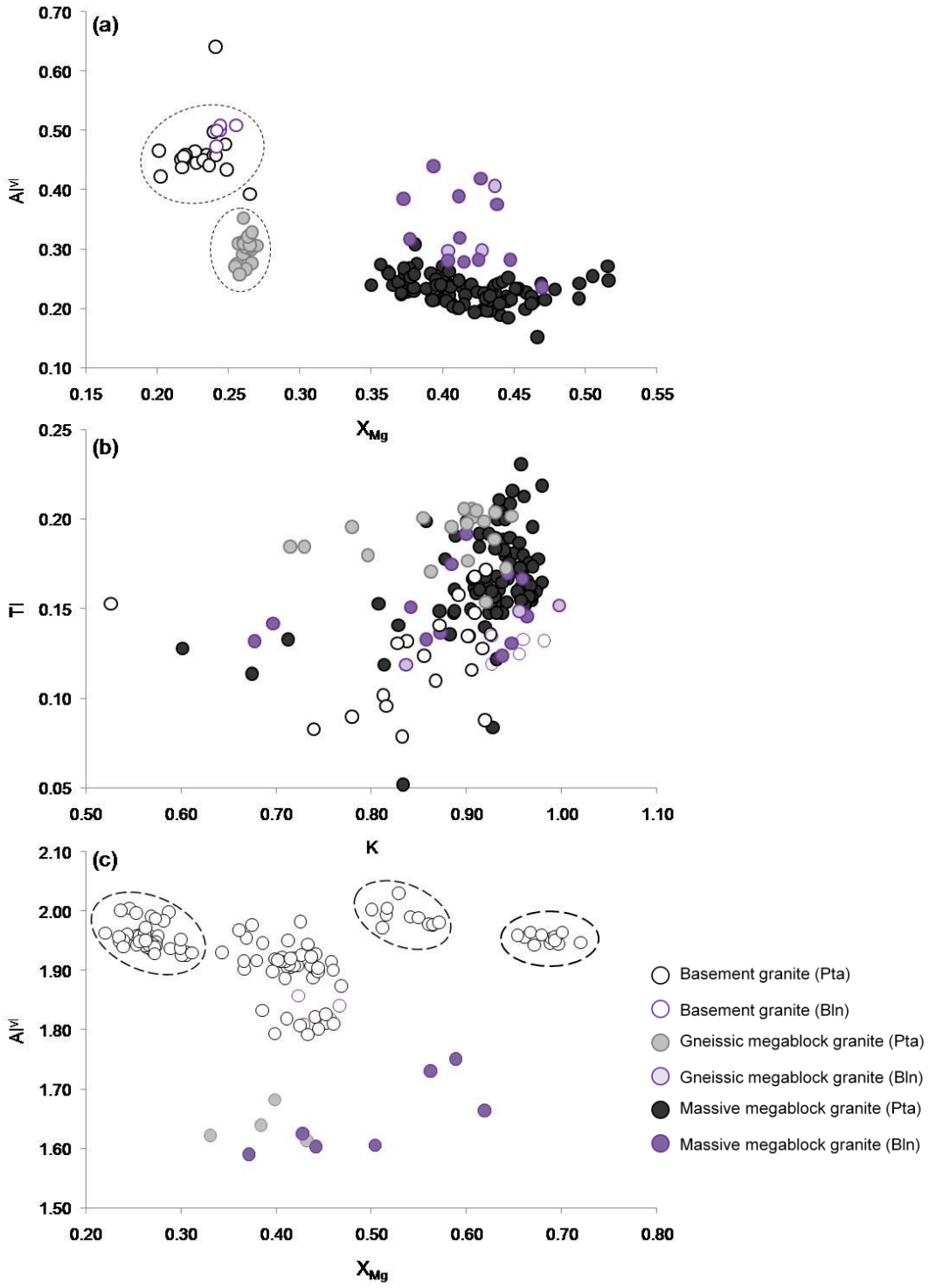

Figure 4.8: (a) X_{Mg} vs. Al^{vi} and (b) K vs. Ti abundances (apfu for 11 oxygens) in Bt and (c) X_{Mg} vs. Al^{vi} abundances (apfu for 11 oxygens) in Ms for the lower basement-derived granite (Bt n = 25; Ms n = 115) and upper gneissic (Bt n = 22; Ms n = 4) and massive (Bt n = 105; Ms n = 9) megablock granites. Dashed lines represent observed groupings. Abbr.: Bln = EMP analyses obtained in Berlin; Bt = biotite; Ms = muscovite (white mica); n = number of analyses; Pta = EMP analyses obtained in Pretoria.

Muscovite X_{Mg} values in the basement granite are in the range X_{Mg} = 0.22-0.72 (mean X_{Mg} = 0.41), in the gneissic megablock granite are in the range X_{Mg} = 0.33-0.43 (mean X_{Mg} = 0.39) and in the massive megablock granite are in the range X_{Mg} = 0.37-0.64 (mean X_{Mg} = 0.51; Figure 4.8c; see Appendices 3a.7 and 3b.11). The basement granite has lower Si:Al (1.08:1) and K:Na (10.69:1) ratios compared to the megablock gneissic (Si:Al = 1.29:1; K:Na = 19.83:1) and massive (Si:Al = 1.25:1; K:Na = 18.84:1) granites (apfu for 11 oxygens; see Appendices 3a.7 and 3b.11). Al^{vi} values (apfu for 11 oxygens) are slightly higher in the basement granite (mean Al^{vi} = 1.93; range Al^{vi} = 1.79-2.03) than in the gneissic (mean Al^{vi} =1.64; range Al^{vi} = 1.61-1.68) and massive (mean Al^{vi} = 1.60; range Al^{vi} = 1.50-1.69) megablock granites (Figure 4.8c; see Appendices 3a.7 and 3b.11).

X_{Mg} values for chlorite (apfu for 14 oxygens) in the upper gneissic (mean X_{Mg} = 0.26; range X_{Mg} = 0.25-0.28) and massive (mean X_{Mg} = 0.43; range X_{Mg} = 0.39-0.47) megablock granites are relatively similar to their biotite counterparts (see Appendices 3a.3 and 3b.3). A single analysis for chlorite in the basement granite sample RG46 contains an X_{Mg} value of 0.20 (see Appendices 3a.3 and 3b.3), much lower than chlorites in the megablock granites. Conversely, the chlorite Al^{vi} value (apfu for 14 oxygens) is the greatest in the basement granite (Al^{vi} = 2.42) compared with the gneissic (mean Al^{vi} = 1.43; range Al^{vi} = 1.09-1.48) and massive (mean Al^{vi} = 1.31; range Al^{vi} = 1.09-1.77) megablock granites (see Appendices 3a.3 and 3b.3).

Compared with garnets in the lower basement-derived mica schist (see Section 4.2.2), the basement granite contains garnets that have higher X_{Mn} values and lower X_{Mg} and X_{Ca} values (Figure 4.3; see Appendices 3a.4 and 3b.5). These garnets also tend to have flat compositional profiles (Figure 4.4c and d). The differences in crystal chemistry combined with the textural differences (see Chapter 2, Section 3.1.4) between mica schist garnets (highly poikilitic and fractured) and granite garnets (commonly idioblastic and less poikilitic) suggest that the latter crystallised from the melt, rather than being an inherited xenocrystic phase from the basement mica schist.

4.3 Geothermobarometry

4.3.1 Introduction

Geothermobarometry is the application of thermodynamics in petrology whereby the *P-T* conditions of an equilibrium mineral assemblage are estimated (Powell and Holland, 2008; Ciocîrdel, 2009). According to Powell *et al.* (2005), a unifying and simplifying principle of metamorphic petrology is that "a mineral assemblage equilibrates continuously on some scale along a *P-T* (pressure-temperature) path while fluid or melt is present, but little or no change occurs while fluid or melt is absent." Consequently, once the fluid or melt in the system is lost, it is assumed that the equilibrium mineral assemblage and compositions are preserved, along with the information relating to the *P-T* conditions at the time of fluid/melt loss (White and Powell, 2002; Powell *et al.*, 2005; Powell and Holland, 2008). This is termed the equilibrium model of metamorphism and allows for the application of equilibrium thermodynamics on mineral assemblages through inverse modelling, for the determination of metamorphic conditions, as well as forward modelling, to assist in understanding metamorphic processes (Powell *et al.*, 2005; White *et al.*, 2008).

A mineral assemblage is considered to be in a state of equilibrium if the assemblage has the lowest Gibbs free energy (ΔG; Spear, 1993; Powell *et al.*, 2005). Before reaching this equilibrium state (also known as peak metamorphic condition; Spear, 1989), however, changes in pressure and temperature during orogenesis or contact metamorphism cause mineral assemblages, modes and compositions to progressively change as they evolve towards a new lowest ΔG equilibrium (White *et al.*, 2008). These changes are driven by chemical potential gradients and achieved through diffusion between and within minerals, and through the growth and consumption of minerals (White *et al.*, 2008).

In terms of thermodynamic relations, any balanced chemical reaction written among phase components in the equilibrium assemblage can also be written in terms of the chemical potentials

of these phase components (Gibbs, 1906; Powell, 1978; Spear, 1989, 1993). This concept can be expanded as a function of pressure (1 bar) and temperature (298 K) to give the following expression (Equation 4.1; see Table 4.3 for symbol definitions; Spear, 1993) for the equilibrium constant (K_{eq}):

$$\Delta G(P,T,X) = 0 = \Delta H(298,1) + \int_{298}^{T} \Delta C_P \, dT + \int_{1}^{P} \Delta V \, dP - T\left(\Delta S(298,1) + \int_{298}^{T} \frac{\Delta Cp}{T} \, dT\right) + RT\ln K_{eq} \quad (4.1)$$

Accepting that the K_{eq} is dependent on pressure and temperature, the above equation is based on the notion that it is possible to determine the value of the equilibrium constant (K_{eq}) by measuring the compositions of co-existing minerals as well as the application of appropriate activity models (Spear, 1989, 1993). Thus, Equation 4.1 is fundamental in establishing the formal thermodynamic relationships between pressure, temperature and mineral composition and can be used to either calculate pressure and temperature from mineral chemistries or to calculate phase equilibria as a function of pressure and temperature (Spear, 1989, 1993).

The calculation of metamorphic phase equilibria is integral to most geothermobarometric methods (Powell and Holland, 2008). It involves solving multiple equations that define the equilibrium conditions of a particular system, which are then compared with what is observed in a sample to infer metamorphic pressures and temperatures (Spear, 1989). These equations are solved using large internally-consistent thermodynamic datasets and activity-composition models, allowing the determination of mineral equilibria that involve solid solutions in complex systems, which can then be plotted on phase diagrams that closely approximate phase relationships in natural systems (Spear and Cheney, 1989; Powell *et al.*, 1998). THERMOCALC (Powell and Holland, 1988, 1994) with AX (an activity-composition calculation programme; Holland and Powell, 2000) is an example of such a software tool. Alternatively, equilibrium assemblage diagrams can be calculated by predicting the stable mineral assemblages based on minimising Gibbs free energy (ΔG), which is

based on the second law of thermodynamics where, at a fixed entropy (S), the equilibrium state is reached in a closed system when the total free energy (G) has reached its minimum value (Callen, 1985; de Capitani and Brown, 1987). An example of a software tool that uses Gibbs free energy (ΔG) minimisation is THERIAK-DOMINO (de Capitani and Brown, 1987; de Capitani, 1994), where the concept is applied by using linear programming combined with the minimisation of single thermodynamic solution functions (Jowhar, 2012).

Table 4.3: Definitions of symbols used in Equation 4.1 (after Spear, 1989, 1993; Powell *et al.*, 1998).

Symbol	Definition	Unit
ΔC_P	Heat capacity change of reaction	$J\ K^{-1}\ mol^{-1}$
dP	Change in pressure	bar
dT	Change in temperature	K
ΔG	Free energy change of reaction	$J\ mol^{-1}$
ΔH	Enthalpy change of reaction	$J\ mol^{-1}$
K_{eq}	Equilibrium constant	-
I	Ionic strength	$mol\ L^{-1}$
n	Total amount in a system	mol
P	Pressure	bar
R	Gas constant (8.3145 $JK^{-1}mol^{-1}$)	$J\ K^{-1}\ mol^{-1}$
ΔS	Entropy change of reaction	$J\ K^{-1}\ mol^{-1}$
T	Temperature	K
ΔV	Volume change of reaction	m^3
X	Composition	-

Geothermobarometric methods can be divided into conventional thermobarometry and pseudosection thermobarometry (Powell and Holland, 2008). Conventional thermobarometry (inverse modelling) is based on Equation 4.1, where balanced chemical reactions are written between the end-members of mineral phases in the equilibrium assemblage (Spear, 1993; Powell and Holland, 2008). Given the sensitivity of mineral compositions to metamorphic *P-T* conditions (Spear, 1993), certain reactions can be used to infer metamorphic temperatures (geothermometers) and pressures (geobarometers). Using Equation 4.1 (Spear, 1989, 1993) with the observed mineral compositions substituted into K_{eq} (Powell and Holland, 2008),

geothermometers can be defined as equilibria that are sensitive to temperature (large ΔS, ΔH and small ΔV), whereas geobarometers can be defined as those equilibria that are sensitive to pressure (large ΔV and small ΔS, ΔH). Types of calibrations used in conventional thermobarometry include exchange thermometers, solvus thermometers and net transfer equilibria (geobarometers; Spear, 1989, 1993).

Pseudosection thermobarometry (forward modelling), on the other hand, is based on the equilibrium mineral assemblages where the chemical composition of the equilibrium volume is used in calculations and projected onto a *P-T* phase diagram (Jowhar, 2012). The equilibrium volume is defined as "the scale on which it is plausible to suggest that the minerals in the mineral assemblage being considered for thermobarometry were in equilibrium with each other" (Powell and Holland, 2008). Differing from a petrogenetic section, where all phases are considered to be in the plane of the section as a result of contact equilibrium, a pseudosection only includes the phases in equilibrium for a single bulk rock composition in the plane of the section (Powell *et al.*, 2005; Jowhar, 2012). A variety of complex systems can be modelled, including the system Na_2O-K_2O-CaO-MgO-FeO-Fe_2O_3-Al_2O_3-SiO_2-TiO_2-H_2O-CO_2 (after Berman and Brown, 1985; de Capitani and Brown, 1987; de Capitani, 1994) and the system MnO-Na_2O-CaO-K_2O-FeO-MgO-Al_2O_3-SiO_2-H_2O-TiO_2-O_2 (also known as the MnNCKFMASHTO system; after Zeh and Holness, 2003; White *et al.*, 2005). The aim of modelling such complex systems is to provide the nearest comprehensive compositional analogue for natural systems, so that results are meaningful in terms of their real world application (e.g. White *et al.*, 2004, 2007, 2008; Ogilvie, 2010).

In recent years, the application of trace element compositions to geothermobarometry has become more common owing to the recognition that the distribution of certain trace elements within the equilibrium mineral assemblage is dependent on pressure and/or temperature (e.g. Heinrich *et al.*, 1997; Yang and Rivers, 2000; Pyle *et al.*, 2001; Zack *et al.*, 2004a; Tomkins *et al.*, 2007). Zack *et al.* (2002) observed that Zr incorporation into rutile in systems with coexisting zircon and quartz appeared to be dependent on temperature. This observation led Zack *et al.*

(2004a) to empirically calibrate a Zr-in-rutile geothermometer for rutile-quartz-zircon mineral assemblages. The presence of prograde rutiles in the lower basement-derived mylonite zone allowed for the application of the Zr-in-rutile geothermometer in this study.

All of the above geothermobarometric methods suffer from some degree of uncertainty. Uncertainties arise from several sources, including (after Spear, 1989, 1993; Zack *et al.*, 2004a; Powell and Holland, 2008):

- General uncertainties:
    - System in question may not represent an equilibrium assemblage;
    - Uncertainties in mineral activity models;
    - Geological uncertainties or bias from mineral compositional heterogeneities;
- For conventional thermobarometry and Zr-in-rutile thermometry:
    - In accuracy of the experimental calibration;
    - Analytical imprecision in microprobe analysis;
    - Uncertainty of the composition and correction factors in electron microprobe standards;
    - Cross correlations between temperature and pressure estimates since all reactions are influenced by both pressure and temperature to some degree; and
- For pseudosection thermobarometry:
    - Misapplication of the relevant thermodynamic model to the equilibrium volume in question.

Owing to the fact that uncertainties increase in size during modelling, these uncertainties must be propagated as far as practical for the results to remain meaningful (Spear, 1993; Powell and Holland, 2008). Although this is relatively simple to do with analytical uncertainties, it is not always possible to take into account systematic uncertainty or bias in the relevant models (Powell, 1985; Powell and Holland, 2008). More often than not, however, this bias is generally unknown, and is usually only considered when evaluating previously produced results (Powell and Holland, 2008).

4.3.2 Constraints on peak *P-T*-X(H_2O) estimates

Before the application of thermodynamics to an equilibrium assemblage system, constraints in terms of *P*, *T* and X(H_2O) must be made since all types of thermobarometry begin with the interpretation of the equilibration volume (Powell and Holland, 2008). In thermodynamics, a constraint is defined as "a state variable associated with some method of changing system energy, which is held constant while minimising a thermodynamic potential" (Anderson, 2005). With regards thermobarometry, these constraints are used to provide the necessary information for the 'starting' guesses (Powell and Holland, 2008). The following outlines the constraints applied to the Eyreville-B target rocks based on petrographic and geochemical observations.

The lower basement-derived section is characterised by the widespread presence of graphite (see Chapter 2, Section 2.3.1). In order for graphite to form, a mixed H_2O-CO_2-CH_4 metamorphic fluid must also be present. Ohmoto and Kerrick (1977) suggested that this fluid must be buffered to the highest possible values of X(H_2O). Under non-ideal conditions, the maximum values for the fluid are X(H_2O) = 0.962, X(CO_2) = 0.019 and X(CH_4) = 0.019 (Valley *et al.*, 1985; Connolly and Cesare, 1993). Despite being a volumetrically minor mineral phase in the lower basement-derived metasediments, the presence of vesuvianite in the calc-silicate rock (see Chapter 2, Section 2.3.1.4) limits the minimum fluid X(H_2O) value to 0.8 (Valley *et al.*, 1985).

Middle to upper amphibolite facies peak metamorphism is observed in the mineral parageneses in the mica schist, amphibolites and calc-silicate rock, with the presence of vesuvianite suggesting a temperature greater that 600°C (Valley *et al.*, 1985). A peak temperature close to the transition from epidote-amphibolite facies to amphibolite facies is suggested by the hornblende-plagioclase±epidote peak assemblage in the amphibolite, where plagioclase is andesinitic (An_{37-42}), epidote has low Ps values (Ps_{19-24}) and titanite is observed (Maruyama *et al.*, 1983; see Section 4.3.2). These temperatures exceed the upper stability limit of chlorite, with final chlorite break down at ~600°C for rocks experiencing intermediate-pressure metamorphism (Spear and Cheney, 1989; Powell and Holland, 1990). However, the coexistence of chlorite and

muscovite in the basement mica schists (see Chapter 2, Section 2.3.1.1) suggests that peak temperatures must have either remained low enough to prevent the melting or subsolidus breakdown of muscovite to K-feldspar (e.g. Fleet *et al.*, 2003), or that chlorite formed as a result of retrogressive metamorphism; the latter corresponds with petrographic observations within the lower basement-derived metasediments. Additionally, the presence of only trace amounts of biotite and garnet in the granites suggests that melting responsible for their formation closely approximated the system $CaO\text{-}K_2O\text{-}NaAlO_2\text{-}Al_2O_3\text{-}SiO_2\text{-}H_2O$ (CKNASH; see Figure 4.9) of Thompson and Tracy (1979). By considering the effects of $X(H_2O)$ and CaO on the minimum granite solidus, the maximum possible metamorphic temperatures experienced by the Eyreville-B borehole core target rocks can be constrained. The melting reaction is displaced up-temperature when involving plagioclase compositions $\geq An_{40}$ (Thompson and Tracy, 1979), and the invariant point is displaced up-pressure by 0.07 GPa in graphite-bearing metapelites (Ashworth and Tyler, 1983; Figure 4.9). It must be remembered, however, that the intrusive nature of the lower basement-derived granite implies that it likely originated at deeper and hotter levels prior to intruding upwards into the mica schists. The absence of in situ melting of the mica schists in the granites leads to the conclusion that the metamorphic thermal peak did not exceed ~650-670°C in the lower basement-derived mica schists.

Althaus (1967) observed that polymorph transformations in the Al_2SiO_5 system are characteristically sluggish below 1 GPa, with sillimanite preferring to nucleate on micaceous minerals (e.g. biotite; Foster, 1977) rather than andalusite or kyanite. However, this transformation may have been aided by either (a) synmetamorphic shear strain, where deformation has provided the pathway for the kyanite-to-sillimanite metamorphic transformation (see Chapter 2, Section 2.4; Rutter and Brodie, 1995), or (b) sillimanite may have formed from another aluminosilicate (e.g. staurolite) via a prograde reaction, such as muscovite + staurolite + chlorite + quartz = aluminosilicate + biotite + H_2O. If the latter scenario is true, the pressure would be constrained at the point where the above reaction meets the andalusite-sillimanite boundary (Figure 4.9). Despite debate regarding the exact location of the andalusite-sillimanite boundary

(see Figure 4.9 caption), the higher pressure triple point is favoured by Pattison and Tracy (1991) for fibrolite formation, which, if the assumption that the fibrolitic knots formed after staurolite is true, places a lower pressure limit of ~0.4 GPa on the prograde *P-T* path in the basement mica schists (Figure 4.9). With regards to the Eyreville-B granites, the average granitic bulk rock compositions (see Chapter 3, Table 3.4) suggest that melting occurred at middle- to shallow-crustal levels (0.2-0.5 GPa) in a H_2O-undersaturated system (see Figure 3.23b; Johannes and Holtz, 1990).

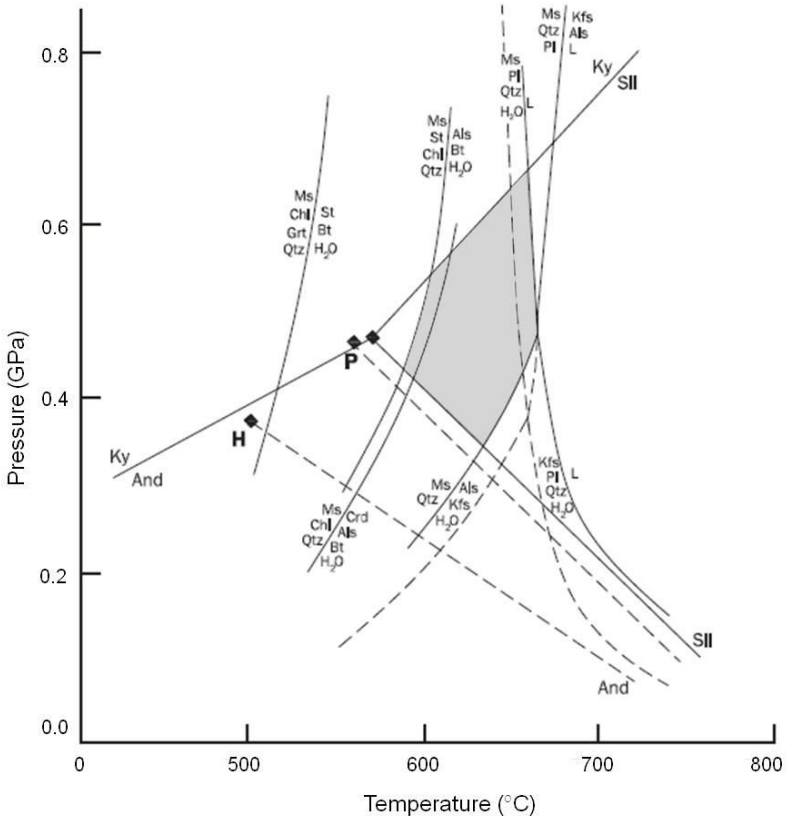

Figure 4.9: *P-T* diagram indicating the relative positions of reactions occurring within the lower basement-derived mica schists within the CKNASH system (modified after Pattison and Tracy, 1991) with the Als phase boundaries (after Holland and Powell, 1998) superimposed. Dashed lines represent the fluid-present Ms melting curves within the CKNASH system (Thompson and Tracy, 1990). Solid lines represent the displaced Ms melting curves where the fluid is in equilibrium with Gr at X(H_2O) = 0.8 (Ashworth and Tyler, 1983). Grey area represents the probable *P-T* conditions, based on mineral stability, under which the basement mica schists formed. P (after Pattison, 1992) and H (after Holdaway, 1971) are triple points that delimit the possible range in *P-T* space for the And-Sil transition as discussed in Pattison and Tracy (1991). Abbr.: Als = aluminosilicate; And = andalusite; Bt = biotite; Chl = chlorite; Crd = cordierite; Gr = graphite; Grt = garnet; Kfs = K-feldspar; Ky = kyanite; L = liquid; Ms = muscovite; Pl = plagioclase; Qtz = quartz; Sil = sillimanite; St = staurolite.

4.3.3 Methodology

A number of geothermometers and geobarometers were applied to the Eyreville-B target rocks. The geothermometers used include Zr-in-rutile thermometry (Zack *et al.*, 2004a; Tomkins *et al.*, 2007), the Grt-Bt mineral pair (Thompson, 1976; Holdaway and Lee, 1977; Ferry and Spear, 1978; Perchuk and Lavrenteva, 1983; Dasgupta *et al.*, 1991; Bhattacharya *et al.*, 1992) and the Hbl-Pl mineral pair (Blundy and Holland, 1990; Holland and Blundy, 1994). The geobarometers used include GASP (garnet-aluminosilicate-quartz-plagioclase; Holland and Powell, 1998) and GPMB (garnet-plagioclase-muscovite-biotite; Holland and Powell, 1998). Based on the geothermometers and geobarometers implemented, the following eight samples were analysed in this study: RG48, RG53, RG54 and RG57 (from the lower basement-derived mica schist), RG40a (from the lower basement-derived granite), RG51 (from the lower basement-derived para-amphibolite) and W51 and W52 (from the upper amphibolite megablock). Table 4.4 lists the geobarometers and geothermometers applied to each of these samples. In addition to the above, samples RG40 (from the lower basement-derived granite), RG53 (from the lower basement-derived mica schist) and W52 (from the upper megablock amphibolite) were selected for *P-T* phase equilibria modelling.

4.3.3.1 Zr-in-rutile geothermometry

Zr-in-rutile geothermometry was performed on two rutile-bearing samples (tourmalinite sample RG54 and tourmaline-rich mica schist sample RG57) from the lower basement-derived mica schists (see Chapter 5, Figure 5.1) using laser ablation (LA)-ICP-MS at the Institut für Geowissenschaften at the Universität Mainz, Germany (see Appendix 4a for mineral compositional data). Only euhedral prograde rutile grains were analysed. The Zr-in-rutile methodology implemented in this study follows that of Luvizotto *et al.* (2009a).

Table 4.4: Geobarometers and geothermometers used on selected samples from the Eyreville-B borehole core. Abbr.: Bt = biotite; Grt = garnet; Hbl = hornblende; Pl = plagioclase; N/A = not applicable.

Sample	Depth (m)	Geobarometer	Geothermometer
Lower basement-derived mica schists			
RG48	1652.02	GASP and GPMB	Grt-Bt mineral pair
RG53	1641.81	GASP and GPMB	Grt-Bt mineral pair
RG54	1638.97	N/A	Zr-in-rutile
RG57	1627.33	N/A	Zr-in-rutile
Lower basement-derived granite			
RG40a	1687.1	GASP and GPMB	Grt-Bt mineral pair
Lower basement-derived para-amphibolite			
RG51	1644.58	N/A	Hbl-Pl mineral pair
Upper amphibolite megablock			
W51	1377.33	N/A	Hbl-Pl mineral pair
W52	1382.97	N/A	Hbl-Pl mineral pair

A New Wave Research UP-213 (wavelength 213 nm) coupled to an Agilent 7500 ce quadruple ICP-MS was used to measure trace element concentrations. Each spot ablated for the samples was 70 µm in size with a laser energy of 3.55 J/cm^2 and a repetition rate of 10 Hz. After measuring a gas blank for 60 s, signals for each spot were recorded for 60 s. Owing to its ability to lower detection limits by a factor of 2 to 3, the carrier gas used was a He-Ar mixture (Jacob, 2006). The plasma torch conditions were optimised to ThO/Th ratios of <0.5%, with no further oxide production corrections applied. For each analysis, ^{49}Ti was used as the internal standard element and TiO_2 was assumed to 100 wt%. Rutile grains were analysed against the NIST SRM 610 glass and the rutile standard R10 (see Table 4.5; Luvizotto *et al.*, 2009a; Jochum *et al.*, 2011). Analytical precision (agreement with accepted values of standards) was better than 10%. Element concentrations were calculated using measurements from the GLITTER software for the following isotopes: ^{51}V, ^{53}Cr, ^{56}Fe, ^{90}Zr, ^{93}Nb, ^{95}Mo, ^{118}Sn, ^{121}Sb, ^{178}Hf, ^{181}Ta, ^{184}W, ^{232}Th and ^{238}U.

Temperatures were calculated using the calibration developed by Tomkins *et al.* (2007), which is based on thermometer equation 4.2 for the *α*-quartz field:

$$T = \frac{83.9 + 0.410P}{0.1428 - R\ln\emptyset} - 273 \quad (4.2)$$

thermometer equation 4.3 for the *β*-quartz field:

$$T = \frac{85.7 + 0.473P}{0.1453 - R\ln\emptyset} - 273 \quad (4.3)$$

and thermometer equation 4.4 for the coesite field:

$$T = \frac{88.1 + 0.206P}{0.1412 - R\ln\emptyset} - 273 \quad (4.4)$$

where *Ø* is Zr is in ppm, *T* is in °C, *P* is in kbar and *R* is the gas constant (0.0083144 kJ K^{-1}; after Tomkins *et al.*, 2007).

Table 4.5: Trace element compositions of the NIST SRM 610 (after Jochum *et al.*, 2011) and R10 (after Luvizotto *et al.*, 2009a) standards used for LA-ICP-MS analysis at the Institut für Geowissenschaften at the Universität Mainz, Germany.

Trace Element	NIST SRM 610 (ppm)	R10 (ppm)
V	450	1279
Zr	448	759
Nb	465	2845
Mo	417	11.2
Sb	396	2.08
Hf	435	37.2
Ta	446	384
W	444	61
Pb	426	0.081
Th	457.2	<0.0035
U	461.5	44.1

4.3.3.2 Conventional geothermobarometry

For the application of conventional geothermobarometers to the target rocks of the Eyreville-B borehole core, Excel spreadsheets, developed by THERMOCALC (Holland and Powell, 1998; http://www.earth.ox.ac.uk/~davewa/pt/th_tools.html), were used to perform the GASP and GPMB barometry (http://www.earth.ox.ac.uk/~davewa/pt/tools/pelite-barometers.xls) and Grt-Bt mineral pair thermometry (www.earth.ox.ac.uk/~davewa/pt/tools/grt-bt.xls) using mineral chemical compositions determined at the University of Pretoria (see Section 4.2.1 for mineral chemistry methodology and Appendix 4b for mineral compositional data). An Excel spreadsheet (www.minsocam.org/MSA/RIM/RiM69_Ch04_hbld_plag_thermo-jla.xls) developed by L. Anderson (2008) from the University of Southern California was used to perform Hbl-Pl thermometry (Blundy and Holland, 1990; Holland and Blundy, 1994). Table 4.6 lists the equilibrium equations on which each geobarometer/thermometer is based. Errors are calculated at 2σ.

4.3.3.3 *P-T* phase equilibria modelling

P-T phase equilibria modelling was performed on three samples (RG53 from the lower basement-derived mica schist, RG40 from the lower basement-derived granite and W52 from the upper megablock amphibolite) using the THERIAK-DOMINO software tool. Input data from XRF bulk rock compositions (see Chapter 3, Section 3.2 for XRF methodology) were converted from wt.% to mol values and then normalised to 1000 (see Table 4.7), with H_2O content calculated by the CIPW norm. The JUN92 database (after Berman, 1988), with the improved solutions models for white mica (Keller *et al.*, 2005) and chlorite (Hunziker, 2003), was used to calculate the equilibrium assemblage diagrams. For the modelling process, starting *P* was set at 0.4 GPa and *T* was set at 600°C, based on estimates determined through Zr-in-rutile thermometry and conventional geothermobarometry (see Section 4.3.4.1, 4.3.4.2 and 4.3.4.3).

Table 4.6: Equilibrium reactions for geothermometers and geobarometers used.

Name	Equilibrium reaction
Geothermometers	
Zr-in-rutile[1]	$SiO_2 + Ti_2ZrO_6 = 2TiO_2 + ZrSiO_4$ (Quartz + Srilankite = Rutile + Zircon)
Grt-Bt mineral pair[2]	$Fe_3Al_2Si_3O_{12} + KMg_3AlSi_3O_{10}(OH)_2 =$ (Almandine + Phlogopite) $Mg_3Al_2Si_3O_{12} + KFe_3AlSi_3O_{10}(OH)_2$ (Pyrope + Annite)
Hbl-Pl mineral pair[3] (Edenite-Tremolite)	$NaCa_2Mg_5Si_4(AlSi_3)O_{22}(OH)_2 + 4SiO_2 =$ (Edenite + Quartz) $Ca_2Mg_5Si_8O_{22}(OH)_2 + NaAlSi_3O_8$ (Tremolite + Albite)
Hbl-Pl mineral pair[3] (Edenite-Richterite)	$NaCa_2Mg_5Si_4(AlSi_3)O_{22}(OH)_2 + 4SiO_2 =$ (Edenite + Quartz) $Na(CaNa)Mg_5Si_8O_{22}(OH)_2 + CaAl_2Si_2O_8$ (Richterite + Anorthite)
Geobarometers	
GASP[4]	$Ca_3Al_2Si_3O_{12} + 2Al_2SiO_5 + SiO_2 = 3CaAl_2Si_2O_8$ (Grossular + Al-silicate + Quartz = Plagioclase)
GPMB-Mg[4]	$Ca_3Al_2Si_3O_{12} + Mg_3Al_2Si_3O_{12} + KAl_2(AlSi_3O_{10})(OH)_2 =$ (Grossular + Pyrope + Muscovite) $3CaAl_2Si_2O_8 + KMg_3(AlSi_3O_{10})F(OH)$ (Anorthite + Phlogopite)
GPMB-Fe[4]	$Ca_3Al_2Si_3O_{12} + Fe_3Al_2Si_3O_{12} + KAl_2(AlSi_3O_{10})(OH)_2 =$ (Grossular + Almandine + Muscovite) $3CaAl_2Si_2O_8 + KFe_3(AlSi_3O_{10})(OH)_{1.5}F_{0.5}$ (Anorthite + Annite)

References: 1 (Zack *et al.*, 2004a; Tomkins *et al.*, 2007); 2 (Thompson, 1976; Holdaway and Lee, 1977; Ferry and Spear, 1978; Perchuk and Lavrenteva, 1983; Dasgupta *et al.*, 1991; Bhattacharya *et al.*, 1992); 3 (Blundy and Holland, 1990; Holland and Blundy, 1994); 4 (Holland and Powell, 1998).

4.3.4 Results

4.3.4.1 Zr-in-rutile thermometry

Using the Tomkins *et al.* (2007) calibration (see Equations 4.2, 4.3 and 4.4) and assuming 0.4 GPa (close to the minimum pressure constraint; see Section 4.3.2), Zr-in-rutile thermometry was performed on 20 grains from sample RG54 (1638.97 m depth) and 8 grains from sample RG57 (1627.33 m depth). However, 3 grains (grains 8, 10 and 11) from sample RG57 contain

Table 4.7: Oxide wt.% and normalised mole values used for THERIAK-DOMINO modelling input data from samples RG53 (from the lower basement-derived mica schist), RG40 (from the lower basement-derived granite) and W52 (from the upper megablock amphibolite).

Oxide	RG53	RG40	W52	Element	RG53	RG40	W52
SiO_2	62.40	74.40	46.30	Si	526.70	551.98	414.31
Al_2O_3	16.40	15.30	18.80	Al	163.15	133.78	198.27
FeO	4.03	1.14	10.71	Fe	56.89	14.15	16.29
MgO	1.00	0.29	6.49	Mg	12.58	3.21	86.58
CaO	2.96	1.21	7.85	Ca	26.77	9.62	75.26
Na_2O	1.64	2.74	2.58	Na	26.84	39.41	44.76
K_2O	3.15	2.71	0.23	K	33.92	25.65	2.63
H_2O	2.72	4.49	0.30	H_2O	15.14	222.20	17.91

insufficient Zr for the application of the thermometer, which may be due to either ilmenite intergrowth with rutile or that rutile grew at the expense of ilmenite (T. Zack, 2010, personal communication). Consequently, results from these grains have not been included in the temperature estimates. A summary of the temperature results calculated at a fixed pressure of 0.4 GPa are shown in Table 4.8 (see Appendix 4a for the full analytical results). The distribution of calculated temperatures for samples RG54 and RG57 is shown in Figure 4.10.

Table 4.8: Average temperature estimates (2σ) from Zr-in-rutile thermometry for samples RG54 and RG57 from the lower basement-derived section. Temperatures calculated at a fixed pressure of 0.4 GPa.

Sample	Average Zr (ppm)	Average Temperature (°C)	Error (°C)	No. of Grains Analysed
RG54	240	606	24	20
RG57	239	606	12	4

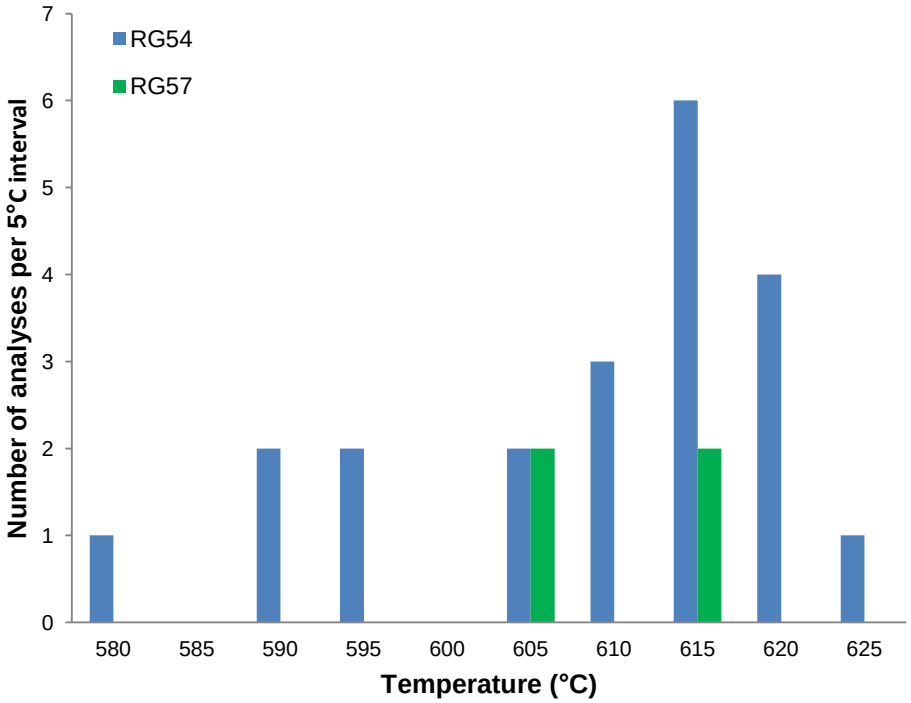

Figure 4.10: Distribution of temperatures calculated from Zr-in-rutile thermometry (assuming 0.4 GPa) for the lower basement-derived samples RG54 and RG57.

Despite the relatively large difference in data set size (n = 20 for RG54 whereas n = 4 for RG57), results from both samples indicate similar Zr contents (239-240 ppm) and peak temperatures (606°C; Table 4.8). However, sample RG54 has a much greater error (± 24 °C) than sample RG57 (± 12 °C), which may be due to the former's larger data set. Sample RG54 shows a nearly normal distribution of temperature, but does exhibit a slight skewness towards lower temperatures (Figure 4.10). Sample RG57, on the other hand, shows a uniform distribution of temperatures for its small data set (Figure 4.9). The consistency of results from both samples suggests that prograde rutile grains experienced an average thermal peak of 606 ± 18°C. This is consistent with closure temperatures for rutile in U/Pb systems estimated at ca. 600 °C (see Chapter 5, Section 5.2.2; Cherniak, 2000).

The Zr-in-rutile thermometry results were calculated using a pressure of 0.4 GPa as it is considered to represent close to the maximum pressure constraint (Section 4.3.2). Temperature calculations using slightly lower (0.3 GPa) and slightly higher (0.5 GPa) pressures did not produce results with greater than 10°C variation (see Appendix 4a). This suggests temperature results produced assuming 0.4 GPa are robust in nature. This is consistent with the geobarometry results determined for the mica schists in Section 4.3.4.3.

4.3.4.2 Conventional geothermometers

Garnet-bearing assemblages

Grt-Bt mineral pair thermometry was performed on two garnet-bearing mica schist samples, RG48 (1652.02 m depth) and RG53 (1641.81 m depth), and one granite sample, RG40a (1687.1 m depth), from the lower basement-derived section. For each sample, two Grt-Bt pairs were selected for analysis and, for each pair, mineral compositions from both garnet cores and garnet rims were used in calculations. Calculations were based on the minimum pressure constraint of 0.4 GPa (see Section 4.3.2). A summary of the results is given in Table 4.9 (see Appendix 4b for the mineral compositional data used). Temperature results based on core garnet compositions within the mineral pair are greater than those generated using rim garnet compositions (Table 4.9).

For the basement mica schist samples, temperature estimates from the Thompson (1976) and Ferry and Spear (1978) calibrations are generally the highest, whereas estimates from the Bhattacharya *et al.* (1992; after Ganguly and Saxena, 1984) calibration produce the lowest results (Table 4.9). The estimated temperatures from garnet cores in each Grt-Bt mineral pair for the samples, ranging between 517 and 685° (with 61% of results lying between 610 and 670°C; mean = 633°C; Table 4.9) are also consistently higher than those calculated for garnet rims, ranging between 451 and 620°C (with 61% of results lying between 510 and 600°C; mean = 567°C; Table 4.9). Also, temperature differences between the core and rim of a single mineral pair can be as much as 73°C (sample RG53-2), although the average temperature difference

between cores and rims is 42°C. Considering textural observations (see Chapter 2, Section 2.4.4) and mineral chemical zoning evidence (see Section 4.2.2), the temperature differences are consistent with the garnet cores preserving peak metamorphic conditions, whereas the rims likely record the retrograde path owing to partial re-equilibration.

Table 4.9: Temperature estimates from the Grt-Bt mineral pair geothermometer for samples RG48 and RG53 (from the lower basement-derived mica schist) and samples RG40a and RG46 (from the lower basement-derived granite) using seven calibrations (see footnote). Temperatures are calculated at a fixed pressure of 0.4 GPa. Abbr.: c = core; r = rim.

Sample	Temperature (°C)						
	T-76	HL-77	FS-78	PL-83	D-91	B-92-HW	B-92-GS
Lower basement-derived mica schist							
RG48-1 (c)	644	623	647	619	622	566	517
RG48-1 (r)	608	592	599	594	590	536	481
RG48-2 (c)	656	633	663	627	652	573	521
RG48-2 (r)	589	576	575	581	569	513	451
RG53-1 (c)	632	613	631	610	570	587	567
RG53-1 (r)	617	600	612	601	562	568	541
RG53-2 (c)	674	647	685	638	587	626	614
RG53-2 (r)	620	603	616	603	550	570	541
Lower basement-derived granite							
RG40a-1 (c)	639	619	640	615	499	528	427
RG40a-1 (r)	613	597	606	598	475	507	404
RG40a-2 (c)	611	595	604	596	470	499	392
RG40a-2 (r)	597	582	585	586	449	496	397

References: T-76 = Thompson (1976); HL-77 = Holdaway and Lee (1977); FS-78 = Ferry and Spear (1978); PL-83 = Perchuk and Lavrenteva (1983); D-91 = Dasgupta *et al.* (1991); B-92-HW = Bhattacharya *et al.* (1992) after Hackler and Wood (1989); B-92-GS = Bhattacharya *et al.* (1992) after Ganguly and Saxena (1984).

Temperature estimates derived from the Grt-Bt mineral pairs for the basement granite sample RG40a show the least temperature differences between garnet cores and rims and generally lie in two distinct ranges: 392-528°C and 582-640°C (Table 4.9). The lower range of temperature estimates was generated using the calibrations derived in Dasgupta *et al.* (1991) and

Bhattacharya *et al.* (1992), after Hackler and Wood (1989) and Ganguly and Saxena (1984), whereas the higher range of temperature estimates was generated using the calibrations derived in Thompson (1976), Holdaway and Lee (1977), Ferry and Spear (1978) and Perchuk and Lavrenteva (1983).

Both temperature estimate ranges are lower than expected for igneous garnets (Table 4.9), which are anticipated to yield temperatures greater than that of the minimum granite solidus, estimated at 675 ± 50°C (Kerrick, 1972; see Figure 4.9). Bhattacharya *et al.* (1992) noted that the reliability of the geothermometry results may be influenced by elevated Mn content in garnets as it affects the Fe-Mg partitioning within Grt-Bt mineral pairs. As such, the geothermometry results in the basement granite sample RG40a are expected to be inaccurate owing to the elevated Mn contents in its garnets (see Section 4.2.4). Although this is clearly the case with the lower temperature estimate range (392-528°C), temperature estimates in the higher range (582-640°C) suggest that these results are more reliable, with two calibrations (Thompson, 1976, and Ferry and Spear, 1978) for the RG40a-1 mineral pair (based on core garnet compositions) generating temperatures within error of the minimum granite solidus temperature (Table 4.9).

The smaller difference in temperature estimates based on garnet core and rim compositions (average 23°C; Table 4.9) corresponds with the chemical (lower pyrope and grossular and higher spessartine mineral chemistries for garnets in the granite compared with the mica schists (see Section 4.2.4) and textural differences compared to the mica schists (see Chapter 2, Section 2.4). These results confirm that the granite garnets are probably not xenocrystic phases from the mica schist but crystallised from the melt instead.

Amphibole-bearing assemblages

The Hbl-Pl mineral pair thermometry was applied to one para-amphibolite sample, RG51 (1644.58 m depth) from the lower basement-derived section, and two amphibolite samples, W51 (1377.33 m depth) and W52 (1382.97 m depth) from the upper amphibolite megablock. For each

sample, two Hbl-Pl mineral pairs were selected for analysis, and for each pair, mineral compositions from both plagioclase cores and plagioclase rims were used in calculations. All calculations assumed a fixed pressure of 0.4 GPa (based on the minimum pressure constraint of 0.4 GPa; see Section 4.3.2). A summary of the results is given in Table 4.10 (see Appendix 4b for the mineral compositional data used).

Temperature estimates from the Edenite-Tremolite solid solution produced much lower results than those estimated from the Edenite-Richterite solid solution (Table 4.10). Relative to the temperature constraints for the Eyreville-B target rocks in Section 4.3.2 (600-670°C), it appears that the Hbl-Pl thermometry based on the Edenite-Tremolite solid solution does not produce useable results. Temperature estimates for the lower basement-derived para-amphibolite based on the Edenite-Richterite solid solution range between 746 and 776°C for plagioclase cores and 734 and 751°C for plagioclase rims, both of which exceed the upper temperature limit of ~670°C (see Section 4.3.2). Furthermore, the Na-content of the plagioclase is considered to be too high for the application of the geothermometer (Holland and Blundy, 1994). Consequently, these results are not considered to be reliable.

Conversely, the temperature estimates based on the Edenite-Richterite solid solution for plagioclase cores from the upper megablock amphibolite range between 656 and 688°C and range between 673 and 688°C for plagioclase rims (Table 4.10). Temperatures estimates using plagioclase rims are consistently higher than those determined for plagioclase cores, which suggests that the plagioclase grains grew along the prograde path. Although these temperature results are somewhat higher than those determined for the lower basement-derived section using Zr-in-rutile thermometry (ca. 606°C; see Section 4.3.4.1), and are at the upper end of the ~670°C temperature constraint, they are still consistent with middle to upper amphibolite facies metamorphic conditions.

Table 4.10: Temperature estimates from the Hbl-Pl mineral pair thermometer (after Blundy and Holland, 1990; Holland and Blundy, 1994) for sample RG51 (from the lower basement-derived para-amphibolite) and samples W51 and W52 (from the upper amphibolite megablock). Temperatures are calculated at a fixed pressure of 0.4 GPa. Abbr.: c = core; r = rim.

Sample	Temperature (°C)	
	Edenite-Tremolite	Edenite-Richterite
Lower basement-derived para-amphibolite		
RG51-1 (c)	341	776
RG51-1 (r)	327	734
RG51-2 (c)	318	746
RG51-2 (r)	319	751
Upper amphibolite megablock		
W51-1 (c)	269	656
W51-1 (r)	276	680
W51-2 (c)	283	688
W51-2 (r)	283	688
W52-1 (c)	280	667
W52-1 (r)	282	673
W52-2 (c)	277	675
W52-2 (r)	276	673

4.3.4.3 Conventional geobarometers

The GASP and GPMB barometers were applied to two garnet-bearing mica schist samples, RG48 (1652.02 m depth) and RG53 (1641.81 m depth) and one granite sample, RG40a (1687.1 m depth), from the lower basement-derived section. For each sample, two garnet assemblages were analysed, and for each assemblage, mineral compositions from both garnet cores and garnet rims were used in calculations. A summary of the results is given in Table 4.11 (see Appendix 4b for the mineral compositional data used).

The application of the GPMB-Fe barometer on samples from both the mica schist and granite sample from the lower basement-derived section produce results that are consistently lower than those generated with the GASP and GPMB-Mg barometers (Table 4.11), with differences

between the average of the latter two barometers with the GPMB-Fe barometer ranging between 0.10 and 0.17 GPa for the mica schist samples and between 0.14 and 0.18 GPa for the granite samples. Consequently, results produced by the GPMB-Fe barometer are regarded as unreliable and they have not been used for further interpretation.

Table 4.11: Pressure estimates from the GASP and GPMB geobarometers (Holland and Powell, 1998) for samples RG48 and RG53 (from the lower basement-derived mica schist) and sample RG40a (from the lower basement-derived granite). Abbr.: c = core; r = rim.

Sample	Pressure (GPa)		
	GASP	GPMB-Mg	GPMB-Fe
Lower basement-derived mica schist			
RG48-1 (c)	0.49	0.48	0.34
RG48-1 (r)	0.51	0.48	0.35
RG48-2 (c)	0.54	0.51	0.36
RG48-2 (r)	0.33	0.32	0.20
RG53-1 (c)	0.55	0.64	0.50
RG53-1 (r)	0.51	0.59	0.45
RG53-2 (c)	0.46	0.61	0.44
RG53-2 (r)	0.39	0.49	0.36
Lower basement-derived granite			
RG40a-1 (c)	0.41	0.49	0.27
RG40a-1 (r)	0.41	0.48	0.27
RG40a-2 (c)	0.30	0.39	0.19
RG40a-2 (r)	0.24	0.36	0.16

Core pressure estimates for garnets from the mica schist samples range from 0.48 to 0.64 GPa, whereas pressure estimates for garnet rims range from 0.32 and 0.59 GPa (Table 4.11). These estimates suggest the pressure conditions under which the garnet cores formed were higher than those under which the garnet rims formed. Pressure estimates derived from garnet cores and rims in sample RG53 tend to be higher than those derived from garnet cores and rims in sample RG48 (Table 4.11), which may suggest that the latter experienced lower pressures than the former. In general, the GASP and GPMB-Mg barometers yielded pressures ≤0.5 GPa (Table

4.11) for mineral pairs from both mica schist samples, which is consistent with the upper pressure constraint in Section 4.3.2. Although it may be suggested that trends within the pressure estimates, together with trends in the temperature estimates (Section 4.3.4.2) , point toward the basement mica schists followed a clockwise *P-T* path, the large error (±0.1 GPa) for both core and rim pressure estimates precludes the ability to determine the trajectory of the *P-T* path (Table 4.11).

For the granite sample RG40a, pressure estimates determined using the GASP and GPMB-Mg barometers generally yielded lower results compared to those determined for the mica schist samples, with most estimates lying between 0.24 and 0.49 GPa (Table 4.11). They also show the least pressure differences between core and rim estimates (Table 4.11), with cores ranging between 0.30 and 0.49 GPa and rims ranging between 0.24 and 0.48 GPa. This suggests a single crystallisation phase, which is is not surprising given that garnet is interpreted as an igneous crystallisation based on textural evidence (see Section 4.3.4.2).

4.3.4.4 *P-T* phase equilibria modelling

P-T phase equilibria modelling using THERIAK-DOMINO (de Capitani and Brown, 1987; de Capitani, 1994) was applied to XRF bulk rock compositions of samples RG53 (1641.81 m depth), W51 (1377.33 m depth) and RG40 (1687.1 m depth) from the lower basement-derived mica schist, lower basement-derived granite and upper megablock amphibolite, respectively. The prograde mineral assemblage for the basement amphibolite sample RG51 could not be modelled using THERIAK-DOMINO owing to the bulk rock composition reflecting minerals from both prograde and retrograde assemblages. In Figures 4.11, 4.12 and 4.13, the modelled *P-T* diagrams for the three samples include the estimated ranges for the peak metamorphic event obtained in the conventional thermobarometry from the previous Sections 4.2.4.2 and 4.2.4.3.

In Figure 4.11, the range of *P-T* estimates from the conventional geothermobarometers plotted for the lower basement-derived mica schist sample RG53 generally corresponds with the peak metamorphic mineral assemblage observed during petrographic analysis (*P* = 0.46-0.64 GPa; *T* =

567-685°C; see Chapter 2, Section 2.3.1.1). However, a small portion of the estimated range of *P-T* conditions under which the mica schist formed includes cordierite. The only basement mica schist sample observed to possibly have once contained cordierite is the biotite schist sample RG70, where very fine-grained white mica aggregates may be pseudomorphs after highly poikilitic porphyroblasts of cordierite. If this interpretation is used, the cordierite porphyroblasts probably underwent pseudomorphism to white mica along the cooling path.

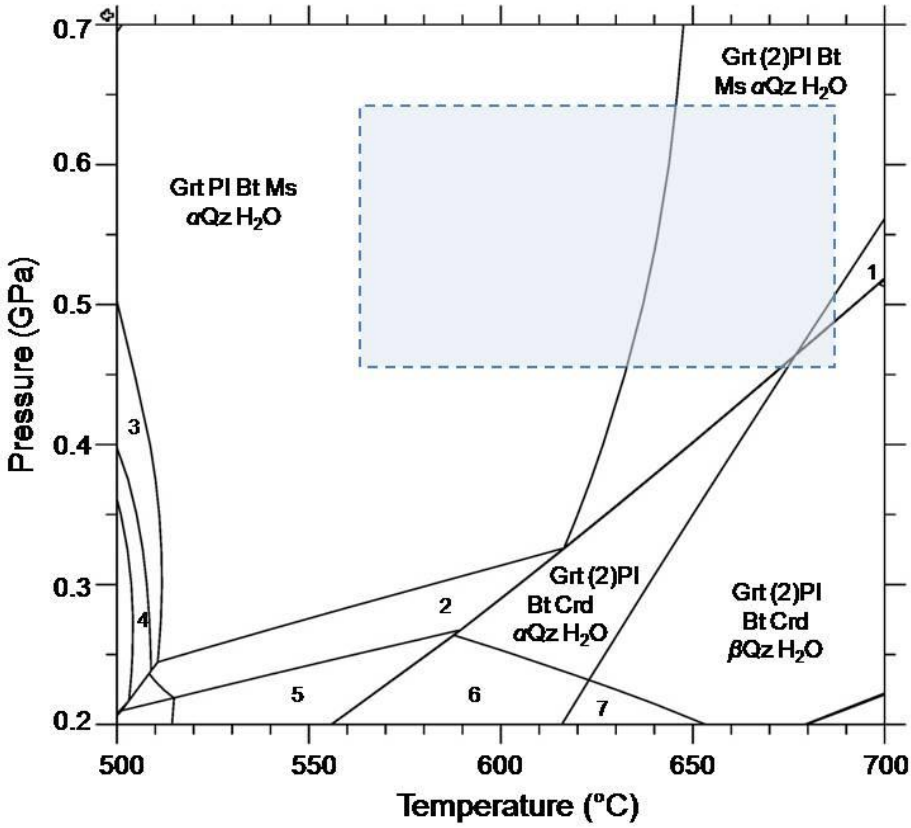

Figure 4.11: *P-T* phase equilibria diagrams using THERIAK-DOMINO for the basement mica schist sample RG53. Assemblages: 1 = Grt (2)Pl Bt Ms *β*Qz H_2O; 2 = Grt Pl Bt Ms Crd *α*Qz H_2O; 3 = Grt Pl Bt Ms Chl *α*Qz H_2O; 4 = Grt (2)Pl Bt Ms Chl *α*Qz H_2O; 5 = Pl Bt Ms Crd *α*Qz H_2O; 6 = (2)Pl Bt Crd *α*Qz H_2O; 7 = (2)Pl Bt Crd *β*Qz H_2O. Symbols: Blue shaded area/dashed line = range of estimated peak *P-T* conditions. Abbr.: Bt = biotite; Chl = chlorite; Crd = cordierite; Grt = garnet; Ms = muscovite (white mica); Pl = plagioclase; (2)Pl = albite and anorthite; Qz = quartz.

For the basement granite sample RG40 (*P* = 0.24-0.49 GPa; *T* = 582-640°C), the presence of a cordierite phase in the mid- to lower portions of the P-T estimates (Figure 4.12) does not

correspond to petrographic observations made in Chapter 2 (Section 2.3.1.6). Although it is possible that the phase was missed during petrographic analysis, the absence of cordierite in the peak mineral assemblage may provide further constraints for the *P-T* conditions under which the granite was formed. This would place the minimum pressure and temperature constraints at ~0.32 GPa and ~580°C, respectively (Figure 4.12).

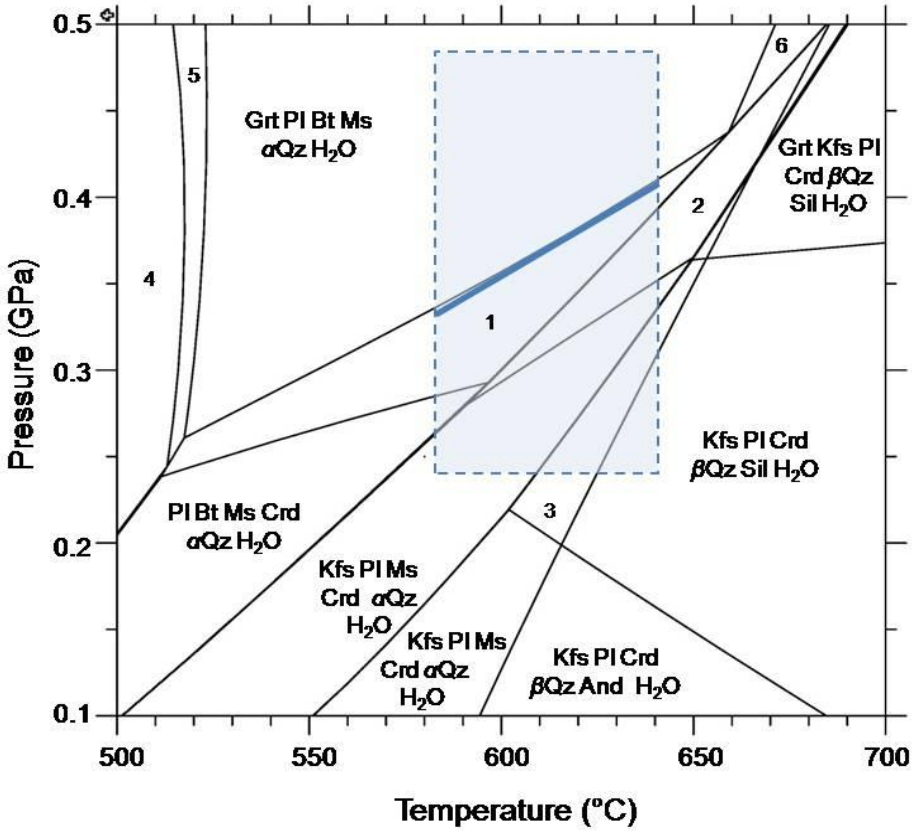

Figure 4.12: *P-T* phase equilibria diagrams using THERIAK-DOMINO for the basement granite sample RG40. Assemblages: 1 = Grt Pl Bt Ms Crd *α*Qz H_2O; 2 = Grt Kfs Pl Ms Crd *α*Qz H_2O; 3 = Kfs Pl Crd *α*Qz Sil H_2O; 4 = Pl Bt Ms Chl *α*Qz H_2O; 5 = Grt Pl Bt Ms Chl *α*Qz H_2O; 6 = Grt Kfs Pl Bt Ms *α*Qz H_2O. Symbols: Blue shaded area/dashed line = range of estimated peak *P-T* conditions; thick blue line = possible minimum *P-T* constraint. Abbr.: And = andalusite; Bt = biotite; Chl = chlorite; Crd = cordierite; Grt = garnet; Kfs = K-feldspar; Ms = muscovite (white mica); Pl = plagioclase; Qz = quartz; Sil = sillimanite.

Finally, in Figure 4.13, the phase equilibria diagram predicts that the mineral assemblage in the upper megablock amphibolite sample W51 (*estimated P* = 0.3-0.5 GPa; *T* = 656-688°C) should

include olivine and spinel, neither of which was observed during petrographic analysis (see Chapter 2, Section 2.3.2). This may suggest that either the bulk rock composition does not represent equilibrium or that the thin section cut from sample W51 does not contain the complete equilibrium mineral assemblage.

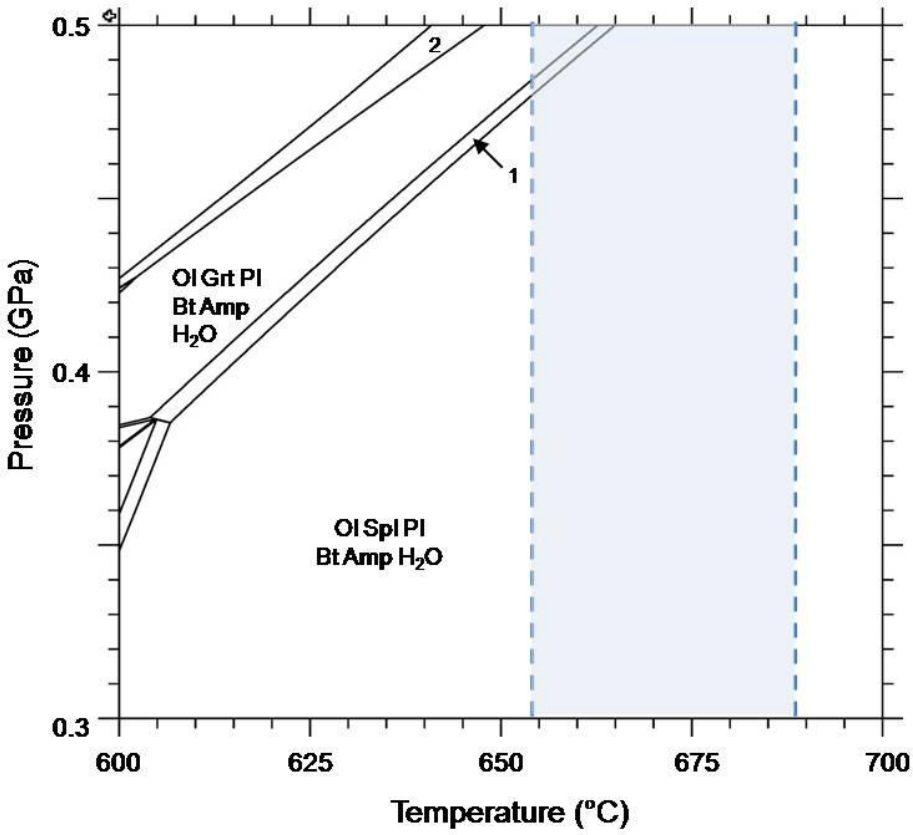

Figure 4.13: *P-T* phase equilibria diagrams using THERIAK-DOMINO for the megablock amphibolite sample W51. Assemblages: 1 = Ol Spl Grt Pl Bt Amp H_2O; 2 = Ol Grt Pl Bt Omp Amp H_2O. Symbols: Blue shaded area/dashed line = range of estimated peak *T* for *P* range of 0.3-0.5 GPa. Abbr.: Amp = amphibole; Bt = biotite; Grt = garnet; Ol = olivine; Omp = omphacite; Pl = plagioclase; Spl = spinel; Qz = quartz.

4.4 Discussion

4.4.1 Metamorphic grade

Metamorphic grade was first introduced by Tilley (1924) as a means to signify the degree of metamorphism as defined by particular pressure-temperature conditions in which the rocks

formed. Although previously considered as only a qualitative term, metamorphic grade is now determined using a variety of qualitative and quantitative methods, including index minerals and mineral zones, metamorphic facies, isograds, bathozones and bathograds, petrogenetic grids and geothermobarometry (Bucher and Grapes, 2011). In this study, metamorphic grade has been constrained by quantitative methods of geothermobarometry (Section 4.3), which was informed by mineral chemistry (Section 4.2).

Prior to the geothermobarometric analysis, however, a number of constraints on *P*-*T*-X(H_2O) were first determined (see Section 4.3.2) based on mineral assemblages found within the lower basement-derived mica schist (see Chapter 2, Section 2.3.1), upper amphibolite megablock (see Chapter 2, Section 2.3.2) and the biotite schist xenoliths in the upper granite megablock (see Chapter 2, Section 2.3.3.3) as well as their respective mineral chemistries (see Sections 4.2.2 and 4.2.3). From this it was deduced that the peak metamorphic event recorded in the lower basement-derived and upper megablock sections of the Eyreville-B borehole core had a minimum fluid X(H_2O) value of 0.8, a pressure minimum of 0.4 GPa and a temperature range between 600 and 670°C (see Section 4.3.2). Where a pressure was required to perform the Zr-in-rutile and conventional geothermometry, the 0.4 GPa constraint was used (see Section 4.3.4.1 and 4.3.4.2).

In the lower basement-derived section, the peak metamorphic temperature experienced was constrained at 606 ± 18°C using Zr-in-rutile thermometry (Section 4.3.4.1). Most of the calculated peak metamorphic temperature estimates determined for Grt-Bt mineral pairs (garnet cores) from the basement mica schist samples are approximately 20 to 40°C higher than the Zr-in-rutile thermometry results (see Section 4.3.4.2), which corresponds with the latter results reflecting a minimum peak metamorphic temperature constraint. In combination with the estimated peak metamorphic pressures (0.46-0.65 GPa; see Section 4.3.4.3), temperature estimates from both Zr-in-rutile thermometry and Grt-Bt mineral pairs are consistent with high-temperature, low pressure metamorphism at mid-amphibolite facies conditions (Eskola, 1920, 1939).

In Section 4.3.4.4, the estimated peak temperatures and pressures were overlaid on *P-T* phase equilibria modelled for sample RG53 using the THERIAK-DOMINO modelling programme (see Figure 4.11). The resultant graph confirms the broad *P-T* estimates generated by the previous geothermobarometric techniques, but it also revealed the high variance nature of the mineral assemblages and, thus, is restricted in its usefulness. And, although the pressure estimates do concur with the petrographic constraints, there is still some uncertainty as to their accuracy, for instance, whether or not fibrolite was formed after staurolite (see Figure 4.9).

With regards to the upper amphibolite megablock, temperatures estimated for Hbl-Pl mineral pairs (656-688°C) are approximately 60 to 70°C and 30 to 50°C higher than the results determined for the lower basement-derived mica schist samples using Zr-in-rutile thermometry and Grt-Bt mineral pair (garnet cores) thermometry, respectively (see Section 4.3.4.2). Despite a somewhat problematic phase equilibria graph for sample W51 (modelled using THERIAK-DOMINO; see Figure 4.13), the temperature results still broadly fall within the temperature constraints given in Section 4.3.2.

The generally lower temperature values determined for garnet rims (most estimates lying between 510 and 600°C; see Table 4.10) from the lower basement-derived mica schists are consistent with both textural (see Chapter 2, Section 2.4.4) and chemical zoning (Sections 4.2.2 and 4.2.3) observed within garnet porphyroblasts associated with the retrograde mylonitic foliation. In Chapter 2, Section 2.4, the presence of certain microstructures in the mylonitised granite (e.g. bookshelf sliding, feldspar subgrain aggregates, neoblastic tails of biotite and chlorite-rich subhorizontal shears) as well as the extensive chlorite-sericite alteration of the mica schists suggests mylonitisation ceased under greenschist facies conditions (Gaipas, 1989), which typically occurs in the 300-500°C range (Eskola, 1939; Bucher and Grapes, 2011).

4.4.2 Geothermal gradient and possible metamorphic evolution

The geothermal gradient of a given continental region is defined as the variation of temperature with depth (e.g. Winter, 2001; van der Pluijm and Marshak, 2004; DiPietro, 2012). Using the temperatures and pressures determined in Section 4.3, the geothermal gradient for the Eyreville-B target rocks can be estimated. By extrapolating from the lower pressure limit of 0.4 GPa (see Section 4.3.2), the metasediments in the lower basement-derived section are interpreted to have experienced peak metamorphism at a depth of ~14 km. This translates into a minimum peak metamorphic geothermal gradient of ~44°C/km (ca. 606°C), which is significantly higher than the average continental geothermal gradient, estimated at 20°C/km (Brown and Mussett, 1993).

Sandiford *et al.* (1998) observed that metamorphism at abnormally high geothermal gradients (>40°C/km) generally results in intermediate- to high-temperature, low-pressure metamorphism at mid- to shallow crustal levels. High-temperature, low-pressure metamorphism has been described in a variety of tectonic settings, including arc-continent and continent-continent collisions, island-arc complexes, volcanic arcs on continental margins, arch-trench systems, back-arc basins and rift settings (De Yoreo *et al.*, 1991, and references therein), which suggests that a single common cause for this type of metamorphism is unlikely (Brown, 1993). Determining the mechanisms through which extreme thermal anomalies are produced to generate the abnormally high geothermal gradients (and the resulting high-temperature, low-pressure metamorphism) has been the subject of many studies (e.g. Oxburgh and Turcotte, 1970, 1971; Lux *et al.*, 1986; England and Thompson, 1984, 1986; Sandiford and Powell, 1986; Wickham and Oxburgh, 1987; Barton and Hanson, 1989; Hanson and Barton, 1989; Loosveld, 1989; Loosveld and Etheridge, 1990; Sandiford *et al.*, 1998), with many authors agreeing that transient advective processes, such as magma ascent and abnormally high heat flows from the mantle, provide much of the heat required to form high-temperature, low-pressure metamorphic conditions (Sandiford *et al.*, 1998). If it is assumed that the lower basement-derived section and upper megablocks of the Eyreville-B borehole core form part of a single metamorphic terrane (see Section 4.4.3), the basement granite and massive megablock granite would provide advective

heat as rising magmas during the M1 metamorphic event (see Chapter 2, Section 2.5). However, other parameters that can be used to provide more information about a high-temperature, low-pressure metamorphic event, including the determination of the trajectory of *P-T* paths and the relative timing of deformation, metamorphism and plutonism (Gibson, 1991), require a study area in which various scenarios can be tested. Consequently, further interpretations of the M1 event within the Eyreville-B borehole core are made in Chapter 6 (Section 6.5), where comparisons are made with surrounding terranes.

4.4.3 Terrane relationships

The information derived from mineral chemistry and geothermobarometry enabled the determination of metamorphic grade and geothermal gradient, components that significantly increase the ability to understand the complex history represented in rocks from the lower basement-derived and upper megablock sections of the Eyreville-B borehole core. This information, combined with results from the other chapters of this study, can be used to ascertain whether these two lithic sections, separated by approximately 154 m of intervening suevitic and lithic impact breccia within the Eyreville-B borehole core (see Chapter 1, Figure 1.15), are in fact related (i.e., formed part of the same terrane).

In Chapter 3 (Section 3.3.3), bulk rock geochemistry revealed that the lower basement-derived and upper megablock granites are calc-alkaline in nature (Figure 3.6), and in Section 3.6.3, that all three granites were emplaced at similar shallow crustal levels (Figure 3.23b). However, in Sections 3.3.3 and 3.6.3 (Figures 3.5, 3.22 and 3.23a), geochemistry also revealed that the lower basement-derived granite is an S-type, metaluminous-to-peraluminous granite that was emplaced in a within-plate tectonic setting, whereas the massive and gneissic megablock granites are I-type, metaluminous granites emplaced in a syn-collisional tectonic setting. Although it is tempting to disregard the latter geochemical dissimilarities between the granites based on the uncertainty of whether the basement granite geochemical results are representative of the rock unit (owing to the very coarse-grained to pegmatitic nature of the basement granite combined with the small

core sample size; see Chapter 2, Section 2.3.1.6 and Chapter 3, Section 3.3.3), petrographic observations indicating that the dominant mica is muscovite corresponds with the basement granite having evolved from a sedimentary source (Chappell *et al.*, 1998). A possible scenario for both the basement S-type and massive megablock I-type granites to have crystallised concurrently (based on geochronological evidence; see Chapter 5, Sections 5.1 and 5.4) is the branch of granite from the parental I-type metaluminous magma may have possibly experienced contamination through the assimilation of reduced and peraluminous sediments as it ascended in the crust (Shearer and Robinson, 1988). Alternatively, melting of separate igneous (e.g. amphibolite) and sedimentary (e.g. pelite) sources produced both I-type and S-type granites, respectively (Chappell and White, 1974).

The two I-type, metaluminous granites in the upper megablock also have dissimilarities, with structural observations of the massive granite intruding the gneissic granite indicating that the latter was the first to crystallise (see Chapter 2, Section 2.3.3). Geochronological studies by Horton *et al.* (2009b) have determined the age of the older, gneissic megablock granite to be 615 ± 7 Ma, thus it probably formed the basement of the terrane, whereas the age of the younger massive granite is 254 ± 3 Ma (see Chapter 5, Section 5.1). Thus, despite the geochemical similarities, the granites were formed and emplaced in two distinct events. U/Pb geochronology performed on rutiles from the lower basement-derived mica schist, however, indicate that peak metamorphism in the lower basement-derived section occurred between 246 and 272 Ma (see Chapter 5, Section 5.2.2), which includes the ca. 254 Ma crystallisation age of the massive megablock granite. This implies that the massive megablock granite intruded and crystallised within the gneissic megablock granite close to peak-metamorphic conditions in the lower basement-derived metasediments succession, which suggests that the upper granite megablock and lower basement-derived section experienced the same metamorphic event (see Chapter 5, Section 5.4). Consequently, the geochronological evidence suggests that the basement granite and massive megablock granite were generated during M1 (see Chapter 2, Section 2.5), intruding into a metamorphic terrane with a gneissic granite basement.

Based on the above conclusion, the lower basement-derived metasediments and the biotite schist xenoliths of the upper granite megablock also should have formed part of the same terrane. However, geochemical analysis (see Chapter 3, Section 3.6.1) revealed that the protoliths for the lower basement-derived metasediments were probably deposited in either a mature island arc or immature magmatic arc tectonic setting (Roser and Korsch, 1986, 1988), whereas the significant component of old continental crust identified within the upper megablock biotite schist xenoliths (see Chapter 3, Section 3.6.1) suggests that the protoliths were most likely deposited during the recycling of a complex orogenic belt (Roser and Korsch, 1988; Simpson, 2010) prior to their incorporation into the magma that gave rise to the massive megablock granite. Thus, despite the fact that both rock units form part of single terrane together with the three granites, their protoliths indicate at least two distinct depositional tectonic settings.

Finally, the upper amphibolite megablock can be linked to the lower basement-derived and upper granite megablocks in at least two ways. Firstly, the amphibolite megablock's amphibolite-facies mineralogy (see Chapter 2, Section 2.3.2) combined with similar estimated temperatures (see Section 4.3.4.2) and cooling ages for amphibole and white mica (see Chapter 5, Section 5.3) suggest it experienced similar peak metamorphic conditions to the lower basement-derived section. The slightly higher temperature estimates determined for the amphibolite megablock compared with temperature estimates for the lower basement-derived mica schists may suggest a slightly deeper level of exhumation for the amphibolite megablock, although errors are considerable. Second, a brecciated granite vein (sample RG04; see Chapter 2, Section 2.3.2) observed to intrude the amphibolite megablock is very similar in mineralogy and texture to what is observed for the massive megablock granite. Although gabbroic and granitic material can evolve from the same parental magma owing to fractional crystallisation (e.g. Winter, 2001), in Chapter 3 (Sections 3.3.3 and 3.6.2), geochemistry revealed that the amphibolite megablock was derived from a tholeiitic magma series, whereas the massive megablock granite was derived from a calc-alkaline magmatic series. Hunter (1998) observed that both tholeiitic and calc-alkaline magmatic series can coexist at similar crustal levels by means of either shallow intracrustal processes or

deep mantle wedge processes. Thus, if the brecciated granite vein within the amphibolite megablock is related to the massive megablock granite, the latter may have been derived from the same tholeiitic parental magma as the megablock amphibolite, with the massive granite subsequently evolving into a calc-alkaline magmatic series. Alternatively, the parental magmas for the precursor to the amphibolite megablock and massive megablock granite are unrelated, evolving separately from each other to similar crustal levels.

Another possibility is that the amphibolite megablock formed part of an ophiolitic complex that was tectonically juxtaposed onto the terrane basement (i.e. the gneissic megablock granite). Geochemistry in Chapter 3 suggested that the precursor to the amphibolite megablock was most likely gabbroic in nature with a minor dioritic component (Section 3.6.2; Figure 3.19). These findings correspond with petrographic observations in Chapter 2 that revealed a grading from gabbro into diorite at the base of the amphibolite megablock (Section 2.3.2). This may be interpreted to reflect a transition from mafic rocks towards more felsic rocks, which is commonly observed within ophiolite complexes, such as the Halifax County Complex (Kite and Stoddard, 1984) and the California Coast Range ophiolite (Hopson *et al.*, 2008). If this is the case for the amphibolite megablock, the ophiolite may have been obducted onto the gneissic megablock granite, which is interpreted to form the basement of the terrane, and later intruded by the massive megablock granite as the latter crystallised.

4.5 Summary

Mineral chemistry (Section 4.2) from the various crystalline rocks types of the lower basement-derived and upper megablocks sections of the Eyreville-B borehole core provides insight into the differences between seemingly similar rock units as well as providing the input data for geothermobarometry (Section 4.3). The mineral assemblages have also been used to determine *P*-*T*-X(H_2O) constraints for the lower basement-derived and upper megablocks sections prior to

the application of the various geothermobarometric techniques, which have constrained X(H_2O) to 0.8, *P* to >0.4 GPa and the *T* range to 600-670°C (Section 4.3.2).

Using the 0.4 GPa pressure constraint, a thermal peak of 606 ± 18°C for the metamorphic event recorded in the lower basement-derived section was determined using Zr-in-rutile thermometry (Section 4.3.4.1), whereas geothermometry performed on Grt-Bt mineral pairs (cores) from two metapelite samples for all calibrations (see Table 4.9) estimated temperatures to be mostly between 610 and 670°C (mean = 633°C; Section 4.3.4.2). Hbl-Pl mineral pairs from the amphibolite megablock estimated temperatures for the peak metamorphic event to range between 656 and 688°C (Section 4.3.4.2), which may suggest a deeper level of exhumation compared with the lower basement-derived mica schists. GASP and GPMB barometry estimated a peak metamorphic pressure range between 0.44 and 0.64 GPa for the lower basement-derived section (Section 4.3.4.3), which is consistent with the constraints given in Section 4.3.2. Although *P-T* phase equilibria diagrams broadly confirm the peak *P-T* estimates (Section 4.3.4.4), the high variance mineral assemblages restrict their usefulness in further interpretations. Both estimated temperatures and pressures determined for the lower basement-derived section based on garnet cores confirm that these rocks experienced a mid-amphibolite facies, mid-crustal, peak metamorphic event (Section 4.4.1). The lower temperature and pressure estimates using garnet rims (Sections 4.3.4.2 and 4.3.4.3) may be reflecting cooling as part of the retrograde S1b mylonitic event. This corresponds with textural and microstructural evidence (see Chapter 2, Section 2.4), which suggests retrograde metamorphism terminated under greenschist metamorphic conditions.

Using the minimum pressure constraint of 0.4 GPa (Section 4.3.2), the geothermal gradient during the metamorphic event recorded in the lower basement-derived and upper megablocks sections of the Eyreville-B borehole core approached ~44°C/km (Section 4.4.2), which generally produces intermediate- to high-temperature, low-pressure metamorphism at mid- to shallow crustal levels (Sandiford *et al.*, 1998). Based on the fact that such metamorphic can conditions

can occur in a wide variety of tectonic environments (De Yoreo *et al.*, 1991) as well as the fact that the tectonic context is missing from the lower basement-derived section and upper megablocks of the Eyreville-B borehole core, further discussion regarding the M1 event continues in Chapter 6, where comparisons with surrounding terranes are made.

Based on the data in chapters 2 to 5, it appears that the crystalline rocks of the lower basement-derived and upper megablocks sections of the Eyreville-B borehole core formed part of single terrane prior to the Chesapeake Bay impact (see Section 4.4.3; Figure 4.14). The lower basement-derived section and upper granite megablock are linked mainly by geochronology, with the crystallisation age of the massive megablock granite (ca. 254 Ma; Horton *et al.*, 2009b) corresponding to the estimated time-span of the prograde-to-peak metamorphic event within the lower basement-derived section (246-272 Ma; see Chapter 5, Section 5.2.2). The age of the gneissic megablock granite (ca. 615 Ma; Horton *et al.*, 2009b) suggests that it formed the basement for the terrane prior to the intrusion of the massive megablock granite. As for the upper amphibolite megablock, it can be linked to the lower basement-derived section through geothermobarometry (Section 4.4.1) and geochronology (Chapter 5, Section 5.4) and to the upper granite megablock by petrographic evidence from the intruding granitic vein interpreted to be related to the massive megablock granite (Chapter 2, Section 2.5.2).

5 GEOCHRONOLOGY

5.1 Introduction

The previous chapters have shown that the Eyreville-B borehole core intersects a variety of metasediments, meta-mafic rocks and granite whose inter-relationships are partially obscured by the disruption caused or complicated by the impact event. Whilst the lower basement-derived granite intruded into the mica schists and structural relationships suggest it crystallised close to the metamorphic peak, its relationship to the massive and gneissic granite varieties of the upper megablock could not be determined. Similarly, although the amphibolite megablock shows a similar metamorphic grade to the lower basement-derived mica schists, no structural relationships could be established to confirm that the metamorphism occurred during a single event. Horton *et al.* (2009b) established zircon U/Pb SHRIMP (Sensitive High Resolution Ion Microprobe) ages that showed the megablock massive granite crystallisation age to be 254 ± 3 Ma, considerably younger than that of the gneissic granite; their Ar/Ar cooling ages for white mica in a different granite pegmatite from the lower basement-derived section showed an age 10 Ma younger (244.1 ± 1.3 Ma; Horton *et al.*, 2009b). This study aims to determine the following for the target rocks of the Eyreville-B borehole core:

(a) The timing of peak metamorphic conditions;

(b) The approximate cooling history for retrograde metamorphic conditions; and

(c) The age inter-relationships between the different rock units.

Two geochronological techniques have been applied to rocks from the amphibolite megablock and the lower basement-derived section of the Eyreville-B borehole core. The two granite varieties of the upper granite megablock were dated by Horton *et al.* (2009b) using the zircon U/Pb SHRIMP method, and have been excluded from this study but are discussed with this study's results in Section 5.4. Motivations for the use of the rutile U/Pb and Ar/Ar geochronological techniques follow.

Compared with zircon and monazite, rutile contains low U concentrations (as little as <0.01 ppm); consequently, the mineral has been less commonly used as a geochronometer (Zack *et al.*, 2011). Reasons for employing the rutile U/Pb geochronometer include (1) the fact that since rutile is assumed to be unstable under low-grade metamorphic conditions, the mineral does not contain any inherited cores from older events (Zack *et al.*, 2004b; Stendal *et al.*, 2006); and (2) Zr in rutile is very sensitive to temperature in rutile-zircon-quartz assemblages, allowing for examination of both age and temperature information within texturally-constrained minerals (Zack *et al.*, 2004a; Watson *et al.*, 2006; Tomkins *et al.*, 2007). In this study, the presence of euhedral rutile grains in the tourmaline-rich mylonite zone (see Chapter 2, Sections 2.3.1.5, 2.3.1.7 and 2.4.1; Figure 5.1) coupled with the scarcity of zircon (Horton *et al.*, 2009a) in the rocks from the lower basement-derived section, motivated for the use of rutile U/Pb geochronology.

Used for both igneous and metamorphic applications, the Ar/Ar geochronometer is a particularly effective geochronometer as it involves a noble, unreactive gas, and has a relatively simple diffusion behaviour (Braun *et al.*, 2006). The geochronometer is able to precisely measure radiogenic Ar since the element is sufficiently rare in rocks (despite it being a secondary constituent of the earth's atmosphere at ~1 wt.%) and is assumed to be absent in the crystal structure at mineral formation (Braun *et al.*, 2006). Motivation for the use of the Ar/Ar geochronometer in this study is due to the abundance of K-rich minerals (e.g. white mica, biotite, amphibolite and K-feldspar which contain elevated levels of ^{39}Ar derived from ^{39}K during irradiation; Scherer, 2007) in the mica schist and granite of the lower basement-derived section and the amphibolite in the upper amphibolite megablock.

The rutile U/Pb and Ar/Ar dating techniques use the concept of thermochronology to determine the apparent age of a rock. In their pioneering studies, Armstrong (1966) and Harper (1967) established that radiometric dating of metamorphic minerals from orogenic belts generally reflect their cooling or thermal histories rather than the age of crystallisation (Dodson, 1979).

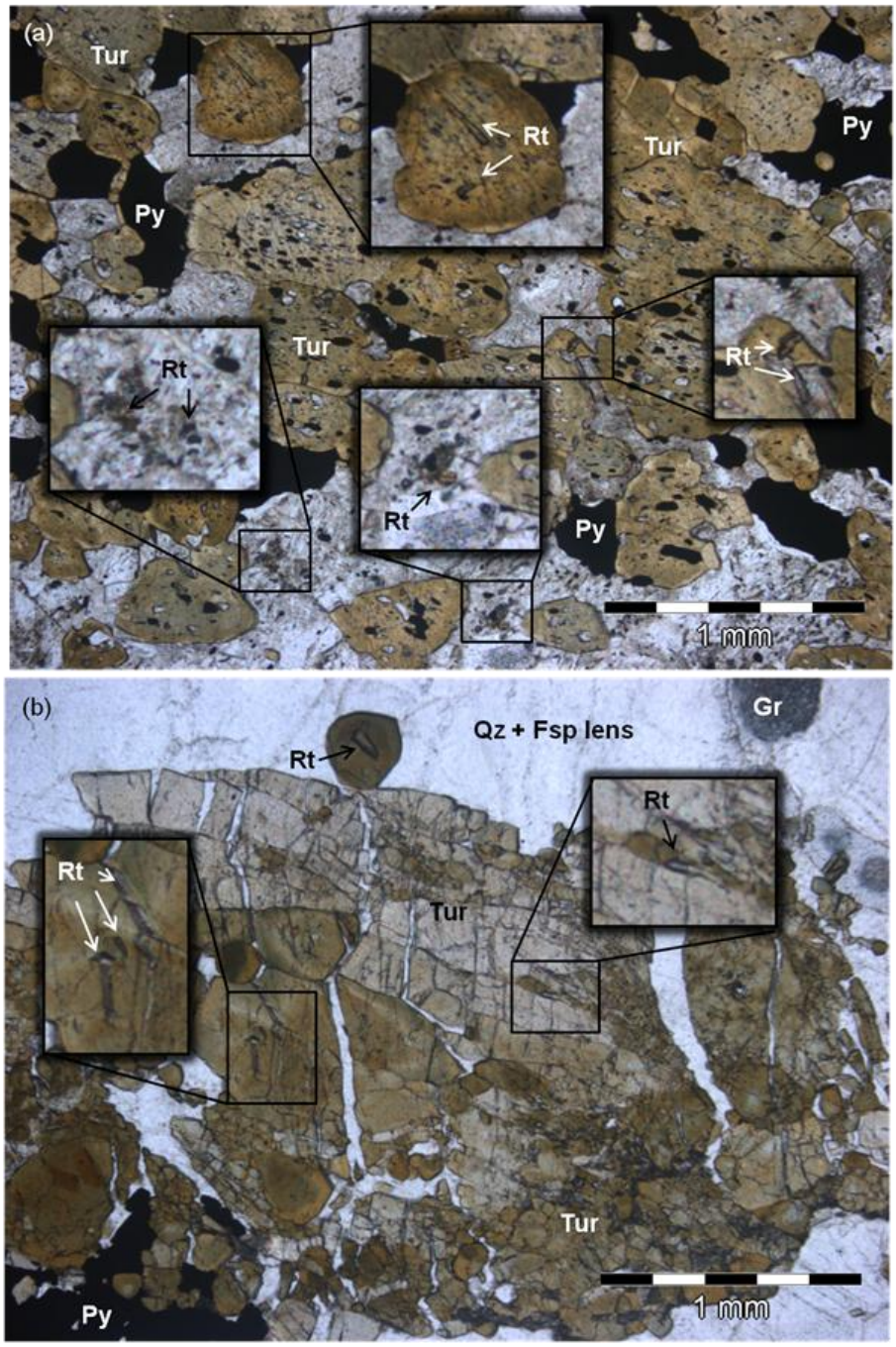

Figure 5.1: Photomicrograph of (a) RG54 (tourmalinite) and (b) RG57 (tourmaline-rich schist) showing the rutile-bearing mineral assemblages. Abbr. (after Siivola and Schmid, 2007; Whitney and Evans, 2010): Fsp – feldspar; Gr – graphite; Py – pyrite; Qz – quartz; Rt – rutile; Tur – tourmaline.

Thermochronology permits the extraction of information regarding a rock's thermal history and is based on the "interplay between the accumulation of daughter product through a nuclear decay reaction in the rock and the removal of daughter product by thermally activated diffusion" (Braun *et al.*, 2006). In the case of the rutile U/Pb method, ^{238}U is the parent to ^{206}Pb (daughter) and ^{235}U is the parent to ^{207}Pb (daughter), whereas for the Ar/Ar method, ^{40}Ar (parent) decays to ^{39}Ar (daughter). Every isotopic system will act as an open system at high temperature (where the daughter product is removed by diffusion more rapidly than it is produced by nuclear decay); as temperature falls, diffusion slows resulting in the retention of progressively larger amounts of the daughter product in the host mineral (Dodson, 1973; Kelley, 2002; Braun *et al.*, 2006). The partial retention zone is a discrete temperature interval at which the switch from open to closed system behaviour occurs (Braun *et al.*, 2006). The temperature at which a system has sufficiently cooled to a point where the diffusion of parent or daughter isotopes out of the system and into the external environment no longer takes place is described as that system's closure temperature (Dodson, 1979; Braun *et al.*, 2006). This is significant as the mineral isotope ratios fixed at the time at which a system (or mineral) reaches its closure temperature will define that system's apparent age (Dodson, 1973). Thus, the knowledge of closure temperatures for the relevant minerals is essential to deciphering the thermal history of the rocks in question.

5.2 Rutile U/Pb geochronology

Rutile is a highly stable mineral during weathering, transport and diagenesis and it is a common component of heavy mineral deposits (Hubert, 1962; Force, 1980; Morton and Hallsworth, 1994). It is also a widely distributed accessory mineral in greenschist to eclogite and granulite facies metamorphic rocks (Luvizotto and Zack, 2009; Meinhold, 2010; Zack *et al.*, 2011). With increasing metamorphism, rutile forms at the expense of ilmenite from low to medium-grade metamorphic conditions (Figure 5.2; Luvizotto *et al.*, 2009b; Meinhold, 2010) such as those observed in the lower basement-derived section of the Eyreville-B borehole core. Demonstrated

to yield precise U/Pb ages, this technique is becoming more popular due to its relative low cost and high throughput of reliable data (Mezger *et al.*, 1989; Zack *et al.*, 2011).

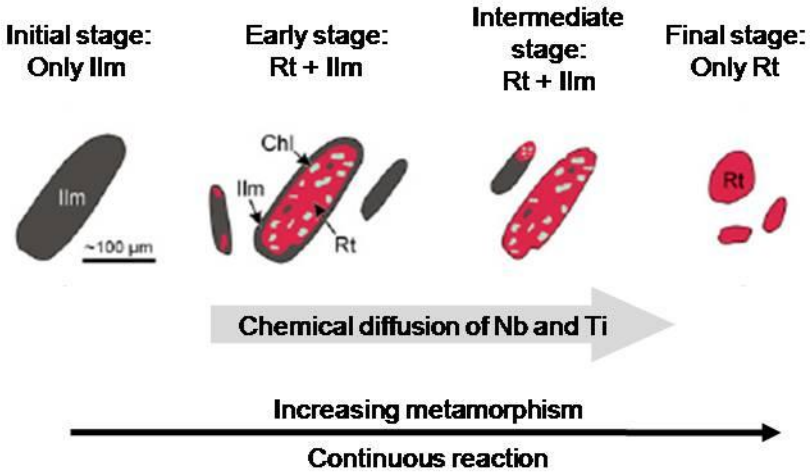

Figure 5.2: Schematic of the prograde formation of rutile from ilmenite under low- to medium-grade metamorphic conditions (after Luvizotto *et al.*, 2009b, and Meinhold, 2010). Abbr. Chl = chlorite; Ilm = ilmenite; Rt = rutile.

5.2.1 Methodology

Rutile is a common accessory phase in the lower basement-derived section, occurring in 11 samples (see Chapter 2, Section 2.3.1). Textural relationships indicate that the rutile formed under prograde to peak metamorphic conditions (e.g. euhedral rutile inclusions in plagioclase porphyroblasts aligned to the foliation inferring rutile mineral growth occurring concurrently with plagioclase mineral growth, etc.; see Chapter 2, Section 2.4.1; Meinhold, 2010). Two samples were identified for U/Pb rutile analysis from the mylonite section of the lower basement-derived section: RG54 (tourmalinite) and RG57 (tourmaline-rich mica schist); these samples were selected due to their relatively abundant rutile component. As discussed in Chapter 2, Section 2.5, the tourmaline mineralisation may have formed either by fluid escape from the nearby post-peak granite pegmatite veins of the mylonite zone, or tourmaline metasomatism may have accompanied mylonitisation. The samples were prepared as polished thin sections at the SGS Lakefield Laboratories (Johannesburg, South Africa). The following methodology follows Zack *et al.* (2011).

LA-ICP-MS analyses were performed at the Institut für Geowissenschaften at the Universität Mainz, Germany, using a New Wave Nd: YAG 213 nm laser coupled to an Agilent 7500 ce quadruple ICP-MS. Cleaning was performed on the samples by polishing the surface with γ-alumina powder to remove any carbon coating, immersion in an ultrasonic bath for five minutes with milli-Q water, and drying with ethanol-soaked kimwipe. Pre-ablating the surface of the thin section with five laser pulses for 30 seconds with a slightly larger diameter than that during analysis was used to minimise common Pb (Pb which is not derived from radioactive decay of Th and/or U in the target phase) contamination during the analytical session, which may skew the analytical results. Before each analysis of 30-50 seconds of laser ablation, the background 30 seconds was measured. Rutile grains were ablated with laser beam diameters of 50-90 μm, a beam energy density of ca. 3.5 J/cm^2, and a 10 Hz repetition rate. Following ablation, the sample cell was flushed by He to carry the aerosol generated during ablation to the ICP-MS. The carrier gas was mixed with Ar prior to reaching the torch in order to produce flow rates of ca. 0.75 l/min He and ca. 0.65 l/m Ar.

Isotopes were measured in time-resolved mode (dwell times for each isotope are detailed in Table 5.1). With an additional 2 ms settling time between isotopes, it was possible to have five mass sweeps per second. This rapid scanning enabled detailed depth profiles of each spot analysis to be obtained, through which heterogeneous material could be detected and excluded. Zr, Th and U concentrations, $^{206}Pb/^{208}Pb$ ratios and $^{206}Pb/^{238}U$ ages were also calculated offline from time-resolved raw counts provided by the ICP-MS.

Owing to rutile being a low-Th phase, Pb can be accurately calculated by measuring ^{208}Pb as ^{208}Pb is not derived from radioactive decay of ^{232}Th (Zack *et al.*, 2011). Similarly, the common Pb component of ^{206}Pb and ^{207}Pb from an analysis can be calculated from given $^{206}Pb/^{208}Pb$ and $^{207}Pb/^{208}Pb$ ratios and ^{208}Pb count rate. The corrected ^{206}Pb and ^{207}Pb count rates are then used to calculate $^{207}Pb/^{206}Pb$, $^{206}Pb/^{238}U$, and $^{207}Pb/^{235}U$ ratios. The decay constants recommended by Steiger and Jäger (1977) have been used for calculating the $^{206}Pb/^{238}U$ and $^{207}Pb/^{235}U$ ages.

Concordia and the weighted $^{206}Pb/^{238}U$ ages for the rutiles analysed were calculated and graphically presented using Isoplot/Ex 3 (Ludwig, 2003; Zack *et al.*, 2011).

Table 5.1: Dwell times for isotopes.

Isotope	Dwell time(ms)
^{90}Zr	10
^{232}Th	10
^{238}U	10
^{206}Pb	30
^{207}Pb	50
^{208}Pb	50

5.2.2 Results

A total of 13 single spot U/Pb analyses were measured by LA-ICP-MS for samples RG54 (1638.97 m depth) and RG57 (1627.33 m depth). Seven rutile grains were analysed for sample RG54 and four rutile grains were analysed for sample RG57, with two of these four grains analysed twice; all grains were ~100 µm in size. Of these analyses, three were discarded owing to irregular ablation signals and a further five analyses were considered unusable owing to unusually high concentrations of common ^{208}Pb, most likely caused by surface contamination. The remaining five useable single-spot U/Pb analyses were corrected for common ^{208}Pb. A summary of the useable results are presented in Table 5.2 (see Appendix 5a for full analytical results).

The rutile U/Pb analyses from both samples were used together to calculate a pooled concordia age of 259 ± 13 Ma, MSWD (mean square of weighted deviates) = 0.054 (Figure 5.3a), with a slightly younger 258 ± 14 Ma age for the $^{206}Pb/^{238}U$ age plot (MSWD = 0.80; Figure 5.3b). Zack *et al.* (2011) noted that, when pooling ages, a 2% uncertainty/error should be added. The MSWD for the concordia age in Figure 5.3a is much lower than errors for individual analyses (Table 5.2). The very low concordia MSWD (Figure 5.3a) may point to an overestimation of errors for single

Table 5.2: LA-ICP-MS data for rutile in samples RG54 and RG57

Sample	Spot #	U (ppm)	Th (ppm)	U/Th	Ratio $^{206}Pb/^{208}Pb^{a}$	Ratio $^{207}Pb/^{235}U^{b}$	± 1 s	Ratio $^{206}Pb/^{238}U^{b}$	± 1 s	rho	Ratio $^{207}Pb/^{206}Pb^{b}$	± 1 s	Age (Ma) $^{207}Pb/^{235}U$	± 1 s	Age (Ma) $^{206}Pb/^{238}U$	± 1 s
RG54	12	13	0.305	0.024	3.7	0.298	0.106	0.0410	0.0020	0.02	0.053	0.019	265	86	259	12
	16	14	0.049	0.003	4.8	0.398	0.116	0.0435	0.0030	0.05	0.066	0.020	340	88	274	19
	18	12	0.195	0.016	2.2	0.129	0.193	0.0423	0.0029	0.00	0.022	0.033	123	190	267	18
RG57	6	27	0.156	0.006	6.5	0.288	0.071	0.0393	0.0019	0.03	0.053	0.013	257	58	249	12
	6	27	0.221	0.008	1.7	0.317	0.209	0.0405	0.0035	0.00	0.057	0.038	279	175	256	21

[a] Raw data
[b] Corrected for common Pb ($^{206}Pb/^{208}Pb$) and machine-induced fractionation

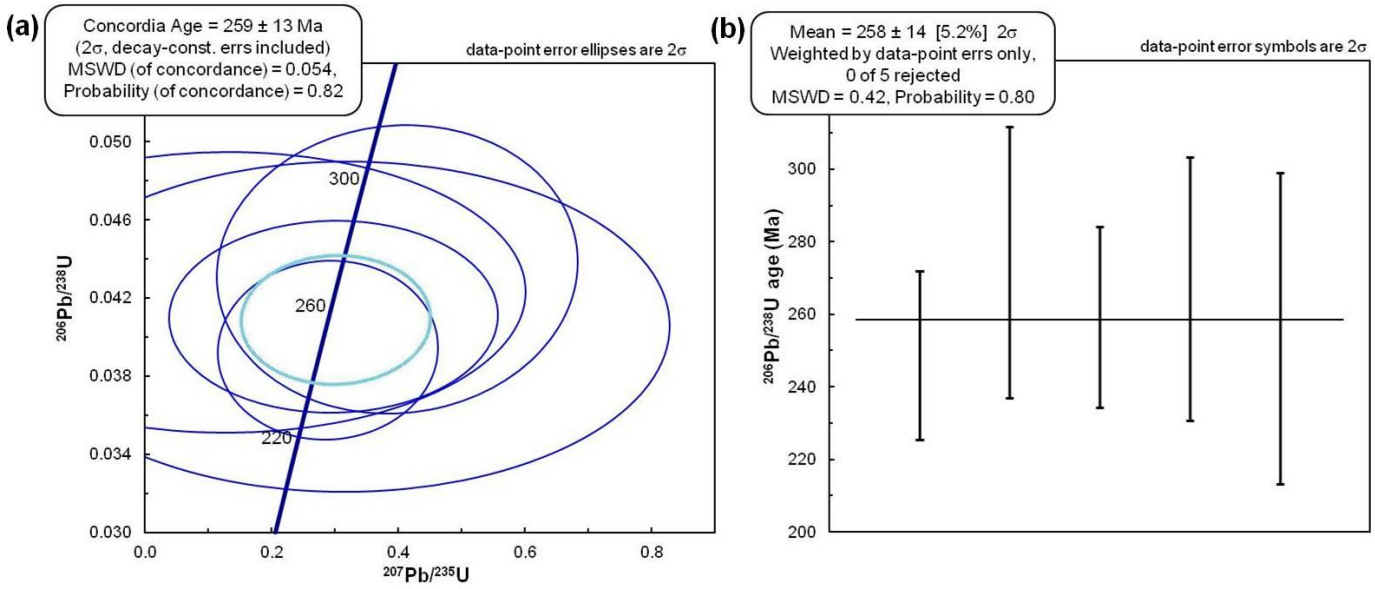

Figure 5.3: (a) Concordia plot and (b) $^{206}Pb/^{238}U$ ages for LA-ICP-MS data of rutiles from samples RG54 and RG57. Errors, MSWD (mean square of weighted deviates) and degree of concordance were calculated using Isoplot (after Ludwig, 2003; Zack *et al.*, 2011).

spots, which may have been caused by changes in signal intensity during an analysis and/or fractionation of $^{206}Pb/^{238}Pb$ ratios during ablation (Zack *et al.*, 2011).

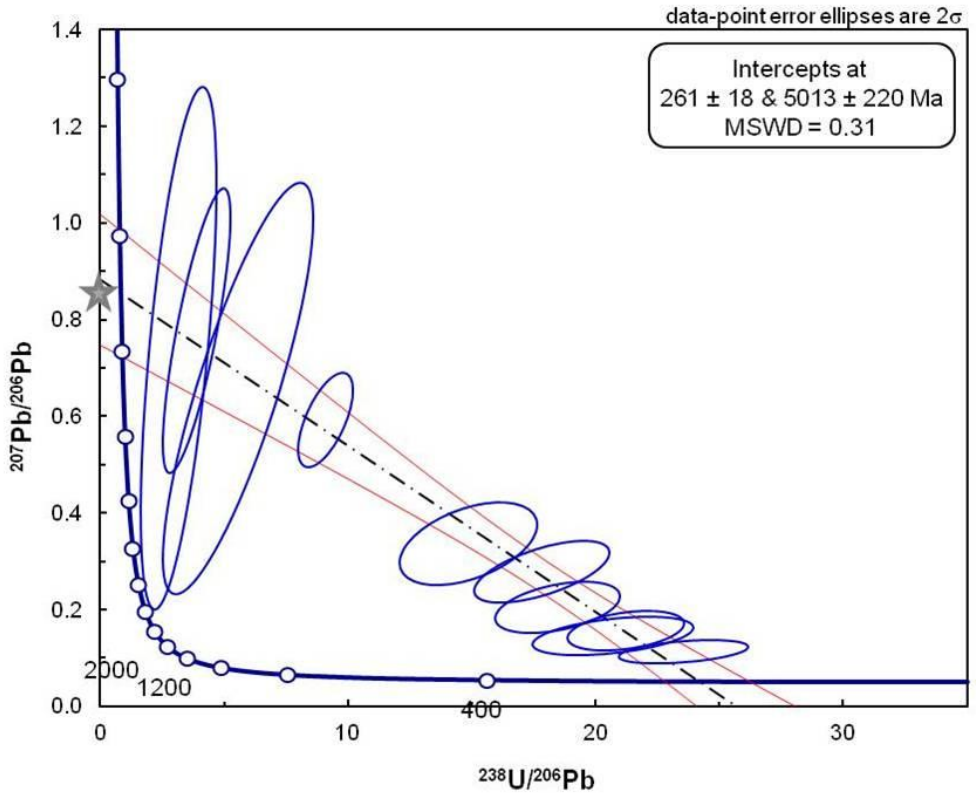

Figure 5.4: Tera-Wasserburg diagram illustrating uncorrected data for rutiles from samples RG54 and RG57. The regression line (black dashed line) intersects the y-axis $^{207}Pb/^{206}Pb$ ratio within error of the current estimate for the continental crust (grey star; Stacey and Kramers, 1975) Abbr.: MSWD = mean square of weighted deviates.

The large 5.2% error observed in the $^{206}Pb/^{238}U$ plot (Figure 5.3b) shows a much greater uncertainty for these results. Such large errors may be induced by unusually high common ^{208}Pb content (Zack, pers. comm. 2010), as observed in the data set. Demonstrating this point, the Terra-Wasserburg diagram in Figure 5.4 illustrates the uncorrected data forming a clear mixing line between common ^{208}Pb (grey star; after Stacey and Kramers, 1975; Zack *et al.*, 2011) and a 261 ± 18 Ma age. Despite the large error, however, the ca. 260 Ma age is a concordant age as it compares well with the ^{208}Pb corrected data plots in Figure 5.2a (259 ± 13 Ma).

The closure temperature for the U/Pb system in rutile has been the cause for some debate. Mezger *et al.* (1989) proposed the closure temperature interval for rutile grains with radii between 90 and 210 μm to occur between 370 and 500°C at a 1-2°C/Ma cooling rate. However, Cherniak (2000) found that, for spherical grains with a cooling rate of 1ºC/Ma, rutile grains with radii of 70 μm have a closure temperature of 576°C and rutile grains with radii of 200 μm have a closure temperature of 617°C. Cherniak (2000) also noted that results from elongate rutile grains tend to have closure temperatures around 17°C higher (~635°C). From these results, Cherniak (2000) deduced a mean closure temperature of ~600°C for ~100 μm rutile grains. To explain the roughly 100°C higher results, Cherniak (2000) postulated that rutile is more retentive of Pb than previously thought.

This higher closure temperature estimate (ca. 600°C) corresponds to the estimates for peak metamorphic temperature using the Zr-in-rutile thermometer (606 ± 18°C; see Chapter 4, Section 4.3.4.1). Despite the fact that Zr diffusion in rutile is sufficiently rapid that re-equilibration occurs subsequent to the timing of mineral crystallisation (e.g. retrogression) especially at higher temperatures, Zr-in-rutile thermometry has been shown to produce accurate temperature results for the timing of rutile mineralisation in medium-grade metamorphic rocks (Watson *et al.*, 2006; Luvizotto *et al.*, 2009b; Meinhold, 2010). Since the rutile closure temperature is within error of that determined for peak metamorphic conditions (see Chapter 4, Section 4.3.4.1), it is interpreted here that the corresponding age of 259 ± 13 Ma reflects the timing of peak metamorphism.

5.3 $^{40}Ar/^{39}Ar$ geochronology

The $^{40}Ar/^{39}Ar$ method has become a widely accepted and utilised method of geochronology due to its broad applicability and data precision (Renne *et al.*, 1998; McDougall and Harrison, 1999; Braun *et al.*, 2006; Scherer, 2007). As noted in the introduction section of this chapter, minerals with elevated levels of ^{39}Ar derived from ^{39}K during irradiation, such as white mica, biotite, amphibole and K-feldspar (Scherer, 2007), can be used. K-feldspar and white mica mineral

separates were obtained from the lower basement-derived section (granite, mica schist and interlayered mylonite) and amphibole and biotite mineral separates from the upper amphibolite megablock (Table 5.3).

Table 5.3: Mineral separates obtained for Ar/Ar geochronological analysis by rock type, sample and depth. Abbr. (after Siivola and Schmid, 2007; Whitney and Evans, 2010): Amp = amphibole; Bt = biotite; Kfs = K-feldspar; WM = white mica.

Rock Type	Sample	Depth (m)	Amp	Bt	Kfs	WM
Megablock amphibolite	RG176	1382.12		✓		
	RG177	1386.60	✓			
Basement granite	RG40	1687.10			✓	✓
	RG167	1655.40			✓	✓
Basement mica schist	RG56	1635.37				✓
	RG169	1687.34				✓
	MJK18	1716.56				✓
	MJK21	1671.86				✓

5.3.1 Methodology

Mineral separates from eight samples were processed for $^{40}Ar/^{39}Ar$ analysis: 2 from the upper amphibolite megablock (RG176 at 1382.12 m depth; RG177 at 1386.6 m depth), 2 from the lower basement-derived granite (RG40 at 1687.1 m depth; RG167 at 1655.4 m depth) and 4 from the lower basement-derived mica schist (RG56 at 1635.37 m depth; RG169 at 1687.43 m depth; MJK18 at 1716.56 m depth; MJK21 at 1671.86 m depth). Hand specimen photographs of these eight samples are included in Figure 5.5 for reference purposes.

Samples were crushed using a mechanical jaw crusher and then dry-sieved. The sieved material was washed and initial mineral separation took place by flotation in water columns. The resulting concentrates were cleaned in an ultrasonic bath with distilled water. The concentrates were sieved again before final separation using a Frantz isodynamic magnetic separator, heavy liquids and paper shaking methods. Hand-picking under a binocular microscope was used for

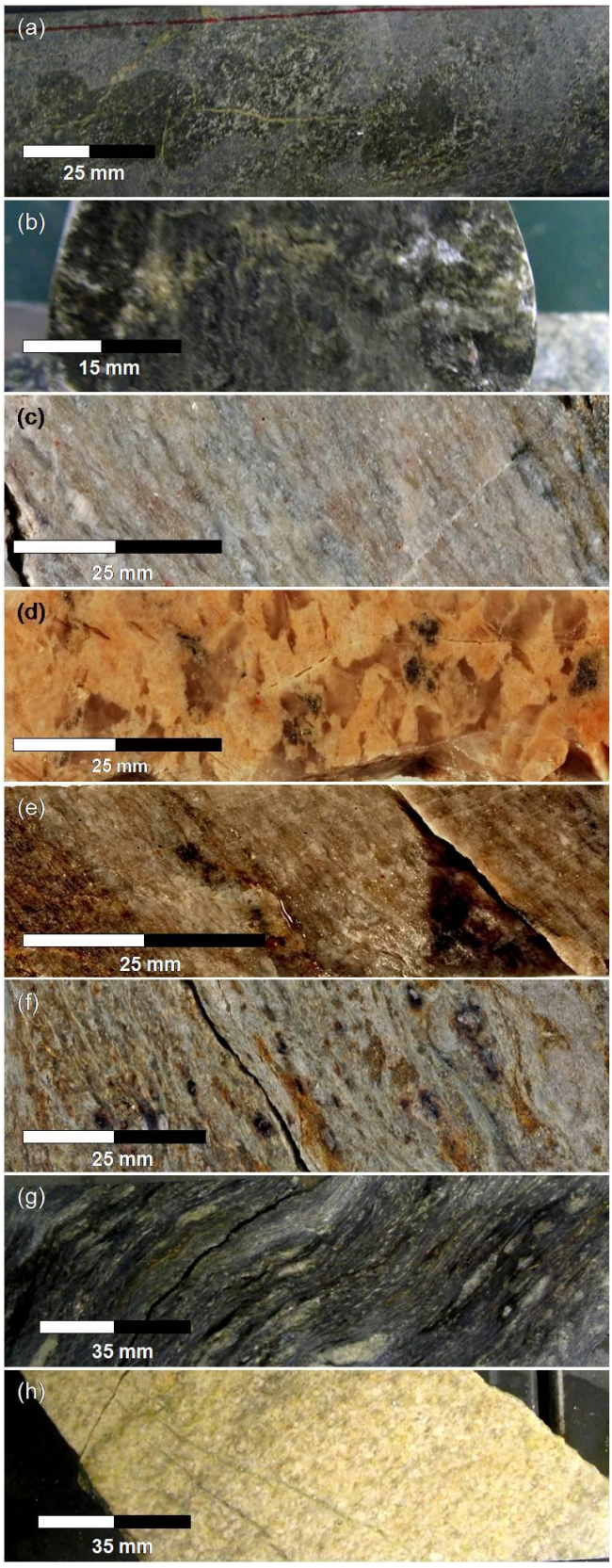

Figure 5.5: Hand specimen photographs for samples (a) RG177, (b) RG176, (c) RG40, (d) RG167, (e) RG169, (f) RG56, (g) MJK18 and (h) MJK21.

final purification (> 99%). Detailed descriptions of the sample preparation and analytical methods utilised here can be found in Haugerud and Kunk (1988) and Kunk *et al.* (2001, 2005).

The mineral concentrates were prepared for irradiation by encapsulating the samples in copper and/or aluminium packets and sealed under vacuum in quartz vials (Kunk *et al.*, 2001). Irradiation took place in the United States Geological Survey TRIGA (Training, Research, Isotopes, General Atomic*)* reactor in Denver, Colorado. At an age of 519.4 Ma, the MMhb-1 Standard was used as the fluence monitor (Alexander *et al.*, 1978; Dalrymple *et al.*, 1981; Kunk *et al.*, 2005). Following irradiation, the samples were sent to the argon dating laboratories at the USGS in Reston, Virginia, where all the ages were determined using the step-heating method. The mineral separates were incrementally heated in a low-blank furnace for 10 minutes per step. After the removal of the reactive gases during each heating step, the samples were analysed in a VG MM 1200b or a MAP 216 mass spectrometer operating in the static mode. An updated version of ArAr* programme (Haugerud and Kunk, 1988) and decay constants recommended by Steiger and Jäger (1977) were used to accomplish data reduction. The plateau ages were defined using the Fleck *et al.* (1977) criteria, as modified by Haugerud and Kunk (1988), where 50% or more ^{39}Ar released from the age spectrum in two or more contiguous steps agree in age within analytical precision limits (±1σ; Kunk *et al.*, 2005). The probability that the steps define a proper plateau is considered acceptable when the *P* (probability) value is > 0.05 (Roddick, 1978; Baksi, 2006).

For the amphibole sample, the inverse isochron age was determined in which, for the results to be meaningful, ≥50% of the ^{39}Ar must be released from the sample, MSWD is ≤2.5 and the calculated initial ^{40}Ar/^{36}Ar ratio is ≥295.5 (Kunk *et al.*, 2005). To improve the fit where results did not meet the above criteria, individual points were deleted from the low- and/or high-temperature portion of the analysis (Kunk *et al.*, 2005).

5.3.2 Results

From the eight samples, 10 mineral separates were generated: 1 amphibole (sample RG177), 1 biotite (sample RG176), 2 K-feldspar (samples RG40 and RG167), 2 igneous white mica (samples RG40 and RG167), and 4 metamorphic white mica (samples RG56, RG169, MJK18 and MJK21). A summary of the interpreted ages for the mineral separates analysed in this study is given in Table 5.4, and the full $^{40}Ar/^{39}Ar$ analytical data is presented in Appendix 5b.

5.3.2.1 Amphibole

Figure 5.6 shows the amphibole age spectrum, K/Cl and inverted isochron diagrams for the amphibolite megablock sample RG177. Although disturbed in the low temperature portion of the spectrum, a plateau age of 249 ± 1.3 Ma, which includes 51% of ^{39}Ar released, was determined (Figure 5.6a). The age range for the mineral separate is between 246 and 328 Ma, with both extremes located in the disturbed low temperature portion of the spectrum (Figure 5.6a). Analysis of the isotope correlation resulted in an inverse isochron age of 249.04 ± 2.1 Ma, including 95.9% of the ^{39}Ar released, with an initial $^{40}Ar/^{36}Ar$ ratio of 312.71 ± 10.64 and MSWD = 0.917 (Figure 5.6b), which correlates with the plateau age within the limits of analytical precision. The scatter of points along the mixing line in the inverse isochron diagram (Figure 5.6b) indicates the presence of excess ^{40}Ar, suggesting that the plateau age reflects the time of cooling.

K/Ca ratios for the amphibole mineral separate show similar disturbances in the low temperature portion of the age spectrum, but are constant onwards from the beginning of the plateau (Figure 5.6a). The slight disturbance early on in the step-heating process suggests the presence of impurities in the form of very small inclusions in the amphibole which were not observed during petrographic analysis (Figure 5.5a; see Chapter 2, Section 2.3.2).

Table 5.4: Compilation of interpreted $^{40}Ar/^{39}Ar$ ages. Abbr.: A = amphibolite; G = granite; LB = lower basement-derived section; MB = megablock section; MS = mica schist; MSWD = mean square of weighted deviates; *P* = probability.

Sample	Locality	Rock Type	Plateau Age (Ma)	*P* value	Age range (Ma)	Isochron Age (Ma)	Initial $^{40}Ar/^{36}Ar$ ratio	^{39}Ar released (%)	MSWD	*P* value
Amphibole										
RG177	MB	A	249.0 ± 1.3	-	246 - 328	249.04 ± 2.13	312.71 ± 10.64	95.9	0.917	-
Biotite										
RG176	MB	A	-	-	-	-	-	-	-	-
K-feldspar										
RG40	LB	G	-	-	210 - 242	-	-	-	-	-
RG167	LB	G	-	-	176 - 241	-	-	-	-	-
White Mica (prograde to peak metamorphism)										
RG56	LB	MS	244.3 ± 1.2*	0.08	212 - 252	244 ± 2	321 ± 10	65.7	2.1	0.04
RG169	LB	MS	242.2 ± 1.1	0.49	82 - 246	242 ± 2	296 ± 6	83.4	1.4	0.2
MJK18	LB	MS	244.0 ± 1.1*	0.09	128 - 254	245 ± 2.0	270 ± 40	53.1	1.7	0.15
MJK21	LB	MS	243.1 ± 1.1*	0.18	162 - 250	243 ± 2.0	298 ± 5	79.9	2	0.04
White Mica (igneous intrusion)										
RG167	LB	G	-	-	190 - 246	234 ± 6	300 ± 30	-	320	0
White mica (mylonitised)										
RG40	LB	G	-	-	67 - 388	247 ± 5	280 ± 30	31.6	0.02	1

- Value could not be determined (see text for details)

* Forced plateau age

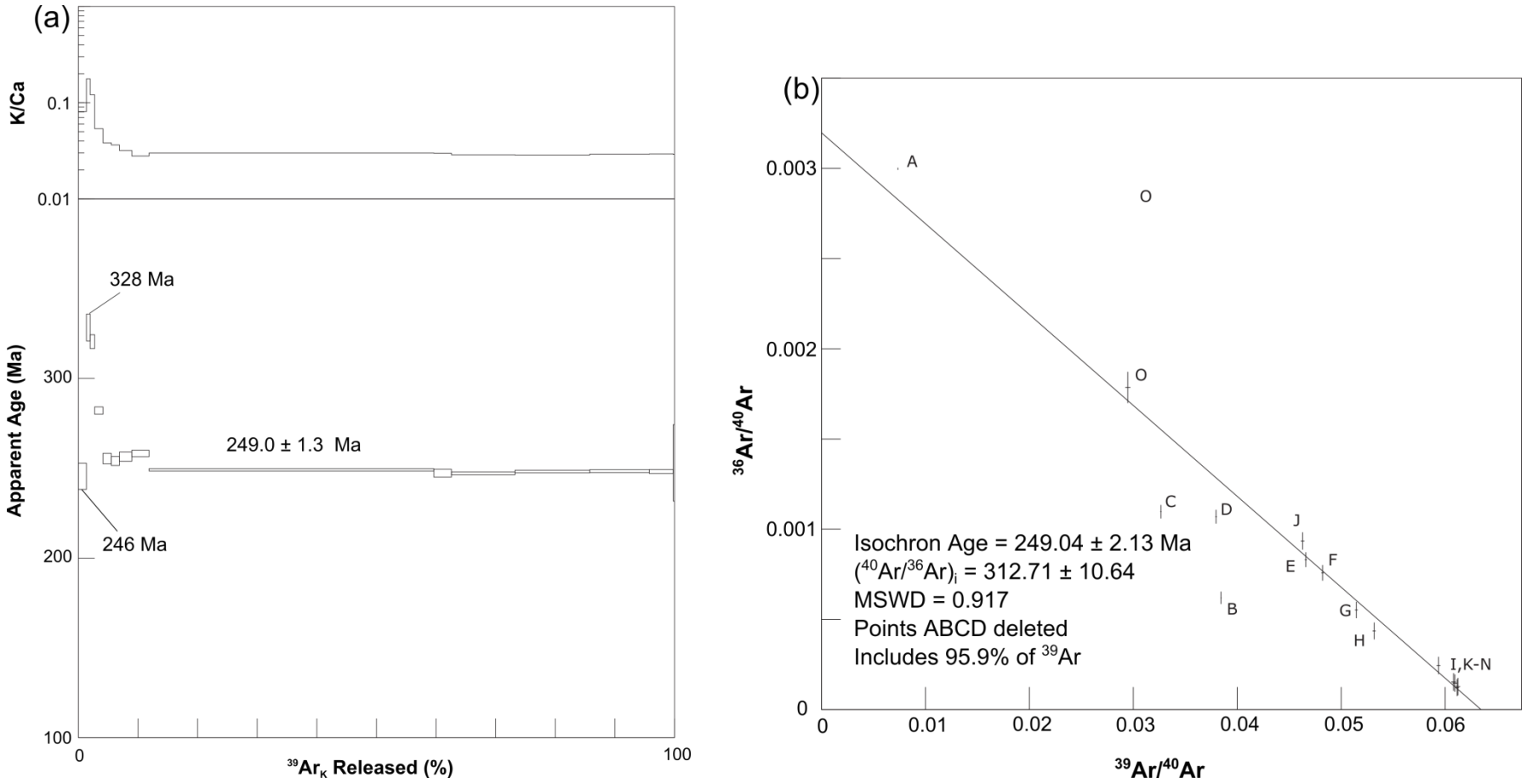

Figure 5.6: Amphibole (a) age spectrum, K/Ca and (b) inverted isochron diagrams for the amphibolite megablock sample RG177. For (a) plateau ages (±1σ), age maxima and age minima are as indicated. For (b), the inverted isochron age is meaningful as MSWD < 2.5 and $(^{40}Ar/^{36}Ar)_i \geq 295.5$ (Kunk *et al.*, 2005). Points A, B, C and D were dropped to improve the fit of the data. Abbr.: MSWD = mean square of weighted deviates.

A number of variables influence the closure temperature for amphibole, including composition, cooling rate and ionic porosity (Dahl, 1996; McDougall and Harrison, 1999; Kunk *et al.*, 2005). In Chapter 4, Section 4.2.3, mineral chemistry analyses of amphiboles in the upper amphibolite megablock revealed Mg-rich compositions that range from pargasitic to tschermakitic hornblende to hornblende. Based on his T_C-Z (closure temperature to ionic porosity) model, Dahl (1996) proposed closure temperatures for amphibole between 475 and 525°C, and also noted that Mg-rich clinoamphiboles tend to have closure temperatures 60 ± 10°C higher than their Fe counterparts. Based on his T_C-Z (closure temperature to ionic porosity) model, Dahl (1996) proposed closure temperatures for amphibole between 475 and 525°C, and also noted that Mg-rich clinoamphiboles tend to have closure temperatures 60 ± 10°C higher than their Fe counterparts. Consequently, it can be interpreted that closure temperatures for the amphiboles in the upper megablock section should be on the upper end of the temperature range. However, experiments undertaken by Harrison (1981) regarding the Ar diffusivity in hornblendes revealed an insensitivity to its Mg/Fe ratio. Furthermore, Harrison (1981) proposed an average of 500 ± 50°C closure temperature for hornblende. Thus, despite the compositional variation in the amphibolite megablock sample, 500°C is an acceptable closure temperature for amphibole (as suggested by Kunk *et al.*, 2005). If, as proposed in Chapter 4, on the basis of similar geochemistry and metamorphic grade, the upper amphibolite megablock is part of the same terrane as the lower basement-derived metasediments, the RG177 amphibole age of ca. 249 Ma may represent closure through the 500°C isotherm during retrograde cooling from a ca. 600°C metamorphic peak.

5.3.2.2 Biotite

As observed in Chapter 4, Section 4.2.3, biotite in the amphibolite megablock (Figure 5.5b) is partially altered to chlorite, making the mineral separating and dating processes difficult. During the step-heating process, the biotite mineral separate from megablock amphibolite sample RG176 released 100% of its ^{39}Ar content in a single step (step B at 1450°C; see Appendix 5b), producing an age of 244.77 ± 0.28 Ma (Table 5.4). Isotope correlation analysis could not be performed since the age spectrum for the biotite mineral separate could not be produced. The

reliability of this age is questioned due to the fact that no plateau age could be produced. Baksi (1996) explained that, for a spectrum age to have geological significance, the bulk of the ^{39}Ar must be released in at least three consecutive steps where step ages overlap. Consequently, this age is considered unreliable despite the fact that it is analogous with spectra ages determined for white mica mineral separates (Section 5.2.4).

5.3.2.3 K-feldspar

The K-feldspar age spectra, K/Cl and K/Ca diagrams for samples RG40 and RG167 are shown in Figure 5.7. The most notable observation for these diagrams is the large amount of disturbance recorded for both samples, resulting in the absence of plateau ages. Furthermore, isochron ages could not be produced (Table 5.4). Both samples have u-shaped to climbing age spectra with much of the age data ranging between 210 and 240 Ma (Figure 5.7). K/Cl and K/Ca ratios show no correlation with the age spectra obtained during the step-heating process (Figure 5.6).

The large amount of disturbance observed in the age spectra in Figure 5.7 probably reflects the incorporation of excess Ar into the K-feldspar mineral lattice. Excess Ar (or ^{40}Ar) is defined as that component of Ar incorporated into minerals by secondary processes, separate from in situ decay (Dalrymple and Lanphere, 1969; McDougall and Harrison, 1999; Kelley, 2002a). Foster *et al.* (1990), Harrison *et al.* (1994) and Zeitler and FitzGerald (1986) observed that u-shaped age spectra patterns from stepwise heating methods in K-feldspar (as seen in Figure 5.7) probably relate to the interplay between the low temperature release of excess Ar from fluid inclusions and the high temperature release of excess Ar from large subgrains during step heating (Kelley, 2002a). As to the geological processes that may have incorporated excess Ar into the K-feldspar grains, Allen and Stubbs, (1982), Smith *et al.* (1994) and Vance *et al.* (1998) observed that excess Ar in shear zones in ancient metamorphic complexes is particularly common (Kelley, 2002b). This is also true in hydrothermal systems associated with large granite intrusions (Kelley *et al.,* 1986; Turner *et al.;* 1993; Kelley, 2002b). The former shear zone scenario applies to sample RG40, which is a fine-grained mylonitised granite sample (Figure

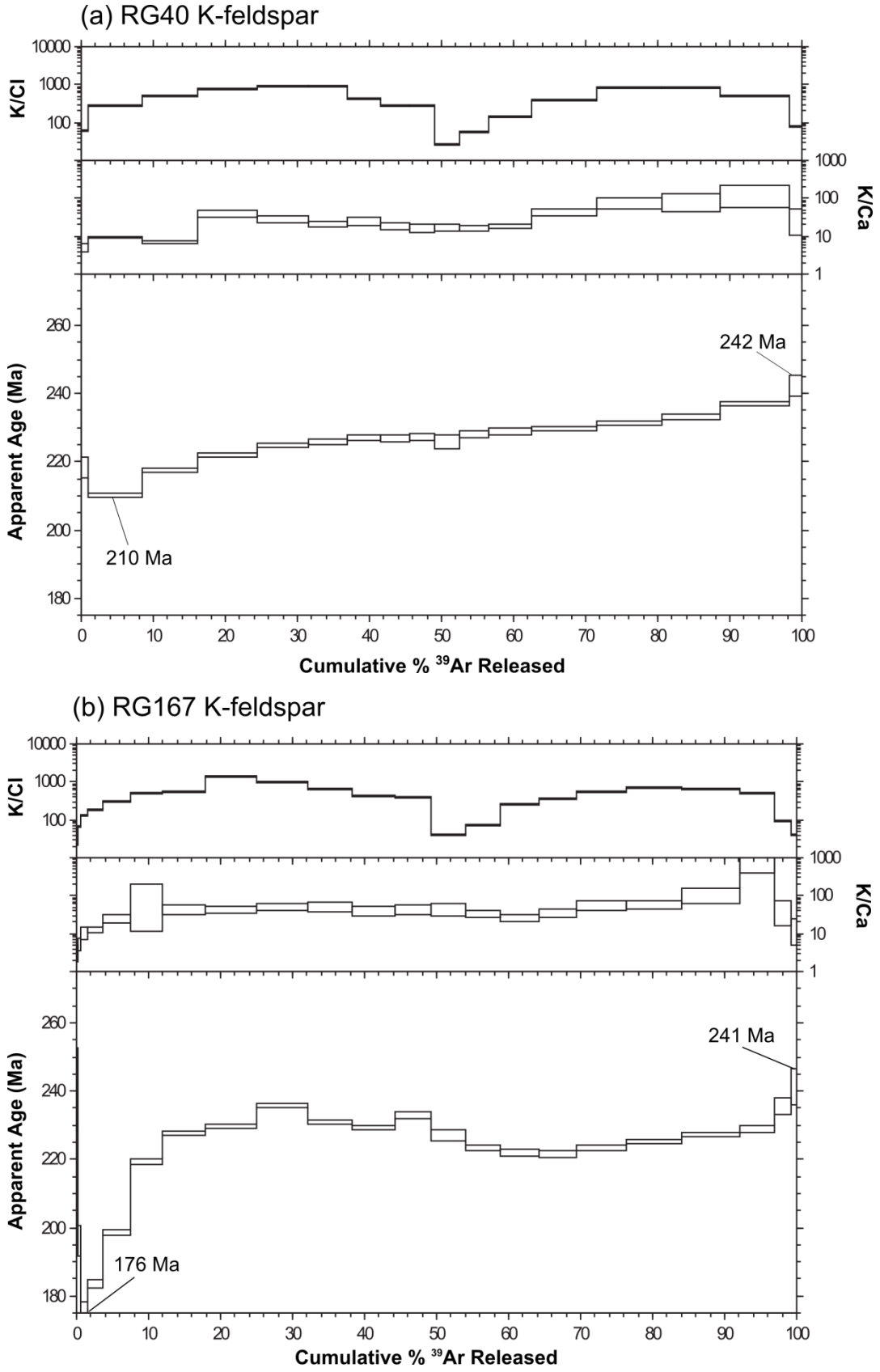

Figure 5.7: K-feldspar age spectra, K/Cl and K/Ca diagrams for samples (a) RG40 and (b) RG167. Age maxima and age minima are as indicated.

5.5c) and the latter hydrothermal veining scenario applies to sample RG167, which is a coarse-grained pegmatitic granite sample (Figure 5.5d).

5.3.2.4 White mica

Igneous, prograde metamorphic and retrograde metamorphic conditions are reflected in the samples from which the six white mica mineral separates were derived. White mica mineral separates were derived from mica schist samples RG169, RG56, MJK18 and MJK21 (Figure 5.5e, f, g and h) in which the mica is found primarily defining the prograde to peak S1 folia (see Chapter 2, Section 2.4.1) and are expected to reflect results associated with these metamorphic conditions. White mica from the pegmatitic granite sample RG167 (Figure 5.5d) is expected to produce results relating to the timing of igneous intrusion into the mica schists during syn-peak metamorphic conditions (Figure 5.9a). Lastly, the white mica mineral separate from the fine-grained mylonitic granite sample RG40 (Figure 5.5c) is a mixed sample and contains at least two generations of white mica (derived from prograde to peak metamorphism mineral growth and later recrystallisation due to retrograde mylonitisation; see Chapter 2, Section 2.4.1). Allaz *et al.* (2011) observed that partial recrystallisation along the retrograde path may induce chemical equilibration and resetting in white mica. Thus, the white mica grown during prograde to peak conditions in this sample is expected to have been at least partially reset during mylonitisation. Consequently, at least one generation of white mica from sample RG40 is expected to reflect the timing of mylonitisation (Figure 5.9b).

Prograde to peak metamorphic white mica

Figure 5.8 shows age spectra, K/Cl and K/Ca diagrams for the prograde to peak metamorphic white mica mineral separates from samples RG169, RG56, MJK18 and MJK21. Age spectra and isochron ages could be produced for all four of the metamorphic white mica mineral separates (Table 5.4). Age spectra for the mineral separates are characterised by relatively flat profiles with minimal disturbance (Figure 5.8). K/Cl ratios are constant with the respective plateaus but decline once plateaux end (Figure 5.8). Highly variable K/Ca ratios for the metamorphic white mica mineral separates indicate the presence of impurities.

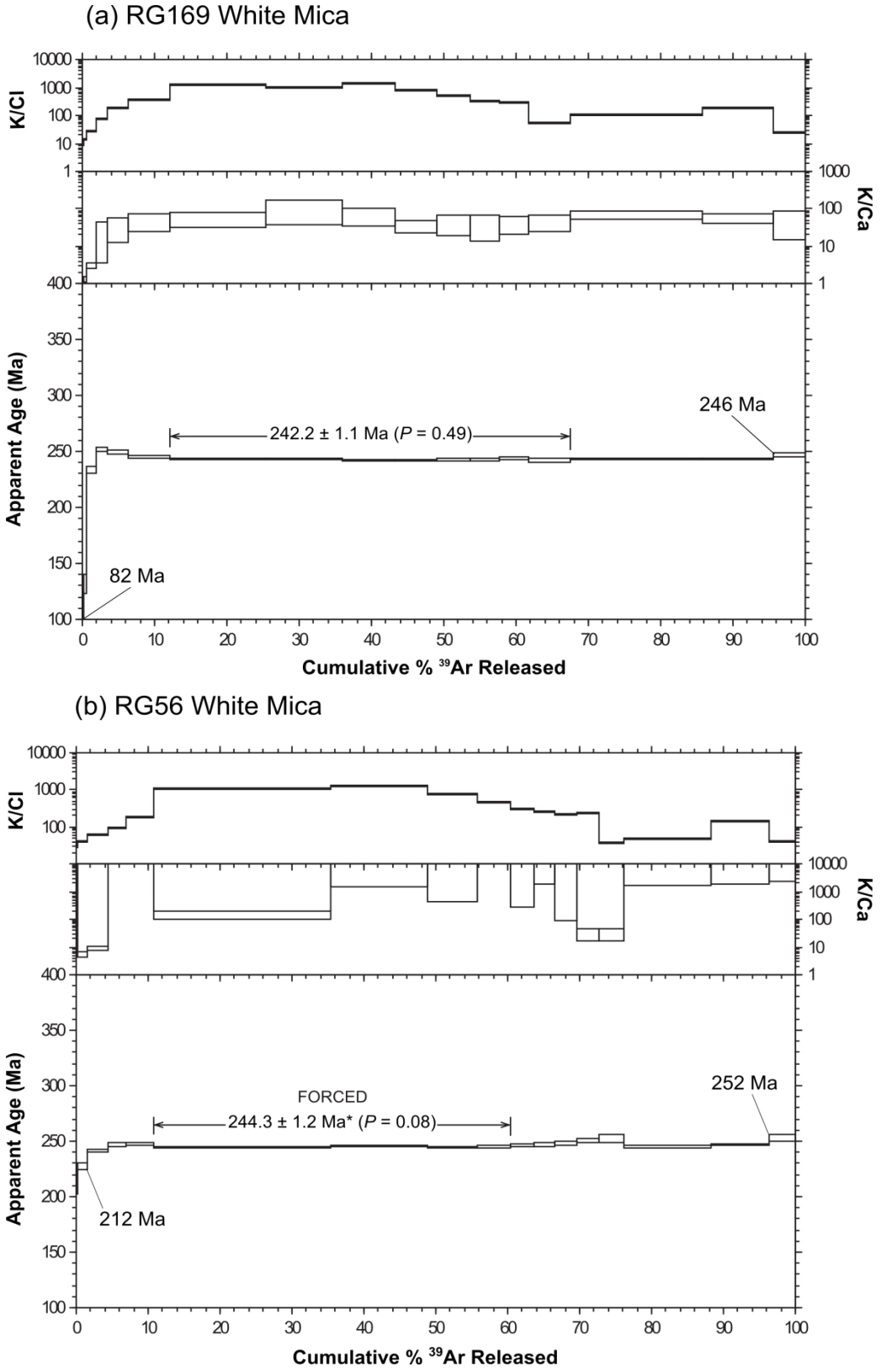

Figure 5.8: White mica age spectra, K/Cl and K/Ca diagrams for mica schist samples (a) RG169, (b) RG56, (c) MJK18 and (d) MJK21. Plateau ages (±1σ), age maxima and age minima are as indicated. Symbols: * = forced plateau age; *P* = probability.

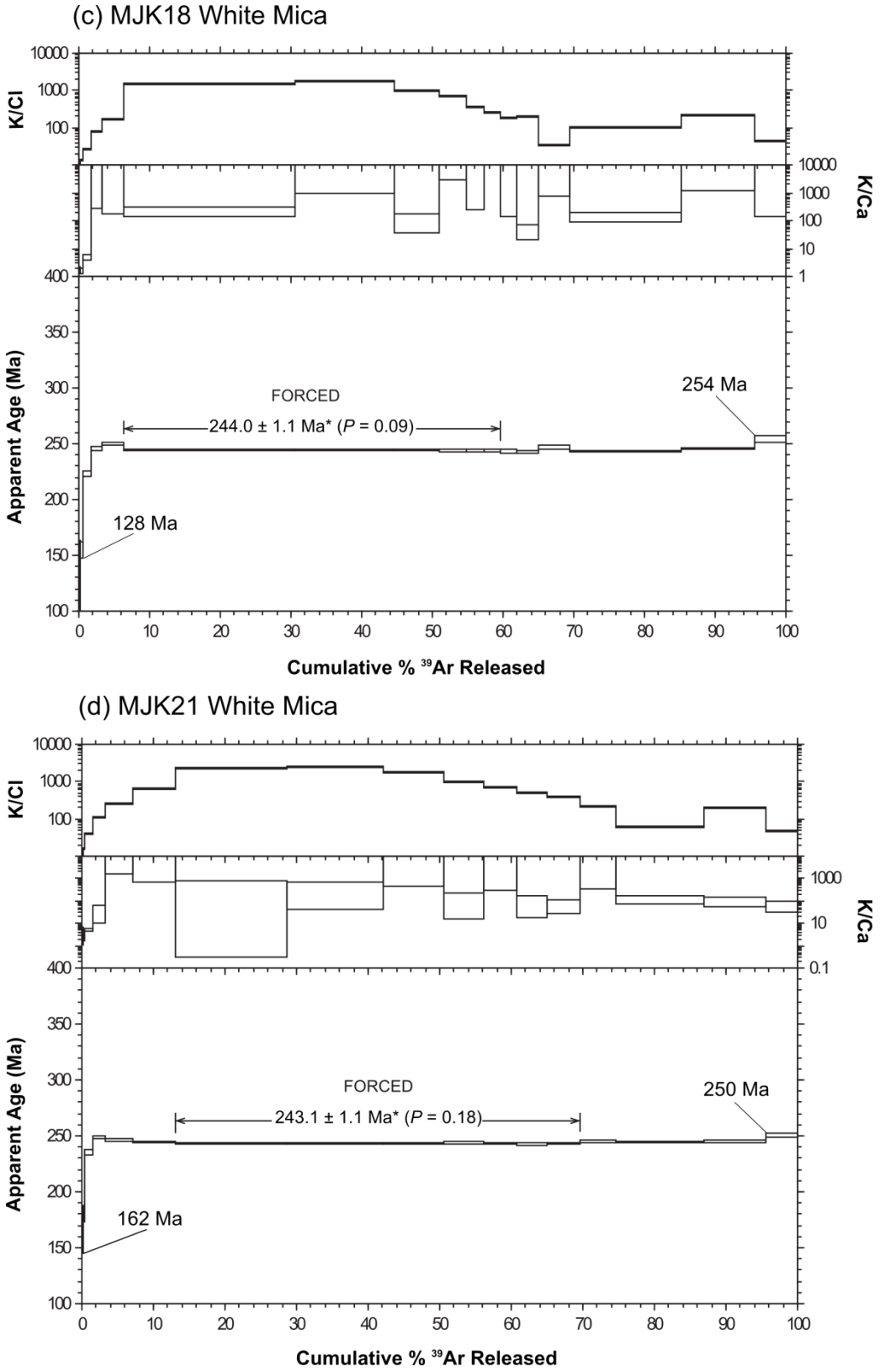

***Figure 5.8 continued*: White mica age spectra, K/Cl and K/Ca diagrams for mica samples (a) RG169, (b) RG56, (c) MJK18 and (d) MJK21. Plateau ages (±1σ), age maxima and age minima are as indicated. Symbol: * = forced plateau age; *P* = probability.**

In Figure 5.8a, only the white mica mineral separate from sample RG169 produced an unforced plateau age (242.2 ± 2 Ma; *P* = 0.49; Table 5.4). The other three white mica mineral separate forced plateau ages were calculated accepting >1σ for the confidence interval of the $^{40}Ar/^{39}Ar$ ratios for the steps defining the plateaux in Figure 5.8b, c and d (Fekiacova *et al.*, 2007). These three samples appear to have experienced some alteration (Figure 5.5 f, g and h), marginally more than that observed in sample RG169, despite their relative locations within the borehole core. This alteration probably caused sufficient disturbance requiring the plateau ages to be forced. However, the three forced plateau ages (RG56 = 244.3 ± 1.2, *P* = 0.08; MJK18 = 244.0 ± 1.1, *P* = 0.09; MJK21 = 243.1 ± 1.1, *P* = 0.18) show robust probability values (>0.05; Roddick, 1978) and are within statistical error of the unforced plateau age for the sample RG169 white mica mineral separate. The average plateau age for the prograde to peak metamorphic white mica is 243 ± 1.1 Ma.

All four prograde to peak metamorphic white mica mineral separates produced isochron ages that have a slightly wider range (242 to 245 Ma; Table 5.4) than observed from the age spectra (242 to 244 Ma; Table 5.4). The isochron ages for the white mica mineral separates from samples RG169 and MJK18 are statistically acceptable as their probability values (*P* = 0.15 and 0.2, respectively) are >0.05 (Table 5.4; Roddick, 1978). However, the isochron ages for the white mica mineral separates from samples RG56 and MJK21 have probability values of 0.04 and are, thus, statistically suspect (Table 5.4; Roddick, 1978).

Hames and Bowring (1994) reported a closure temperature for Ar in white mica at 350 ± 50°C (Braun *et al.*, 2006). As such, it is interpreted here that the average plateau age of 243 ± 1.1 Ma for the four white mica mineral separates indicates the time of cooling through the ~350°C isotherm following peak metamorphism.

Igneous white mica

Figure 5.7 shows the age spectra, K/Cl and K/Ca diagrams for the igneous white mica samples RG167 and RG40. Similar to their respective K-feldspar mineral separates (Figure 5.6); spectra

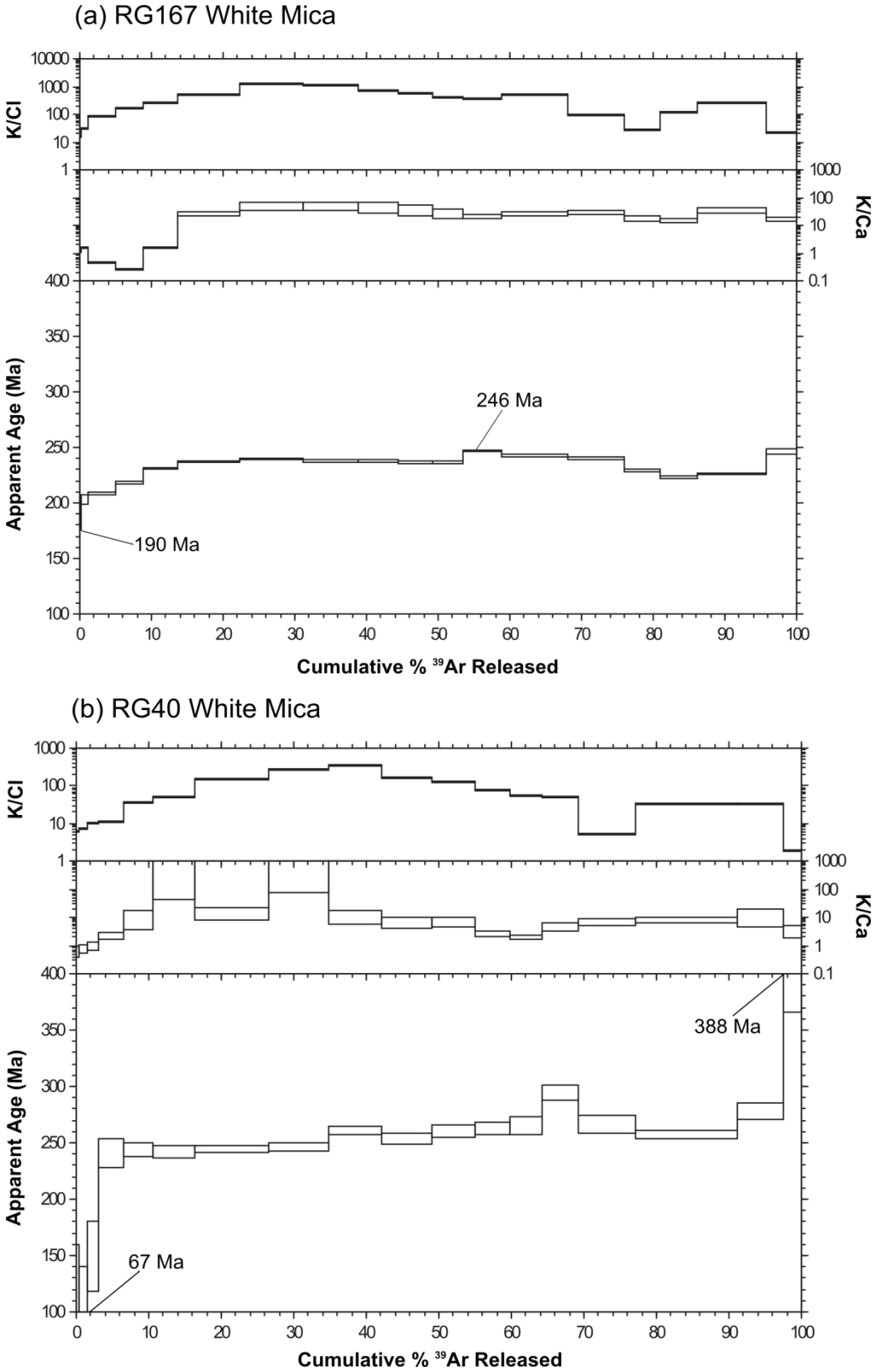

Figure 5.9: White mica age spectra, K/Cl and K/Ca diagrams for granitic samples (a) RG167 and (b) RG40. Plateau ages (±1σ), age maxima and age minima are as indicated.

plateau ages could not be produced for either sample (possible causes are discussed in Section 5.4.1). The variable K/Cl and K/Ca ratios for both samples (Figure 5.9) are reminiscent of the respective K-feldspar mineral separates (Figure 5.6).

The igneous white mica mineral separate from sample RG167 has a humped age spectrum (Figure 5.9a) with an age range (190-246 Ma) similar to that observed from its K-feldspar counterpart (176-241 Ma; Table 5.4; Figure 5.6b). The isochron age for sample RG167 is the youngest age produced for all mineral separates at 234 ± 6 Ma with an initial $^{40}Ar/^{36}Ar$ ratio of 300 ± 30 (Table 5.4). The large error (MSWD = 320) coupled with the nil probability value (*P* = 0) make this an imprecise age which is statistically unacceptable and should not be used (Roddick, 1978; Baksi, 1996).

Sample RG40 has a climbing age spectrum (Figure 5.8b) with the broadest age range observed of all the mineral separates, ranging from 67 to 388 Ma (Table 5.4); it must be noted, however, that much of the age spectrum for white mica in this sample lies between 240 and 294 Ma (Figure 5.8b; Appendix 5b). As discussed in Section 5.3.2.3 and the introduction to Section 5.3.2.4, sample RG40 is a fine-grained granite that underwent mylonitisation and associated recrystallisation shortly after its intrusion into the lower basement-derived mica schists during pre- to syn-peak metamorphic conditions (see Chapter 2, Section 2.4.1), resulting in at least two generations of white mica (prograde to peak mineral growth and retrograde recrystallisation), which may be the reason responsible for the broad age range and the lack of a plateau age.

The isochron age for sample RG40 is 247 ± 5 Ma ($^{40}Ar/^{36}Ar_i$ = 280 ± 30; MSWD = 0.02) and is the oldest Ar/Ar age produced for all mineral separates other than the amphibole for amphibolite megablock sample RG177 (ca. 249 Ma; Table 5.4). The probability of the accuracy of this age is relatively high (*P* = 1.00) despite the fact that it only includes 31.6% of the ^{39}Ar released (Table 5.4). This slightly older age may reflect the mylonitisation age since textural arguments in Chapter 2, Section 2.4.1 recognised that mylonitisation occurred shortly after peak metamorphic conditions, resulting in much recrystallisation of minerals including white mica. This is

demonstrated in sample RG40 where white mica fish are abundant (see Chapter 2, Section 2.4.3), suggesting that the older ca. 247 Ma event recorded by white mica in sample RG40 reflects the timing of mylonitisation. It must be noted, however, that this is still within error of the average plateau age obtained for the prograde to peak metamorphic white mica mineral separates (243 ± 1.1 Ma).

5.4 Discussion

Application of the two geochronological techniques has provided a peak metamorphic age, a mylonitisation age and a number of cooling ages from the mid-amphibolite facies metamorphic rocks in both the lower basement-derived granite and mica schist and the amphibolite megablock of the Eyreville-B borehole core. These ages have been graphically presented in the thermal-decay or time-temperature curve in Figure 5.10 to illustrate the probable cooling history if it is the same for all of these rocks.

The sequence of events illustrated on the thermal decay curve in Figure 5.10 is based on the results of this study and are interpreted to occur as follows. (1) Peak metamorphism as recorded by rutiles in the lower basement-derived mica schist mylonite section (259 ± 13 Ma; Section 5.2). (2) Cooling of peak metamorphic conditions though the 500°C isotherm at 249 ± 1.3 Ma as recorded by the amphibolite megablock amphibole mineral separate (Section 5.3.2.1). (3) Age of mylonitisation (247 ± 5 Ma) at 350 ± 50°C as recorded by the white mica mineral separate from the mylonitised granite sample RG40 (Section 5.3.2.4). (4) Continuing cooling history (243 ± 1.1 Ma) through at 350°C isotherm as recorded in the white mica mineral separates from the lower basement-derived mica schists (Section 5.3.2.4).

In Figure 5.11, zircon U/Pb SHRIMP ages for the massive and gneissic granite varieties of the upper megablock as well as an Ar/Ar age for the pegmatitic granite in the lower basement-derived section compiled by Horton *et al.* (2009b) have been included into the thermal decay curve from Figure 5.10. The granite crystallisation temperature used in Figure 5.11 (675 ± 50°C)

is based on the minimum granite solidus curve at 0.5 GPa (after Kerrick, 1972). The addition of these data to the data set compiled by this study allows for a more comprehensive analysis of the metamorphic events recorded in the Eyreville-B target rocks.

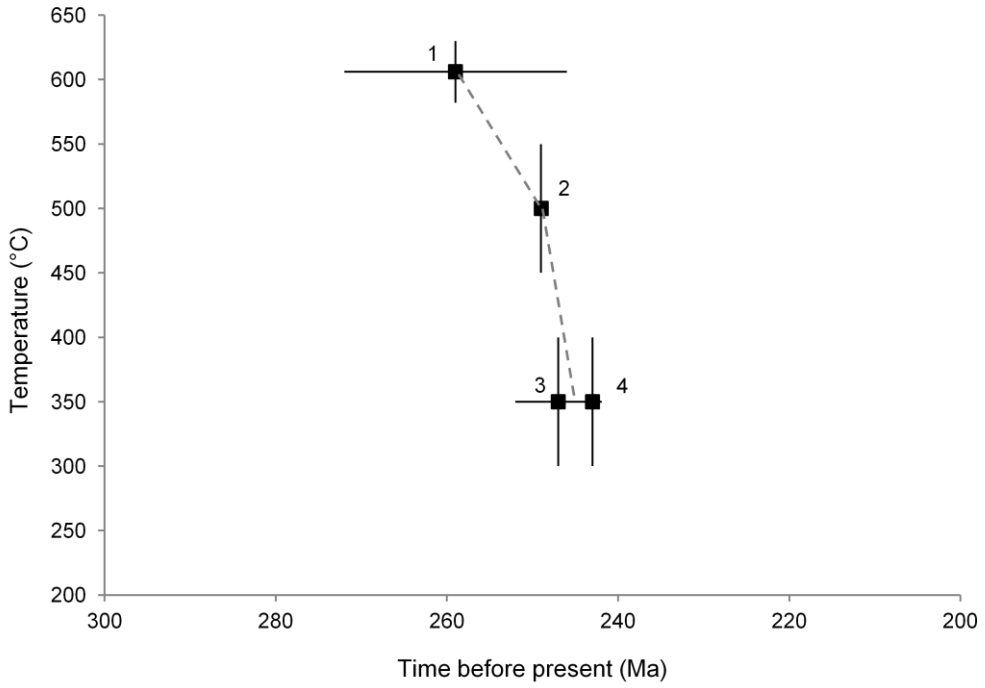

Figure 5.10: Thermal decay curve showing the cooling path for the target rocks of Eyreville-B borehole core based on this study's results. Refer to the explanation of numbered labels in text. Closure temperatures used: rutile = 606 ± 18°C (Chapter 4, Section 4.3.4.1); amphibole = 500 ± 50°C (Harrison, 1981); muscovite/white mica = 350 ± 50°C (Hames and Bowring, 1994). Symbols: black squares and lines = data points with errors from this study; grey dashed line = projected cooling history.

The updated sequence of events illustrated in Figure 5.11 interpreted for the Eyreville-B target rocks follows (refer to Figure 5.10 discussion for numbers 2, 4, 5 and 7). (1) Intrusion and crystallisation of the precursor to gneissic granite in the upper megablocks section at 615 ± 7 Ma during a previous metamorphic event (Horton *et al.* 2009b). (2) Peak metamorphism in the lower basement-derived mica schist mylonite section at 259 ± 13 Ma. (3) Intrusion and crystallisation of the massive granite into the gneissic granite of the upper megablocks section at 254 ± 3 Ma (Horton *et al.*, 2009b). (4) Cooling of the amphibolite megablock through the 500°C isotherm at 249 ± 1.3 Ma. (5) Mylonitisation of the lower basement-derived section at 247

± 5 Ma (see Figure 5.10 discussion). Cooling of the lower basement-derived granite through the 350°C isotherm took place at (6) 244.1 ± 1.3 Ma (Horton *et al.*, 2009b) and in the basement mica schists (7) at 243 ± 1.1 Ma.

In Figure 5.11, the massive megablock granite (number 3) lies within error of peak metamorphism at 254 ± 3 Ma (number 2), indicating that the younger granite intruded and crystallised into the megablock granite gneiss syn- to post-peak metamorphic conditions (errors in peak metamorphism and granite crystallisation temperatures overlap). Similar to the gneissic variety, the massive megablock granite formed from an igneous protolith in a syncollisional environment (see Chapter 3, Section 3.6.3). Thus, age of crystallisation of the massive granite at syn- to post-peak metamorphism corresponds with its chemistry. This ties the granite megablock to the same terrane as the mica schist and granite in the lower basement-derived section and the upper amphibolite megablock (as established in Section 5.3.2.1). Consequently, the more robust age of 254 ± 3 Ma from the massive granite in the upper megablocks section is here inferred to reflect peak metamorphism in Eyreville-B target rocks.

The average cooling rate from peak mid-amphibolite facies metamorphic conditions (259 ± 13 Ma) to greenschist conditions through the retrograde mylonitisation (249 to 243 Ma) is approximately 16°C/Ma (grey dashed line in Figures 5.10 and 5.11). However, if the more reliable crystallisation age of the massive granite in the upper megablocks section (254 ± 3 Ma; Horton *et al.*, 2009b) is assumed to reflect the timing of peak metamorphism in the lower basement-derived mica schists, an alternative linear cooling rate is inferred (red dashed line in Figure 5.11), approximating 21°C/Ma.

5.5 Summary

Previous geochronological studies undertaken for rocks in the Eyreville-B borehole core included zircon U/Pb SHRIMP ages of 615 ± 7 Ma for the gneissic granite and 254 ± 3 Ma for

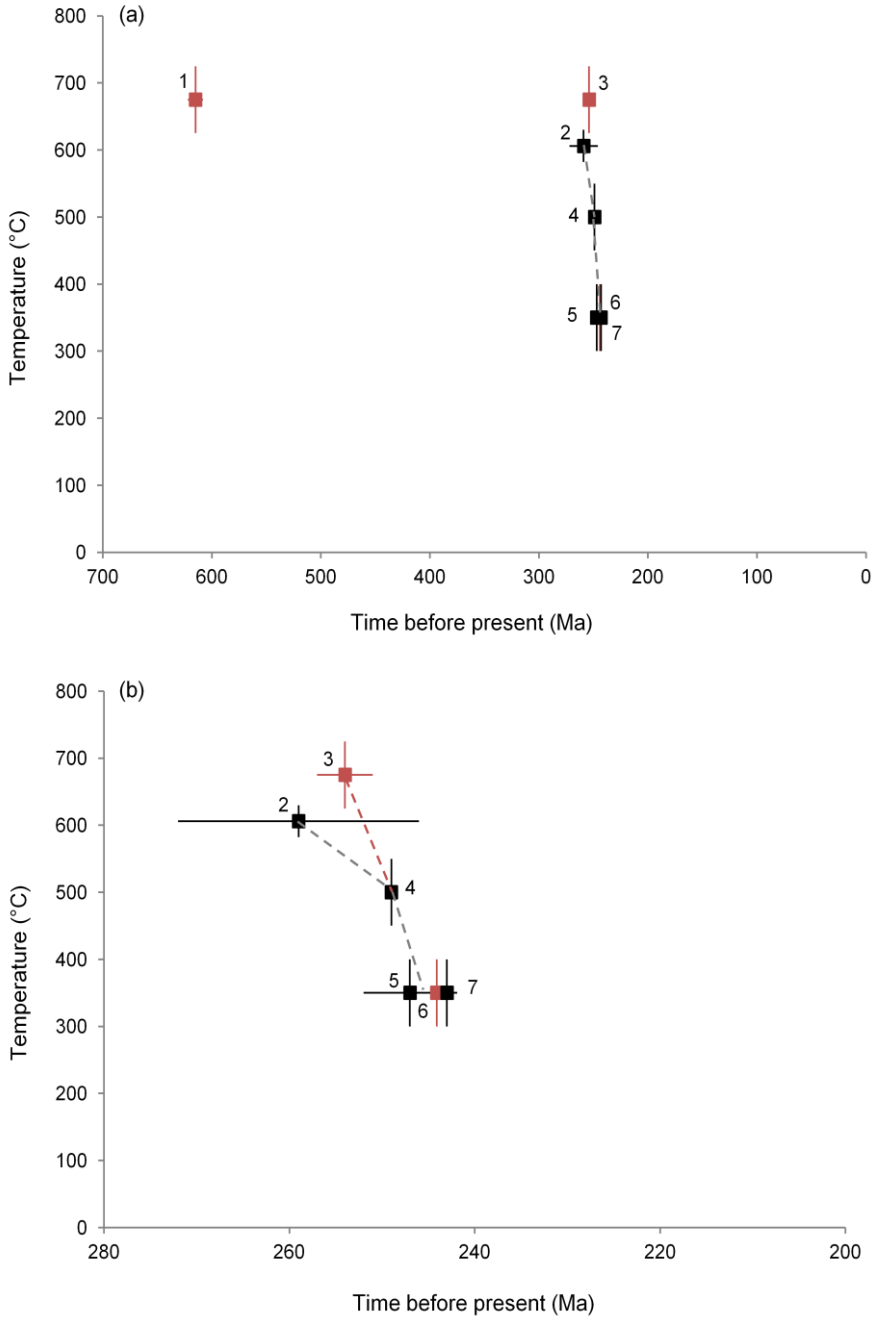

Figure 5.11: (a) Thermal-decay curve showing complete crystallisation and cooling history as recorded in the target rocks of the Eyreville-B borehole core. (b) Magnified view of the cooling history from 280 to 200 Ma. Refer to the explanation of numbered labels in text. Granite crystallisation temperature is 675 ± 50°C (after Kerrick, 1972). Closure temperatures: rutile = 606 ± 18°C (Chapter 4, Section 4.3.4.1); amphibole = 500 ± 50°C (Harrison, 1981); muscovite/white mica = 350 ± 50°C (Hames and Bowring, 1994). Symbols: red squares and lines = data points with errors derived from Horton *et al.* (2009b); black squares and lines = data points with errors from this study; grey dashed lines = projected cooling history; red dashed line = alternative cooling history.

the massive granite from the upper granite megablock, and an Ar/Ar cooling age of 244.1 ± 1.3 Ma from a white mica mineral separate derived from a pegmatitic granite sample from the lower basement-derived section (Horton *et al.*, 2009b). The geochronological techniques used in this study revealed a peak metamorphic rutile U/Pb age of 259 ± 13 Ma for mica schists in the lower basement-derived mylonite zone, which is in agreement with the igneous crystallisation age of zircon determined for the massive granite in the upper megablocks section.

Ar/Ar geochronology revealed a mylonitisation age of 247 ± 5 Ma for white mica in a mylonitised granite sample from the lower basement-derived section and cooling ages for amphibole and white mica mineral separates from the upper amphibolite megablock (249 ± 1.3 Ma) and lower basement-derived mica schists (243 ± 1.1 Ma), respectively. Some of the Ar/Ar geochronological data was not sufficiently reliable due to partial resetting of the analysed minerals and thus could not be used for geologic interpretations, such as the K-feldspar mineral separates derived from granite samples of the lower basement-derived section.

Based on chemistry and geochronology, the upper granite megablock, upper amphibolite megablock and lower basement-derived section are compatible with the same terrane, which experienced a ca. 250 Ma metamorphic event. This suggests that the terrane comprises sediments that deposited onto and mafic rocks that intrude an older ca. 615 Ma gneissic granite basement and experienced regional metamorphism to mid-amphibolite facies conditions. This will be discussed further in Chapter 6.

6 DISCUSSION AND CONCLUSIONS

The excavation of the Chesapeake Bay impact structure (CBIS) into the Appalachian orogenic belt of the eastern USA and its sedimentary cover (the Atlantic Coastal Plain) led to massive rock failure in the annular trough after the initial impact, resulting in the slumping, sliding and displacement of megablocks of sedimentary and crystalline basement sequences into the central crater (see Chapter 1, Figures 1.12 and 1.14; Poag *et al.*, 2004). In addition to revealing the sequences directly caused by the impact, the ICDP-USGS drilling of the CBIS has allowed the first substantial analysis of metamorphic and igneous rocks in the easternmost portions of the Appalachian orogen (also known as the Appalachian Piedmont; Milici, 1995) that are concealed beneath thick sedimentary deposits of the Atlantic Coastal Plain along the east coast of the USA. The pre-impact target rock units of the Eyreville-B borehole core have also been investigated as part of the ICDP-USGS drilling of the CBIS by Horton *et al.* (2009a, 2009b), Skála *et al.* (2009), Schmitt *et al.* (2009) and Vanko (2009).

Rock sequences from below (the lower basement-derived crystalline section; Chapter 2, Figure 2.1) and above the impactites section (upper granite and amphibolite megablocks; Chapter 2, Figure 2.11) of the Eyreville-B borehole core were investigated in this study by:

- Petrographic description and structural analysis (Chapter 2),
- Bulk rock and REE (rare earth elements) geochemical classification (Chapter 3),
- Mineral chemistry and geothermobarometry (Chapter 4), and
- Geochronological characterisation (Chapter 5).

This final chapter aims to discuss the findings from this study in the context of the regional geology and other published work from the ICDP-USGS project, and present an interpretation of the pre-impact geological history of the crystalline basement rocks.

6.1 Geological setting

The following section provides a summary of the details given in Chapter 1, Section 1.1 regarding the evolution of the Appalachian orogen and the tectonostratigraphic terranes in the vicinity of the CBIS (Figure 6.1 and Tables 6.1 and 6.2).

The Appalachian orogen formed over a period of ~1000 million years, from the Late Mesoproterozoic assembly of the supercontinent Rodinia (ca. 1200 Ma; Faill, 1997), through the Early Ordovician rifting of Rodinia and opening of the Iapetus Ocean (ca. 700 Ma; Horton *et al.*, 1989) to the opening of the Rheic Ocean (at the expense of the Iapetus Ocean; ca. 465; Murphy and Nance, 2013) and subsequent accretion of several micro-continents onto the Laurentian margin through a number of orogenic events during the Palaeozoic (~550-260 Ma; Horton *et al.*, 1989, 1991, 1994; Rankin, 1994), culminating with the Late Palaeozoic assembly of the supercontinent Pangaea (McMenamin and McMenamin, 1990; Faill, 1997; Hatcher, 2010). The orogen is exposed from Alabama to Newfoundland along the eastern margin of the North American continent (see Chapter 1, Figure 1.2) and forms the basement of the Atlantic Coastal Plain (Faill, 1997; Horton *et al.*, 1989, 1991, 1994).

At least five orogenic events have been described in parts of the Appalachian orogen: the Penobscottian (550-480 Ma; Drake *et al.*, 1989; Rankin, 1994; Zagorevski *et al.*, 2007; van Staal *et al.*, 2009), Taconian (495-440 Ma; Horton *et al.*, 1989; Rankin, 1994; Hibbard *et al.*, 2007a; van Staal *et al.*, 2009; Murphy and Nance, 2013), Salinic (450-423 Ma; van Staal *et al.*, 1998, 2009; Waldron *et al.*, 2009; Murphy *et al.*, 2010), Acadian (421-350 Ma; Murphy *et al.*, 1999; Murphy and Keppie, 2005) and Alleghanian (325-260 Ma; Hatcher, 1989, 2002; Horton *et al.*, 1989; Nance and Linnemann, 2008) orogenies.

The Penobscottian orogeny involved the generation of a magmatic arc on the peri-Gondwanan margin of the Iapetus Ocean that later obducted onto a peri-Gondwanan micro-continent (formed by the amalgamation of several peri-Gondwanan terranes rifted from Gondwana with the opening of the Rheic Ocean; Faill, 1997; Hibbard *et al.*, 2007a; Murphy *et al.*, 2010; Nance

and Linnemann, 2008). The Taconian orogeny followed a similar sequence of events as the Penobscottian orogeny, except that its magmatic arc formed on the peri-Laurentian margin of the Iapetus Ocean, and obducted onto a peri-Laurentian micro-continent (an amalgamation of terranes that separated from Laurentia during the rifting stage of the disassembly of Rodinia; Hibbard *et al.*, 2007a; van Staal *et al.*, 2009; Murphy and Nance, 2013). Both peri-Laurentian and peri-Gondwanan micro-continents had accreted onto the Laurentian margin by ca. 440 Ma (Horton *et al.*, 1989; Rankin, 1994; Hibbard *et al.*, 2007a).

The Salinic and Acadian orogenies involved the accretion of peri-Gondwanan micro-continents onto the Laurentian margin as the Iapetus Ocean progressively closed (Murphy *et al.*, 2010; Murphy and Nance, 2013). This accretion of these peri-Gondwanan micro-continents (Baltica, Carolina, Ganderia and Meguma) resulted in the formation of Laurussia (Hibbard *et al.*, 2007a; Murphy *et al.*, 2010). The final orogenic event, the Alleghanian orogeny, occurred as Gondwana collided with Laurussia as the Rheic Ocean closed and is the last compressional event to affect the Mid-Atlantic region (Horton *et al.*, 1989, 1991; Rankin, 1994; Faill, 1998; Hatcher, 2002; Ettensohn, 2008).

The above orogenic events, and accompanying closure of the Iapetus and Rheic oceans, resulted in the accretion of tectonostratigraphic terranes to the Laurentian margin (Horton *et al.*, 1989, 1991, 1994; Rankin, 1994). The locations of the suture zones associated with the closure of the Iapetus and Rheic oceans as proposed by Lefort (1988) and Lefort and Max (1991) are shown in Figure 6.1a. The exact locations of these zones are in dispute as they are buried beneath the sediments of the Atlantic Coastal Plain and have been identified based solely on geophysical evidence (Lefort, 1988; Lefort *et al.*, 1988; Lefort and Max, 1991; West, 1998; Hibbard, 2000; Murphy *et al.*, 2006). Consequently, the interpretation of the origin of certain terranes of the Appalachian orogen (i.e. Laurentian, Iapetan or peri-Gondwanan) has been cause for much controversy (Murphy *et al.*, 2006; Hibbard *et al.*, 2007a).

Erosion of the Appalachian orogen and subsequent deposition of sediments during the Mesozoic and Cenozoic has complicated the identification and interpretation of the underlying tectonostratigraphic terranes that were accreted to the Laurentian margin as the Iapetus and Rheic oceans closed (Horton *et al.*, 1989; Rankin, 1994). Information regarding the subsurface geology of the Appalachian orogen and subsequent interpretation of the various tectonostratigraphic terranes has been gathered through surface geology extrapolation, gravity, magnetic and seismic geophysical studies, and limited borehole information (Horton *et al.*, 1989, 1991). In the vicinity of the CBIS (Figure 6.1b), terranes include the Roanoke Rapids, Hatteras, Spring Hope, Carolina, Crabtree (not shown in Figure 6.1b; see Figure 1.9), Falls Lake, Sussex, Goochland, Chopawamsic, Potomac composite and Jefferson terranes (Figure 6.1b; Horton *et al.*, 1989, 1991, 1994); the first six terranes form part of the amalgamated volcanic arc Carolina Zone (see Chapter 1, Section 1.1.2.1; Hibbard *et al.*, 2002). A summary table of the characteristics of these terranes is given in Table 6.1.

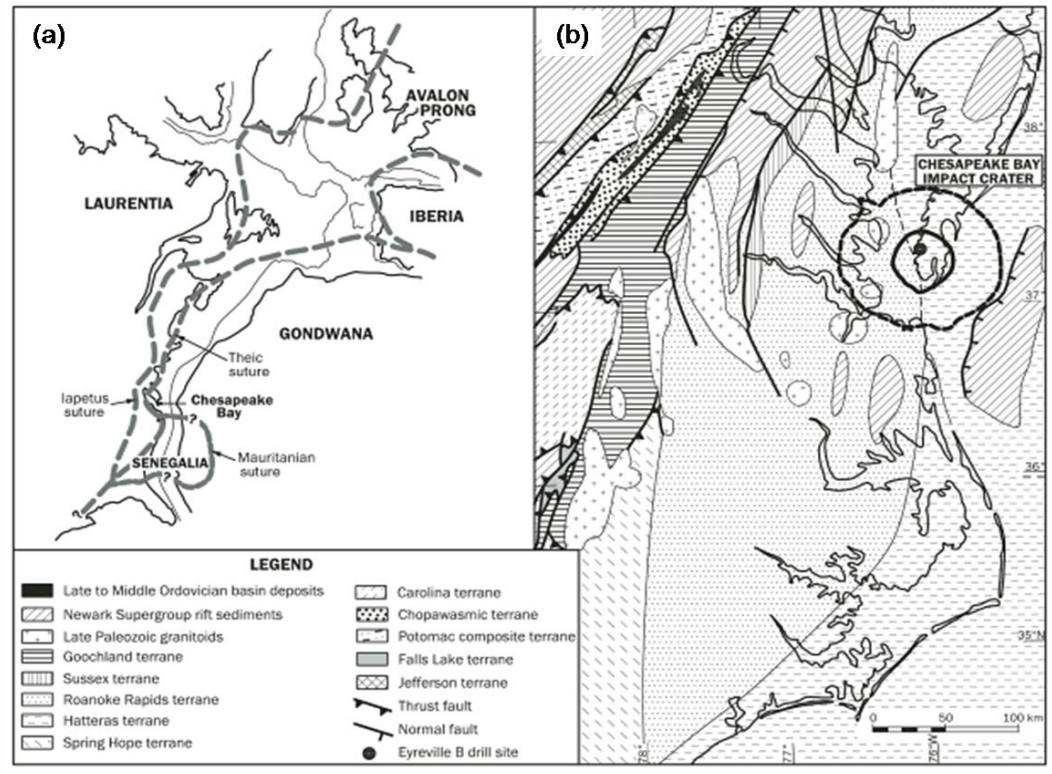

Figure 6.1: (a) Plate reconstruction of the Palaeozoic sutures between Laurentia and Gondwana showing the location of the CBIS (after Lefort, 1988; Lefort and Max, 1991). (b) Tectonostratigraphic terrane map of the Central Appalachians showing the location of the CBIS (after Horton *et al.*, 2005b).

Table 6.1: Characteristics of terranes in the vicinity of the CBIS (as seen in Figure 6.1b).

Terrane	Units	Lithologies	Structural relationships	Noteworthy intrusions	Age	Metamorphic grade
Carolina Zone[1]						
Roanoke Rapids[1,2]	Halifax County Complex[1,2,3]	Intrusive complex comprising ultramafics, gabbroids, felsic plutonics and basaltic rocks[3]	Bounded by the Hollister and Gaston Dam faults on west, Richmond Basin on north and bounded by the Hatteras terrane on the east (boundary covered by Atlantic Coastal Plain sediments)[1,2]	Ultramafics, gabbroids and felsic plutonics[3]	Undetermined; > 292 ± 31 Ma (maximum age for Hollister mylonite zone)[3,4]	Greenschist to epidote-amphibolite[1,2,3]
	Roanoke Rapids Complex[1,2,5]	Intrusive trondhjemitic to quartz-dioritic core surrounded by felsic metavolcanic and metavolcaniclastic rocks[1,5]		Trondhjemitic to quartz-dioritic pluton[1,5]	Metagranodiorite: 672 ± 2 Ma (U/Pb zircon)[7]; Metatonalite: ca. 668 Ma (^{207}Pb/^{206}Pb zircon)[8]	Greenschist to epidote-amphibolite[1,2]
	Easonburg Formation[1,2,6]	Felsic volcanic and phyllitic volcaniclastic rocks[1,6]		Metagranite and metatonalite[7,8]	Metagranite: 615 ± 1 Ma (U/Pb zircon)[7]; Metatonalite: ca. 607 Ma (^{207}Pb/^{206}Pb zircon)[8]	Greenschist[1,2]
Hatteras[2,]	Hatteras[2,9]	Granitic rocks intruding Bt gneiss, Grt-bearing schist and carbonatised amphibolite[10]	Bounded on west by Roanoke Rapids terrane and covered by Atlantic Coastal Plain sediments on east[2]	Intrusive complex including Amp-Qz monzonite (AQM) and Grt-Crd-Bt granite (GCBG)	AQM: 630 ± 39 Ma and GCBG: 583 ± 46 Ma (Rb/Sr whole rock)[11]	Amphibolite[2,9,10]
Spring Hope[1,2]	Upper[12]	Volcanogenic metasedimentary rocks[1,12]	Bounded by Nutbush Creek fault zone on west and Hollister fault zone on east[1]	Metagabbro and metadiorite[2]	549 ± 4 Ma and 551 ± 2 Ma (U/Pb zircon)[7]	Greenschist[1]
	Lower[12]	Felsic and minor mafic metavolcanic rocks[1,12]			590 ± 3 Ma (U/Pb zircon)[13]	Greenschist[1]

Terrane	Units	Lithologies	Structural relationships	Noteworthy intrusions	Age	Metamorphic grade
Carolina[1,2]	Virgilina sequence[1,2]	Felsic-intermediate metavolcanic rocks, metaclastic turbidites and metabasalt[1]	Bounded on west by Charlotte terrane and Goochland, Falls Lake, Crabtree and Mesozoic basins to the east[1]	Roxboro metagranite (RMG), Vance Country pluton (VCP) and Parks Crossroads granodiorite (PCG)[1]	Volcanic and plutonic rocks: 620 ± 20 Ma (U/Pb zircon)[10] and 620-616 Ma (U/Pb zircon)[11]; RMG, VCP and PCG ca. 546 Ma (U/Pb zircon)[1,14]	Greenschist[1,2]
	Albemarle sequence[1,2]	Felsic and mafic volcanic rocks and epiclastic sedimentary rocks[1]	Bounded on west by Charlotte terrane and covered by Atlantic Coastal Plain sediments on east[1]	Gabbro dykes, sills and small laccoliths[15]	Basal Uwharrie Formation: 586 ± 10 Ma (U/Pb zircon)[16] and 551 ± 8 Ma (U/Pb zircon)[17,18]	Greenschist[1,2]
	South Carolina sequence[1,2]	Intermediate to felsic pyroclastic rocks and metasedimentary rocks[1]	Bounded on west by Charlotte terrane and covered by Atlantic Coastal Plain sediments on east[1]	N/A	Basal Persimmon Fork Formation: ca. 580-545 Ma (U/Pb zircon)[19,20,21]	Greenschist[1,2]
	Cary sequence[1,2]	Dacitic crystal-lithic tuffs with minor phyllites and mafic rocks[1,22]	Narrow strip bounded on west by Uchee terrane and Savannah River terrane on east[1]	Felsic plutons[1,6,22]	Felsic metavolcanics: 575 ± 12 Ma (U/Pb zircon)[13]	Greenschist[1,2]
Crabtree[1,2]	Crabtree[1,2]	Felsic gneiss, Grt-St schist, Grt-Ky schist and graphitic schist[1,23]	Bounded by Nutbush Creek fault zone on west, the Falls Lake terrane to the northwest and Raleigh terrane to the east[1,22]	Crabtree Creek pluton (CCP)[1]	CCP: 542 Ma ($^{207}Pb/^{206}Pb$ zircon)[4]; 554, 564 and 566 Ma ($^{207}Pb/^{206}Pb$ zircon)[13]	Amphibolite[23]

Terrane	Units	Lithologies	Structural relationships	Noteworthy intrusions	Age	Metamorphic grade
Falls Lake[1,2]	Falls Lake[1,2]	Mafic and ultramafic blocks, micaceous quartzofeldspathic rocks (MQ) and pelitic schists[1,2]	Bounded by Albemarle sequence to the north, the Crabtree terrane to the south, Mesozoic basins to the west and truncated by the Nutbush Creek fault zone on east[1]	Crabtree Creek pluton (CCP)[1]	MQ: ca. 590 Ma ($^{207}Pb/^{206}Pb$ zircon)[13]	Upper greenschist to middle amphibolite[24]
Other						
Sussex[2,25]	Sussex[2,25]	Laminated siliceous metavolcanic rocks and calcareous metasiltstone, Bt-Ep-Grt-Amp schist and gneiss, metagabbro, metadiorite and Bt-Qz monzonite[2,25]	Bounded by the Goochland terrane on west and the Roanoke Rapids terrane on east[2,25]	N/A	Undetermined	Greenschist[2,25]
Goochland[2,25]	State Farm Gneiss[2,25]	Felsic to intermediate gneiss[26,27]	Bounded on west from the Chopawamsic terrane by the Spotsylvania fault zone and on the east by the Hylas fault zone[27,28]	N/A	ca. 1046-1023 Ma (U/Pb zircon)[29]	Granulite[31]
	Sabot Amphibolite[2,25]	Amphibolite inter-layered with Bt gneiss[27]		Montpelier Anorthosite (MA)[26,27]	MA: 1045 ± 10 Ma (U/Pb zircon)[27]	Granulite[31]
	Maidens Gneiss[2,25]	Layered metavolcanic and metasedimentary rocks[25,27]			Granitic gneiss:1035 ± 5 Ma (U/Pb zircon)[30]	Granulite[31]
Chopa-wamsic[2,25]	Ta River Metamorphic Suite[2,25]	Amphibolite interlayered with Bt gneiss and schist[2,25]	Bounded on west from the Potomac terrane by the Chopawamsic fault and from the Goochland terrane by the	N/A	Undetermined	Amphibolite[26,33]

Terrane	Units	Lithologies	Structural relationships	Noteworthy intrusions	Age	Metamorphic grade
	Chopawamsic Formation[2,25]	Mafic and felsic metavolcanic rocks[26]	Spotsylvania fault zone on east[26,27]	Columbia pluton (CP)[34]	Metavolcanic rocks: ca. 470 Ma (U/Pb zircon)[32,33]; CP: 457 ± 7 Ma (U/Pb SIMS)[34]	Greenschist to amphibolite[26,33]
	James Run Formation[2,25]	Predominantly felsic intergraded volcanic and volcaniclastic rocks[2]		N/A	Undetermined	Greenschist to amphibolite[26,33]
	Arvonia and Quantico Formations[2,25]	Metasedimentary rocks containing fossils (brachiopods, trilobites, bryozoans, echinoderms and crinoids stems)[2,25,23]		N/A	Late Ordovician (~460-440 Ma)[33]	Greenschist to amphibolite[26,33]
Potomac composite[2,35]	Mather Gorge Formation[35]	Domains[35]: Blockhouse Point (BPD; sericite phyllonites and minor ultramafic rocks), Bear Island (BID; metagreywacke, ultramafic rocks, migmatite, granodiorite, quartz-mica schists and amphibolite), Stubblefield Falls (SFD; magmatic to phyllonitic schist with minor amphibolite and diamictite)	Bound by Pleasant Grove fault on west and Plummers Island fault on east[35]	Bear Island Granodiorite (BIG) and associated pegmatites and lamprophyre dykes intrude into the BID[35]	BPD: ca. 940 Ma (U/Pb zircon)[36] BID: ca. 540 Ma (U/Pb zircon)[36] BIG: ca. 440 Ma (U/Pb zircon)[36]	Greenschist to amphibolite[35]

Terrane	Units	Lithologies	Structural relationships	Noteworthy intrusions	Age	Metamorphic grade
	Sykesville Formation[35]	Diamictite containing amphibolite, migmatite, schist, metagreywacke, granofels, phyllonite, metabasalt and vein quartz clasts[37]	Bound by Plummers Island fault on west and Rock Creek shear zone on east[35]	Georgetown Intrusive Suite (GIS; Bt-Hbl tonalite), Dalecarlia Intrusive Suite (DIS; Bt and Ms-Bt monzogranite) and the Kensington Tonalite (KT; Ms-Bt tonalite)[37,38]	GIS: 472 ± 4 Ma (SHRIMP U/Pb zircon)[38] DIS: 478 ± 6 Ma (SHRIMP U/Pb zircon)[38] KT: 463 ± 8 Ma (SHRIMP U/Pb zircon)[38]	Upper amphibolite[35]
	Laurel Formation[35]	Quartz and meta-arenite fragments and Ms-Bt schist in a quartzo-feldspathic matrix[37]	Bound by Rock Creek shear zone on west and covered by Atlantic Coastal Plain sediments[35]	Kensington Tonalite (KT; Ms-Bt tonalite)[38]	Laurel Formation: ca. 520 Ma (U/Pb zircon)[28] KT: 463 ± 8 Ma (SHRIMP U/Pb zircon)[38]	Upper amphibolite[35,37]
Jefferson[2,25]	Jefferson[2,25]	Gneiss, schist, amphibolite and ultramafic rocks[2,25]	Bounded on northwest and beneath by Laurentia and the Potomac composite terrane on the east[2]	Elkahatchee pluton (EP)[25]	EP: 490 ± 28 Ma (Rb/Sr whole rock)[25,39]	Greenschist to granulite[2]

Mineral abbreviations: Amp = amphibole; Bt = biotite; Crd = cordierite; Ep = epidote; Grt = garnet; Hbl = hornblende; Ky = kyanite; Ms = muscovite; St = staurolite; Qz = quartz (after Whitney and Evans, 2010). References: 1 (Hibbard *et al.*, 2002); 2 (Horton *et al.*, 1989); 3 (Kite and Stoddard); 4 (Russell *et al.*, 1985); 5 (Horton and Stoddard, 1986); 6 (Farrar, 1985); 7 (Coler and Samson, 2000); 8 (Horton and Stern, 1994); 9 (Daniels and Ziets, 1978); 10 (Denison *et al.*, 1967); 11 (Russell *et al.*, 1981); 12 (Carpenter *et al.*, 1995); 13 (Goldberg, 1994); 14 (Wortman *et al.*, 2000); 15 (Conley and Bain, 1965); 16 (Wright and Seiders, 1980); 17 (Ingle, 1999); 18 (Ingle-Jenkins *et al.*, 1999); 19 (Carpenter *et al.*, 1982); 20 (Dallmeyer *et al.*, 1986); 21 (Barker *et al.*, 1998); 22 (Blake *et al.*, 1999); 23 (Robitaille, 2004); 24 (Horton *et al.*, 1986); 25 (Rankin, 1994); 26 (Spears *et al.*, 2004); 27 (Aleinikoff *et al.*, 1996); 28 (Horton *et al.*, 2005b); 29 (Owens and Tucker, 2003); 30 (Horton *et al.*, 1995); 31 (Farrar, 1984); 32 (Horton *et al.*, 1998); 33 (Coler *et al.*, 2000); 34 (Wilson, 2001); 35 (Kunk *et al.*, 2004); 36 (Southworth *et al.*, 2006); 37 (Southworth, 2002); 38 (Aleinikoff *et al.*, 2002); 39 (Russell *et al.*, 1987).

Table 6.2: Tectonic setting and proposed source of origin for terranes in the vicinity of the CBIS (as seen in Figure 6.1b).

Terrane	Tectonic Setting	Source of origin
Carolina Zone		
Roanoke Rapids	Volcanic arc[1]	Peri-Gondwanan[1]
Hatteras	Volcanic arc[1,2,3]	Peri-Gondwanan[2,3]
Spring Hope	Volcanic arc[1]	Peri-Gondwanan[1]
Carolina	Volcanic arc[1]	Peri-Gondwanan[1]
Crabtree	Volcanic arc[1]	Peri-Gondwanan[1]
Falls Lake	Volcanic arc[1]	Peri-Gondwanan[1]
Other		
Sussex	Mélange[2,4]	Undetermined
Goochland	Laurentian slice[5]/ accreted micro-continent[2,4]	Disputed (Laurentian[5]/ Peri-Gondwanan[2,4])
Chopawamsic	Volcanic arc[2,4]	Iapetan[6]
Potomac composite	Mélange[2,4]	Iapetan[6]
Jefferson	Accretionary complex[2,4]	Iapetan[6]

References: 1 (Hibbard *et al.*, 2002); 2 (Horton *et al.*, 1989); 3 (Horton *et al.*, 2005b); 4 (Rankin, 1994); 5 (Bartholomew and Tollo, 2004); 6 (Hibbard *et al.*, 2007a)

6.2 Lithologies

This study identified eight major crystalline basement rock types within the Eyreville-B borehole core, namely the mica schist, para-amphibolite, calc-silicate and granite of the lower basement-derived section, and the ortho-amphibolite, granite gneiss and massive granite with biotite schist xenoliths of the upper megablocks section. The following section includes the comparisons of these rocks with those in the surrounding terranes.

6.2.1 Lower basement-derived section

The lower basement-derived section of the Eyreville-B borehole core is divided into two rock components; a metasedimentary sequence and a coarse-grained to pegmatitic granite that intrudes the metasediments.

6.2.1.1 Metasedimentary sequence

Petrographic analysis of the lower basement-derived metasedimentary sequence revealed the presence of mica schist, para-amphibolite and calc-silicate rocks (see Chapter 2, Section 2.3.1); prior to metamorphism, these were shale, greywacke and marl sediments, respectively (see Chapter 3, Section 3.6.1). The mica schist is composed of muscovite, quartz, plagioclase, biotite and graphite, with lesser amounts of fibrolite, garnet, tourmaline, pyrite, rutile and pyrrhotite (Chapter 2, Section 2.3.1.1). The mineral assemblages for the para-amphibolite and calc-silicate rocks, both found within a mylonite zone (see Chapter 2, Figure 2.1), are amphibole-plagioclase-epidote-biotite-K-feldspar-quartz-titanite-calcite and vesuvianite-plagioclase-quartz-epidote, respectively (see Chapter 2, Sections 2.3.1.3 and 2.3.1.4). The occurrence of minor biotite schist and tourmalinite is also observed in the lower basement-derived metasedimentary sequence (see Chapter 2, Sections 2.3.1.2 and 2.3.1.5).

The provenance for the metasedimentary sequence is somewhat ambiguous based on geochemical analyses, with results spanning passive margin, active margin and island arc sediments (see Chapter 3, Section 3.6.1). However, 74 % of the sediments have an igneous provenance, most of which is intermediate igneous (see Chapter 3, Figures 3.16 and 3.17), indicating either a mature island arc or immature continental magmatic arc tectonic setting. Based on this evidence, the metasedimentary sequence is interpreted to have been deposited in either of the two volcanic arc tectonic settings.

According to Horton *et al.* (2005b), the CBIS formed in rocks from the Roanoke Rapids (western portion) and Hatteras (eastern portion) terranes (Figure 6.1b). The Roanoke Rapids terrane in the underlying western portion of the CBIS comprises a mafic-ultramafic suite (Halifax County complex) and a volcanic-plutonic complex (Roanoke Rapids complex) surrounded by a sequence of felsic volcanic and phyllitic volcaniclastic rocks (Easonburg Formation), which were subjected to greenschist to epidote-amphibolite grade conditions (see Chapter 1, Section 1.1.2; Table 6.1; Kite and Stoddard, 1984; Farrar, 1985; Horton *et al.*, 1989; Hibbard *et al.*, 2002). The Hatteras terrane, underlying the eastern portion of the CBIS, is composed of amphibolite-facies

pelitic schists and gneisses that have been intruded by granitic to dioritic plutonic rocks (see Chapter 1, Section 1.1.2; Table 6.1; Denison *et al.*, 1967; Daniels and Zietz, 1978; Horton *et al.*, 1989). Little to no quantitative data are available for metasedimentary and metavolcaniclastic rocks of these two terranes; consequently, comparisons between these rocks and those of the Eyreville-B borehole core are based on qualitative analysis.

The amphibolite-facies metasediments of the Eyreville-B borehole core (see Section 6.5) compare well with the amphibolite-facies rocks of the Hatteras terrane, where Denison *et al.* (1967) observed biotite schist, with large (2 mm) poikiloblastic garnet porphyroblasts, and carbonatised amphibolite comprising hornblende, plagioclase, iron oxides and calcite veins, with calcite and micas locally replacing hornblende. Although the minor biotite schist component in the lower basement-derived section lacks garnet, the size of garnet porphyroblasts in the basement mica schist is comparable to those observed by Denison *et al.* (1967). The basement para-amphibolite also shows similar mineral assemblages and calcite alteration to that seen in the Hatteras terrane's carbonatised amphibolite (Denison *et al.*, 1967). In comparison, the lower, greenschist facies, felsic volcanic and phyllitic volcaniclastic rocks of the Roanoke Rapids terrane show greater similarities to lithic clasts found within the intervening impactite sequence of the Eyreville-B borehole core (see Chapter 1, Figure 1.15). Jolly (2011) identified at least 17 types of lithic clasts in the impactite sequence, where phyllites were the most common lithic clast and felsic gneiss clasts slightly less abundant.

Horton *et al.* (1989, 1991) proposed that the amphibolite facies Hatteras terrane may be a higher-grade equivalent of the greenschist-facies Roanoke Rapids terrane. If this is true, the terrane would form part of the Carolina Zone, a cluster of mainly Neoproterozoic to early Palaeozoic terranes located along the eastern flank of the Southern Appalachians (see Chapter 1, Section 1.1.2; Hibbard *et al.*, 2002). Predominantly comprising meta-igneous rocks with an associated metasedimentary component, the Carolina Zone forms one of the late Neoproterozoic to Cambrian composite volcanic arc systems accreted to Laurentia in Late Ordovician to Silurian time (Hibbard *et al.*, 2002). Consequently, the Hatteras terrane would also

be associated with active margin tectonic settings, such as arc volcanism, and compare favourably with the possible tectonic settings proposed for the Eyreville-B borehole core metasedimentary rocks (see Chapter 3, Figures 3.16 and 3.17). Although not definitive, the metasedimentary rocks of the lower basement-derived section share more diagnostic characteristics (e.g. mineral assemblage, tectonic setting, metamorphic grade, etc.) with the metasedimentary rocks of the Hatteras terrane than the Roanoke Rapids terrane, and it is more likely that they form part of the former terrane.

6.2.1.2 Granite

The granite of the lower basement-derived section is pegmatitic to coarse-grained and is composed of K-feldspar, plagioclase, quartz and muscovite with minor biotite and garnet (see Chapter 2, Section 2.3.1.6). Petrographic and geochemical analysis on two fine-grained samples (RG40 and RG61) from the basement granite, which are considered to be representative of this rock unit, revealed it to be a peraluminous, S-type granite that was generated in a within-plate tectonic setting (see Chapter 2, Section 2.3.1.6; Chapter 3, Sections 3.3.3 and 3.6.3, Figures 3.5, 3.22 and 3.23). Difficulties in sampling the pegmatitic granite owing to large grain size prevented precise determination of the depth of melting/crystallisation (see Chapter 3, Figure 3.23b).

From Virginia to Georgia, the Central and Southern Appalachians are intruded by Alleghanian-age granitic plutons ranging from 330-260 Ma (Horton *et al.*, 1987; Coler *et al.*, 1997; Speer *et al.*, 1994). Most of the ~60 plutons are leucocratic, metaluminous, biotite- and hornblende-bearing granites and granodiorites (Figure 6.2a); however, there are at least eight plutons that are peraluminous in nature, containing muscovite, garnet and/or cordierite, similar to what is observed for the lower basement-derived granite (Speer *et al.*, 1994).

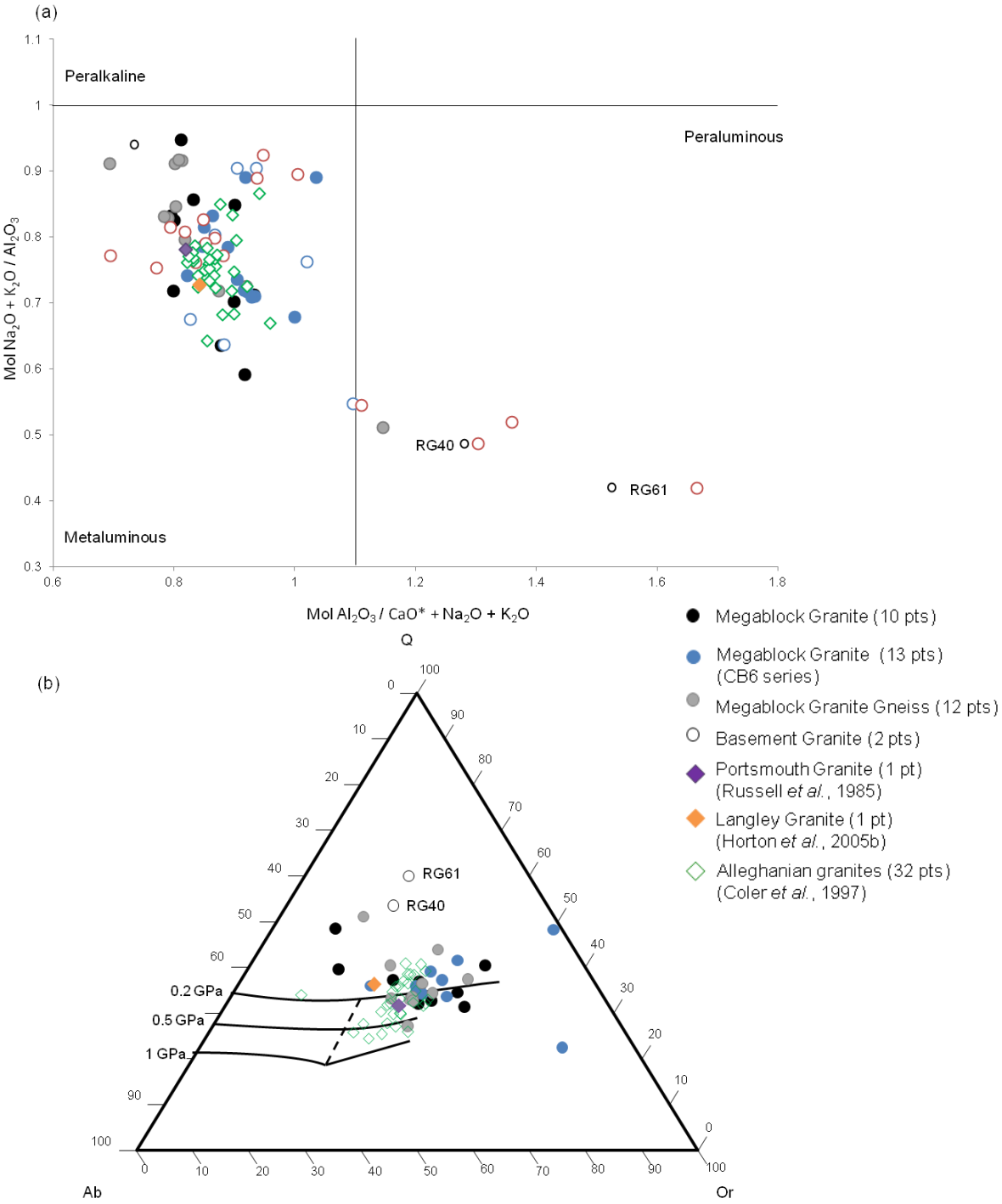

Figure 6.2: Comparisons between the granites from the Eyreville-B borehole core, the Langley Granite from the Langley borehole core and the Alleghanian-age granitic plutons from the eastern portion of the Appalachian orogen (data from Russell *et al.*, 1985; Coler *et al.*, 1995; Horton *et al.*, 2005b). (a) ASI diagram (after Shand, 1927; Chappell and White, 1974) and (b) ternary Ab-Qz-Or diagram including cotectic curves in an H_2O-undersaturated system (after Johannes and Holtz, 1991). Dashed line represents the water-undersaturated curve for a_{H2O} = 0.8 crustal fluids in equilibrium with graphite (after Johannes and Holtz, 1991). Abbr. ASI = alumina saturation index (after Shand, 1927); Ab = albite; Or = orthoclase; Qz = quartz (mineral abbreviations after Whitney and Evans, 2010).

In petrography and age, the nearest, most similar, Alleghanian-age pluton to the basement granite is the Portsmouth Granite, located approximately 50 km to the southwest in the Roanoke Rapids terrane (Horton *et al.*, 1989). The Portsmouth Granite is also a non-foliated, coarse-grained, muscovite- and biotite-bearing granite (Russell *et al.*, 1985). Dated at 263 ± 25 Ma using Rb-Sr whole rock geochronology (Russell *et al.*, 1985; Samson *et al.*, 1995), the Portsmouth Granite is approximately 10 Ma older than the peak metamorphic event (although within error) recorded in the Eyreville-B borehole core (254 ± 3 Ma; see Chapter 5, Section 5.4; Section 6.6; Horton *et al.*, 2009b). The crystallisation age of the basement granite could not be determined through U/Pb zircon geochronology (see Section 6.6), with the closest age from white mica Ar/Ar geochronology being 243 ± 1.1 Ma (see Chapter 5, Section 5.3.2.4). Microstructural observations of the lower basement-derived granite revealed that it does not contain the prograde to syn-peak metamorphic foliation seen in the mica schists, but that it is strongly mylonitised together with the mica schists in the mylonite zone (see Chapter 2, Section 2.4.1), suggesting intrusion occurred slightly after peak metamorphic conditions (ca. 254 Ma) but prior to the onset of the retrograde mylonitic event (cooling through the 500°C isotherm dated at ca. 247 Ma; see Chapter 5, Section 5.4; Section 6.5). The inferred age range (between 254 and 247 Ma) for the lower basement-derived granite might be interpreted to fall within error of the Rb/Sr whole rock 260 ± 25 Ma crystallisation age Russell *et al.* (1985) determined for the Portsmouth Granite. However, as observed in the large error (± 25 Ma) determined for the Portsmouth Granite, Rb/Sr whole rock geochronology does not always produce precise ages (Davis *et al.*, 2003). Nevertheless, the 254-247 Ma age range for the lower basement-derived section suggests that it was emplaced during the last stages of the Alleghanian orogeny (330-260 Ma; Horton *et al.*, 1989).

With regards to ASI (alumina saturation index; Figure 6.2a), the Portsmouth Granite is unlike the representative fine-grained samples (RG40 and RG61) from the lower basement-derived granite as it does not appear to be peraluminous in nature. This suggests that the Portsmouth Granite has an igneous protolith (I-type granite; Chappell and White, 1974) in contrast to the basement granite's sedimentary source (S-type granite; Chappell and White, 1974; see Chapter

3, Section 3.3.3). However, the metaluminous ASI (Figure 6.2a) of the Portsmouth Granite contradicts its peraluminous mineralogy (contains muscovite; Russell *et al.*, 1985) as well as $^{87}Sr/^{86}Sr$ isotopic ratios (>0.71) and ^{18}O values (>8.9%) that indicate a sedimentary origin (S-type granite; Chappell and White, 1974; Speer *et al.*, 1994; Samson *et al.*, 1995). Since the I- and S-type classification system is based on petrological, geochemical and isotopic features (Chappell *et al.*, 1998), Speer *et al.* (1994) interpreted a continental crustal origin for the Portsmouth Granite.

In Figure 6.2b, the Portsmouth Granite plots at slightly lower pressures than the 0.2 GPa cotectic curve (for granitic melts in a H_2O-undersaturated system; after Johannes and Holtz, 1991), indicating melting and magma emplacement occurred at shallow crustal levels. Since the large dispersion in data from samples of the lower basement-derived granite precludes determination of emplacement levels from Figure 6.2b, it cannot be certain whether these conditions were comparable with those of the Portsmouth Granite and other Alleghanian-age plutons. However, despite differing mineralogy, geochemistry and source rock, Speer *et al.* (1994) observed that most of the Alleghanian-age plutons were emplaced at middle to shallow crustal levels (0.2-0.5 GPa; Figure 6.2b) based on geobarometric techniques applied to rocks in their contact aureoles and granite crystallisation. Consequently, the lower basement-derived granite may have been emplaced at similar levels.

6.2.2 Upper megablocks section

Two rock types comprise the upper megablocks section of the Eyreville-B borehole core; the ~13-m-thick amphibolite megablock, and the ~275-m-thick granite megablock. Included into the granite megablock are the biotite schist xenoliths.

6.2.2.1 Amphibolite megablock

The amphibolite of the upper megablocks section is composed of amphibole, plagioclase, biotite and quartz, with accessory epidote, chalcopyrite, pyrrhotite, pyrite, magnetite and titanite (see

Chapter 2, Section 2.3.2). Geochemical analysis in Chapter 3 (Section 3.6.2) combined with textural observations in Chapter 2 (Section 2.4) and by Horton *et al.* (2009b) indicate that the megablock amphibolite is a metamorphosed tholeiitic gabbro that probably emplaced in an island arc tectonic setting (Figures 3.19, 3.20 and 3.21). Comparisons between the upper amphibolite megablock and the mafic-ultramafic rocks of the Halifax County Complex in the Roanoke Rapids terrane, which Horton *et al.* (2005b) proposed to underlie the western portion of the CBIS (Figure 6.1), are shown in Figure 6.3.

In the Halifax County Complex, Kite and Stoddard (1984) observed four basic rock groups: ultramafics, gabbroids, felsic plutonic rocks and basaltic rocks. In Figure 6.3, the average compositions of nine recognised mafic-ultramafic rocks from the Halifax County Complex are plotted with samples from the upper amphibolite megablock for selected major element oxides against SiO_2. Generally, samples from the amphibolite megablock tend to be slightly enriched in TiO_2, Al_2O_3, Fe_2O_3 and Na_2O (Figure 6.3a, b, c and f) and depleted in MgO and CaO (Figure 6.3d and e) compared to the Halifax County Complex rocks. The amphibolite megablock shares the greatest geochemical similarities with average compositions of the basaltic rocks (metabasalt and, to a lesser extent, the basaltic amphibolite and amphibolite) of the Halifax County Complex (Figure 6.3). This is surprising since textural observations made in Chapter 2, Section 2.4, and by Horton *et al.* (2009b) indicate that a relict igneous (gabbroic/dioritic) texture is locally preserved in the amphibolite megablock and, consequently, greater similarities with the gabbroid rocks were expected. However, TiO_2, Al_2O_3, MgO and CaO content within sample RG06 from the amphibolite megablock, whose precursor is interpreted to be diorite (see Chapter 3, Section 3.6.2, Figure 3.19), shows the strongest correlation with the quartz diorite sample from the Halifax County Complex (Figure 6.3). This may suggest that this portion of the amphibolite megablock may preserve the initial stages of transition from mafic material towards more felsic material within an ophiolitic complex, which is the proposed origin for the Halifax County Complex (Kite and Stoddard, 1984).

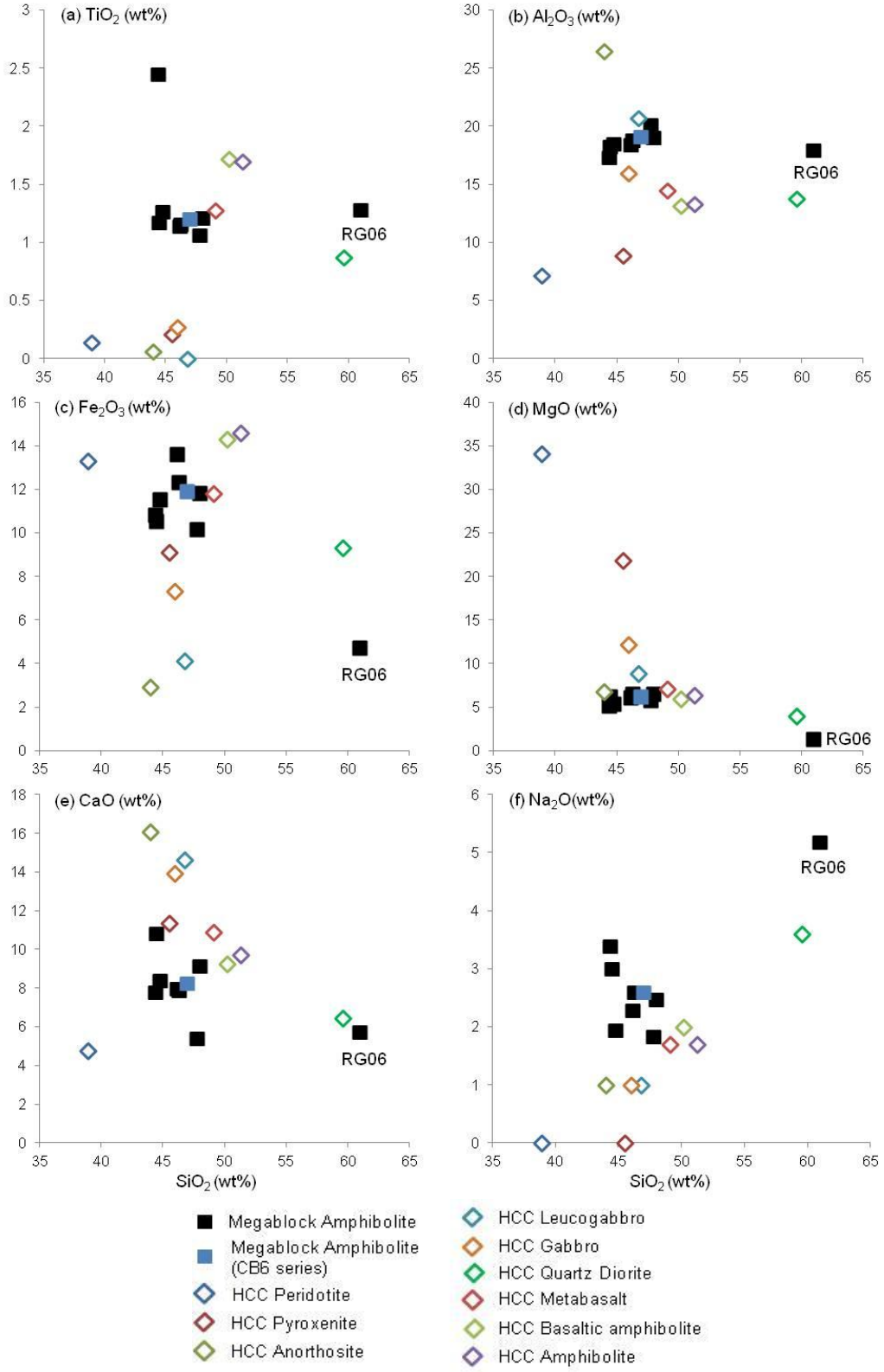

Figure 6.3: Harker diagrams showing selected major element oxides (TiO_2, Al_2O_3, Fe_2O_3, MgO, CaO and Na_2O) plotted against SiO_2 for the megablock amphibolite of the Eyreville-B borehole core and the mafic-ultramafic rocks of the Halifax County Complex (data from Kite and Stoddard, 1984). Abbr.: HCC = Halifax County Complex.

Kite and Stoddard (1984) proposed that the Halifax County Complex is a tholeittic island-arc ophiolite based on the following mineralogical, lithological and geochemical evidence (Horton *et al.*, 1989): (1) The sequence of rock units (peridotite and dunite-pyroxenite-gabbroid-diorite) and clinopyroxene-bearing plutonic rocks compare well with cumulate sequences observed in many ophiolites (Hopson *et al.*, 1975; George, 1978; Himmelberg and Loney, 1980; Sinton, 1980; Pallister and Hopson, 1981). (2) The increasing Fe enrichment through the ultramafic-gabbroic-basaltic sequence is typical of trends observed in oceanic tholeiites (Irvine and Baragar, 1971; Norman and Strong, 1975). (3) Rare earth element geochemical studies of the Halifax County Complex show the gabbroids as more primitive (less differentiated) than the basalts, and the basalts exhibit rare earth element characteristics comparable with island-arc tholeiites (Jakes and Gill, 1970; Kite and Stoddard, 1984). Although comparisons between the Halifax County Complex and the amphibolite megablock are limited, bulk rock major and trace element analysis (see Chapter 3, Section 3.6.2, Figure 3.21) as well as rare earth element analysis (see Chapter 3, Section 3.5.2, Figure 3.15b) indicates that the amphibolite megablock also likely formed in an island-arc setting. Therefore, it is possible that the mid-amphibolite grade metamorphosed gabbroic rock of the amphibolite megablock (see Section 6.4) is an intrusive equivalent of the greenschist basaltic rocks of the Halifax County Complex that experienced metamorphic conditions slightly greater than observed in the Halifax County Complex. Alternatively, the amphibolite megablock may form part of a similar ophiolitic complex in the amphibolite-facies Hatteras terrane that has yet to be identified in the latter.

The amphibolite megablock is also intruded by a brecciated biotite granite vein towards the base of the megablock (see Chapter 2, Section 2.3.2). As its mineralogy and texture closely resembles the massive megablock granite, it has been interpreted to be derived from the same source (see Chapter 2, Section 2.5.3), which is discussed in Section 6.2.2.2. Consequently, it is deduced that the amphibolite megablock forms part of the same metamorphic terrane as the upper granite megablock and that it was emplaced prior to peak metamorphism.

6.2.2.2 Granite megablock

The gneissic granite of the upper megablock is composed of K-feldspar, quartz, plagioclase and biotite, with lesser amounts of pyrite and magnetite (see Chapter 2, Section 2.3.3.1). The pervasive gneissic fabric is defined by aligned biotite grains alternating with K-feldspar (see Chapter 2, Sections 2.3.3.1 and 2.4.1). Geochemical analysis shows that it is a metaluminous, I-type granite that was emplaced in a syn-collisional environment at middle to shallow crustal levels (0.2-0.5 GPa) under H_2O-undersaturated conditions (see Chapter 3, Section 3.3.3, Figures 3.5, 3.22 and 3.23). Although very similar to Alleghanian-age granites in the eastern portion of the Central and Southern Appalachians in terms of mineralogy and geochemistry (Figure 6.2; Speer *et al.*, 1994), the gneissic granite is considerably older (ca. 615 Ma; Horton *et al.*, 2009b). Rocks of similar age are observed in the Roanoke Rapids terrane and are discussed in detail in Section 6.6.

Similar to the gneissic granite, the mineral assemblage of the intruding massive biotite granite of the upper megablocks section includes K-feldspar, quartz, plagioclase, biotite and pyrite, but also includes minor amounts of muscovite and magnetite (see Chapter 2, Section 2.3.3.2). It is also metaluminous in nature (Figure 6.2a) and was emplaced at middle to shallow crustal levels (0.2-0.5 GPa) under H_2O-undersaturated conditions (see Chapter 3, Section 3.3.3, Figures 3.5, 3.22 and 3.23). It compares well with the Alleghanian-age granites located within the eastern portion of the Central and Southern Appalachians in terms of mineralogy, ASI and levels of emplacement (Figure 6.3; Speer *et al.*, 1994). Similar to the lower basement-derived granite, the age of the massive granite (ca. 254 Ma; Horton *et al.*, 2009b) suggests that it was emplaced during the latter stages of the Alleghanian orogeny (Horton *et al.*, 1989; Speer *et al.*, 1994).

The megablock biotite schist xenoliths are almost exclusively found in the massive granite variety in the granite megablock, although rare xenoliths are observed in the granite gneiss. The mineralogy of the biotite schists includes biotite, plagioclase, quartz, pyrite, epidote and minor amounts of amphibole (see Chapter 2, Section 2.3.3.3). The geochemistry of the biotite schist xenoliths suggests that they are metamorphosed shale derived from eroded old continental

crust that was later deposited in an active margin setting most likely associated with recycling of complex orogenic belts (see Chapter 3, Section 3.6.1, Figures 3.16 and 3.17), differentiating them from the metasediments of the lower basement-derived section (see Section 6.2.1.1). Although the biotite schist xenoliths superficially resemble the biotite schist in the lower basement-derived section in terms of mineralogy and geochemistry (see Chapter 2, Sections 2.3.1.2 and 2.3.3.3; Chapter 3, Section 3.6.1, Figures 3.16 and 3.17), the basement biotite schist shows extensive hydrothermal alteration, causing uncertainty with regards to any inferred geochemical protoliths and provenance interpretations (Schmitt *et al.*, 2009). Consequently, comparisons with the megablock biotite schist xenoliths are tenuous.

It is also possible that, rather than reflecting a sedimentary source, the biotite schist xenoliths represent a restite component generated from partial melting during the metamorphic event associated with the generation of the massive megablock granite. However, foliated mica-rich restites are typical of S-type granites derived during anatexis (Williamson *et al.*, 1997), whereas I-type restites are characterised by clinopyroxene and amphibole phases (Wall *et al.*, 1987; Stephens, 2001). It is more likely that the biotite schist xenoliths observed in the upper granite megablock were scavenged from wall rock as the magma that gave rise to the massive megablock granite ascended through the crust (see Chapter 2, Sections 2.3.3.2 and 2.3.3.3; Chapter 3, Section 3.6.1). Such a process is termed stoping, where significant temperature differences between wall rock and magma at shallow crustal levels produce the necessary thermal stress to fracture the wall rock (Glazner and Bartley, 2006). Such wall-rock xenoliths have been documented in some of the Alleghanian granitoids in the Central and Southern Appalachians (Speer *et al.*, 1994).

6.3 Structure

As established in Chapter 2 (Section 2.4), at least two deformation events are preserved in the lower basement-derived section of the Eyreville-B borehole core (D1 and D2). The granitic gneiss of the upper granite megablock also contains evidence for at least one deformational

event (see Chapter 2, Section 2.4). Structural evidence for the Chesapeake Bay impact is also discussed in this section.

6.3.1 D1 event

Macro- and microstructural analysis of the lower basement-derived rocks of the Eyreville-B borehole core revealed evidence for a diachronous D1 event: a prograde mica foliation (S1a) in the mica schists, and a retrograde mylonitic foliation (S1b) and lineation (L1b) in the mica schists and granite veins of the mylonite zone (see Chapter 2, Section 2.4.1). Cumulative analysis of the mica schist foliation indicates a moderate to shallow dip (mean ~30°) from horizontal (see Chapter 2, Section 2.4.1) at present. Microstructural evidence in the lower basement-derived section (see Chapter 2, Section 2.4.1) suggests that the prograde and retrograde fabrics were generated during a single, continuous, non-coaxial event. Metamorphic grade (Section 6.4) and the age of metamorphism (Section 6.5) suggest that the D1 event in the lower basement-derived section occurred as part of the Alleghanian orogeny.

The Alleghanian orogeny is characterised by a Barrovian metamorphic sequence from chlorite to sillimanite zone (amphibolite facies) from west to east in the Appalachian orogen (Kunk *et al.*, 2004). Features of the Alleghanian orogeny include regional ductile deformation localised along the eastern margin of Laurentia, fold-and-thrust structures in the Appalachian basin and deformation and metamorphism in the hinterland as well as the widespread magmatism in the form of granitic intrusions discussed in Sections 6.2.1.2 and 6.2.2.2 (Horton *et al.*, 1987; Speer *et al.*, 1994; Faill, 1998). Geologists have attempted to document the sequence of events that the Alleghanian orogeny followed in different parts of the Southern and Central Appalachians (e.g. Dallmeyer *et al.*, 1986; Secor *et al.*, 1986; Dallmeyer, 1989; Stoddard *et al.*, 1991; Rankin, 1994; Faill, 1998; Hatcher, 2002). In most cases, Alleghanian tectonism can be separated into three phases: regional metamorphism and pluton emplacement, widespread deformation, and dextral shearing (Faill, 1998). However, the sequence of these phases appears to vary in different areas of the Central and Southern Appalachians. Although Dallmeyer's (1989) observations in the eastern Piedmont of Georgia and South Carolina (Southern Appalachians)

concurs with the above sequence, Stoddard *et al.* (1991) observed in the eastern Piedmont of North Carolina near Raleigh that deformation occurred prior to the thermal peak of regional amphibolite-facies metamorphism and plutonism (Rankin, 1994). In both the Central and Southern Appalachians, however, the transpressional dextral shearing event is considered the last phase of the Alleghanian orogeny.

If the lower basement-derived section was not rotated significantly as a consequence of the impact, the present subhorizontal orientation of the mylonitic S-C and S-C' structures observed in the lower basement-derived section would be indicative of reverse slip sense, consistent with a thrusting component in the D1 event. This is similar to what Bobyarchick (1981) observed in the Eastern Piedmont fault system where he proposed that penecontemporaneous strike-slip motion and thrusting occurred during the late stages of the Alleghanian orogeny. However, seismic profiling of the Eyreville borehole cores by Catchings *et al.* (2008) revealed that the ICDP-USGS drilling of the CBIS did not intersect the true crater basement, which caused Gohn *et al.* (2008) to propose that the lower basement-derived section forms part of the slumped transient crater wall and is not in situ basement (see Section 6.3.3). As such, it is possible that the foliation orientations may originally have been either more steeply or shallowly dipping, which might indicate either thrusting or extensional shear movement. Although subhorizontal extensional shearing concomitant with medium- to high-grade metamorphism has been observed in several metamorphic belts (e.g. Davis, 1987) and rift environments (e.g. Wickham and Oxburgh, 1985), this type of extension is not documented in any of the other Appalachian terranes (e.g. Horton *et al.*, 1989, 1991, 1994; Rankin, 1994). It is more likely that the S1 foliations are thrust-related features corresponding with the convergence-related thrust and/or transpressive tectonics which characterise the Appalachian terranes (e.g. Hatcher, 2002; Hackley *et al.*, 2007; Hatcher *et al.*, 2007).

In the older granite of the upper megablock, a prograde gneissic foliation and a localised retrograde mylonitic foliation and lineation are observed (see Chapter 2, Section 2.4.1). Owing to the limited vertical exposure of the Eyreville-B borehole core, inter-relationships between the

gneissic granite and surrounding rocks are absent, and the kinematic relationship between the gneissic granite and lower basement-derived section is unclear since the evidence that gneissic foliation developed during shearing is equivocal (see Chapter 2, Section 2.4.1). However, the gneissic nature of the older megablock granite limits the metamorphic grade of the foliation-forming event to at least amphibolite facies (Myers, 1978). Within the vicinity of the CBIS, only two regional metamorphic events reached such high grades: the granulite facies Grenville orogeny (Gates and Glover, 1989) at ca. 1.1 Ga (Horton *et al.*, 1989), and the amphibolite-facies Alleghanian orogeny (Kunk *et al.*, 2004) between 325-260 Ma (Hatcher, 1989, 2002; Horton *et al.*, 1989). The ca. 615 Ma age of the older gneissic granite in the upper megablock (see Section 6.6; Horton *et al.*, 2009b) eliminates the possibility of deformation during the Grenville orogeny. As such, it is inferred that the foliation-forming event was part of the Alleghanian orogeny. The absence of sufficient structural evidence prevents the development of a sound argument linking the gneissic foliation of the upper granite megablock to the D1 shearing event in the lower basement-derived section. However, based on what is observed, it is more likely that the prograde gneissic foliation formed during the earlier stages of the diachronous Alleghanian orogeny (regional metamorphism and/or widespread deformation; Faill, 1998) rather than the final dextral shearing stage. This assumption is based on two observations: (1) deformed Alleghanian plutons in the region of the CBIS tend to be associated with retrogressive mylonitic shear zones (e.g. Petersburg Granite in the Hylas zone; Gates and Glover, 1989) and show much greater intensities of deformation and retrogression than that seen in the gneissic megablock; and (2) the unfoliated nature of the younger megablock granite that intruded the megablock granite gneiss (the timing of which has been interpreted to reflect peak metamorphism at 254 ± 3 Ma; Horton *et al.*, 2009b; see Sections 6.5 and 6.6) suggests that peak metamorphism in the target rocks of the Eyreville-B borehole core was not a foliation-forming event. Thus, the gneissic foliation in the older megablock granite must have occurred prior to peak metamorphism and not as a result of retrogression.

6.3.2 D2 event

The second deformation event recorded in the target rocks of the Eyreville-B borehole core, D2, is defined by mesoscopic breccias in the form of a narrow, anastomosing or branching fracture network that is locally cataclastic (Chapter 2, Section 2.4.2). The fractures are locally sub-parallel to the core, are typically filled by chlorite and/or calcite, and contain chloritic slickensides with an obliquely plunging lineation (L2). This fracture network is most commonly observed in the lower basement-derived section, although minor chlorite-filled fractures are also observed in the upper amphibolite and granite gneiss megablocks (see Chapter 2, Sections 2.3.1, 2.3.2 and 2.3.3.1). Where sub-vertical (D2) fractures are observed to locally cross-cut breccias in hand specimen, microscopic evidence of truncation and/or displacement is absent, which suggests fracture formation was penecontemporaneous with brecciation (see Chapter 2, Section 2.4.2).

Brecciation in the lower basement-derived calc-silicate is associated with extensive calcite-epidote-quartz±chlorite fracture fill and, although it superficially resembles the D2 fracture networks, brecciation is more extensive and matrix-supported (see Chapter 2, Sections 2.3.1.8 and 2.4.2). The calc-silicate breccias share many similar features with the calcite-cemented breccias observed in the felsic gneiss blocks within the impactite sequence; truncated calcite veins and fractures along the edges of the felsic gneiss blocks indicate that at least some brecciation occurred prior to the Chesapeake Bay impact (see Chapter 2, Section 2.4.2; Horton *et al.*, 2009b; Jolly, 2011). The extensive brecciation and retrogression observed in both the lower basement-derived calc-silicate and felsic gneiss blocks of the impactite sequence relative to the lower basement-derived mica schists may reflect the greater competence the former compared to the mica schists during the mylonitic D1b deformation. D2 calcite veins locally cross-cut brecciation in the felsic gneiss blocks of the Eyreville-B impactite sequence. Whilst this may suggest a pre-D2 timing for these breccias, the complex nature of fracturing processes, which can lead to the overprinting of fracture sets during a single fracturing (D2) event cannot be discounted.

The D2 event has two possible causes, depending on whether substantial rotation of the rocks occurred during the impact. If little rotation occurred, the D2 fractures are subvertical faults overprinting with a pervasive shallow-dipping syn-metamorphic fabric. These observations correspond with many tectonic reconstructions that favour initial thrusting and subsequent retrograde strike-slip faulting along late Alleghanian dextral strike-slip faults (Rankin, 1994). However, the possibility cannot be discounted that the subvertical faults could represent more than one event. This is demonstrated in the second possibility for the D2 fracture network, where post-orogenic Mesozoic faulting, most commonly observed in the Alleghanian granites of the Appalachian Piedmont (Bartholomew and Van Arsdale, 2012), may have been the cause for the fracture network. During the Jurassic rifting (northwest-southeast extension), reactions between hydrothermal fluids and wall rocks of fractures and veins generated by the failed north-south rifting in the Triassic resulted in the alteration of plagioclase feldspar to K-feldspar, otherwise known as “pinking” (Mauldin *et al.*, 1997; Bartholomew *et al.*, 1997; Bartholomew and Van Arsdale, 2012; Evans and Bartholomew, 2000). This alteration is similar to what is observed at the base of the upper granitic megablock where K-feldspar alteration is associated with a fracture network (see Chapter 2, Section 2.3.3). Consequently, it is possible that the calcite- and/or quartz-filled D2 fractures in the Eyreville-B target rocks are a late-Alleghanian feature, whereas the fracture sets associated with “pinking” alteration in the lower portions of the upper granite megablock might have been the result of post-orogenic hydrothermal alteration during Mesozoic normal faulting.

6.3.3 Chesapeake Bay impact event

Other than polymict impact breccia and suevite dikes in the upper 60 m of the lower basement-derived section (see Section 2.4.2; Horton *et al.*, 2009a), no evidence of impact-related features has been found during this study. However, Horton *et al.* (2009a) recorded the occurrence of weakly to moderately shocked quartz in a single thin section from a cataclastic granite located adjacent to a suevite vein in the lower basement-derived section at 1607 m depth. The lack of shock-induced features in the lower basement-derived section suggests that this block was

derived from the outer parts of the transient crater and that the polymict breccias and suevites were injected during the cratering process (Horton *et al.*, 2009b).

As for the upper granitic and amphibolite megablocks, the absence of both shock metamorphism and impact breccia dykes led Horton *et al.* (2009b) to propose that these clearly allochthonous blocks originated in unshocked bedrock outside of the transient crater wall. This most likely occurred when the central crater widened beyond the transient crater by the inward collapse of bedrock (see Chapter 1, Section 1.2, Figure 1.14; Horton *et al.*, 2009b). The sand in which the amphibolite megablock lies below the upper granite megablock (see Chapter 1, Figure 1.15; Chapter 2, Figure 2.11) was identified by Self-Trail *et al.* (2009) to have been derived from the lowermost part of the Potomac Formation (see Chapter 1, Section .1.3, Figure 1.11). Horton *et al.* (2007) suggested that the sand provided a low-friction substrate on and within which the megablocks were transported. Based on the location of the Eyreville drill site relative to the centre of the CBIS (~9 km northeast) and modelling by Collins and Wünnemann (2005) and Collins *et al.* (2008), which indicates the central crater expanded from a 14 km radius (transient crater) to a 20 km radius, the upper amphibolite and granite megablocks must have been transported between 5 and 11 km laterally to the current position (Horton *et al.*, 2009b). It is less clear how far the lower basement-derived section was transported.

6.4 Metamorphic grade

The grade of metamorphism recorded in the target rocks of the Eyreville-B borehole core is best observed in the metasediments of the lower basement-derived section and the biotite schist xenoliths and amphibolite of the upper megablock section. In the lower basement-derived section, fluid composition and mineral assemblages were used to constrain peak *P*-*T*-X(H_2O) conditions (see Chapter 4, Section 4.3.2). The presence of graphite in the mica schists and vesuvianite in the calc-silicate rocks constrains X(H_2O) to between 0.8 and 0.9 (see Chapter 4, Section 4.3.2; Ohmoto and Kerrick, 1977; Valley *et al.*, 1985). The presence of vesuvianite also indicates that peak metamorphic temperatures exceeded 600°C (Valley *et al.*, 1985). These

temperature estimates are supported by the hornblende-plagioclase±epidote mineral assemblage in the para-amphibolite, which suggests peak metamorphic conditions close to the transition between epidote-amphibolite and amphibolite facies (Maruyama *et al.*, 1983). The absence of in situ granite melting in the lower basement-derived section constrains the upper limit for peak temperatures at ~650-670°C (Table 6.3; Pattison and Tracy, 1991). With regards to peak metamorphic pressures, fibrolitic knots formed after suspected staurolite in the mica schists constrain the lower pressure to >0.4 GPa (Table 6.3; Pattison and Tracy, 1991), whereas the fact that the petrogenesis for the average composition of the lower basement-derived granite is consistent with melting and emplacement occurring between 0.2 and 0.5 GPa (Table 6.3; see Chapter 3, Section 3.6.3, Figure 3.23b; Section 6.2, Figure 6.2), places an upper pressure limit of 0.5 GPa (see Chapter 4, Section 4.3.2).

Using these constraints in combination with Zr-in-rutile, Grt-Bt and Hbl-Pl geothermometry and GASP (Grt-Als-Qz-Pl) and GPMB (Grt-Pl-Ms-Bt) geobarometry (Table 6.3; see Chapter 4, Section 4.3), the peak metamorphic conditions were determined as mid-amphibolite facies (606 ± 18°C and 0.4 GPa) for the lower basement-derived mica schists. Although temperature estimates from the Hbl-Pl mineral pairs were somewhat higher for the amphibolite megablock (670-690°C; see Chapter 4, Section 4.3), these temperatures are still consistent with mid- to upper-amphibolite facies conditions (Hietanen, 1967). The mineral assemblage in the biotite schist xenoliths suggests that they also experienced at least mid-amphibolite facies conditions (see Chapter 4, Section 4.4.2). In comparison, rocks of the Roanoke Rapids terrane underlying the western portion of the CBIS reach a maximum grade of epidote-amphibolite facies (Table 6.1; Kite and Stoddard, 1984; Farrar, 1985; Horton *et al.*, 1989), and the easterly portion of the CBIS is underlain by the mid-amphibolite facies Hatteras terrane (Table 6.1; Denison *et al.*, 1967; Daniels and Ziets, 1978; Horton *et al.*, 1989). The peak metamorphic conditions recorded in the lower basement-derived section and upper amphibolite and granite megablocks of the Eyreville-B borehole core are more consistent with the latter terrane, supporting the arguments made in Section 6.2.1.1. The phyllites in the impactite sequence identified by Jolly (2011) and in

older borehole cores in the western portion of the CBIS are more consistent with the greenschist nature of the Roanoke Rapids terrane.

6.5 Timing and nature of metamorphism

In Chapter 5, geochronological studies of samples from the lower basement-derived section and upper amphibolite megablock were used to constrain timing of the peak amphibolite grade metamorphic and D1a deformation events preserved in the target rocks of the Eyreville-B borehole core, as well as its subsequent cooling history. Using U/Pb rutile geochronology, peak metamorphism in the mica schists of the lower basement-derived section was constrained at 259 ± 13 Ma (Table 6.3; see Chapter 5, Section 5.2.2). This age is within statistical error of the U/Pb zircon 254 ± 3 Ma age Horton *et al.* (2009b) determined for the massive granite in the upper granite megablock (Table 6.3; see Section 6.6). The massive granite's syn-collisional tectonic setting and the syn- to post-peak metamorphic timing of crystallisation ties the granite to the same terrane as the lower basement-derived mica schists and amphibolite megablock (Table 6.3; see Chapter 5, Section 5.4; Section 6.7). Consequently, the more robust 254 ± 3 Ma age has been inferred to reflect the timing of peak metamorphism. Retrograde cooling of the Eyreville-B target rocks was constrained using Ar/Ar geochronology (Table 6.3; see Chapter 5, Section 5.3). In the upper amphibolite megablock, cooling through the 500°C isotherm occurred at 249 ± 1.1 Ma (Table 6.3; see Chapter 5, Section 5.3.2.1). In the lower basement-derived section, a fine-grained mylonitised granite sample was interpreted to constrain the timing of mylonitisation at 247 ± 5 Ma (Table 6.3; see Chapter 5, Section 5.3.2.4), whereas Horton *et al.* (2009b) determined that cooling of the granite through the 350°C isotherm occurred at 244.1 ± 1.3 Ma. The latter age corresponds closely with Ar/Ar cooling ages through the 350°C isotherm (ca. 243 ± 1.1 Ma) determined in this study for the lower basement-derived mica schists (Table 6.3; see Chapter 5. Section 5.3.2.4).

As discussed in Chapter 1, Section 1.1, and Section 6.1, continental collision during the amphibolite facies Alleghanian orogeny occurred from 325 to 260 Ma (Hatcher, 1989, 2002;

Horton *et al.*, 1989). Although the 254 ± 3 Ma age for peak metamorphism in the Eyreville-B target rocks is only slightly less than the lower limit of the Alleghanian orogeny, metamorphic cooling ages determined in this study are approximately 10 Myr younger. Additionally, emplacement of the massive megablock and basement granites is constrained as late Permian (see Section 6.6). Based on these ages, it is suggested that the younger limit of the diachronous Alleghanian orogeny in the vicinity of the Eyreville site be revised by 10 Myr.

Table 6.3: Summary of estimated conditions and timing of metamorphism and deformation experienced by the Eyreville-B rock units analysed in this study.

Lithology	Metamorphic grade	Pressure	Temperature	Geochronology	Deformation
Upper megablocks section					
Amphibolite	Amphibolite	0.4 GPa[1]	670-680°C (Hbl-Pl)	249 ± 1.1 Ma (Ar/Ar)	D1
Massive granite	N/A	0.2-0.5 GPa[2]	650-670°C[3]	254 ± 3 Ma[4] (U/Pb SHRIMP zircon)	Post-tectonic
Gneissic granite	Amphibolite	0.2-0.5 GPa[2]	650-670°C[3]	615 ± 7 Ma[4] (U/Pb SHRIMP zircon)	Pre-D1 (?)
Lower basement-derived section					
Mica schists	Amphibolite	0.4 GPa (GASP and GPMB)	606 ± 18°C (Zr-in-rutile)	259 ± 13 Ma (U/Pb rutile) 243.1 ± 1.1 Ma (Ar/Ar)	D1a and D1b
Granite	N/A	0.2-0.5 GPa[2]	650-670°C[3]	247 ± 5 Ma (Ar/Ar)	post-D1a but pre-D1b

[1] Pressure estimate determined for mica schists from GASP and GPMB geobarometers
[2] Pressure estimates from Johannes and Holtz (1991)
[3] Temperature estimates from Pattison and Tracy (1991)
[4] Granite crystallisation ages determined by Horton *et al.* (2009b)

Structural evidence in the Eyreville-B target rocks and comparison with regional structures suggest that the M1 metamorphic event was probably induced by thrusting (see Section 6.3). Syn-metamorphic thrust-related deformation, however, would be difficult to explain. Simplistically, heat flow initially decreases during thrusting in a thickening-related burial setting; however, heating of these rocks occurs during exhumation as a result of this thickening

(England and Thompson, 1984). Consequently, the thermal response to thrusting and deformation may overlap if the thrusting event is sufficiently long-lived and/or if other heat sources in complex orogens such as the Appalachians speed up the metamorphic response to thrusting. Such heat sources may include the advection heat by magma and/or emplacement of hot thrust sheets. The presence of such heat sources are commonly observed in high-temperature, low-pressure metamorphic terranes (Sandiford and Powell, 1991), which corresponds with findings in Chapter 4 (Section 4.4.2) where such metamorphic conditions are implied by the very steep metamorphic thermal gradient (44°C/km; Sandiford *et al.*, 1998). Sandiford and Powell (1991) observed that three different mechanisms within the continental lithosphere may provide the advective heat transfer for high-temperature, low-pressure terranes, namely erosion, penetrative deformation and migrating melts. Speer *et al.* (1994) suggested that, rather than being the cause, the Alleghanian plutons were emplaced as a result of metamorphism during the orogeny (see Section 6.6). Synchronous deformation and metamorphism caused by the emplacement of hot thrust sheets was proposed by Hackley *et al.* (2007) to explain the amphibolite-grade metamorphism experienced by certain parts of the Carolina terrane. It is possible, at least in part, that the emplacement of such hot thrust sheets on the lower basement-derived metasediments produced the heat energy required for deformation. Unfortunately, the lack of vertical exposure of the Eyreville-B target rocks limits the ability to fully assess the large-scale metamorphic context of the rocks. Additionally, the high-variance metamorphic assemblage of the basement mica schists precludes the ability to tightly constrain the *P-T* path, which may have assisted in the clarification this problem.

Cooling rates determined from thermochronological studies (such as completed in this study and Horton *et al.*, 2009b) can be used to obtain information that may constrain the evolution of exhumed continental crust (Dunlap, 2000). Using the determined ages from this study and Horton *et al.* (2009b), a cooling rate approximating 21°C/Ma for the Eyreville-B target rocks was established (see Chapter 5, Section 5.4, Figure 5.11). This is consistent with the 25°C/Ma cooling rate Burton and Kunk (2006) established for the amphibolite facies Ashe Metamorphic Suite from the Blue Ridge Belt in southwestern North Carolina and the ca. 20°C/Ma cooling rate

observed in the South Carolina Kiokee belt (Dallmeyer *et al.*, 1986; Snoke and Frost, 1990). The relatively rapid cooling histories preserved in these rocks and the Eyreville-B target rocks correspond with results from fluid inclusion studies completed by Evans and Bartholomew (2000), who proposed rapid isobaric cooling occurred in the last phases of the Alleghanian orogeny.

6.6 Age and nature of intrusions

As discussed in Sections 6.2, 6.3 and 6.5, petrographic and structural evidence has revealed three granite intrusions in the Eyreville-B target rocks: a pegmatitic to coarse-grained granite in the lower basement-derived section and the gneissic and massive granites in the upper granite megablock (see Chapter 2, Figures 2.1 and 2.11). In the upper granite megablock, Horton *et al.* (2009b) established a U/Pb zircon age of 615 ± 7 Ma for the older gneissic granite. This Neoproterozoic age is within error of at least four granitoid intrusions in the Roanoke Rapids terrane. The Langley Granite, sampled by the USGS-NASA drilling of the Langley borehole core located in the southwestern portion of the CBIS annular trough (Horton *et al.*, 2005a), has been dated at 612 ± 10 Ma using U/Pb zircon SHRIMP geochronology (Horton *et al.*, 2005b). Owens *et al.* (2010b) dated the trondhjemitic Three Creek pluton at 613.6 ± 0.9 Ma using U/Pb zircon CA-TIMS (Chemical Abrasion – Thermal Ionization Mass Spectrometry) geochronology. A metagranite near Skippers, Virginia, was dated by Coler and Samson (2000) to have a U/Pb zircon age of 615 ± 0.6 Ma. Finally, a metatonalite that most likely intruded the Easonburg Formation was dated using $^{207}Pb/^{206}Pb$ zircon geochronology to be ca. 607 Ma in age (Horton and Stern, 1994). Consequently, it is likely that the gneissic megablock granite was emplaced during the same magmatic pulse that occurred between 607 and 615 Ma.

Older rocks are also documented in the Roanoke Rapids terrane. In the Roanoke Rapids Complex, preliminary $^{207}Pb/^{206}Pb$ zircon ages at ca. 668 Ma were determined for a metatonalite (Horton and Stern, 1994), a U/Pb zircon 672 ± 2 Ma age was determined for a metagranodiorite (Coler and Samson, 2000), and a ca. 673 Ma U/Pb zircon age was determined for

metavolcanics using CA-ID-TIMS (Chemical Abrasion – Isotope Dilution – Thermal Ionization Mass Spectrometry) geochronology (Owens *et al.*, 2011). This apparent bimodal age relationship led Hibbard *et al.* (2002) to propose Stage I magmatism in the Carolina Zone (see Chapter 1, Section 1.1.2.1) involved a diachronous event, where granitoid intrusions were emplaced in island arc volcanics at ca. 670 Ma, and in volcanogenic sediments between 615 and 607 Ma. However, the interpreted ca. 55 Ma duration of this event is a very long time span for a single event and it seems more likely that each age group represents a discrete magmatic pulse. Such an interpretation has been proposed by Owens and Hamilton (2013), who attribute the ca. 670 Ma event to an older arc phase and the ca. 615 Ma event to a younger, juvenile, arc phase. This scenario would suggest that the crust in the Roanoke Rapids terrane is older than 660 Ma, with the implications that the terrane may have been a separate crustal block prior to 660 Ma, which later amalgamated with other terranes of the Carolina Zone prior to the second phase of arc magmatism recorded throughout the Carolina Zone (Owens and Hamilton, 2013).

As discussed in Section 6.5, crystallisation of the massive granite of the upper megablock occurred at 254 ± 3 Ma (Horton *et al.*, 2009b), and has been used to constrain the timing of peak metamorphism. Owing to the scarcity of zircons in the lower basement-derived section (Horton *et al.*, 2009a), the basement granite could not be directly dated. However, structural evidence in combination with metamorphic cooling ages (see Sections 6.3 and 6.5) constrain the timing at which emplacement of the basement granite occurred (post-peak metamorphism but pre-retrograde mylonitisation). Consequently, emplacement of the basement granite is interpreted to have taken place between ca. 254 and ca. 247 Ma. This Permian age constraint places it along with the massive megablock granite as among the youngest events yet recorded in the Alleghanian orogeny. The ages of these two granites, combined with the ca. 240-250 Ma metamorphic cooling ages, further justifies extending the younger limit of the diachronous Alleghanian orogeny in the vicinity of the Eyreville site by 10 Myr.

The ages and compositional similarities of the two younger Eyreville-B granites to other Alleghanian granites in the Central and Southern Appalachians were previously discussed in

Section 6.2. The Alleghanian granites range in age from 335 to 263 Ma and appear to have been emplaced concurrently with Alleghanian ductile deformation, which provided the heat energy required for melting by either decompression, heat advection, flux production and/or the provision of fluid flux pathways (Speer *et al.*, 1994; Hibbard *et al.*, 2002). Consequently, Speer *et al.* (1994) proposed that the magmatic event was a result of the Alleghanian deformation rather than the cause. This last statement corresponds well with observations made by Pindell and Dewey (1982) and Nelson (1992), who suggested that the generation of the granite plutons was a consequence of continental collision rather than from melting above a subduction zone (Rankin, 1994).

6.7 Tectonic implications

In Chapters 4 and 5 (Sections 4.4.3 and 5.4), the upper amphibolite and granite megablocks were linked to the lower basement-derived section based on mineralogy, structural evidence, geochemistry, geothermobarometry and geochronology, suggesting that they form part of the same terrane (see Sections 6.2, 6.3, 6.4 and 6.5). Nonetheless, the relatively higher metamorphic grade preserved in the megablock amphibolite and biotite schist xenoliths, combined with the predicted lateral distance that the megablocks travelled during the Chesapeake Bay impact event (see Section 6.3.3) might suggest that these rocks form part of a separate terrane from the lower basement-derived section. The Hatteras terrane, however, is the only amphibolite-grade terrane within the 5-11 km distance from the Eyreville-B borehole core (see Figure 6.1, Table 6.1). Consequently, it is tentatively concluded that the rocks from the Eyreville-B borehole core analysed in this study form part of the amphibolite facies Hatteras terrane.

Observations from this study have revealed that the CBIS excavated a complex succession of rocks that reflect the histories of multiple events. As discussed in Chapter 1, Section 1.1 and Section 6.1, the evolution of the Appalachians involved at least five orogenic episodes that culminated in the final configuration of the Pangaea supercontinent (Murphy *et al.*, 2010).

Petrography and geochemistry link the lower basement-derived metasediments, the biotite schist xenoliths and the upper amphibolite megablock to rocks of the Carolina Zone, a composite volcanic arc system that experienced at least three discrete magmatic pulses (see Chapter 1, Section 1.1.2.1 and Section 6.2; Hibbard *et al.*, 2002; Owens and Hamilton, 2013). Owens and Hamilton (2013) observed that evidence for a ca. 670 Ma magmatic pulse is only preserved in the Roanoke Rapids terrane. Considering the more evolved crustal component for this phase in the Roanoke Rapids terrane (Hibbard *et al.*, 2002), it may be likely that the protolith for the biotite schist xenoliths has its origins in this oldest arc phase. Additionally, correlations between the amphibolite megablock and ophiolitic Halifax County Complex suggests that the amphibolite megablock could have formed either as an intrusive body or as part of an ophiolite complex generated during the initial stages of island arc development (Kite and Stoddard, 1984), and may have also formed part of the oldest arc phase recorded in the Roanoke Rapids terrane prior to its amalgamation with other terranes of the Carolina Zone (see Section 6.6; Owens and Hamilton, 2013). This may explain the relatively greater similarities between the biotite schist xenoliths and amphibolite megablock compared with the lower basement-derived metasediments. The problems arising from such a speculation are based on the much higher metamorphic grade experienced by the biotite schist xenoliths and amphibolite megablock relative to the Roanoke Rapids terrane, although the temperature estimates are somewhat equivocal (Section 6.4). However, as noted previously, these rocks most likely form part of the Hatteras terrane, which has been proposed by Horton *et al.* (2005b) to be a higher grade equivalent of the Roanoke Rapids terrane.

After the amalgamation of the Roanoke Rapids terrane with the Carolina Zone, the second phase of magmatism relating to a more juvenile, felsic, island arc occurred at ca. 615-607 Ma (Hibbard *et al.*, 2002; Owens and Hamilton, 2013). The differences in the geochemistry and tectonic setting between the lower basement-derived metasediments and the megablock biotite schist xenoliths suggest that the protoliths for the former were deposited subsequent to the latter. Consequently, the protoliths of the para-amphibolite and calc-silicate in the lower

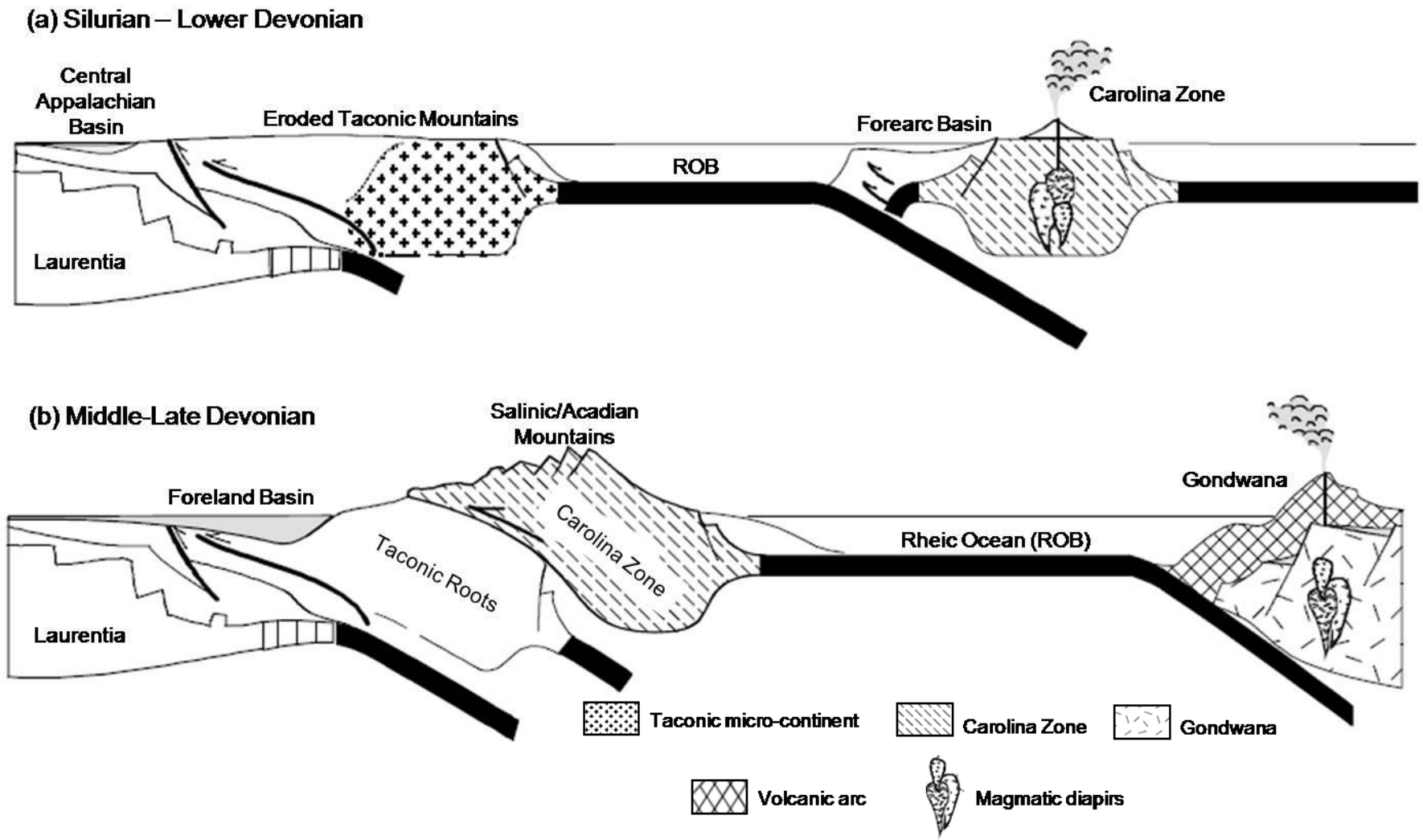

Figure 6.4: Schematic cross sections showing the latter stages of the Carolina Zone accretion onto the Laurentian margin from (a) the Silurian to Lower Devonian, (b) the Middle-Late Devonian and (c) the Middle Devonian, followed by (d) the Late Permian collision between Laurentia and Gondwana (diagrams modified after Fichter and Baedke, 1999). See text for explanation. Abbr. ROB = remnant ocean basin.

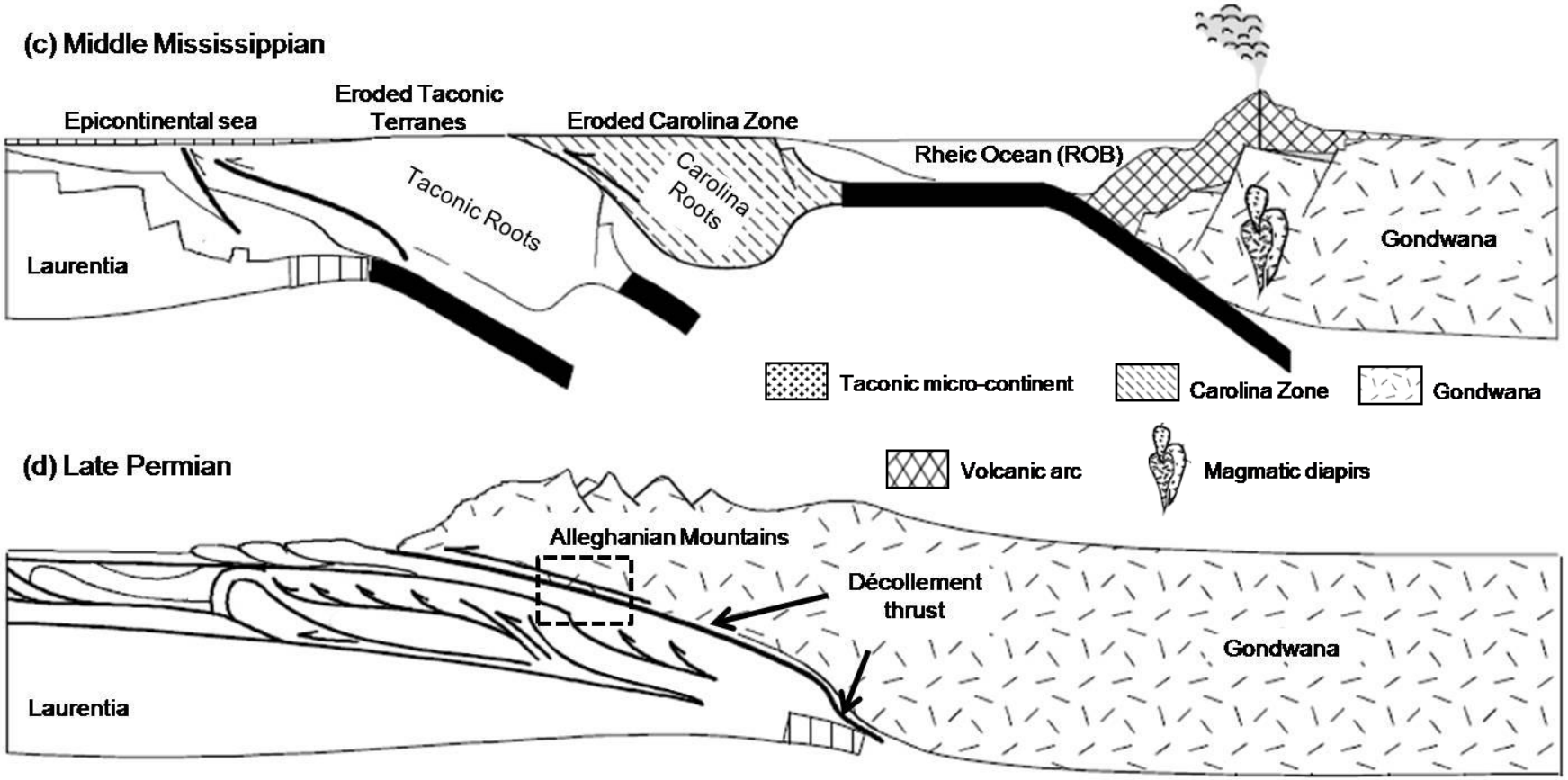

Figure 6.4 (continued): **Schematic cross sections showing the latter stages of the Carolina Zone accretion onto the Laurentian margin from (a) the Silurian to Lower Devonian, (b) the Middle-Late Devonian and (c) the Middle Devonian, followed by (d) the Late Permian collision between Laurentia and Gondwana (diagrams modified after Fichter and Baedke, 1999). See text for explanation. Abbr. ROB = remnant ocean basin.**

basement-derived section of the Eyreville-B borehole core could have been deposited during this stage as turbidites in the fore-arc basin of the Carolina Zone (Figure 6.4a; see Chapter 3, Section 3.6.2), and were possibly later incorporated with the similar-aged volcanogenic protoliths of the lower basement-derived mica schists (see Chapter 3, Section 3.6.1) as the Carolina Zone migrated towards and accreted to Laurentia (Figure 6.4b). The Neoproterozoic age of the gneissic megablock granite (ca. 615 Ma; Horton *et al.*, 2009b) suggests that its emplacement also took place during this second stage of magmatism in the Carolina Zone (Owens and Hamilton, 2013). Together, the metasediments and the megablock granite gneiss, as well as the biotite schist xenoliths and amphibolite megablock, probably formed part of a Neoproterozoic basement (Figure 6.4c), which has also been observed in other drill cores (e.g. USGS-NASA Langley and Bayside cores; Horton *et al.*, 2005b).

As discussed in Section 6.1.1, the Alleghanian orogeny in the Central and Southern Appalachians was a décollement tectonism that involved much of the previously metamorphosed and deformed eastern Laurentia (Faill, 1998). Geiser (1988) suggested that the line of emergence of the décollement thrust from the crust (Figure 6.4d) lay under northern Chesapeake Bay (Faill, 1998). If this hypothesis is true, the Eyreville-B target rocks would be located near the internal zone of the Alleghanian orogenesis (see dashed block in Figure 6.4d). Magmatism associated with the Alleghanian orogeny (not shown in Figure 6.4d) resulted in the emplacement and rapid cooling of the multiple Alleghanian granitoid intrusions, most likely including the lower basement-derived granite and the upper massive megablock granite, at middle to shallow crustal levels (Speer *et al.*, 1994).

Rapid exhumation of the Alleghanian orogen associated with Mesozoic crustal extension, as noted by Jamieson and Beaumont (1988) and Snoke and Frost (1990), may have resulted in the erosion of much, if not all, of the westward-overriding Gondwana plate. Since the estimated depth of penetration for the CBIS is in excess of 5 km, it is possible that the Chesapeake Bay impact crater excavated rocks of either Laurentian and/or peri-Gondwanan affinity. The petrographic, chemical and geochronology evidence from the target rocks of the Eyreville-B

borehole core, however, show greater resemblance to rocks of the peri-Gondwanan Roanoke Rapids and Hatteras terranes of the Carolina Zone, and are consequently also interpreted to be peri-Gondwanan in origin.

6.8 Conclusions

Analysis of the target rocks from the Eyreville-B borehole core has provided new information that can be applied to current models regarding the Appalachian basement beneath the Atlantic Coastal Plain sediments. Despite the limited sample size and vertical exposure of the Eyreville-B borehole core target rocks, comparisons with neighbouring terranes resulted in the following conclusions:

- Mineralogy, geochemistry, metamorphic grade and structural evidence in rocks from both the lower basement-derived section and upper megablocks section suggest that these rocks form part of the same amphibolite-facies terrane, which is most likely to be the Hatteras terrane.
- If the Hatteras terrane is a higher grade equivalent of the Carolina Zone Roanoke Rapids terrane (as proposed by Horton *et al.*, 2009b), the biotite schist xenoliths and amphibolite megablock were most likely deposited/emplaced during the oldest arc phase recorded in the Roanoke Rapids terrane at ca. 670 Ma.
- The age of the megablock granite gneiss suggests that it was emplaced during the second, more juvenile, island arc event recorded in the Carolina Zone at ca. 615-607 Ma, along with the deposition of the protoliths for the lower basement-derived metasediments.
- The D1 deformation and M1 metamorphic events recorded in rocks of the Eyreville-B borehole core analysed in this study suggest peak metamorphic conditions involved fluid compositions $X(H_2O)$ between 0.8 and 0.9, temperatures at ca. 600°C and pressures at ca. 0.4 GPa, occurring at ca. 254 Ma. This was followed by rapid retrograde cooling that began at ca. 249 Ma through the 500°C isotherm in the upper amphibolite megablock and continued through the 350°C isotherm at ca. 243 Ma in the

lower basement-derived section, with mylonitisation in the basement section possibly taking place at ca. 247 Ma.

- The late Permian timing and amphibolite-facies grade of the M1 metamorphic event recorded in the Eyreville-B borehole core suggest it occurred during the late stages of the diachronous Alleghanian orogeny. Although considered a separate event in this study, the D2 fracturing event was also most likely a late Alleghanian feature; the fracture sets and associated pinking at the base of the upper granite megablock gneiss were most likely caused by Mesozoic normal faulting.
- The massive granite in the megablock, which was emplaced during prograde- to peak metamorphic conditions, and the lower basement-derived pegmatitic granite, which was emplaced shortly after peak metamorphism but prior to the onset of retrograde mylonitisation, show many petrographic, geochemical and geochronological similarities with other Alleghanian granites in the region and are among the youngest events recorded in the orogeny, possibly revising the lower limit of the Alleghanian orogeny.
- Rapid exhumation and resultant erosion of as much as 10 to 15 km of the crust during the Mesozoic crustal extension may have allowed for the CBIS to excavate rocks of either Laurentian and/or peri-Gondwanan affinity. Comparative analysis of the Eyreville-B borehole core target rocks with the Roanoke Rapids and Hatteras terranes suggests that they have a peri-Gondwanan origin.

6.9 Recommendations

The ICDP-USGS drilling of the CBIS has provided access to the deepest-seated rocks yet recovered of the underlying Appalachian Piedmont. This study has attempted to describe and analyse these rocks using petrography, geochemistry, structure, geothermobarometry and geochronology. However, the final geodynamic analysis and interpretation of the Eyreville-B target rocks has proved difficult owing to ambiguous results caused mainly by the small sample size and lack of vertical exposure from the borehole core. Future studies which may prove useful to confirm and constrain these results include isotopic geochemistry to enable more

robust protolith and tectonic setting interpretations and comparisons with neighbouring terranes, thus testing the conclusions of this study and fluid inclusion studies to determine fluid compositions and trapping conditions, which can be used to better constrain metamorphic conditions experienced by the target rocks of the Eyreville-B borehole core (if not excessively altered by the impact fluids) as well as the orientation of particularly the D1 structures.

REFERENCES

Aleinikoff, J.N., J.W. Horton, Jr. and M. Walter, 1996, Middle Proterozoic age of the Montpelier Anorthosite, Goochland terrane, eastern Piedmont, Virginia: Geological Society of American Bulletin, v. 108, p. 1481-1491.

Aleinikoff, J.N., J.W. Horton, Jr., A.A. Drake, Jr. and C.M Fanning, 2002, SHRIMP and conventional U-Pb ages of Ordovician granites and tonalites in the Central Appalachian Piedmont: Implications for Paleozoic tectonic events: American Journal of Science, v. 302, p. 50.

Alexander, E.C., Jr., G.M. Michelson and M.A. Lanphere, 1978, MMhb-1: A new ^{40}Ar-^{39}Ar dating standard, *in* Zartmand, R.E. (ed.), Short papers for the Fourth International Conference, Geochronology, Cosmochronology, Isotope Geology: U.S. Geological Survey Open-File Report 78-701, p. 6-8.

Allaz, J., M. Engi, A. Berger and I.M. Villa, 2011, The Effects of Retrograde Reactions and of Diffusion on ^{40}Ar-^{39}Ar Ages of Micas: Journal of Petrography, v. 52, no. 4, p. 691-716.

Allen, A.R. and D. Stubbs, 1982, An ^{40}Ar/^{39}Ar study of a polymetamorphic complex in the Arunta Block, central Australia: Contributions to Mineralogy and Petrology, v. 79, p. 319-332.

Althaus, E., 1967, The Triple Point Andalusite-Sillimanite-Kyanite: An Experimental and Petrologic Study: Contributions to Mineralogy and Petrology, v. 16, p. 29-44.

Anderson, G.M., 2005, Truth and beauty in thermodynamics: Canadian Mineralogist, v. 43, p. 11-19.

Armstrong, R. L., E. Jãger and P. Eberhardt, 1966, A comparison of K-Ar and Rb-Sr ages on Alpine biotites: Earth and Planetary Science Letters v. 1, p. 13-19.

Ashworth, J.R., and I.M. Tyler, 1983, The distribution of metamorphic temperatures around the Strontian granodiorite: Geological Magazine, v. 120, p. 281-290.

Bailey, C.M. and B.E. Owens, 2012, Traversing suspect terranes in the central Virginia Piedmont: From Proterozoic anorthosites to modern earthquakes: GSA Field Guides, v. 29, p. 327-344.

Bakker, H.E., K. de Jong, H. Helmers and C. Biermann, 1989, The geodynamic evolution of the Internal Zone of the Betic Cordilleras (south-east Spain): a model based on structural analysis and geothermobarometry: Journal of Metamorphic Geology, v. 7, p. 359-381.

Baksi, A.K., 2006, Guidelines for assessing the reliability of $^{40}Ar/^{39}Ar$ plateau ages: Application to ages relevant to hotspot tracks, accessed from www.mantleplumes.org on 7 August 2013.

Barker, A.J., 1994, Interpretation of porphyroblast inclusion trails: limitations imposed by growth kinetics and strain rates: Journal of Metamorphic Geology, v. 12, p. 681-694.

Barker, A.J., 1998, Introduction to Metamorphic Textures and Microstructures (2nd ed.): Cheltenham, Stanley Thornes Ltd, 243 p.

Barker, C., D.T. Secor, Jr., J. Pray and J.W. Horton, Jr., 1998, Age and deformation of the Long town meta granite, South Carolina Piedmont: a possible constraint on the origin of the Carolina terrane: Journal of Geology, v. 106, p. 713-725.

Bartholomew, M.J. and R.B. Van Arsdale, 2012, Structural controls on intraplate earthquakes in the eastern United States, *in* Cox, R.T., M.P. Tuttle, O.S. Biyd and J. Locat (eds.), Recent Advances in North American Paleoseismology and the Neotectonics East of the Rockies: Geological Society of America Special Paper 439, p. 165-190.

Bartholomew, M.J. and R.P. Tollo, 2004, Northern ancestry for the Goochland terrane as a displaced fragment of Laurentia: Geology, v. 32, p. 669-672.

Bartholomew, M.J., R.D. Heath, B.M. Brodie and S.E. Lewis, 1997, Post-Alleghanian deformation of Alleghanian granites (Appalachian Piedmont) and the Atlantic Coastal Plain: Geological Society of America Abstracts with Programs, v. 29, p. 4.

Barton, M.D. and R.B. Hanson, 1989, Magmatism and the development of low-pressure metamorphic belts: implications from the western United States and thermal modelling: Geological Society of America Bulletin, v. 101, p. 1051-1065.

Bartosova K., D. Mader, R.T. Schmitt, L. Ferrière, C. Koeberl, W.U. Reimold and F. Brandstätter, 2009, Chapter 18, Geochemistry of the impact breccia section (1397 – 1551 m depth) of the Eyreville drill core, Chesapeake Bay impact structure, USA, *in* Gohn, G.S., C. Koeberl, K.G. Miller and W.U. Reimold (eds.), The ICDP-USGS Deep

Drilling Project in the Chesapeake Bay Impact Structure: Results from the Eyreville Core Holes: Geological Society of America Special Paper 458, p 397-433.

Bell, T.H. and C. Cuff, 1989, Dissolution, solution transfer, diffusion versus fluid flow and volume loss during deformation/metamorphism: Journal of Metamorphic Geology, v. 7, p. 425-447.

Berman, R.G. and T.H. Brown, 1985, Heat capacity of minerals in the system Na_2O-K_2O-CaO-MgO-FeO-Fe_2O_3-Al_2O_3-SiO_2-TiO_2-H_2O-CO_2: representation, estimation, and high temperature extrapolation: Contributions to Mineralogy and Petrology, v. 89, p. 168-183.

Berman, R.G., 1988, Internally-consistent thermodynamic data for minerals in the system Na_2O-K_2O-CaO-MgO-FeO-Fe_2O_3-Al_2O_3-SiO_2-TiO_2-H_2O-CO_2: Journal of Petrology, v. 29, p. 445-522.

Bhatia, M.R. and K.A.W. Crook, 1986, Trace element characteristics of greywackes and tectonic setting discrimination of sedimentary basins: Contributions to Mineralogy and Petrology, v. 92, p. 181-193.

Bhattacharya, A., L. Mohanty, A. Maji, S.K. Sen and M. Raith, 1992, Non-ideal mixing in the phlogopite-annite binary: Constraints from experimental data on Fe-Mg partitioning and the reformulation of the biotite-garnet geothermometer: Contributions to Mineralogy and Petrology, v. 111, p. 87-93.

Blake, D. E., and E.F. Stoddard, 1993, The Crabtree Creek pluton: A deformed mid-Palaeozoic(?) stitching pluton on the west flank of the Raleigh metamorphic belt: Geological Society of America Abstracts with Programs, v. 25, p. 4.

Blake, D., 1994, Intrusive and deformational relationships of the Crabtree Creek pluton in west Raleigh, *in* Stoddard, E. and D. Blake (eds.), Geology and Field Trip Guide, Western Flank of the Raleigh Metamorphic Belt, North Carolina: Carolina Geological Society Field Trip Guidebook, North Carolina Geological Survey, p. 25-37.

Blake, D., E.F. Stoddard, M. Heller, R. Carpenter, A. Carpenter and J.R. Butler, 1999, Raleigh 100K Statemap project: Geologic relationships of the southwestern Raleigh metamorphic belt in North Carolina: Geological Society of America Abstracts with Programs, v. 31, p. A-3.

Blundy, J.D. and T.J.B. Holland, 1990, Calcic amphibole equilibria and a new amphibole-plagioclase geothermometer: Contributions to Mineralogy and Petrology v. 104, p. 208-224.

Bobyarchick, A., 1981, The Eastern Piedmont fault system and its relationship to Alleghanian tectonics in the southern Appalachians: Journal of Geology, v. 89, p. 335-347.

Bohor, B.F., W.J. Betterton and E.E. Foord, 1988, Coesite, glass, and shocked quartz at DSDP Site 612; Evidence for nearby impact in the late Eocene: Lunar and Planetary Science Conference, 19th, Houston, Tex., March 14–18, 1988, Abstracts, p. 114–115.

Boltin, W.R. and E.F. Stoddard, 1987, Transition from Eastern slate belt to Raleigh belt in the Hollister Quadrangle, North Carolina: Southeastern Geology, v. 27, p. 185-205.

Braun, J., P. van der Beek and G. Batt, 2006, Quantitative Thermochronology: Numeral Methods for the Interpretation of Thermochronological Data: New York, Cambridge University Press, 272 p.

Brown, G.C. and A.E. Mussett, 1993, The Inaccessible Earth: An Integrated View of Its Structure and Composition: London, Chapman and Hall, 288 p.

Brown, M., 1993, *P-T-t* evolution of orogenic belts and the causes of regional metamorphism: Journal of the Geological Society of London, v. 150, p. 227-241.

Brown, P.M., J.A. Miller and F.M. Swain, 1972, Structural and stratigraphic framework and spatial distribution of permeability of the Atlantic Coastal Plain, North Carolina to New York: U.S. Geological Survey Professional Paper 796, 79 p.

Bucher, K. and R. Grapes, 2011, Petrogenesis of Metamorphic Rocks (8th ed.): Berlin, Springer-Verlag, 428 p.

Burton, W.C. and M.J. Kunk 2006, Evidence for Taconian and Alleghanian orogenesis in the Eastern Blue Ridge near Highlands, NC: Geological Society of America Abstracts with Programs, v. 38, p. 20.

Callen, H.B., 1985, Thermodynamics and an Introduction to Thermostatistics (2nd ed.): New York, John Wiley and Sons, 493 p.

Carpenter, R., L. Odom and M. Hartley, 1982, Geochronological investigation of the Lincolnton metadacite, Georgia and South Carolina, *in* Bearce, D., W. Black, S. Kish and J. Tull

(eds.), Tectonic Studies in the Talledega and Carolina Slate Belts, Southern Appalachian Orogen: Geological Society of America Special Paper 191, p. 145-152.

Carpenter. P., III, R. Carpenter and E.F. Stoddard, 1995, Rock sequences in the eastern half of the Raleigh 30X60–minute quadrangle, North Carolina – A progress report – STATEMAP II project: Geological Society of America Abstracts with Programs, v. 27, p. 41.

Catchings, R.D., D.S. Powars, G.S. Gohn, J.W. Horton, Jr., M.R. Goldman and J.A. Hole, 2008, Anatomy of the Chesapeake Bay impact structure revealed by seismic imaging, Delmarva Peninsula, Virginia, U.S.A.: Journal of Geophysical Research, v. 113, B08413, 23 p.

Cederstrom, D.J., 1945a, Selected well logs in the Virginia Coastal Plain north of James River: Virginia Geological Survey Circular, v. 3, p. 1-81.

Cederstrom, D.J., 1945b, Geology and ground-water resources of the coastal plain in south-eastern Virginia: Virginia Geological Survey Bulletin, v. 63, p. 1-384.

Cederstrom, D.J., 1946, Chemical character of ground water in the coastal plain of Virginia: Virginia Geological Survey Bulletin, v. 4, p. 13-322.

Chappell, B.W. and A.J.R. White, 1974, Two contrasting granite types: Pacific Geology, v. 8, p. 173–174.

Chappell, B.W. and A.J.R. White, 1984, I- and S-type granites in the Lachlan Fold Belt, southeastern Australia, *in* Keqin, X. and T. Guangchi (eds.), Geology of Granites and Their Metallogenic Relations: Beijing: Science Press, p. 87–101.

Chappell, B.W. and A.J.R. White, 1992, I- and S-type granites in the Lachlan Fold Belt: Transactions of the Royal Society of Edinburgh: Earth Sciences, v. 83, p. 1–26.

Chappell, B.W., C.J. Bryant, D. Wyborn, A.J.R. White and I.S. Williams, 1998, High- and Low-Temperature I-type Granites: Resource Geology, v. 48, p. 225-235.

Cherniak, D.J., 2000, Pb diffusion in rutile: Contributions to Mineralogy and Petrology, v. 193, p. 1998-207.

Ciocîrdel, M., 2009, Geothermometry and the Principal Types of Geothermometers Used in Petrology: Petroleum-Gas University of Ploiesti Bulletin, v. 61, p. 47-56.

Coler, D.G. and S.D. Samson, 2000, Characterization of the Spring Hope and Roanoke Rapids terranes, southern Appalachians: A U-Pb geochronologic and Nd isotopic study: Geological Society of America Abstracts with Programs, v. 32, p. A-11-A-12.

Coler, D.G., G.L. Wortman, S.D. Samson, J.P. Hibbard and R. Stern, 2000, U-Pb geochronologic, Nd isotopic and geochemical evidence for the correlation of the Chopawamsic and Milton terranes, Piedmont Zone, southern Appalachian Orogen: Journal of Geology, v. 108, p. 363-380.

Coler, D.G., S.D. Samson and J.A. Speer, 1997, Nd and Sr isotopic constraints on the source of Alleghanian granites in the Raleigh metamorphic belt and Eastern Slate Belt, southern Appalachians, U.S.A.: Chemical Geology, v. 134, p. 257–275.

Collins, G.S. and K. Wünnemann, 2005, How big was the Chesapeake Bay impact?: Insight from numerical modelling: Geology, v. 33, p. 925-928.

Collins, G.S., T. Kenkmann, G.R. Osinski and K. Wünnemann, 2008, Mid-sized complex crater formation in mixed crystalline-sedimentary targets: Insight from modelling and observation: Meteoritics & Planetary Science, v. 43, p. 1955-1977.

Colman-Sadd, S.P., G.R. Dunning and T. Dec, 1992, Dunnage-Gander relationships and Ordovician orogeny in central Newfoundland: a sediment provenance and U/Pb age study: American Journal of Science, v. 292, p. 317-355.

Coney, L., 2009, Mineralogy and geochemistry of the impact breccias of the Bosumtwi impact structure, Ghana: Genesis and secondary processes. Unpublished PhD thesis, University of the Witwatersrand, Johannesburg, South Africa, 299 p.

Coney, P. J., D.L. Jones and J.W.H. Monger, 1980, Cordilleran suspect terranes: Nature, v. 288, p. 329-333.

Conley, J. and G. Bain, 1965, Geology of the Carolina slate belt west of the Deep River-Wadesboro Triassic Basin, North Carolina: Southeastern Geology, v. 6, p. 117-138.

Connolly, J.A.D. and B. Cesare, 1993, C-O-H-S fluid composition and oxygen fugacity in graphitic metapelites: Journal of Metamorphic Geology, v. 11, p. 379-388.

Crowley, W.P., 1976, The geology of the crystalline rocks near Baltimore and its bearing on the evolution of the eastern Maryland Piedmont: Maryland Geological Survey Report of Investigation no. 27, 39 p.

Dahl, P.S., 1996, The effects of composition on retentivity of argon and oxygen in hornblende and related amphiboles: A field-tested empirical model: Geochimica et Cosmochimica Acta, v. 60, no. 19, p. 3687-3700.

Dallmeyer R.D., J.E. Wright, D.T. Secor, Jr. and A.W. Snoke, 1986, Character of the Alleghanian orogeny in the southern Appalachians: Part II. Geochronological constraints on the tectonothermal evolution of the eastern Piedmont in South Carolina: Geological Society of America Bulletin, v. 97, p. 1329-1344.

Dallmeyer, R.D., 1989, Contrasting accreted terranes in the southern Appalachian orogen and Atlantic-Gulf coastal plains and their correlation with West African sequences, *in* Dallmeyer, R.D. (ed.), Terranes in the Circum-Atlantic Paleozoic Orogens: Geological Society of America Special Paper 230, p. 247-267.

Dalrymple, G.B. and M.A. Lanphere, 1969, Potassium–Argon Dating, Principle Techniques and Applications to Geochronology: San Francisco, Freeman, 258 p.

Dalrymple, G.B., E.C. Alexander, M.A. Lanphere, and G.P. Kraker, 1981, Irradiation of samples for $^{40}Ar/^{39}Ar$ dating using the Geological Survey TRIGA Reactor: U.S. Geological Survey Professional Paper 1176, p. 55.

Dalziel, I.W.D. and M.A.S. McMenamin, 1995, Are Neoproterozoic glacial deposits preserved on the margins of Laurentia related to the fragmentation of two supercontinents?: comment and reply: Geology, v. 23, p. 959-960.

Daniels, D.L. and I. Ziets, 1978, Geolgoic interpretation of aeromagnetic maps of the Coastal Plain region of South Carolina and parts of North Carolina and Georgia: U.S. Geological Survey Open-File Report 78-261, 62 p., appendix.

Dasgupta, S., P. Sengupta, D. Guha and M. Fukuoka, 1991, A refined garnet-biotite Fe-Mg exchange geothermometer and its application in amphibolites and granulites: Contributions to Mineralogy and Petrology, v. 109, p. 130-137.

Davis, D.W., I.S. Williams and T.E. Krogh, 2003, Chapter 6, Historical Development of Zircon Geochronology, *in* Hanchar, J.M. and W.O. Hoskin (eds.), Zircon: Reviews in Mineralogy and Geochemistry, v. 53, p. 145-182.

Davis, G.H., 1987, A shear-zone model for the structural evolution of metamorphic core complexes in southeastern Arizona, *in* Coward, M.P., J.F. Dewey and P.L. Hancock (eds.), Continental Extensional Tectonics: Geological Society of London, Special Publication 28, p. 247-266.

de Capitani, C. and T.H. Brown, 1987, The computation of chemical equilibrium in complex systems containing non-ideal solutions: Geochimica et Cosmochimica Acta, v. 51, p. 2639-2652.

de Capitani, C., 1994, Gleichgewichts-Phasendiagramme: Theorie und Software: Berichte der Deutschen Mineralogischen Gesellschaft, v. 6, p. 48.

De Yoreo, J.J., D.R. Lux and C.V. Guidotti, 1991, Thermal modelling in low-pressure/high-temperature metamorphic belts: Tectonophysics, v. 188, p. 209-238.

Deer, W.A., R.A. Howie and J. Zussman, 1992, An Introduction to the Rock-Forming Minerals (2nd ed.): Essex, Longman Scientific and Technical, 696 p.

Denison, R.E., H.P. Raveling and J.T. Rouse, 1967, Age and descriptions of subsurface basement rocks, Pamlico and Albemarle Sound area, North Carolina: American Association of Petroleum Geologists Bulletin, v. 51, p. 268-272.

Dewey, J.F., M.J. Kennedy and W.S.F. Kidd, 1983, A geotraverse through the Appalachians of Northern Newfoundland, *in* Rast, N. and F.M. Delaney (eds.), Profiles of Orogenic belts: American Geophysical Union Geodynamics Series, v. 10, p. 205-241.

Dickinson, W.R. and C.A. Suczek, 1979, Plate Tectonics and Sandstone Compositions: The American Association of Petroleum Geologists Bulletin, v. 63, p. 2164-2182.

DiPietro, J.A., 2012, Landscape Evolution in the United States: An Introduction to the Geography, Geology and Natural History: Waltham, Elsevier, 480 p.

Dodson, M.H., 1973, Closure temperature in Cooling Geochronological and Petrological Systems: Contributions to Mineralogy and Petrology, v. 40, p. 259-274.

Dodson, M.H., 1979, Theory of Cooling Ages: Lectures in Isotope Geology, p. 194-202.

Drake, A. A., Jr., and A.J. Froelich, 1986, Geologic map of the Annandale quadrangle, Fairfax and Arlington Counties, and Alexandria City, Virginia: USGS Map GQ-1601, scale 1:24,000.

Drake, A.A., A.K. Sinha, J. Laird and R.E. Guy, 1989, The Taconic orogen, *in* Hatcher, R.D., Jr., W.A. Thomas and G.W. Viele (eds.), The Appalachian-Ouachita Orogen in the United States (Geology of North America, Vol. F-2): Geological Society of America, Boulder, Colorado, p. 101-177.

Drake, A.A., Jr. and B.A. Morgan, 1981, The Piney Branch complex – a metamorphosed fragment of the central Appalachian ophiolite in northern Virginia: American Journal of Science, v. 281, p. 484-508.

Drake, A.A., Jr. and P.T. Lyttle, 1981, The Accotink schist, Lake Bancroft metasandstone, and Popes Head Formation – keys to understanding of the tectonic evolution of the northern Virginia Piedmont: USGS Professional Paper 1205, 16 p.

Drake, A.A., Jr., 1985, Metamorphism in the Potomac composite terrane, Virginia-Maryland: Geological Society of America Abstracts with Programs, v. 17, no. 7, p. 566.

Drake, A.A., Jr., 1986, Probable Late Proterozoic rocks of the central Appalachian Piedmont: Geological Society of America Abstracts with Programs, v. 18, p. 14.

Drake, A.A., Jr., 1987, Pre-Taconian deformation in the Pedmont of the Potomac Valley – Penobscottian, Cadomian, or both?, in Contribution to Virginia Geology-V (Harris volume): Virginia Division of Mineral Resources Publication 74, p. 1-18.

Drake, A.A., Jr., 1998, Geologic map of the Kensington Quadrangle, Montgomery County, Maryland: USGS Map GQ-1774, scale 1:24,000.

Dunlap, W.J., 2000, Nature's diffusion experiment: The cooling-rate cooling-age correlation: Geology, v. 28, p. 139-142.

England, P.C. and A.B. Thompson, 1984, Pressure-temperature-time paths of regional metamorphism: I. Heat transfer during the evolution of regions of thickened continental crust: Journal of Petrology, v. 25, p. 894-928.

England, P.C. and A.B. Thompson, 1986, Some thermal and tectonic models for crustal melting in continental collision zones, *in* Coward, M and A.C. Ries (eds.), Collision Tectonics, Special Publication 19, p. 83-94

Eskola, P., 1920, The mineral facies of rocks: Norsk geologisk tidsskrift, v. 6, p. 143-194.

Eskola, P., 1939, Die metamorphen Gesteine, *in* Barth, T.F.W., C.W. Correns and P. Eskola (eds.), Die Entstehung der Gesteine: Berlin, Springer, p. 263-407.

Etheridge, M.A., 1983, Differential stress magnitudes during regional deformation and metamorphism: Upper bound imposed by tensile fracturing: Geology, v. 11, p. 231-234

Ettensohn, F.R., 2008, Chapter 4, The Appalachian Foreland Basin in Eastern United States: Sedimentary Basins of the World, v. 5, p. 105-179.

Evans, M.A. and M.J. Bartholomew, 2000, Crustal Fluid Evolution and Changes in Deformation Conditions during Regional Syn- to Post-Orogenic Exhumation: Southeastern Piedmont, Southern Appalachians: U.S. Department of Energy, Contract No. DE-AC09-96SR18500, accessed from http://sti.srs.gov/fulltext/ms2000187/ms2000187.html on 28 June, 2013.

Everett, J.R., M. Morisawa and N.M. Short, 1986, Tectonic Landforms, in Short, N.M. and R.W. Blair, Jr. (eds.), Geomorphology from Space: A Global Overview of Regional Landforms: NASA Special Publication 486, 717 p.

Ewing, M., A.P. Crary and H.M. Rutherford, 1937, Geophysical investigations in the emerged and submerged Atlantic Coastal Plain, Part I, Methods and results: Geological Society of America Bulletin, v. 48, p. 753-802.

Faill, R.T., 1997, A geologic history of the north-central Appalachians: Part 1. Orogenesis from the Mesoproterozoic through the Taconic orogeny: American Journal of Science, v. 297, p. 551-619.

Faill, R.T., 1998, A geologic history of the north-central Appalachians: Part 3. The Alleghany orogeny: American Journal of Science, v. 298, p. 131-179.

Farrar, S.S., 1984, The Goochland granulite terrane: remobilized Grenville basement in the eastern Virginian Piedmont: Geological Society of America Special Paper 194, p. 215-227.

Farrar, S.S., 1985, Tectonic evolution of the easternmost Piedmont, North Carolina, Geological Society of America Bulletin, v. 96, p. 362-380.

Fekiacova, Z., D.F. Mertz and P. Renne, 2007, Geodynamic setting of the Tertiary Hocheifel volcanism (Germany), Part I: $^{40}Ar/^{39}Ar$ dating, *in* Ritter, J. and U. Christensen (eds.), Mantle Plumes - A Multidisciplinary Approach, Springer, p. 185-206.

Ferrière, L., C. Koeberl, W.U. Reimold, L. Hecht and K. Bartosova, 2009, The origin of "toasted" quartz in impactites revisited: 40th Lunar and Planetary Science Conference, CD-ROM, abstract n. 1751.

Ferry, J.M. and F.S. Spear, 1978, Experimental Calibration of the Partitioning of Fe and Mg Between Biotite and Garnet: Contributions to Mineralogy and Petrology, v. 66, p. 113-117.

Fichter L.S. and S.J. Baedke, 1999, Cross-sections Divided into Fourteen Stages A-M, *in* The Geologic Evolution of Virginia and the Mid-Atlantic Region: Harrisonburg Virginia, James Madison University's Department of Geology and Environmental Sciences, accessed from http://csmres.jmu.edu/geollab/vageol/vahist/13xsect.pdf on 9 January, 2014.

Fleck, R.J., J.F. Sutter and D.H. Elliot, 1977, Interpretation of discordant $^{40}Ar/^{39}Ar$ age-spectra of Mesozoic tholeiites from Antarctica: Geochimica et Cosmochimica Acta, v. 41, p. 15-32.

Fleet, M.E., W.A. Deer, R.A. Howie and J. Zussman, 2003, Rock-Forming Minerals: Micas (2nd ed.): Geological Society of London, v. 3A, 758 p.

Force, E.R., 1980, The provenance of rutile: Journal of Sedimentary Petrology, v. 50, p. 485-488.

Foster, C.T., Jr., 1977, Mass transfer in sillimanite-bearing pelitic schists near Rangeley, Maine: American Mineralogist, v. 62, p. 727-746.

Foster, D.A., T.M. Harrison, P. Copeland and M.T. Heizler, 1990, Effects of excess argon within large diffusion domains on K-feldspar age spectra: Geochimica et Cosmochimica Acta, v. 54, p. 1699-1708.

French, B.M., 1998, Traces of Catastrophe: A Handbook of Shock-Metamorphic Effects in Terrestrial Meteorite Impact Structures: Lunar and Planetary Institute, LPI Contribution 954, 120 p.

Ganguly, J. and S.K. Saxena, 1984, Mixing properties of aluminosilicate garnets: constraints from natural and experimental data, and application to geothermobarometry: American Mineralogist, v. 69, p. 88-97.

Gapais, D., 1989, Shear structures within deferred granites: Mechanical and thermal indicators: Geology, v. 17, p. 1144-1147.

Gapais, D., 1989, Shear structures within deformed granites: Mechanical and thermal indications: Geology, v. 17, p. 1144-1147.

Gates, A.E. and L. Glover, III, 1989, Alleghanian tectono-thermal evolution of the dextral transcurrent Hylas zone, Virginia Piedmont, U.S.A.: Journal of Structural Geology, v. 11, p. 407-419.

Geiser, P.A., 1988, Mechanisms of thrust propagation: some examples and implications for the analysis of overthrust terranes: Journal of Structural Geology, v. 10, p. 829-845.

George, R.P., Jr., 1978, Structural petrology of the Olympus ultramafic complex in the Troodos ophiolite, Cyprus: Geological Society of America Bulletin, v. 86, p. 845-865.

Gibbs, J.W., 1906, The Scientific Papers of J. Willard Gibbs, PhD, LLD: Volume 1: Thermodynamics: New York, Longmans, Green and Company, 434 p.

Gibson, R.L., 1991, Hercynian low-pressure-high-temperature regional metamorphism and subhorizontal foliation development in the Canigou massif, Pyrenees, France–Evidence for crustal extension: Geology, v. 19, p. 380-383.

Gibson, R.L., G.N. Townsend, J.W. Horton, Jr. and W.U. Reimold, 2009, Chapter 12, Pre-impact tectonothermal evolution of the crystalline basement-derived rocks in the ICDP-USGS Eyreville B core, Chesapeake Bay impact structure, *in* Gohn, G.S., C. Koeberl, K.G. Miller and W.U. Reimold (eds.), The ICDP-USGS Deep Drilling Project in the Chesapeake Bay Impact Structure: Results from the Eyreville Core Holes: Geological Society of America Special Paper 458, p. 235–254.

Gibson, T.G., 1983, Key foraminifera from upper Oligocene to lower Pleistocene strata of the central Atlantic Coastal Plain, *in* Ray, C.E. (ed.), Geology and palaeontology of the Lee Creek Mine, North Carolina; I: Smithsonian Contributions to Palaeobiology, no. 53, p. 355–453.

Glass, B.P., 1989, North American tektite debris and impact ejecta from DSDP site 612: Meteoritics, v. 24, p. 209-218.

Glazner, A.F. and J.M Bartley, 2006, Is stoping a volumetrically significant pluton emplacement process?: Geological Society of America Bulletin, v. 118, p. 1185-1195.

Glover, L., III. And A.K. Sinha, 1973, The Virgilina deformation, a late orogenic event in the central Piedmont of Virginia and North Carolina: American Journal of Science, v. 273-A, p. 234-251.

Glover, L., III., 1989, Tectonics of the Virginia Blue Ridge and Piedmont: Culpeper to Richmond, Virginia: *in* Metamorphism and tectonics of eastern and central North America, Field Trip Guidebook T363: American Geophysical Union, International Geologic Congress, 28th Guidebook, 59 p.

Glover, L., III., N.H. Evans, J.G. Patterson and W.R. Brown, 1989, Tectonics of the Virginia Blue Ridge and Piedmont: Culpepper to Richmond, Virginia, *in* Metamorphism and tectonics of eastern and central North America, Field Trip Guidebook T363: American Geophysical Union, International Geologic Congress, 28th Guidebook, 59 p.

Gohn G.S., C. Koeberl, K.G. Miller, W.U. Reimold, J.V. Browning, C.S. Cockell, J.W. Horton, Jr., T. Kenkmann, A.A. Kulpecz, D.S. Powars, W.E. Sanford and M.A. Voytek, 2009, Deep drilling in the Chesapeake Bay impact structure – An overview *in* Gohn, G.S., C. Koeberl, K.G. Miller and W.U. Reimold (eds.), The ICDP-USGS Deep Drilling Project in the Chesapeake Bay Impact Structure: Results from the Eyreville Core Holes: Geological Society of America Special Paper 458, p. 1-20.

Gohn, G.S., C. Koeberl, K.G. Miller, W.U. Reimold, C.S. Cockell, J.W. Horton, Jr., W.E. Sanford and M.A. Voytek, 2006, Chesapeake impact structure drilled: Eos (Transactions), American Geophysical Union, v. 8735, p. 349-360.

Gohn, G.S., C. Koeberl, K.G. Miller, W.U. Reimold, J.V. Browning, C.S. Cockell, J.W. Horton, Jr., T. Kenkmann, A.A. Kulpecz, D.S. Powars, W.E. Sanford and M.A. Voytek, 2008, Deep drilling into the Chesapeake Bay impact structure: Science, v. 320, p. 1740–1745.

Gohn, G.S., K.G. Miller and J.E. Quick, 2004, ICDP Workshop Report: Deep drilling in the central crater of the Chesapeake Bay impact structure, Virginia, USA: International Continental Scientific Drilling Program Newsletter, v. 6, p. 30-35.

Goldberg, S.A., 1994, U-Pb geochronology of volcanogenic terranes of the eastern North Carolina Piedmont: preliminary results, *in* Stoddard, E.F. and D. Blake (eds.), Geology and Field Trip Guide, Western Flank of the Raleigh Metamorphic Belt, North Carolina: Carolina Geological Society Field Trip Guidebook, North Carolina Geological Survey, Raleigh, NC, p. 13-17.

Goldsmith, J.R., 1982, Review of the behaviour of plagioclase under metamorphic conditions: American Mineralogist, v. 67, p. 643-652.

Goodwin, B.K., 1970, Geology of the Hylas and Midlothian quadrangles, Virginia: Virginia Division of Mineral Resources, Report of Investigations, v. 23, plates 1 and 2, scale 1:24,000.

Grapes, R. And M. Otsuki, 1983, Peristerite compositions in quartzofeldspathic schists, Franz Josef-Fox Glacier Area, New Zealand: Journal of Metamorphic Petrology, v. 1, p. 47-61.

Groat, L.A., F.C. Hawthorne and T.C. Ercit, 1992, The chemistry of vesuvianite: Canadian Mineralogist, v. 30, p. 19-48.

Gromet, L.P., R.F. Dymek, L.A. Haskin and R.L. Korotev, 1984, The “North American shale composite”: Its compilation, major and trace element characteristics: Geochimica et Cosmochimica Acta, v. 48, p. 2469-2482.

Hackler, R.T. and B.J. Wood, 1989, Experimental determination of Fe and Mg exchange between garnet and olivine and estimation of Fe-Mg garnet mixing properties: American Mineralogist, v. 74, p. 994-999.

Hackley, P.C., J.D. Peper, W.C. Burton and J.W. Horton, Jr., 2007, Northward extension of Carolina slate belt stratigraphy and structure, south-central Virginia: Results from geologic mapping: American Journal of Science, v. 307, p. 749-771.

Hames, W.E. and S.A. Bowering, 1994, An empirical evaluation of the argon diffusion geometry in muscovite: Earth and Planetary Science Letters, v. 124, p. 161-167.

Hanson, R.B. and M.D. Barton, 1989, Thermal development of low-pressure metamorphic belts: results from two-dimensional numerical models: Journal of Geophysical Research, v. 94(B8), p. 10363-10377.

Harper, C. T., 1967, The geological interpretation of potassium-argon ages of metamorphic rocks from the Scottish Caledonides: Scottish Journal of Geology, v. 8, p. 46-66.

Harris, N.B.W., J.A. Pearce and A.G. Tindle, 1986, Geochemical characteristics of collision-zone magmatism: Geological Society of London, Special Publications, v. 19, p. 67-81.

Harrison, T.H., 1981, Diffusion of ^{40}Ar in Hornblende: Contributions to Mineralogy and Petrology, v. 78, p. 324-331.

Harrison, T.M., M.T. Heizler, O.M. Lovera, W. Chen and M. Grove, 1994, A chlorine disinfectant for excess argon released from K-feldspar during step heating: Earth and Planetary Science Letters, v. 123, p. 95-104.

Hatcher, R.D., Jr., 1989, Tectonic synthesis of the U.S. Appalachians, *in* Hatcher, R.D., Jr., W.A. Thomas and G.W. Viele (eds.), The Appalachian-Ouachita Orogen in the United States (Geology of North America, Vol. F-2): Geological Society of America, Boulder, Colorado, p. 511-536.

Hatcher, R.D., Jr., 2002, Alleghanian (Appalachian) orogeny, a product of zipper tectonics: Rotational transpressive continent-continent collision and closing of ancient oceans along irregular margins, *in* Martínez Catalán, J.R., R.D. Hatcher, Jr., R. Arena and F. Díaz García (eds.), Variscan-Appalachian dynamics: The building of the late Paleozoic basement: Geological Society of America Special Paper 364, p. 199–208.

Hatcher, R.D., Jr., 2010, The Appalachian orogen: A brief summary: Geological Society of America Memoirs, v. 206, p. 1-19.

Haugerud, R.A. and M.J. Kunk, 1988, ArAr*: A computer program reduction of ^{40}Ar-^{39}Ar data: U.S. Geological Survey Open-File Report 88-261, 68 p.

Hawarth, R.T., D.L. Daniels, H. Williams and I. Zietz, 1980, Bouguer gravity map of Appalachian orogen: Map 3, Memorial University of Newfoundland, St. Johns, scale 1:1,000,000.

Heinrich, W., G. Andrehs and G. Franz, 1997, Monazite–xenotime miscibility gap thermometry I: An empirical calibration: Journal of Metamorphic Geology, v. 15, p. 3-16.

Henry, D.J., and C.V. Guidotti, 1985, Tourmaline as a petrogenetic indicator mineral: an example from the staurolite metapelites of NW Maine: American Mineralogist, v, 70, p. 1-15.

Herron, M.M., 1988, Geochemical classification of terrigenous sands and shales from core or log data: Journal of Sedimentary Petrology, v. 58, p. 820-829.

Hibbard, J. P., and S.D. Samson, 1995, Orogenesis exotic to the Iapetan cycle in the southern Appalachians, *in* Hibbard, J. P., C.R. van Staal and P.A. Cawood (eds.), Current perspectives in the Appalachian-Caledonian orogen: Geological Association of Canada Special Paper 41, p. 191-205.

Hibbard, J.P., 2000, Docking Carolina: Mid Paleozoic accretion in the southern Appalachians: Geology, v. 28, p. 127-130.

Hibbard, J.P., C.R. van Staal and B.V. Miller, 2007b, Links between Carolinia, Avalonia, and Ganderia in the Appalachian peri-Gondwanan Realm, *in* Evenchick, C.A. (ed.), Whence the Mountains? Inquiries into the Evolution of Orogenic Systems: A Volume in Honour of Raymond A. Price: Geological Society of America Special Paper 433, p. 291-311.

Hibbard, J.P., C.R. van Staal and D.W. Rankin, 2007a, A comparative analysis of pre-Silurian crustal building blocks of the northern and southern Appalachian orogen: American Journal of Science, v. 307, p. 23-45.

Hibbard, J.P., E.F. Stoddard, D.T. Secor and A.J. Dennis, 2002, The Carolina Zone: overview of Neoproterozoic to Early Paleozoic peri-Gondwanan terranes along the eastern Flank of the southern Appalachians: Earth-Science Reviews, v. 57, p. 299-339.

Hietanen, A., 1967, On the Facies Series in Various Types of Metamorphism: Journal of Geology, v. 75, p. 187-214.

Himmelberg, G.R. and R.A. Loney, 1980, Petrology of ultramafic and gabbroic rocks of the Canyon Mountain ophiolite, Oregon: American Journal of Science, v. 280-A, p. 232-268.

Holdaway, M.J. and S.M. Lee, 1977, Fe--Mg Cordierite Stability in High-Grade Pelitic Rocks Based on Experimental, Theoretical, and Natural Observations: Contributions to Mineralogy and Petrology, v. 63, p. 175-198.

Holdaway, M.J., 1971, Stability of andalusite and the aluminium silicate phase diagram: American Journal of Science, v. 271, p. 97-131.

Holland, T.J.B., and J.D. Blundy, 1994, Non-ideal interactions in calcic amphiboles and their bearing on amphibole-plagioclase thermometry: Contributions to Mineralogy and Petrology, v. 116, p. 433-447.

Holland, T.J.B., and R. Powell, 1998, An internally consistent thermodynamic data set for phases of petrological interest: Journal of Metamorphic Geology, v. 16, p. 309-343.

Holland, T.J.B., and R. Powell, 2000, AX: A Program to Calculate Mineral End-Members from Chemical Analyses (Usually from an Electron Microprobe): Cambridge, Cambridge University Press, 11 p.

Hopson, C.A., S.J. Frano, E.A. Pessagno, Jr. and J.M. Mattinson, 1975, Preliminary report and geologic guide to the Jurassic ophiolite near Point Sal, southern California coast: Geological Society of America, 71st Annual Meeting Cordilleran Section, Field Trip, n. 5, 36 p.

Hopson, R.F., J.W. Hillhouse and K.A. Howard, 2008, Dike orientations in the Late Jurassic Independence dike swarm and implications for vertical-axis tectonic rotations in eastern California, *in* Wright, J.E. and J.W. Shervais (eds.), Ophiolites, Arcs and Batholiths: A tribute to Cliff Hopson: Geological Society of America Special Paper 438, p. 481-498.

Horton J.W., Jr., D.S. Powars and G.S. Gohn, 2005a, Studies of the Chesapeake Bay impact structure – Introduction and discussion, Chapter A, *in* Horton, J.W., Jr., D.S. Powars and G.S. Gohn (eds.), Studies of the Chesapeake Bay Impact Structure—The USGS-NASA Langley Borehole core, Hampton, Virginia, and Related Borehole cores and Geophysical Surveys: U.S. Geological Survey Professional Paper 1688, p. A1–24.

Horton, J.W., Jr. and E.F. Stoddard, 1986, The Roanoke Rapids complex of the Eastern slate belt, Halifax and Northampton Counties, North Carolina, *in* Neathery, T.L. (ed.),

Southeastern Section of the Geological Society of America: Boulder, Colorado, Geological Society of America, Centennial Field Guide, v. 6, p. 217-222.

Horton, J.W., Jr. and G.A. Izett, 2005, Crystalline-Rock Ejecta and Shocked Minerals of the Chesapeake Bay Impact Structure, USGS-NASA Langley Core, Hampton, Virginia, with Supplemental Constraints on the Age of Impact, *in* Horton, J.W., Jr., D.S. Powars and G.S. Gohn (eds.), Studies of the Chesapeake Bay Impact Structure—The USGS-NASA Langley Borehole core, Hampton, Virginia, and Related Borehole cores and Geophysical Surveys: U.S. Geological Survey Professional Paper 1688, p. E1-30.

Horton, J.W., Jr. and T.W. Stern, 1994, Tectonic significance of preliminary uranium-lead ages from the eastern Piedmont of North Carolina: Geological Society of America Abstracts with Programs, v. 26, p. 21.

Horton, J.W., Jr., A.A. Drake and D.W. Rankin, 1989, Tectonostratigraphic terranes and their Paleozoic boundaries on the central and southern Appalachians, *in* Dallmeyer, R.D. (ed.), Terranes in the Circum-Atlantic Paleozoic orogens: Geological Society of America Special paper 230, p. 213-245.

Horton, J.W., Jr., A.A. Drake and D.W. Rankin, 1994, Terranes and Overlap Sequences in the Central and Southern Appalachians, An Expanded Explanation for Part of the Circum-Atlantic Terrane Map: U.S. Geological Survey Open-File Report 94-682, 40 p.

Horton, J.W., Jr., A.A. Drake, D.W. Rankin and R.D. Dallmeyer, 1991, Preliminary Tectonostratigraphic Terrane Map of the Central and Southern Appalachians: U.S. Geological Survey Miscellaneous Investigations Series Map I-2163, scale 1:2,000,000.

Horton, J.W., Jr., D.E. Blake, A.S. Wylie, Jr. and E.F. Stoddard, 1986, Metamorphosed mélange terrane in the eastern Piedmont of North Carolina: Geology, v. 14, p. 551-553.

Horton, J.W., Jr., J.N. Aleinikoff and W.C. Burton, 1995, Mesoproterozoic and Neoproterozoic terranes in the eastern Piedmont of Virginia, implications of coordinated field studies and U-Pb geochronology: Geological Society of America Abstracts with Programs, v. 27, p. 397.

Horton, J.W., Jr., J.N. Aleinikoff, A.A. Drake, Jr. and M.C. Fanning, 1998, Significance of Middle to Late Ordovician volcanic-arc rocks in the central Appalachian Piedmont, Maryland and Virginia: Geological Society of America Abstracts with Programs, v. 30, p. 125.

Horton, J.W., Jr., J.N. Aleinikoff, M.J. Kunk, C.W. Naeser and N.D. Naeser, 2005b, Petrography, structure, age, and thermal history of granitic coastal plain basement in the Chesapeake Bay impact structure, USGS-NASA Langley core, Hampton, Virginia, Chapter B, *in* Horton, J.W., Jr., D.S. Powars and G.S. Gohn (eds.), Studies of the Chesapeake Bay Impact Structure—The USGS-NASA Langley Borehole core, Hampton, Virginia, and Related Borehole cores and Geophysical Surveys: U.S. Geological Survey Professional Paper 1688, p. B1–29.

Horton, J.W., Jr., M.J., Kunk, H.E. Belkin, J.N. Aleinikoff, J.C., Jackson and I-M. Chou, 2009b, Chapter 14, Evolution of crystalline target rocks and impactites in the Chesapeake Bay impact structure, ICDP-USGS Eyreville B core, *in* Gohn, G.S., C. Koeberl, K.G. Miller and W.U. Reimold (eds.), The ICDP-USGS Deep Drilling Project in the Chesapeake Bay Impact Structure: Results from the Eyreville Core Holes: Geological Society of America Special Paper 458, p. 277-316.

Horton, J.W., Jr., R.L. Gibson, W.U. Reimold, A. Wittmann, G.S. Gohn and L.E. Edwards, 2009a, Chapter 2, Geologic columns for the ICDP-USGS Eyreville B core, Chesapeake Bay impact structure: Impactites and crystalline rocks, 1766 to 1096 m depth, *in* Gohn, G.S., C. Koeberl, K.G. Miller and W.U. Reimold (eds.), The ICDP-USGS Deep Drilling Project in the Chesapeake Bay Impact Structure: Results from the Eyreville Core Holes: Geological Society of America Special Papers, v. 458, p. 21-50.

Howell, D.G. and D.L. Jones, 1984, Tectonostratigraphic terrane analysis and some terrane vernacular, in Howell, D.G., D.L. Jones, A. Cox and A. Nur (eds.), Proceedings of the Circum-Pacific Terrane Conference: Stanford University Publications in Geological Sciences, v. 18, p. 6-9.

Hubert, J.F., 1962, A zircon–tourmaline–rutile maturity index and the interdependence of the composition of heavy mineral assemblages with the gross composition and texture of sandstones: Journal of Sedimentary Petrology, v. 32, p. 440-450.

Hunter, A.G., 1998, Intracrustal Controls on the Coexistence of Tholeiitic and Calc-alkaline Magma Series at Aso Volcano, SW Japan: Journal of Petrology, v. 39, p. 1255-1284.

Hunziker, P., 2003, The stability of tri-octahedral Fe^{2+}-Mg-Al chlorite: A combined experimental and theoretical study. Unpublished PhD thesis, University of Basel, Switzerland.

Ingle, S., 1999, Age and tectonic significance of the Uwharrie Formation and Albemarle Group, Carolina slate belt. Unpublished MSc thesis, University of Florida, Gainesville, USA, 96 p.

Ingle-Jenkins, S., P. Mueller and A. Heatherington, 1999, Evidence for Mesoproterozoic basement in the Carolina and other southern Appalachian terranes: Geological Society of America Abstracts with Programs, v. 31, p. A-22.

Irving, T.N. and W.R.A. Baragar, 1971, A guide to the chemical classification of the common volcanic rocks: Canadian Journal of Earth Sciences, v. 8, p. 523-548.

Jacob, D.E., 2006, High sensitivity analysis of trace element poor geological reference glasses by laser-ablation inductively coupled plasma mass spectrometry (LA-ICPMS): Geostandards and Geoanalytical Research, v. 30, p. 221-235.

Jakes, P. and J. Gill, 1970, Rare earth elements and the island arc tholeiite series: Earth and Planetary Science Letters, v. 9, p. 17-28.

Jamieson, R.A. and C. Beaumont, 1988, Orogeny and metamorphism: A model for deformation and pressure-temperature-time paths with applications to the central and southern Appalachians: Tectonics, v. 7, p. 417-445.

Jarosewich, E., 2002, Smithsonian Microbeam Standards: Journal of Research of the National Institute of Standards and Technology, v. 107, p. 681-685.

Jarvis, K.E., 1988, Inductively coupled plasma mass spectrometry: A new technique for the rapid or ultra-trace level determination of the rare-earth elements in geological materials: Chemical Geology, v. 68, p. 31-39.

Jochum, K.P., U. Weis, B. Stoll, D. Kuzmin, Q. Yang, I. Raczek, D. E. Jacob, A. Stracke, K. Biraum, D.A. Frick, D. Günther and J. Enzweiler, 2011, Determination of Reference Values for NIST SRM 610–617 Glasses Following ISO Guidelines: Geostandards and Geoanalytical Research, v. 35, p. 397-429.

Johannes, W., and F. Holz, 1990, Formation and composition of H_2O-undersaturated granitic melts, *in* Ashworth, J.R., and M. Brown (eds.), High-Temperature Metamorphism and Crustal Anatexis: The Mineralogical Society Series, v. 2, p. 87-104.

Johnson, S.E., 1999, Porphyroblast microstructures: A review of current and future trends: American Mineralogist, v. 84, p. 1711-1726.

Johnson, S.E., 2009, Porphyroblast rotation and strain localization: Debate settled: Geology, v. 37, p. 663-666.

Johnson, S.S., 1977, Gravity map of Virginia, simple Bouguer anomaly: Virginia Division of Mineral Resources, scale: 1:500,000.

Jolly, L.C., 2011, Petrographic and geochemical analysis of the impactite succession in the Eyreville B drill core, Chesapeake Bay impact structure, Virginia, USA. Unpublished MSc thesis, University of the Witwatersrand, Johannesburg, South Africa, 268 p.

Jones, D.L., 1983, Recognition, character and analysis of tectonostratigraphic terranes in western North America: Journal of Geological Education, v. 31, p. 295-303.

Jones, D.L., D.G. Howell, P.J. Coney and J.W.H. Monger, 1983, Recognition, character and analysis of tectonostratigraphic terranes in western North America, *in* Hashimoto, M. and S. Uyeda (eds.), Advances in earth and planetary sciences: Tokyo, Terra Scientific Publishing Co., p. 31-35.

Jowhar, T.N., 2012, Computer Programs for P-T History of Metamorphic Rocks using Pseudosection Approach: International Journal of Computer Applications, v. 41, p. 18-25.

Keller, L.M., C. de Capitani and R. Abart, 2005, A quaternary solution model for white micas based on natural coexisting phengite-paragonite pairs: Journal of Petrology, v. 46, p. 2129-2144.

Kelley, S., 2002a, K-Ar and Ar-Ar Dating: Reviews in Mineralogy and Geochemistry, v. 47, p. 785-818.

Kelley, S., 2002b, Excess argon in K-Ar and Ar-Ar geochronology: Chemical Geology, v. 188, p. 1-22.

Kelley. S., G. Turner, A.W. Butterfield and T.J. Shepherd, 1986, The source and significance of argon isotopes in fluid inclusions from areas of mineralisation: Earth and Planetary Science Letters, v. 79, p. 303-318.

Keppie, J.D., J. Dostal, J.B. Murphy and R.D. Nance, 1996, Terrane transfer between eastern Laurentia and western Gondwana in the Early Paleozoic: constraints on global reconstructions, *in* Nance, R.D. and M.D. Thompson (eds.), Avalonian and related peri-Gondwanan terranes of the circum North Atlantic: Geological Society of America Special Paper, v. 304, p. 369-380.

Kerrick, D.M., 1972, Experimental determination of muscovite + quartz stability with $P_{H_2O} < P_{total}$: American Journal of Science, v. 272, p. 946-958.

Kite, L.E. and E.F. Stoddard, 1984, The Halifax County Complex: oceanic lithosphere in the eastern North Carolina Piedmont: Geological Society of America Bulletin, v. 95, p. 422-432.

Klein, C., 2002, The 22nd Edition of the Manual of Mineral Science: New York, John Wiley and Sons, Inc., 641 p.

Koeberl, C. and A.A. Anderson, 1996, The Manson impact structure, Iowa: Anatomy of an impact crater: Geological Society of America Special Paper 302, p. 1-468.

Krynine, P.D., 1946, The Tourmaline Group in Sediments: Journal of Geology, v. 54, p. 65-87.

Kunk, M.J. R.P. Wintsch, C.W. Neaser, N.D. Naester, C.S. Southworth, A.A. Drake, Jr. and J.L. Becker, 2005, Contrasting tectonothermal domains and faulting in the Potomac terrane, Virginia-Maryland – discrimination by $^{40}Ar/^{39}Ar$ and fission-track thermochronology: Geological Society of America Bulletin, v. 117, no. 9/10, p. 1347-1366.

Kunk, M.J., J.A. Winick and J.O. Stanley, 2001, $^{40}Ar/^{39}Ar$ Age-Spectrum and Laser Fusion Data for Volcanic Rocks in West Central Colorado: U.S. Geological Survey Open-File Report 01-472, 94 p.

Kunk, M.J., R.P. Wintsch, C.S. Southworth, B.K. Mulvey, C.W. Naeser and N.D. Naeser, 2004, Multiple Paleozoic metamorphic histories, fabrics, and faulting in the Westminster and Potomac terranes, central Appalachian Piedmont, northern Virginia and southern

Maryland, *in* Southworth, S., and W. Burton (eds.), Geology of the national capital region – field trip guidebook: U.S. Geological Survey Circular 1264, p. 163–188.

Leake, B.E., 1978, Nomenclature of amphiboles: Mineralogical Magazine, v. 42, p. 533–563.

Lefort, J.P. and M.D. Max, 1991, Is there Archean crust beneath the Chesapeake Bay?: Tectonics, v. 10, p. 213-226.

Lefort, J.P. M.D. Max and J. Roussel, 1988, Geophysical evidence for the location of the NW boundary of Gondwanaland and its relationship with two older satellite sutures, *in* Harris, A.L. and D.J. Fettes (eds.), The Caledonian-Appalachian Orogen: Geological Society of London, Special Publication 38, p. 49-60.

Lefort, J.P., 1988, Imprint of the Reguibat uplift (Mauritania) on to the central and southern Appalachians of the USA: Journal of African Earth Sciences, v. 7, p. 433-442.

LeVan, D.C. and R.F. Pharr, 1963, A magnetic survey of the coastal plain in Virginia: Virginia Division of Mineral Resources Report of Investigations 4, p. 1-17.

Lister, G.S., and A.W. Snoke, 1984, S-C Mylonites: Journal of Structural Geology, v.6, p. 617-638.

Little, N.C., L.J. Kosakowsky, R.J. Speakman, M.D. Glascock and J.C. Lohse, 2004, Characterisation of Maya pottery by INAA and ICP-MS: Journal of Radioanalytical and Nuclear Chemistry, v. 262, p. 103-110.

Loosveld, R. J. H. and M.A. Etheridge, 1990, A model for low-pressure facies metamorphism during crustal thickening: Journal of Metamorphic Geology, v. 8, p. 257-267.

Loosveld, R.J.H., 1989, The synchronism of crustal thickening and low-pressure facies metamorphism in the Mount Isa inlier, Australia 2: Fast convective thinning of mantle lithosphere during crustal thickening: Tectonophysics, v. 165, p. 191-218.

Ludwig, K.R., 2003, Isoplot/Ex 3.00: A geochronological toolkit for Microsoft Excel. Berkeley Geochronological Centre: Special Publication, v. 4.

Lumpkin, B., E. Stoddard and D. Blake, 1994, The Raleigh graphite schist, *in* Stoddard, E. and D. Blake (eds.), Geology and Field Trip Guide, Western Flank of the Raleigh Metamorphic Belt, North Carolina: Carolina Geological Society Field Trip Guidebook, North Carolina Geological Survey, p. 19-24.

Luvizotto, G.L. and T. Zack, 2009, Nb and Zr behaviour in rutile during high-grade metamorphism and retrogression: An example from the Ivrea-Verbano Zone: Chemical Geology, v. 261, p. 303-317.

Luvizotto, G.L., T. Zack, H.P. Meyer, T. Ludwig, S. Triebold, A. Kronz, C. Münker, D.F. Stockli, S. Prowatke, S. Klemme, D.E. Jacob and H. von Eynatten, 2009a, Rutile crystals as potential trace element and isotope mineral standards for microanalysis: Chemical Geology, v. 261, p. 346-369.

Luvizotto, G.L., T. Zack, S. Triebold and H. von Eynatten, 2009b, Rutile occurrence and trace element behaviour in medium-grade metasedimentary rocks: example from the Erzgebirge, Germany: Mineralogy and Petrology, v. 97, no. 3-4, p. 233-249.

Lux, D. R., J.J. De Yoreo, C.V. Guidotti and E.R. Decker, 1986, Role of plutonism in low-pressure metamorphic belt formation: Nature, v. 323, p. 794-797.

Marr, J.D., Jr., 1985, Day one, Geology of the crystalline portion of the Richmond 1° x 2° quadrangle: A progress report, *in* Geology of portions of the Richmond 1° x 2° quadrangle: Annual Virginia Geological Field Conference, p. 1-22.

Martin, A.J. and B.E. Owens, 2012, Implications of c. 550 Ma crystallisation of the Sabot Amphibolite protolith in the Goochland terrane of the Central Virginia Piedmont: Geological Society of America Abstracts with Programs, v. 44, p. 172.

Maruyama, S., J.G. Liou and K. Suzuki, 1982, The peristerite gap in low-grade metamorphic rocks: Contributions to Mineralogy and Petrology, v. 81, p. 268-276.

Maruyama, S., K. Suzuki and J.G. Liou, 1983, Greenschist-Amphibolite Transition Equilibria at Low Pressures: Journal of Petrology, v. 24, p. 683-604.

Mason, R., 1990, Petrology of metamorphic rocks: London, Unwin Hyman, 230 p.

Mauldin, J., J. Shervais and A.J. Dennis, 1997, Petrologic and structural constraints on the classification of crystalline basement beneath the Savanna River Site, SC: Geological Society of America Abstracts with Programs, v. 29, p. 455.

McDonough, W.F. and S.-s. Sun, 1995, The composition of the Earth: Chemical Geology, v. 120, p. 223-253.

McDougall, I. and T.M. Harrison, 1999, Geochronology and thermochronology by the $^{40}Ar/^{39}Ar$ method: Oxford, New York University Press, 269 p.

McLennan, S.M, 1993, Weathering and Global Denudation: Journal of Geology, v. 101, p. 295-303.

McLennan, S.M., S. Hemming, D.K. McDaniel and G.N. Hanson, 1993, Geochemical approaches to sedimentation, provenance and tectonics, *in* Johnson, M.J. and A. Basu (eds.), Processes Controlling the Composition of Clastic Sediments: Geological Society of America Special Paper 284, 21-40.

McMenamin, M.A.S. and D.L.S. McMenamin, 1990, The emergence of animals. The Cambrian breakthrough: New York, Columbia University Press, 217 p.

Meinhold, G., 2010, Rutile and its applications in earth sciences: Earth-Science Reviews, v. 102, p. 1-28.

Mezger, K., G.N. Hanson and S.R. Bohlen, 1989, High-precision U-Pb ages of metamorphic rutile: application to the cooling history of high-grade terranes: Earth and Planetary Science Letters, v. 96, p. 106-118.

Middlemost, E.A.K., 1994, Naming materials in the magma/igneous rock system: Earth-Science Reviews, v. 37, p. 215-224.

Milici, R.C., 1995, Blue Ridge Thrust Belt (068), Piedmont Province (069), Atlantic Coastal Plain Province (070), Adirondack Province (071), and New England Province (072) in Gautier, D. L., Dolton, G. L., Takahashi, K. I., and Varnes, K. L. (eds.), National Assessment of United States oil and gas resources-results, methodology, and supporting data: U.S. Geological Survey Digital Data Series DDS-30.

Miller, C.F., 1985, Are Strongly Peraluminous Magmas Derived from Pelitic Sedimentary Sources?: Journal of Geology, v. 93, p. 673-689.

Mixon, R.B., C.R. Berquist, Jr., W.L. Newell, G.H. Johnson, D.S. Powars, J.S. Schindler and E.K. Rader, 1989, Geologic map and generalized cross sections of the coastal plain and adjacent parts of the Piedmont, Virginia: USGS Miscellaneous Investigations Series Map I-2033, 2 sheets, scale 1:250,000.

Morton, A.C. and C.R. Hallsworth, 1994, Identifying provenance-specific features of detrital heavy mineral assemblages in sandstones: Sedimentary Geology, v. 90, p. 241-256.

Mose, D.G. and M.S. Nagel, 1982, Plutonic events in the Piedmont of Virginia: Southeastern Geology, v. 23, p. 25-39.

Murphy, J.B. and J.D. Keppie, 2005, The Acadian orogeny in the northern Appalachians: International Geology Review, v. 47, p. 663-687.

Murphy, J.B. and R.D. Nance, 2008, The Pangea conundrum: Geology, v. 36, p. 703-706.

Murphy, J.B. and R.D. Nance, 2013, Speculations on the mechanisms for the formation and breakup of supercontinents: Geoscience Frontiers, v. 4, p. 185-194.

Murphy, J.B., C.R. van Staal and J.D. Keppie, 1999, Is the mid to late Paleozoic Acadian Orogeny a plume-modified Laramide-style orogeny?: Geology, v. 27, p. 653-656.

Murphy, J.B., G. Gutierrez-Alonzo, R.D. Nance, J. Fernandez-Suarez, J.D. Keppie, C. Quesada, R.A.. Strachan and J. Dostal, 2006, Origin of the Rheic Ocean: Rifting along a Neoproterozoic suture?: Geology, v. 34, p. 325-328.

Murphy, J.B., J.D. Keppie, R.D. Nance and J. Dostal, 2010, Comparative evolution of the Iapetus and Rheic Oceans: A North America perspective: Gondwana Research, v. 17, p. 482-499.

Myers, J.S., 1978, Formation of banded gneisses by deformation of igneous rocks: Precambrian Research, v. 6, p. 43-64.

Nance, R.D. and U. Linnemann, 2008, The Rheic Ocean: Origin, Evolution and Significance: Geological Society of America Today, v. 18, p. 4-12.

Nance, R.D., G. Gutiérrez-Alonso, J. D. Keppie, U. Linnemann, J.B. Murphy, C. Quesada, R.A. Strachan and N.H. Woodcock, 2012, A brief history of the Rheic Ocean: Geoscience Frontiers, v. 3, p. 125-135.

Nelson, K.D., 1992, Are crustal thickness variations in old mountain belts like the Appalachians a consequence of Lithospheric deformation?: Geology, v. 20, p. 498-502.

Nesbitt, B.E. and E.J. Essene, 1982, Metamorphic thermometry and barometry of a portion of the southern Blue Ridge Province: American Journal of Science, v. 282, p. 701-729.

Nesbitt, H.W. and G.M. Young, 1982, Early Proterozoic climates and plate motions inferred from major element chemistry of lutites: Nature, v. 299, p. 715-717.

Neuman, R.B., 1967, Bedrock geology of the Shin Pond and Stacyville Quadrangles, Penobscot County, Maine: USGS Professional paper 524-I, 37 p.

Norman, R.E. and D.F. Strong, 1975, The geology and geochemistry of ophiolitic rocks exposed at Ming's Bight, Newfoundland: Canadian Journal of Earth Sciences, v. 12, p. 777-797.

Obradovich, J., L.W. Snee and G.A. Izett, 1989, Is there more than one glassy impact layer in the late Eocene?: Geological Society of America Abstracts with Programs, v. 21, p. 134.

Ogilvie, P., 2010, Metamorphic Studies in the Vredefort Dome, South Africa. Unpublished PhD thesis, University of the Witwatersrand, Johannesburg, South Africa, 720 p.

Ohmoto, H. and D. Kerrick, 1977, Devolatization equilibria in graphitic systems: American Journal of Science, v. 277, p. 1013-1044.

Ordóñez-Calderón, J.C., A. Polat, B.J. Fryer, J.E. Gagnon, J.G. Raith and P.W.U. Appel, 2008, Evidence for HFSE and REE mobility during calc-silicate metasomatism, Mesoarchean (~3075 Ma) Ivisaartoq greenstone belt, southern West Greenland: Precambrian Research, v. 161, p. 317.

Owens, B. and R. Tucker, 2003, Geochronology of the Mesoproterozoic State Farm gneiss and associated Neoproterozoic granitoids, Goochland terrane, Virginia: Geological Society of America Bulletin, v. 115, p. 972-982.

Owens, B.E. and M.A. Hamilton, 2013, New U-Pb zircon ages from the Roanoke Rapids terrane, eastern Piedmont province, Virginia: Implications for assembling Carolinia: Geological Society of America Abstracts with Programs, v. 45, p. 810.

Owens, B.E. and S.D. Samson, 2004, Nd-isotopic constraints on the magmatic history of the Goochland terrane, easternmost Grenville crust in the southern Appalachians: Geological Society of America Memoir, v. 197, p. 601-608.

Owens, B.E., R. Buchwaldt and C.R. Shirvell, 2010a, Geochemical and geochronological evidence for Devonian magmatism revealed in the Maidens gneiss, Goochland terrane, Virginia: Geological Society of America Memoir, v. 206, p. 725-738.

Owens, B.E., M.A. Hamilton and S.P. Hess, 2010b, Three Creek pluton: A Neoproterozoic trondhjemitic to tonalitic intrusion in the Roanoke Rapids terrane, eastern Piedmont province, Virginia: Geological Society of America Abstracts with Programs, v. 42, p. 103.

Owens, B.E., M.A. Hamilton, C.R. Berquist, Jr. and P.L. Harner, 2011, Field, geochemical and geochronological evidence for two pulses of Neoproterozoic magmatism in the Roanoke Rapids terrane, eastern Piedmont province, Virginia: Geological Society of America Abstracts with Programs, v. 43, p. 271.

Oxburgh, E.R. and D.L. Turcotte, 1970, The thermal structure of island arcs: Geological Society of America Bulletin, v. 81, p. 1665-1668.

Oxburgh, E.R. and D.L. Turcotte, 1971, Origin of paired metamorphic belts and crustal dilation in island arc regions: Journal of Geophysical Research, v. 76, p. 1315-1327.

Pallister, J.S. and C.A. Hopson, 1981, Samail ophiolitic plutonic suite: Filed relations, phase variation, cryptic variation and layering and a model of a spreading ridge magma chamber: Journal of Geophysical Research, v. 86, p. 2593-2644.

Passchier, C.W. and R.A.J. Trouw, 2005, Microtectonics: Berlin, Springer, 366 p.

Paterson, S.R., Vernon, R.H. and Robisch, O.T., 1989, A review of criteria for the identification of magmatic and tectonic foliations in granitoids: Journal of Structural Geology, v. 11, p. 349-363.

Pattison D.R.M. and R.J. Tracy, 1991, Phase equilibria and thermobarometry of metapelites, *in* Kerrick, D.M., ed., Contact Metamorphism: Mineralogical Society of America Reviews in Mineralogy, v. 26, p. 105-206.

Pattison, D.R.M., 1992, Stability of andalusite and sillimanite and the Al_2SiO_5 triple point: Constraints from the Ballachulish aureole, Scotland: Journal of Geology, v. 100, p. 423-446.

Pattison, D.R.M., and R.J. Tracy, 1991, Phase equilibria and thermobarometry of metapelites, *in* Kerrick, D.M. (ed.), Contact Metamorphism: Mineralogical Society of America Reviews in Mineralogy, v. 26, p. 105–206.

Pavlides, L., 1980, Revised nomenclature and stratigraphic relationships of the Fredericksburg Complex and Quantico Formation of the Virginia Piedmont: USGS Professional Paper 1146, 29 p.

Pearce, J.A. and M.J. Norry, 1979, Petrogenetic implications of Ti, Zr, Y and Nb variations in volcanic rocks: Contributions to Mineralogy and Petrology, v. 69, p. 33-47.

Pearce, J.A., S.J. Lippard and S. Roberts, 1984, Characteristics and tectonic significance of supra-subduction zone ophiolites: Geological Society of London, Special Publications, v. 16, p. 77-94.

Pearce, J.A., T. Alabaster, A.W. Shelton and M.P. Searle, 1981, The Oman Ophiolite as a Cretaceous Arc-Basin Complex: Evidence and Implications: Philosophical Transactions of the Royal Society of London, Series A, Mathematical and Physical Sciences, v. 300, p. 299-317.

Pedersen, R.B., J. Malpas and T. Falloon, 1996, Chapter 1, Petrology and geochemistry of gabbroic and related rocks from Site 894, Hess Deep, in Mével, C., K.M. Gillis, J.F. Allan and P.S. Meyer (eds.), Proceedings of the Ocean Drilling Program, Scientific Results, v. 147, p. 3-19.

Perchuk, L.L., and I.V. Lavrenteva, 1983, Experimental investigation of exchange equilibria in the system garnet-cordierite-biotite, *in* Saxena, S.K. (ed.), Advances in Physical Geochemistry, Volume 3: New York, Springer-Verlag, p. 199–239.

Pettijohn, F.J., 1957, Sedimentary Rocks (2nd ed.): New York, Harper, 718 p.

Pichler, H. and C. Schmitt-Riegraf, 1997, Rock-forming Minerals in Thin Section: London, Chapman and Hall, 221 p.

Pidgeon, R.T. and M.R.W. Johnson, 1974, A comparison of zircon U-Pb and whole-rock Rb-Sr systems in three phases of the Carn Chuinneag Granite, Northern Scotland: Earth and Planetary Science Letter, v. 24, p. 105-112.

Pindell, J. and J.F. Dewey, 1982, Permo-Triassic reconstruction of western Pangea and the evolution of the Gulf of Mexico/Caribbean region: Tectonics, v. 1, p. 179-212.

Poag, C.W. and L.W. Ward, 1993, Allostratigraphy of the U.S. Middle Atlantic continental margin – Characteristics, distribution, and depositional history of principal unconformity-

bounded Upper Cretaceous and Cenozoic sedimentary units: USGS Professional Paper 1542, 81 p.

Poag, C.W. and M.P. Aubry, 1995, Upper Eocene impactites of the U.S. East Coast: Depositional origins, biostratigraphic framework, and correlations: Palaios, v. 10, p. 16-43.

Poag, C.W., 1996, Structural outer rim of Chesapeake Bay impact crater: Seismic and bore hole evidence: Meteoritics and Planetary Science, v. 31, p. 218-226.

Poag, C.W., 1997, The Chesapeake Bay bolide impact: a convulsive event in Atlantic coastal plain evolution: Sedimentary Geology, v. 108, p. 45-90.

Poag, C.W., 1997, The Chesapeake Bay bolide impact: A convulsive event in Atlantic Coastal Plain evolution: Sedimentary Geology, v. 108, p. 45-90.

Poag, C.W., 1999, Secondary craters from the Chesapeake Bay impact: 30th Annual Lunar and Planetary Science Conference, abstract no. 1047.

Poag, C.W., 2000, Nature and distribution of deposits derived from the Chesapeake Bay submarine impact: Geological Society of America Abstracts with Programs, v. 32, p. A-163.

Poag, C.W., C. Koeberl and W.U. Reimold, 2004, The Chesapeake Bay Impact Crater – Geology and Geophysics of a Late Eocene Submarine Impact Structure: New York, Springer-Verlag, 552 p. plus CD-ROM.

Poag, C.W., D.R. Hutchinson, S.M. Colman and M.W. Lee, 1999, Seismic expression of the Chesapeake Bay impact crater: Structural and morphologic refinements based on new seismic data: Geological Society of America Special Paper 339, p. 149-164.

Poag, C.W., D.S. Powars, L.J. Poppe and R.B. Mixon, 1994, Meteoroid mayhem in Ole Virginny: Source of the North American tektite strewn field: Geology, v. 22, p. 691-694.

Poag, C.W., D.S. Powars, L.J. Poppe, R.B. Mixon, L.E. Edwards, D.W. Folger and S. Bruce, 1992, Deep Sea Drilling Project Site 612 bolide event: New evidence of a late Eocene impact-wave deposit and a possible impact site, U.S. east coast: Geology, v. 20, p. 771-774.

Poag, C.W., D.S. Powars, R.B. Mixon, L.E. Edwards, D.W. Folger, L.J. Poppe and S. Bruce, 1991, An upper Eocene impact-wave(?) deposit beneath Chesapeake Bay: Geological Society of America Abstracts with Programs, v. 23, p. A-460.

Poag, C.W., J.B. Plescia and P.C. Molzer, 2002, Ancient impact structures on modern continental shelves: The Chesapeake Bay, Montagnais, and Toms Canyon craters, Atlantic margin of North America: Deep-Sea Research II, v. 49, p. 1081-1102.

Poland, F.B., 1976, Geology of the rocks along the James River between Sabot and Cedar Point, Virginia. Unpublished MSc thesis, Virginia Polytechnic Institute and State University, United States, 98 p.

Pollock, J.C., 2008, The Neoproterozoic-Early Palaeozoic Tectonic Evolution of the Peri-Gondwana Margin of the Appalachian Orogen: An Integrated Geochronological, Geochemical and Isotopic Study from North Carolina and Newfoundland. Unpublished PhD thesis, North Carolina State University, United States of America, 208 p.

Powars, D.S. and T.S. Bruce, 1999, The effects of the Chesapeake Bay impact crater on the geologic framework and the correlation of hydrogeologic units of the lower York-James Peninsula, Virginia: USGS Professional Paper 1612, 82 p.

Powars, D.S., 2000, The effects of the Chesapeake Bay impact crater on the geological framework and correlation of hydrogeologic units of the lower York-James peninsula, Virginia: USGS Professional Paper 1612, 53 p.

Powars, D.S., C.W. Poag and R.B. Mixon, 1993, The Chesapeake Bay “impact crater,” stratigraphic and seismic evidence: Geological Society of America Abstracts with Programs, v. 25, p. A-378.

Powars, D.S., R.B. Mixon and S. Bruce, 1992, Uppermost Mesozoic and Cenozoic geological cross-section, outer coastal plain of Virginia, *in* Gohn, G.S. (ed.), Proceedings of the 1988 USGS workshop on the geology and geohydrology of the Atlantic Coastal Plain: USGS Circular, v. 1059, p. 85-101.

Powars, D.S., R.B. Mixon, L.E. Edwards, C.W. Poag and S. Bruce, 1990, Cross section of Cretaceous and Cenozoic strata, Norfolk arch to Salisbury basin, outer coastal plain of Virginia: Geological Society of America Abstracts with Programs, v. 22, p. 57.

Powars, D.S., R.B. Mixon, L.E. Edwards, G.W. Andrews and L.W. Ward, 1987, Evidence for Paleocene and lower Eocene pinch-outs on the north flank of the Norfolk arch, Eastern Shore of Virginia: Geological Society of America Abstracts with Programs, v. 19, p. 124.

Powell, R. and T.J.B Holland, 1988, An internally consistent dataset with uncertainties and correlations: 3. Applications to geobarometry, worked examples and a computer program: Journal of Metamorphic Geology, v. 6, p. 173-204.

Powell, R. and T.J.B. Holland, 1994, Optimal geothermometry and geobarometry: American Mineralogist, v. 79, p. 120-133.

Powell, R. and T.J.B. Holland, 2008, On thermobarometry: Journal of Metamorphic Geology, v. 26, p. 155-179.

Powell, R., 1978, Equilibrium Thermodynamics in Petrology: An Introduction: London, Harper and Row, 284 p.

Powell, R., 1985, Geothermometry and geobarometry: a discussion: Journal of the Geological Society of London, v. 142, p. 29-38.

Powell, R., and T.J.B. Holland, 1990, Calculated mineral equilibria in the pelitic system, KFMASH K_2O-FeO-MgO-Al_2O_3-SiO_2-H_2O: The American Mineralogist, v. 75, p. 367–380.

Powell, R., M. Guiraud and R.W. White, 2005, Truth and beauty in metamorphic phase-equilibria: Conjugate variables and phase diagrams: Canadian Mineralogist, v. 43, p. 21-33.

Powell, R., T.J.B. Holland and B. Worley, 1998, Calculating phase diagrams involving solid solutions via non-linear equations, with examples using THERMOCALC: Journal of Metamorphic Geology, v. 16, p. 577-588.

Price, J.R. and M.A. Velbel, 2003, Chemical weathering indices applied to weathering profiles developed on heterogeneous felsic metamorphic parent rocks: Chemical Geology, v. 202, p. 397-416.

Pyle, J.M., F.S. Spear, R.L. Rudnick, W.F. McDonough, 2001, Monazite-xenotime-garnet equilibrium in metapelites and a new monazite-garnet thermometer: Journal of Petrology, v. 42, p. 2083-2107.

Rankin, D.W., 1988, The Jefferson terrane of the Blue Ridge tectonic province: An exotic accretionary prism: Geological Society of America Abstracts with Programs, v. 20, p. 310.

Rankin, D.W., 1994, Continental margin of the eastern United States; past and present, *in* Speed, R.C. (ed.), Phanerozoic Evolution of North American Continent-Ocean Transitions: Boulder, Colorado, Geological Society of America, Decade of North American Geology, Continent-Ocean Transect Volume, p. 129–218.

Rankin, D.W., A.A. Drake, Jr., L. Glover, III., R. Goldsmith, L.M. Hall, D.P. Murray, N.M. Ratcliff, J.F. Read, D.T. Secor, Jr. and R.F. Stanley, 1989, Pre-orogenic terranes, in Hatcher, R.D., Jr., W.A. Thomas and G.W. Viele (eds.), The Appalachian-Ouachita Orogen in the United States (Geology of North America, Vol. F-2): Geological Society of America, Boulder, Colorado, p. 7-100.

Renne, P. R., D.B. Karner and K.R. Ludwig, 1998, Absolute ages aren't exactly: Science, v 282, p. 1840-1841.

Robitaille, K.R., 2004, Geology and terrane relationships of the Tar River area, Franklin and Granville Counties, North Carolina. Unpublished MSc thesis, University of North Carolina, Wilmington, USA, 157 p.

Roddick, J.C., 1978, The application of isochron diagrams in ^{40}Ar-^{39}Ar dating: A discussion: Earth and Planetary Science Letters, v. 48, p. 185-208.

Rodgers, J., 1970, The tectonics of the Appalachians: New York, Wiley InterScience Publishers, 271 p.

Rollinson, H., 1993, Using Geochemical Data: Evaluation, Presentation, Interpretation: London, Longman Group UK Limited, 352 p.

Roser, B.P. and R.J. Korsch, 1986, Determination of tectonic setting of sandstone–mudstone suites using SiO_2 content and K_2O/Na_2O ratio: Journal of Geology, v. 94, p. 635-650.

Roser, B.P. and R.J. Korsch, 1988, Provenance signatures of sandstone–mudstone suites determined using discriminant function analysis of major-element data: Chemical Geology, v. 67, p. 119-139.

Russell, G.S., A.L. Odom and W. Russell, 1987, Uranium-lead and rubidium-strontium isotopic evidence for the age and origin of granitic rocks in the northern Alabama Piedmont, *in* Drummond, M.S. and N.L. Green (eds.), Granites of Alabama: Tuscaloosa, Geological Society of Alabama, p. 239-249.

Russell, G.S., C.W. Russell, J.A. Speer and L. Glover, III, 1981, Rb-Sr evidence of latest Precambrian to Cambrian and Alleghanian plutonism along the eastern margin of the sub-coastal plain Appalachians, North Carolina and Virginia: Geological Society of America Abstracts with Programs, v.13, p. 543.

Russell, G.S., J.A. Speer and C.W. Russell, 1985, The Portsmouth granite, a 263 Ma post-metamorphic biotite granite beneath the Atlantic coastal plain, Suffolk, Virginia: Southeastern Geology, v. 26, p. 81-93.

Rutter, E.H. and K.H. Brodie, 1995, Mechanistic interactions between deformation and metamorphism: Geological Journal, v. 30, p. 227-240.

Sabet, M.A., 1973, Gravity and magnetic investigation, Eastern Shore area, Virginia: Geological Society of America Bulletin, v. 84, p. 2119-2126.

Samson, S.D., D.G. Coler and J.A. Speer, 1995, Geochemical and Nd-Sr-Pb isotopic composition of Alleghanian granites of the southern Appalachians: Origin, tectonic setting, and source characterization: Earth and Planetary Science Letters, v. 134, p. 359–376.

Sandiford, M. and R. Powell, 1986, Deep crustal metamorphism during continental extension: modern and ancient examples: Earth and Planetary Science Letters, v. 79, p. 151-158.

Sandiford, M., M. Hand and S. McLaren, 1998, High geothermal gradient metamorphism during thermal subsidence: Earth and Planetary Science Letters, v. 163, p. 149-165.

Scherer, A., 2007, $^{40}Ar/^{39}Ar$ dating and errors: Oberseminar 09.01.2007 Institut für Geologie, TU Bergakademie Freiberg, 11 p.

Schmitt, R.T., A. Wittmann and D. Stöffler, 2004, Geochemistry of drill core samples from Yaxcopoil-1, Chicxulub impact crater, Mexico: Meteoritics and Planetary Sciences, v. 39, p. 979-1001.

Schmitt, R.T., K. Bartosova, W.U. Reimold, D. Mader, A. Wittmann, C. Koeberl and R.L. Gibson, 2009, Chapter 22, Geochemistry of impactites and crystalline basement-derived lithologies from the ICDP-USGS Eyreville A and B drill cores, Chesapeake Bay impact structure, Virginia/USA, *in* Gohn, G.S., C. Koeberl, K.G. Miller and W.U. Reimold (eds.), The ICDP-USGS Deep Drilling Project in the Chesapeake Bay Impact Structure: Results from the Eyreville Core Holes: Geological Society of America Special Paper 458, p. 481-541.

Scholz, C.H., 1988, The brittle – plastic transition and the depth of seismic faulting: Geologische Rundschau, v.77, p. 319-328.

Searle, M.P. and R.K. Stevens, 1984, Obduction processes in ancient, modern and future ophiolites, *in* Gass, I.G., S.J. Lippard and A.W. Shelton (eds.), Ophiolites and Oceanic Lithosphere: Journal of the Geological Society of London Special Publication, v. 13, p. 303-319.

Secor, D.T., Jr., A.W. Snoke, K.W. Bramlett, O.P. Costello and O.P. Kimbrell, 1986, Character of the Alleghanian orogeny in the southern Appalachians: Part I. Alleghanian deformation in the eastern Piedmont: Geological Society of America Bulletin, v. 97, p. 1319-1328.

Self-Trail, J.M., L.E Edwards and R.J. Litwin, 2009, Chapter 28, Paleontological interpretations of crater processes and infilling of synimpact sediments from the Chesapeake Bay impact structure, *in* Gohn, G.S., C. Koeberl, K.G. Miller and W.U. Reimold (eds.), The ICDP-USGS Deep Drilling Project in the Chesapeake Bay Impact Structure: Results from the Eyreville Core Holes: Geological Society of America Special Paper 458, p. 617-632.

Shand, S.J., 1927, The Eruptive Rocks: New York, Van Nostrand, 360 p.

Shearer, C.K. and P. Robinson, 1988, Petrogenesis of metaluminous and peraluminous tonalites within the Merrimack Synclinorium: Hardwick Tonalite, Central Massachusetts: American Journal of Science, v. 288-A, p. 148-195.

Shimamoto, T., 1989, The origin of *S-C* mylonites and a new fault zone model: Journal of Structural Geology, v.11, p. 51-64.

Shirvell, C.R., R.J. Tracy and B.E. Owens, 2004, Palaeozoic (not Mesoproterozoic) high-grade metamorphism in the Goochland terrane, Virginia: New results from electron microprobe dating of monazite: Geological Society of America Abstracts with Programs, v. 36, p. 80.

Sibson, R.H., 1977, Fault rocks and fault mechanisms: Journal of the Geological Society of London, v. 133, p. 191-213.

Siivola, J. and R. Schmid, 2007, List of mineral abbreviations, in Fettes, D. and J. Desmons (eds.), Metamorphic Rocks: A Glossary of Terms, Recommendations of the International Union of Geological Sciences Subcommission on the Systematics of Metamorphic Rocks: Cape Town, Cambridge University Press, p. 93-110

Simpson, G.D.H., 2010, Formation of accretionary prisms influenced by sediment subduction and supplied by sediments from adjacent continents: Geology, v. 38, p. 131-134.

Sinton, J.M., 1980, Petrology and evolution of the Red Mountain ophiolite, New Zealand: American Journal of Science, v. 280-A, p. 296-328.

Skála, R., F. Langenhorst and A. Deutsch, 2009, Chapter 19, Geochemical characteristics of basement target rocks, suevitic glasses from the Eyreville B drill core, Chesapeake Bay impact structure, and three bediasites, *in* Gohn, G.S., C. Koeberl, K.G. Miller and W.U. Reimold (eds.), The ICDP-USGS Deep Drilling Project in the Chesapeake Bay Impact Structure: Results from the Eyreville Core Holes: Geological Society of America Special Paper 458, p. 435-445.

Smith, P.E., D. York, R.M. Easton, Ö. Özdemir and P.W. Layer, 1994, A laser $^{40}Ar/^{39}Ar$ study of minerals across the Grenville Front: investigations of reproducible excess Ar patterns: Canadian Journal of Earth Sciences, v. 31, no. 5, p. 808-817.

Smulikowski, W., J. Desmons, D.J. Fettes, B. Harte, F.P. Sassi and R. Schmidt, 2007, A systematic nomenclature for metamorphic rocks: 2. Types, grade and facies of metamorphism: Recommendations by the IUGS Subcommission on the Systematics of Metamorphic Rocks, web version 01.02.2007.

Snoke, A. and R. Frost, 1990, Exhumation of high pressure pelitic schist, Lake Murray spillway, South Carolina: evidence for crustal extension during Alleghanian strike-slip faulting: American Journal of Science, v. 290, p. 853-881.

Southworth, S, 2002, Digital Geologic Map and Database of the Frederick 30' x 60' Quadrangle, Maryland, Virginia, and West Virginia: U.S. Geological Survey Open-File Report 02-437, 79 p.

Southworth, S., A.A. Drake, Jr., D.K. Brezinski, R.P. Wintsch, M.J. Kunk, J.N. Aleinikoff, C.W. Naeser and N.D. Naeser, 2006, Central Appalachian Piedmont and Blue Ridge tectonic transect, Potomac River corridor, *in* Pazzaglia, F.J., ed., Excursions in Geology and History: Field Trips in the Middle Atlantic States: Geological Society of America Field Guide 8, p. 135–167.

Spear, F.S., 1989, Petrologic determination of metamorphic pressure-temperature-time paths, *in* Spear, F.S. and S.M. Peacock (eds.), Metamorphic pressure-temperature-time paths, Short Course in Geology (American Geophysical Union), v. 7, p. 1-55.

Spear, F.S., 1993, Metamorphic Phase Equilibria and Pressure-Temperature-Time Paths: Mineralogical Society of America, 799 p.

Spear, F.S., and J.T. Cheney, 1989, A petrogenetic grid for pelitic schists in the system SiO_2-Al_2O_3-FeO-MgO-K_2O-H_2O: Contributions to Mineralogy and Petrology, v. 101, p. 149–164.

Spears, D.B., B.E. Owens and C.M. Bailey, 2004, Trip 7: The Goochland-Chopawamsic Terrane Boundary, Central Virginia Piedmont, *in* Southworth, S. and W. C. Burton (eds.), Geology of the National Capital Region – Field Trip Guidebook: U.S. Geological Survey Circular 1264, p. 223-245.

Speer, J.A., H.Y McSween, Jr. and A.E. Gates, 1994, Generation, Segregation, Ascent and Emplacement of Alleghanian Plutons in the Southern Appalachians: Journal of Geology, v. 102, p. 249-267.

Stacey, J.S. and J.D. Kramers, 1975, Approximation of terrestrial lead isotope evolution by a 2-stage model: Earth and Planetary Science Letters, v. 26, p. 207-221.

Stampfli, G.M. and G.D. Borel, 2002, A plate tectonic model for the Paleozoic and Mesozoic constrained by dynamic plate boundaries and restored synthetic oceanic isochrones: Earth and Planetary Science Letters, v. 196, p. 17-33.

Stanley, R.S. and N.M. Ratcliff, 1985, Tectonic synthesis of the Taconian orogeny in western New England: Geological Society of America Bulletin, v. 96, p. 1227-1250.

Steiger, R.H. and E. Jäger, 1977, Subcommission on geochronology: Convention on the use of decay constants in geo- and cosmochronology: Earth and Planetary Science Letters, v. 36, p. 359-362.

Stendal, H., S.F. Toteu, R. Frei, J. Penaye, U.O. Njel, J. Bassahak, J. Nni, B. Kankeu, V. Ngako and J.V. Hell, 2006, Derivation of detrital rutile in the Yaoundé region from the Neoproterozoic Pan-African belt in southern Cameroon (Central Africa): Journal of African Earth Sciences, v. 44, p. 443-458.

Stephens, W.E., 2001, Polycrystalline amphibole aggregates (clots) in granites as potential I-type restite: An ion microprobe study of rare-earth distributions: Australian Journal of Earth Sciences: An International Geoscience Journal of the Geological Society of Australia, v. 48, p. 591-601.

Stevens, R.K., 1970, Cambro-Ordovician flysch sedimentation and tectonics in west Newfoundland and their possible bearing on a Proto-Atlantic ocean, *in* Lajoie, J. (ed.), Flysch Sedimentology in North America: Geological association of Canada Special Paper 7, p. 165-177.

Stoddard, E., A. Wylie and D. Blake, 1989, Metamorphosed chromitite in the Falls Lake mélange, North Carolina Piedmont, *in* Mittwede, S. and E. Stoddard (eds.), Ultramafic Rocks of the Appalachian Piedmont: Geological Society of America Special Paper 231, p. 33-44.

Stoddard, E.F., S.S. Farrar, J.W. Horton, Jr., R. Butler and R. Druhan, 1991, The eastern Piedmont in North Carolina, *in* Horton, J.W., Jr. and V. Zullo (eds.), The Geology of the Carolinas: The University of Tennessee Press, Knoxville, TN, p. 79-92.

Stoddard, E.F., V.V. Cavaroc and R.D. McDaniel, 1978, Status of geologic research in the Raleigh belt, *in* Snoke, A.W. (ed.), Geological investigations of the eastern Piedmont,

southern Appalachians (Fieldtrip Guidebook) : Columbia, South Carolina Geological Survey, p. 8-12.

Stöffler, D., 1971, Progressive metamorphism and classification of shocked and brecciated crystalline rocks at impact craters: Journal of Geophysical Research, v. 76, p. 5541-5551.

Taylor, P.T., I. Zietz and L.S. Dennis, 1968, Geologic implications of aeromagnetic data for the eastern continental margin of the United States: Geophysics, v. 33, p. 755-780.

Taylor, S.R. and S.M. McLennan, 1985, The Continental Crust: Its Composition and Evolution: Oxford, Blackwell, 312 p.

Taylor, S.R., 1989, Geophysical framework of the Appalachians and adjacent Grenville province, *in* Pakiser, L.C. and W.D. Mooney (eds.), Geophysical framework of the continental United States: Geological Society of America Memoir, v. 172, p. 317-348.

Teifke, R. H., 1973, Stratigraphic units of the Lower Cretaceous through Miocene series, in Geologic Studies, Coastal Plain of Virginia: Virginia Division of Mineral Resources Bulletin, v. 83, p. 1-78.

Thomas, W.A., 2006, Tectonic inheritance at a continental margin: GSA Today, v. 16, p. 4-11.

Thomas, W.A., T.M. Chowns, D.L. Daniels, T.L. Neathery, L. Glover, III. and R.J. Gleason, 1989, The subsurface Appalachians beneath the Atlantic and Gulf Coastal Plains, *in* Hatcher, R.D., Jr., W.A. Thomas and G.W. Viele (eds.), Geology of North America: The Appalachian-Ouachita Orogen in the United States: (Geology of North America, Vol. F-2): Geological Society of America, Boulder, Colorado, p. 445-458.

Thompson, A.B., 1976, Mineral reactions in pelitic rocks: II. Calculation of some *P*-*T*-X(Fe-Mg) phase relations: American Journal of Science, v. 276, p. 425–454.

Thompson, A.B., and R.J. Tracy, 1979, Model systems for anatexis of pelitic rocks: II. Facies series melting and reactions in the system CaO-K_2O-$NaAlO_2$-Al_2O_3-SiO_2-H_2O: Contributions to Mineralogy and Petrology, v. 70, p. 429-438.

Thompson, J.B., 1957, The graphical analysis of the mineral assemblages in pelitic schists: American Mineralogist, v. 42, p. 842-858.

Thompson, J.B., Jr., W.A. Bothner, P. Robinson, Y.W., Isachsen and K.D. Klitgord, 1993, A guide to continent ocean transect E-1 Adirondacks to Georges Bank, *in* Thompson, J.B., Jr., W.A. Bothner, P. Robinson and K.D. Klitgord (eds.), E-1 Adirondacks to Georges Bank: Geological Society of America Centennial Continent/Ocean Transect no. 17, 55 p.

Tilley, C.E., 1924, Contact metamorphism in the Comrie area of the Perthshire Highlands: Quarterly journal of the Geological Society of London, v. 80, p. 22-70.

Tomkins, H.S., R. Powell and D.J. Ellis, 2007, The pressure dependence of the zirconium-in-rutile thermometer: Journal of Metamorphic Geology, v. 25, p. 703-173.

Townsend, G.N., R.L., Gibson, J.W. Horton, Jr., W.U. Reimold, R.T Schmitt and K. Bartosova, 2009, Chapter 13, Petrographic and geochemical comparisons between the lower crystalline basement-derived section and the granite megablock and amphibolite megablock of the Eyreville B core, Chesapeake Bay impact structure, USA, *in* Gohn, G.S., C. Koeberl, K.G. Miller and W.U. Reimold (eds.), The ICDP-USGS Deep Drilling Project in the Chesapeake Bay Impact Structure: Results from the Eyreville Core Holes: Geological Society of America Special Paper 458, p. 255-275.

Tull, J. F., C.I. Barineau, P.A. Mueller and J.L. Wooden, 2007, Volcanic arc emplacement onto the southernmost Appalachian Laurentian shelf: Characteristics and constraints: Geological Society of America Bulletin, v. 119, p. 261-274.

Turner, G., P. Burnard, J.L. Ford, J.D. Gilmour, I.C. Lyon and F.M. Stuart, 1993, Tracing fluid sources and interactions: Philosophical Transactions of the Royal Society of London, Series A-Mathematical Physical and Engineering Sciences, v. 344, p. 127-140.

Valley, M.J., D.R. Peacor, J.R. Bowman, E.J. Essene and M.J. Allard, 1985, Crystal chemistry of a Mg-vesuvianite and implications of phase equilibria in the system CaO-MgO-Al_2O_3-SiO_2-H_2O-CO_2: Journal of Metamorphic Geology, v. 3, p. 137-153.

Valverde-Vaquero, P., C.R. van Staal, V. McNicoll and G.R. Dunning, 2005, Mid-Late Ordovician magmatism and metamorphism along the Gander margin in central Newfoundland: Journal of the Geological Society of London, v. 162, p. 1-16.

van der Pluijm, B.A. and S. Marshak, 2004, Earth Structure: An introduction to structural geology and tectonics (2nd ed.): New York, Norton and Company, 656 p.

van Staal, C. J.B. Whalen, P. Valverde-Vaquero, A. Zagorevski and N. Rogers, 2009, Pre-Carboniferous, episodic accretion-related, orogenesis along the Laurentian margin of the northern Appalachians: Geological Society of London, Special Publication 327, p. 271-316.

van Staal, C., J. Dewey, C. Mac Niocaill and W. McKerrow, 1998, The Cambrian-Silurian tectonic evolution of the northern Appalachians and British Caledonides: history of a complex, west and southwest Pacific-type segment of the Iapetus, *in* Blundell, D. and A. Scott (eds.), Lyell: The Past is the Key to the Present: Geological Society of London, Special Publication 143, p. 199-242.

van Staal, C.R., 1994, The Brunswick subduction complex in the Canadian Appalachians: record of the Late Ordovician to Late Silurian collision between Laurentia and the Gander margin of Avalon: Tectonics, v. 13, p. 946-962.

Vance, D., M. Ayres, S.P. Kelley and N.B.W. Harris, 1998, The thermal response of a metamorphic belt to extension: constraints from laser Ar data on metamorphic micas: Earth and Planetary Science Letters, v. 162, p. 153-164.

Vanko, D.A., 2009, A petrographic and fluid inclusion assessment of hydrothermal alteration of some impactites and crystalline rocks in the Chesapeake Bay impact structure, ICDP-USGS Eyreville B core: Geological Society of America, Special Paper 458, p. 543-557.

Veevers, J.J., 1994, Pangea: Evolution of a supercontinent and its consequence for Earth's paleoclimate and sedimentary environments: Geological Society of America Special Paper 288, p. 13-24.

Waldron, J.W.F., C.E. White, S.M. Barr, A. Simonetti and L.M. Heaman, 2009, Provenance of the Meguma terrane, Nova Scotia: rifted margin of early Paleozoic Gondwana: Canadian Journal of Earth Sciences, v. 46, p. 1-8.

Walker, K.R., G.A. Joplin, J.F. Lovering and R. Green, 1960, Metamorphic and metasomatic convergence of basic igneous rocks and lime-magnesia sediments of the Pre-Cambrian

of north-western Queensland: Journal of the Geological Society of Australia, v. 6, p. 149-177.

Wall, V.J., J. D. Clemens and D. B. Clarke, 1987, Models for Granitoid Evolution and Source Compositions: Journal of Geology, v. 95, p. 731-749.

Ward, L.W. and G.L. Strickland, 1985, Outline of Tertiary stratigraphy and depositional history of the U.S. Atlantic Coastal Plain, *in* Poag, C.W. (ed.), Geologic Evolution of the United States Atlantic Margin: New York, Van Nostrand Reinhold, p. 87-123.

Ward, L.W. and K. Krafft, 1984, Stratigraphy and palaeontology of the outcropping Tertiary bed in the Pamunkey River region, central Virginia Coastal Plain: Guidebook for Atlantic Coastal Plain Geological Association 1984 Field Trip: Atlantic Coastal Plain Geological Association, 280 p.

Watson, E.B., D.A. Wark and J.B. Thomas, 2006, Crystallisation thermometers for zircon and rutile: Contributions to Mineralogy and Petrology, v. 151, p. 413-433.

Weill, D.F. and M.J. Drake, 1973, Europium Anomaly in Plagioclase Feldspar: Experimental Results and Semiquantitative Model: Science, v. 180, p. 1059-1060.

West, T., 1998, Structural analysis of the Carolina-Inner Piedmont terrane boundary: implications for the age and kinematics of the central Piedmont suture, a terrane boundary that records Paleozoic Laurentia-Gondwana interactions: Tectonics, v. 17, p. 379-394.

White, A.J.R., and B.W. Chappell, 1983, Granitoid types and their distribution in the Lachlan fold belt, southeastern Australia, *in* Roddick, J.A. (ed.), Circum-Pacific Plutonic Terranes: Geological Society of America Memoir 159, p. 21-34.

White, R.W. and R. Powell, 2002, Melt loss and the preservation of granulite facies mineral assemblages: Journal of Metamorphic Geology, v. 20, p. 621-632.

White, R.W., N.E. Pomroy and R. Powell, 2005, An in-situ metatexite–diatexite transition in upper amphibolite facies rocks from Broken Hill, Australia: Journal of Metamorphic Geology, v. 23, p. 579-602.

White, R.W., R. Powell and J.A. Baldwin, 2008, Calculated phase equilibria involving chemical potentials to investigate the textural evolution of metamorphic rocks: Journal of Metamorphic Geology, v. 26, p. 181-198.

White, R.W., R. Powell and J.A. Halpin, 2004, Spatially-focussed melt formation in aluminous metapelites from Broken Hill, Australia: Journal of Metamorphic Geology, v. 22, p. 825-845.

White, R.W., R. Powell and T.J.B. Holland, 2007, Progress relating to calculation of partial melting equilibria for metapelites: Journal of Metamorphic Geology, v. 25, p. 511-527.

Whitney, D.L. and B.W. Evans, 2010, Abbreviations for names of rock-forming minerals: American Mineralogist, v. 95, p. 185-187.

Wickham, S.M. and E.R. Oxburgh, 1987, Low-pressure regional metamorphims in the Pyrenees and its implications for the thermal evolution of rifted continental crust: Philosophical Transactions of the Royal Society of London A, v. 321, p. 219-242.

Wickham, S.M. and E.R. Oxburgh, 1985, Continental rifts as a setting for regional metamorphism: Nature, v. 318, p. 330-333.

Williams, H. and R.K. Stevens, 1974, The ancient continental margin of eastern North America, *in* Drake, C.L. (ed.), The geology of continental margins: New York, Springer-Verlag, p. 781-796.

Williams, H., 1979: Appalachian orogen in Canada: Canadian Journal of Earth Sciences, v. 16, p. 792-807.

Williams, M.L., 1994, Sigmoidal inclusion trails, punctuated fabric development, and interactions between metamorphism and deformation: Journal of Metamorphic Geology, v. 12, p. 1-21.

Williamson, B.J., H. Downes, M.F. Thirlwall and A. Beard, 1997, Geochemical constraints on restite composition and unmixing in the Velay anatectic granite, French Massif Central: Lithos, v. 40, p. 295-319.

Wilson, J., 2001, U/Pb zircon ages of plutons from the central Appalachians and GIS-based assessment of plutons with comments on their regional tectonic significance.

Unpublished MSc thesis, Virginia Polytechnic Institute and State University, Blacksburg, USA, 121 p.

Winter, J.D., 2001, An Introduction to Igneous and Metamrophic Petrology: New Jersey, Prentice Hall, 697 p.

Withjack, M.O., R.W. Schlische, M.L. Malinconico and P.E. Olsen, 2012, Rift-basin development: lessons from the Triassic-Jurassic Newark Basin of eastern North America, *in* Mohriak, W.U., A. Danforth, P.J. Post, D.E. Brown, G.C. Tari, M. Nemcŏk and S.T. Sinha (eds.), Conjugate Divergent Margins: Journal of the Geological Society of London Special Publication 369.

Woollard, G.P., W.E. Bonini and R.P Meyer, 1957, A seismic refraction study of the Atlantic Coastal Plain and continental shelf between Virginia and Florida: Wisconsin University Department of Geology Report, Contract N7 ONR-28512, p. 1-128.

Wortman, G., S.D. Samson and J. P. Hibbard, 2000, Precise U-Pb zircon constraints on the earliest magmatic history of the Carolina terrane: Journal of Geology, v. 108, p. 321-338.

Wright, J. and V. Seiders, 1980, Age of zircon from volcanic rocks of the central North Carolina Piedmont and tectonic implications for the Carolina volcanic slate belt: Geological Society of America Bulletin, v. 91, p. 287-294.

Yang, P. and T. Rivers, 2000, Trace element partitioning between coexisting biotite and muscovite from metamorphic rocks, Western Labrador: Structural, compositional and thermal controls: Geochimica et Cosmochimica Acta, v. 64, p. 1451-1472.

Young, G.M., 1995, Are Neoproterozoic glacial deposits preserved on the margins of Laurentia related to the fragmentation of two supercontinents?: Geology, v. 23, p. 153-156.

Zack, T, A. Kronz, S.F. Foley and T. Rivers, 2002, Trace element abundances in rutiles from eclogites and associated garnet mica schists: Chemical Geology, v. 184, p. 97–122.

Zack, T., D.F. Stockli, G.L. Luvozotto, M.G. Barth, E. Belousova, M.R. Wolfe and R.W. Hinton, 2011, In situ U-Pb rutile dating by LA-ICP-MS: ^{208}Pb correction and prospects for geological applications: Contributions to Mineralogy and Petrology, v. 162, p. 515-530.

Zack, T., H. von Eynatten and A. Kronz, 2004b, Rutile geochemistry and its potential use in quantitative provenance studies: Sedimentary Geology, v. 171, p. 37-58.

Zack, T., R. Moraes and A. Kronz, 2004a, Temperature dependence of Zr in rutile: empirical calibration of a rutile thermometer: Contributions to Mineralogy and Petrology, v. 148, p. 417-488.

Zagorevski, A., C.R. van Staal, V.C. McNicoll and N. Rogers, 2007, Upper Cambrian to Upper Ordovician peri-Gondwanan island arc activity in the Victoria Lake Supergroup, Central Newfoundland: Tectonic development of the Ganderian margin: American Journal of Science, v. 307, p. 339-370.

Zeh, A. and Holness, M., 2003, The effect of reaction overstep on garnet microtextures in metapelitic rocks of the Ilesha Schist Belt, SW Nigeria: Journal of Petrology, v. 44, p. 967-994.

Zeitler, P.K. and J.D. FitzGerald, 1986, Saddle-shaped $^{40}Ar/^{39}Ar$ age spectra from young, microstructurally complex potassium feldspars: Geochimica et Cosmochimica Acta, v. 50, p. 1185-1199.

Zen, E-an, D.B. Stewart and L.R. Fyffe, 1986, Paleozoic tectonostratigraphic terranes and their boundaries in the mainland Northern Appalachians: Geological Society of America Abstracts with Programs, v. 18, p. 800.